Preprints

FOURTH CONFERENCE ON SATELLITE METEOROLOGY AND OCEANOGRAPHY

May 16–19, 1989

San Diego, Calif.

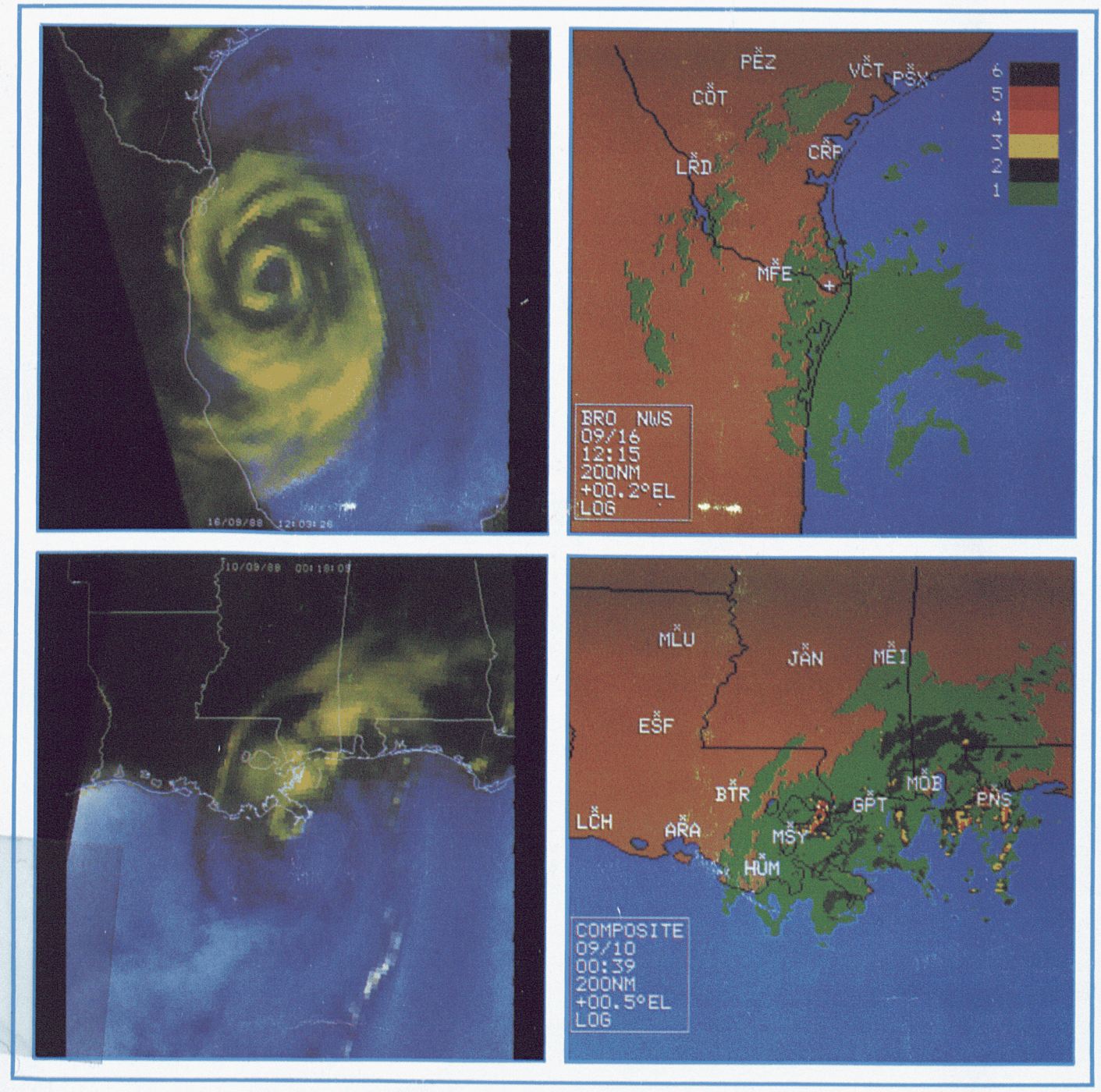

AMERICAN METEOROLOGICAL SOCIETY

AMERICAN METEOROLOGICAL SOCIETY

45 BEACON STREET, BOSTON, MASSACHUSETTS 02108

PERIODICALS—1989°

	Nonmember Prices
JOURNAL OF THE ATMOSPHERIC SCIENCES (ISSN 0022-4928) Volume 46, 1989. Semi-monthly Original research papers related to the atmospheres of the earth and other planets with emphasis on the quantitative and deductive aspects of the physics and dynamics of atmospheric processes and phenomena.	$295.00* $30.00†
JOURNAL OF APPLIED METEOROLOGY (ISSN 0894-8763) Volume 28, 1989. Monthly Original papers and critical surveys concerned with the applications of the atmospheric sciences to operational and practical goals. Its editorial scope encompasses the full range of applications of meteorology to safety, health, industry, the economy, and general well-being of the human community.	$150.00* $20.00†
JOURNAL OF PHYSICAL OCEANOGRAPHY (ISSN 0022-3670) Volume 19, 1989. Monthly Original research and survey papers devoted to the communication of knowledge concerning the physics and chemistry of the oceans and of the processes coupling the sea to the atmosphere. Papers will deal with the theoretical and observational aspects of topics such as: ocean circulation, surface waves, internal waves, inertial oscillations, oceanic turbulence, interpretive regional studies, and oceanic tides and other long-wave phenomena.	$170.00* $20.00†
MONTHLY WEATHER REVIEW (ISSN 0027-0644) Volume 117, 1989. Monthly Original research and survey papers concerned with weather analysis and forecasting (non-operational); observed and modeled circulations including techniques development and verification studies, and seasonal-annual weather summaries.	$195.00* $20.00†
JOURNAL OF ATMOSPHERIC AND OCEANIC TECHNOLOGY (ISSN 0739-0572) Volume 6, 1989. Bimonthly Original research and survey papers related to instrument-system descriptions, exploratory measurement techniques, calibration methods, and performance analyses for the mainstream of atmospheric and oceanic technology, including the development of data-acquisition hardware, real-time and post-analysis software, and signal-processing techniques.	$125.00* $15.00†
WEATHER AND FORECASTING (ISSN 0882-8156) Volume 4, 1989. Quarterly Original research and survey papers immediately related to the operational forecasting or weather events significant to operational forecast problems including such topics as operational-forecasting techniques, applications of new analysis methods, forecasting-verification studies, and case studies with direct application to forecasting.	$100.00* $15.00†
JOURNAL OF CLIMATE (ISSN 0894-8755) Volume 2, 1989. Monthly Articles concerned with climate data and analysis, long-term atmospheric variability (seasonal, interannual), climate change and prediction on seasonal and longer time scales, and the impacts of climate change on society.	$150.00* $20.00†
BULLETIN OF THE AMERICAN METEOROLOGICAL SOCIETY (ISSN 0003-0007) Volume 70, 1989. Monthly The official organ of the Society, devoted to editorials, topical reports to members, articles, professional and membership news, conference announcements, programs, and summaries, book reviews, and Society activities.	$60.00* $20.00†
METEOROLOGICAL & GEOASTROPHYSICAL ABSTRACTS (ISSN 0026-1130) Volume 40, 1989. Monthly Abstracts of current world literature in meteorology, climatology, aeronomy, planetary atmospheres, solar-terrestrial relations, hydrology, oceanography, glaciology, cosmic rays, and radioastronomy. The abstracts of books, articles, and reprints are arranged by subject categories with extensive cross-referencing. Monthly author, subject, and geographical indexes. Information on the computerized MGA data base, 1970–1985, may be obtained by writing to the Society.	$600.00* $20.00†
METEOROLOGICAL & GEOASTROPHYSICAL ABSTRACTS (ANNUAL INDEXES) Vol. 38, Jan.–Dec. 1987. Annually Cumulative Author, Subject, and Geographic Indexes.	$200.00* $3.00†

°The availability and prices of back issues of AMS periodicals will be furnished on request.

*Subscriptions are accepted on calendar year basis only. †Surface postage and handling for foreign subscriptions.

TL
798
.M4
C61
1989

FOURTH CONFERENCE ON SATELLITE METEOROLOGY AND OCEANOGRAPHY

May 16–19, 1989 San Diego, Calif.

Sponsored by
American Meteorological Society

Cover: Comparison of Special Sensor Microwave/Imager (SSM/I) data with nearly simultaneous radar data. The 86 GHz horizontal polarization is displayed through the red and green guns, while the 37 GHz vertical polarization is displayed through the blue gun. Radar data, with colors corresponding to VIP (intensity) levels, was obtained through the Alden C2000R Weather Display System.

Upper left:	SSM/I data of Hurricane Gilbert at 1203 GMT 16 September 1988
Upper right:	NWS radar data from Brownsville, Tex. at 1215 GMT 16 September 1988
Lower left:	SSM/I data of Hurricane Florence at 0018 GMT 10 September 1988
Lower right:	NWS radar data composited from Slidell, La. and Pensacola, Fla. at 0039 GMT 10 September 1988

Imagery courtesy of Andrew J. Negri and Edward B. Rodgers, NASA/Goddard Space Flight Center, Greenbelt, Md.

Copyright © 1989, *American Meteorological Society*. This copyright notice applies only to the overall collection of papers; authors retain their individual rights and should be contacted directly for permission to use their material separately. Contact AMS for permission pertaining to the overall collection. The manuscripts reproduced herein are unrefereed papers presented at the **Fourth Conference on Satellite Meteorology and Oceanography**; their appearance in this collection does not constitute formal publication.

LIBRARY
AUG 3 1 1989
N.O.A.A.
U S Dept of Commerce

AMERICAN METEOROLOGICAL SOCIETY
45 Beacon Street, Boston, Massachusetts, USA 02108

National Oceanic and Atmospheric Administration
TIROS Satellites and Satellite Meteorology

ERRATA NOTICE

One or more conditions of the original document may affect the quality of the image, such as:

Discolored pages
Faded or light ink
Binding intrudes into the text

This has been a co-operative project between the NOAA Central Library and the Climate Database Modernization Program, National Climate Data Center (NCDC). To view the original document contact the NOAA Central Library in Silver Spring, MD at (301) 713-2607 x124 or Library.Reference@noaa.gov.

HOV Services
Imaging Contractor
12200 Kiln Court
Beltsville, MD 20704-1387
January 26, 2009

Blank page retained for pagination

FOREWORD

As mentioned in the Call for Papers, the focus of this conference is on the use of satellites for observing the tropical atmosphere and oceans. Since the Third Conference in Anaheim, much more research has been conducted on the use of new sensors or combinations of sensors to learn more about the tropics as well as other regions of the world. Many of the 66 presentations and 26 posters reflect the use of satellite data to determine rainfall, winds, temperatures, and other important weather or sea surface information. Other papers describe preparations for the Tropical Rainfall Measurement Mission, future systems, or experiments.

Thanks to Dr. Gary Barnes and his program committee, four joint sessions will be held with the 18th Conference on Hurricanes and Tropical Meteorology. These sessions will highlight the respective roles of satellites and aircraft in tropical cyclone forecasting as well as specific applications of satellite observations in the tropics.

It is very encouraging to see the scope of research efforts in studying the tropical oceans and atmosphere, and to see the important contribution satellites have made in this area over the past several decades. The continuing synergism of scientific and operational talents in each of these areas should pay great dividends through more accurate and timely forecasting of major tropical systems in the future.

Floyd F. Hauth
Program Chairperson

PROGRAM COMMITTEE **Floyd F. Hauth, Chairperson**

Dan McMorrow
Anthony Mostek
Andrew Negri
Hans Rosendal
Larry Stowe
Paul Twitchell
Thomas H. Vonder Haar
Greg Wilson

AMS 1989 COMMITTEE ON SATELLITE METEOROLOGY AND OCEANOGRAPHY

Philip A. Durkee, Chairperson

Dennis Chesters
Kenneth R. Hardy*
Floyd F. Hauth
Robert Introne, Jr.
Eric Mollo-Christensen
Anthony Mostek
Larry Stowe
Gerard Szejwach
Paul Twitchell
Greg Wilson*

*1988 Committee members

TABLE OF CONTENTS

		Page
FOREWORD		i
AUTHOR INDEX		xi

JOINT SESSION 1: THE ROLE OF SATELLITE OBSERVATIONS IN THE TROPICS (Joint with Hurricane and Tropical Meteorology Conference)

Chairperson: William K. M. Lau, NASA/GSFC, Greenbelt, Md.

J1.1	OVERVIEW OF THE TROPICAL RAINFALL MEASURING MISSION (TRMM). Joanne Simpson, NASA/GSFC, Greenbelt, Md.	J1
J1.2	ON THE USE OF SATELLITE DERIVED HEATING RATES TO INITIALIZE TROPICAL FORECASTS. W. A. Heckley, G. Kelly and M. Tiedtke, ECMRWF, Reading, U. K.	J3
J1.3	INTERANNUAL VARIABILITY OF THE EARTH'S CLIMATE DURING THE LAST DECADE AS OBSERVED BY THE NIMBUS-7 SPACECRAFT. P. E. Ardanuy and D. V. Hoyt, Res. & Data Systems Corp.; H. L. Kyle and D. Han, NASA/GSFC, Greenbelt, Md.	J5
J1.4	PASSIVE MICROWAVE RETRIEVALS OF RAINFALL AND RAIN SYSTEM STRUCTURE. Christian Kummerow, NASA/GSFC, Greenbelt; and I. Hakkarinen, General Sciences Corp. (GSC), Laurel, Md.	J8
J1.5	CLOUD MODEL-BASED SIMULATIONS OF SATELLITE MICROWAVE DATA AND THEIR APPLICATION TO AN SSM/I RAIN ALGORITHM. Robert F. Adler, A. J. Negri, and W.-K. Tao, NASA/GSFC, Greenbelt; and N. Prasad, GSC, Laurel, Md.	J12

JOINT SESSION 2: THE ROLE OF SATELLITE OBSERVATIONS IN TROPICAL CYCLONE RESEARCH AND FORECASTING (Joint with Hurricane & Tropical Meteorology)

Chairperson: William Gray, Colorado State Univ., Fort Collins, Colo.

J2.1	HURRICANE TYPHOON MOTION FROM VERY HIGH RESOLUTION MODEL FORECASTS. T. N. Krishnamurti, H. S. Bedi, and D. Oosterhof, Florida State Univ., Tallahassee, Fla.	J16
J2.2	ON GENERALIZING THE THEORY OF TROPICAL CYCLONES TO INCLUDE ENVIRONMENTAL INFLUENCES. R. T. Merrill, CIMSS, Univ. of Wisconsin, Madison, Wis.	J19
J2.3	THE UTILITY OF SPECIAL SENSOR MICROWAVE/IMAGER DATA IN THE OPERATIONAL ANALYSIS OF TROPICAL CYCLONES. Edward N. Rappaport, NOAA/NHC, Coral Gables; and P. G. Black, NOAA/HRD, Miami, Fla.	J21
J2.4	IMPROVING OBJECTIVE SATELLITE ESTIMATES OF TROPICAL CYCLONE INTENSITY. Raymond M. Zehr, NOAA/NESDIS and CIRA, Colorado State Univ., Fort Collins, Colo.	J25

SESSION 3: TROPICAL RAINFALL MEASURING MISSION (TRMM) I

Chairperson: Andrew Negri, NASA/GSFC, Greenbelt, Md.

3.1	NONLINEAR ESTIMATION OF MONSOON RAINFALL FROM RADAR AND RAINGAGE DATA. W. F. Krajewski and D.-S. Lin, Univ. of Iowa, Iowa City, Iowa	1
3.2	TROPICAL OCEANIC RAINFALL ESTIMATION FROM MICROWAVE RADIOMETRY. Kyung-Sup Shin, Korea Advanced Inst. of Science & Technology, Seoul, Korea; P. E. Riba and G. R. North, Texas A&M Univ., College Station, Tex.	5

Note: Joint session papers appear edged in gray at the back of this volume.

Page

3.3 EMPIRICAL STUDIES OF THE MICROWAVE RADIOMETRIC RESPONSE TO RAINFALL IN THE TROPICS AND MIDLATITUDES. G. W. Petty and K. B. Katsaros, Univ. of Washington, Seattle, Wash. 9

3.4 AIRBORNE RADAR AND RADIOMETRIC MEASUREMENTS FOR TRMM ALGORITHM DEVELOPMENT. Robert Meneghini and T. T. Wilheit, NASA/GSFC, Greenbelt, Md.; K. Nakamura and T. Kozu, Comm. Res. Lab., Tokyo, Japan *

3.5 ON THE CALIBRATION OF CLIMATOLOGICAL SATELLITE RAINFALL MEASUREMENTS USING A TRANSPORTABLE GROUND-BASED POLARIZATION RADAR. A. R. Jameson and L. S. Chiu, Applied Res. Corp., Landover, Md. 13

SESSION 4: TRMM II

Chairperson: Andrew Negri, NASA/GSFC, Greenbelt, Md.

4.1 CONCEPTUAL DESIGNS OF RAIN RADARS IN THE TROPICAL RAINFALL MEASURING MISSION AND ON THE JAPANESE EXPERIMENT MODULE AT THE MANNED SPACE STATION PROGRAM. K. Okamoto, J. Awaka, T. Ihara, K. Nakamura, and T. Kozu, Comm. Res. Lab., Tokyo; and T. Manabe, ATR Optical & Radio Comm. Res. Labs., Osaka, Japan 18

4.2 DETECTION OF THE DIURNAL CYCLE IN RAINFALL FROM THE TRMM SATELLITE. T. L. Bell, NASA/GSFC, Greenbelt, Md. 22

4.3 COMPARING RAIN ESTIMATION DESIGNS. Gerald R. North and S. Nakamoto, Texas A&M Univ., College Station, Tex. 24

4.4 COMPARISON OF RAINFALL PROFILES RETRIEVED FROM DUAL-FREQUENCY RADAR AND FROM COMBINED RADAR AND PASSIVE MICROWAVE RADIOMETRIC MEASUREMENTS. J. Weinman, Appl. Res. Corp., Landover; R. Meneghini, NASA/GSFC, Greenbelt, Md.; and K. Nakamura, Comm. Res. Lab., Tokyo, Japan 27

4.5 AIRCRAFT MICROWAVE OBSERVATIONS AND SIMULATIONS OF DEEP CONVECTION AT 18-183 GHZ. H.-Y. M. Yeh, Caelum Res. Corp., Silver Spring; N. Prasad, R. A. Mack, and I. M. Hakkarinen, GSC, Laurel; and R. F. Adler, NASA/GSFC, Greenbelt, Md. 31

JOINT SESSION 5: THE ROLE OF AIRCRAFT RECONNAISSANCE IN TROPICAL CYCLONE FORECASTING
(Joint with Hurricane & Tropical Meteorology)

Chairperson: Thomas H. Vonder Haar, Colorado State Univ., Fort Collins, Colo.

J5.1 TECHNIQUES DEVELOPMENT PROGRAM AT THE JOINT TYPHOON WARNING CENTER. Joel D. Martin, Joint Typhoon Warning Ctr., Nimitz Hill, Guam J29

J5.2 FORECASTING TYPHOONS WITHOUT AIRCRAFT RECONNAISSANCE AT THE JOINT TYPHOON WARNING CENTER. Daniel McMorrow, Joint Typhoon Warning Ctr., Nimitz Hill, Guam J32

J5.3 TROPICAL CYCLONE CENTER-FIXING USING DMSP SSM/I DATA. C. S. Velden, W. S. Olson, and B. A. Roth, Univ. of Wisconsin, Madison, Wis. J36

J5.4 IMPACTS OF AIRCRAFT RECONNAISSANCE "FIXES" ON TROPICAL CYCLONE TRACK PREDICTIONS. R. C. Sheets, NOAA/NHC, Coral Gables, Fla. *

J5.5 THE AMS STUDY OF IMPACT OF AIRCRAFT RECONNAISSANCE ON TROPICAL CYCLONE ANALYSIS-FORECASTING. W. Gray, Colorado State Univ., Fort Collins, Colo.; C. Guard, Scott AFB, Ill.; C. Neumann, NOAA, Miami, Fla.; and T. Tsui, NEPRF, Monterey, Calif. J40

Note: Joint session papers appear edged in gray at the back of this volume.

*Manuscript not available; if received in time, it will appear prior to joint papers at back of book.

Page

SESSION 6: WEATHER ANALYSIS AND FORECASTING I

Chairperson: Daniel J. McMorrow, Joint Typhoon Warning Ctr., Nimitz Hill, Guam

6.1 SSM/I OBSERVATION OF TROPICAL CYCLONE GALE FORCE VICINITY WINDS. Charles R. Holliday and Kenneth R. Waters, AFGWC, Offutt AFB, Neb. 267

6.2 STRUCTURE OF TROPICAL CYCLONES AND SURROUNDING REGIONS AS DETERMINED FROM OLS AND SSM/I IMAGERY ANALYSIS. Morton Glass and Gerald W. Felde, AFGL, Hanscom AFB, Mass. 35

6.3 A MICROWAVE, VISIBLE, AND INFRARED EVALUATION OF TROPICAL STORM FLOYD. Ralph Ferraro, SM Systems and Res. Corp., Landover, Md.; J. C. Alishouse, R. Scofield, and A. Timchalk, NOAA/NESDIS, Washington, D.C.; and W. Jiankang, SMC, Beijing, PRC 39

6.4 IMAGES OF PRECIPITATION PATTERNS ASSOCIATED WITH TROPICAL CYCLONES USING THE SSM/I 85 GHZ CHANNEL. Thomas F. Lee and Allan Caughey, NEPRF, Monterey, Calif. 45

6.5 TROPICAL SYNOPTIC COMPOSITES IN VAS, OLR, AND TOVS RADIANCE DATA. James P. McGuirk, Texas A&M Univ., College Station, Tex. 49

SESSION 7: WEATHER ANALYSIS AND FORECASTING II

Chairperson: Daniel J. McMorrow, Joint Typhoon Warning Ctr., Guam

7.1 MULTISPECTRAL IMAGE ANALYSIS OF HURRICANE GILBERT. Thomas J. Kleespies, AFGL, Hanscom AFB, Mass. 55

7.2 TROPICAL SYNOPTIC SCALE MOISTURE FIELDS OBSERVED FROM THE NIMBUS-7 SMMR. J. D. Fink and J. P. McGuirk, Texas A&M Univ., College Station, Tex. 59

7.3 SAHELIAN AFRICA CONVECTIVE SYSTEMS DESCRIBED FROM METEOSAT ISCCP B2 DATA. Michel Desbois, Brigitte Gnamien, and Theoneste Kayiranga, CNRS/LMD, Palaiseau Cedex, France 61

7.4 QUANTITATIVE SATELLITE ANALYSES OF FOUR TROPICAL CYCLONES DURING AMEX/EMEX. Debra Lubich, CIRA, Colorado State Univ.; and R. M. Zehr, NOAA/NESDIS, Fort Collins, Colo. 63

7.5 THE DIURNAL VARIATION OF CONVECTIVE CLOUDINESS ALONG THE INTERTROPICAL CONVERGENCE ZONE (ITCZ). J. F. W. Purdom, NOAA/NESDIS; F. Weng and T. H. Vonder Haar, CIRA, Colorado State Univ., Fort Collins, Colo. 67

SESSION 9: RAINFALL STUDIES I

Chairperson: Hans Rosendal, NOAA/NWS/WFO, Honolulu, Hawaii

9.1 ESTIMATES OF GATE CONVECTIVE AND STRATIFORM RAINFALL DERIVED FROM RADAR AND SATELLITE DATA. Andrew J. Negri and R. F. Adler, NASA/GSFC, Greenbelt, Md. 71

9.2 HOW UNIVERSAL ARE THE GATE RAINFALL STATISTICS? Kyung-Sup Shin, Korea Advanced Inst. of Science and Technology, Seoul, Korea; P. E. Riba, Y.-S. Ahn, and G. R. North, Texas A&M Univ., College Station, Tex. 75

9.3 TROPICAL OCEANIC RAINFALL: ESTIMATION FROM SMMR AND SSM/I. C. Prabhakara, NASA/GSFC, Greenbelt, Md.; Giuseppe Dalu, CNR, Inst. di Fisica dell'Atmos., Rome, Italy; and B. E. Vollmer, Applied Res. Corp., Landover, Md. 79

9.4 SSM/I RADIANCES CORRELATED WITH 15 MINUTE RAIN GAUGE DATA. Roy W. Spencer and R. E. Hood, NASA/MSFC, Huntsville, Ala. 83

*Manuscript not available; if received in time, it will appear prior to joint papers at back of book.

Page

9.5 MULTICHANNEL MICROWAVE-BASED PRECIPITATION RETRIEVAL USING AN EXPERT SYSTEM APPROACH WITH SSM/I MEASUREMENTS. Kyung-Whan Oh, E. A. Smith, and A. Kandel, Florida State Univ., Tallahassee, Fla. *

SESSION 10: RAINFALL STUDIES II

Chairperson: Hans Rosendal, NOAA/NWS/WFO, Honolulu, Hawaii

10.1 SSM/I LIQUID AND FROZEN PRECIPITATION PATTERNS IN HURRICANE GILBERT. R. W. Spencer and R. E. Hood, NASA/MSFC, Huntsville, Ala. 86

10.2 A RAINGAGE, RADAR, AND SATELLITE SIMULATION STUDY OF THE ESTIMATION OF CONVECTIVE RAINFALL BY AREA-TIME INTEGRALS. David A. Short, NASA/GSFC, Greenbelt; D. B. Wolff, Applied Res. Corp., Landover, Md.; D. Rosenfeld, Hebrew Univ., Jerusalem, Israel; and D. Atlas, Bethesda, Md. 90

10.3 IR SATELLITE ESTIMATIONS OF RAIN IN SAHELIAN AFRICA: STUDY OF DIFFERENT SPATIAL AND TEMPORAL RESOLUTIONS. Isabelle Jobard and Michel Desbois, CNRS/LMD, Palaiseau Cedex, France 94

10.4 THE COLD CORE LOW ANALYSIS DURING TAMEX. Koung-Ying Liu and Tian-Yow Shyu, Chinese AF, Weather Wing, Taiwan, ROC 96

10.5 ESTIMATING TROPICAL RAINFALL FROM MULTIPLE SOURCES OF INFORMATION. Phillip A. Arkin and J. E. Janowiak, NOAA/NWS/NMC, Washington, D.C. 100

POSTER SESSION 8A: TROPICAL METEOROLOGY AND SATELLITE OBSERVATIONS IN THE TROPICS (Parallel with Hurricane & Tropical Meteorology JP8B)

Chairperson: Anthony Mostek, NOAA/NWS/NMC, Washington, D.C.

JP8A.1 COMPARISON OF SSM/I RAINRATES AND SURFACE WINDS WITH THE CORRESPONDING CONVENTIONAL DATA IN THE NORTHWEST PACIFIC TYPHOONS. G. V. Rao, E. Ciardi, and D. Rhudy, St. Louis Univ., St. Louis, Mo. 104

JP8A.2 TROPICAL STORM UPPER LEVEL FLOW PATTERNS DETERMINED FROM MESOSCALE CLOUD MOTION VECTORS. Gary Ellrod, NOAA/NESDIS, Washington, D.C. 108

JP8A.3 MOISTURE RETRIEVALS FROM THE GOES VAS. Christopher M. Hayden, NOAA/NESDIS, Univ. of Wisconsin; and A. J. Schreiner, Univ. of Wisconsin, Madison, Wis. 112

JP8A.4 UPPER TROPOSPHERIC DRYNESS IN WALKER/HADLEY CIRCULATION -- A NEW SATELLITE PERSPECTIVE. Arthur C. Neuendorffer, NOAA/NESDIS, Washington, D.C. *

JP8A.5 GROUND TRUTH OBSERVATIONS FOR TRMM. Otto W. Thiele, NASA/GSFC, Greenbelt, Md. 118

JP8A.6 THE GROUND TRUTH ANALYSIS OF RAIN GAUGE DATA FOR THE TRMM PROJECT. Karen J. Kowalewsky, Applied Res. Corp., Landover; and O. Thiele, NASA/GSFC, Greenbelt, Md. 121

JP8A.7 INTERDIURNAL VARIABILITY OF DEEP CONVECTION OVER TROPICAL AFRICA DURING THE SUMMER OF 1983. Adel F. Hanna and B. W. Crissman, Res. Triangle Inst., Research Triangle Park, N.C. 124

JP8A.8 RAINFALL ESTIMATION USING T.I.R. METEOSAT IMAGERY OVER THE WESTERN SAHEL (1986-87). M. Carn, J. P. Lahuec, D. Dagorne, and B. Guillot, CMS, Lannion, France 126

JP8A.9 MONTHLY PRECIPITATION ESTIMATES FROM THE SSM/I ON DMSP. Thomas T. Wilheit, A. T. C. Chang, and A. Sharma, NASA/GSFC, Greenbelt, Md. *

JP8A.10 ANALYSIS OF THE OPTICAL PROPERTIES OF HAWAIIAN CONVECTIVE WARM BAND CLOUDS. A. Rigaud, C. Pontikis, and S. Bouadjadj, Meteorologie Nat'l., Magny les Hameaux, France 130

*Manuscript not available; if received in time, it will appear prior to joint papers at back of book.

Page

JP8A.11 TROPICAL APPLICATION OF TECHNIQUES TO MEASURE SURFACE EMITTANCE AND CLOUD LIQUID WATER CONTENT OVER LAND. Andrew S. Jones and T. H. Vonder Haar, CIRA, Colorado State Univ., Fort Collins, Colo. 133

JP8A.12 THE INFLUENCE OF ATMOSPHERIC STRATIFICATION ON SCATTEROMETER DATA. Jean-Francois Louis and R. N. Hoffman, AER, Inc., Cambridge, Mass. 137

JP8A.13 A COMPARISON OF VAS AND ODW DATA AROUND A SUBTROPICAL COLD LOW. James L. Franklin and J. Kaplan, NOAA/HRD, Miami, Fla.; C. S. Velden, Univ. of Wisconsin; and C. M. Hayden, NOAA/NESDIS, Madison, Wis. 141

JP8A.14 SATELLITE OBSERVATIONS OF HURRICANE GILBERT. Eugene Kratz, R. Ferraro, M. E. Maiden, and D. Carr, S M Systems and Res. Corp., Landover; J. Alishouse and H. F. Drahos, Jr., NOAA/NESDIS, Suitland, Md. 145

JP8A.15 WATER VAPOR RETRIEVAL FROM NOAA SATELLITES. Y. Tahani, A. Chedin, and N. A. Scott, CNRS/LMD, Palaiseau Cedex, France 147

JP8A.16 MOISTURE STRUCTURE OF TROPICAL CLOUD SYSTEMS AS INFERRED FROM SSM/I. Franklin R. Robertson, NASA/MSFC, Huntsville, Ala. 151

JP8A.17 MOISTURE CONVERGENCE DURING A CONVECTIVE FLARE-UP IN THE TROPICS. Ellen Steiner, CIRES, Univ. of Colorado, Boulder, Colo. 154

JP8A.18 SIMULATED APPEARANCE OF AN EVOLVING SUPERCELL HAIL STORM AT SSM/I MICROWAVE FREQUENCIES. Eric Smith and H. J. Cooper, Florida State Univ., Tallahassee, Fla.; A. Mugnai, Inst. di Fisica dell'Atmos., Frascati, Italy; and G. J. Tripoli, Univ. of Wisconsin, Madison, Wis. 158

JP8A.19 TIME EVOLUTION OF CLOUD FIELDS FROM ISCCP OBSERVATIONS. G. G. Campbell and T. H. Vonder Haar, CIRA, Colorado State Univ., Fort Collins, Colo. 161

JP8A.20 SHORT-TIME-SCALE FLUCTUATION OF TROPICAL CONVECTION ABOVE AFRICA AND THE ATLANTIC OCEAN. J. Ph. Duvel, CNRS/LMD, Palaiseau Cedex, France 165

JP8A.21 IMPACT OF VAS RETRIEVALS ON A SIMULATION OF RETURN FLOW IN THE GULF OF MEXICO. Robert M. Aune, NOAA/NESDIS, Madison, Wis. 169

JP8A.22 ESTIMATION OF FREQUENCY-WAVE NUMBER SPECTRUM IN GATE RAIN DATA. Shoichiro Nakamoto, J. B. Valdes, and G. R. North, Texas A&M Univ., College Station, Tex. 172

JP8A.23 A MODEL FOR ATMOSPHERIC BRIGHTNESS TEMPERATURES OBSERVED BY THE SPECIAL SENSOR MICROWAVE IMAGER (SSM/I). Grant W. Petty and K. B. Katsaros, Univ. of Washington, Seattle, Wash. 175

JP8A.24 CHARACTERISTICS OF THE GOES I-M IMAGER AND SOUNDER. Edward Koenig, ITT Aerospace/Optical Div., Fort Wayne, Ind. 179

JP8A.25 CHARACTERISTICS OF AVHRR/3 AND HIRS/3 FOR NOAA-K, L, M. Larry Owens, D. Ceckowski, and A. J. Ames, ITT Aerospace/Optical Div., Fort Wayne, Ind. 183

JP8A.26 DETERMINATIONS OF CLOUD LIQUID WATER IN THE TROPICS FROM THE SSM/I. John Alishouse, NOAA/NESDIS, Washington, D.C.; C. Swift, Univ. of Massachusetts, Amherst, Mass.; C. Ruf, JPL, Pasadena, Calif.; and S. Snyder and J. Vongsathorn, S M Systems and Res. Corp., Landover, Md. 187

JOINT SESSION 11: TROPICAL CYCLONES: SATELLITE APPLICATIONS (Joint with Hurricane and Tropical Meteorology)

Chairperson: Robert Merrill, CIMSS, Univ. of Wisconsin, Madison, Wis.

J11.1 **REMOTE SENSING OF OCEAN SURFACE WINDS WITH THE SSM/I. Mark Goodberlet, Univ. of Massachusetts, Amherst, Mass. J42

**Max Eaton Prize Candidate

Note: Joint session papers appear edged in gray at the back of this volume.

*Manuscript not available; if received in time, it will appear prior to joint papers at back of book.

Page

J11.2 UPPER-TROPOSPHERIC INFLUENCES ON WESTERN PACIFIC TROPICAL CYCLONE INTENSITY CHANGE AS INFERRED FROM SATELLITE OZONE OBSERVATIONS. E. B. Rodgers, NASA/GSFC, Greenbelt; and J. Stout, GSC, Laurel, Md. J46

J11.3 **FORECASTING 30 KNOT WIND RADIUS IN WEST PACIFIC TROPICAL CYCLONES USING GEOSTATIONARY INFRARED SATELLITE DATA. D. N. Shoemaker, Colorado State Univ., Fort Collins, Colo. J48

J11.4 A USE OF WATER VAPOR IMAGERY IN FORECASTING HURRICANE MOTION. James Lushine, WSFO, Miami, Fla. J50

J11.5 PRECIPITABLE WATER AND LIQUID WATER IN TROPICAL CYCLONES AS ESTIMATED FROM SSM/I. H.-J. Huang, Univ. of N. Carolina, Asheville, N.C.; and F. R. Robertson, NASA/MSFC, Huntsville, Ala. J52

SESSION 12: CORRELATION STUDIES WITH CLOUD/RADIATION DATA

Chairperson: Larry Stowe, NOAA/NESDIS, Camp Springs, Md.

12.1 SPACE-TIME VARIABILITY OF TROPICAL CONVECTION. Harry H. Hendon, M. Salby, K. Tanaka, K. Woodberry, and P. Callaghan, Univ. of Colorado, Boulder, Colo. 190

12.2 TEMPORAL CHARACTERISTICS OF TROPICAL CONVECTION. Lorraine A. Remer and B. C. Weare, Univ. of California, Davis, Calif. 194

12.3 THE CLOUD AND SURFACE CONTRIBUTIONS TO THE NET RADIATION BALANCE DURING THE 1982-83 EL NINO. Byung-Ju Sohn and E. A. Smith, Florida State Univ., Tallahassee, Fla. 198

12.4 ANNUAL AND SEMIANNUAL CYCLES OF THE OUTGOING LONGWAVE RADIATION AND DIVERGENT CIRCULATION OVER THE TROPICS. Tsing-Chang Chen and R.-Y. Tzeng, Iowa State Univ., Ames, Iowa *

12.5 COMPARISONS BETWEEN METEOSAT WATER VAPOUR RADIANCE AND ECMWF ANALYSED FIELDS FOR JULY 1985. Laurence Picon, CNRS/LMD, Palaiseau Cedex, France 202

12.6 AN ATTEMPT TO REMOTELY SENSE FROM SPACE THE SURFACE HEAT BUDGET OVER THE INDIAN OCEAN DURING THE 1979 MONSOON. Catherine Gautier and R. Frouin, Scripps Inst., La Jolla, Calif. *

12.7 ANALYSIS OF SURFACE SOLAR IRRADIANCE VARIABILITY DURING THE 1982-83 EL NINO. Beth Chertock and R. Frouin, Scripps Inst., La Jolla, Calif. *

SESSION 13: MULTISPECTRAL STUDIES

Chairperson: Paul Twitchell, Office of Naval Res., Arlington, Va.

13.1 ATMOSPHERIC TEMPERATURE RETRIEVAL FROM SATELLITE MICROWAVE MEASUREMENTS. Martha E. Maiden, M. V. Piepgrass, D. R. Donahue, and M. Sylva, S M Systems and Res. Corp., Landover; and H. F. Drahos, Jr., NOAA/NESDIS, Suitland, Md. 204

13.2 HIGH RESOLUTION DEPICTION OF SST AND SSC FROM MAMS DATA. Christopher C. Moeller, L. E. Gumley, and K. I. Strabala, CIMMS, Univ. of Wisconsin; and W. P. Menzel, NOAA/NESDIS, Madison, Wis. 208

13.3 ESTIMATION OF SURFACE SKIN TEMPERATURES OVER THE TIBETAN PLATEAU FROM AVHRR SPLIT WINDOW MEASUREMENTS. Lei Shi and E. A. Smith, Florida State Univ., Tallahassee, Fla. 213

13.4 CLOUD TYPES AND SST OVER THE TROPICAL PACIFIC OCEAN DERIVED FROM NOAA-9 SPLIT WINDOW DATA. Toshiro Inoue, MRI, Ibaraki, Japan 217

**Max Eaton Prize Candidate

Note: Joint session papers appear at the back of this volume.

*Manuscript not available; if received in time, it will appear prior to joint papers at back of book.

Page

13.5 DETERMINATIONS OF TOTAL PRECIPITABLE WATER IN THE TROPICS FROM THE SSM/I. John Alishouse, NOAA/NESDIS, Washington, D.C.; S. Snyder and J. Vongsathorn, S M Systems and Res. Corp., Landover, Md. 221

SESSION 14: TEMPERATURE AND WATER VAPOR RETRIEVAL

Chairperson: Paul Twitchell, Office of Naval Res., Arlington, Va.

14.1 THE CLASSIFICATION OF ATMOSPHERIC PARAMETERS OVER THE OCEANS USING PRINCIPAL COMPONENT ANALYSIS OF SSM/I MEASUREMENTS. Russell A. Ambroziak and J. D'Aguanno, NOAA/NESDIS, Washington, D.C.; and R. R. Ferraro, S M Systems and Res. Corp., Landover, Md. 224

14.2 CLUSTERING OF SATELLITE/SOUNDING RADIANCES TO MAXIMIZE MESOSCALE METEOROLOGICAL DETAIL. Donald W. Hillger and J. F. W. Purdom, NOAA/NESDIS and CIRA, Colorado State Univ., Fort Collins, Colo. 228

14.3 TOVS AND THERMODYNAMIC CONTROLS ON TROPICAL DEEP CONVECTION. Siri Jodha S. Khalsa, CIRES, Univ. of Colorado, Boulder, Colo. 232

14.4 MULTISPECTRAL RETRIEVAL OF RAINFALL RATES USING THE SPECIAL SENSOR MICROWAVE/IMAGER (SSM/I). William S. Olson, F. J. LaFontaine, W. L. Smith, and B. A. Roth, CIMSS, Univ. of Wisconsin, Madison, Wis.; and C. D. Kummerow, NASA/GSFC, Greenbelt, Md. 263

14.5 UNIQUE SIGNATURES OF SYNOPTIC FEATURES IN TIROS N SATELLITE DATA. G. A. White, III and J. P. McGuirk, Texas A&M Univ., College Station, Tex. 236

SESSION 15: WIND STUDIES

Chairperson: Greg Wilson, NASA/MSFC, Huntsville, Ala.

15.1 GLOBAL DATA ASSIMILATION OF SSM/I WIND SPEED MEASUREMENTS. James S. Goerss, NEPRF, Monterey, Calif. 238

15.2 ASSIMILATION OF AUTOMATED WINDS DERIVED FROM GOES MULTISPECTRAL IMAGERY. Steven D. Swadley and J. S. Goerss, NEPRF, Monterey, Calif. 242

15.3 ADVANCES IN THE AUTOMATED PRODUCTION OF WIND ESTIMATES FROM GEOSTATIONARY SATELLITE IMAGERY. Robert T. Merrill, CIMSS, Univ. of Wisconsin, Madison, Wis. 246

SESSION 16: FUTURE SYSTEMS

Chairperson: Greg Wilson, NASA/MSFC, Huntsville, Ala.

16.1 NASA'S EARTH OBSERVING SYSTEM. James C. Dodge, NASA, Washington, D.C. *

16.2 SATELLITE OBSERVATIONS OF TROPICAL CYCLONES DURING THE 1990'S. William E. Shenk and E. B. Rodgers, NASA/GSFC, Greenbelt, Md.; and S. Chang, Naval Res. Lab., Washington, D. C. 250

16.3 AUTOMATIC ANALYSIS OF STEREOSCOPIC GOES/GOES AND GOES/NOAA IMAGE PAIRS FOR MEASUREMENT OF HURRICANE CLOUD TOP HEIGHT AND STRUCTURE. A. F. Hasler and J. Strong, NASA/GSFC, Greenbelt; H. Pierce and R. H. Woodward, GSC, Laurel, Md. 255

16.4 FOURIER TRANSFORM SPECTROSCOPY FOR IMPROVED ATMOSPHERIC SOUNDING FROM SPACE. Steven H. Silverman and D. D. LaPorte, Santa Barbara Res. Ctr., Goleta, Calif.; and H. E. Revercomb, CIMSS, Univ. of Wisconsin, Madison, Wis. 259

*Manuscript not available; if received in time, it will appear prior to joint papers at back of book.

AUTHOR INDEX

		Paper	Page
A	Adler, Robert F.	4.5	31
		9.1	71
		J1.5	J12
	Ahn, Yoo-Shin	9.2	75
	Alishouse, John	6.3	39
		JP8A.14	145
		13.5	221
		JP8A.26	187
	Ames, A. J.	JP8A.25	183
	Ambroziak, Russell A.	14.1	224
	Ardanuy, P. E.	J1.3	J5
	Arkin, Philip A.	10.5	100
	Atlas, D.	10.2	90
	Aune, Robert M.	JP8A.21	169
	Awaka, J.	4.1	18
B	Bedi, H. S.	J2.1	J16
	Bell, Thomas L.	4.2	22
	Black, Peter G.	J2.3	J21
	Bouadjadj, S.	JP8A.10	130
C	Callaghan, Pat	12.1	190
	Campbell, G. G.	JP8A.19	161
	Carn, M.	JP8A.8	126
	Carr, Deborah	JP8A.14	145
	Caughey, Allan	6.4	45
	Ceckowski, D.	JP8A.25	183
	Chang, Alfred T. C.	JP8A.9	*
	Chang, S.	16.2	250
	Chedin, A.	JP8A.15	147
	Chen, Tsing-Chang	12.4	*
	Chertock, Beth	12.7	*
	Chiu, L. S.	3.5	13
	Ciardi, E.	JP8A.1	104
	Cooper, Harry J.	JP8A.18	158
	Crissman, Bobby W.	JP8A.7	124
D	D'Aguanno, Jane	14.1	224
	Dagorne, D.	JP8A.8	126
	Dalu, G.	9.3	79
	Desbois, Michel	7.3	61
		10.3	94
		12.5	202
	Dodge, James C.	16.1	*
	Donahue, D. R.	13.1	204
	Drahos, H. F., Jr.	13.1	204
		JP8A.14	145
	Duvel, J. Ph.	JP8A.20	165
E	Ellrod, Gary	JP8A.2	108
F	Ferraro, Ralph	6.3	39
		JP8A.14	145
		14.1	224
	Felde, Gerald W.	6.2	35
	Fink, J. D.	7.2	59
	Franklin, James L.	JP8A.13	141
	Frouin, Robert	12.6	*
		12.7	*
G	Gautier, Catherine	12.6	*
	Glass, Morton	6.2	35
	Gnamien, Brigitte	7.3	61
	Goerss, James S.	15.1	238
		15.2	242
	Goodberlet, M.	J11.1	J42
	Gray, W.	J5.5	J40
G	Guard, C.	J5.5	J40
	Guillot, B.	JP8A.8	126
	Gumley, Liam E.	13.2	208
H	Hakkarinen, I.	4.5	31
		J1.4	J8
	Han, D.	J1.3	J5
	Hanna, Adel F.	JP8A.7	124
	Hasler, A. F.	16.3	255
	Hayden, C. M.	JP8A.3	112
		JP8A.13	141
	Heckley, W. A.	J1.2	J3
	Hendon, Harry	12.1	190
	Hilger, Donald W.	14.2	228
	Hoffman, R. N.	JP8A.12	137
	Holliday, Charles R.	6.1	267
	Hood, Robbie E.	9.4	83
		10.1	86
	Hoyt, D. V.	J1.3	J5
	Huang, H.-J.	J11.5	J52
I	Ihara, T.	4.1	18
	Inoue, Toshiro	13.4	217
J	Jameson, A. R.	3.5	13
	Janowiak, John E.	10.5	100
	Jiankang, W.	6.3	39
	Jobard, Isabelle	10.3	94
	Jones, Andrew S.	JP8A.11	133
K	Kandel, Abraham	9.5	*
	Kaplan, John	JP8A.13	141
	Katsaros, K. B.	3.3	9
		JP8A.23	175
	Kayiranga, Theoneste	7.3	61
	Kelly, G.	J1.2	J3
	Khalsa, Siri Jodha S.	14.3	232
	Kleespies, Thomas J.	7.1	55
	Koenig, Edward	JP8A.24	179
	Kowalewsky, Karen	JP8A.6	121
	Kozu, Toshiaki	3.4	*
		4.1	18
	Krajewski, W. F.	3.1	1
	Kratz, Eugene	JP8A.14	145
	Krishnamurti, T. N.	J2.1	J16
	Kummerow, Christian D.	14.4	263
		J1.4	J8
	Kyle, H. L.	J1.3	J5
L	LaFontaine, Frank J.	14.4	263
	Lahuec, J. P.	JP8A.8	126
	LaPorte, Daniel D.	16.4	259
	Lee, Thomas F.	6.4	45
	Lin, D.-S.	3.1	1
	Liu, Koung-Ying	10.4	96
	Louis, J. F.	JP8A.12	137
	Lubich, Debra	7.4	63
	Lushine, J. B.	J11.4	J50
M	Mack, R. A.	4.5	31
	Maiden, Martha E.	JP8A.14	145
		13.1	204
	Manabe, T.	4.1	18
	Martin, J. D.	J5.1	J29
	McGuirk, James P.	6.5	49
		7.2	59
		14.5	236
	McMorrow, D.	J5.2	J32
	Meneghini, Robert	3.4	*
		4.4	27

*Paper not available; if received in time, it will appear in back of book.

AUTHOR INDEX

		Paper	Page
M	Menzel, W. Paul	13.2	208
	Merrill, Robert T.	15.3	246
		J2.2	J19
	Moeller, Christopher C.	13.2	208
	Mugnai, Alberto	JP8A.18	158
N	Nakamoto, Shoichiro	4.3	24
		JP8A.22	172
	Nakamura, Kenji	3.4	*
		4.1	18
		4.4	27
	Negri, Andrew J.	9.1	71
		J1.5	J12
	Neuendorffer, Arthur C.	JP8A.4	*
	Neumann, C.	J5.5	J40
	North, Gerald R.	3.2	5
		4.3	24
		9.2	75
		JP8A.22	172
O	Oh, Kyung-Whan	9.5	*
	Okamoto, K.	4.1	18
	Olson, William S.	14.4	263
		J5.3	J36
	Oosterhof, D.	J2.1	J16
	Owens, Larry	JP8A.25	183
P	Petty, G. W.	3.3	9
		JP8A.23	175
	Picon, Laurence	12.5	202
	Piepgrass, M. V.	13.1	204
	Pierce, H.	16.3	255
	Pontikis, C.	JP8A.10	130
	Prabhakara, C.	9.3	79
	Prasad, N.	4.5	31
		J1.5	J12
	Purdom, J. F. W.	7.5	67
		14.2	228
R	Rao, G. V.	JP8A.1	104
	Rappaport, Edward N.	J2.3	J21
	Remer, Lorraine A.	12.2	194
	Revercomb, H. E.	16.4	259
	Rhudy, D.	JP8A.1	104
	Riba, Phil E.	3.2	5
		9.2	75
	Rigaud, A.	JP8A.10	130
	Robertson, Franklin R.	JP8A.16	151
		J11.5	J52
	Rodgers, Edward B.	16.2	250
		J11.2	J46
	Rosenfeld, D.	10.2	90
	Roth, Barry A.	14.4	263
		J5.3	J36
	Ruf, Christopher	JP8A.26	187
S	Salby, Murry	12.1	190
	Schreiner, A. J.	JP8A.3	112
	Scofield, Roderick	6.3	39
	Scott, N. A.	JP8A.15	147
	Sharma, Awdhesh	JP8A.9	*
	Sheets, R. C.	J5.4	*
	Shenk, William E.	16.2	250
	Shi, Lei	13.3	213
	Shin, Kyung-Sup	3.2	5
		9.2	75
S	Shoemaker, D. N.	J11.3	J48
	Short, David A.	10.2	90
	Shyu, Tian-Yow	10.4	96
	Silverman, Steven H.	16.4	259
	Simpson, Joanne	J1.1	J1
	Smith, Eric A.	9.5	*
		JP8A.18	158
		12.3	198
		13.3	213
	Smith, William L.	14.4	263
	Snyder, Sheila	13.5	221
		JP8A.26	187
	Sohn, Byung-Ju	12.3	198
	Spencer, Roy W.	9.4	83
		10.1	86
	Steiner, Ellen	JP8A.17	154
	Stout, J.	J11.2	J46
	Strabala, Kathy I.	13.2	208
	Strong, J.	16.3	255
	Swadley, Steven D.	15.2	242
	Swift, C.	JP8A.26	187
	Sylva, M.	13.1	204
T	Tahani, Y.	JP8A.15	147
	Tanaka, Ken	12.1	190
	Tao, W. -.K	J1.5	J12
	Thiele, Otto W.	JP8A.5	118
		JP8A.6	121
	Tiedtke, M.	J1.2	J3
	Timchalk, Andrew	6.3	39
	Tripoli, Gregory J.	JP8A.18	158
	Tsui, T.	J5.5	J40
	Tzeng, Ren-Yow	12.4	*
V	Valdes, J. B.	JP8A.22	172
	Velden, Christopher S.	JP8A.13	141
		J5.3	J36
	Vollmer, B. E.	9.3	79
	Vonder Haar, T. H.	JP8A.11	133
		JP8A.19	161
		7.5	67
	Vongsathorn, Jennifer	13.5	221
W	Waters, Kenneth R.	6.1	267
	Weare, Bryan C.	12.2	194
	Weinman, James	4.4	27
	Weng, F.	7.5	67
	White, G. A., III	14.5	236
	Wilheit, Thomas T.	3.4	*
		JP8A.9	*
	Wolff, David B.	10.2	90
	Woodberry, Karen	12.1	190
	Woodward, R. H.	16.3	255
Y	Yeh, H.-Y. M.	4.5	31
Z	Zehr, Raymond M.	7.4	63
		J2.4	J25

*Paper not available; if received in time, it will appear in back of book.

NONLINEAR ESTIMATION OF MONSOON RAINFALL FROM RADAR AND RAINGAGE DATA

Witold F. Krajewski and Dah-Syang Lin

Department of Civil and Environmental Engineering
and
Iowa Institute of Hydraulic Research
The University of Iowa
Iowa City, Iowa 52242-1585

1. INTRODUCTION

One of the main objectives of the planned Tropical Rainfall Measuring Mission (TRMM) will be to provide estimates of monthly rainfall averaged over 5° by 5° areas in the tropics (Simpson, 1988). Rainfall estimates will be based on data from multiple sensors installed on the TRMM low altitude non-Sun-synchronous satellite. These data will represent indirect measurements and, as such, can be corrupted by high measurement error. In addition to measurement error, TRMM rainfall estimates will be characterized by a sampling error due to non-continuous areal coverage by the satellite (Bell,1987; North 1987). In order to get a better handle on the accuracy of TRMM rainfall, an extensive validation experiments are being planned (Thiele, 1987). As part of the validation activities several testing sites were selected around the globe. At these sites extensive measurements of surface rainfall are being collected by various ground-based sensors. The idea is to compare TRMM rainfall estimates with more accurate estimates based on sensors such as meteorological radars and raingage networks. However, for this approach to work satisfactorily, one needs to provide not only fairly accurate estimates of surface rainfall but also accurate estimates of the uncertainties of these estimates.

It is the objective of this paper to describe some preliminary results of initial analysis leading to estimates of climatological rainfall and its uncertainties. The data used were collected during AMEX in Darwin, Australia in 1987 and 1988 and include radar and raingage observations. The rainfall estimation approach adopted in this study is based on stochastic interpolation methods investigated earlier by Krajewski (1987), Creutin et al. (1988), Delrieu et al (1988), Azimi-Zonooz et. al. (1989), and Seo et al (1989). The methods produce rainfall estimates by optimally combining radar and raingage measurements. Both, the results of numerical simulation experiments conducted by Krajewski and his colleagues, and the results obtained from real world data by Creutin and his group, indicate that combining radar and raingage observations increases the accuracy of rainfall estimates as compared to estimates obtained from each sensor alone. However, the performance of the merging methods depends on many factors which are not fully examined yet.

In the following chapters we will describe a nonlinear merging methodology called disjunctive cokriging, first used to combine radar and raingage data by Azimi-Zonooz et al (1989), we will discuss estimation issues as they relate to time and space scales of interest to TRMM, and will present results of raingage data analysis for a data set obtained by NASA from Darwin, Australia.

2. THE ESTIMATION METHOD

Disjunctive kriging, which is a nonlinear stochastic interpolation method of spatial data was first proposed by a French mathematician Matheron (Matheron, 1976). Since, the method has been investigated and applied in various fields such as mining engineering, agricultural research and hydrological studies (Puente and Bras, 1982; Yates, 1986).

The disjuctive estimator of rainfall at a location u_0 is obtained by a linear combination of nonlinear functions f_i's and h_j's

$$\hat{R}_{DCK}(u_0)=\sum_{i=1}^{n_g} f_i[g(u_i)] + \sum_{j=1}^{n_r} h_j[r(u_j)] \qquad (1)$$

where $g(u_i)$ and $r(u_j)$ are the standard normal random variables obtained from raingage and radar observations, respectively, from the locations in the vicinity of u_0. The functions f and

g are unknown and need to be estimated. It seems like a hopeless task, unless we use transformed variables and approximate these functions with some polynomial. The transforrmations used to transfer raingage observations $G(u_i)$ and radar observations $R(u_j)$ are defined as

$$G(u_i)=\Phi_g[g(u_i)]=\sum_{k=0}^{k_g} C_k H_k[g(u_i)] \qquad (2)$$

$$R(u_j)=\Phi_r[r(u_j)]=\sum_{k=0}^{k_r} D_k H_k[r(u_j)] \qquad (3)$$

where H_k is a Hermite polynomial of order k, and g and r are the standard normal random variables which are obtained from transforms

$$g(u_i)=\Phi_g^{-1}[G(u_i)] \qquad (4)$$

$$r(u_i)=\Phi_r^{-1}[R(u_i)] \qquad (5)$$

Making use of the fact that Hermite polynomials are orthogonal with respect to standard normal density function one can evaluate the coefficients C_k (and D_k) from

$$C_k=(k!)^{-1}(2\pi)^{-1/2}\int_{-\infty}^{\infty}\Phi(y)H_k(y)e^{-1/2y^2}dy \qquad (6)$$

Eq. (6) can be solved by numerical integration, or, if $\Phi(y)$ is approximated linearly - analyticaliy. For details of analytical solution see Puente and Bras (1982) or Krajewski and Azimi-Zonooz (1987). Once the transforms $\Phi_g[g(u_i)]$ and $\Phi_r[r(u_j)]$ are obtained, Hermite expansion can be used to approximate the functions f_i and h_j.Expanding the disjunctive estimator, Eq. (1), in a series of Hermite polynomials gives the following linear relationship

$$\hat{R}_{DCK}(u_0)=\sum_{k=0}^{k_g}\sum_{i=1}^{n_g} f_{ik}H_k[g(u_i)] + \sum_{k=0}^{k_r}\sum_{j=0}^{n_r} h_{jk}H_k[r(u_j)] \qquad (7)$$

where f_{ik} and h_{jk} are coefficients of Hermite expansion. These coefficients can be obtained from the solution of the following constrained minimization problem:

$$Var\{R(u_0)-\hat{R}_{DCK}(u_0)\}\rightarrow min \qquad (8)$$

subject to:

$$E\{R(u_0)-\hat{R}_{DCK}(u_0)\}=0 \qquad (9)$$

The solution is given in terms of a system of linear equations

$$\sum a_{ik}\,\rho^k_{g\alpha i}+\sum b_{jk}\,\rho^k_{gr\alpha j}=\rho^k_{g0\alpha} \quad \text{for } i,\alpha=1,\ldots,n_g$$

$$\sum b_{ik}\,\rho^k_{g\beta i}+\sum b_{jk}\,\rho^k_{gr\beta j}=\rho^k_{g0\beta} \quad \text{for } j,\beta=1,\ldots,n_r$$

$$k=1,\ldots,k_{max} \qquad (10)$$

and

$$f_{ik}=C_k a_{ik} \qquad (11)$$

$$h_{jk}=C_k b_{jk} \qquad (12)$$

where ρ_{gai} and $\rho_{r\beta j}$ are correlation functions of the gage and radar fields, ρ_{graj} and $\rho_{rg\beta i}$ are cross correlation functions between radar and gage fields, ρ_{g0a} is the correlation function of point to be estimated and gage field, and $\rho_{rg0\beta}$ is the cross correlation function between point to be estimated on the gage field and the radar field. The correlations involved are computed after the original fields are transformed into standard Gaussian fields. The parameter k_{max} is the maximum order of Hermite polynomials expansion.

Based on the above description the computational algorithm can be summarized as follows:

1. Transform the original fields into standard Gaussian fields
2. Compute spatial correlation functions for the transformed fields
3. Determine the coefficients of the linear expansion of the nonlinear functions of observations (Eq. (7)).
4. Perform estimation at the desired number of locations in the estimation domain.

For details of the algorithm the interested reader is refered to Azimi-Zonooz et. al. (1989). Disjunctive kriging also provides, in addition to optimal estimates, estimation variance.

It should be pointed out that disjunctive kriging is based on the assumption of second order homogeneity of the underlying process of spatial rainfall. This assumption seems reasonable in the case of Darwin data since most of the land under the radar umbrella is rather flat, with the highest point being 250 m above sea level. However, checking the validity of this assumption and evaluation of the quantitative effects of its potential violation remain to be investigated.

Another important consideration concerns the probability distribution of the rainfall data. The method of disjunctive kriging offers improvement over standard linear estimation if the data are highly skewed. Preliminary analysis of the Darwin data seems to support this hypothesis. However, if the data can be well approximated by the lognormal distribution then it can be shown that the problem of disjunctive kriging is equivalent to a transformed linear estimation.

3. PRELIMINARY ANALYSIS

Since the main objective of this investigation is to develop a framework for optimal estimation of climatological rainfall using radar and raingage data, the central question is to determine the most advantageous time scale to perform estimation. It is clear that on the time scale of the resolution of the data (1 min for rain gages and 5 min for the radar) both sensors are characterized by high measurement noise and also rainfall at this scale exhibits very weak spatial dependence (correlation). Also, from the estimation point of view, the most favorable scale has to be linked to the spacing of the raingage network and the results of radar-raingage cross correlation. The minimum distance between two rain gages in the Darwin network is about 14 km (Figure 1) and this fact immediately suggests that the optimal scale should be somewhere above the hourly scale. The preliminary computations support this hypothesis.

Figure 2 shows the spatial correlation function computed from hourly accumulations while Figure 3 shows the results for daily data. The fitted function is an exponential selected here arbitrarily. Also, the effect of spatial anisotropy was not taken into account in the computations. It is clear the estimates of the correlation function for hourly data is associated with high uncertainty

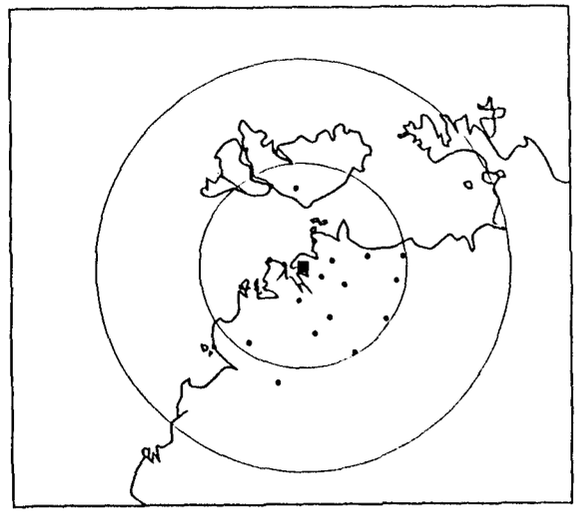

Figure 1. Schematic representation of raingage network near Darwin, Australia. Position of the radar is indicated by the solid square in the middle. The circles indicate 100 km and 200 km ranges.

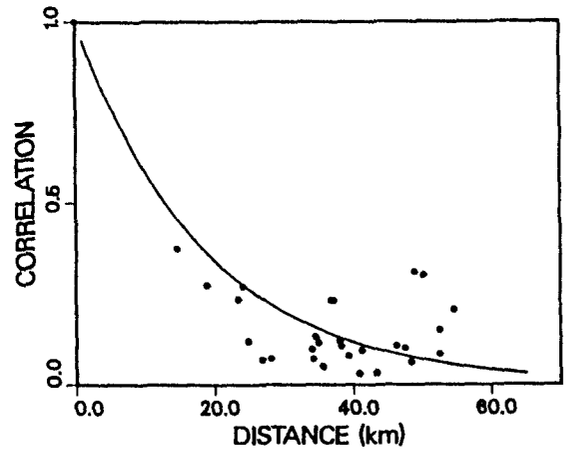

Figure 2. Correlation function of hourly raingage data. The exponential model was fitted by using the least-square technique.

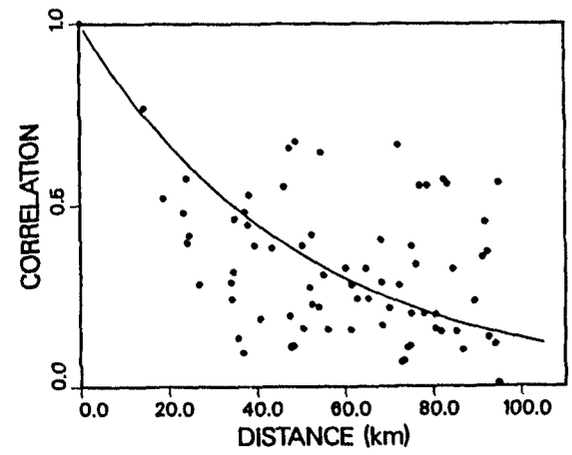

Figure 3. Correlation function of daily rainfall accumulations.

due to the lack of data at short distances. Also, the correlation values at the distances corresponding to typical interstation distances is not very significant. This suggests that at the time scale of up to one hour the best estimate of spatial rainfall is simply an areal average. The correlation of the daily data is, as expected, higher but it is also associated with significant scatter. However, from the point of view of joint radar and raingage estimation, the most important question is the nature of radar-raingage cross correlation. This remains to be investigated.

Acknowledgements

This material is based on work supported by the National Aeronautics and Space Administration. The authors are grateful for this support.

REFERENCES

Azimi-Zonooz A., W.F. Krajewski, D.J. Seo, and D.S. Bowles, 1989: Spatial rainfall estimation by linear and nonlinear cokriging of radar and raingage data. *Journal of Stochastic Hydrology* (in press).

Bell, T.L., 1987: A space-time stochastic model of rainfall for satellite remote-sensing studies. *Journal of Geophysical Research,* 92, D8, 9631-9643.

Creutin, J. D., Delrieu G. and Lebel T. 1988: Rain measurement by raingage-radar combination: A geostatistical approach. *Journal of Atmospheric and Oceanic Technology.* 5(1), 102-115.

Delrieu, G., A. Bellon and J.D. Creutin. 1988: Estimation de Lames d'Eau Spatiales a l'Aide de Donnees de Pluviometres et de Radar Meteorologique - Application au Pas de Temps Journalier dans la Region de Montreal., *Journal of Hydrology*, 98, 315-344.

Krajewski, W. F., 1987: Cokriging Radar-Rainfall and Raingage Data, *Journal of Geophysical Research*, 92 (D8), 9571-9580.

Krajewski, W. F. and Azimi-Zonooz, A., 1987: Hermite approximation of anamorphosis function, Technical Note No 10. Hydrologic Research Laboratory, National Weather Service, Silver Spring, Maryland.

Matheron, G. A., 1976: Simple Substitute for Conditional Expectation: the Disjunctive Kriging. Proceedings of the NATO Advanced Studies Institute "Geostat 75", D Reidel Publishers, Dordrecht, Netherlands.

North, G. R., 1987: Sampling Studies for Satellite Estimation of Rain. Proceedings of the Tenth Conference on Probability and Statistics, American Meteorological Society, Boston, Mass.

Puente, C. E. and R. L. Bras, 1982: A Comparison of Linear and Nonlinear Random Field Estimators, R. M. Parsons Laboratory, Technical Report 287, M.I.T., Cambridge, Mass.

Seo, D. J., W. F. Krajewski, D. S. Bowles, 1988: A Stochastic Interpolation of Rainfall Data from Raingages and Radar Using Cokriging: 1, Design of Experiments. Submitted to *Water Resources Research.*

Simpson J. (Ed), 1988: Report of the Science Steering Group for a Tropical Rain Measuring Mission, NASA Goddard Space Flight Center, Greenbelt , Maryland.

Thiele, O. 1987: Validating Space Observations of Rainfall, Proceedings of International Symposium on Tropical Precipitation Measurements, Tokyo, Japan.

Yates, S.R., 1986: Disjunctive Kriging: Cokriging, *Water Resources Research*, 22(10),1371-1376.

3.2

Tropical Oceanic Rainfall Estimation from Microwave Radiometry

Kyung-Sup Shin*, Phil E. Riba, and Gerald R. North

Climate System Research Program
Department of meteorology
Texas A&M University, College Station, Texas

1. Introduction

The objective of this study is to propose and test a new algorithm to retrieve area-time averaged rainrates in global dimension in anticipation of the Tropical Rainfall Measuring Mission (TRMM; Simpson et al. 1988). Our approach utilizes a single channel microwave observation and limits to the tropical oceanic rainfall. It is well appreciated that rainfall retrieval from a single channel informaton has some limitation due to changing surface emissivity on different surface characteristics, atmospheric water vapor, and non-raining cloud liquid water contents. Approach from multi-channel information is desirable in principle, and the sensitivity of different microwave frequencies has been tested by many previous investigators (Huang and Liou 1983, Wu and Weinman 1984, Smith and Mugnai 1988, and many others). Smith and Kidder (1978) also attempted to use multi-spectral information on rainfall retrieval.

It is suggested that retrieval of area-time averaged rainfall over ocean from a single channel information may be possible because of relatively uniform ocean back ground. Some biases due to changing atmospheric conditions can be adjusted statistically if their characteristics can be identified for a long time and over large area. Similar studies have been attempted by Kidder and Vonder Haar (1977) for depicting rainfall frequencies over oceans, and by Rao et al., (1976) for producing Global Oceanic Rainfall Atlas by using Nimbus-5 Electrically Scanning Microwave Radiometer (ESMR-5). The same data set used by Rao et al. was used in this study. To our knowledge, a multi-channel or multi-spectral approaches have never been applied to the global scale of rainfall retrieval. In any case, the improvement of understanding for the single channel case should be a good first step toward development of multichannel algorithms.

* *Current affiliation*: Korea Advanced Institute of Science and Technology, Seoul, Korea.

2. Microwave radiative transfer through rain-layer

A simple microwave radiative transfer model which is similar to Wilheit et al. (1977) except for excluding scattering effect by raindrops was developed. Results show remarkable agreement with the Wilheit curve without scattering. Using the model developed, more cases for different atmospheric models were calculated and the results were fitted by the saturation exponential curve of $T_B = A - Be^{-CR}$ as a $T - R$ relation. Here A is the saturation temperature (281K in this model) and B is the dynamic range of temperature variation. $A - B = T_0$ will be the temperature when $R = 0$, henceforth T_0 will be referred to as *background temperature*.

First, variations of T_0 and C are investigated for 11 different atmospheric conditions by changing cloud liquid water content and water vapor amount when R=0 within the scope of the Wilheit model. The results are summarized in Table 1. Table 1 shows that the coefficient of C is only a function of freezing level height. All 11 cases are essentially the same value of C regardless of different T_0 (or B). The saturation exponentional $T - R$ relation is in very good agreement with the calculated brightness temperatures. In all cases, the R^2 value is greater than .97 and average difference between them is less than 1K in tropical conditions (3 to 5 km freezing level). Curve fitting of C with respect to freezing level height (z in km) shows that the C increases with freezing level height (optical thickness) possibly in a quadratic form

$$C = 0.004 + 0.026z + 0.0045z^2.$$

Rao et al. (1976) and Kidder and Vonder Haar (1977) used a threshold temperature for a given freezing level to identify a raining pixel. Their approaches, in other words, used fixed values of T_0 and C which are determined only by freezing level height estimated from climatology. But it is easy to imagine that T_0 is different from place to place and day to day in spite of the same freezing level height. Rainfall retrieval from a single snap shot is the problem of finding the values of T_0 and C. But in the problem of monthly average of snap shots, the T_0 and C will form certain statistical distributions, possibly a normal distribution. If we find a proper way to estimate their distributions, the overall retrieval accuracy will be improved.

Table 1 Fitted regression coefficients of T_0 and C by $T_B = A - Be^{-CR}$ for given atmospheric conditions and freezing level height. Cloud liquid water (l_c) are placed below freezing level as 500 m thick, and temperature profile is determined by a constant lapse rate of 6.5°/km from freezing level (see Wilheit et al., 1977).

RH(%)	$l_c(g/m^3)$	Freezing level (km)				
		1	2	3	4	5
50	0.0	130(.036)	132(.078)	137(.125)	144(.179)	156(.241)
50	0.5	136(.036)	138(.078)	142(.125)	150(.179)	161(.241)
50	1.0	141(.036)	143(.077)	148(.125)	155(.179)	165(.241)
80	0.0	132(.036)	136(.078)	144(.125)	156(.180)	172(.245)
80	0.25	135(.036)	139(.076)	147(.123)	158(.177)	174(.240)
80	0.5	137(.036)	142(.076)	149(.123)	161(.177)	177(.240)
80	0.75	140(.036)	144(.076)	152(.123)	163(.177)	179(.240)
80	1.0	143(.036)	147(.077)	154(.125)	166(.180)	181(.246)
100	0.0	132(.036)	137(.078)	146(.125)	160(.181)	178(.247)
100	0.5	138(.036)	143(.077)	151(.125)	164(.181)	182(.247)
100	1.0	143(.036)	148(.077)	157(.125)	169(.181)	186(.247)

$T_0(C)$

3. Data

The ESMR-5 brightness temperature data set from December 1973 to November 1974 were analyzed. ESMR-5 measured at 19.35 GHz with horizontal polarization and scanned ±50 degrees accross the flight path in 78 steps. It flew in a sun-synchronous polar orbit with local noon and midnight equator crossing times (see Wilheit (1972) for more detail).

In preliminary analysis, the authors found that the data contain a significant bias with scan angles. NASA initially corrected the data by using global average statistics of scan angle bias (personal communication with Wilheit). This adjustment based on global average left significant bias on scan angles locally, especially in the tropics. More adequate data correction methods by using microwave radiative consequences is currently investigating by the author's team. However, at this stage, we have found that the 21 pixels near nadir (scan position 29 through 49 corresponding ±12° scan angles) are fairly consistent and free of bias. But temperatures measured at night at scan positions of 36 through 43 are consistently lower than at adjacent positions by about 4K, which is suggesting obvious instrument problem. Therefore, additional correction was applied to those positions at night observations by adding 4K. Similar corrections were also applied by Kidder and Vonder Haar (1977) and Short (1988).

As a consequence, the original ESMR-5 data with ±12° scan angles were used in this study. Because of narrow scan width, a large sampling error is expected for monthly rainfall estimates. The formula proposed by Shin and North (1988) predicts about 20 % sampling error on monthly 5° × 5° area averaged rainrate estimates. Due to the data limitation, seasonal average rainrate is tested in this study, and this will give about 10 % sampling error. More complete monthly based area averaged rainrate estimations should be waited until an adequate correction factors are applied to the whole scan positions.

4. Retrieval algorithm

a) Histogram analysis

At each 5° × 5° grid box, the ESMR-5 brightness temperatures of FOV were collected for each season over the tropical Pacific and Atlantic. Then the collected brightness temperatures were analyzed on a histogram of 5K bin at each grid and each season. Figure 1 shows an example of such a histogram. It ranges generally from 130 to 260K. It shows a skewed distribution which has a long tail at higher temperatures suggesting FOVs of raining cases. The temperatures on the colder side suggest FOVs of non-raining cases. Although there is no rain, the back ground temperature, T_0, can be different due to different atmospheric conditions as seen in Table 1. We assume that the distribution of T_0 is normal when they are collected in a large area and for a long time. Therefore, it is suggested that the histogram is composed by the sum of the normal distribution of colder temperatures of non-raining cases and rain distribution of warmer temperatures, and the peak of histogram represents the average T_0 in that area during the season, the mean of normal distribution.

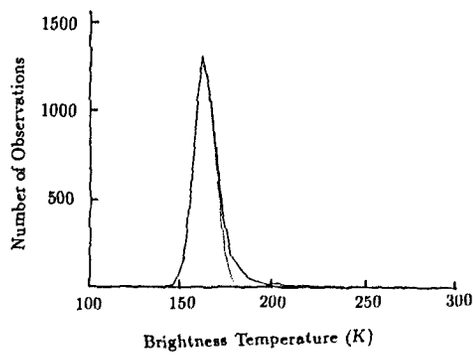

Fig. 1 An example of histogram of brightness temperatures for a season and in a 5° × 5° grid box over ocean. The dotted line indicates the best fit of normal distribution from cold temperature to the peak +5K of the histogram.

An iteration method was developed to separate the normal distribution of non-raining cases and raining distribution. By classifying the shape of each histogram and using the peak as a first guess of mean of the normal distribution, the mean and variance of T_0 are estimated by searching a best fit of the histogram (dashed line in Fig. 1). In this procedure, only the distribution of colder temperatures up to the peak +5K is used. Then the residual at warmer temperatures was suggested as a rain distribution. A very similar concept is currently being investigated by Chang and Wilheit (1988) independently.

Figure 2 shows the histograms (solid lines), fitted normal distributions (dashed lines) at each grid box over ocean along a given latitude band. The mean and variance of the estimated normal distribution are different in each grid box. The mean gives information of the average atmospheric water vapor and cloud water, while the variance includes the fluctuation of those in space and time.

b) Rain estimation

First the rain probability (P) was estimated at each grid box by considering the number of rain pixels out of total number in the histogram. The brightness temperatures of rain cases were converted to rainrates using the $T-R$ relation in section 2. Again,

$$T_B(R) = 281 - Be^{-C(z)R}$$

where $C = 0.004 + 0.026z + 0.0045z^2$, z the freezing level height in km, and B is the dynamic range of a given background temperature. The freezing level height was estimated from the zonally symmetric climatological data

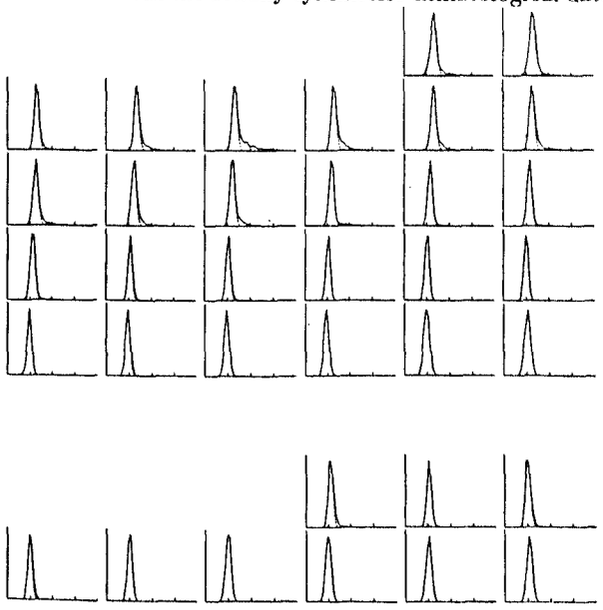

Fig. 2 Histograms (solid) and the fitted normal distribution (dashed) along a latitude band of 10-15°S at winter. Longitude increases from left to right, top to bottom with 5°. The blanks indicate the grid areas blocked over land (see Fig. 3). The coordinates of each histogram is the same as Fig. 1. The maximum number of observations is normalized to be same.

similar to Kidder and Vonder Haar (1976). The B is estimated from the average background temperature estimated from the peak of histogram. At each grid box, the estimated rainrate ($\hat{R}$) is

$$\hat{R} = P \sum_{i}^{N} f(T_i)\hat{R}_i(T_i)$$

where $f(T_i)$ is the probability density function of brightness temperatures when raining, and $\hat{R}_i$ is the estimated rainrate at the i-th bin.

c) Beam filling error adjustment

Due to the large FOV of the microwave sensor with respect to spatial scale of tropical rain, the rainfall distribution inside a FOV is hardly uniform. The sensor measures integrated radiances of non-uniform rainrates as a single value. Because of the non-linear (saturated exponential) $T-R$ relationship, retrieved rainrate from measured radiance is not the same as real average rainrate. This error is called the beam filling error and has been noticed in radar meteorology. Smith and Kidder (1978), Austin and Geotis (1978), and Lovejoy and Austin (1980) have addressed this problem and their results showed that estimated rainrates from microwave observation consistently underestimate the observed (or simulated) rainrates by a factor of about .5 to .6 with large variances. Recently, a more comprehensive study on beam filling problem has been conducted by Short (1988). His ensemble FOV model based on the gamma probability distributed rainrates within a FOV predicts that the ratio of rainrate estimated from microwave sensor to real rainrate (beam filling correction factor, κ) can be parameterized by

$$\kappa = \frac{-F\alpha\beta C}{ln(1 + F[\{1 + \beta C\}^{-\alpha} - 1])} \qquad (1)$$

where F is the fraction of the FOV covered by rainy area, α and β the shape and scale parameters of gamma distribution, respectively, and C the exponent determined by freezing level height. The '-' sign indicates underestimation. Using the parameter values found in GATE, κ is 2.2. It is impossible at this stage to say that whether the parameters in GATE represent the ITCZ condition throughout the tropics. However, in the absence of better information, the same factor of $\kappa = 2.2$ is multiplied to the estimated rainrate ($\hat{R}$) throughout the tropics in this study. In fact, the variation of κ with time and space remains an open question.

5. Results and discussion

Fig. 3 shows the seasonal 5° × 5° area averaged rainfall retrieved by the proposed algorithm in this study. The results were compared to the precipitation climatology from ship observations for the years of 1950-72 over the Pacific by Dorman and Bourke (1979) (hereafter will be referred to as DB). However, direct comparison is not meaningful because of the difference in time and averaging area. (2° latitude × 5° longitude averaging were used in DB). Larger area averaging may reduce the mean rainrate for a local scale such as narrow band of ITCZ.

Comparison shows that the retrieved rainfall represents the major rainy regions, the ITCZ and SPCZ, and major dry regions. The movement of major rainy and dry regions are well described and the absolute values of rainfall look quite comparable with DB. However, there are several discrepancies with DB, and they are likely to be unrealistic.

At winter, at 25-30° N, rainfall seems to be overestimated. The same is true at the southern latitude at summer. It is suggested that the rainfall at these latitudes in these seasons have extra-tropical characteristics which are driven by synoptic patterns rather than by convective mechanisms. Therefore the spatial scale is larger than that of tropical rainfall. Also the freezing level height is lower than in the tropics. But the same beam filling correction factor of 2.2 has been multiplied to the entire domain. From eq. (1), the beam filling correction factor should be different (must be small) because different rainfall characteristics will affect the parameters of F, α, β, and low freezing level will affect to C.

For entire seasons, the retrieved rainfall at the east coast of Australia tends to be overestimated. The careful check of histograms in this region shows consistent long tails to higher temperatures in every season, which is suggesting errors due to ground effects. The ESMR-5 data have been reported to have location errors of up to 40 km (Short 1988). Therefore, we cannot exclude the chance of counting the pixels over ground as a rainy pixels. Side lobes of the antenna pattern may also enhance this effect. This effect may also be accounted to other regions of many islands although careful efforts to eliminate pixels over major islands have been tried.

References

Austin, P. M., and S. G. Geotis, 1978: Evaluation of the quality of precipitation data from a satellite-borne radiometer. *Final Report under NASA grant NSG 5024*, Massachusetts Institute of Technology, Cambridge, MA, 30 pp.

Chang A. T. C, and T. T. Wilheit, 1988: Rainfall index over ocean derived from SSM/I data, *Proceedings of the International Geoscience and Remote Sensing Society, Edinburgh, Scottland*, 251-252.

Dorman C. E., and R. H. Bourke, 1979: Precipitation over the Pacific ocean, 30°S to 60°N, *Mon. Wea. Rev.*, 107, 896-910.

Huang R., and K.-N. Liou, 1983: Polarized microwave radiation transfer in precipitating cloudy atmoapheres: applications to window frequencies, *J. Geophys. Res.*, 88, 3885-3893.

Kidder S. Q., and T. H. Vonder Harr, 1977: Seasonal oceanic precipitation frequencies from Nimbus 5 microwave data, *J. Geophys. Res.*, 82, 2083-2086.

Lovejoy, S., and G. L. Austin, 1980: The estimation of rain from satellite-borne microwave radiometers, *Quart. J. Roy. Meteor. Soc.*, 106, 255-276.

Rao, M. S. V., W. V. Abbott, and J. S. Theon, 1976: Satellite derived global oceanic rainfall atlas, NASA SP-410, Washington, D. C.

Shin, K.-S., and G. North, 1988: Sampling error study for rainfall estimate by satellite using a stochastic model, itJ. Appl. Moteor, 27, 1218-1231.

Short, D. A., 1988: Remote sensing of oceanic rainrates by passive microwave sensors: a statistical-physical approach, Ph.D dissertation, Texas A&M University, College Station, TX.

Simpson, J. R., R. Adler and G. North, 1988: A proposed tropical rainfall measuring mission (TRMM) satellite, *Bull. Amer. Meteor.Soc.*, 69, 278-295.

Smith E. A., and S. Q. Kidder, 1978: A multispectral satellite approach to rainfall estimates, Research report, Colorado State University, Fort Collins, CO.

Smith E. A., and A. Mugnai, 1988: Radiative transfer to space through a precipitating cloud at multiple microwave frequencies. Part II: Results and analysis, *J. Appl. Meteor.*, 27, 1074-1091.

Wilheit T. T., 1972: The electrically scanning microwave radiometer (ESMR) experiment, in *The Nimbus-5 User's Guide*, edited by R. R. Sabatini, pp 59-104, NASA Goddard Space Flight Center, Greenbelt, MD.

Wilheit T. T., A. T. C. Chang, M. S. V. Rao, E. B. Rodgers, and J. S. Theon, 1977: A satellite technique for quantitatively mapping rainfall rates over the oceans, *J. Appl. Meteor.*, 16, 551-560.

Wu, R., and J. A. Weinman, 1984: Microwave radiances from precipitating clouds containing aspherical ice, combined phase and liquid hydrometeors. *J. Geophys. Res.*, 89, 7170-7148.

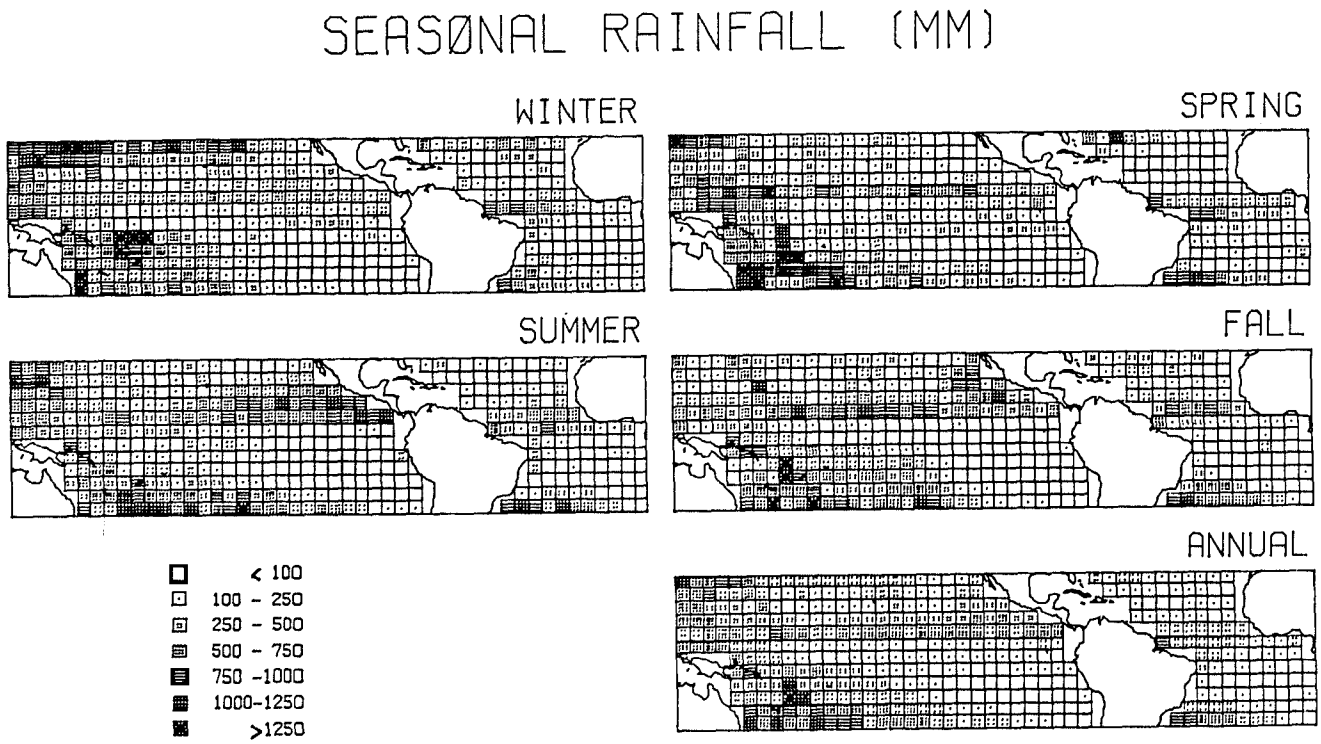

Fig. 3 The seasonal and annual rainfall (mm/season) over the Pacific and Atlantic in 1974 estimated from ESMR-5 data.

EMPIRICAL STUDIES OF THE MICROWAVE RADIOMETRIC RESPONSE TO RAINFALL IN THE TROPICS AND MIDLATITUDES

Grant W. Petty and Kristina B. Katsaros

University of Washington
Seattle, Washington

1. INTRODUCTION

During the past decade, interest in satellite passive microwave radiometry as a tool for monitoring global precipitation has increased, as the result of encouraging experience with sensors such as the Scanning Multichannel Microwave Radiometer (SMMR) and the new Special Sensor Microwave Imager (SSM/I). The planned Tropical Rainfall Measuring Mission (TRMM), for example, will rely heavily on passive microwave observations from space to contribute to its goal of creating a precipitation climatology for the tropical oceans (Simpson et al., 1988). There is also growing interest among midlatitude researchers in the ability of microwave radiometers to map precipitation within midlatitude frontal cloud bands (e.g., Katsaros and Lewis, 1986).

Despite recent advances in the theoretical modelling of microwave radiative transfer in rain clouds, observational data continue to play an indispensable role in helping define the capabilities and limitations of satellite microwave sensors. Comparisons to date have concentrated mainly on convection observed by radar over and near the continental United States.

With this in mind, we present some results of quantitative comparisons between satellite microwave radiometer observations and digital radar observations of equatorial convective cloud clusters and midlatitude frontal precipitation.

2. SMMR OBSERVATIONS OF TROPICAL PRECIPITATION COMPARED WITH DIGITAL RADAR

2.1 Data

During the Winter Monsoon Experiment (WMONEX), conducted in December 1978, a WR-73 digital radar belonging to the Massachussetts Institute of Technology was sited at Bintulu (3.2N, 113.0E) on the northwest coast of the island of Borneo. This radar obtained three-dimensional reflectivity patterns, to a nominal range of 256 km, of tropical convective cloud clusters appearing as local diurnal circulations interacted with the larger scale monsoon flow.

During the same period, the Scanning Multichannel Microwave Radiometer (SMMR) was in operation aboard the polar-orbiting Nimbus 7 satellite, sampling an 800 km swath at 6.6, 10.7, 18, 21 and 37 GHz, in dual polarization. Despite the narrow swath width and the alternating day duty cycle of the instrument, two cloud clusters were observed nearly simultaneously by both the SMMR and the MIT radar. These occurred on 11 December and 23 December 1978, in each case near 0400 UTC (noon local time).

2.2 SMMR Algorithm

We restrict our attention here to the SMMR channels having the best spatial resolution, namely the two 37 GHz channels (vertical and horizontal polarization), with a gridded ("CELL-ALL" format) resolution of approximately 30 km.

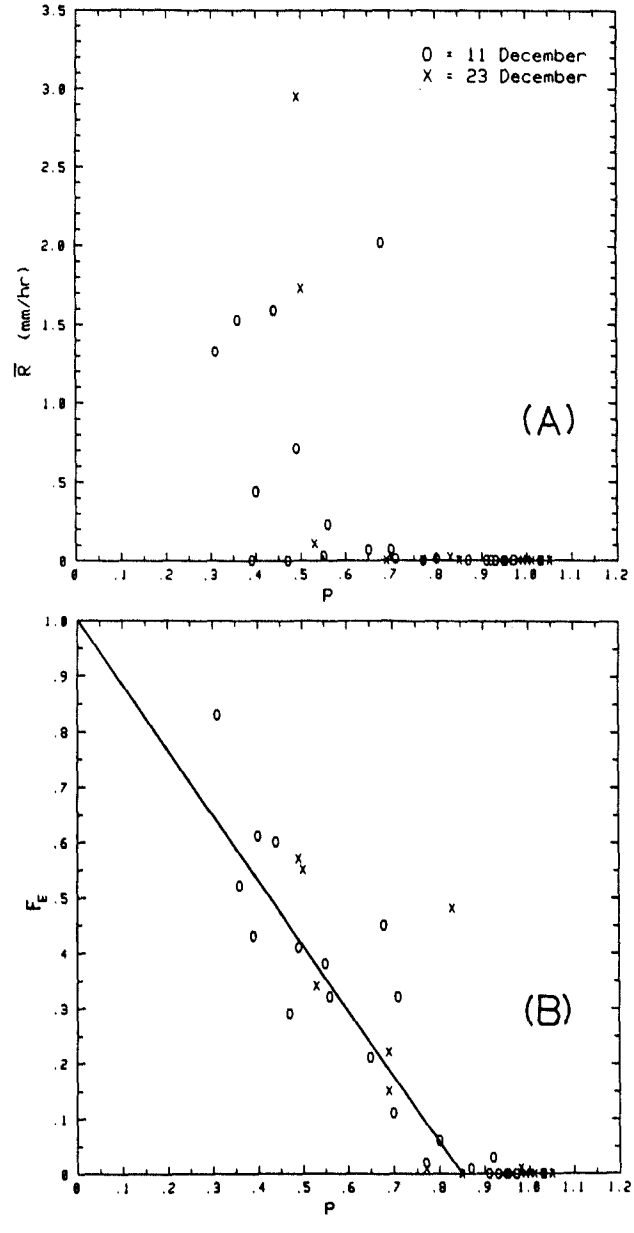

Figure 1. SMMR 37 GHz normalized polarization compared with (a) FOV-averaged rain rate and (b) fractional echo coverage F_E, for two tropical cloud clusters in WMONEX.

Two approaches to the interpretation of 37 GHz T_B in terms of precipitation parameters have been employed in earlier studies. The first is the so-called emission-based method (e.g., Wilheit et al., 1977), wherein increases in T_B are interpreted in terms of increasing atmospheric opacity due to increasing rain rate. The second is the dual-channel, scattering-based method proposed by Spencer (1986), on the basis of the observation that strong convection containing frozen precipitation aloft can depress T_B substantially below the normally elevated values expected from rain cloud emission alone.

Here, we pursue a third attenuation-based approach, wherein decreases in the polarization difference ($T_{B,V} - T_{B,H}$) are interpreted in terms of decreasing visibility of the highly polarized ocean surface (e.g., Spencer et al., 1983; Ferraro et al., 1988). We offer a refinement which should improve quantitative interpretation of polarization differences.

We divide the observed polarization difference by a hypothetical "clear-sky" polarization difference appropriate to cloudless, but otherwise similar, conditions for the time and location in question, defining a non-dimensional normalized polarization P:

$$P = \frac{(T_{B,V} - T_{B,H})}{(T_{B,V} - T_{B,H})_{CLR}}. \qquad (1)$$

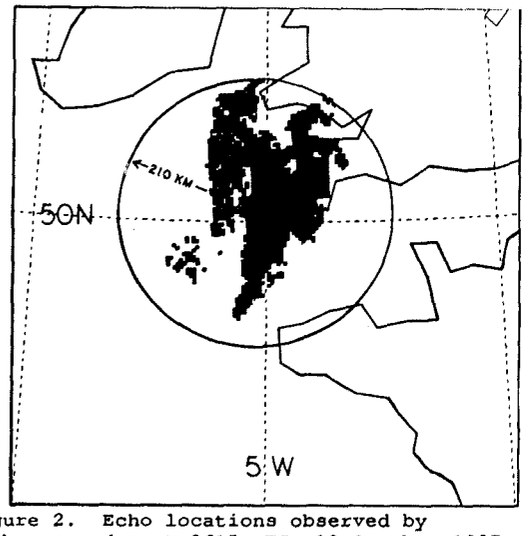

Figure 2. Echo locations observed by Camborne radar at 0615 UTC, 19 October 1987. Black represents reflectivity exceeding minimum detectable signal.

The clear-sky polarization difference can be estimated from models or climatology, or by using a histogram technique applied to actual data, as was done here. In the WMONEX cases, the clear-sky 37 GHz polarization typically ranged from 40 K to 50 K, depending mainly on water vapor content and surface roughness.

P thus ranges from about unity, in the complete absence of clouds, to zero, in the presence of completely opaque, unbroken rain clouds. This assumes that polarization effects due to preferentially oriented hydrometeors are insignificant, an assumption which appears valid for our data.

The motivation for the use of P lies in its relatively simple physical interpretation: under the assumption of plane-parallel geometry, we have found P to be approximately equal to the square of rain cloud transmittance, independent of other sources of variability, such as atmospheric water vapor content and surface temperature. The use of P, therefore, may permit more meaningful empirical comparisons between data obtained under widely differing conditions. See Petty and Katsaros (1989) for a more comprehensive discussion.

2.3 Results

Average rain rate and fractional echo coverage were computed from the radar data for each overlapping SMMR pixel. A plot of average rain rate $\bar{R}$ versus the 37 GHz P values (Fig. 1a) exhibits an unimpressive correlation ($r = -0.48$). In contrast, a plot of fractional echo coverage, F_E, versus P (Fig. 1b) shows a much more pronounced correlation ($r = -0.81$). The observed relationship between F_E and P may be summarized as follows:

$$F_E \simeq \begin{cases} 1 - \frac{P}{0.85}, & \text{for } P < 0.85 \\ 0, & \text{for } P > 0.85 \end{cases}. \qquad (2)$$

That T_B variations in these cases are dominated by changes in fractional coverage by rain, rather than footprint-averaged rain rate, is consistent with the conclusions of Spencer et al. (1983) and Ferraro et al. (1988) for convection over the Gulf of Mexico.

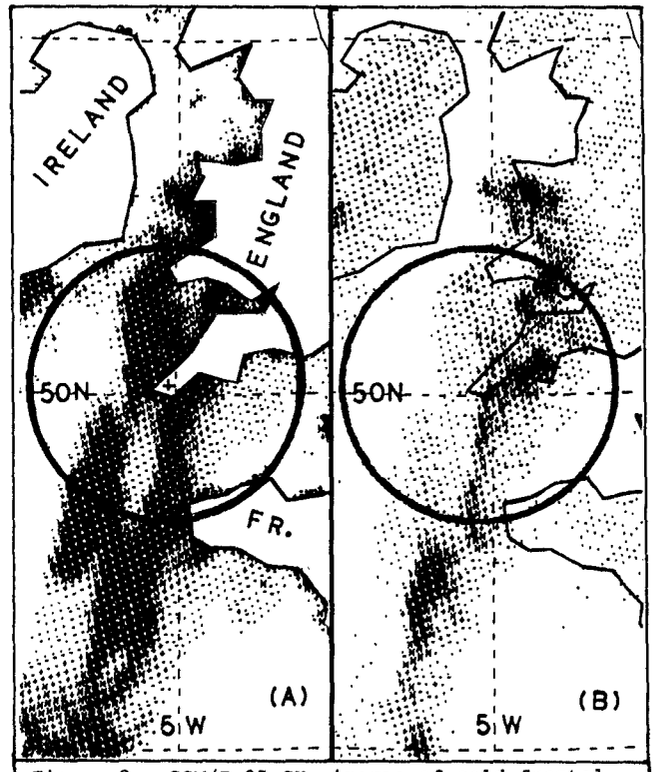

Figure 3. SSM/I 85 GHz images of cold frontal precipitation at 0613 UTC, 19 October 1987. (a) polarization difference (K). Darkest shading indicates values < 10 K ; white indicates > 35 K. (b) scattering signal (eqn. 3). Darkest shading > 8 K ; white < -2 K. Circles correspond to radar range limit shown in Figure 2.

3. SSM/I OBSERVATIONS OF MIDLATITUDE FRONTAL PRECIPITATION COMPARED WITH DIGITAL RADAR

3.1 Instrument characteristics

The Special Sensor Microwave Imager (SSM/I), launched in July 1987, is an improved microwave radiometer with better calibration characteristics and better sampling than the older SMMR. It has five channels (19.35, 22.235 and 37 GHz, all except 22.235 GHz in both vertical and horizontal polarization) corresponding roughly to the three highest frequencies (18, 21 and 37 GHz) of the SMMR, plus two new channels at 85.5 GHz (vertical and horizontal polarization).

All of the SSM/I frequencies, excepting perhaps the water vapor sensitive channel at 22.235 GHz, have potential application to satel-

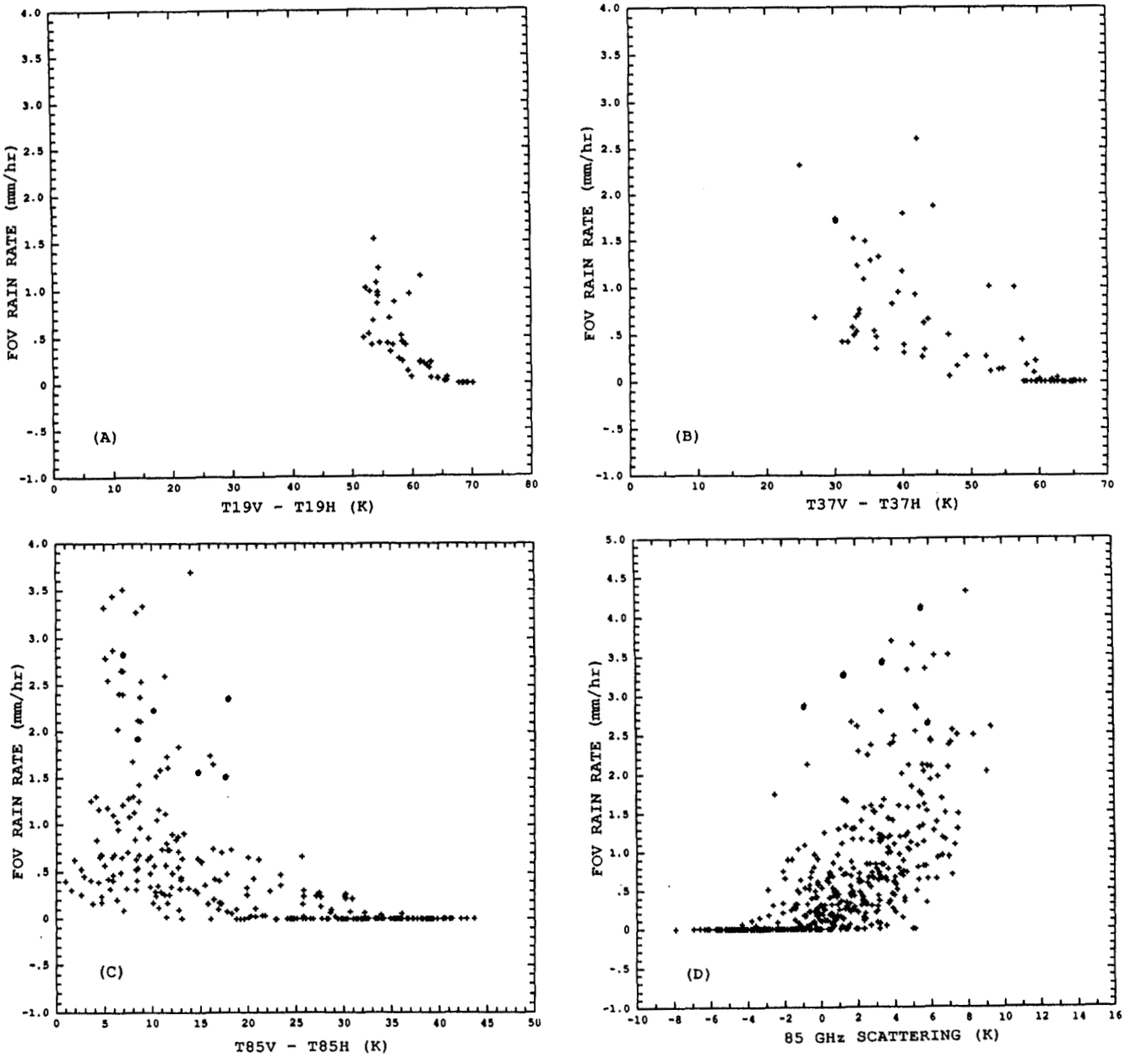

Figure 4. SSM/I observables compared with FOV-averaged radar rain rate for midlatitude oceanic frontal precipitation in IOP #1 (19 October 1987) of the Fronts 87 experiment. (a) 19.35 GHz polarization, (b) 37 GHz polarization, (c) 85.5 GHz polarization, (d) 85.5 GHz volume scattering.

lite-based precipitation estimates, albeit with differing characteristic spatial resolutions and sensitivities to rain, as well as varying sensitivity to other geophysical parameters.

As for SMMR, the polarization difference at a given frequency may be taken as a crude measure of atmospheric opacity, although at 85 GHz this interpretation must be applied with caution due to the polarizing effects of oriented ice particles.

Theoretical and observational studies (e.g., Hood and Spencer, 1988; Hakkarinen and Adler, 1988) have indicated that the SSM/I 85 GHz channels could potentially be important for observing distributions of heavier precipitation, due to their high sensitivity to volume scattering by precipitation size ice particles frequently present in moist convection. The method of Spencer (1986) appears to take on new significance when adapted to the SSM/I 85 GHz channels, the higher spatial resolution (15 km) making them even more attractive for this purpose.

The scattering signal may be extracted from dual polarization 85 GHz T by considering only variations in $(T_{B,V}, T_{B,H})$-space which are orthogonal to the variations due to atmospheric absorption and emission in the absence of scattering. In practice, this means computing the distance in $(T_{B,V}, T_{B,H})$-space between a dual-polarization brightness temperature pair and a hypothetical "pure emission" line which is chosen to pass through coordinate pairs representative of the open ocean, on one extreme, and of optically thick, but non- scattering, water clouds, on the other (Spencer, 1986). For the case presented here, we calculate the scattering signal as

$$S = .387T_{B,H} - .922T_{B,V} + 143.8 \qquad (3)$$

3.2 Data

The Mesoscale Frontal Dynamics Project/ Fronts 87 experiment was conducted during part of the Fall and Winter of 1987. One aim of the proj-

ect was to investigate frontal structure over the eastern North Atlantic. Rain-gauge calibrated digital radars operating at several locations in England and France recorded precipitation patterns in selected North Atlantic frontal systems as they moved through the area.

During Intensive Operating Period (IOP) #1, at 0615 UTC on 19 October 1987, cold frontal precipitation was sampled nearly simultaneously by the Camborne 10 cm radar (50.06N, 5.35W) and the SSM/I. Radar echo locations are depicted in Fig. 2. The SSM/I 85 GHz polarization and scattering signal are depicted in Fig. 3a and 3b, respectively.

3.3. Results

Qualitatively, 85 GHz polarization differences less than 15 K (dark areas in Fig. 3a) appear to closely correspond to areas of radar echo, except in the more distant portions of the southwest quadrant. We believe that some discrepancies may be due to deficiencies in the radar coverage, as the radar site is known to be less than optimal. A narrow, north-south oriented band of enhanced 85 GHz scattering (Fig. 3b) closely corresponds to a distinct line of heavier radar rain rate (not shown). Moreover, the scattering signal is easily discernible over land, in contrast to other microwave indices of precipitation.

Scatter plots of FOV-averaged rain rate versus 19, 37 and 85 GHz polarization difference and 85 GHz volume scattering signal are presented in Fig. 4. In contrast to the tropical cases examined earlier, there is a clear correlation here between FOV-averaged rain rate and all four SSM/I observables. Sensitivity to rain rate increases with increasing frequency, as expected. The 85 GHz polarization difference saturates at very low rain rates, and then assumes a value near 10 K with increasing rain rates, presumably due to the presence of preferentially oriented scatters. Despite considerable noise, much of which may in fact be due to residual errors in the navigation of the SSM/I data or to radar errors, the 85 GHz scattering signal (Fig. 4d) clearly contains some information on rain rate even in this relatively weak stratiform rainband.

At 19.35, 37 and 85 GHz, polarization differences less than 65 K, 60 K and 25 K, respectively, appear to indicate precipitation for this midlatitude case. In contrast, rain was associated only with 37 GHz polarization differences below 35 K in the WMONEX cases, mainly due to much larger contribution to atmospheric attenuation by water vapor. Note, however, that if we compute P by dividing the observed polarizations in Fig. 4b by a "clear-sky" value of about 65 K, we find that P = 0.85 once again gives a reasonable threshold for the appearance of rain, as in the tropical case.

4. CONCLUSIONS

The data presented here, though limited in quantity and scope, succeed in illustrating the considerable differences between the microwave response to rainfall in the equatorial tropics, and to stratiform rain in oceanic midlatitude fronts. The most important differences appear to be due to the different spatial characteristics of stratiform and convective rainfall and to the different background brightness temperature fields associated with tropical and midlatitude levels of atmospheric water vapor.

The SSM/I 85 GHz scattering signal appears to provide relatively high-resolution information on precipitation patterns in midlatitude oceanic fronts, and has the additional advantage of being equally useful over land.

ACKNOWLEDGEMENTS:

We are grateful to Robert W. Lunnon of the British Meteorological Office for providing the digital radar data from the Fronts 87 experiment. SSM/I brightness temperatures made available by Frank J. Wentz and Erika Francis of Remote Sensing Systems, Inc. WMONEX radar data were provided by Mr. Spiro Geotis and Professor Earl Williams at MIT. Nimbus-7 SMMR data were processed by the SMMR Information Processing Team of the Nimbus Project and made available by the National Space Science Data Center at Goddard Space Flight Center. This work was supported by NASA grants NAG5-784 and NAG5-943.

REFERENCES:

Ferraro, R.R., J.C. Alishouse, and J.V. Fiore 1988: Comparison of weather radar and satellite-based passive microwave observations of rainfall over land and oceans. Preprints, Third Conference on Satellite Meteorology and Oceanography, Feb. 1-5, 1988, Anaheim CA, Amer. Meteor. Soc., 309-314

Hakkarinnen, I.M, and R.F Adler 1988: Observations of precipitating convective systems at 92 and 183 GHz: Aircraft results. Meteorol. Atmos. Phys., 38, 164-182

Hood, R.E., and R.W. Spencer, 1988: Thunderstorm ice induced brightness temperature depressions at 18, 37, and 92 GHz during COHMEX and their implications for satellite precipitation retrievals. Preprints, Third Conference on Satellite Meteorology and Oceanography, Feb. 1-5, 1988, Anaheim CA, Amer. Meteor. Soc., 303-308

Katsaros, K.B., and R.M. Lewis, 1986: Mesoscale and synoptic scale features of North Pacific weather systems observed with the Scanning Multichannel Microwave Radiometer on Nimbus 7. J. Geophys. Res., 91, 2321-2330

Petty, G.W., and K.B. Katsaros, 1989 : Precipitation observed over the South China Sea by the Nimbus 7 Scanning Multichannel Microwave Radiometer during WMONEX. Accepted for publication in J. Appl. Meteor.

Simpson, J., R.F. Adler, and G.R. North, 1988: A proposed Tropical Rainfall Measuring Mission (TRMM) satellite. Bull. Amer. Met. Soc., 69, 278-295

Spencer R.W., B.B. Hinton, and W.S. Olson 1983: Nimbus-7 37 GHz radiances correlated with radar rain rates over the Gulf of Mexico. J. Clim. Appl. Meteor., 22, 2095-2099

Spencer, R.W. 1986: A satellite passive 37 GHz scattering based method for measuring oceanic rain rates. J. Climate Appl. Meteor., 25, 754-766

Wilheit, T.T., A.T.C Chang, M.S.V. Rao, E.B. Rodgers and J.S. Theon 1977: A satellite technique for quantitatively mapping rainfall rates over the ocean. J. Appl. Meteor., 16, 551-560

3.5

ON THE CALIBRATION OF CLIMATOLOGICAL SATELLITE RAINFALL MEASUREMENTS USING A TRANSPORTABLE GROUND-BASED POLARIZATION RADAR

A. R. Jameson

and

L. S. Chiu

Applied Research Corporation
Landover, Maryland

1. INTRODUCTION

Over the last several years the importance of tropical precipitation on global circulation has become increasingly apparent. Yet in much of the tropics, which is largely oceanic, rainfall measurements are meager. Although some improvements in measuring rainfall at a limited number of specific locations is possible, obtaining meaningful rainfall estimates on a global scale can only be achieved using satellites. Essentially this is the basis for the proposed Tropical Rainfall Measurement Mission (TRMM)(see Simpson et al., 1988).

Proposed satellite instrumentation includes both radiometers and radars. Aside from considerations of measurement geometry, both instruments have strengths and ambiguities. While radiometers are relatively inexpensive, even multiple frequencies provide little height resolution. The retrieval of rainfall rate from brightness temperatures can be obscured by several factors including scattering by high altitude ice (Wilheit et al., 1977; Wu and Weinmann, 1984), characteristic of intense rain producing systems, and by the unknown depth of the atmosphere containing rain (Wilheit et al., 1977). As shall be shown below, at lower microwave frequencies the brightness temperature (T_B) is also somewhat sensitive to the drop size distribution which can vary between different locations and seasons.

While radars are considerably more expensive, they can, in principle, provide important measurements of the distribution of the precipitation with height as well as measurements of the thickness of the atmosphere containing rain. An important limitation on the use of spaceborne radar measurements is the difficulty of converting radar reflectivity (Z) to rainfall rate estimates (R) with useful accuracy. While many of the current geometric limitations on accurately measuring Z from space can be overcome (Atlas and Moore, 1987), variations in the drop size distribution remain a significant source of uncertainty.

Recently, however, a technique (HART) has been proposed (Atlas et al., 1988; Rosenfeld et al., 1988) for circumventing much of this problem when measuring rainfall over large areas. Because of the statistical properties of the rainfall (Kedem et al., 1989), Atlas et al. show that the area average rainfall rate <R> can be estimated accurately from the fractional area covered by R greater than some arbitrary but small threshold τ. Furthermore, if the radar reflectivity factor corresponding to τ (Z_τ) is known, then it is only necessary to measure the area covered by Z_τ in order to estimate <R>. This technique obviously has great potential practical importance for estimating global tropical precipitation using spaceborne (and ground-based) radars provided Z_τ is known. This quantity is likely to depend upon rainfall type (convective, monsoonal, stratiform), location, and season. The HART method, therefore, must be calibrated.

Similarly, the retrieval of rainfall rate estimates from brightness temperatures can be improved if the statistics on the depth of the atmosphere containing rain, the thickness of the ice hydrometeors overlying the raining layer, and the average drop size distribution are known as functions of rainfall type, location and season. From statistical analyses it should be possible to improve the correlations between R and T_B or even to develop an approach analogous to HART for estimating <R>.

There are at least two methods when attempting to relate observables. One is to measure simultaneously the quantities at the same location. This, for example, is the standard approach for developing radar Z-R relations. A less common but potentially useful approach is to independently develop the probability or cumulative distributions for both quantities. A matching of the distributions can then be used to specify unknown parameters in the relation.

Recently, this latter method has been suggested as the preferred approach for calibrating the HART method. Unlike the direct correlation of quantities, this distribution matching method has the distinct and important advantage that it does not require simultaneous observations of parameters. This is particularly convenient when attempting to correlate measurements involving ground-based and moving platforms such as aircraft and satellites. As will be demonstrated below, however, it is important to collect the measurements of all observables at the same spatial resolution.

2. EFFECT OF RESOLUTION ON GATE RAINFALL PROBABILITY DISTRIBUTIONS

The GATE rainrate data compiled by Patterson et. al. (1979) can be used to

TABLE 1. ESTIMATED PARAMETERS OF THE CUMULATIVE DISTRIBUTION AND CONTRIBUTION TO TOTAL RAINFALL

RESOL'N	P(%)	a	C_{10}	C_{50}	C_{90}	W_{10}	W_{50}	W_{90}
GATE PHASE I RR=0.51 mm/hr								
4 (km)	13	3.85	.18	1.61	9.4	1.81	9.44	39.8
8	19	2.65	.07	.85	7.0	1.41	8.00	30.0
16	30	1.72	.02	.39	5.0	1.10	6.48	22.4
32	46	1.11	.009	.19	3.2	.80	4.72	15.1
64	62	0.83	.007	.15	2.3	.55	3.24	10.0
128	86	0.60	.004	.13	1.9	.05	2.00	7.0
256	95	0.54	.007	.21	1.9	.05	1.54	3.6
GATE PHASE II RR=0.38 mm/hr								
4	10	3.79	.18	1.50	8.9	1.80	9.50	44.5
8	16	2.41	.06	.70	6.0	1.23	7.76	33.1
16	26	1.46	.02	.30	4.0	.90	5.37	26.3
32	42	0.89	.008	.18	2.5	.60	3.55	10.0
64	64	0.59	.005	.12	1.6	.40	2.45	9.0
128	84	0.45	.004	.13	1.5	.03	1.45	5.0
256	97	0.39	.014	.21	1.2	.04	0.85	2.3

unit: mm/hr

illustrate the effect of resolution on the probability distribution of rainrates, for example. In these calculations, we use a square centered around the B-scale area of GATE which encompasses an area of 256 by 256 km (64 by 64 4-km pixels). Rainrates for 8, 16, 32, 64, 128 and 256 km pixels are calculated using adjacent 4 km pixels. The cumulative distribution (C) and the contribution to the total rainfall (W) at these different resolutions are calculated. [See Chiu (1988) for a detailed description.] Table 1 is a summary of the fraction of rainy pixels (p), the mean rainrate a (conditional on rain), the 10, 50 and 90 percentiles for the cumulative distribution (C_{10}, C_{50}, C_{90}) of the rainy pixels and the percentiles for contribution to the total rainfall (W_{10}, W_{50}, W_{90}).

The space-time average rainrate (RR) is the product of p times a. Since RR is constant with resolution, p must decrease as a increases with increasing resolution. At a resolution of 4 km, (the resolution of the proposed TRMM radar) for GATE I (II), p is about 13% (10%) and a is 3.85 (3.79) mm/hr. On the other hand, at a resolution of 8 km (the resolution of the proposed microwave TRMM radiometers), p is 19% (16%), while a is 2.65 (2.41) mm/hr. Obviously this discrepancy between mean rainrates (and p) suggests that the probability distribution is also likely to be altered by measurement resolution.

Kedem and Chiu (1987) proposed a stochastic model for rainrate and showed that in some asymptotic limits, the distribution approaches a lognormal distribution. The 4 km pixel rainrates in GATE can be modeled rather well by a mixed lognormal distribution (Kedem et al. 1989). Fig.1 shows the cumulative distribution for resolutions of 4 km and 256 km

Fig.1: Cumulative distribution of rainrates for 256 km (upper) and 4 km (lower) resolution for GATE I (left) and II (right). The x and y axes are scaled so that a lognormal distribution appears as a straight line. y-axis is Log_{10} of the rainrate (mm/hr). x values of -0.9, -0.48, 0., 0.48 and 0.9 correspond to the 10, 25, 75 and 90 percentiles.

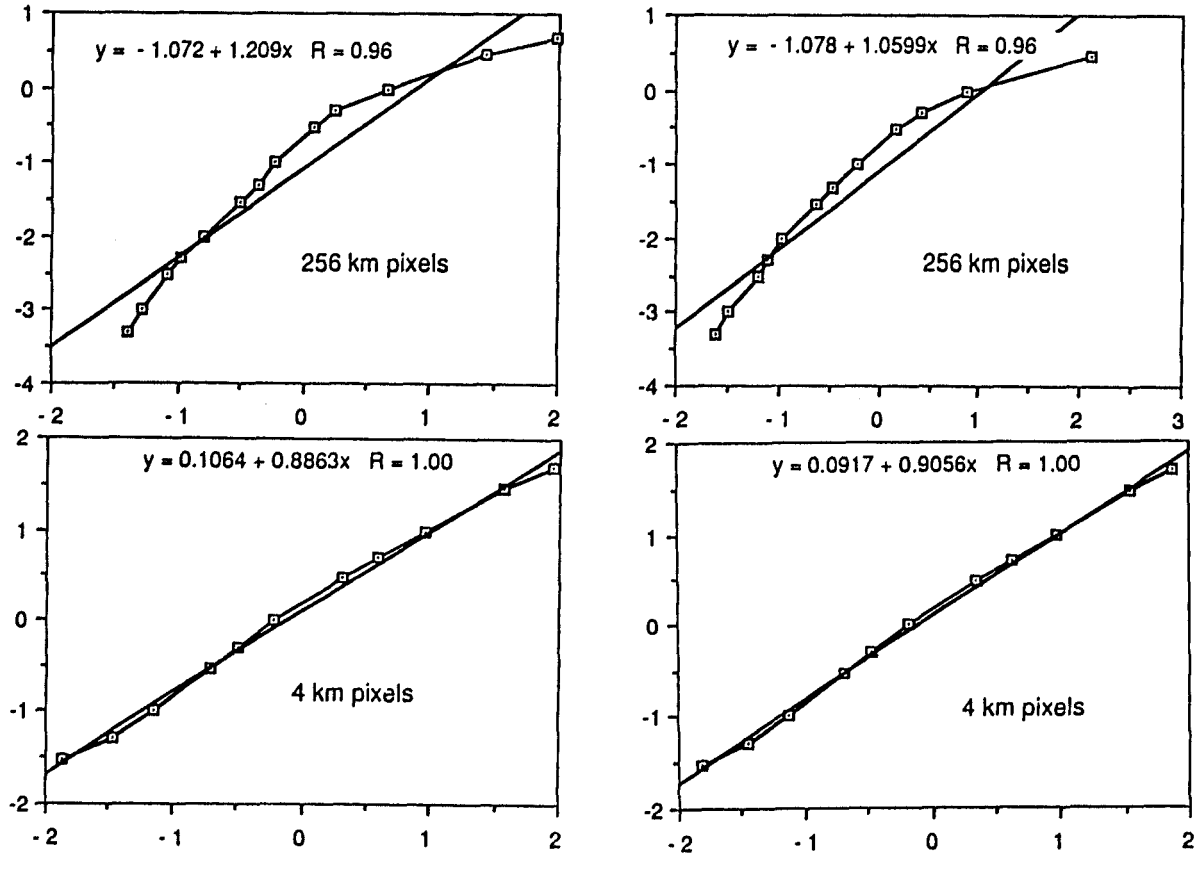

for both phases of GATE. The x and y axis have been scaled so that a lognormal distribution appears as a straight line. Clearly, while the linear fit at the 4 km resolution is almost perfect, the curvature at the 256 km resolution indicates that the cumulative distribution deviates significantly from that of a lognormal distribution. Thus, not just the mean values but the distributions themselves are functions of measurement resolution. Care must, therefore, be taken when comparing probability distributions measured at different resolutions.

3. A TRANSPORTABLE GROUND-BASED POLARIZATION RADAR AS A CALIBRATION TOOL

Using the matched distribution method for calibration of techniques such as HART requires, therefore, a means of measuring rainfall over areas the size of the footprints of satellite instruments. Although raingages can provide some information, they at best represent point measurements over only a limited ensemble of incremental areas contained within a region of interest. In contrast remote sensing instruments measure over an entire region. In general, then, an accurate comparison between remote sensing measurements and raingages over substantial areas requires a prohibitively expensive dense gage network. A transportable polarization radar, on the other hand, may provide a reasonable alternative.

For years conventional radars have been used to estimate rainfall rates using the reflectivity factor (Z). Unfortunately, since Z depends both on the drop concentration and the drop size distribution, many different combinations of these two factors can yield the identical Z. Consequently attempts to measure rainfall using Z alone are highly variable and depend upon particular meteorological circumstances (Battan, 1973). Specifically not all drop size distributions are of the particular form specified by Marshall and Palmer (1948) (e.g., Ulbrich, 1983) . As a result there has been an interest in using additional radar parameters in order to constrain some of this variability.

In particular radars capable of measurements at different polarizations provide several additional parameters to constrain rainfall estimates. While a detailed discussion is beyond the space and scope of this paper, the parameters include: (1) the differential reflectivity (ζ) (the ratio of Z measured using horizontal polarization to that at vertical polarization (Seliga and Bringi, 1976); (2) the mean and variance of the reflectivity weighted ratio of backscattered amplitudes corresponding to horizontal and vertical polarizations (Y) (Jameson, 1989); and (3) the propagation differential phase shift between horizontal and vertical polarizations (Δ_{HV}) (Jameson, 1985; Sachidananda and Zrnic', 1986). Because raindrops are nearly oblate, the first two quantities provide an estimate of the backscattered power weighted mean drop shape (axis ratio) and variance of drop shapes (Jameson, 1983a, 1987).

Since this axis ratio is a direct function of the drop size (Pruppacher and Pitter, 1972; Beard and Chuang, 1987) the polarization parameters can be used to estimate the reflectivity weighted mean and variance of a drop size distribution of quiescent drops (Jameson, 1983a; 1989). In principle these quantities can reduce the variability in instantaneous 'point' estimates of the rainfall rates (Seliga and Bringi, 1976; Jameson, 1983b) to better than ±15%-30%. Using raingages as 'truth', differential reflectivity experiments yield estimates which are within ±35% of raingage values (Goddard and Cherry, 1984). Polarization radar are likely to be further improved using the mean and variance of the amplitude ratio (Jameson, 1989). A further significant reduction in estimate uncertainty is also likely when estimates are over substantial areas. Most importantly these estimates can be made over regions of the size of the footprints of airborne and spaceborne remote sensing instruments. Perhaps better than any other method, polarization radars can, therefore, provide the rainfall rate probability distributions for the proper application of the matched distribution method for calibrating HART in different locations and seasons. They can also provide information to help reduce the variability of rainrate estimates from radiometers.

4. THE APPLICATION OF POLARIZATION RADAR DATA TO THE INTERPRETATION OF BRIGHTNESS TEMPERATURES

It is now well known that brightness temperatures (T_B) can be affected by such factors as the depth and type of ice overlying regions of rain as well as the depth of the raining layer. Because polarization radars can readily discriminate ice from water hydrometeors (e.g., Hall et al., 1984), they can provide important statistical information of these parameters at representative locations and seasons.

Another factor which has received little attention is the effect of the variability of the drop size distribution on T_B. While it appears that attenuation (and consequently radiometric rainrate estimates) are fairly insensitive to variations in the drop size distribution at frequencies around 37 GHz (e.g., Atlas and Ulbrich, 1977), it is not true for frequencies less than about 30 GHz. Lower frequencies, however, are particularly useful for measurements at higher rainfall rates ($\gtrsim$10 mm hr^{-1}) which cause saturation at higher frequencies.

Using the solution of Weinman and Davies (1978), T_B at a frequency of 9.3 GHz are calculated at nadir for an ice free simple model of a homogeneous 4 km thick isothermal layer of rain extending to infinity in the horizontal . For simplicity it is assumed that the drops are distributed exponentially according to

$$N(D)dD = N_0 \exp(-\Lambda D)\, dD \qquad (1)$$

where N(D)dD is the concentration of drops of size D to D+dD, and N_0 and Λ (the slope) are distribution parameters which can be related to the rainfall rate. These relationships, however, vary as illustrated by the differences between Marshall-Palmer type distributions and those of Sekhon and Srivastava (1971), for example. The extinction coefficient and albedo are then calculated for a range of median volume diameters (D_0) (that drop size which splits the liquid water content between drops larger than D_0 and those smaller) keeping the minimum and maximum drop sizes fixed at 100 μm and 6 mm, respectively.

The results for four rainfall rates are presented in Fig.2 where the deviation of the brightness temperature from that for the Marshall-Palmer drop size distribution are plotted as a function of D_0. Obviously deviations of only a few 0.1 mm in D_0 can significantly affect T_B particularly as the rainfall rate increases. Since it is unlikely that the Marshall-Palmer (or any other) distribution will be applicable at all times and locations around the globe, it would be particularly useful to develop a climatologically meaningful set of drop distribution relations similar to those prescribed by Marshall-Palmer or Sekhon and Srivastava at representative locations and seasons in key areas.

Compared to numerous extensive and expensive networks of raingages, a transportable polarization radar may be the best method for obtaining such information over substantial areas. For example, if the average form for a drop size distribution is known to be exponential, the polarization measurement of parameters such as differential reflectivity provide not only estimates of the rainfall rate over an area but estimates of D_0 (or equivalently the slope of the distribution) as well (see Fig.2). It should be possible, therefore, to develop relations between N_0, Λ, and the rainfall rate better tuned to the climate at particular locations and seasons than Marshall-Palmer relations. It is also conceivable that through the technique of probability distribution matching the polarization radar rainfall statistics might also be used to develop a technique analogous to HART for the interpretation of T_B.

5. A CONCLUDING REMARK

The development and use of spaceborne instruments for monitoring geophysical parameters and particularly rainfall on a global scale guarantees that the next several years will be a particularly exciting. However, while the design, assembly and launch of new equipment tends to consume a great deal of attention and effort, these activities should not be allowed to become a major distraction from the scientific goals. It would be unfortunate indeed if large sums of money were spent to obtain space measurements without a concomitant adequate expenditure for ground-based instruments to assure the most accurate and complete scientific use of these exciting space measurements.

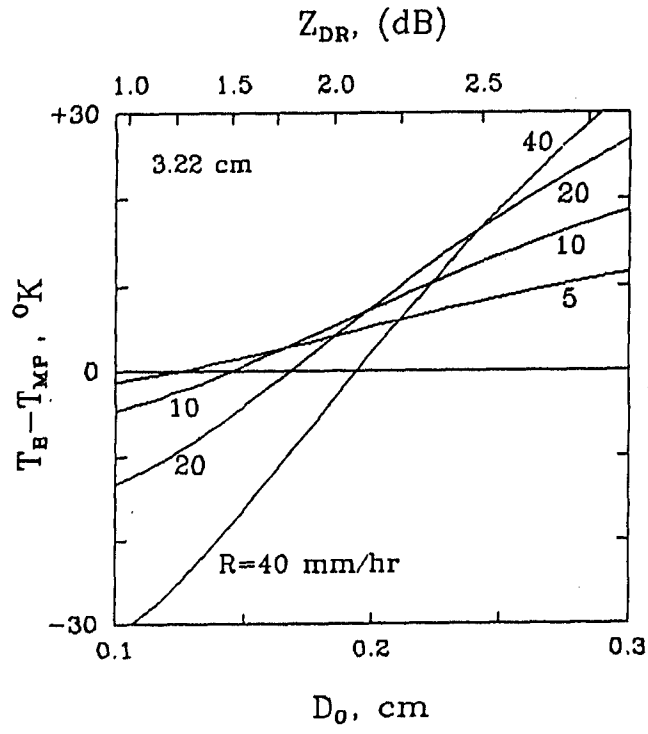

Fig.2: Plot of the difference in brightness temperature at a wavelength of 3.22 cm between that for a model cloud and that corresponding to an assumed Marshall Palmer distribution versus the median volume drop diameter (D_0). The corresponding differential reflectivity (Z_{DR}) is indicated at the top.

Acknowledgements:

This work was funded by grants NAS5-30083, NAS5-30303, and NAS5-27796 from the National Aeronautics and Space Administration.

6. REFERENCES

Atlas, D., D. Rosenfeld, and D.A. Short, 1988: The estimation of convective rainfall by area integrals. Part I: The theoretical and empirical basis. Conf. Mesoscale Precip. Analysis, Simulation, and Forecasting. MIT, Cambridge.

Atlas, D., and R.K. Moore, 1987: The measurement of precipitation with synthetic aperture radar. J. Atmos. Oceanic Technol., 4, 368-376.

Atlas, D., and C.W. Ulbrich, 1977: Path and area-integrated rainfall measurement by microwave attenuation in the 1-3 cm band. J. Appl. Meteor., 16, 1322-1331.

Battan, L.J., 1973: Radar Observation of the Atmosphere, Univ. Chic. Press, 324 pp.

Beard, K.V., and C. Chuang, 1987: A new model for the equilibrium shape of raindrops. J. Atmos. Sci., 44, 1509-1524.

Chiu, L. S., 1988: Rain estimation from satellites: Areal rainfall-rain area relation. Third Conf. on Satellite Meteorology and Oceanography (Anaheim, CA), Amer. Meteor. Soc., Boston, 363-368.

Goddard, J.W.F., and S.M. Cherry 1984: The ability of dual-polarization radar (copolar linear) to predict rainfall rate and microwave attenuation. Radio Sci., 19, 201-208.

Hall, M.P.M., J.W.F. Goddard, and S.M. Cherry, 1984: Identification of hydrometeors and other targets by dual-polarization radar. Radio Sci., 19, 132-140.

Jameson, A.R., 1983a: Microphysical interpretation of multi-parameter radar measurements in rain. Part I: Interpretation of polarization measurements and estimation of raindrop shapes. J. Atmos. Sci., 40, 1792-1802.

Jameson, A.R., 1983b: Microphysical interpretation of multi-parameter radar measurements in rain. Part II: Estimation of raindrop distribution parameters by combined dual-wavelength and polarization measurements. J. Atmos. Sci., 40, 1803-1813.

Jameson, A.R., 1985: Microphysical interpretation of multi-parameter radar measurements in rain. Part III: Interpretation and measurement of propagation differential phase shift between orthogonal linear polarizations. J. Atmos. Sci., 42, 607-614.

Jameson, A.R., 1987: Relations among linear and circular polarization parameters measured in canted hydrometeors. J. Atmos. Oceanic Technol., 4, 634-645.

Jameson, A.R., 1989: The interpretation and meteorological application of radar backscatter amplitude ratios at linear polarizations. J. Atmos. Oceanic Technol., 6, in press.

Kedem, B. and Chiu, L. S., 1987: On the lognormality of rain rate. Proc. Nat'l. Acad. Sci. USA 84, 84, 901-905.

Kedem, B., Chiu, L. S., and North, G., 1989: Estimation of mean rain rate: Application to satellite observations. J. Geophy. Res., submitted.

Marshall, J.S., and W.M. Palmer, 1948: The distribution of raindrops with size. J. Meteor., 10, 25-29.

Patterson, V.L., Hudlow, M.D., Pytlowany, P.J., Richards, F. P., and Hoff, J.D., 1979: GATE radar rainfall processing system. NOAA Tech. Memp. EDIS 26, Nat'l Oceanic and Atmospheric Admin., Washington, D.C.

Pruppacher, H.R., and R.L. Pitter, 1971: A semi-empirical determination of the shape of cloud and raindrops. J. Atmos. Sci., 28, 86-94.

Rosenfeld, D., D. Atlas, and D.A. Short, 1988: The estimation of convective rainfall by area integrals. Part II: The height-area threshold (HART) method. Conf. Mesoscale Precip. Analysis, Simulation, and Forecasting. MIT, Cambridge.

Sachidananda, M., and D.S. Zrnic', 1986: Differential propagation phase shift and rainfall rate estimation. Radio Sci., 21, 235-247.

Sekhon, R.S., and R.C. Srivastava, 1971: Doppler radar observations of drop-size distributions in a thunderstorm. J. Atmos. Sci., 28, 983-994.

Seliga, T.A., and V.N. Bringi, 1976: Potential use of radar differential reflectivity measurements at orthogonal polarizations for measuring precipitation., J. Appl. Meteor., 15, 69-76.

Simpson, J., R.F. Adler, and G.R. North, 1988: A proposed satellite Tropical Rainfall Measuring Mission (TRMM). Bull. Amer. Meteor. Soc., 69, 278-295.

Ulbrich, C.W., 1983: Natural variations in the analytic form of the raindrop size distribution. J. Climate Appl. Meteor., 22, 1764-1775.

Weinman, J.A., and R. Davies, 1978: Thermal microwave radiances from horizontally finite clouds of hydrometeors. J. Geophys. Res., 83, 3099-3107.

Wilheit, T.T., A.T.C. Chang, M.S.V. Rao, E.B. Rodgers, and J.S. Theon, 1977: A satellite technique for quantitatively mapping rainfall rates over the oceans. J. Appl. Meteor., 16, 551-560.

Wu, R., and J.A. Weinman, 1984: Microwave radiances from precipitating clouds containing aspherical ice, combined phase, and liquid hydrometeors. J. Geophys. Res., 89, 7170-7178.

4.1

CONCEPTUAL DESIGNS OF RAIN RADARS IN THE TROPICAL RAINFALL MEASURING MISSION AND ON THE JAPANESE EXPERIMENT MODULE AT THE MANNED SPACE STATION PROGRAM

Ken'ichi Okamoto, Jun Awaka, Toshio Ihara, Kenji Nakamura and Toshiaki Kozu
Communications Research Laboratory, Ministry of Posts and Telecommunications,
2-1, Nukui-kitamachi 4-chome, Koganei-shi, Tokyo, 184, Japan

Takeshi Manabe
ATR Optical and Radio Communications Research Laboratories,
TWIN-21 MID Tower, 2-1-61, Shiromi, Higashi-ku, Osaka, 540, Japan

1. INTRODUCTION

Rainfall of the tropical region where about 60% of the global rainfall is concentrated is the driving force of the global climate system. Tropical rain affects global climate change, global heat balance, and the global water cycle. However, quantative measurement data on tropical rain, especially over the ocean or over the tropical rain forest have been very sparse until now. Recently, the importance of measuring tropical rain has been recognized by many meteorologists in the world and some spaceborne missions to measure tropical rain by radar have been proposed by the USA, Japan and France. The Phase-A study of TRMM (Tropical Rainfall Measuring Mission) has been performed and Prephase-B studies have been continuing now under joint efforts between the USA and Japan.(1) The phase-A study of BEST (Bilan Energétique du Système Tropical) was started by France in 1988.(2) In addition to these free flying satellite projects, rain radar missions have been proposed on the international manned space station. They are the TRAMAR (Tropical Rain Mapping Radar) proposed by the USA,(3) and the rain radar on the JEM (Japanese Experiment Module). This paper briefly introduces the conceptual design of both the TRMM rain radar and the rain radar on the JEM which CRL (Communications Research Laboratory) has worked on to date.

2. CONCEPTUAL DESIGN STUDY OF TRMM RAIN RADAR

TRMM has three mission instruments to observe rain from space. They are Advanced Very High Resolution Radiometer (AVHRR), two microwave radiometers (ESMR and SSM/I) and the rain radar. The mission concept for the TRMM satellite with these sensors is shown in Fig. 1. The altitude of the TRMM satellite is 350 km and the orbit inclination was selected as 35° to include observation of the "baiu" front around Japan. The main purpose of TRMM is to measure the monthly averaged precipitation in pixel areas of 500 x 500 km between latitudes of ± 35° with an accuracy of 10 %. Although rain radar is a powerful means to observe rain and is widely used on the ground, a spaceborne rain radar has not yet been realized. Only a spaceborne rain radar can quantitatively measure rain rate distributions and vertical rain profiles on such a global scale. TRMM is now planned to be launched in 1994 by a Japanese H-II rocket and the TRMM rain radar may become the first spaceborne rain radar.

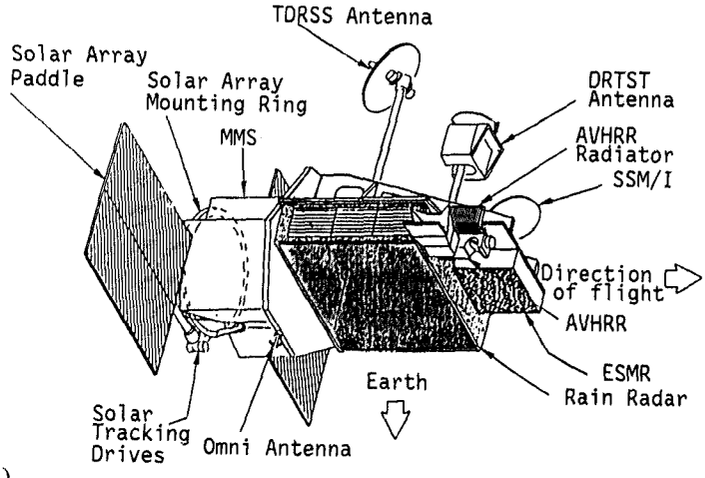

Fig.1 Conceptual Design for the TRMM Satellite

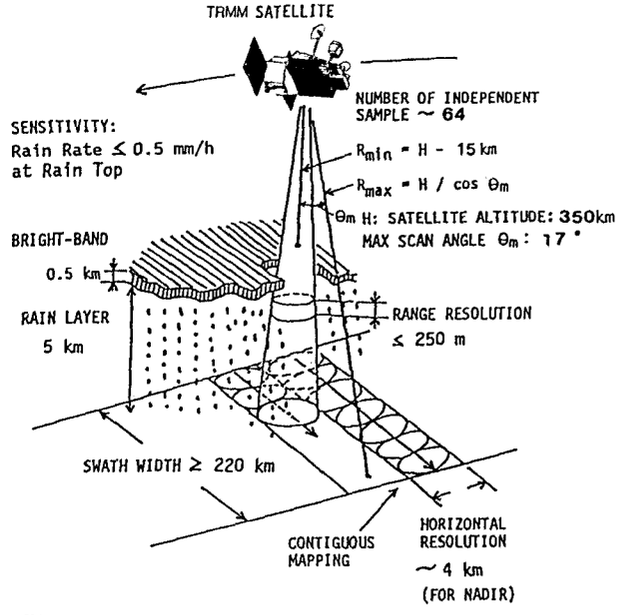

Fig.2 Mission Requirements for the Radar and Precipitation Model

Figure 2 shows mission requirements for the radar and precipitation model. The mission requirements were basically specified by NASA. The single frequency of 13.8 GHz was selected by considering three points: (1) to obtain a sufficient dynamic range at the rain bottom; (2)

to obtain a sufficiently narrow beam width to attain the required spatial resolution under the antenna hardware limitations; (3) frequency allocation of ITU table. The satellite altitude of 350 km was determined to provide fine horizontal resolution and to avoid the large air drag. Although a larger swath is preferable, it causes height smearing at the scan edge and small dwell time in the angle bin direction. A swath width of 220 km is a compromise between scientific requirements and the engineering limitations. The range resolution of 250 m is a meteorological requirement which is necessary to study details of the clouds or cloud cluster activities. The horizontal resolution of 4 km and the minimum measurable rain rate are also reasonable compromises. The independent sample number of 64 means the signal fluctuation of about 0.7 dB.

In the precipitation model which we adopt, the rain is assumed uniform and extends to a height of 5 km. The thickness of the bright band or the melting layer is 0.5 km and the attenuation coefficient in the melting layer is assumed to be twice as large as that of rain below the melting layer.

In the TRMM rain radar, the radar antenna beam must scan a swath width of 220 km in the cross-track direction every 0.6 s in order to observe a raining area without any gaps between scanning lines which are perpendicular to the moving direction of the satellite. Therefore, high speed electric scanning becomes essential.

In trade-off studies, three major competitive items were discussed for the selection of a preferred candidate for the TRMM rain radar. These competitive items were (1) a pulse compression radar vs conventional type radar, (2) a passive array radar with TWTA (Travelling Wave Tube Amplifier) vs active array radar with SSPA (Solid State Power Amplifier), and (3) antenna types (planar array antenna vs cylindrical parabolic).

Figure 3 shows a layout for the active array radar selected as a reliable candidate for the TRMM radar after the trade-off studies. Although active array radars are intricate in structure and require relatively large sizes and weights, total system loss becomes small because transmission lines between the antenna and transmitters/ receivers are short and phase shifter losses can be compensated by SSPA and LNA (Low Noise Amplifier). The total system is

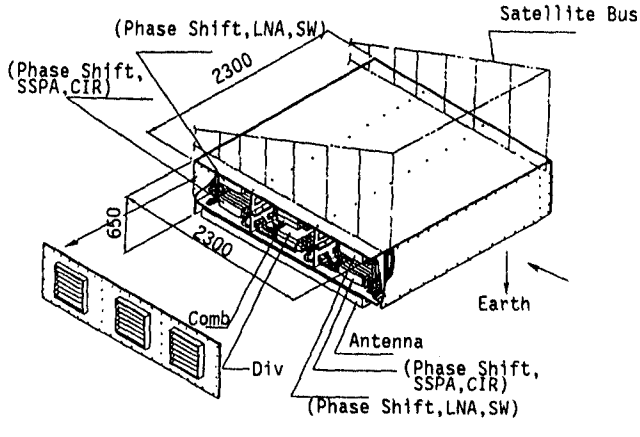

Fig.3 System Layout for the TRMM Rain Radar (Active array radar)

more reliable because it is still operational if some parts of the transmitters or receivers are broken in active array. In this figure, the total system is placed in a thermal control unit. The maximum power of the SSPA with GaAs FETs, which can be obtained in the present technology, under the configuration shown in the Figure 3 is about 10 W with a hybrid of two-stage SSPAs. A peak power of 571.2 W can be attained with present technology. The MMIC (Monolithic Microwave Integrated Circuit) technology is also introduced to reduce the weight in the active array radar. Main system parameters and estimated values of power consumption and weight of the active array type TRMM rain radar are shown in Table 1. The minimum detectable rain rate at the rain top is 0.4 mm/h at the scan edge and the measurable rain rate at the rain bottom is between 0.4-52 mm/h at nadir, with a signal to noise ratio of 0 dB. The attained horizontal resolution at nadir is 4.3 km and the range resolution is 250 m. The swath width is 220 km as indicated in Figure 1. The number of independent sample of 64 is achieved by the combination of variable PRF and the non-linear scanning method.

Table 1. Main System Parameters of TRMM Rain Radar

Frequency	13.8 GHz
Antenna	
Type	Planar array
Gain	47.7 dB
Beam width	0.71 x 0.71 degs.
Aperture	2.2 m x 2.2 m
Sidelobe level	less than -35dB
Scan angle	± 17.0 degs.
Transmitter	
Type	SSPA (x 131)
Peak power	572.1 W
Pulse width	1.67 μ s
PRF (Variable PRF *1)	4126 Hz
Receiver	
Noise figure	2.5 dB
Band width	0.78 MHz
Dynamic range	More than 70 dB
Smin	-112.6 dBm
Required S/N	0 dB
Total system loss	2.0 dB
Number of independent samples (Variable PRF + Non-linear scan)	≅64
Data rate	85 kbps
Power consumption(*2)	224 W
Weight(*2)	328 kg

(*1) Margin due to the altitude variation of the satellite is assumed ±5.5 km.
(*2) Including margin

3. CONCEPTUAL DESIGN STUDY OF RAIN RADAR ON THE JAPANESE EXPERIMENT MODULE

The JEM comprises an important part of the International Manned Space Station Program. The altitude of JEM is 250 nautical miles (463 km) and the orbit inclination is 28.5° . This orbit inclination is suitable for the frequent observation of the tropical rainfall. JEM is a multipurpose experimental module which consists of a pressurized module (PM), exposed facility

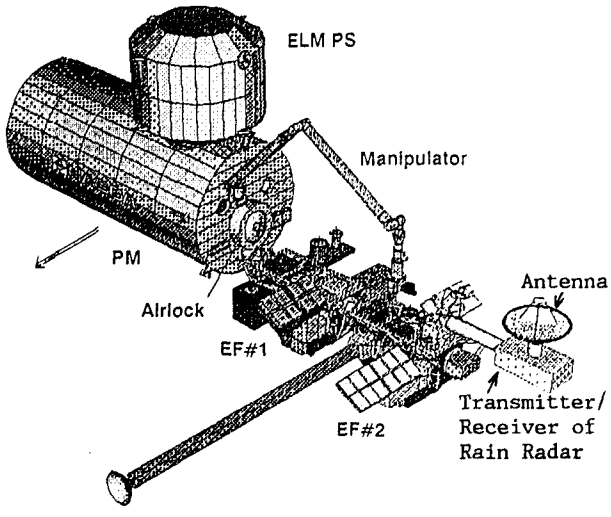

Fig.4 Baseline Configurations of JEM and Antenna, Transmitter and Receiver for Rain Radar

(EF) and experiment logistics module (ELM). Figure 4 shows the baseline configuration of JEM. Furthermore, observation from JEM provides the advantages of hands-on ease of maintenance and repair. Experiments in earth observation, solar system astronomy and the technology & physical science/ communication will be made at the exposed facility EF#1 and EF#2 shown in the Figure 4. In the earth observation experiment, three reference missions are now finally selected which affect the details of the EF. These three reference missions are the dual-frequency (10 GHz, 24.15 GHz) rain radar to observe tropical rainfall, lidar to observe atmospheric trace gases or aerosols and to measure three- dimensional wind velocity, and visible and IR multispectral vertical sounders to observe tropical land and ocean where the source of energy that drives the global climate system originates.

The rain radar experiment is closely related to the large antenna assembly and measurement experiment at the technology & physical science/communication experiment field. Figure 4 shows the large aperture antenna which will be assembled by the manipulator. As the first step of the development of a dual-frequency rain radar, a conceptual design of the rain radar was made by utilizing this antenna. The 10 GHz and 24.15 GHz frequencies were again selected according to the frequency allocation table of ITU. According to the mission requirements for the rain radar, a horizontal resolution of 4 km at nadir with a satellite altitude of 463 km and a range resolution of 300 m were selected. The swath width is 300 km. The mimimum detectable rain rate at the rain top is 1 mm/h at both 10 GHz and 24.15 GHz and a rain rate between 1 mm/h and 50 mm/h is expected to be measured at the rain bottom at 10 GHz, with a signal-to- noise ratio of 3 dB. The main system parameters of the rain radar on JEM are shown in Table 2. A basic assumption is to use the Cassegrain parabolic antenna assembled by the technology & physical science/communication experiment. The same antenna is commonly used by both

Table 2. Main System Parameters of the Rain Radar on JEM

	X-band	K-band
Frequency	10 GHz	24.15 GHz
Antenna		
Type	Cassegrain antenna commonly used for both frequencies	
Aperture	4.4 m	1.8 m
Gain	50.2 dB	50.2 dB
Beam width	0.5 x 0.5 degs	0.5 x 0.5 degs
Sidelobe level	-30 dB	-30 dB
Scan angle	± 18.0 degs.	± 18.0 degs.
Transmitter		
Type	TWTA	TWTA
Peak power	500 W	200 W
Pulse width	2μs	2μs
PRF (fixed)	3046 Hz	3046 Hz
Receiver		
Noise figure	2.5 dB	3.0 dB
Band width	0.6 MHz	0.6 MHz
Smin	-113.7 dBm	-112.2 dBm
Required S/N	3 dB	3 dB
Total system loss	2.0 dB	2.5 dB
Number of independent sample	24 multiplied by integers	24 multiplied by integers
Data rate	186 kbps	186 kbps
Power consumption	610 W	
Weight	420 kg	

frequencies, and the TWTA is selected for the transmitter. The matched beam antenna system is used to reduce the effective aperture size at K-band. It is planned to scan the sub-reflector of the Cassegrain antenna mechanically in this type of radar in order to reduce the reaction caused by the antenna scanning. An important activity will be to establish the algorithm for retrieval of rain rate from the dual-frequency rain radar on planned for JEM by comparing this sensor's data with ground truth data.

In addition to this class rain radar, system designs for two more advanced types of radars have been made. Both radars adopt electric scanning-type phased-array antennas. They are, (1) an offset parabolic cylindrical antenna with the SSPAs and (2) a planar array antenna with SSPAs (the same type radar as that of TRMM).

4.CONCLUSIONS

Conceptual designs for the rain radars on TRMM and on JEM were briefly shown. The TRMM rain radar adopts an active array radars at 13.8 GHz. The critical components of this type of radar are the solid state elements of the transmitters and receivers and slotted wave-guide antenna. The development of these critical components at the BBM level is now being made at CRL. Also a preliminary design of the TRMM rain radar will be made. A more detailed system design of rain radar on JEM will also be made to meet the mission requirements.

REFERENCES

(1) K.Okamoto et al., "A feasibility study of rain radar for the Tropical Rainfall Measuring Mission", J. Commun. Res. Lab., Vol. 35, No. 145, pp.109-208, 1988.

(2) Marzoug,M., P. Amayenc and N.Karouche, "Design of a spaceborne radar for tropical rain mapping at the climatological scale" Proc. of IGARSS'88, pp.247-248, 1988.

(3) G.R. North et al., "Tropical Rain Mapping Radar(TRAMAR), A proposal to the NASA for the A.O. No. OSSA-1-88 on the EOS", Vol.1, 1988.

DETECTION OF THE DIURNAL CYCLE IN RAINFALL FROM THE TRMM SATELLITE

Thomas L. Bell

Laboratory for Atmospheres / Code 613
Goddard Space Flight Center
Greenbelt, MD 20771

1. INTRODUCTION

The statistics of rainfall change with the time of day, responding to the daily passage of the sun. The nature of this *diurnal cycle* varies from region to region on the earth and from season to season. Determining this variability is important both for comparing predictions of atmospheric models to actual atmospheric behavior and for making sure that estimates of total rainfall from low-altitude satellites are not biassed because of the nonuniformity of their temporal coverage. Randall (1989) has recently described general circulation model results for the diurnal cycle.

NASA is exploring the possibility of mounting an experiment specifically designed to obtain the climatology of rain rates in the tropics, the Tropical Rainfall Measuring Mission (TRMM). Although there are no data from the proposed TRMM satellite to work with yet, we can ask how well the diurnal cycle in rainfall will be detectable when the satellite is eventually collecting data, given the satellite's proposed sampling characteristics. We shall discuss here analyzing data for the diurnal cycle, taking into account the fact that the satellite visits will be irregularly spaced in time. We shall also estimate the accuracy with which the first few harmonics of the diurnal cycle can be detected from several months of satellite data, using rainfall statistics observed during the Global-Atmospheric-Research-Program Atlantic Tropical Experiment (GATE).

A more detailed discussion of these ideas can be found in Bell and Reid (1989).

2. DETECTION OF THE DIURNAL CYCLE

The satellite passes over a given geographical location at times t_m, providing estimates $R(t_m)$ of the rain rate averaged over a given area, which we shall take to be of the order of 500 km × 500 km in size. (The times t_m are indexed by the integer m). From these observations we wish to discover how rain statistics vary with the time of day. We focus here on the variations in the climatic mean, expressing the variation as a Fourier series

$$\langle R(t)\rangle = r_0 + r_1\cos(\omega_d t - \varphi_1) + r_2\cos(2\omega_d t - \varphi_2) + \dots , \qquad (1)$$

where the angular brackets indicate a climatic average, r_0 represents the mean daily rainfall, r_1 and φ_1 are the amplitude and phase for simple sinusoidal variation of the mean, and $\omega_d = 2\pi/(24 \text{ hours})$ is the diurnal frequency. In order to simplify the discussion further, we shall neglect the higher harmonics in what follows, though they can be important in many areas of the world. It is not difficult to extend the treatment to include them.

The amplitude and phase of the diurnal cycle can be estimated from a month of observations with a least squares fit of (1) to the observations $R(t_m)$; that is, by minimizing

$$\sum_{m=1}^{N} [r(t_m) - R(t_m)]^2 \quad , \qquad (2)$$

where N is the number of satellite observations during the month. Having obtained such a fit, we must then decide whether the amplitude r_1 is statistically significant, given the sample size (1 month) from which it was obtained. A number of approaches have been suggested for determining the statistical significance of r_1. If the time series $R(t_m)$ is sufficiently long, the statistics of r_1^2 can be approximated by a chi-squared variable with two degrees of freedom,

$$r_1^2 \sim \frac{1}{2}\langle r_1^2\rangle \chi_2^2 \qquad (3)$$

where $\langle r_1^2\rangle$ is the estimated mean square amplitude under the null hypothesis that there is no diurnal cycle. This may be estimated directly from the data set by breaking the time series up into small sections, assumed to be uncorrelated with each other, and using the variance of the diurnal amplitude among the various sections as an estimate. Press and Teukolsky (1988) discuss this problem further. Zwiers and Hamilton (1986) suggest using the power spectrum at frequencies near ω_d. Bell and Reid explore modeling the time series as an autoregressive process to estimate $\langle r_1^2\rangle$.

3. DETECTABILITY OF GATE-LIKE DIURNALITY

In order to evaluate TRMM's ability to establish diurnal cycles in tropical rain, some representative data are needed. The GATE data were taken in the neighborhood of the Inter-Tropical Convergence Zone (ITCZ) during the summer of 1974 off the west coast of Africa. Although these statistics may not be entirely representative of what may be found in the ITCZ further away from the continents, the data are well studied and provide areally averaged rain rates within a 400 km diameter circle. Data being collected in preparation for TRMM from various radar sites may help soon in learning about the variability in tropical rain statistics.

Areally averaged rain rate in Phase I of GATE, covering June 28 to July 16, has mean 0.49 mm/h and variance 0.51 mm^2/h^2. The least squares fit yields r_1 = 0.22 mm/h peaking at about 2:30 in the afternoon local time (1600 UT). A correlation time of approximately 8 hours is found for the areally averaged rain rate, and, if the approach in Bell and Reid (1989) is followed with the assumptions described above, the amplitude of the diurnal cycle is significant at p = 0.03. GATE Phase II, covering July 26 to August 13, shows a diurnal amplitude of

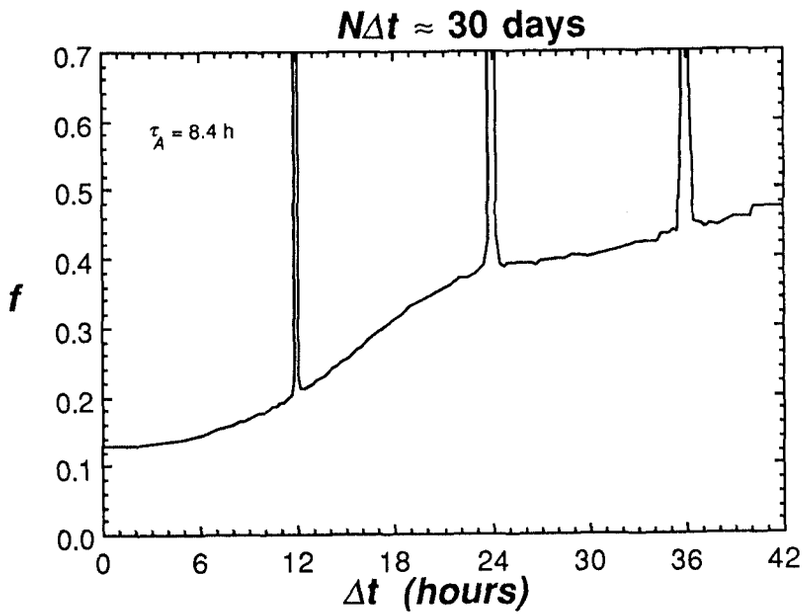

Fig. 1. Plot of $f(N, \Delta t, \tau_A)$ in Eq. (4) as a function of sampling interval, for τ_A = 8.4 hours, using one month of data.

only 0.11 mm/h. The variance is also smaller, but not small enough to make the diurnal amplitude statistically significant for Phase II. (It is also noteworthy that the fits to the 12-hour cycle—the "semi-diurnal" cycle—have negligible amplitudes and are not statistically significant in either Phase.)

In order to determine how small a diurnal cycle can be detected by the TRMM satellite, we need to estimate the quantity $\langle r_1^2 \rangle$ for satellite observations. It is in general a complicated function of the precise sequence of observing times t_m of the satellite. However, near the equator the satellite visits an area at approximately equally spaced times slightly less than 12 hours apart (although it does not always view the entire area), such that during the course of a month the area is viewed during most of the hours of the day. We can easily calculate $\langle r_1^2 \rangle$ assuming equally spaced observations and a temporal autocorrelation of the area-averaged rain rate that decreases exponentially with lag. With these assumptions $\langle r_1^2 \rangle$ can be written as

$$\langle r_1^2 \rangle = \sigma_A^2 f^2(N, \Delta t, \tau_A) \quad , \qquad (4)$$

where σ_A^2 is the variance of area-averaged rain rate, Δt is the interval between satellite observations, τ_A is the correlation time of the area-averaged rain, and N is the number of observations during the month.

Extrapolation of GATE statistics to areas larger than the GATE area is discussed in detail in Bell *et al.* (1989). For an area of size 600 km × 600 km we shall assume the variance σ_A^2 to be about 1/4 of the variance seen in GATE-sized areas (~ 300 km × 300 km). If we take the correlation time to be 8.4 hours, which is a straightforward estimate of the autocorrelation time of area-averaged GATE rain rates obtained by Bell and Reid (1989), we can compute f in (4) as a function of Δt. It is shown in Fig. 1. For Δt in the neighborhood of 12 hours (but different enough from 12 hours that the entire diurnal cycle is observed during a month) we see that $f \approx 0.2$. Using the 5% critical value $\chi_2^2 \approx 6.0$ in (3), we find that a diurnal amplitude $r_1 = 0.12$ mm/h could be detected: that is, a diurnal cycle whose amplitude is 25% of the mean could be detected at the 0.05 significance level. The diurnal amplitude found in GATE I, discussed above, would be easily detectable with the satellite. This result is not sensitive to our choice for τ_A, but is sensitive to the estimate of σ_A^2.

4. CONCLUSION

The TRMM satellite appears able to provide good estimates of the diurnal cycle, especially if data are averaged over larger areas and longer time periods. It will however be important to learn how rain rate statistics in different locations and seasons may differ from what was found in GATE, and to evaluate how much our conclusions may be affected by these differences.

5. REFERENCES

Bell, T.L., A. Abdullah, R.L. Martin, and G.R. North, 1989: Sampling errors for satellite-derived tropical rainfall: Monte Carlo study using a space-time stochastic model. Submitted to *J. Geophys. Res. (Atmos.)*.

Bell, T.L., and N. Reid, 1989: Statistical problems in rainfall measurements from space. Submitted to *J. Amer. Stat. Assoc.–Appl.*

Press, W.H., and S.A. Teukolsky, 1988: Search algorithm for weak periodic signals in unevenly spaced data. *Computers and Physics 2*, 77-82.

Randall, D.A., 1989: Why is there a diurnal cycle of precipitation over the oceans? Presented at the Symposium on the Rôle of Clouds in Atmospheric Chemistry and Global Climate, Jan. 29 - Feb. 3, Anaheim, California, sponsored by the American Meteorological Society.

Zwiers, F. and K. Hamilton, 1986: Simulation of solar tides in the Canadian Climate Centre general circulation model. *J. Geophys. Res. 91D*, 11877-11896.

COMPARING RAIN ESTIMATION DESIGNS

Gerald R. North and Shoichiro Nakamoto
Climate System Research Program
College of Geosciences
Texas A&M University
College Station, TX 77843-3146

1. INTRODUCTION

Space-time averages of rain rates are needed in several applications, but are difficult to estimate because the methods always leave gaps in the measurements in space or time. Usually one must be content with certain sparce sampling designs on the area-time volume. The problem is exacerbated by the complicated and largely unknown statistical structure of rain rate fields. These evolving fields may be considered as space-time stochastic processes, but the statistics are hardly of the type routinely encountered in most applications. For example, they exhibit an extreme deviation from gaussian. Most of the probability is concentrated in a spike at zero rain rate-- it is only raining a few percent of the time at a point (or over a small area) in space. To further complicate matters the continuum part of the pdf is reasonably close to lognormal, a distribution known to have a rather fat tail (Kedem and Chiu, 1987).

The point to point autocorrelation structure of rain rate fields is also problematic. Studies from the GATE [GARP (=Global Atmospheric Research Programme) Atlantic Tropical Experiment] rain data set (Hudlow and Paterson, 1979) show that the correlations are not of a simple short range type, but rather tend to be power law dependent over a range from 4 km separation out to possibly 70 km (Bell, 1987; Bell et al., 1988). The autocorrelation times for area average rain rates depend strongly upon the magnitude of the area, being nearly a linear increase with length of the cell (Bell, 1987; North, 1987).

There is clearly a need to have better measurements of the statistical properties of rain rate fields to help in arriving at sensible sampling designs, but we are left at this time with pitifully few observations of the type necessary to answer all of our design questions. Unfortunately, the need to acquire area-time data sets over the whole globe for the applications mentioned above, especially those requiring large expenditures for space-based observational programs, force us to take up the problem even with incomplete knowledge of rain rate statistics in space and time. We have especially in mind the meeting of recently discussed requirements of the atmospheric dynamics community for a precipitation data set that is of about 15% accuracy for month averages and for areas of about 500 by 500 km (Simpson et al., 1988). For example, we wish to know how many rain gages are necessary in such an averaging cell to ensure that the sampling errors (and instrument errors) will not exceed the tolerances set by the users. There is also the possibility of measuring the precipitation rates from low orbiting satellites that pass over the averaging cell. The sampling scheme of such a spaceborne sensor is very different from the gages in that the satellite returns to the cell after finite intervals (close to 12 hours) and takes a snapshot of the entire cell (or some fraction of its area). Hence, this design is gappy in time but continuous in space -- quite the opposite of the gage design which is gappy in space but continuous in time.

In this study we present a formalism that allows the computation of sampling errors because of space-time gaps through an expression that is essentially a design-dependent filter that acts upon the space-time spectrum of the rain rate field. This allows a clear separation of the rainfield structure and the design problems.

2. SPECTRAL FORMALISM

Consider a random field $\psi(\vec{r}, t)$ defined in the x, y plane and along the time axis, t. Let the ensemble average of $\psi(\vec{r}, t)$ be zero and its variance at a point in space-time be σ^2. In most of what follows we will be interested in space-time averages of $\psi(\vec{r}, t)$,

$$\Psi \equiv \frac{1}{TL^2} \int_{-\frac{L}{2}}^{\frac{L}{2}} \int_{-\frac{L}{2}}^{\frac{L}{2}} \int_{-\frac{T}{2}}^{\frac{T}{2}} \psi(\vec{r}, t)\, dx\, dy\, dt$$

We assume the field $\psi(\vec{r}, t)$ is statistically homogeneous and isotropic in space and stationary in time; its ensemble mean can be taken as zero The ensemble mean of Ψ, denoted $\langle\Psi\rangle$, vanishes. The variance of Ψ can be computed from

$$\langle\Psi^2\rangle = \frac{1}{(L^2T)^2} \iiiint\!\!\int \langle\psi(\vec{r}\,', t')\psi(\vec{r}, t)\rangle d^2\vec{r}\,'\, d^2\vec{r}\, dt\, dt'$$

where the integrals run over the volume of the space-time box. The integrand above is the space-time lagged covariance. For spatially homogeneous and temporally stationary fields this function is a function only of $\vec{\xi} = \vec{r} - \vec{r}$, and $\tau = t - t'$. We denote the lagged covariance by

$$\langle \psi(\vec{r}\,', t')\psi(\vec{r}, t)\rangle = \sigma^2 \rho(\vec{\xi}, \tau)$$

where $\rho(\vec{\xi}, \tau)$ is the space-time lagged autocorrelation. We define the normalized wave number-frequency spectrum of the space-time field by the Fourier Transform (FT) of the autocorrelation

$$S(\vec{v}, f) = \iiint \rho(\vec{\xi}, \tau) e^{2\pi i(\vec{\xi}\cdot\vec{v} + f\tau)} d^2\vec{\xi} d\tau$$

where the integrals run over all space. It follows that

$$\iiint S(\vec{v}, f) d^2\vec{v} df = \rho(0, 0) = 1$$

Also of interest is the FT of the field itself

$$\tilde{\psi}(\vec{v}, f) = \iiint e^{2\pi i(\vec{v}\cdot\vec{r} + ft)} \psi(\vec{r}, t) d^2\vec{r} dt$$

and its FT inverse

$$\psi(\vec{r}, t) = \iiint e^{-2\pi i(\vec{v}\cdot\vec{r} + ft)} \tilde{\psi}(\vec{v}, f) d^2\vec{v} df$$

where again all three limits are from minus to plus infinity. Using the above Fourier Transform pair, the normalized spectrum can be expressed in terms of the inverse FT as follows:

$$\langle \tilde{\psi}(\vec{v}', f')\tilde{\psi}(\vec{v}, f)\rangle = \sigma^2 \delta^{(2)}(\vec{v}' - \vec{v})\delta(f' - f) S(\vec{v}, f)$$

In deriving the last formula we made use of the well-known formula:

$$\int_{-\infty}^{\infty} e^{ikx}\, dx = 2\pi\delta(k)$$

After some rearrangements we may construct the variance of the space-time average:

$$\langle \Psi^2\rangle = \sigma_V^2 =$$
$$\sigma^2 \iiint G(\pi v_1 L)^2 G(\pi v_2 L)^2 G(\pi f T)^2 S(\vec{v}, f) d^2\vec{v} df$$

where $G(\pi x)^2 \equiv (\sin(\pi x) / \pi x)^2$ is familiar from time series analysis (Blackman and Tukey, 1959). An interpretation of (10) is that the space-time box averaging of the field is represented as a three dimensional low pass filter acting on the space-time power spectrum of the field.

Also of interest is the spatial average of the random process over the cell area L^2. The variance of the spatial average can be represented in a similar form:

$$\sigma_A^2 = \sigma^2 \iiint G(\pi v_1 L)^2 G(\pi v_2 L)^2 S(\vec{v}, f) d^2\vec{v} df$$

Clearly, $\sigma_V^2 \le \sigma^2$ and $\sigma_A^2 \le \sigma^2$, since $\iiint S(\vec{v}, f) d^2\vec{v} df = 1$ and $G^2 \le 1$, $S \ge 0$. Note that S has units $(length)^2 time$.

An intent of this paper is to systematically analyze the errors incurred in estimating Ψ by various statistical measurement designs. For example, one design of interest is that of a low altitude satellite that passes over the area L^2, taking an instantaneous area average, then returning at intervals Δt until the entire period T is covered. The snapshot area-means are then averaged to form an estimate of the space-time average over the volume $L^2 T$.

3. MEAN SQUARED ERRORS AND SAMPLING DESIGNS

Consider the satellite overflight case discussed above. The estimator may be written

$$\Psi_S = \frac{1}{NL^2} \sum_{n=0}^{N-1} \iint \psi(\vec{r}, (n + \tfrac{1}{2})\Delta t) d^2\vec{r}$$

where N is the total number of visits in the averaging interval ($T = N\Delta t$) and the integral is over the box . The last expression can also be written

$$\Psi_S = \frac{1}{L^2 T} \iiint K(\vec{r}, t)\psi(\vec{r}, t) d^2\vec{r} dt$$

where

$K(\vec{r}, t) = \Delta t \sum \delta(t - (n - \tfrac{1}{2})\Delta t)$ is a kernel representative of the discrete time sampling design.

Now consider the mean square error made in estimating Ψ using this design

$$\varepsilon^2 = \langle (\Psi - \Psi_S)^2 \rangle$$

Using the Fourier representation we may write

$$\varepsilon^2 = \iiint |H(\vec{v}, f)|^2 S(\vec{v}, f) d^2\vec{v} df$$

This is the desired form which indicates the error as a filtered integral over all frequencies and wave numbers of the space-time spectrum of the geophysical process. Note that the information about the design and the properties of the rain rate field are clearly factored.

Specifically in the case of the satellite design

$$|H_S(\vec{v}, f)| = G(\pi v_1 L) G(\pi v_2 L) G(\pi f T)\left(1 - \frac{1}{G(\pi f \Delta t)}\right)$$

The most important factor in $|H(\vec{v}, f)|^2$ is $G(\pi f T)^2 \left(1 - \frac{1}{G(\pi f \Delta t)}\right)^2$ which can be written

$$B(f) = \frac{\sin^2(\pi f N \Delta t)}{N^2 \sin^2(\pi f \Delta t)} (1 - G(\pi f \Delta t))^2, \quad N\Delta t = T \qquad (\#)$$

This form is easily analyzed if it is noted that

$$\lim_{N \to \infty} \frac{\sin^2 N\pi\Delta t f}{N \sin^2 \pi\Delta t f} = \frac{1}{\Delta t} \sum_{n=-\infty}^{\infty} \delta\left(f - \frac{n}{\Delta t}\right)$$

which is a series of spikes at $f = \frac{n}{\Delta t}$, for all positive and negative integers n; it is known as the Dirac comb (Blackman and Tukey, 1959). The second

factor in (#) is unity at each of the spikes except at n= 0, where it vanishes. Thus, the error becomes to a very good approximation

$$\varepsilon^2 \approx \frac{\sigma^2 \alpha}{L^2} \frac{1}{N\Delta t} \int df \sum_{n=01} \frac{\delta(f - \frac{n}{\Delta t})}{1 + 4\pi^2 f^2 \tau_0^2} \tag{20}$$

In the special case of interest, $N\Delta t = T$, $\Delta t \approx \tau_0$, $N = 60$. The product of (#) and the spectrum are schematically depicted in Fig. 1, but for $N = 10$. Note that the spikes are 6 times narrower for $N = 60$. This figure shows clearly how well the series converges. Using (#) we may write

$$\varepsilon^2 \approx \sigma_A^2 \frac{1}{\pi^2} \frac{\Delta t}{T} \frac{\Delta t}{\tau_0}$$

Inserting the numbers: $\varepsilon \approx .04\,\sigma_A$; in other words the error is expected to be about 4 % of the area average rain rate standard deviation. Scaling our results to account for the fact that satellites only visit part of the square on each visit and the fact that larger boxes are nominally used in the satellite application, we arrive at an error of 10.4% which agrees with recent studies by Bell et al. (1988) and Shin and North (1988).

It is interesting to return to the interpretation of (#). Consider the meaning of the sum contributing to mean square error. Note that the sum consists of contributions from the power spectrum at harmonics (Fig. 1) of the frequency $\frac{1}{\Delta t}$, twice the so-called Nyquist frequency. The smaller the

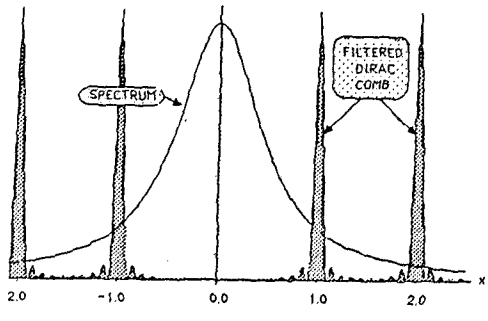

Figure 1. The filter $B(f)$ with a plot of the temporal spectrum for zero spatial wave number. Note that the filter picks up contributions to the error from the temporal spectrum at twice the Nyquist frequency and all of the harmonics of it. Since the spectrum falls off as the square of frequency, the series of contributions picked up by the Dirac Comb converges rapidly.

spectrum is at frequencies above this important value, the smaller will be the error. In fact, if the spectrum is zero above some critical frequency that is below the Nyquist frequency, there will be no error; this is equivalent to the famous "sampling theorem", well known in communications theory (e.g., Blackman and Tukey, 1959). The conclusion is that the errors will be quite small ($\approx 4\%$) when the satellite revisit time is the same as or smaller than the autocorrelation time for the time series generated area average of the field.

4. CONCLUSIONS

We have presented a formalism that should prove useful in future studies that evaluate sampling strategies for geophysical fields. The formalism is simple and intuitive: factoring the dependence of the physical phenomenon (space-time spectrum) away from the dependence on the measurement design (spectrum filter). We find small (about 5%) sampling errors for a satellite design that makes cell-wide snapshot evaluations of the averaging cell about once every autocorrelation time for the large scale field.

We believe the formalism presented here can be used in several studies involving rain parameter estimation. For example, one can take into account the actual satellite visiting sequence and its partial covering of cells on individual visits by suitable random variable techniques. One can also take into account the measurement errors associated with individual instruments such as thermal noise in microwave radiometers. The formalism can be extended to evaluate designs for estimating diurnal harmonic amplitudes as well as various low frequency oscillitory phenomena in the global atmospheric system. A similar formalism can be used in modeling the ground truth process in satellite retrievals. Finally, optimum weighting strategies can be developed for combining designs into grander systems. We anticipate that some restrictions such as the spatial homogeneity assumption can be relaxed with the use of location dependent spatial correlation statistics and their associated expansion functions.Another interesting example of use of the formalism is to construct the analogous filter for a regular array of rain gages. This problem also has a simple analytical solution (North and Nakamoto, 1989)

REFERENCES

Bell, T. L., 1987: A space-time stochastic model of rainfall for satellite remote-sensing studies. J. Geophys. Res. Atmos., Vol.92, No. D8, pp. 9631-964, August 20, 1987.

Bell, T. L., A. Abdullah, R. Martin and G. R. North, 1988: Monte Carlo study of sampling errors for satellite-derived tropical rainfall using space-time stochastic model. Submitted to J. Geophys. Res.

Blackman, R. B. and J. W. Tukey, 1959: **The Measurement of Power Spectra**. Dover Publications, New York, 190 pp.

Hudlow, M. and V. Paterson, 1979: GATE Radar Rainfall Atlas. NOAA Special Report, available from U.S. Government Printing Office, Washington, DC 20402, 158 pp.

Kedem, B. and L. Chiu, 1987: On the lognormality of rain rate. Proc. Nat. Acad. Sci., February issue.

North, G. R., 1987: Sampling studies for satellite estimation of rain. Tenth Conference on Probability and Statistics. Oct. 4-5, 1987. Edmonton, Alta., Canada. Published by the Am. Meteor. Soc., Boston, Mass.

Shin, K.-S. and G. R. North, 1989: Sampling error study for rainfall estimates by satellite using a stochastic model. Tenth Conference on Probability and Statistics. Oct. 4-5, 1987, Edmonton, Alta., Canada. Published by the Am. Meteor. Soc., Boston, Mass.

Simpson, J., R. Adler and G. R. North, 1988: On some aspects of a proposed tropical rainfall measuring mission (TRMM). Bull. Meteor. Soc., Vol. 69, No. 3, March 1988.

COMPARISON OF RAINFALL PROFILES RETRIEVED FROM DUAL-FREQUENCY RADAR AND FROM COMBINED RADAR AND PASSIVE MICROWAVE RADIOMETRIC MEASUREMENTS

J. A. Weinman

Applied Research Corp.
8201 Corporate Dr. #920
Landover, MD 20785

R. Meneghini

Code 675
Goddard Space Flight Ctr
Greenbelt, MD 20771

K. Nakamura

Communication Research Lab.
2-1 Nukui-Kitamachi, 4 Chome
Tokyo, Japan 184

1. INTRODUCTION:

Latent heat is a prominent component of the energy budget of the tropical atmosphere. Trenberth et al. (1988) recently demonstrated that rainfall anomalies off the coast of Peru in early 1988 contributed to the north American drought later that year. A crucial consideration in their study was knowledge of the altitude at which the latent heat was released into the atmosphere. A space-borne Tropical Rain Measuring Mission, TRMM, is under consideration to provide climatological data on tropical precipitation, see Simpson et al.(1988). This satellite mission will employ a radar that operates at 14 GHz. and a dual polarized, multispectral passive radiometer that operates at 18, 22, 37 and 85.6 GHz.

The following study presents an analysis of data from a dual frequency X and Ka band radar and an X band radiometer. The precipitation profiles retrieved from combined radar and microwave radiometer measurements are compared to those derived only from dual frequency radar measurements to determine the performance of the combined radar-radiometer precipitation retrievals. Because of size and weight limitations on antennae as well as resolution considerations, airborne radars operate at higher frequencies than those employed by operational ground-based weather radars. As a consequence, attenuation is a serious limitation on the retrieval of rainfall profiles. The present study illustrates a method to retrieve rainfall rate profiles from attenuated radar returns and passive radiometric data. This data was obtained from flights that occurred during a 1985-1986 Communications Research Laboratory/NASA rain measuring experiment near Wallops Island, VA. over the Atlantic Ocean.

2. RADAR AND RADIOMETRIC INSTRUMENTATION:

The X and Ka band radar and radiometer that was used in this study have been described by Okamoto et al.(1982). The characteristics of the radar -radiometer system are described in Table 1.

TABLE 1. Characteristics of the C.R.L. Airborne Sensor

	X Band	Ka Band
Radar:		
Frequency (GHz.)	10	34.45
Magnetron Peak Power (Kw.)	20	10
Pulse Repetition Freq. (Hz.)	440	440
Pulse Duration (μs)	0.5	0.5
Receiver Bandwidth (MHz.)	2	2
Receiver Noise Figure (dB.)	5.3	9.6
Dynamic Range (dB.)	80	80
Antenna,Offset Paraboloid: (Common to both radiometer and radar.)		
Diameter (cm)	26	7.5
Scan Angle* (°)	± 23 (operated at nadir in this study)	
* Note that all devices could view nearly the same rain volume.		
Gain (dB)	26	26
3 dB Beamwidth (°)	8.0x8.0	8.0x8.0
Radiometer:		
Type, Null-balancing Dicke.		
Noise Figure (dB)	6	
Integration Time (s.)	.25	
Temperature Resolution (K)	.5	
Absolute Accuracy (K)	± 2	
Dynamic Range (K)	50 - 400	

3. THEORY OF PRECIPITATION RATE PROFILE RETRIEVALS:

3. A. 1) Retrieval of the Path Integrated Extinction from X Band Radiometry

The extinction coefficient, k(z), in dB/km is a function of altitude, z, measured from the ground in the subsequent development. The extinction coefficient consists of three components, namely: $k_l(z)$, $k_i(z)$ and $k_{cl}(z)$, the extinction coefficients of the liquid hydrometeors, the ice hydrometeors and the nonprecipitating cloud droplets respectively. We assume that the extinction coefficients depend upon the rainfall rate, R, as:

$$\bar{k}\ (\mathrm{dB/km}) = \alpha * R^{\beta} \quad (\mathrm{mm/h}) \tag{1}$$

where the constants α and β depend upon the frequency of the radiation and the phase of the hydrometeors. These constants are presented in Table 2. The values for liquid hydrometeors are taken from Atlas et al. (1984) and those for ice hydrometeors are fitted to the theoretical results of Kummerow and Weinman (1988).

The values of the extinction coefficient of the nonprecipitating liquid cloud drops are also presented in Table 2. The nonprecipitating liquid droplets are assumed to be uniformly distributed with a density of .4 gm/m³ from the cloud base at 2 km to the top of the rain cloud, z*, or to the flight altitude, H, whichever was the lowest.

The extinction coefficient of the precipitation only is:

$$\bar{k}(z) = k(z) - k_{cl}(z) \tag{2}$$

A first order estimate of the rain within the cloud was obtained from a radiative transfer model that relates the X band emitted radiance to the path integrated extinction:

$$\tau(\mathrm{dB}) = \int_0^{z^*} \bar{k}(z')\, dz' = \bar{k}\ z^* \tag{3}$$

where $\bar{k}(z)$ is the X band extinction coefficient of the rain and $\bar{k}$ is its mean value. The X band extinction coefficient is relatively insensitive to ice hydrometeors that have a small scattering coefficient. Heights are identified in Fig. 1.

The temperature profile is assumed to diminish linearly at a lapse rate of 6.5 K/km from the value at the surface, namely 20°C. The assumed sea surface temperature is 15°C. The value of z* is thus 3.5 km.

TABLE 2: Parameters used to compute radiative quantities.

	Liquid		Ice	
Frequency (GHz)	10	35	10	35
α (dB/km)	1.30 (-2)	.219	2.42 (-4)	1.28 (-2)
β	1.16	1.04	1.22	1.42
D (mm³/m³)	275	450	4.1 (3)	1.0 (4)
d	1.55	1.15	1.00	.84
k(dB/km)(0°C)	3.67 (-2)	.416	---	---
$\lvert K_{cl}\rvert^2$ (0°C)	.928	.882	.197	.197

* The radiative parameters for liquid water were computed at the ambient temperatures for each level; the values at 0°C are selected to be representative.

A one layer plane parallel radiative transfer model was used to compute the X band radiances in units of brightness temperature as a function of slant path integrated extinction, τ/μ, where μ is the cosine of the viewing angle. The model assumed that only liquid hydrometeors were present up to the level, z*. Details of the derivation of that model were presented by Weinman and Davies (1978).

The present analysis requires the inverse result, namely the path integrated extinction as a function of X band radiance. A simple analytical expression that was fitted to the model output can be used for that purpose; it is accurate to 5%:

$$\tau/\mu\ (\mathrm{dB}) = 7.12 - 1.42 \ln[\ 263.3 - I(K)\ ] \tag{4}$$

$$110\ K < I < 257\ K$$
$$0.7 < \mu < 1$$

3.A. 2) Derivation of the Path Integrated Extinction in the Ka Band

Once the mean rainfall rate, $\bar{R}$, within the rain column is determined from the X band radiometric measurements by Eqs. (1), (3) and (4) the slant path extinction can be derived for subsequent Ka band radar retrievals by employing those same equations with the α and β appropriate to 35 GHz, see Table 2.

3.A. 3) Derivation of the Path Integrated Extinction by Dual Frequency Radar Methods Only

Using radar data only, the path integrated attenuation was determined by means of a dual wavelength surface reference technique, DSRT, over the ocean, see Meneghini and Atlas (1986). These measurements provide a validation of the radiometrically derived τ.

For a down viewing air-borne radar in the presence of rain along the beam, the backscattered power from the surface depends upon the path integrated extinction along the beam and the scattering cross section of the surface, σ. Because both τ and σ are unknown, a measurement made at a neighboring rain free location, $\bar{\sigma}$, can provide an estimate of σ. If the surface returns exceed both the rain echo and the receiver noise at the range corresponding to z = 0, then the largest source of error arises from fluctuations in $\bar{\sigma}/\sigma$. Data taken over a wind roughened ocean at wind speeds between 1 and 20 m/s produce a change that is less than 10 dB, see Jones et. al. (1977).

In the dual frequency version of this method, the differential path integrated attenuation estimate takes the form:

$$\Delta\tau = \int_0^{z^*} [\, k_{35}(z') - k_{10}(z') \,]\, dz' \qquad (5)$$

$$= \frac{1}{\gamma} \ln\left[\tilde{P}_{35}(0)\, P_{10}(0) \,/\, P_{35}(0)\, \tilde{P}_{10}(0) \right]$$

where $P_i(0)$ and $\tilde{P}_i(0)$ are the powers reflected from the sea surface, $z = 0$, beneath the rain column and from a nearby rain free region respectively at the frequencies designated by i and $\gamma = .461$.

The primary advantage of the DSRT is that the variance of the of the estimate of $\Delta\tau$ is reduced to the extent that σ is correlated at the two frequencies.

3.B. 1) Retrieval of Rainfall Extinction Profiles from Radar Returned Power

The nadir viewing radar measures returned power that is described by the radar equation:

$$P(z) = \frac{C\, |K|^2 Z(z) \exp(-\gamma \int_z^{z^*} k(z')\, dz') + \bar{e} + e'}{(H - z)^2} \qquad H > z^* \qquad (6)$$

where P(z) is the power received by the airborne radar at height, H, that has been singly scattered from height z. The liquid hydrometeor cloud extends to a height of z*. If the aircraft flight altitude, H, is less than z*, then z* must be replaced by H. A minor problem must be overcome if z* > H, namely the radar does not respond to precipitation within 500 m of the aircraft. The rain within that range interval extinguishes the backscattered signal but no scattered signal can be measured, see Fig. 1. The constant, C, contains instrument parameters.

Noise in the instrument consists of a mean value that can be subtracted from the measured power, $\bar{e}$, and a part that is undetermined and therefor cannot be subtracted from the measured power, e'.

The backscattering at 180° is proportional to, $|K|^2 Z(z)$. This quantity varies with altitude and its value depends phase and the rainfall rate of the hydrometeors.

$$Z = D * R^d \ (\text{mm/h}) \qquad (7)$$

For heights less than z* all of the hydrometeors are assumed to be liquid and the hydrometeors are assumed to be dry graupel above z_m. The dependence of the backscattering coefficients, D and d, on the rainfall rate are taken from the work of Douglas (1964), see Table 2.

The term, $|K|^2$, depends upon the phase of the hydrometeors, see Table 2.

An effective reflectivity can be defined at each frequency.

$$\zeta(z) = |K|^2 * Z(z) \,/\, \bar{k} \qquad (8)$$

The quantity, $\zeta(z)$, is relatively insensitive to the rainfall intensity; however a first guess can be provided from the mean rainfall rate, $\bar{R}$, obtained from the X band radiometric brightness temperature provided by Eqs. (3) and (1).

The received power is corrected for range and extinction due to nonprecipitating drops, and the mean noise, $\bar{e}$, is removed:

$$S(z) = (P(z) - \bar{e})\ (H - z)^2 \exp(\gamma \int_{(z-2)}^{z^*} k_{cl}(z')\, dz') \,/\, (C\, \zeta(z)) \qquad (9)$$

Inserting Eq.(9) into Eq.(6) yields:

$$S(z) = \tilde{k}(z) \exp(-\gamma \int_z^{z^*} \tilde{k}(z')\, dz') \qquad (10)$$

which is a function of the extinction coefficient of the hydrometeors only.

Taking logarithms of both sides of Eq. (10) and differentiating that equation with respect to z, yields a Bernoulli equation whose solution was presented by Hitschfeld and Bordan (1954). They used the value of the extinction coefficient closest to the radar as a boundary condition. In the case of a nadir viewing radar, that is the extinction coefficient at the top of the precipitating cloud which is $\tilde{k}(z^*)$.

Another solution can be found by employing the path integrated extinction defined in Eq. (3) to derive the $\tilde{k}(z^*)$. Integrating the solution to the Hitschfeld-Bordan equation from 0 to z* yields:

$$\tilde{k}(z^*) = \frac{1 - \exp(-\gamma\tau)}{\gamma \int_0^{z^*} S(z') \,/\, S(z^*)\, dz'} \qquad (11)$$

Expressing $\tilde{k}(z^*)$ in terms of τ, permits Eq.(11) to be introduced into the Hitschfeld-Bordan equation to yield:

$$\tilde{k}(z) = \frac{S(z)\ [\, 1 - \exp(-\gamma\tau)]}{\gamma\, [\int_0^z S(z')\, dz' + \exp(-\gamma\tau) \int_z^{z^*} S(z')\, dz']} \qquad (12)$$

see Meneghini et al. (1983) and Weinman et al. (1988).

3.B.2) Optimal Rainfall Rate Profile from Returned Radar Power in the Presence of Noise

An analysis of errors in the extinction coefficient introduced by noise shows that the errors in the extinction coefficient are far greater near the surface than near the top of the rain column. This follows because the residual effects of noise are erroneously corrected for range squared and two way path attenuation.

In order to overcome the noise contamination problem we seek an optimal rainfall rate profile, $R_o(z')$, that simultaneously minimizes the effect of noise in the radar return and the departure of the optimal rainfall rate profile from the mean rainfall rate, $\bar{R}$, that was inferred from the radiometrically measured path integrated extinction, see Eqs. (1), (3), and (7).

This is achieved by defining a quantity that is minimized:

$$\psi_i = \int_0^{z^*} [R_o(z') - R_i(z')]^2 + \Lambda_i(z')\, [\, R_o(z') - \bar{R}_i \,]^2 dz' = \text{minimum} \qquad i = 10,35 \qquad (13)$$

where R(z') is the rainfall rate profile that is retrieved from the extinction coefficient profile computed from Eqs.(1) and (12). The index identifies the frequency in GHz that is being considered.

The Lagrange multiplier is proportional to the ratio of the two quadratic terms that appear in Eq. (13):

$$\Lambda_i(z') = \left[\frac{\bar{e}\ (H - z')^2\ R(z')}{C\ \zeta(z')\ S(z')\ \beta\ \bar{R}\ f} \right]_i^2 \qquad (14)$$

where f is an empirically adjusted fraction of $\bar{R}$ that provides an acceptable deviation of $R_o(z')$ from R. In practice, $f = 1$.

The optimal $R_{o,i}(z)$ is found by setting the derivative of ψ_i with respect of $R_{o,i}(z)$ to zero so that:

$$R_{o,i}(z) = \left[\frac{R(z) + \Lambda(z)\, \bar{R}}{[\, 1 + \Lambda(z)\,]} \right]_i \qquad (15)$$

As a final step, the $R_{o,i}(z)$ is renormalized so that its mean value is $\bar{R}$ between 0 and z*.

3.B.3) Retrieval of the Ice Hydrometeor Profile Above the Melting Layer

Only ice hydrometeors are assumed to exist above the -35C isotherm at z_m so that Eq. (6) can be used to determine the backscattering due ice hydrometeors.

The constant, C, that appears in Eq.(6) was determined by matching the returned power computed for a rainfall rate profile at $0 < z < z^*$ to the measured returned power, P(z), in that altitude interval.

The extinction due to ice hydrometeors can be neglected in the top most cloud layer and the backscatter coefficient can be used to derive the "rainfall rate" of that layer. The extinction that affects the return from the next layer can be derived from the preceding layer and the backscatter coefficient can be used to compute the "rainfall rate" of the ice hydrometeors in each layer down to z_m.

3.B.4) Retrieval of the Rainfall Rate in the Melting Layer

The extinction and backscattering coefficients in the melting layer are complicated functions of the rainfall rate because the phase of the hydrometeors is changing with height. Accordingly, the "rainfall rate" for $z_o < z < z_m$ is represented by a parabolic curve that is fitted in a least square sense to layers below z_o and above z_m.

3.B.5) Retrieval of Rainfall Profiles from Dual Frequency Radar Measurements Only

An optimizing procedure similar to that used in Eq. (13) et.seq. was used to obtain a rainfall rate profile from the combined dual frequency radar returns. The quantity

$$\psi_{DFR} = \int_0^{z^*} [\, R_o(z') - R_{35}(z')]^2 + \Lambda(z')\, [\, R_o(z') - R_{10}(z')]^2 dz' = \text{minimum} \qquad (16)$$

The Lagrange multiplier in this case is a proportional to the ratio of the two quadratic terms that appear in Eq. (16), i.e.

$$\Lambda(z') = \left[\frac{\bar{e}\ (H - z')^2\ R(z')}{C\ \zeta(z')\ \beta\ S(z')} \right]_{35}^2 \Bigg/ [f(z')\, R(z')]_{10}^2 \qquad (17)$$

where the denominator is proportional to the error introduced by the noise in the Ka band return. The numerator is proportional to the uncertainty in the rainfall rate retrieved from the X band radar; it is caused by hail or mixed phase precipitation that is most likely above 1 km. It is proportional to a fractional part, f(z'), of the rainfall profile, R(z'), retrieved by the X band radar.

Setting the derivative of ψ_{DFR} with respect to $R_o(z')$ to zero as before yields:

$$R_o(z) = \frac{R_{35}(z) + \Lambda(z)\, R_{10}(z)}{[\, 1 + \Lambda(z)\,]} \qquad (18)$$

Finally, the $R_o(z)$ is renormalized so that its mean value between 0 and z* is $\bar{R}$.

4. EXPERIMENTAL RESULTS AND DISCUSSION:

4.A) Determination of Path Integrated Extinction from Dual Frequency Radar and from Passive Radiometric Measurements:

The path integrated extinction was derived from the X band measured radiometric brightness temperature. The path integrated extinction was also determined by measuring the reflection of the radar power from the sea surface with both the X and Ka band radars. A comparison of the mean rainfall rates derived from Eqs. (1), (3) and (4) and Eqs. (1), (3), and (5) is presented in Fig. 2. For the cases considered here, the two techniques provide average rainfall rates that agree within about 25%. The mean rainfall rates for the sample studies that were used in this study are presented in the captions of Figs. (3-b) and (4-b).

4.B) Retrieval of Profiles of Rainfall Rates from Single Frequency Radar and Passive Radiometric Measurements and from Dual Frequency Radar Returns:

Examples of returned range squared corrected radar power and noise profiles are presented in Figs.3 and 4-a. Because the noise in the X band was negligible, only the Ka band noise is presented. We applied the algorithm to Ka band radar returns, even though we had to derive the path integrated extinction for that channel from the X band radiometric value, because we wish to illustrate the impact of strong extinction and serious noise effects upon the retrieved profiles.

Fig. 3-b compares the precipitation retrieval profiles obtained from X and Ka band radars with constraints imposed by the path integrated extinction. The present algorithm appears to operate in the presence of ice and melting layers provided that all of the ice hydrometeors remain above the freezing level. It is noteworthy that the Ka band retrieval below 1.25 km approaches 12 mm/h, where the algorithm tends to replace the noise contaminated part of the retrieval with the mean value of the rainfall rate. Because the Ka band rainfall does not diminish as the X band retrieval below 1 km, it cannot increase as much above 2 km and still preserve the path integrated extinction. The dual frequency radar retrieved profile follows the Ka band near the top of the rain layer and it follows the X band return near the surface where the Ka radar return is masked by receiver noise. The normalizing condition imposed by $\bar{R}$ produces a slight shift in the composite profile.

Fig. 4-b shows X and Ka band retrievals that are in excellent agreement. The reason for that appears to be that the signal/noise ratio was acceptable for both radar returns and that no ice hydrometeors appear to have been present. It is noteworthy that the Ka band retrieval near the surface tends toward the mean rainfall rate while the X band retrieval continues its monotonic trend near the surface. The reason for this is that Eq.(18) mixes the mean extinction coefficient with the noisy retrieved value mostly at the lowest and noisiest level. The rainfall rate retrieved above 1.5 km from the Ka radar exceeds the value obtained from the X band radar because the algorithm requires the path integrated extinction to be fixed. As a consequence a modestly underestimated rainfall rate near the surface is compensated by a corresponding overestimate aloft. The dual frequency radar rainfall retrieval again falls between the two radar-radiometer retrievals.

5. DISCUSSIONS:

The present technique is applicable only over the ocean if a single frequency radiometer is used. Space and air-borne rain observation systems now utilize or are planned to utilize multifrequency radiometers. Approximate estimates of the integrated path extinction and the hydrometeor phase profile can be derived from such data, see Kummerow et al. (1988). Moreover a multi frequency radiometric technique is applicable over both land and sea. In view of these findings, a single frequency radar operating from space in conjunction with multifrequency passive radiometers shows promise of being able to provide cost effective spaceborne measurements of global tropical rainfall distributions.

REFERENCES:

Atlas, D., C.W. Ulbrich, R. Meneghini (1984) The Multiparameter Remote Measurement of Rainfall, Radio Sci., 19, 3 - 22

Douglas, R.H. (1964) Hail Size Distribution, Proc. 11th Radar Wea. Conf., Am. Met. Soc., Boston, MA., 146 - 149.

Hitschfeld, W., J. Bordan (1954) Errors Inherent in the Radar Measurement of Rainfall at Attenuating Wavelengths. J. Met., 11, 58-67.

Jones, W. L., L.C. Schroeder, and J.L. Mitchell, (1977:) Aircraft Measurements of the Microwave Scattering Signature of the Ocean, IEEE, AP-25, 52-61.

Kummerow, C.D., J. A. Weinman (1988) Radiative Properties of Deformed Hydrometeors for Commonly Used Passive Microwave Frequencies, IEEE Trans. on Geosci. and Rem. Sens., 26, 629-638

Kummerow, C.D., R.A. Mack, I.M. Hakkarinen (1988) A Self Consistency Approach to Improve Microwave Rainfall Rate Estimation from Space. Submitted to J. App. Met.

Meneghini, R.J., J. Eckerman, D.Atlas (1983) Determination of Rain Rate from a Spaceborne Radar Using Measurements of Total Attenuation, IEEE Trans. Geosci. and Rem. Sensing, GE-21 , 34 - 43

Meneghini, R., D. Atlas (1986) Simultaneous Ocean Cross Section and Rainfall Measurements from Space with a Nadir Looking Radar. J. Atm. and Oc. Tech., 1, 400-413

Okamoto, K., S. Yoshikado, H. Masuko, T.Ojima, N. Fugono, K. Nakamura, J. Awaka, H. Inomata, (1982) Airborne Microwave Rain Scatterometer/Radiometer, Int. J. Remote Sensing, 1, 277-294

Simpson, J., R.F. Adler, G.R. North (1988) A Proposed Tropical Rainfall Measuring Mission (TRMM) Satellite, Bull. Am. Met. Soc., 69, 278 - 295

Trenberth, K.E., G.W. Branstator, P.A. Arkin (1988) Origins of the 1988 North American Drought, Science, 242, 1640 - 1645

Weinman, J.A., R, Davies (1978) Thermal Microwave Radiances from Horizontally Finite Clouds of Hydrometeors, J. Geophys. Res., 83, 3099 -3107

Weinman, J.A., C.D. Kummerow, C.S. Atwater (1988) An Algorithm to Derive Precipitation Profiles from a Downward Viewing Radar and a Multifrequency Passive Radiometer, Proc. of IGARSS '88 Symposium, Edinburgh Scotland, Sept. 13-16, Ref. ESA SP-284 (IEEE 88CH2497-6)

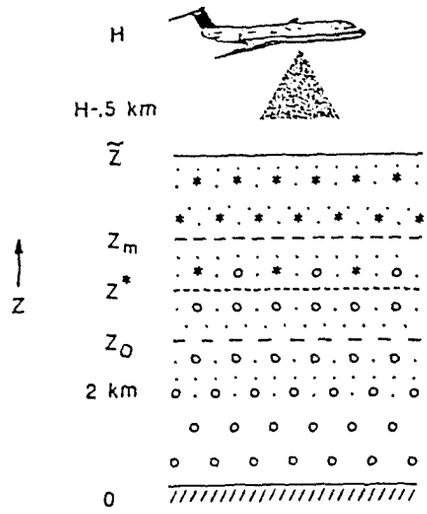

FIGURE 1

Fig. 1: Schematic view of the rainfall profile retrieval showing the various geometric quantities used in the present analysis. (•) non precipitable cloud drops, (*) ice hydrometeors, (o) rain. The following heights are: z_o, freezing level (0°C isotherm); z^*, top of the rain layer (400 m above the freezing level); z_m, top of the melting layer (-35°C isotherm); z, top of the precipitating cloud.

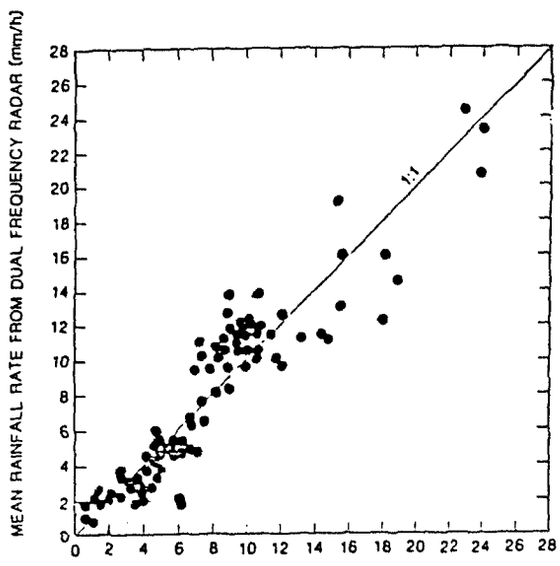

FIGURE 2

Fig. 2: Comparison of mean rainfall rates, $\bar{R}$, retrieved from the X band passive microwave radiometer data and from the X - Ka band dual frequency radar reflections from the sea surface. The solid line represents a 1:1 correspondence.

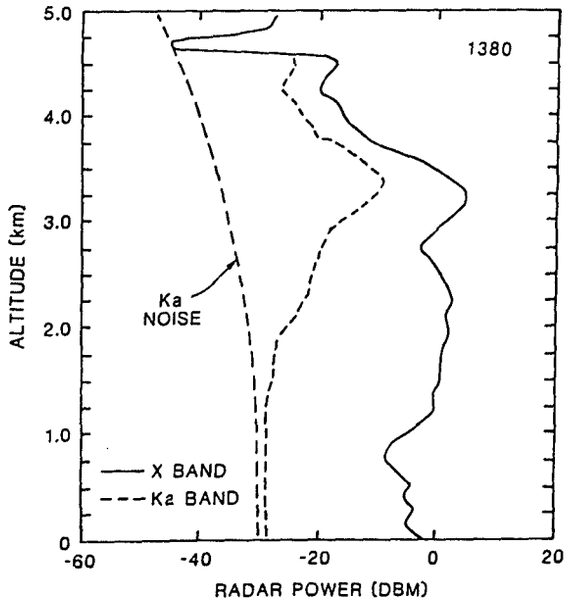

FIGURE 3a

Fig. 3 - a: Profiles of the range square corrected returned radar power in dB for X and Ka band radars for sample #1380. The Ka band range square corrected noise in dB is also shown. X band (———), Ka band (- - - -).

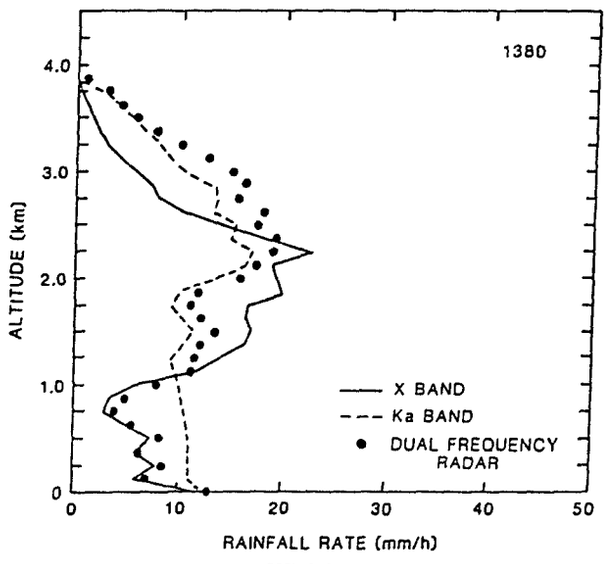

FIGURE 3b

Fig. 3 - b: Profiles of rainfall rate (mm/h) retrieved from the algorithm that combines single frequency radiometric and radar data. X band (————), Ka band (- - - -). These results are compared to those obtained from the dual frequency radar algorithm, (● ● ● ●). The data are derived from sample #1380 for which H = 5.1 km, I = 176.6 K, $\bar{R}$(radiometric) = 11.9 mm/h and $\bar{R}$(DSRT) = 12.8 mm/h.

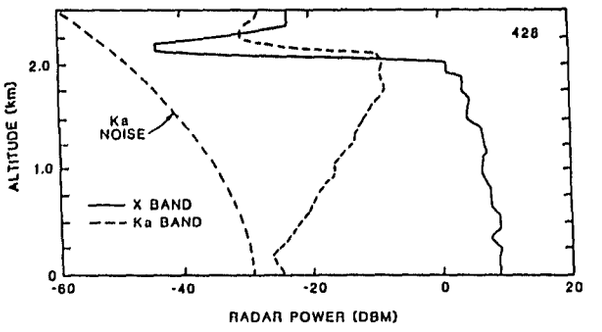

FIGURE 4a

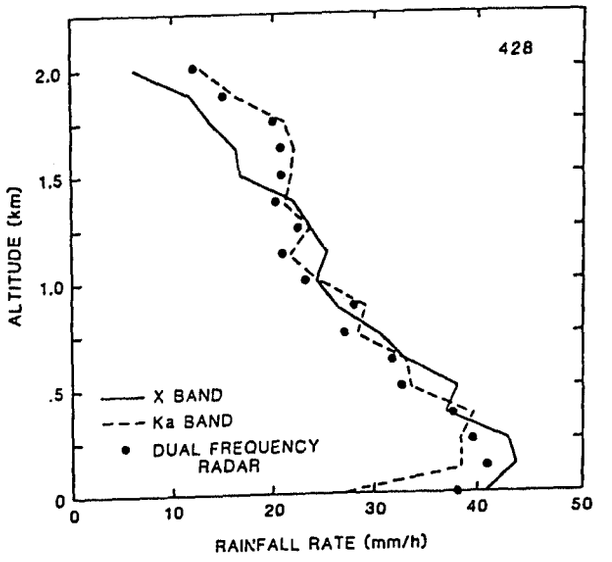

FIGURE 4b

Fig. 4 - a/b: Same as above for sample #428 for which H = 2.55 km, I = 212.0 K, $\bar{R}$(radiometric) = 26.5 mm/h, $\bar{R}$(DSRT) = 28.9 mm/h.

4.5

AIRCRAFT MICROWAVE OBSERVATIONS AND SIMULATIONS OF DEEP CONVECTION AT 18-183 GHZ.

H.-Y. M. Yeh[2], N. Prasad[3], and R. F. Adler[1], R. A. Mack[3], and I. M. Hakkarinen[3]

[1] NASA/Goddard Space Flight Center, Greenbelt, MD 20771
[2] Caelum Research Corporation, Silver Spring, MD 20901
[3] General Sciences Corporation, Laurel, MD 20707

1 INTRODUCTION

A radiative transfer model is used for simulating the aircraft multichannel microwave observations and for the study of 29 June 1986 storm system during COHMEX. The integrated aircraft data from the Multi-spectral Cloud Radiometer (MCR), Advanced Microwave Moisture Sounder (AMMS), and Microwave Precipitation Radiometer (MPR) are shown in Figs. 1a and b for flight lines 1 and 2, respectively. Ground-based radar data are used to derive hydrometeor profiles of the storm, based on which the microwave upwelling brightness temperatures at the top of the atmosphere are calculated. Various vertical hydrometeor phase profiles and different particle size distributions are experimented in the model, and the results are compared with the aircraft radiometric data. It is found that the brightness temperatures are directly affected by the complex nature of hydrometeors including size distribution and mixture of ice/water phases.

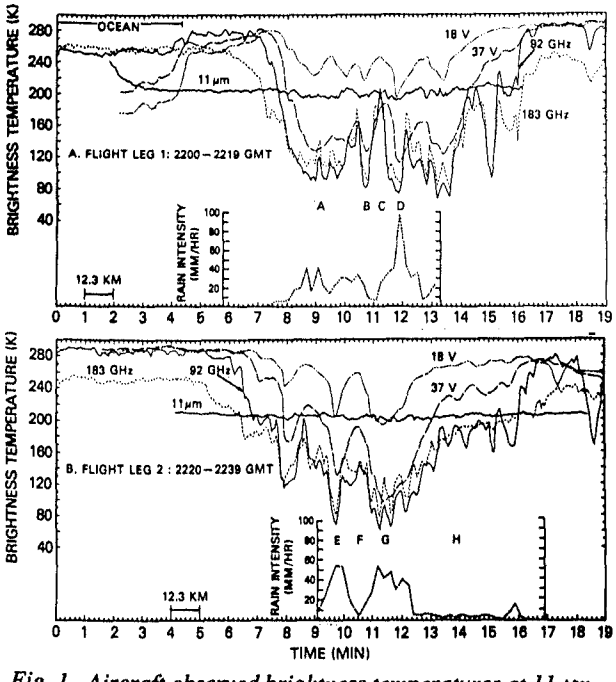

Fig. 1. Aircraft observed brightness temperatures at 11 μm (MCR), 18 and 37 GHz (MPR), and 92 and 181 GHz (AMMS). Also shown is the low-level radar-based rain rate over the portion of the flight path where the radar data is available: (a) flight line 1, 2200 to 2219 GMT; and (b) flight line 2, 2220 to 2239 GMT.

2 MICROWAVE RADIATIVE TRANSFER MODEL

The basic model used for calculating microwave upwelling brightness temperature (T_B) is a revision of the model used by Wilheit et al. (1982). This model has been modified to include the capabilities of handling mixed phase layers and detailed vertical structure of the atmosphere (Szejwach et al., 1986). The atmosphere is divided into up to 200 layers of equal optical thickness. The optical thickness is a result from the combination of gaseous and hydrometeor extinction in the atmosphere. In this study, precipitating ice and two classes of liquid (cloud water and rainwater) are given in hydrometeor profiles. The amounts of these three classes of hydrometeors are determined by radar reflectivities and the vertical phase distribution that is assumed in the model. Computation of the extinction, scattering, absorption coefficients and phase function is performed according to the Mie theory. These radiative parameters are then integrated by the given size distribution

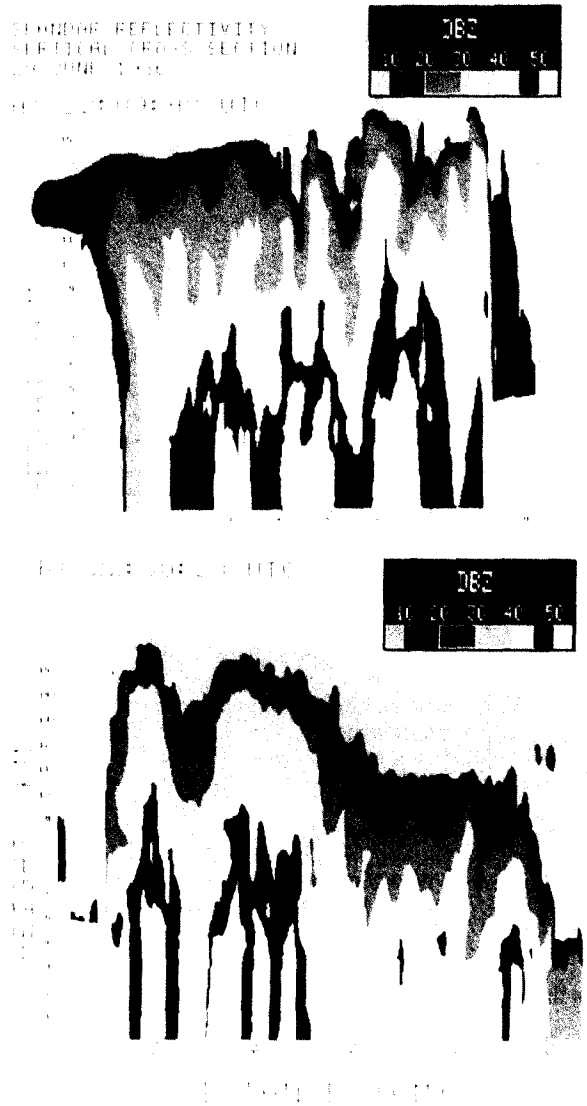

Fig. 2. The SPANDAR radar reflectivity cross section corresponding to (a) flight line 1, and (b) flight line 2. The reflectivities are extrapolated from the layers with existing radar data to the ground and to 16 km altitude.

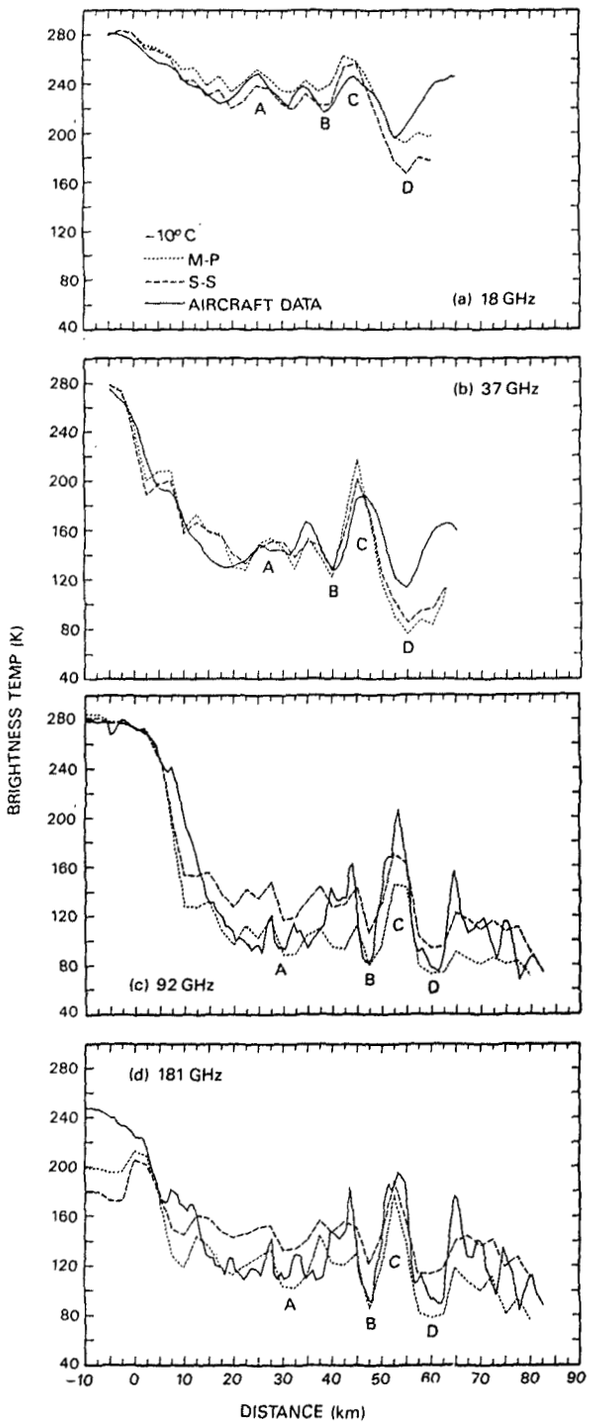

Fig. 3. Comparsion of aircraft data and model results using the M-P and S-S size distributions for flight line 1 at (a) 18 GHz, (b) 37 GHz, (c) 92 GHz, and (d) 181 GHz. The phase transition is assumed at -10°C..

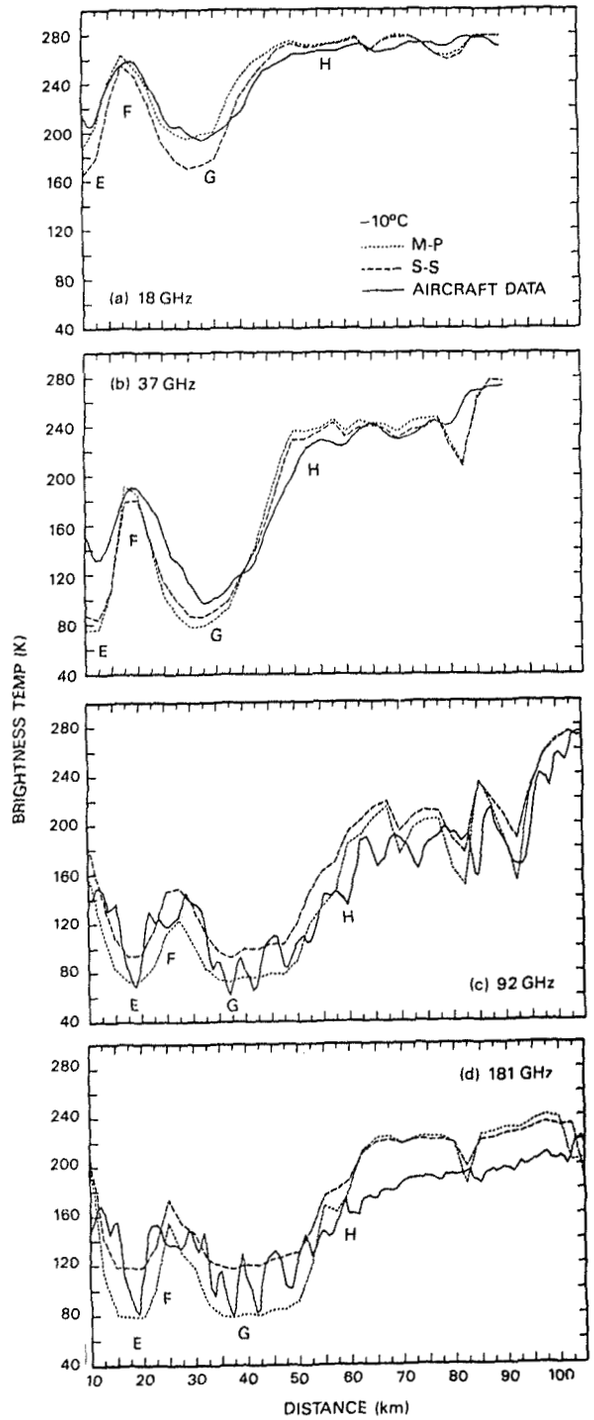

Fig. 4. Same as Fig. 3, except for flight line 2.

in the radiative transfer model.

3 UTILIZATION OF RADAR REFLECTIVITIES AS INPUT TO RADIATIVE MODEL

Due to the restriction of elevation angle and the effect of the curvature of the Earth, the original radar volume scans were limited to certain heights. In this investigation, the radar reflectivities have been extrapolated from the layers with existing radar data to the ground and to the maximum cloud altitude (16 km) for the model calculations (as shown in Figs. 2a and b for flight lines 1 and 2, respectively). Each vertical hydrometeor profile is divided into three different sections: the first section, above a given level, consists of ice particles only; the second section has a mixture of both ice and liquid phases with ice (liquid) water content linearly decreasing (increasing) from the all-ice to the all-liquid level; and the third section, in which only liquid phase is present. Three phase transition temperatures, -30°C, -20°C and -10°C are used to define the threshold between the first and second sections. The transition from the second to third section is fixed at the melting layer (0°C) for all simulations.

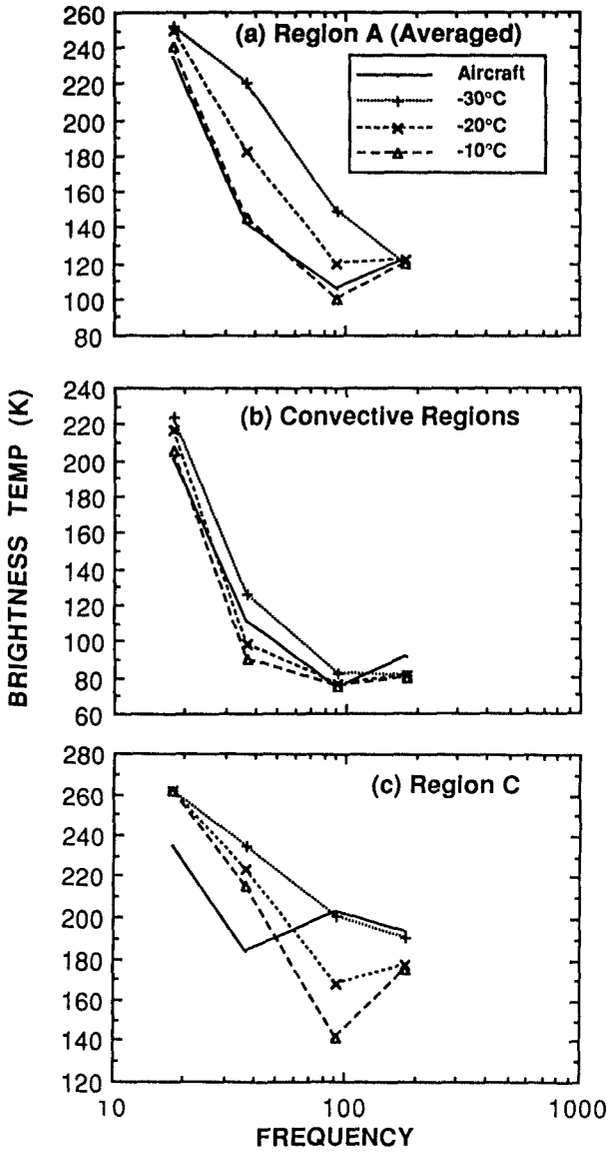

Fig. 5. Model simulated brightness temperature as a function of frequency and phase trnasition. The calculations are based on the profiles (a) in the weakening convective region A, (b) in convective cores (averaged coldest T_B of B, D, E, and G), and (c) in region C.

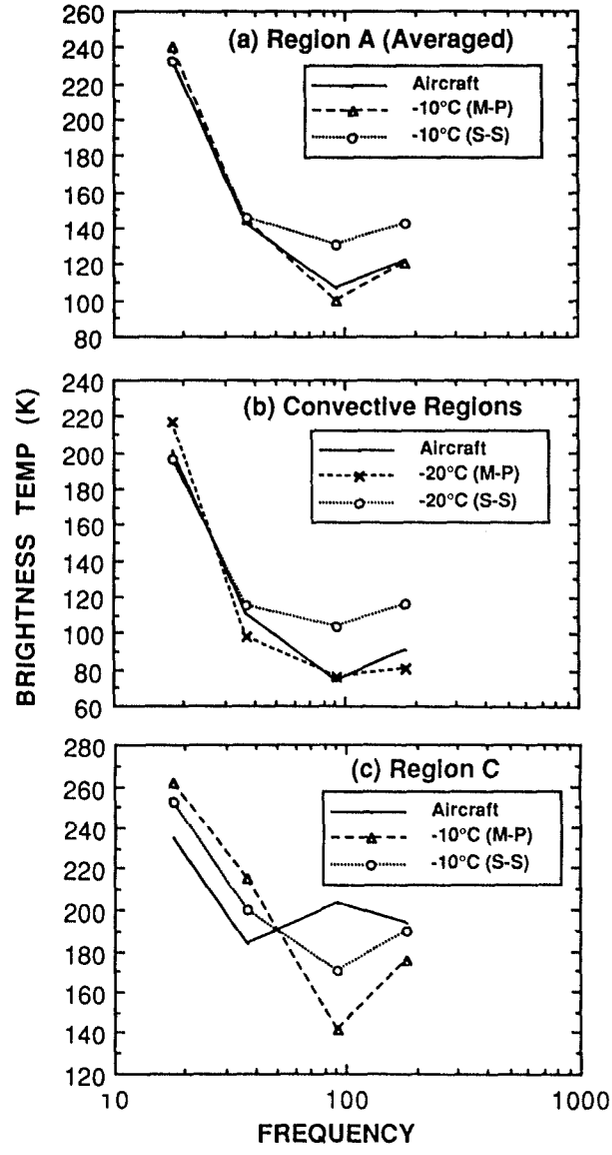

Fig. 6. Same as Fig. 5, except for the comparison of model results using the M-P and S-S size distributions.

In the model simulations, we use the Marshall and Palmer (1948; M-P) distribution for a sensitivity study of the upwelling T_B effected by various phase profiles. In addition, the Sekhon and Srivastava (1979; S-S) distribution is used to study the effect of particle size on the microwave measurements.

4. SIMULATIONS OF OBSERVED BRIGHTNESS TEMPERATURES AT 18, 37, 92, AND 181 GHZ

The model simulations at different frequencies are shown in Figs. 3 and 4, assuming phase transitions at -10°C, for flight lines 1 and 2, respectively. We first discuss the effect of hydrometeor phases on the microwave radiation based solely on the M-P size distribution. When the phase transition is assumed at -30°C, the model results at all frequencies are generally too warm (see Figs. 5a and b). The only exceptions are the simulations at higher frequencies (92 and 181 GHz) in the convective cores and the sharp break in the cloud area (*C*) (Fig. 5b and c), where large quantity of small ice particles in the upper troposphere effectively scatter the upwelling radiation from below. The same amount of ice, however, is not enough to diffuse the microwave radiation at the lower frequencies. When the phase transition is lowered to -20°C level, the calculated T_B become colder because of the stronger scattering effect from more ice. At the lower frequencies, the model results are still too warm compared to the aircraft data, except in the convective cores.

When the phase transition is moved to -10°C, the calculated T_B at 18 GHz are significantly reduced especially over the convective cores (*D* in Fig. 3a and *E*, *G* in Fig. 4a). The calculated temperatures at 18 GHz in the *C* and *H* regions are not significantly changed regardless of the increase of ice content phase. At 37 GHz, the simulated T_B's are greatly affected by the additional amounts of ice in the atmosphere (Figs. 3b and 4b), especially over the weakening convective region (*A*). The simulated temperatures in the convective cores (*D*, *G* and *E*) are reduced to about 75 K, and become colder than aircraft

measurements by at least 20 K. The pattern of the simulated brightness temperatures at 92 and 181 GHz is changed little by giving more ice, except those in *C* and *H*.

For the effect of particle size on the T_B, the model results using the two different size distributions are close to each other when the phase transition is at -30°C. The charactericstics of the two size distributions tend to depart from each other further as ice content increases; the S-S distribution generally has more larger ice particles, which scatter more effectively the lower frequency radiation, as compared to the M-P distribution. As total ice content in the cloud increases by lowering phase transition to -20°C, results of using the two size distributions become more distinctive at 18 and 92 GHz (see Fig. 6b). At 18 GHz, the calculated T_B using the S-S distribution decrease more than those using the M-P distribution. But the tendency is opposite at 92 GHz, at which the model results using the S-S size distribution are hardly changed by increasing the ice content. When the phase transition is moved to -10°C, at 18 GHz, the computed T_B's using the M-P distribution become colder and closer to the radiometric data, especially in the deep convective regions (~195 K), where the results of using the S-S distribution are too cold (~165 K) (Figs. 3a, and 4a). The model results at 37 GHz are not very sensitive to the difference in size distributions used in the calculations. It is, however, noted that the model results show an opposite tendency in deep and weak convective areas with the M-P and S-S size distributions. At both 92 and 181 GHz, the simulations using the S-S distribution are warmer than those using the M-P distribution almost in all regions. This can be attributed to two reasons: (a) the ice contents calculated based on the S-S distribution are less than those using the M-P distribution for radar reflectivities greater than 35 dBZ, and (b) the S-S distribution produces a higher concentration of large particles, but the overall concentration is much lower than the M-P distribution.

From Fig. 5a, a phase transition to all ice at -10°C appears to give the best overall answer in the weakening convective region (*A*). Fig. 5b, however, shows that over the convective cores (averaged coldest T_B's in *B, D, E* and *G* regions), the best agreement between the model results and aircraft data is by assuming the phase transistion to be at -20°C. Compared to weak convections (e.g. *A* region), more supercooled liquid water is likely to be present at the upper atmosphere in areas with deep convection.

In Fig. 5c, the unique breaking area *C* shows that the aircraft data at 37 GHz is colder than that at 92 GHz due to the difference in viewing geometry. No simulation using the M-P distribution can properly reproduce the trend of T_B's as a function of frequency. Although the radar reflectivity in the *C* area is quite weak, the simulated T_B's using two size distributions show distinctive results as a function of frequency (Fig. 6c). The S-S distribution tends to have results closer to the observed data although there is still a large discrepancy. It is possible that in this region, fewer but larger particles (such as graupel) are predominant, because they have more scattering effect on the low frequency than on the high frequency channels.

5. CONCLUSIONS

Results of the comparison between model simulations and aircraft observations indicate that (1) the M-P distribution well represents the ice particle size distribution, especially in the upper tropospheric portion of the cloud; (2) the S-S distribution, which has a higher concentration of large particles, appears to better simulate the particle size at the lower portion of the cloud, which has more effect on the T_B's at 18 and 37 GHz; (3) in deep convective regions, significant supercooled water must be present up to the -20°C layer, while in less convective areas frozen hydrometeors should be predominant above -10°C layer.

Acknowledgments. The authors are thankful to Dr. James Dodge and NASA's Mesoscale Atmospheric Processes Program for support of this project, and Mr. Rich Fulton for providing a software for computing hydrometeor profiles from radar reflectivities.

REFERENCES

Marshall, J. S., and W. M. Palmer, 1948: The distribution of raindrops with size. *J. Meteor.*, **5**, 165-166.

Sekhon, R. S. and R. C. Srivastava, 1970: Snow size spectra and radar reflectivity. *J. Atmos. Sci.*, **27**, 299-307.

Szejwach, G., R. F. Adler, I. Jobard, and R. A. Mack, 1986: A cloud model-radiative model combination for determining microwave TB-rain rate relations. Second Conf. on Sat. Meteor./Remote Sensing and Appl., Amer. Metero. Soc. May 13-16, Williamsburg, VA, 444-449.

Wilheit, T. T., A. T. C. Chang, J.L. King, E.B. Rodgers, R.A. Nieman, B.M. Krupp, A.S. Milman, J.S. Stratigos, and H. Siddalingaiah, 1982: Microwave radiometric observations near 19.35, 92 and 183 GHz of precipitation in tropical strom Cora. *J. Appl. Meteor.*, **21**, 1137-1145.

STRUCTURE OF TROPICAL CYCLONES AND SURROUNDING REGIONS AS DETERMINED FROM OLS AND SSM/I IMAGERY ANALYSIS

Morton Glass and Gerald W. Felde

Air Force Geophysics Laboratory
Hanscom AFB, Massachusetts

1.0 INTRODUCTION

A new microwave imaging sensor was successfully launched by the Defense Meteorological Satellite Program (DMSP) on June 19, 1987. This seven channel passive radiometer is known as the Special Sensor Microwave/Imager (SSM/I). Visible and infrared (IR) imagery data from the Operational Linescan System (OLS) are collected on the same DMSP spacecraft as the SSM/I. This set of coincident DMSP spacecraft data provide a new means of meteorological analysis.

A group of tropical cyclones of varying peak intensities occurring in the western North Pacific during 1988 were selected for study. Analyses based entirely on the use of SSM/I and OLS DMSP spacecraft data were performed. Alternative data sources for tropical cyclone analysis need to be explored, since reconnaissance flights by the Air Force were discontinued in this region in September 1987. Imagery analysis for two stages during the life cycle of Typhoon Pat are presented in this paper. One case is for an early stage when the storm is at tropical storm strength and is intensifying. The other case is for conditions when the storm is at typhoon strength and is just beginning to weaken.

2.0 OLS AND SSM/I INSTRUMENT DESCRIPTIONS

The DMSP spacecraft carrying the OLS and SSM/I instruments is designated F8. It is in a sun synchronous, near-polar orbit at an altitude of 833 km with an inclination of 98.8 degrees and an orbital period of 102 minutes. Data are obtained at approximately 6 a.m. and 6 p.m. local time. Both the OLS and SSM/I data swaths are centered on the satellite subtrack. The SSM/I swath is 1394 km wide and the OLS swath is about twice as wide.

The OLS has been the primary meteorological sensor on DMSP spacecraft since 1976. It is a scanning radiometer that measures upwelling radiation in two broad spectral bands, one in the visible (0.4 - 1.1 micrometer) and the second in the thermal IR (10.2 - 12.8 micrometer) regions. Data are available at resolutions of 0.6, 2.8, or 5.6 km depending on the selected processing mode. For a complete description of the OLS see Haig (1982) and Heacock (1985).

The SSM/I is a seven channel passive scanning radiometer that detects upwelling polarized microwave radiation form the earth/atmosphere system. The instrument is sensitive to four frequencies: 19.35, 22.2, 37, and 85.5 GHz. Two polarizations, vertical (V) and horizontal (H), are available at each frequency, except 22.2 GHz which has only V polarization. The SSM/I measures emitted energy at spatial intervals of 12.5 km at 85 GHz and 25 km at the three lower frequencies. The sensor footprints are almost circular and range in diameter from 55 km at 19 GHz down to 15 km at 85 GHz. The conical scan geometry of the SSM/I results in a constant zenith angle of 53.1 degrees. Further details on the SSM/I are given by Hollinger and Lo (1983) and Hollinger et al. (1987).

3.0 SSM/I ENVIRONMENTAL PARAMETER ALGORITHMS

Hughes Aircraft Company, the SSM/I instrument manufacturer, developed algorithms for estimating several surface and atmospheric parameters from SSM/I brightness temperatures. Two of them, surface wind speed and rain rate, are of particular interest for tropical cyclone analysis. These two algorithms, as well as most of the other parameter extraction algorithms, use the microwave brightness temperatures as independent variables in linear regression equations. Details on the extraction of environmental parameters are given by Lo (1983), Hughes Aircraft Company (1985), and Hollinger et al. (1987).

Radiation measured by the SSM/I (in either of two orthogonal polarizations) comes from three sources - atmospheric emission, surface emission, and atmospheric emission reflected from the surface. Energy from the latter two sources is attenuated by some loss factor in passing through the atmosphere. For microwave radiation, the important atmospheric parameters that attenuate are water vapor, oxygen, and liquid water (both in the form of cloud water and rain). However, clouds or rain also considerably increase the atmospheric emission. In the extreme, clouds or rain totally obscure the surface, producing a satellite measurement that is related only to atmospheric phenomena. In general, the microwave signal reaching the satellite is partially due to the earth background surface and partiallly due to the overlying atmosphere within its field of view. Clouds and rain become more transparent as the microwave frequency

decreases. The 22 GHz channel is sensitive to atmospheric water vapor because there is a resonance line at this frequency. Microwave energy emitted or scattered by the atmosphere is unpolarized. On the other hand, microwave energy emitted or reflected by the surface is polarized.

Surface wind speeds can be estimated over ocean backgrounds from SSM/I data because the surface emissivity is related to its roughness. Emissivity increases with increased water surface roughness as winds increase. Brightness temperatures from the following four channels are used in the SSM/I equation for surface wind speeds over an ocean background: 19 GHz-H, 22 GHz-V, 37 GHz-V, and 37 GHz-H. Clouds will also increase brightness temperatures, but not significantly in the channels of primary importance for the estimation of surface wind speed. Rain over an ocean background also increases the brightness temperatures. This is partly due to increased emission from the water mass in the atmosphere and partly due to roughening of the surface by falling rain. It is for this reason, that surface wind is not estimated when heavy rain is detected. Note that surface wind speed can not be estimated over land.

There are SSM/I algorithms for estimation of rain rate over both land and ocean backgrounds. For ocean backgrounds, brightness temperatures from the following four channels are used: 19 GHz-H, 22 GHz-V, 37 GHz-V, and 37 GHz-H. In general, the SSM/I sees a region of rain as an area of warm brightness temperatures over the otherwise cold (in terms of brightness temperatures) ocean. Microwave radiation is significantly absorbed and reemitted by atmospheric raindrops. This effect also takes place for cloud-sized droplets at 85 GHz. Over a reflecting water surface, this signal is strongly enhanced. The basis of the rain rate algorithm over ocean is that initially the 19 and 37 GHz brightness temperatures increase as rain rates increase up to a moderate rain rate, after which the brightness temperatures decrease as the rain rates increase further. This reduction in brightness temperatures for larger rain rate values is due to scattering by the large raindrops and/or ice particles present in heavy rain.

4.0 CASE STUDIES

Typhoon Pat occurred from October 18 to 23, 1988 in the western North Pacific. It's track is shown in Fig. 1. This track was obtained from positions listed in the tropical cyclone warning bulletins issued by the Joint Typhoon Warning Center (JTWC) in Guam.

During the life of the storm, the DMSP satellite made 71 orbits. The storm was at least partially in view of the SSM/I scan during 8 of these orbits. Two cases were selected for study.

SSM/I and OLS data for the first case discussed in the next section are from revolution 6903 of the DMSP F8 satellite which ascended over the area of interest at approximately 22Z on October 20, 1988. Pat has

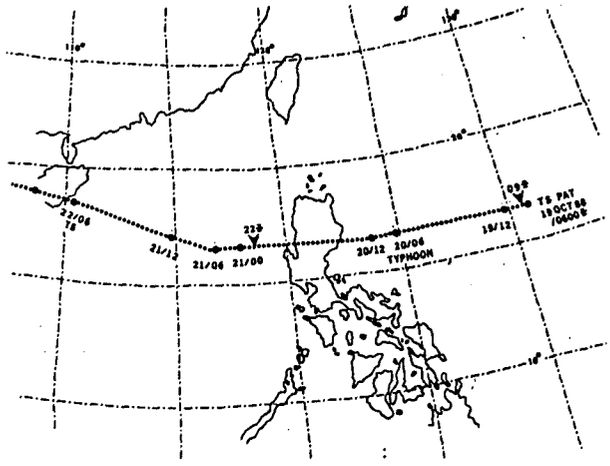

Fig. 1. Track of Typhoon Pat, Oct. 19 - 22, 1988.

typhoon strength at this time and is beginning to decay. The JTWC bullentins stated the storm winds to be 90 with gusts to 110 knots at 12Z on October 20, 1988 and to be 65 with gusts to 80 knots at 00Z on October 21, 1988.

SSM/I and OLS data for Case 2 are from revolution 6881. The satellite was descending over the area of interest at about 09Z on October 19, 1988. Pat is a tropical storm at this time and is intensifying. The JTWC bulletins indicate Pat's winds to be 45 with gusts to 55 knots at 06Z on October 19, 1988 and to be 50 with gusts to 65 knots at 12Z on October 19, 1988.

The SSM/I and OLS imagery data were processed and analyzed using the Air Force Geophysics Laboratory (AFGL) Interactive Meteorological System (AIMS). AIMS is a distributed system of mini- and micro-computers that was developed to support research in remote sensing at AFGL. Two image processing workstations are part of this system. A complete description of AIMS is given by Gustafson et al. (1987).

For each case, OLS visible and IR images were generated from 5.6 km resolution data. The OLS images were not remapped. They were displayed in scan format to take advantage of the full resolution of the data. Images of SSM/I brightness temperature fields for 37 and 85 GHz and the surface wind speed and rain rate fields obtained from the SSM/I operational algorithms were also produced. These coarser resolution fields were remapped into the OLS scan format to allow for easy comparison to the OLS images and generation of various OLS and SSM/I composite images of the storm.

5.0 RESULTS

An OLS IR grayshade image and an SSM/I 85 GHz-H grayshade image for Case 1 (typhoon stage) are shown in Figs. 2 and 3, respectively. In both images, grayshades change from dark to light as brightness temperatures decrease. The cloud tops of Typhoon Pat (white - cold) are very distinct in Fig. 2. However,

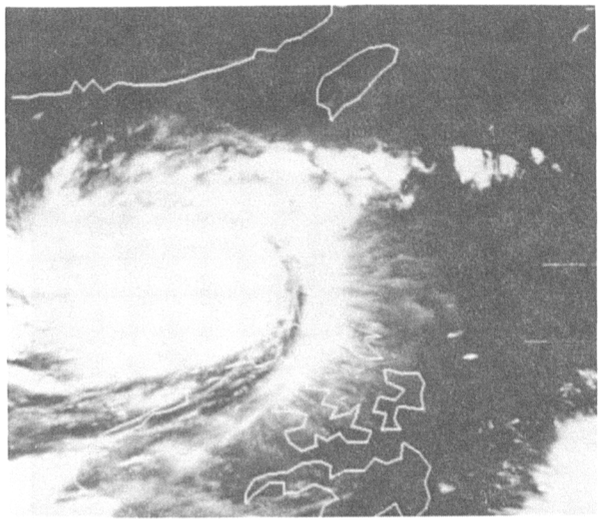

Fig. 2. OLS IR image for Case 1 (Typhoon) - 22Z on Oct. 20, 1988.

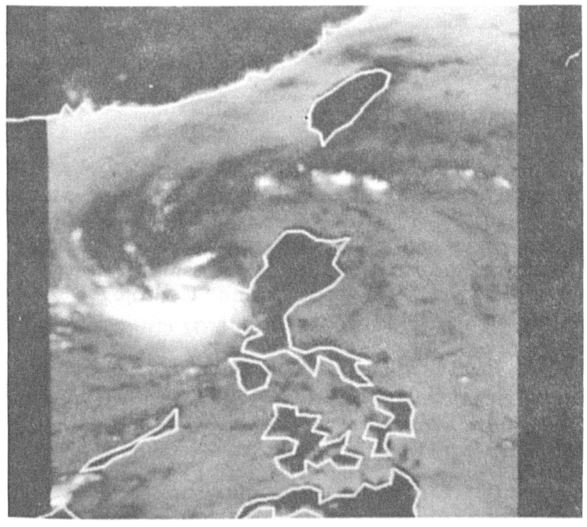

Fig. 3. SSM/I 85 GHz-H image for Case 1 (Typhoon) - 22Z on Oct. 20, 1988.

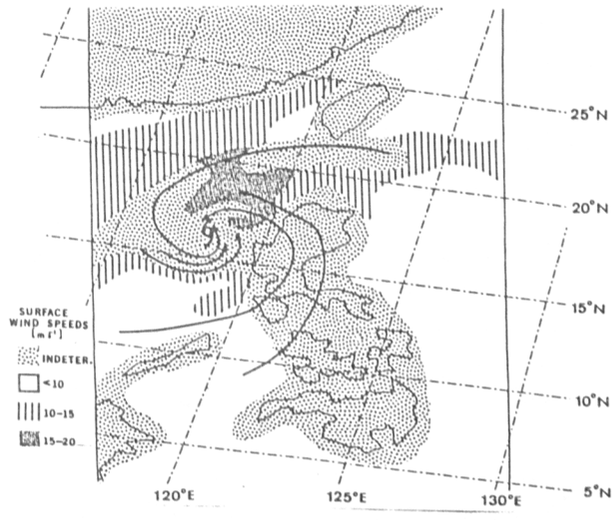

Fig. 4. SSM/I-derived surface wind speeds (m/s) for Case 1 (Typhoon) - 22Z on Oct. 20, 1988.

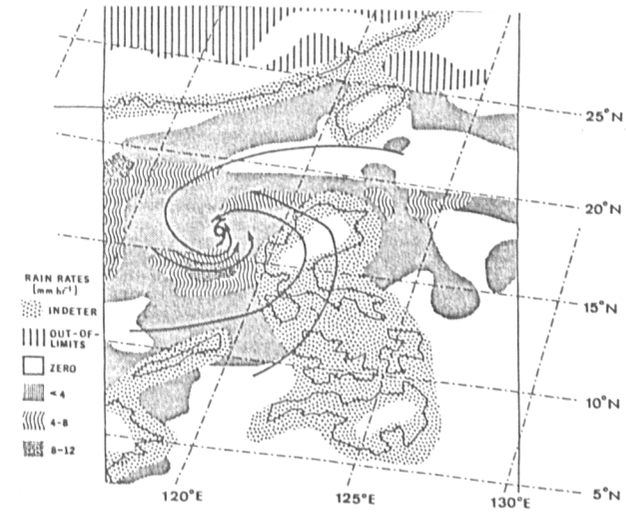

Fig. 5. SSM/I-derived rain rates (mm/hr) for Case 1 (Typhoon) - 22Z on Oct 20, 1988.

the thick cirrus shield obscures the non-cirrus cloud band structure of the storm. Therefore the surface location of the storm center is not evident since there is no well defined eye.

The strong contrast between land and ocean backgrounds is evident in the microwave image (Fig. 3). Land has warm brightness temperatures (dark grayshades), while ocean has cold (light grayshades) ones. Cirrus clouds are transparent over all backgrounds. Non-cirrus clouds have a warm signature (dark grayshades) over ocean backgrounds. There is one exception, well-developed convective clouds have a strong cold signature over ocean (as well as land). The cold signature of deep convective clouds results from scattering by the thick layer of large ice particles present in the upper regions of these clouds. This was first observed by Wilheit (1982) with a 92 GHz radiometer flown on an aircraft. The non-cirrus cloud band structure is readily seen in the 85 GHz image (dark grayshades) with the embedded intense convective cells highlighted (bright grayshades within the dark grayshade bands).

Analysis of this cloud band structure seen in the 85 GHz image and the OLS IR image of the cirrus shield led to an estimated storm center location of 16.4 degrees N and 118.3 degrees E at 22Z on October 20, 1988. This location agrees well with the storm track shown in Fig. 1. The main cloud bands and storm center location were superimposed on contour analyses of derived wind speed and rain rate fields. These are shown in Figs. 4 and 5, respectively.

The wind and rain patterns qualitatively fit the storm center and cloud band structure. Wind and rain maxima are located near the storm center. Note the location of the indeterminate areas in both figures. The SSM/I wind algorithm is unable to provide estimates in areas of heavy rain over ocean, or over

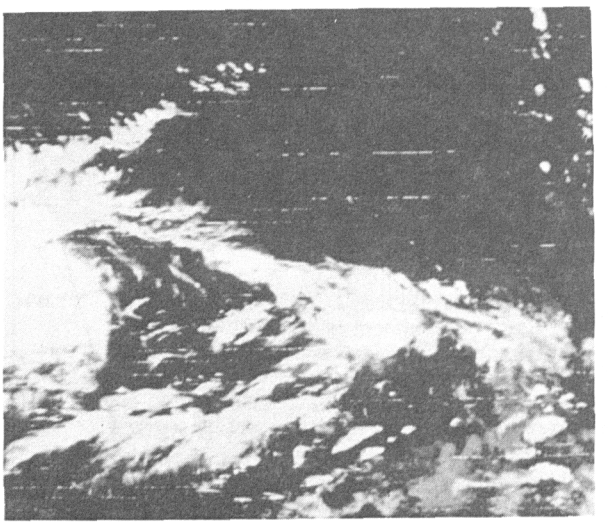

Fig. 6. OLS IR image for Case 2 (Tropical Storm) - 09Z on Oct. 19, 1988.

Fig. 7. SSM/I 85 GHz-H image for Case 2 (Tropical Storm) - 09Z on Oct. 19, 1988.

land and coastal regions. The rain algorithm is unable to provide estimates over coastal boundary regions. Some areas of out-of-limits values are seen in Fig. 5. This means that the numerical rain rate values returned were not physically realistic.

An OLS IR grayshade image and an SSM/I 85 GHz-H grayshade image for when Pat was designated a Tropical Storm (Case 2) is shown in Figs. 6 and 7, respectively. Although the storm is poorly defined at this stage, as evidenced by the IR imagery, the cloud bands observed using the 85 GHz clearly show the organization of the convective activity and make it possible to estimate the location of the storm center. The estimated storm center location is 16.1 degrees N and 130.3 degrees E at 09Z on October 19,1988. This location agrees well with the JTWC storm track depicted in Fig. 1. The patterns in the SSM/I derived wind speed and rain rate fields (not shown) fit the storm center and cloud band structure well. Note that a large cloud band on the eastern perimeter of the storm is seen in the IR image for Case 1 (Fig. 2) when the storm is at typhoon strength. This cloud band is absent 37 hours earlier when ths storm is at tropical storm strength (Fig. 6). Also note there is an extensive deep convective band (bright grayshades) just south of the storm center which can be seen in the 85 GHz image for Case 1 (Fig. 2). This feature is not present for Case 2 (Fig. 7). The maximum derived rain rate for this case was 9 mm/hr; for the typhoon (Case 1) the maximum rain rate was 11 mm/hr.

6.0 CONCLUSIONS

Coinicident SSM/I (microwave) and OLS (visible and IR) imagery data show promise as a new tool for delineating the cloud band structure, locating the intense convective cells within the cloud bands, and locating the storm center of tropical cyclones. Wind speed and rain rate fields derived from SSM/I algorithms agreed qualitatively with known features of tropical cyclones. These derived parameters will become more useful as algorithms are refined.

7.0 REFERENCES

Gustafson, G., D. Roberts, C. Ivaldi, R. Schechter, T. Kleespies, K. Hardy, R. d'Entremont, G. Felde, and R. Lynch, 1987: The AFGL Interactive Meteorological System. Preprints, Third International Conference on Interactive Information and Processing Systems for Meteorology, Oceanography, and Hydrology, AMS, Boston, MA, 151-154.

Haig, T. O., 1982: The Role of Meteorological Satellites in Tactical Battlefield Weather Support. AFGL Technical Report AFGL-TR-82-0124, AFGL, Hanscom AFB, MA.

Heacock, L. E., editor, 1985: Envirosat-2000 Report, Comparison of the Defense Meteorological Satellite Program (DMSP) and the NOAA Polar-orbiting Operational Environmental Satellite (POES) Program. U.S. Department of Commerce, Washington, DC.

Hollinger, J., R. Lo, G. Poe, R. Savage, and J. Peirce, 1987: Special Sensor Microwave/Imager User's Guide. Naval Research Laboratory, Washington, DC.

Hollinger, J. P., and R. C. Lo, 1983: SSM/I Project Summary Report. Naval Research Laboratory Technical Memorandum Report 5055, Washington, DC.

Hughes Aircraft Company, 1985: Special Sensor Microwave/Imager (SSM/I) Technical Operating Report (TOR). Contract F04701-84-C-0036.

Lo, R. C., 1983: A Comprehensive Description of the Mission Sensor Microwave Imager (SSM/I) Environmental Parameter Extraction Algorithm. Naval Research Laboratory Technical Memorandum Report 5199, Washington, DC.

Wilheit, T. T., A. T. C. Chang, J. L. King, E. B. Rodgers, R. A. Nieman, B. M. Krupp, A. S. Milman, J. S. Stratigos, and H. Siddalingaiah, 1982: Microwave radiometric observations near 19.35, 92, and 183 GHz of precipitation in tropical storm Cora. J. Appl. Meteor., 21, 1137-1145.

A MICROWAVE, VISIBLE, AND INFRARED EVALUATION OF TROPICAL STORM FLOYD

Ralph R. Ferraro

S M Systems and Research Corporation
8401 Corporate Drive, Suite 510
Landover, MD 20785

John C. Alishouse

Roderick Scofield

Wang Jiankang*

Andrew Timchalk

NOAA/NESDIS
Washington, DC 20233

*Visiting Scientist, Satellite Meteorological Center, State Meteorological Administration, Beijing, Peoples Republic of China

1. INTRODUCTION

Present operational rainfall retreival estimates used by NOAA are based upon satellite measurements taken in the visible and infrared (IR). Such techniques utilize cloud top temperatures and cloud growth and other satellite signatures to estimate half hourly rainfall accumulations (Scofield, 1987). Other rainfall techniques based upon the visible and IR have been developed by Griffith, et al. (1978), Wu, et al. (1985), Richards and Arkin (1981), and Adler and Negri (1988).

A much more direct measure of rainfall intensity can be obtained by passive microwave measurements. Many promising investigations using the Nimbus-7 SMMR indicate that oceanic rainfall properties such as intensity and areal extent can be retrieved from microwave radiometers (Alishouse, et al., 1988; Spencer, et al., 1983; Olson, 1986). The recent launch of the DMSP Special Sensor Microwave/Imager (SSM/I) has added new excitement in the retreival of rainfall via passive microwave measusrements. This operational instrument includes a dual-polarization channel at 85 GHz which is highly sensitive to rain over land and ocean.

It is the purpose of this paper to investigate the value of combining the microwave data with the visible and IR. The feasibility of developing a tri-spectral approach to rainfall estimation is needed as there are plans to include a microwave instrument on future NOAA polar orbiting (beginning in the early 1990's) and geostationary platforms. An ensemble of satellite and ground data have been obtained for Tropical Storm Floyd which affected south Florida on October 12, 1987. Although Floyd was a minimal tropical storm, an interesting comparison has been made for a light to moderate band of rain showers over southern Florida.

2. BACKGROUND

2.1 Tropical Storm Floyd

Tropical Storm Floyd became the sixth named tropical disturbance of 1987 on October 10, just off the coast of Nicaragua (Case, 1988). Floyd headed northward and grazed the western tip of Cuba late on October 11. Floyd was upgraded to a hurricane on the morning of the 12th when winds were measured at 80 mph by aircracft reconnaissance, but attained hurricane strength for only 12 hours. On October 12, Floyd passed over the Florida Keys with wind gusts of 80 mph then rapidly weakened as it moved northeastward and interacted with a frontal boundary across central Florida. A band of two to four inch of rainfall occured over Southern Florida on October 12 due to the interaction of Floyd with the frontal boundary.

2.2 Microwave Response to Rain

Unlike the visible and IR which infer rain intensity by cloud top temperatures, cloud structure, etc., the microwave radiation in atmospheric window channels penetrates the cloud layer and responds primarily to the rain layer. Since the emissivity at microwave frequencies vary with surface type and frequency, the effects of rain on the resultant satellite measured brightness temperatures (TB) are different over land and ocean. Over vegetated land, the emissivity is high and constant with frequency. The main effect of rain is the reduction in TB due to the scattering of the upwelling radiation by precipitation size ice particles. This scattering increases with frequency, so the 85 GHz channel will be the most sensitive to rain over land and a decrease in TB with frequency is a strong indicator of rain. One complicating factor is the partial beam filling of the footprint with rain. This becomes more dominant with lower frequencies (i.e., larger footprints).

Over the ocean, the emissivity is low and increases with frequency. The presence of clouds and very light rain is to increase the TB since the upwelling oceanic radiation is absorbed and re-emitted at the cloud temperature, which is radiometrically warmer than the ocean surface. In regions of very light rain or very small convective showers, the presence of precipitation size ice particles is small compared to the microwave footprints. Thus, the observed TB will continue to increase with rainrate. However, as the intensity of rain increases, the presence of the rain layer and precipitation size ice particles initiates a scattering process which reduces the TB. This rain rate at which the reduction in TB occurs is inversely proportional to frequency, so the 85 GHz observations will begin to decrease at much lower rain rates than those at 19 GHz. Finally, with the presence of ice, the higher frequencies (37 and 85 GHz) will respond very similarly over land and ocean.

2.3 Previous Combined Microwave, Visible and IR Studies

Similar studies have been performed by other investigators. Wilheit, et al. (1982) and Hakkarinen and Adler (1988) have used radiometers flown on high altitude aircraft to investigate the sensitivity of the 92 and 183 GHz channels to precipitation. Results from these studies indicate that strong scattering signals occur at these frequencies in the presence of convective storms. Inverse relationships between the 19 GHz and 92 GHz channels were evident over the ocean. In addition, the microwave radiation was not affected by the presence of cirrus and thus, detailed structure of the convective cores were found with the microwave data which was not found in the visible and IR. Spencer, et al. (1988) have taken a look at different storms using the SSM/I observations. They found the scattering signature at 85 GHz to be the same over land and water. Again, they were able to detect better storm structure with the microwave than the GOES visible and IR due to the cirrus penetration by the SSM/I.

3. DATA SOURCES

The source of the microwave data is the SSM/I instrument, which operates at dual-polarization at 19, 37, and 85 GHz and at 22 GHz vertical polarization. These seven channels are measured at a fixed conical scan angle of 50 degrees and have constant footprint sizes which range from 69 by 53 km at 19 GHZ, 50 by 40 km at 22 GHz, 37 by 29 km at 37 GHz, and 15 by 13 km at 85 GHz. All the channels are sampled every 25 km in the along- and across-scan directions while the 85 GHz channel is sampled in between these points for a 12.5 km sample spacing. More details of the SSM/I instrument are given by Hollinger, et al. (1987). Digital data from DMSP orbits 1615 (1124 UTC) and 1622 (2326 UTC) on October 12 were used.

Visible and IR data from the GOES satellite were obtained in the form of hard copy images for October 12, 1987. In addition, all the aviation surface weather observations and six-hour rainfall totals for the state of Florida were obtained. Relatively high resolution 24 hour rainfall observations were obtained from NMC.

Three forms of radar data were obtained. The first was the microfilm scenes of the PPI scans at the various NWS WSR-57 installations in Florida. The scenes give the rainfall exent and the intensities in DVIPS. The second type of radar data was digital in form and obtained from NOAA/AOML. The data was from the Key West radar and is the form of dBZ values gridded to 2.25 km grid cells (Dodge, et al., 1987). Finally, hourly Manually Digitized Radar (MDR) charts were also obtained near the times of the SSM/I passes.

4. DATA ANALYSIS AND RESULTS

Out of the two SSM/I passes near the Florida region on October 12, only the descending pass at 2326 UTC detected the precipitation associated with the remnants of Floyd and the frontal boundary. Unfortunately, the earlier pass near the time of Floyds' peak intensity just grazes the eastern edge of the storm. At 2326 UTC, only light to moderate rain was reported at a few

stations (Daytona Beach, Miami, Fort Lauderdale, Homestead, and Orlando) with the main rain area off the east coast of Florida. However, a small band of rain was detected by radar from just north of Lake Okeechobee and southward for about 50 miles. We chose to analyze this band of rain first since it proved to be a challenging one for both the IR and microwave due to its rather small size, light to moderate rainfall rate, and location over land. Results from the larger area of rain offshore will be presented at the conference.

4.1 GOES IR Analysis

GOES IR imagery for 2331 UTC are presented in Figure 1a. Manually computed IR digital temperatures (°C) are shown in Figure 1b. Satellite derived rainfall estimates (Scofield, 1987) for the half hour period between 2300 and 2330 UTC are shown in Figure 1c. The area over southern Florida where the comparisons are being made is indicated by a box. A small north-south convective cloud band (C-B) is located within the box. The IR imagery and digital analysis shows two areas of cold IR temperatures (-70°C) embedded within this convective cloud band. The southern cold topped area produced raifall estimates of 1 to 3 inches, whereas the northern one ranged from 0.25 to 0.6 inches. A sequence of half hourly IR images showed that the cloud band (C-B) only persisted over the same area for a 2 to 3 hour period before moving eastward and dissapating. At this time Floyd was poorly organized with the main rain area east of Florida and a low center located just south of Miami.

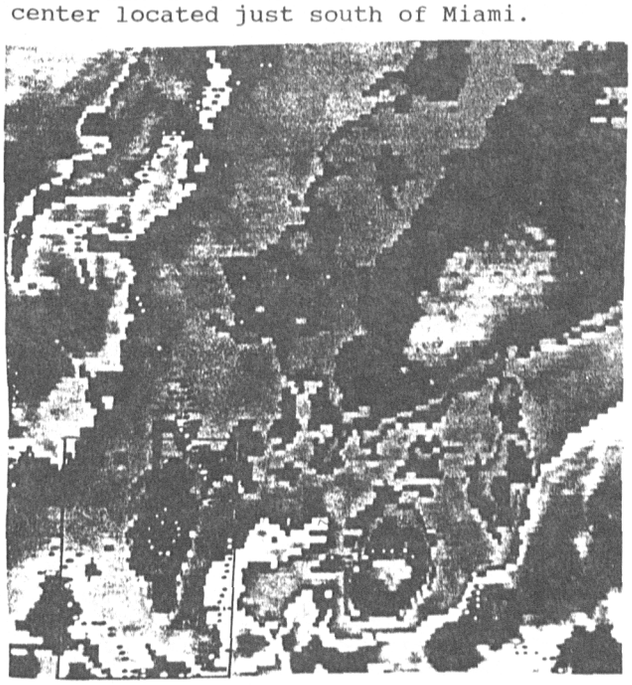

FIGURE 1A. GOES IR IMAGE FOR 2331 UTC ON 12 OCTOBER 1987.

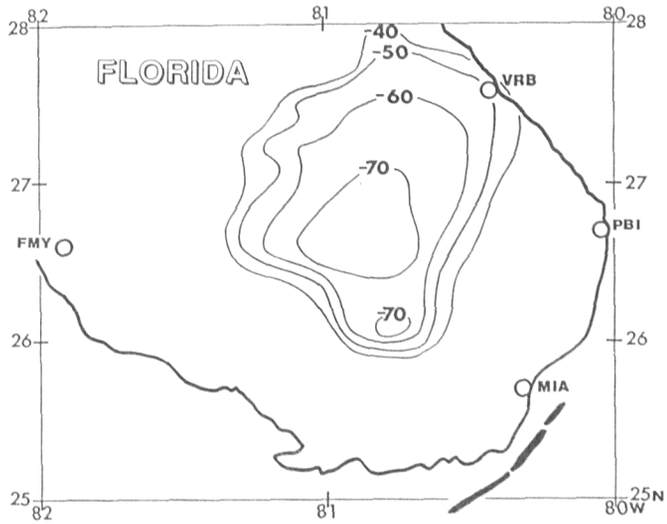

FIGURE 1B. MANUALLY COMPUTED GOES IR TEMPERATURES (°C).

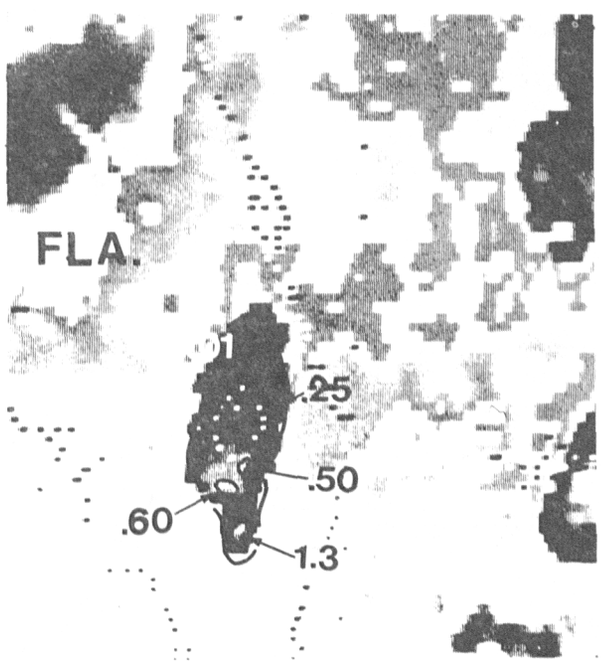

FIGURE 1C. NESDIS HALF HOURLY RAINFALL ESTIMATES FOR 2300 TO 2330 UTC.

4.2 SSM/I Analysis

An objective analysis scheme was used in order to compare output from the SSM/I channels. A complication was the varying footprint sizes of the SSM/I channels with frequency. A Barnes (1964) objective analysis scheme as modified by Koch, et al. (1983) for use with satellite data was used to process the data and grid it at 0.1 degrees latitude and longitude. Values of K=500 and Rmax=40 were used for the 19, 22 and 37

GHz data and K=300 and Rmax=25 were used for the 85 GHz data. Objective analyses were performed on the data from all of the SSM/I channels. However, due to the limited space in this paper, mapped data are presented for only three channels: 19, 37, and 85 GHz, horizontal polarization (HP).

Figures 2 through 4 show SSM/I 19, 37, and 85 GHz TB's gridded every 0.1 degree in a three degree latitude by 2 degree longitude area centered over the convective rain band.

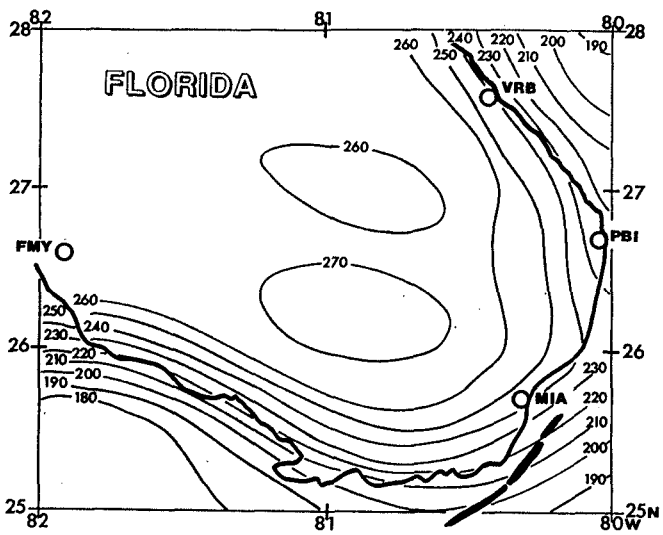

FIGURE 2. SSM/I 19 GHZ HP TB (K) FOR 2326 UTC ON 12 OCTOBER 1987.

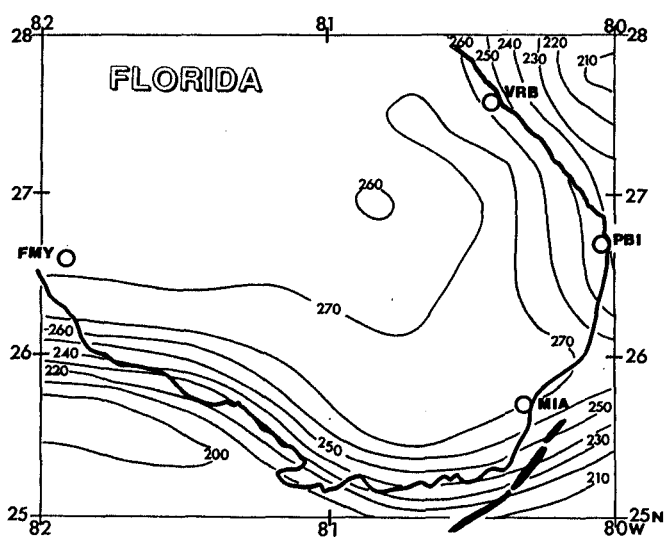

FIGURE 3. SSM/I 37 GHZ HP TB (K).

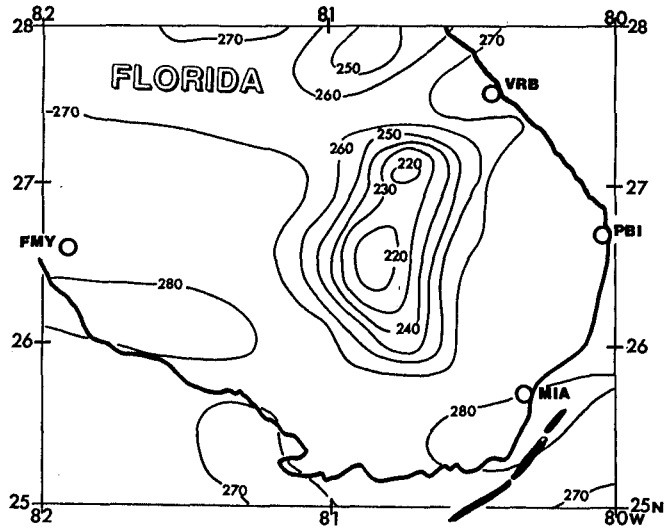

FIGURE 4. SSM/I 85 GHz HP TB (K).

At 19 GHz, the most striking feature is the contrast between land and water. This is due to the large emissivity difference between the two surfaces. Notice the Florida coastline, where TB differences of near 90 K are evident. The broad coastline feature is in response to the large footprint at 19 GHz. Lake Okeechobee is also evident. At 37 GHz, similar features are seen, although the coastline is better defined due to the higher resolution of this channel. The 85 GHz scene is dramatically different. First, the land/water contrast is not clearly observed. This is due to the higher emissivity of the ocean at 85 GHz and the presence of clouds over the water. The most striking feature is the cold band of TB's which are centered near 26.6 N and 80.8 W. This is the region of rain associated with the convective rain band shown in Figure 1. TB depressions of over 60 K are caused by this band of rain. The TB depressions are caused by the scattering process previously described. Finally, there appears to be two centers of cold TB's, most likely associated with areas of heavier rain.

4.3 Comparisons of Satellite and Surface Observations

Figure 5 shows two radar depictions of the rain band. Figure 5a shows the Key West radar data for 2326 UTC (dBZ) which has been gridded to the same projection as ths SSM/I data while Figure 5b shows the Miami radar PPI (DVIPS) for 2325 UTC. Both radars agree fairly well in intensity, with the Key West values probably too low due to the large distance (75 to 100 miles) from the radar

site. Some displacement in positioning is evident but again this can be attributed to the large distance of the rain echoes from Key West. The rainfall intensities for DVIP level 2 using a convective Z-R relationship is 0.2 to 1.1 inches per hour.

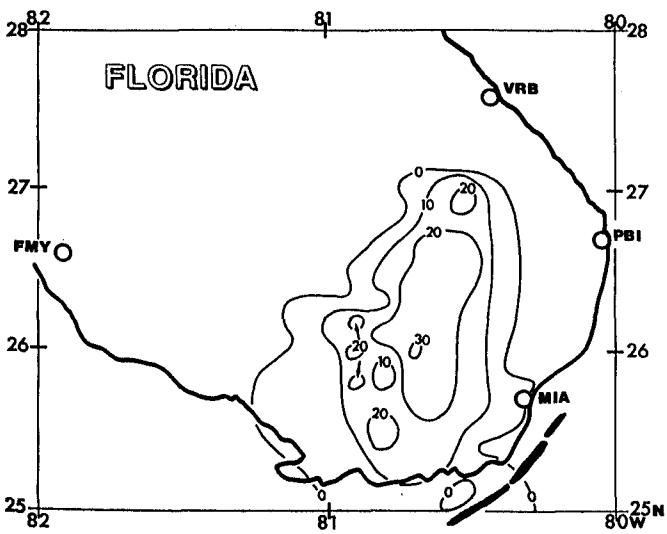

FIGURE 5A. KEY WEST RADAR REFLECTIVITIES (DBZ) FOR 2326 UTC.

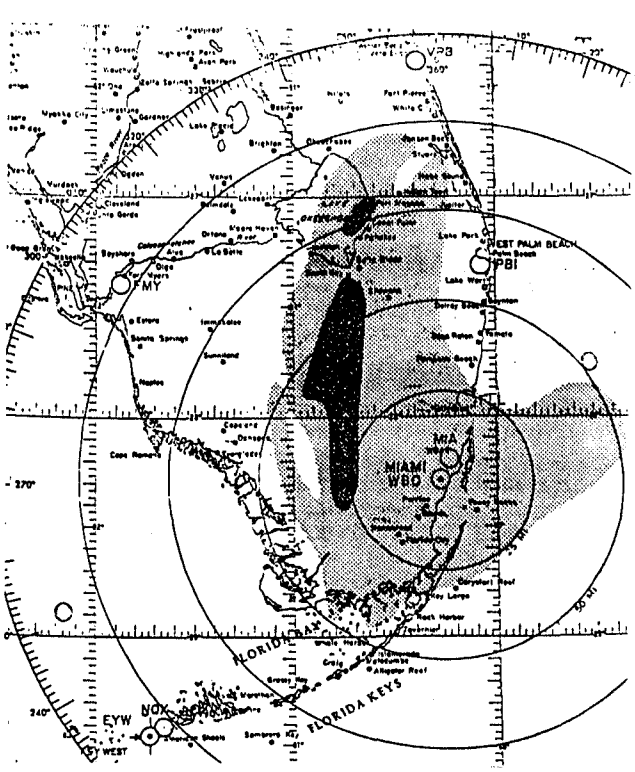

FIGURE 5B. MIAMI RADAR REFLECTIVITIES (DVIPS) FOR 2325 UTC.

The SSM/I 85 GHz and enhanced GOES IR scene are in qualitative agreement in delinating the rain area. However, there are a few important differences. The SSM/I data shows a much more detailed TB field over the rain band than the IR indicating the heavier rain areas. Note the location of the two coldest areas (TB < 220 K) which match up well with the centers of the PPI DVIP level 2. The IR scene for this region is much less detailed. An exception to this is the new convective growth in the southern edge of the rain band which is not detected by the SSM/I. There is some hint of the smaller, but probably more intense rain cell in the Key West radar. Also, the MDR chart for UTC GMT indicated a small area of DVIP level 5 over southern Florida, possibly in response to this cell. As was shown in figure 1c, the NESDIS operational rainfall estimates placed the heaviest amounts with this cell.

5. SUMMARY

In this brief study, we have made a comparison between the SSM/I and GOES IR signatures for a small rain band over southern Florida associated with the remnanats of Tropical Storm Floyd. As was the case with previous investigations, the 85 GHz channels provide the most information for the detection of precipitation. The main advantage of the microwave data over the IR is the deliniation of heavier rain cores which are obscurred by cirrus in the IR. This leads to areal overestimates of rainfall with the IR. The main advantage of the IR over the microwave is the detection of new convective growth which is too small to be detected by the microwave footprints. This would lead to rainfall intensity underestimates with the microwave. It is apparent that the shortcomings of the two instruments tend to compensate one another, thus leading to the conclusion that a the combination of the two with the visible offers the best satellite derived rainfall analysis. More cases are needed to better understand how best to combine the microwave, IR, and visible into a tri- spectral technique.

6. ACKNOWLEDGEMENTS

The authors would like to thank Ted Funk of the Synoptic Analysis Branch of NESDIS for computing the rainfall estimates and John Shadid for the final draft of the figures and illustrations.

7. REFERENCES

Adler, R.F. and A.J. Negri, 1988: A satellite infrared technique to estimate tropical convective and stratiform rainfall. J. Appl. Meteor., 27, 30-51.

Alishouse, J.C., R.R. Ferraro and J.V. Fiore, 1988: Inference of oceanic rainfall properties from the Nimbus-7 SMMR. Submitted to J. Appl. Meteor.

Barnes, S.L., 1964: A technique for maximizing details in numerical weather map analysis. J. Appl. Meteor.,3, 396-409.

Case, R.A., 1988: Atlantic hurricanes-a subdued season. Weatherwise, 41, 25-29.

Dodge, P.M., M. Black, R.W. Burpee and F.D. Marks, 1987: Time lapse radar imagery from land-falling hurricanes. Proc. 17th Conf. on Hurricanes and Tropical Meteorolgy, Miami, FL, AMS, Boston, MA.

Griffith, C.G., W.L. Woodley, P.G. Grube, D.W. Martin, J. Stout and D.N. Sikdar, 1978: Rain estimation from geosynchronous satellite imagery: Visible and infrared studies. Mon. Wea. Rev., 106, 1153-1171.

Hakkarinen, I.M. and R.F. Adler, 1988: Observations of Precipitating convective systems at 92 and 183 GHz: Aircraft results. Meteorol. Atmos. Phys.,38, 164-182.

Hollinger, J., R. Lo, G. Poe, R. Savage, and J. Pierce, 1987: Special Sensor Microwave/Imager User's Guide. Naval Research Laboratory, Washington, DC, 122 pp.

Koch, S.E., M. Desjardins, and P.J. Kocin, 1983: An interactive Barnes objective analysis scheme for use with satellite and conventional data. J. Climate Appl. Meteor., 22, 1487-1503.

Olson, W.S., 1986: Model-based retreival of tropical cyclone rainfall rates using the Nimbus-7 SMMR. Proc. 2nd Conf. on Satellite Meteorology/Remote Sensing and Apllications, Williamsburg, VA, AMS, Boston, MA.

Richards, F. and P. Arkin, 1981: On the relationship between satellite-observed cloud cover and precipitation. Mon. Wea. Rev., 109, 1081-1093.

Scofield, R.A., 1987: The NESDIS operational convective precipitation estimation technique. Mon. Wea. Rev, 115, 1773-1792.

Spencer, R.W., B.B. Hinton, and W.S. Olson, 1983: Nimbus-7 37 GHz radiances corredlated with radar rain rates over the Gulf of Mexico. J. Climate Appl. Meteor., 25, 754-766.

Spencer, R.W., H.M. Goodman and R.E. Hood, 1988: Precipitation retreival over land and ocean with the SSM/I, part I: Identification and characteristics of the scattering signal. In press.

Wilheit, T.T., A.T.C. Chang, J.L. King, E.B. Rodgers, R.A. Nieman, B.M. Krupp, A.S. Milman, J.S. Stratigos, H. Siddalingaiah, 1982: Microwave radiometric observations near 19.35, 92, and 183 GHz of precipitation in tropical storm Cora. J. Appl. Meteor.,21,1137-1145.

Wu, R., J.A. Weinman and R.T. Chin, 1985: Determination of rainfall rates from GOES satellite images by a pattern recognition technique. J. Atmos. Oceanic Technol., 2, 314-330.

6.4

IMAGES OF PRECIPITATION PATTERNS ASSOCIATED WITH TROPICAL CYCLONES USING THE SSM/I 85 GHz CHANNEL

Thomas F. Lee and Allan Caughey
Naval Environmental Prediction Research Facility
Monterey, CA 93943-5006

1. INTRODUCTION

Images produced from the Defense Meteorological Satellite Program's (DMSP) Special Sensor Microwave Imager (SSM/I) show detailed precipitation patterns within tropical cyclones. Such information, based on the 85 GHz channel, can significantly aid forecasting and nowcasting. Many important aspects of tropical cyclones can now be observed, which could not be easily inferred from visible or infrared (IR) images. This case study documents a developing tropical cyclone using the SSM/I 85 GHz channel.

Satellite microwave data from tropical cyclones have been available for years, but the coarse spatial resolution has limited the effectiveness of images. Using the Electrically Scanning Microwave Radiometer data from Nimbus 5, Rodgers and Adler (1981) produced a 19 GHz image which showed a rain-free eye of a developing typhoon before the eye appeared on IR imagery. At this frequency the rain signal results from the enhanced emission from large water droplets; thus a rain area over a sea surface is associated with greater brightness temperatures than the surrounding areas (Wilheit et al., 1977). Precipitation-sized ice particles have a relatively minor effect on the brightness temperatures at this frequency (Wilheit et al., 1982). 19 GHz images of precipitation are also available from the SSM/I, but their usefulness is limited. First, it is often difficult to distinguish rain from nonraining liquid clouds (Spencer et al., 1989). Second, the footprint size is approximately 60 km, which tends to smooth out important detail.

At 85 GHz the dominant signature produced by precipitation arises mainly from scattering by precipitation-sized ice particles above the freezing level rather than from emission by water droplets. This scattering produces lower brightness temperatures over areas of significant precipitation than over surrounding areas. Spencer et al. (1989) document that precipitation is strongly indicated in cloud systems with 85 GHz temperatures below about 255 K, regardless of the freezing level. Thus, the application of this threshold can delineate precipitation in a variety of climate zones. Despite the two distinct physical mechanisms responsible for precipitation signatures at 19 GHz vs 85 GHz, the spatial agreement between the two channels is rather good (Wilheit et al. 1982; Spencer et al., 1989). The SSM/I 85 GHz channel produces superior images because of better spatial resolution and sharper delineation of precipitation from non-precipitating clouds.

2. DATA

The 85 GHz data are available from the spacecraft at about 15 km resolution. At the Fleet Numerical Oceanographic Center (FNOC) the data are interpolated into a data base with resolution of approximately 18 km. In addition to the 85 GHz images, co-located visible and IR images are available at about 4 km resolution in the FNOC data base.

On images of the 85 GHz data, we use the convention commonly used on IR images: low brightness temperatures are depicted in bright grayshades, high brightness temperatures in dark grayshades. Thus, areas of precipitation (low brightness temperatures) are bright relative to the background. Away from regions of precipitation or significant liquid water clouds, gradients of water vapor over the ocean also appear prominently on 85 GHz images. Unlike IR images, however, on which water vapor-laden regions show up as relatively cold (relatively bright grayshades), 85 GHz images depict such areas as relatively warm (relatively dark grayshades). Coastlines appear naturally on 85 GHz images as a result of the warmer brightness temperatures over land than over the ocean.

3. CASE STUDY

Figure 1 shows an 85 GHz image of tropical storm Florence (maximum sustained winds: 60 kt) in the Gulf of Mexico on 9 September 1988 at 1149 UTC. She became a hurricane later in the day before going ashore in Louisiana. In the 85 GHz (horizontal polarization) image (Figure 1) a large area of precipitation surrounds a rain-free eye. Associated precipitation extends northeastward and crosses the coastline. In addition, a narrow spiral band of precipitation appears to the southeast of the center. Despite the prominent signature of the rain-free eye on Figure 1, the DMSP visible and IR images (Figures 2-3) show little trace of this center. The dense cirrus canopy, opaque at visible and IR frequencies but transparent at 85 GHz, explains the differences seen on Figures 1-3.

Consistent with the IR image, a trace of IR cloud top temperatures through a cross-section (Figure 4) indicates only the high cirrus canopy (pixels 85 through 168). The trace of 85 GHz brightness temperatures reveals the presence and strength of the convection under the cirrus canopy. The application of the 255 K precipitation threshold (Spencer et al., 1989) shows the eye wall precipitation as pronounced spikes

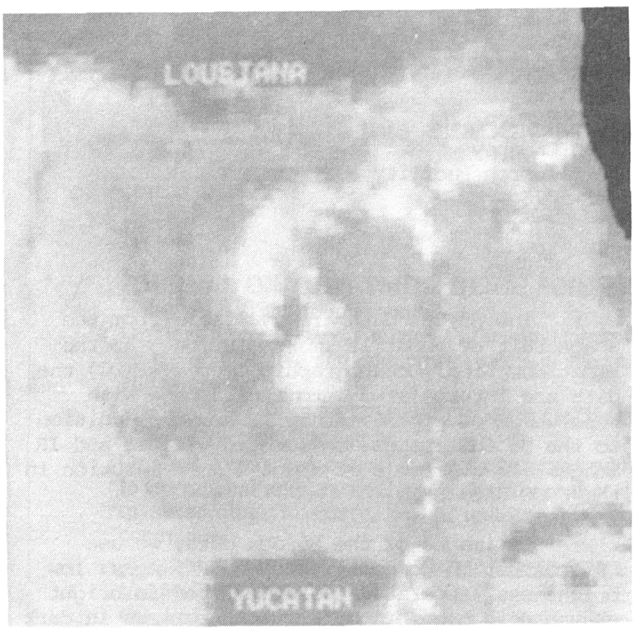

Fig. 1. SSM/I 85 GHz image (horizontal polarization) of tropical storm Florence in the Gulf of Mexico, 1149 UTC on 9 September 1988.

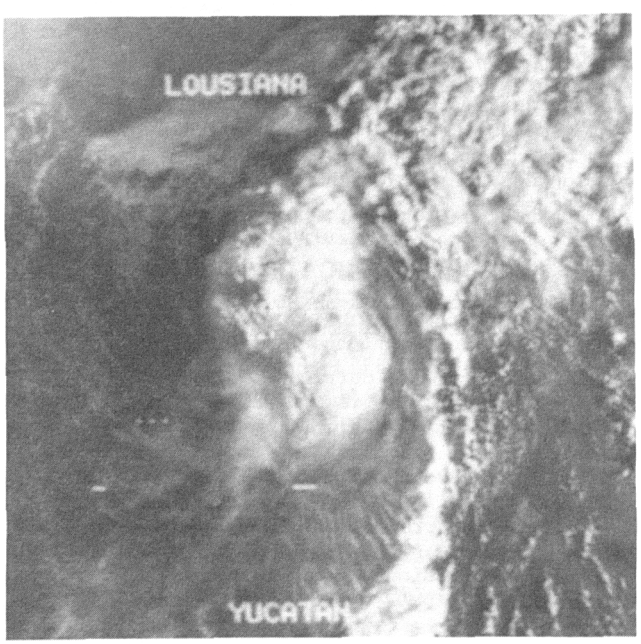

Fig. 2. Visible image of tropical storm Florence, 1149 UTC on 9 September 1988.

(stippled on Figure 4). In between the two peaks of precipitation lies a warm, rain-free eye.

The distribution of water vapor around Florence can also be qualitatively inferred from Figure 4. In the generally southerly flow on the eastern side of the storm, vapor-laden air is

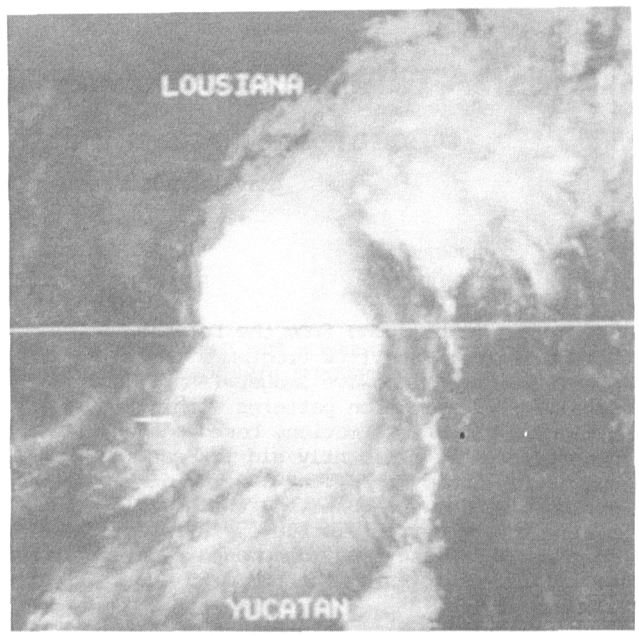

Fig. 3. IR image of tropical storm Florence, 1149 UTC on 9 September 1988. Horizontal line indicates position of cross-section (Fig. 4).

advected from the tropics. The emission from this vapor and from embedded water clouds adds substantially to the emission from the sea surface, producing 85 GHz temperatures near 260 K. On the western side of the storm, however, a more continental flow helps import drier air into the area. This dry air contributes relatively little additional energy to the radiance from the sea surface. Therefore, the 85 GHz satellite brightness temperatures in this region average around 235 K, low enough to be incorrectly flagged as precipitation by the 255 K threshold (hatched on Figure 4).

These two distinct regions of atmospheric water vapor content can be also be seen on the 85 GHz image (Figure 1): the bright grayshades west of the storm indicate relatively little water vapor in the lower atmosphere; the darker grayshades east of the storm indicate a more moist boundary layer. Fortunately, an analyst viewing the image would probably not misinterpret the bright western region as precipitation, since the visible and IR images (Figures 2-3) confirm that the area is clear. For more ambiguous cases, Spencer et al. (1989) have developed a polarization-corrected 85 GHz image that eliminates any false precipitation signals caused by water surfaces.

4. DISCUSSION

Much of the current research into SSM/I data emphasizes algorithms which combine the different channels to produce quantitative parameters (rain rate, water vapor, liquid water, etc.). This case study shows, however, that even

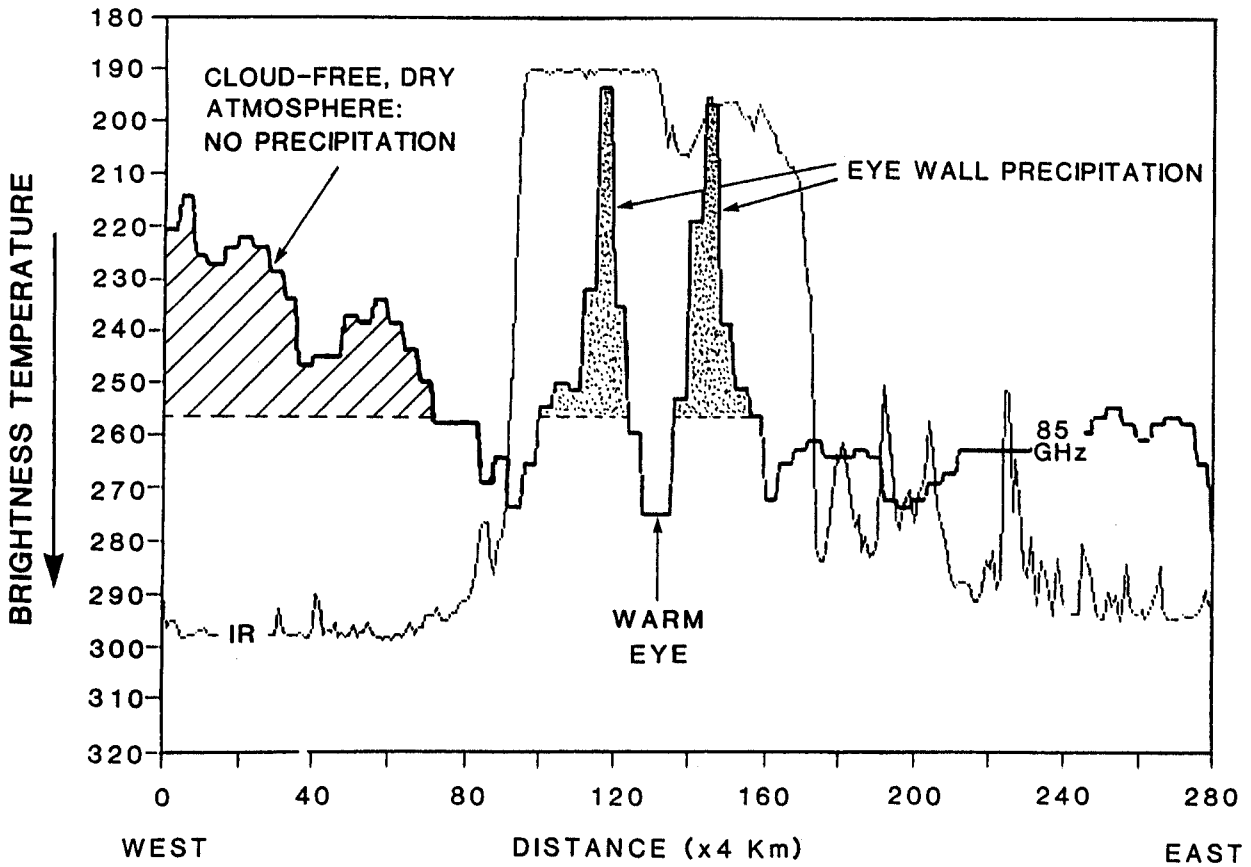

Fig. 4. Cross-section of IR (fine trace) and 85 GHz horizontal polarization (bold trace) channels through tropical storm Florence, 1149 UTC on 9 September 1988. Stippling indicates precipitation using a 85 GHz threshold of 255 K; hatching indicates a "false" precipitation signal using the same threshold. Location of the cross-section indicated on Fig. 3.

unprocessed images of 85 GHz data provide useful, easy-to-interpret forecast products. To the extent that 85 GHz images are made available to duty forecasters of tropical cyclones, significant improvements in analysis and forecasting should result.

For example, incorporation of 85 GHz images should improve the Dvorak technique (1984) which requires analysis of IR and visible images to produce an estimate of tropical cyclone strength. At present, the detection of eyes in developing storms, a required step in the Dvorak technique, is often possible only during the daytime when visible images images give a more detailed view of the storm than do IR images. Sometimes even a visible image fails to delineate the eye (e.g., Figure 2). 85 GHz images, on the other hand, are available both day and night and should always show eyes as they develop.

The operational use of the 85 GHz image could also support reconnaissance aircraft penetrating tropical cyclones. At the present, visible and IR images provide only sketchy pre-takeoff information about the structure of the storm core. 85 GHz images, on the other hand, often show significant asymmetries of convection within the eye wall, indicating regions where penetrations might be carried out with relative ease and safety. Also, features of special research interest, such as double eye walls, could be identified on images, giving research crews advance guidance for upcoming flights.

5. ACKNOWLEDGMENTS

Mr. Jim Clark and PH1 Ken Bolden helped produce the satellite images. Dr. Paul Tag helped guide the progress of the research.

6. REFERENCES

Dvorak, V. F., 1984: Tropical cyclone intensity analysis using satellite data. NOAA Technical Report NESDIS 11, U.S. Department of Commerce, Washington DC, 47 pp.

Frank, W. M., 1987: Tropical Cyclone Formation. A Global View of Tropical Cyclones, R. L. Elsberry, Ed., based on the International Workshop on Tropical Cyclones (Bangkok, Thailand), November 25-December 5, 1985, Office of Naval Research, 53-90.

Rodgers, E. B., and R. F. Adler, 1981: Tropical cyclone rainfall characteristics as determined from a satellite passive microwave radiometer. Mon. Wea. Rev., 109, 506-521.

Spencer, R. W., H. M. Goodman and R. E. Hood, 1989: Precipitation retrieval over land and ocean with the SSM/I: Identification and characteristics of the scattering signal. Accepted by Journal of Atmospheric and Oceanic Technology.

Wilheit, T. T., A. T. C. Chang, M. S. V. Rao, E. B. Rodgers, and J. S. Theon, 1977: A satellite technique for quantitatively mapping rainfall rates over the oceans. J. Appl. Meteor., 16, 551-560.

_____, T. T., J. L. King, E. B. Rodgers, R. A. Nieman, B. M. Krupp, A. S. Milman, J. S. Stratigos, and H. Siddalingaiah, 1982: Microwave radiometric observations near 19.35, 92, and 183 GHz of precipitation in tropical storm Cora. J. Appl. Meteor., 21, 1137-1145.

6.5

TROPICAL SYNOPTIC COMPOSITES IN VAS, OLR AND TOVS RADIANCE DATA

James P. McGuirk

Department of Meteorology
Texas A&M University
College Station, Texas 77843-3146

1. INTRODUCTION

1.1 Background

Understanding the transient structure of the tropical Pacific atmosphere is hampered by lack of data. Larger spatial and temporal scale features can be examined through smoothing of the data across the larger scales. This procedure fails for synoptic scale features over the Pacific because the resolution of the data normally exceeds the size of the system. A second problem is that the synoptic scale signal of satellite observations in the tropics is weak at best. Most operational techniques emphasize information associated with the vertical structure of the observations and the atmospheric systems themselves. It is curious that operational meteorologists turn first to the horizontal structure of satellite observations.

This paper contrasts the horizontal structure of specific tropical synoptic features with those of a zonal mean ITCZ. Two hypotheses are assumed:

i. The cool season Pacific ITCZ oscillates between two states: a zonally symmetric state, referred to as a quiescent state; and a locally convectively active, meridionally oriented state, referred to as a tropical plume. McGuirk et al. (1987) presented evidence substantiating this modal behavior in the ITCZ.

ii. Satellite channel radiances possess signals sufficiently strong to reveal horizontal, as well as the vertical, structure of these synoptic ITCZ variations. Preliminary work (not reported herein) suggest that these horizontal signals are not captured well in modern analysis systems, even though the vertical structure often is specified accurately. These signals can be resolved by averaging over many events, or compositing, instead of smoothing temporal and spatial scales.

Conclusions are made regarding the two different appearances of the ITCZ--a weakly convective, zonally symmetric state and a locally, synoptically-active convective state. Of primary significance is how a number of different satellite systems view these distinctive states.

1.2 Data

The two ITCZ modes are contrasted in four different forms of satellite radiance data:

i. Daily, gridded (2.5°x2.5°) OLR, from which tropical convective cloud can be inferred;

ii. Digitized, gridded (3.5°x3.5°) GOES VAS water vapor imagery (6.7 μm), which possesses a weighting function peak at approximately 500 mb for climatological moisture distributions.

iii. Analyzed brightness temperatures (3.75°x3.75°) of TOVS water vapor channels from the NOAA 7 and 8 polar orbiters(6.7 μm [500 mb]; 7.3 μm [700 mb] is available but similar). Since this instrument is used for sounding reconstruction, data are absent in overcast regions.

iv. Analyzed brightness temperature vectors, as in iii, except for a nearly complete set of TOVS channels with weighting function peaks in the troposphere (HIRS and MSU); these channels are indicators of both thermal and moist structure.

In all cases the data are composited over many events to minimize the effects of missing data, sampling errors and variability of individual systems.

2. ZONAL ITCZ VS. SYNOPTIC PLUME

Hayes and McGuirk (1989) describe a procedure for identifying and quantifying periods of significant convection along the ITCZ. Figure 1 contrasts periods during which the ITCZ is active all the way across the Pacific with periods when the ITCZ is active at a single point (165°W) with no *a priori* knowledge of convective activity elsewhere. If attention is focused on active behavior at a point, the resultant pattern is strongly meridional and of synoptic scale. The pattern resembles a tropical plume. For strong zonally symmetric (at least across the Pacific) active convection, the signal is weaker and no significant synoptic detail is apparent. Correspondence between the two sets of days comprising these composites is not good; active convection at 165°W does not imply a strong or weak ITCZ. The zonally symmetric composite is the strong convection extreme of the quiescent mode; the quiescent mode typically is much weaker than that in Fig. 1. Even so, the convective maximum in the zonally symmetric ITCZ is significantly weaker (about 10 W/m²) than in the tropical plume mode. The dry subsidence region is also organized zonally, with comparable anomaly magnitudes in both composites.

Figure 2 compares OLR composites of many occurrences of synoptic scale tropical plumes with many days when no tropical plumes were observed. Days comprising composites in Fig. 2 are not the same as those composited in Fig. 1. The tropical plume composite is centered--in latitude, longitude and time--on the initiation of the plume and its intersection with the ITCZ; the pattern is similar to that generated by Lin and Mock (1986). Plume patterns are associated with locally active meridional overturning; that is, a local Hadley cell.

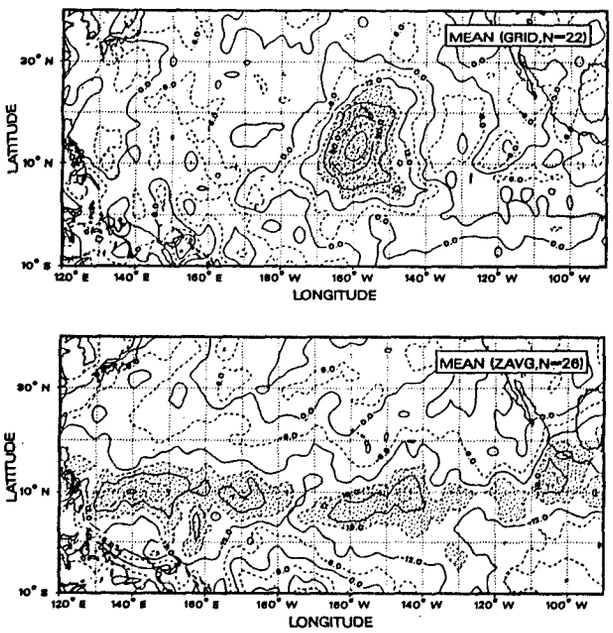

Fig. 1. (top) OLR composite anomaly map of 22 d of active convection at 165°W; (bottom) as in top, except 26 d with zonally averaged active convection. Contour interval is 6 W/m²; active convection regions are shaded.

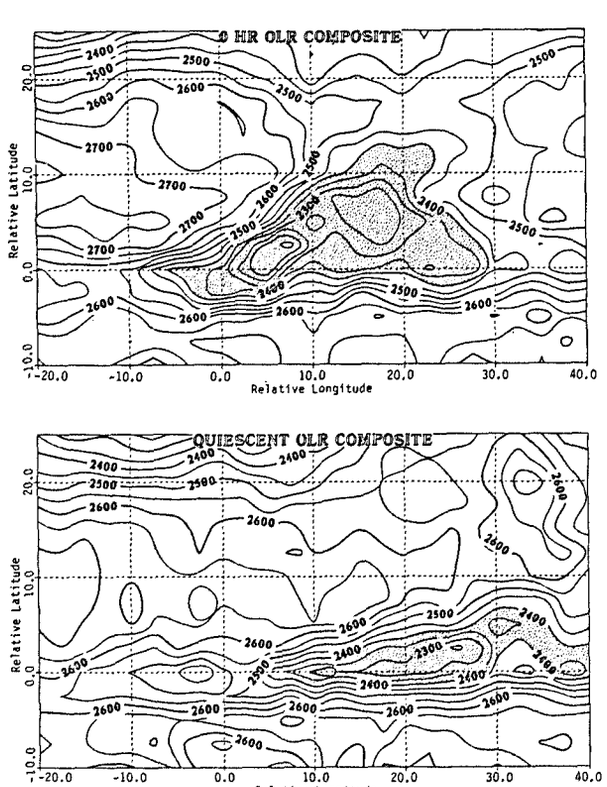

Fig. 2. (top) OLR composites of 35 tropical plumes, centered at the plume origin at 0° relative longitude and the ITCZ, and (bottom) 35 quiescent days. Units in 0.1 W/m²; high cloud regions are shaded.

When plumes are not active, the ITCZ is predominantly zonal and convectively weaker (10–15 W/m² warmer). The dry subsidence region poleward of the active convection (the subtropical high) is larger, more zonally oriented, and not as cloudy or warm (5–10 W/m² cooler). Thus, in the zonally symmetric mode, it can be inferred that the Hadley cell is weaker.

Figure 3 reproduces the composite events from Fig. 2, as viewed in VAS water vapor imagery. The patterns are similar but not identical. The wave nature of the plume and the contrast between zonally symmetric and plume states is stronger in the vapor imagery. Smaller scale details are different in the two views of the composite. A subset of the composite cases is shown in Fig. 4, as viewed in TOVS vapor channel data (6.7 μm). The plume composite has had the climatological brightness temperatures subtracted from it. The quiescent composite is apparently dissimilar to those in Figs. 2 and 3, only partly because of the larger domain represented; between 105° and 165°W the ITCZ is oriented more SW–NE and is displaced about 5° farther south. The subtropical high appears to be more of an east-west wave feature, rather than a zonally banded one because of its weakness in the eastern Pacific. The quiescent mode however more nearly resembles Figs. 2 and 3 than the climatological mean over which data were analyzed. The ITCZ is disappears east of 110°W. The plume composite of Fig. 4 implies a significant amplification of the climatological pattern and generally resembles the vapor imagery composite in Fig. 3. Within the plume region, all cloudy observations are absent in Fig. 4; therefore, Fig. 4 underestimates the plume signal.

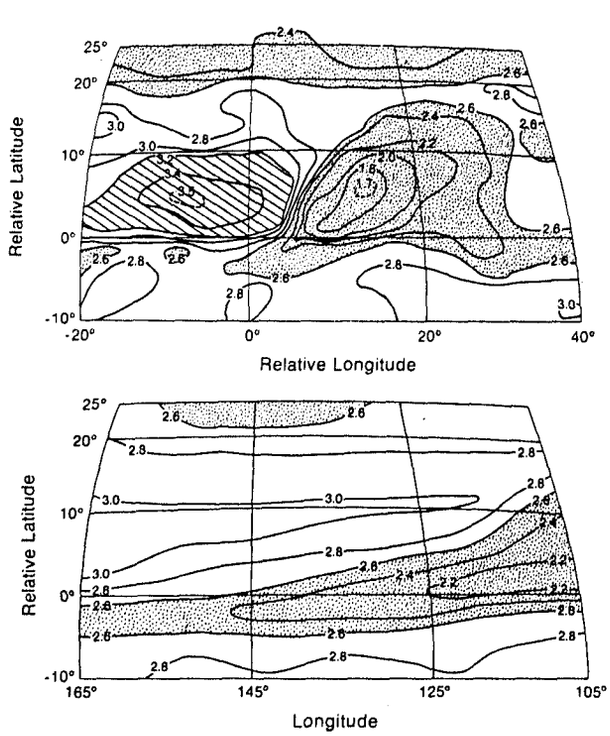

Fig. 3. As in Fig. 2, except for GOES VAS water vapor imagery composites. Units from 1–4 correspond to gray-scale from white (cloud) to black (clear); shading denote brightest clouds.

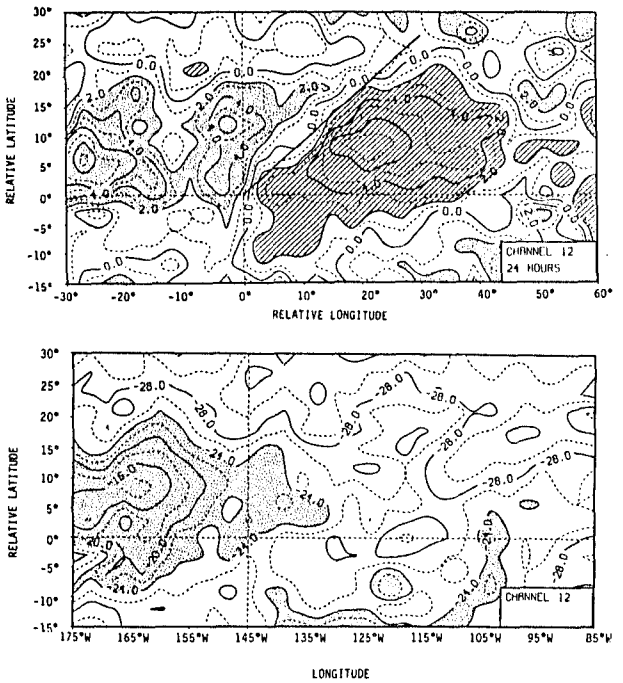

Fig. 4. (top) Anomalies of TOVS 6.7 μm water vapor brightness temperature composites of 17 plume events and (bottom) 17 "quiescent" days. Units in °C with shading dry and hatching/heavy line moist.

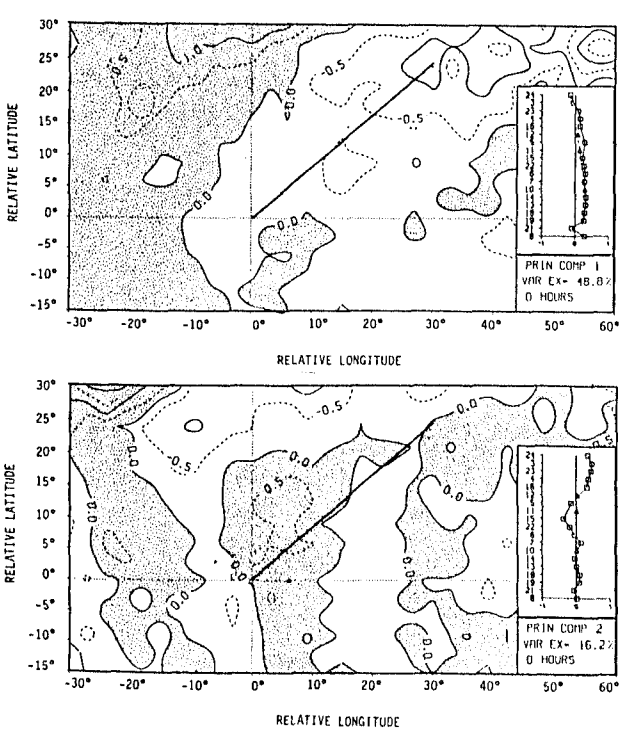

Fig. 5. EOF decompositions of TOVS tropospheric channel radiance observations for 17 plume events. Insets show approximate vertical structure and % eddy variance explained: (top) tropospheric average temperature and (bottom) tropospheric thermal wave--warm over cold; mappings give amplitudes with positive regions shaded.

Finally Fig. 5 presents two empirical orthogonal function decompositions of TOVS tropospheric channels for the Fig. 4 plume composites identifying two thermal patterns valid at the origin of the plumes. The insets show the approximate vertical thermal structure and the amount of total channel variance explained (the zonally symmetric structure has already been removed). The upper panel is a tropospheric average temperature signal, warm to the west of the plume, cold to the east. The lower panel depicts a synoptic scale, equivalent barotropic, upper tropospheric wave. Within the plume, the structure is warm air over cold, with the opposite to the west of the plume origin.

3. PRECURSOR SIGNALS

Figure 6 depicts composite maps of VAS imagery, OLR analysis, TOVS water vapor analysis and the EOF thermal wave 24 to 48 h before composite plume initiation; that is, mean precursor forecast signals. A strong (useful) wave signature appears in the vapor imagery, less strongly and a slightly different configuration in the TOVS vapor composite, not at all in the OLR analysis, and very strongly in the upper tropospheric thermal wave (TOVS). The OLR fails because, at times long before plume initiation, insufficient vertical motion has been generated to develop an organized cloud field; the OLR however does demonstrate the difference between the quiescent mode and the plume precursor phase--the quiescent case represents a relatively active, but zonally symmetric ITCZ. The discrepancies between TOVS and VAS vapor channels is unclear, but should be related to the overall discrepancy between the climatological patterns of the two systems. The TOVS thermal pattern demonstrates that dynamical disturbances exist already at this time in the deep tropics, even before any tropical development has occurred in conjunction with the mid latitude trough (a common feature associated with plumes and identified in the northwest corner of the VAS vapor composite of Fig. 6).

4. COMPARISON AND SUMMARY

The major differences between the observing systems deal with resolution and clouds. VAS imagery is continuous and interprets clouds simply as very wet regions. TOVS either corrects the observations to an equivalent no-cloud brightness temperature, or makes no observation at all in overcast cloud. OLR detects only cloud; moist unsaturated regions are equivalent to dry. Thus as tropical plumes evolve, they will be underestimated seriously by TOVS, which eliminates observations in the cloud plume region; the same problem exists in active ITCZ regions (like the quiescent mode). Resolution should not be a problem in these analyses because the compositing technique will minimize sampling errors. The discrepancy which exists between the vapor channels (TOVS and VAS), particularly in precursor stages when cloud contamination is minimized, is more difficult to understand. For pattern differentiation, vapor

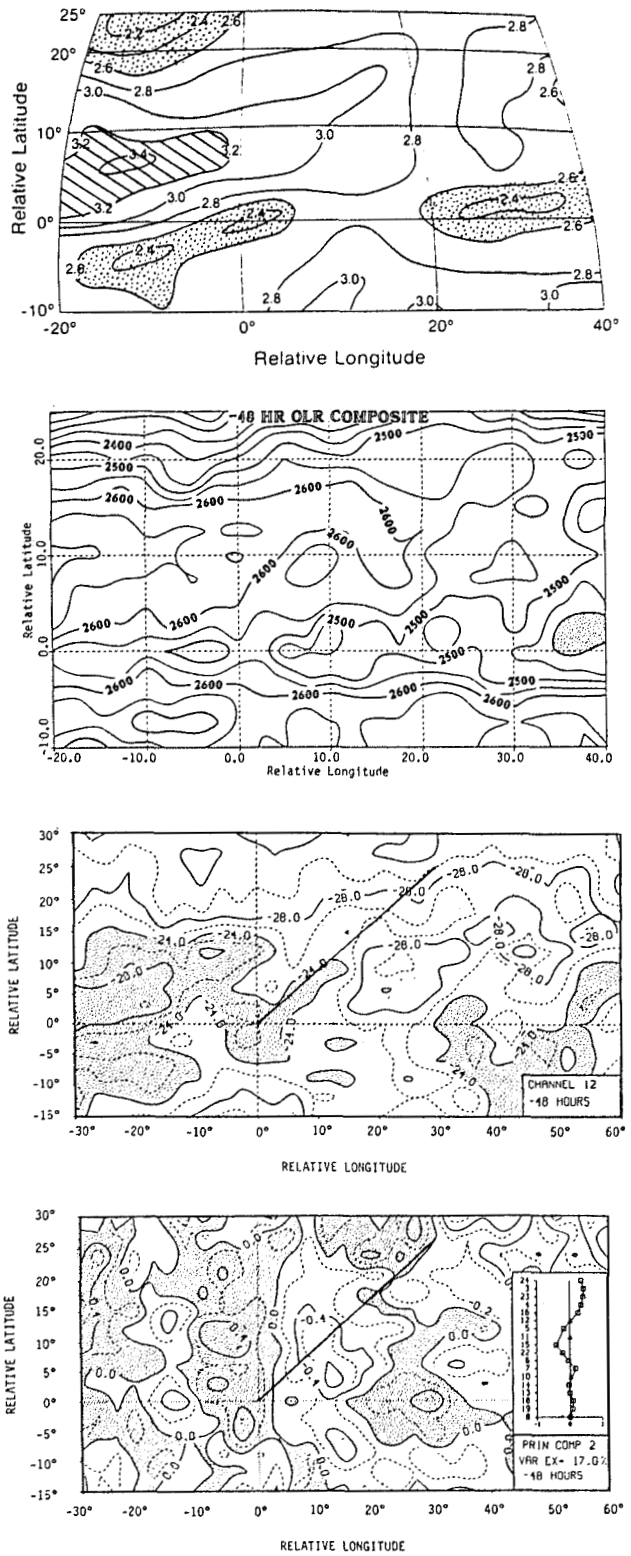

Fig. 6. Precursor composite signatures (24-48 h before plume initiation) for VAS imagery (top), OLR analysis (2nd), TOVS vapor channel (3rd), and TOVS thermal wave (bottom). Shading consistent with previous figures.

imagery may be superior to both vapor soundings channels and OLR because it senses meaningful information in both cloudy and cloud free regions.

The most significant results are:

i. All the satellite sensors detect similar and useful patterns;

ii. The patterns are sufficiently different that independent synoptic information is available in each;

iii. Cloud, vapor and temperature information each can be isolated;

iv. Tropical signatures are sufficiently strong that useful signatures can be detected in both moisture and thermal patterns both in the presence of clouds and even before their development;

v. The ITCZ exhibits a zonally symmetric convective phase and an enhanced regional convective phase (plumes), both of which can be differentiated from climatological mean behavior.

5. ACKNOWLEDGEMENTS

The research reported here is supported by NASA's George C. Marshall Space Flight Center, under Contract No. NAS-37284.

6. REFERENCES

Hayes, P.M., and J.P. McGuirk, 1989: Active modes of the Pacific ITCZ, *Preprints, AMS 18th Conf. on Hurricanes and Tropical Meteorology*, San Diego, May 1989.

Lin, R-Q., and D.K. Mock, 1986: A test of the ECMWF model in tropical synoptic-scale diagnosis. *Mon. Wea. Rev., 114*, 1519-1538.

McGuirk, J.P., A.H. Thompson and N.R. Smith, 1987: Moisture bursts over the tropical Pacific Ocean, *Mon. Wea. Rev., 115*, 787-798.

Blank page retained for pagination

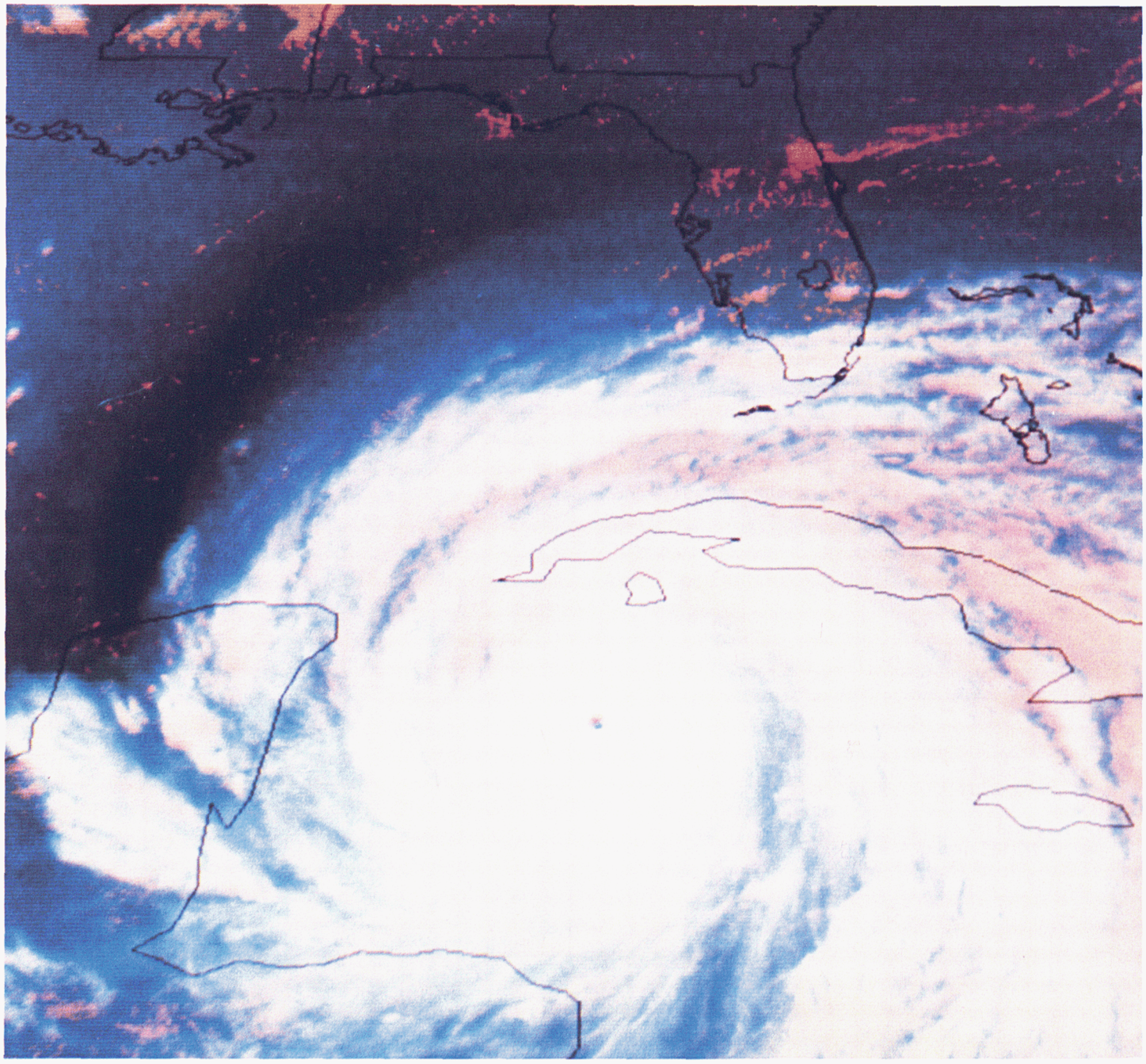

Figure 4. Paper 7.1 Multispectal Image Analysis of Hurricane Gilbert, Thomas J. Kleespies.

Multispectral image of Hurricane Gilbert taken by the VISSR Atmospheric Sounder on GOES East at 2130 UT on 13 September 1989. The image was constructed by driving the red color gun of the monitor with visible imagery, green with 11 micrometer infrared (VAS band 8), and blue with 6.7 micrometer water vapor imagery (VAS band 10). Low clouds appear bright in the visible, but dark (warm) in the infrared, and non-existent in water vapor imagery (water vapor imagery does not see the surface), so they appear red overall, as can be seen in the vicinity of Florida. High clouds are apparent in all three bands, so they appear white, as can be seen in the major rain bands. In the region of the Gulf of Mexico to the northwest of the hurricane which is free of mid and high level clouds, dry subsiding air due to hurricane dynamics has a darker appearance than the surrounding blue tinted regions which contain more moisture at upper levels of the troposphere.

MULTISPECTRAL IMAGE ANALYSIS OF HURRICANE GILBERT

Thomas J. Kleespies
Satellite Meteorology Branch
Atmospheric Sciences Division
Air Force Geophysics Laboratory
Hanscom AFB MA 01731

1.0 INTRODUCTION

One of the early applications of meteorological satellite imagery was positioning of tropical cyclones. However, since these early satellites were polar orbiting, a particular tropical cyclone was viewed only a few times per day. This task became much easier with the advent of geosynchronous satellites. But the early geosynchronous satellites ATS 1,2 and 3 in the late 1960's and early 1970's carried only visible imagers, and thus were restricted to observations during the local daylight. The launch of ATS-6 in 1974 brought the first infrared imager to geosynchronous orbit, and weather forecasters for the first time were able to observe and track tropical cyclones from space twenty-four hours a day (Duback and Ng, 1988)

When GOES 4 became operational in 1980 it brought new and improved imaging capabilities with the VAS instrument. The VAS is a 13 channel spin-scan radiometer, able to produce imagery or sounding data. When producing imagery, it can simultaneously image in the visible, plus two, three or four different infrared bands. When sounding, visible and up to twelve infrared bands are acquired, with the scan mirror dwelling on a particular scan line for a number of spins in order to observe the same area with different bands and to reduce instrumental noise (NASA, 1980).

A good example of early bispectral techniques to deduce cloud properties is given by Reynolds and VonderHaar(1977). The use of infrared water vapor imagery to observe the near storm environment around tropical storms was explored by Rodgers and Stout (1983), Nunez and Stout (1984), and Velden(1987). Menzel et al (1983) use the VAS sounding channels in a retrieval type approach to estimate cloud top height.

Multispectral image analysis can be considered to be a mature field in the area of land resources remote sensing (see for example Moik (1980), Schowengerdt (1983)). However, there seems to be few references to multispectral image analysis of scenes of meteorological interest, possibly because full color image processors have only recently become "affordable" to the meteorological community. Notable among these references are d'Entremont and Thomason (1987) who discussed some of the theory behind multispectral AVHRR imagery in some detail, and Kleespies et al, (1987) who presented SMMR and GOES multispectral imagery. The particular three bands used to create the imagery discussed in this paper were first brought to the author's attention by Zehr (1984). In his oral presentation, he showed GOES imagery which combined the visible, 11 μm infrared, and 6.7 μm water vapor channels into a single false color image. This paper uses these three channels to examine the near environmental features of the atmosphere around Hurricane Gilbert.

2.0 METHODOLOGY

The AFGL Interactive Meteorological System (AIMS) is a cluster of VAX minicomputers and workstations used for research purposes at AFGL. AIMS routinely acquires and processes North American surface and upper air data, and GOES Multispectral Imagery. Imagery can be displayed on any one of three Adage 3000 image processors. Each of the Adages has a minimum address space of 1024x1024x32 bits deep. In low resolution mode, any 512x512 portion can be displayed. The image depth can be partitioned in a large number of ways, depending upon the application. Since the Adage is a full color display device, it requires that the video chain contain at least twenty-four bits of imagery; eight bits each for the red, green and blue channels. These channels can actually be remapped arbitrarily at the bit level via a cross-bar-switch. The high level eight bits are nominally reserved for overlays. Monochrome image display, such as for a single channel image, is accomplished by copying the same eight bit image to all three channels (red, green and blue). Full color image display, such as with a color photograph, is attained by placing the monochrome intensity of the red component of the image in the red channel, and similarly for the green and blue channels. Multispectral imagery is achieved in the same fashion as for full color imagery, but since there is not necessarily a correspondence between the spectral regions used and the human range of vision, the selection as to which spectral band to place into which RGB channel is somewhat arbitrary, and relies to some degree on individual taste (there is a human factors consideration when applied to individuals with impaired color vision). Figure 1 is a schematic of the spectral band/channel selection for the multispectral imagery discussed in this paper. The infrared band is VAS band 8 and the water vapor band is VAS band 10.

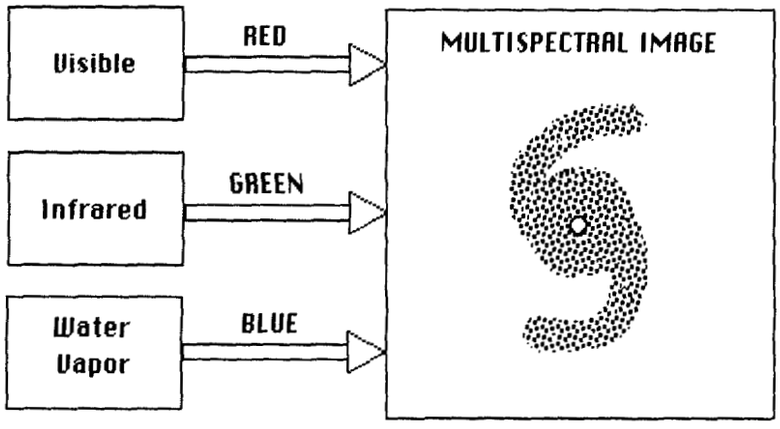

Figure 1. Spectral Band-Channel assignment for display of multispectral imagery on AIMS Adage 3000.

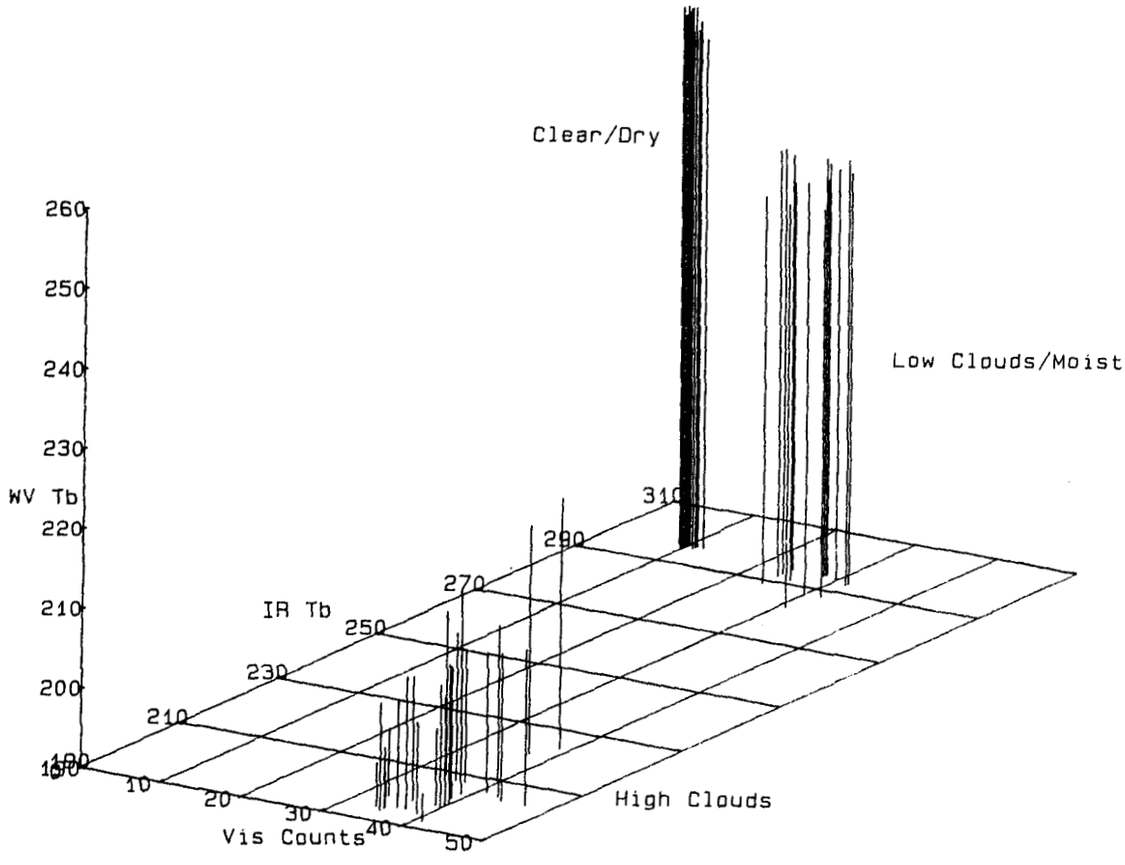

Figure 3. Three-space scatter diagram of selected cloud features from the 2130 UT 13 Sep 1988 GOES E multispectral image of Hurricane Gilbert. The coordinates represented by the pixel values for visible counts, infrared and water vapor brightness temperatures are at the top of the vertical lines. The drop lines from these coordinates to the visible-infrared plane are to help relieve the ambiguity of perception when viewing a three-space plot in perspective. As per Figure 1, the visible axis can be thought of the red axis in the RGB model, similarily the infrared can be thought as the green axis, and the water vapor can be thought as the blue axis.

3.0 RESULTS

In daylight, all clouds appear to be some degree of brightness in the visible, although there has been reported some relationship between albedo and cloud height (Griffith and Woodley, 1973). Away from sunglint the ocean surface appears fairly dark. In the infrared there is a general inverse relationship between brightness temperature and cloud height, the warm clouds tops are lower in the atmosphere, and the cold cloud tops are higher in the atmosphere. Water vapor imagery requires some interpretation. In the water vapor absorption band around 6.7 μm, virtually no radiation emitted from the surface reaches the instrument, so a scene with no clouds appears to be quite cold compared to a window channel. The VAS instrument measures the integrated radiance emitted by the water vapor in the upper troposphere. Since this channel is near the center of the absorption band, it saturates fairly high in the troposphere. If the upper troposphere is relatively dry, some the radiation that is sensed by the instrument is emitted deep in the atmosphere, and with normal lapse rates, the resulting brightness temperature is consequently warmer than that emitted from an atmosphere with a relatively moist upper troposphere.

The interplay between these three bands when displayed as multispectral imagery yield a rich diversity of color. The general features are quite clear. Low clouds appear red or magenta, since they are bright in the visible (red), dark in the infrared (green) and non discernable in water vapor (blue). High clouds appear yellow or white, since they are relatively bright in all three bands. In clear air, regions of dry-subsiding air have a dark appearance (dark in the visible over the ocean, warm-dark in the infrared, dry-dark in the water vapor band). Moist areas in the upper troposphere have a blue tint, even over the underlying low and mid-level clouds (water vapor band is cold-bright). Figure 2 is an example of the the three images that produced the multispectral imagery described in this paper. Figure 4 is the multispectral representation and is the color insert to these proceedings. Of real interest is the fact that the subsidence associated with the hurricane dynamics is very apparent in the water vapor imagery in the northwest sector outside of the outer rain band. Additionally, it is possible to see the low level clouds between the rain bands in the multispectral imagery, which would be difficult to discern with single channel imagery.

Figure 3 is a three-space scatter diagram of visible counts versus infrared and water-vapor brightness temperatures for a few select cloud types in the hurricane Gilbert environment. Since the three axes in Figure 3 correspond directly to the red, green and blue axes of a RGB color model, it is clear why the different cloud types come out so distinctly in the multispectral imagery.

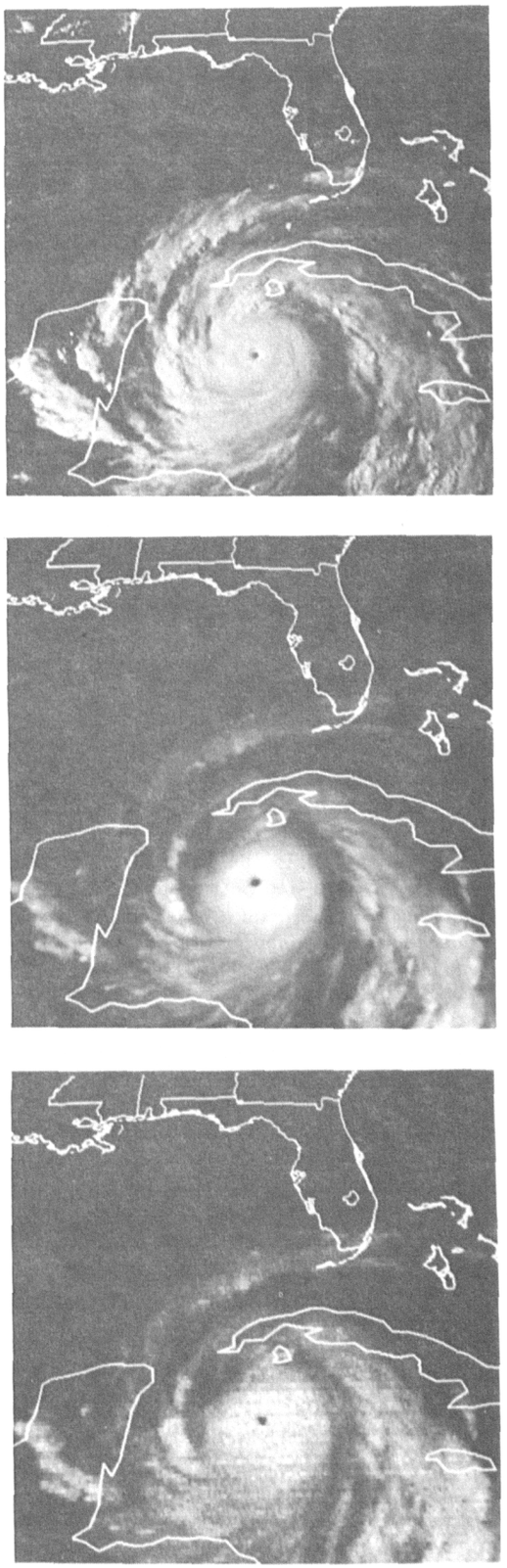

Figure 2. GOES E imagery of Hurricane Gilbert at 2130 UT 13 Sep 1988. Top picture is Visible, middle is 11 μm infrared, bottom is 6.7 μm water vapor.

4.0 SUMMARY

This paper presents a method of multispectral display and analysis of VAS imagery and applies it to the case of Hurricane Gilbert. The technique allows the viewer to unambiguously differentiate between low and high level clouds at a glance, and to identify regions of subsidence associated with the secondary circulation of a major tropical storm.

5.0 REFERENCES

d'Entremont, R. P., and L. W. Thomason, (1987): Interpreting Meteorological Satellite Images Using a Color-Composite Technique, *Bull. Am. Met. Soc.*, 68(7), pp 762-768.

Duback, Leland L, and Carolyn Ng, 1988: *Compendium of Meteorological Space Programs, Satellites and Experiments,* National Space Science Data Center, World Data Center A for Rockets and Satellites, 88-03,

Griffith, C. G. and Woodley, W. L., 1973: On the Variation with Height of the Top Brightness of Precipitating Convective Clouds, *J. Appl. Met.*, 12, pp 1086-1089.

Kleespies, T. J., R. P. d'Entremont, G. W. Felde, K. R. Hardy, L. W. Thomason, G. B. Gustafson C. F. Ivaldi, 1987: Application of the AFGL Interactive Meteorological System to Atmospheric Research, *Preprints, Third International Conference, Interactive Information and Processing Systems for Meteorology, Oceanography, and Hydrology,* New Orleans, LA, AMS, Boston MA, pp 198-201.

Menzel, W. P., W. L. Smith, and T. R. Stewart, 1983: Improved Cloud Motion Wind Vector and Altitude Assignment using VAS, *J. of Climate and App. Met.*, 22, pp377-384.

Moik, J. G., 1980: Digital Processing of Remotely Sensed Images, *NASA SP-341,* GSFC, Greenbelt, MD., 330pp.

NASA, and Hughes Aircraft Company, 1980: *Geostationary Operational Environmental Satellite GOES D,E,F Data Book*

Nunez, E., and J. Stout, 1984: Tropical Storm Moisture and Subsidence Patterns as revealed by the VISSR Atmospheric Sounder (VAS) Water Vapor Channel. *Postprints of the 15th Conf. on Hurricanes and Tropical Meteorology,* Miami, FL, AMS, Boston, MA, pp 256-260.

Reynolds, D.W., and T.H. VonderHaar, 1976: A Bispectral Method for Cloud Parameter Determination, *Monthly Weather Review,* 105, pp 446-457.

Rodgers, E. B., and J. Stout, 1983: The Inference of Tropical Cyclone Dynamics using GOES/VISSR/VAS data. *VISSR Atmospheric Sounder (VAS) Research Review,* J. R. Greaves, Editor. NASA Conf. Publications 2253, GSFC, Greenbelt, MD.

Schowengerdt, R. A., 1983: *Techniques for Image Processing and Classification in Remote Sensing,* Academic Press, 249 pp.

Velden, C. S., 1987: Satellite Observations of Hurricane Elena (1985) using the VAS 6.7 μm "Water-Vapor" Channel, *Bull. Am. Met. Soc.*, 68(3), pp 210-215.

6.0 LIST OF ACRONYMS

AFGL	Air Force Geophysics Laboratory
AIMS	AFGL Interactive Meteorological System
ATS	Applied Technology Satellite
AVHRR	Advanced Very High Resolution Radiometer
GOES	Geostationary Operational Environmental Satellite
RGB	Red-Green-Blue
SMS	Synchronous Meteorological Satellite
SMMR	Scanning Multichannel Microwave Radiometer
VAS	VISSR Atmospheric Sounder
VAX	Virtual Address eXtension
VISSR	Visible Infrared Spin Scan Radiometer

TROPICAL SYNOPTIC SCALE MOISTURE FIELDS OBSERVED FROM THE NIMBUS-7 SMMR

J. D. Fink and J. P. McGuirk

Department of Meteorology, Texas A&M University
College Station, TX 77843-3146 (409-845-4431)

1. INTRODUCTION

Nimbus-7 SMMR brightness temperatures from a 7 days in January 1979 and a 3 days in May 1979 are used to estimate precipitable water over the tropical eastern Pacific Ocean. The estimates are made from an algorithm developed by Wilheit and Chang (1980). The SMMR estimates are compared within the context of five typical tropical synoptic features: Tropical Plume (TP), a synoptic cloud system described by McGuirk et al. (1987); Subtropical High (STH); Active ITCZ (AITCZ); Quiescent ITCZ (QITCZ); Equatorial Dry Zone (EDZ), a subsidence region between 90° and 120° W.

Comparisons are made between the SMMR based precipitable water estimates and each of the following: TIROS-N 7.3 and 6.7 micrometer water vapor channels (TOVS 11 and TOVS 12, respectively), TIROS-N 10.5-12.5 micrometer Outgoing Longwave Radiation (OLR), and a model estimate from the European Center for Medium Range Weather Forecasts (ECMWF).

2. WATER VAPOR EVALUATION

SMMR estimates of precipitable water have a rms difference with respect to radiosondes of only 2.5 kg m^{-2} at a resolution of 60 km; therefore they will be treated as "ground truth".

2.1 Correlations and Mean Synoptic Structure

A set of 540 concurrent observations over the entire period are available for the five moisture estimators. Collocated cross correlations between the estimators are presented in Table 1a. Each estimator provides information about the moisture in the atmosphere when compared to SMMR; the best correlation is with the ECMWF analysis and then with TOVS 11. Though TOVS 11 and TOVS 12 are highly correlated, the SMMR and TOVS 11 correlation is superior because the TOVS 12 is too sensitive to insignificant upper tropospheric moisture; this sensitivity leads to serious errors in relatively dry atmospheres. The SMMR and OLR correlation of −0.56 is a precipitable water and cloud correlation; the correlation is not high because cloud cover (cirrus) does not guarantee a deep layer of moisture.

The data were separated geographically by feature and cross correlations were computed. Half of the correlations within the five synoptic features were not significantly different from zero, due only in part to the small sample sizes. Results are shown in Table 1b for TPs, with statistically insignificant correlations deleted. Table 1b is exceptional only in that most correlations are significant for TPs. The only insignificant correlations are those between ECMWF and infrared satellite observations. The interpretation of Table 1 is that (a) represents primarily interregional variation and (b) represents intrasystem variations associated with synoptic structure. Only small intrasystem signals exist, and these signals are largest in TPs and the AITCZ, where observed variability is largest.

Table 1a. Correlation of precipitable water estimates.

	TOVS 11	TOVS 12	OLR	ECMWF
SMMR	−.61	−.48	−.56	.70
TOVS 11	*	.89	.66	−.56
TOVS 12	*	*	.55	−.44
OLR	*	*	*	−.44

Table 1b. Correlation of precipitable water within TPs.

SMMR	−.35	−.36	−.28	.46
TOVS 11	*	.90	.60	
TOVS 12	*	*	.55	
OLR	*	*	*	

Comparisons of individual SMMR estimates with TOVS 11 and ECMWF estimates are shown in Fig. 1. Although correlations are good, scatter in the two plots is large. SMMR estimates span nearly the entire range for every ECMWF and TOVS 11 value.

Mean values and standard deviations within the five features showed that the TP and AITCZ had the highest moisture contents and standard deviations. SMMR and ECMWF possessed mean values within TPs and QITCZs that are statistically alike, implying that TPs resemble a QITCZs; the main difference is that TPs have a larger standard deviation than QITCZs.

2.2 Prediction of Precipitable Water

SMMR observation are estimated by multiple regression of TOVS 11, TOVS 12, OLR, and the ECMWF analysis, listed in order of decreasing importance. All four coefficients were statistically significant and the regression had a coefficient of determination $R^2 = 0.67$. Fig. 2 compares the resulting predicted and observed SMMR. The largest under predictions occurred within the AITCZ region, typically 15 kg m^{-2}. The largest overpredictions occurred within TPs and the EDZ, typically 10 kg m^{-2}. Inspite of the systematic nature of prediction errors, no statistically significant regressions were obtained within

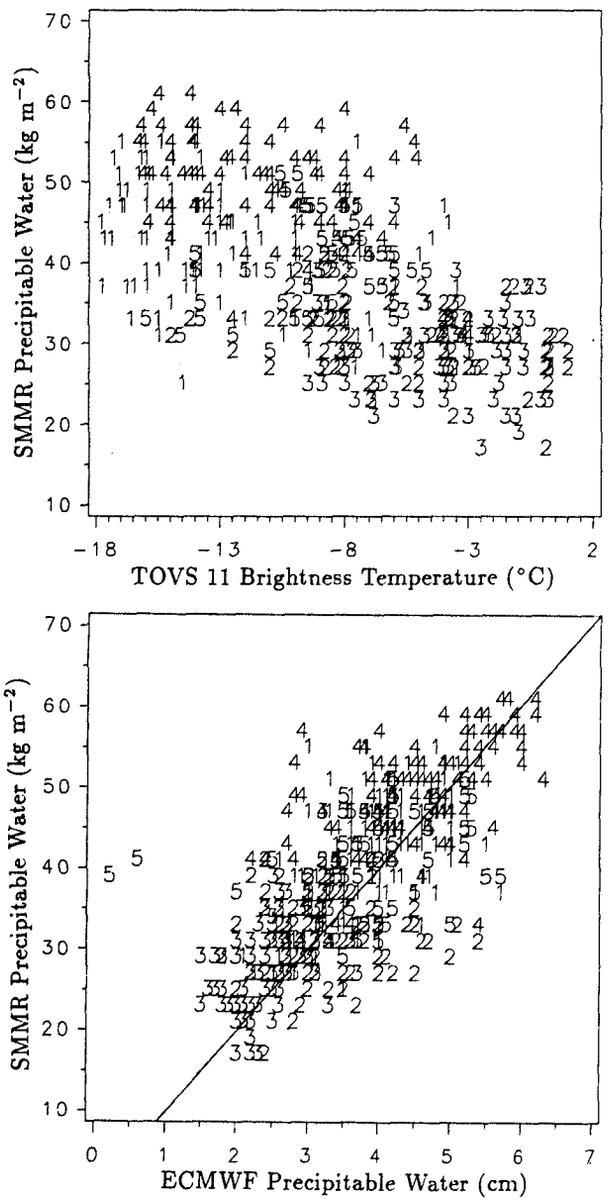

Fig. 1(top). Plot of SMMR precipitable water vs. TOVS 11 brightness temperature. (bottom) SMMR precipitable water vs. ECMWF. Data points 1=TP, 2=EDZ, 3=STH, 4=AITCZ, 5=QITCZ. The straight line would be a perfect fit.

synoptic features.

Figure 3 compares SMMR, ECMWF and predicted SMMR along the western edge of a single SMMR pass. The ECMWF estimates two maxima, at 3° N and 15° S, corresponding to an AITCZ and Southern Hemisphere convection; at 30° N is the dry STH. SMMR detects a similar pattern except the AITCZ is wetter. and the moist region is continuous into the southern hemisphere. The predicted SMMR nearly corrects for the ECMWF underprediction from 5 to 15° S; unfortunately it over predicts the moisture in the STH at 30° N.

3. SUMMARY

All five water vapor estimators are correlated; unfortunately most of the correlation is explained by regional differences, not by synoptic structures. Most of the geographical SMMR variation can be predicted from a model and infrared satellite observations. These predictions can differentiate between the TPs, EDZ, STH, AITCZ, and QITCZ.

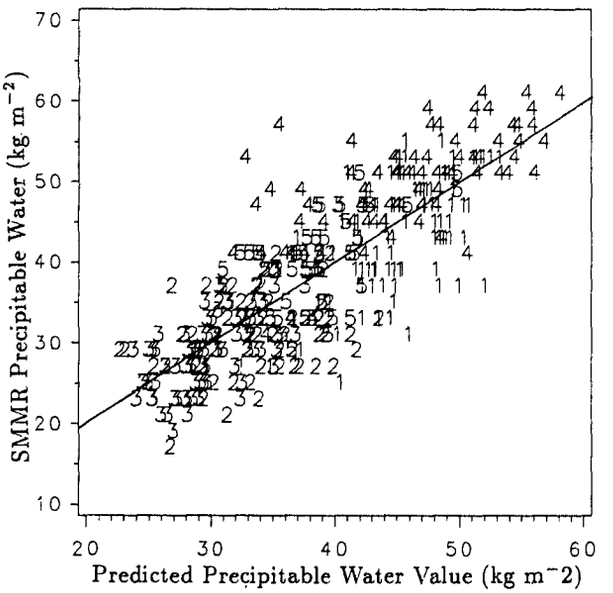

Fig. 2 Same as Fig. 1 except SMMR precipitable water vs. predicted SMMR precipitable water.

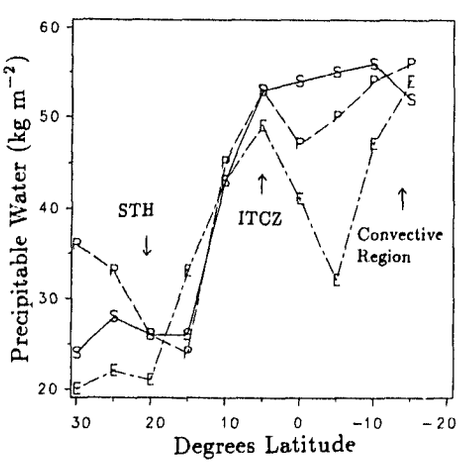

Fig. 3. Plot of SMMR (S), Predicted SMMR (P), and ECMWF (E) along the western edge of a SMMR pass at 160° W about 1200 GMT May 16, 1979.

4. ACKNOWLEDGMENTS

The research is sponsored by NASA's George C. Marshall Space Flight Center, under Contract No. NAS-37284. Jeffrey Fink acknowledges the support of the United States Air Force Institute of Technology.

5. REFERENCES

McGuirk, J.P., A.H. Thompson and N.R. Smith, 1987: Moisture bursts over the tropical Pacific Ocean, *Mon. Wea. Rev.*, *115*, 787–798.

Wilheit, T.T., and A.T.C. Chang, 1980: An algorithm for retrieval of ocean surface and atmospheric parameters from the observations of the Scanning Multichannel Microwave Radiometer, *Radio Science*, *15*, 525–544.

SAHELIAN AFRICA CONVECTIVE SYSTEMS DESCRIBED FROM METEOSAT ISCCP B2 DATA

Michel Desbois, Brigitte Gnamien and Théoneste Kayiranga

LMD/CNRS
Palaiseau, France

1. INTRODUCTION

The large scale behaviour of convective clouds over tropical continents can be described from geostationary satellites IR imagery, specially with the ISCCP level B data set, allowing to follow the evolution of the cold cloud tops. Recent studies using this principle have shown the large amplitude of the convective cloudiness fluctuations and the large extent of the areas affected, specially in the African ITCZ *(Duvel, 1988; Desbois et al., 1988)*. In this last paper, the association of the diurnal cycle of convective clouds to orography was again clearly shown : maximum cycle over mountaineous areas and over regions where breeze type circulations are likely to occur. In other areas like the flat regions of Sahel, it was noticed that propagating convective systems were also submitted to a large diurnal evolution.

The aim of the present paper is to describe some of the characteristics of the diurnal cycle of convective clouds over Africa, at large and regional scales, and to examine the respective roles of local convection and propagating systems. The periods studied are July 1983 and July 1985, corresponding respectively to a dry month and a more normal one in Sahelian regions.

2. AMPLITUDE AND PHASE OF THE DIURNAL CYCLE

One of the indicators we have computed to characterize the diurnal cycle amplitude is based on the maximum difference between the frequency of occurences of cold clouds (below -40°C), as they appear in the infrared window channel (10.5-12.5 μm) at the different hours. The knowledge of the number of events for a particular hour for a given pixel allows to control the statistical significance of the results. The maps produced are presented on figure 1, showing a close association with orography, but also large amplitudes over some other areas, with large interannual differences.

From the hourly maps of the monthly number of occurences of clouds colder than -40°C, maps of the hour of maximum "cold cloudiness occurence" can be constructed to characterize the phase of the cycle. Mountain regions can be distincted by a cloud growth maximum occuring in the beginning of the afternoon, i.e. earlier in the day than for other regions. Downwind of these regions, there is often a delay of the phase of the cloud cycle from East to West corresponding to phase speeds of the order of 10-15 m/s, similar to the one of squall lines, but not far neither from the wind velocity in the upper troposphere.

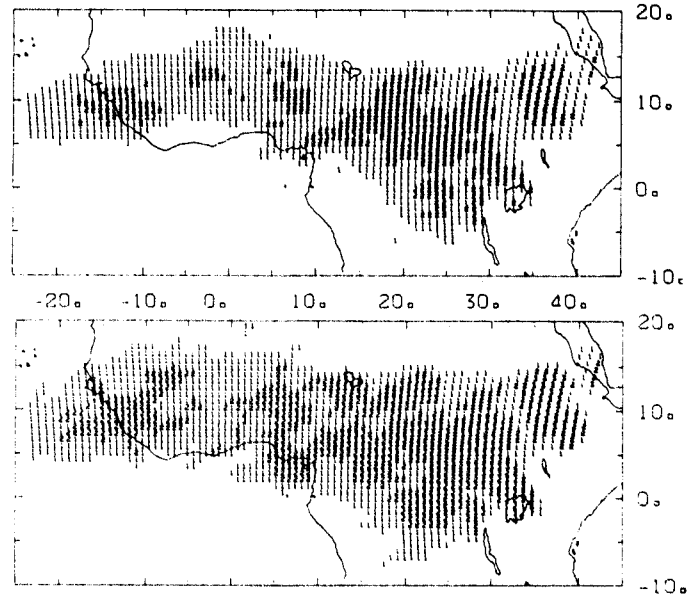

Fig. 1. Amplitude of the cycle for July 1983 (top) and 1985 (bottom). Moderate: 1; Medium: 2; High: 3.

Most of the large scale interannual differences appear to be related in a complex way to the position relative to the mean ITCZ and the orography, the coastal effects and the occurence of squall lines. But no general rule appears, and a regional examination of the interannual differences is necessary.

3. EXAMPLE OF REGIONAL BEHAVIOUR : THE WEST AFRICAN COAST

This area is marked by a North-West to South-East coastline, backed by a moderately high moutain range, composed from the Fouta-Djalon in the North and the Guinean ridge in the South. The low layers of the atmosphere are characterized over the sea by a South Westerly to Westerly flow (monsoon flow). This mean flow weakens over the continent, specially near the mountain range. The Easterly wind at 700 hPa is on the average stronger in 1983 (10 m/s) than in 1985 (5 m/s). On the contrary, at 200 hPa, the Easterlies are stronger in 1985.

The diurnal amplitude of the cycle (Figure 2) appears to be the highest over the Fouta-Djalon for both years. But the remaining distribution is very different : in 1985, a band of maxima lies just beyond the coastline from Senegal to Liberia, and the oceanic maximum occurs more South than in 1983, but significant

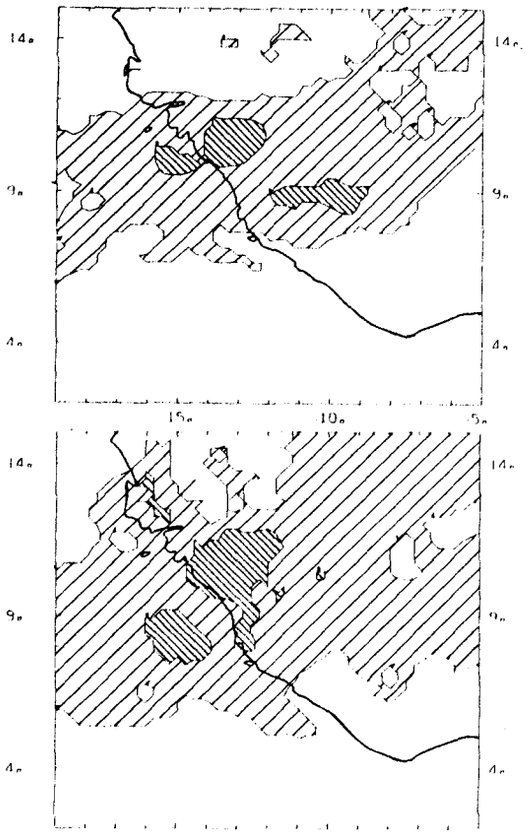

Fig. 2. Amplitude of the cycle over West African Coast. Isolines represent 4 and 8 occurences.

values are found over a much wider area, facing the coastline. Over the continent, the maximum frequency of cold clouds occurs around 18:00 local time over the mountains, but also along the coastline in 1985. Over the ocean, the areas of maximum cycle correspond to a maximum frequency time around 4:30 in 1983 and 7:30 in 1985. A westward advection of this maximum is noticed in 1983. This advection does not appear clearly in 1985.

These elements suggest the following behaviour : In July 83 (see §4.), propagating events are predominant over the area, and a land-sea breeze circulation can establish only in the zone of the highest mountains (Fouta-Djalon). Reversely, in July 85, the weak 700 hPa Easterly flow allows the development of breeze circulations along the whole coastal region.

4. SQUALL LINES AND LOCAL CONVECTION

Main characteristics of squall lines occuring in July 1983 and July 1985 have already been described in Desbois et al. (1988). We precise here the number of squall lines compared to the total number of convective events :

For each pixel, the monthly total number of occurences of clouds colder than -40°C is computed ; then, using the criteria of Desbois et al (1988) for the identification of squall lines, the number of such occurences due to the passage of a squall line is also recorded. The

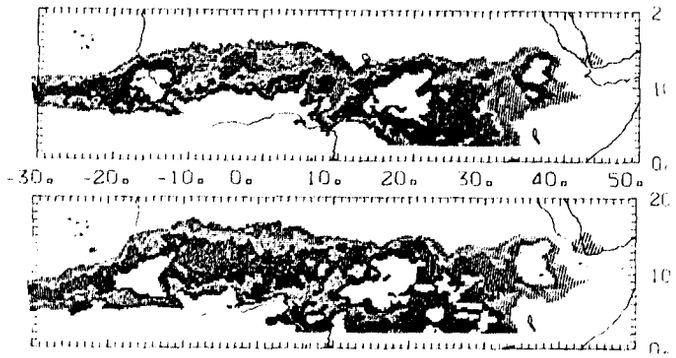

Fig. 3. Occurences of clouds colder than -40°C, for July 83 and 85. Isolines : 10 to 30

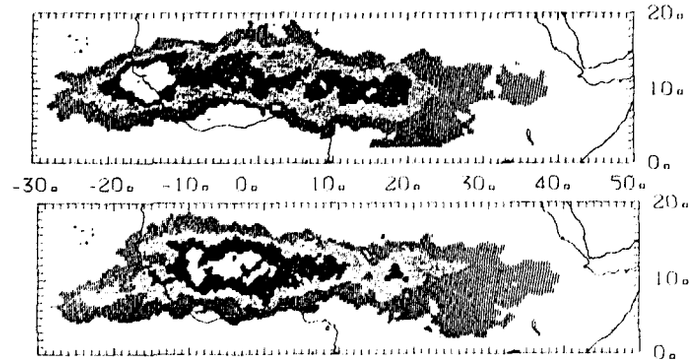

Fig. 4. Occurences of squall lines for July 83 and 85. Isolines : 1 to 15

results are presented on Figures 3 and 4, for July 1983 and July 1985.

The number of cold clouds presents approximately the same distribution in 1983 and 1985, despite the overall larger amount in 1985 : the maxima are located over the mountains and some coastal regions. Squall lines are affecting also the same general area for both years, around 10°N. However, the distribution of these squall lines occurence is very different for the two months : squall lines are passing over the West African coast much more often in 1983 than 1985. Over the continental regions, in 1985, the number of squall lines is larger and they are more concentrated from the South-West of lake Chad to Guinea mountains. The proportion of these events overpasses 50% over most of the sahelo-soudanian regions situated West of lake Chad, reaching 65% in some particular places.

References

Desbois M., T. Kayiranga, B. Gnamien, S. Guessous and L. Picon, 1988 : Characterization of some elements of the sahelian climate and their interannual variations for July 83, 84 and 85 from the analysis of METEOSAT ISCCP data. *J. Climate*, 1, *867-904*.

Duvel J.P., 1988 : Analysis of diurnal, interdiurnal and interannual variations during northern hemisphere summers using Meteosat infrared channels. *J. Climate*, 1, *471-484*.

7.4

QUANTITATIVE SATELLITE ANALYSES OF FOUR TROPICAL CYCLONES DURING AMEX/EMEX

Debra A. Lubich [1]
Raymond M. Zehr [2]

[1]Cooperative Institute for Research in the Atmosphere (CIRA)
Colorado State University, Fort Collins, CO 80523-0033

[2]Regional and Mesoscale Meteorology Branch
Satellite Applications Laboratory
NOAA/NESDIS, Fort Collins, CO 80523-0033

1. INTRODUCTION

The Equatorial Mesoscale Experiment (EMEX) was conducted in northern Australia from January 8 to February 18 of 1987. Following the onset of the northern Australia monsoon in mid-January, four tropical cyclones developed in the Australian region. This paper reports on digital satellite data analyses covering the life cycles of the four storm systems. The analyses reveal the distribution and amount of deep convective clouds with respect to cyclone center. These observations are compared to previous results of an extensive study regarding NW Pacific tropical cyclones from 1983-1984 (Zehr, 1988). The results of objective estimates of cyclone intensity using the digital satellite data are also discussed.

2. GMS SATELLITE DATA

Digital visible and infrared satellite data from the Japanese Geostationary Meteorological Satellite (GMS) were obtained from NESDIS. The GMS satellite has a sub-point of 0 degrees latitude, 140 degrees E. longitude, with a sub-point resolution of 2.5 km and 5.0 km for visible and infrared data, respectively. The GMS data used in this study were extracted from the ISCCP (International Satellite Cloud Climatology Project) archive as three hourly full disk imagery with a visible and infrared resolution of 10 km. Each data point (pixel) has a digital count value which has been calibrated to radiance. For infrared image data, the radiance can be converted to a brightness temperature (T_B) or equivalent blackbody temperature. The infrared data is sensed at a wavelength of 11.2 micrometers, therefore the clear atmosphere is nearly transparent and T_B can be used as a measure of the radiative temperature of a cloud top. However, clouds with emissivity much less than 1.0 (e.g. thin cirrus) will have a brightness temperature much warmer than their cloud top temperature. The range of T_B associated with each count value varies from approximately 0.5 ^{0}C to 2.0 ^{0}C, giving a resolution of approximately 1.5 ^{0} C at typical cloud top temperature.

Additional digital satellite data, including data from the NOAA polar orbiting satellites, have been processed and are available for the EMEX/AMEX period (Lubich and Zehr, 1987; Stephens and Greenwald, 1988).

3. NORTHERN AUSTRALIAN TROPICAL CYCLONES OF JAN-FEB, 1987

An extensive scientific network was available for data collection during EMEX and the concurrent investigations of phase II of the Australian Monsoon Experiment (AMEX). Research aircraft were deployed from Darwin to investigate areas of significant convective activity (Martin et al, 1987). Simultaneous monitoring of convection and the large scale monsoonal flow via a wide network provided data which is currently being used in more detailed analyses of the relationship between monsoon convection and enhanced westerly winds. This network included a radar and sounding array which utilized the existing regional network plus the special AMEX observation sites designed to concentrate on the convectively active region of the Gulf of Carpentaria (Holland et al, 1986).

General large scale circulation throughout most of the Australian region indicated that an El Nino-Southern Oscillation (ENSO) event was occurring, resulting in a suppression of tropical cyclogenesis. Normally, the monsoon trough, characterized by deep westerlies to the north and deep easterlies to the south, produces heavy rainfall accompanying numerous mesoscale convective systems. The monsoon trough to the west of the Australian continent was rather poorly developed for most of the Australian cyclone season (Manchur, 1987). However, active monsoonal conditions in mid January interrupted

NAME	DURATION (including tropical depression)	ATTAINED CYCLONE INTENSITY	EST. LOWEST CENTRAL PRESSURE (MB)	MAX. WIND (KM/HR)
Connie	1/15 - 1/23	1/17 1200 UTC	950	149
Irma	1/18 - 1/21	1/19 1200 UTC	984	n.a.
Damien	1/31 - 2/9	2/3 0000 UTC	980	97
Jason	2/6 - 2/13	2/7 0600 UTC 2/12 1800 UTC	965	110

Table 1. Tropical cyclones in the EMEX/AMEX study area, 1987.

the ENSO effect for approximately one month, allowing the development of 4 tropical cyclones during the EMEX investigations (Table 1). Three of the four cyclones (IRMA, CONNIE and JASON) had coastal crossings from sea to land. Two cyclones (IRMA and JASON) formed in spite of unfavorable upper air conditions. TC CONNIE may have had an important role in the genesis of IRMA. Figure 1 illustrates the paths of the four tropical cyclones. (Manchur, 1987).

4. ANALYSIS

Zehr (1988) utilized the GMS digital infrared data in an extensive study of 48 tropical storms and typhoons which occurred in the NW Pacific from 1983-84. Time series of the number of pixels (hence area) corresponding to various T_B threshholds for various circular areas with respect to cyclone center were plotted for each tropical cyclone. Characteristics of tropical cyclones revealed by this technique are: 1) diurnal variation of deep convection with an early morning maximum in cold cloud area; 2) a convective maximum coinciding with genesis; and 3) a convective maximum preceding maximum storm intensity, coinciding with maximum rate of intensity increase.

Similar time series were computed from the GMS IR data for the life-cycles of the four tropical cyclones which occurred during EMEX. Best track information obtained from the Australian Bureau of Meteorology Research Centre (BMRC) was used to determine the storm centers of the four tropical cyclones.

5. RESULTS

5.1 Diurnal Variation

The cloud areas colder than -75° C within 2 degrees latitude (220 km) of storm center are plotted in Figure 2 for each tropical cyclone. All four storms exhibited distinct diurnal variation in cold cloud amount during some portion of their life cycle. However, the time of day at which deep convective clouds reach a maximum depends on whether the cyclone is located over land or over water. Tropical Cyclone CONNIE (Fig. 2a) showed a late afternoon (2000 local

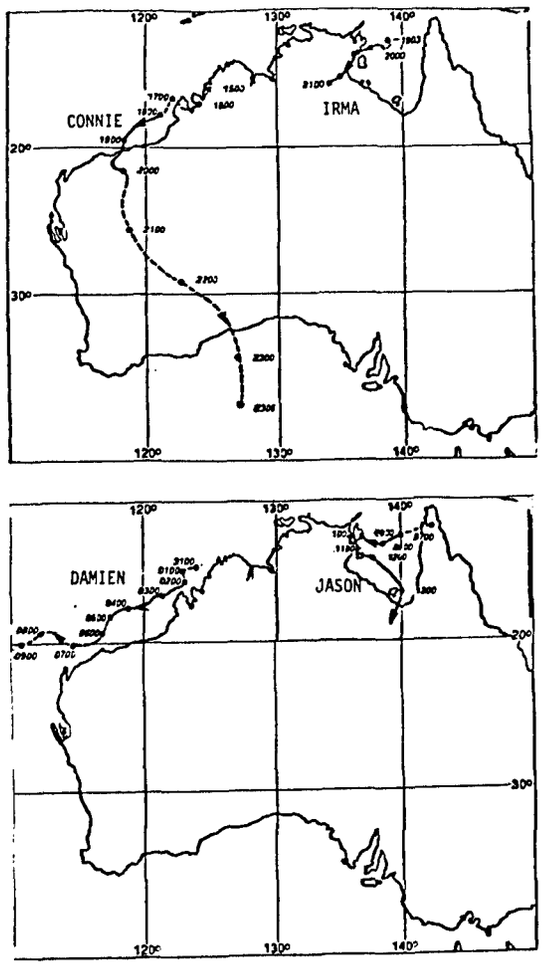

Figure 1. Paths of the four tropical cyclones. Times are labeled as DDHH.

time) maximum on the 16th while located mostly over land, and an early morning maximum (0500 local) on the 18th (UTC) when it was offshore. Tropical Cyclone IRMA (Fig. 2b) had a very distinct early morning maximum while it was over the Gulf of Carpentaria. DAMIEN (Fig. 2c), which remained offshore its entire life cycle, has an early morning maximum, while JASON (Fig. 2d) shows a double maximum during some of its lifetime due to its close proximity to the coastline.

The diurnal variations which appear in Figure 2 agree with previous studies. Zehr (1987) showed a large persistent morning maximum in cold cloud area with NW Pacific typhoons far removed from continental influences. Williams and Houze (1987) illustrated the double maximum in the diurnal convective cycle with winter monsoon cloud clusters. They showed cloud areas defined by a -60° C threshold to reach maximum coverage over land at 1600-2300 local time and over sea at 0400-1200 local time.

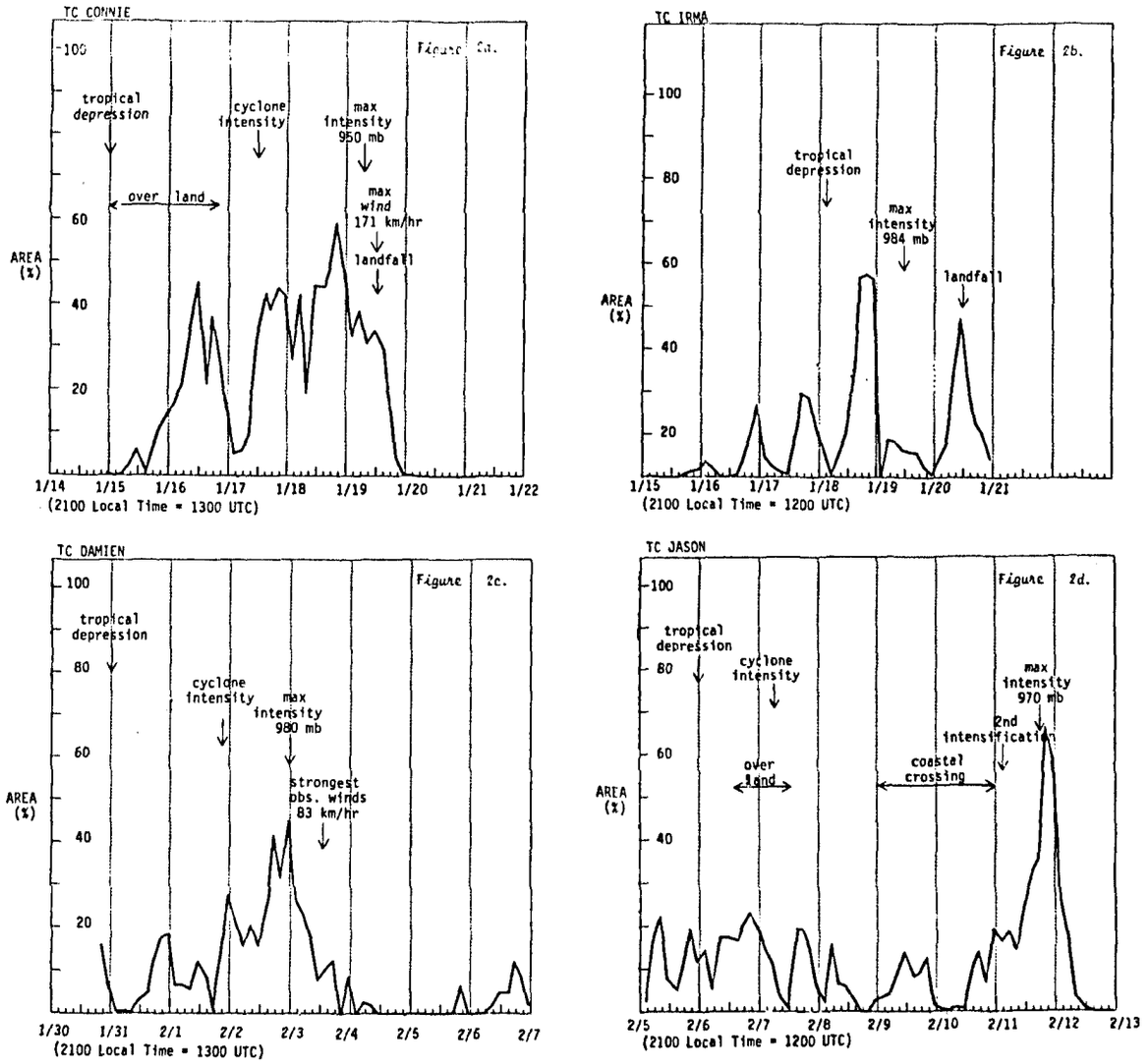

Figure 2. Time series for 0-2° radius from storm center, areas colder than -75° C for all four tropical cyclones. Plotted times are in UTC.

5.2 Intensity

Maximum cold cloud areas are generally associated with deepening typhoons. The 83-84 NW Pacific results (Zehr, 1988) show a consistent convective area maximum prior to maximum tropical cyclone intensity. Zehr also observed that intensity change rather than maximum intensity showed a better correlation to deep convection as measured by the -75 ° C cloud areas at radius 0-2 degrees.

The minimum sea-level pressures (MSLP) for TC CONNIE and TC JASON are plotted in Figure 3. The post-analysis MSLP data were obtained from the BMRC. Only CONNIE and JASON showed intensification characterized by more than a 25 mb/day decrease in MSLP. Note that the MSLP decreases with each tropical cyclone occur during an active convective period (allowing for the diurnal variation). Note that the time period during which CONNIE deepened the most (Fig. 3a) corresponds to prolonged active convection (Fig. 2a). This example fits well with the findings of Zehr (1989). JASON shows a convective maximum (Fig. 2b) near the time of maximum intensity. However, the imminent landfall of JASON at this time is probably influencing both the MSLP and the convective activity.

In addition, a technique following the approach of Dvorak (1984) was applied to the digital IR data. The technique aims at improving objective estimates of tropical cyclone intensity from satellite data. The algorithm developed by Dvorak extracts two temperatures from the IR data and relates them to current intensity. A 55 km (30 n. mi.) circle centered on the eye is used to find the surrounding temperature. The "surrounding temperature" is defined as the warmest pixel located on the circle. Intensity increases as the surrounding temperature decreases. The warmest IR pixel in the eye is the other temperature, and intensity increases as eye temperature

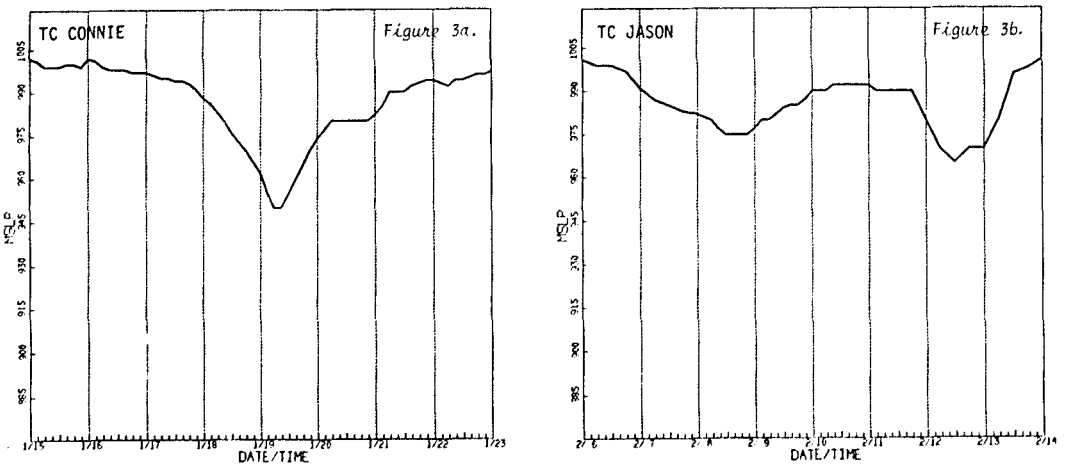

Figure 3. Minimum Sea-Level Pressure plots for TC CONNIE and TC JASON.

increases. Dvorak expresses intensity in terms of an index or T-no. corresponding to typical daily intensity changes. T-no. can be converted to maximum sustained wind speed and minimum sea-level pressure (MSLP).

The Dvorak digital IR technique was developed for hurricanes exhibiting well-defined eyes in the satellite imagery. Only CONNIE developed a well-defined eye, and for only a very short period. Therefore, the digital IR technique was largely ineffective for use with the four tropical cyclones which occurred during EMEX.

6. SUMMARY

Digital satellite data have been analyzed from four tropical cyclones which occurred in northern Australia during the 1987 Equatorial Mesoscale Experiment. The results compare favorably in two areas with results obtained from previous anaylses of 48 NW Pacific tropical storms and typhoons. 1) A distinct diurnal variation in convective cloud amounts is apparent, with early morning maximums in cold cloud area for tropical cyclones located over the sea. 2) The areas in 0-2° latitude radius, colder than -75° C show a relationship to the rate of MSLP decreases.

Due to the generally weak nature of the Australian tropical cyclone season from 1986-1987, and to the proximity of the storms to the Australian continent, comparisons with regard to cyclone intensity estimates from Dvorak's digital IR technique could not be made.

7. ACKNOWLEDGEMENTS

Portions of this research were supported by NOAA Grant NA-85-RAH-05045 and National Science Foundation contract grant no. ATM-8617856.

8. REFERENCES

Dvorak, V.F. 1984: Tropical cyclone intensity analysis using satellite data. NOAA Tech. Rep. NESDIS 11, 47 pp.

Holland, G.J., J.L. McBride, R.K. Smith, D. Jasper, and T.D. Keenan, 1986: The BMRC Australian Monsoon Experiment: AMEX. Bul. Amer. Meteor. Soc., 67, 1466-1472.

Lubich, D.A. and R.M. Zehr, 1988: The use of polar orbiter data in tropical weather system analysis. Preprints 3rd Conf. on Satellite Meteorology and Oceanography, Anaheim, Amer.Meteor. Soc., 209-214.

Manchur, W., 1987: The Australian tropical cyclone season 1986-87. Aust. Met. Mag., 95-102.

Martin, S.C., V. Kondratiev, T.D. Keenan and A.L. West, 1987: The AMEX radar system. Aust. Met. Mag., 143-151.

Stephens, G.L. and T.J. Greenwald, 1988: An atlas of the satellite observations during the EMEX aircraft missions. Dept. of Atmos. Sci., Colo. State Univ., Ft. Collins, CO, 80523.

Williams, M. and R.A. Houze, 1987: Satellite observed characteristics of winter monsoon cloud clusters. Mon. Wea. Rev., 115, 505-519.

Zehr, R.M., 1987: The diurnal variation of deep convective clouds and cirrus with tropical cyclones. Preprints 17th Conf. on Hurricanes and Tropical Meteorology, Miami, Amer. Meteor. Soc., 276-279.

____, 1988: Satellite diagnosis of tropical cyclones. Preprints 3rd Conf. on Satellite Meteorology and Oceanography, Anaheim, Amer. Meteor. Soc., 241-246.

____, 1989: Improving objective satellite estimates of tropical cyclone intensity. Preprints, 4th Conf. on Satellite Meteorology and Oceanography, San Diego, Amer. Meteor. Soc.

7.5

THE DIURNAL VARIATION OF CONVECTIVE CLOUDINESS ALONG THE INTER-TROPICAL CONVERGENCE ZONE (ITCZ)

James F.W. Purdom
NOAA/NESDIS/RAMM

Fuzhong Weng
PRC

Thomas H. Vonder Haar
Atmospheric Science Department

and

Cooperative Institute for Research in the Atmosphere (CIRA)
Colorado State University
Fort Collins, Colorado 80523

1.0 INTRODUCTION

The diurnal variation of tropical convection has been studied by Gray and Jacobsen (1977) in addressing tropical rainfall, and by Zehr (1987) in addressing tropical cyclone cloudiness in the Western Pacific. However, neither of those studies addressed the diurnal variation of deep convection along the inter-tropical convergence zone. In this study, the diurnal variation of deep convection along the ITCZ was studied using infrared data from the GOES-East and GOES-West satellites. The period covered by this ongoing study is from mid-December, 1988 to the end of January, 1989. GOES-East data were available for the entire study period. However, with the loss of GOES-West on January 21, that satellite's data only covers up to that time. The area covered by the study is shown in Figure 1, as is the mean position of the ITCZ for the study period. Results from our ongoing study should be useful for global modeling activities, radiation budget studies, regional scale climatological activities and for the development of local forecasting aids, to name but a few possible applications. We plan to expand the study to include the diurnal variation of stratiform cloudiness over the region.

2.0 METHODOLOGY

The study region was divided into equal area of subregions 15 by 15 degrees on either side of the equator, Figure 1. Using the NOAA VAS Data Utilization (VDUC) workstation at CIRA, GOES-East and GOES-West 11 um satellite imagery were received at 3 hourly intervals (beginning at 0000 GMT for GOES-East and 0015 GMT for GOES-West). The resolution of the infrared data on the VDUC covering the area shown in Figure 1 was 16 km. Those data were remapped into a Mercator projection, with the spatial resolution of the infrared imagery after remapping being approximately 20 km by 20 km. Reduction in resolution of the original 8 km infrared data to 16 km is accomplished in a VDUC routine that selects the first 8 km by 8 km infrared pixel in a 16 by 16 km area and assigns that value to the 16 by 16 km pixel, all other infrared pixels within that area are discarded. The percentage of cloudiness for each of the 15 by 15 degree subregions was assessed in the following temperature ranges (all degrees Celsius) : +10 to -10, -11 to -40, -41 to -60, -61 to -73 and colder than -73. For December and January, the warmest cloudiness studied in the region was +10 to -10. That cloud is assumed to be weak convection and/or mid-level stratiform in character: generally in the tropics this would cover cloud tops between 650 and 450 mb, well above the trade inversion. Cloudiness in the other temperature ranges are interpreted similar to Zehr (1987): -11 to -40, thin cirrus and some mid-level cloudiness; -41 to -60, mostly anvil cloudiness and some convection; while cloudiness colder than -61 was assumed to be active deep convection. The averages were calculated by summing the number of pixels in a given temperature range for each time and subregion and then dividing by the number of days for that month. In assessing the diurnal character of cloudiness, it must be realized that in regions where cloudiness exists colder than the temperature range being studied, that much of the cloud range being studied might be obscured by higher clouds. Therefore, a representative assessment might not be possible.

3.0 RESULTS

Results for the time period are shown in Table 1, with plots for the four temperature ranges showing results for four subregions (E, M, U and X) given in Figures 2-6. Areas A to X in Table 1, correspond to the subregions shown in Figure 1. The maxima of cloudiness in the +10 to - 10 range, the -41 to -60 range, and that colder than -61 for each subregion is specified in Table 1 by use of an alpha numeric code. In that code, m and p represent morning and afternoon, respectively, while A denotes a strong signal and B denotes a weak signal. The number before the m or p gives the local time of the maxima. An asterisk (*) means that the maxima was not a distinct signal (not like the afternoon convective maxima at U in Figure 2) but occurred within a broad time period of large values (as with the morning weak convection/mid-level maxima in subregion M that is shown in Figure 5). For example, if a combination of 3mA* occurs in a subregion, it means strong (A) morning maximum at 3 am local time (3m), with the maxima being a peak within a broad time period (*) of large values. No letters (blank) for a subregion means no obvious maxima of cloudiness for either morning or night. For the subregions in Figures 2-6, subregion M is mostly ocean but includes some islands, subregions E and X cover only ocean, and subregion U is over South America.

In general, the convective maximum occurring over land in the afternoon shows up well. The results shown in Figure 2 clearly show a strong convective maxima (colder than -61) over subregion U. That maxima is accompanied by an increase in cloudiness in the -41 to -60 range (Figure 3), which should represent anvil cloudiness and smaller showers. The strong convective signals are then followed by a steady increase in cloudiness in the -11 to -40 range that appears to peak at 1 am local (Figure 4). That warmer cloudiness is most likely debris due to the earlier convection, however, the peak

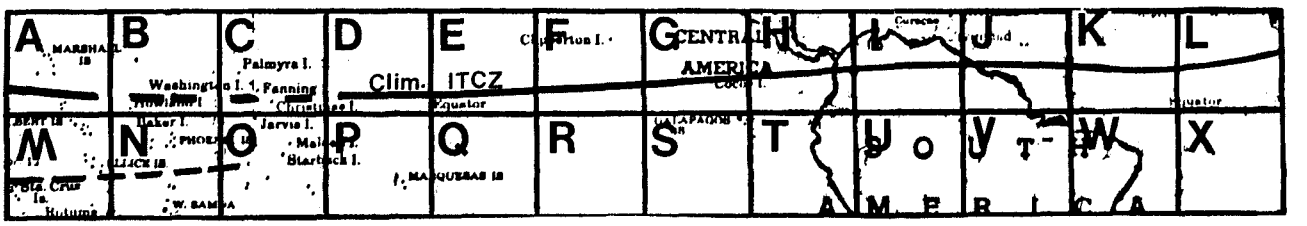

Figure 1. Area covered by the study. The common area viewed by both satellites, mentioned in the text is E, M, U, X. The climatological position of the ITCZ is indicated.

TABLE 1. CLOUD MAXIMA BY AREA
DECEMBER 1988 AND JANUARY 1989

AREA	+10 TO -10		-41 TO -60		LESS THAN -61	
	DEC	JAN	DEC	JAN	DEC	JAN
A	2mA	2mB	2pB	2pB	8pB	
B	1mB*	3mB	3mB	3pB		
C	4mB*		10mB	1pB		
D	2mB*			2pB		
E	1mA	1mA	6mB			
F	1mA*	2mB*	1pA		7mB	
G	3mA*	2mB				
H	3mA	4mA	3pB*			
I	4mA	4mA	4pA	6pA	4pB	4pB
J	5mB*	3mA	5pB	2pB		
K	0mA	3mB	1pB	3pB		7mB*
L	2mA	2mB*	1pB		9mB	4mB*
M	1mB*	5mB*	2pA	5pA	2mA*	5mA
N	1mB*	2mA	3pA	3pA	4mA*	5mB*
O	2mB	4mB			4mB	
P	2mB					
Q	6mB	5mB*		9pB*		10m8pB
R	4mA	4mA				
S	4mA	5mA	8mB			
T	5mA	4mA	3pB	3pB		
U	6mA	7mA	4pA	4pA	4pA	4pA
V	5mA	5mA	5pA	6pA	5pA	5pA
W	3mB*	3mB	3pA	4pB	6pB	6pB
X	3mA	4mB	4pB			

shown at 1 am may be misleading since higher cloudiness may well be shielding the lower cloud from view. Note that this cloudiness steadily decreases after 1 am, another sign that its formation mechanism is due to the earlier convection. As the cloudiness in the -11 to -40 range decreases, cloudiness in the +10 to -10 range (Figure 5) is seen to gradually increase, with a morning maxima at around 7 am, however, the same care in interpreting cloudiness in the -11 to -40 range applies here. With the onset of daytime heating that cloudiness rapidly decreases. Figure 6 shows the total cloud cover (all cloud colder than +10) as a function of time. Notice that in subregion U total cloudiness (colder than +10) begins to increase with the onset of deep convection around 1 pm, and peaks around 12 hours later. It is interesting to note that the area covered by this cloudiness is well over an order of magnitude larger than the amount of deep convection that more than likely led to its being. Similar trends for the various temperature ranges were found in the coastal areas covered by subregions I and W.

A maxima in deep convective cloudiness was found in the early morning hours (between 4 am and 7 am) over several of the oceanic subregions, Figure 1 and Table 1. This correlates well with the studies of Zehr (1987) and Gray and Jacobsen (1977) previously mentioned. It should be realized that the months of December and January are normally accompanied by weak convection along the ITCZ for the region of this study, with the strongest areas being west of the area covered by GOES-West. However, the western most subregion, subregion M, was active with a very definite diurnal cycle exhibiting a maxima in the early morning hours around 5 am. As can be seen in Figure 2, the difference between the active convection over land (subregion U) as compared to the active region over water (subregion M) is striking. There is a much stronger diurnal variation in the strong convective activity for subregion U (land) than subregion M (water). However, the overall amount of convective activity in subregion M is much greater than that for subregion U. The diurnal signal in progressively warmer categories for subregion M lag one another by about 4 to 6 hours; this is similar to earlier findings by Zehr (1987) in studying tropical cyclones, and is attributed mainly to debris from the active convection and its slow dissipation in a very moist environment.

It is interesting to note, that with the exception of subregion U (which is over central South America), that the subregions all show a maxima in cloudiness in the +10 to -10 range that begins to decrease prior to sunrise, Figure 5 and Table 1. That maxima generally occurs around 1 am to 4 am over ocean regions, and in some cases is strong and well defined, as in subregions E and X, while in others it is part of

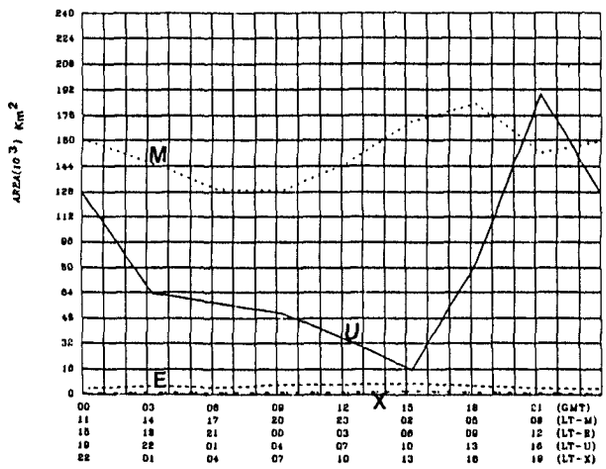

Figure 2. Diurnal variation of cloud cover for selected areas for both months for cloud colder than -61 Celsius. LT stands for local time for the indicated subregion.

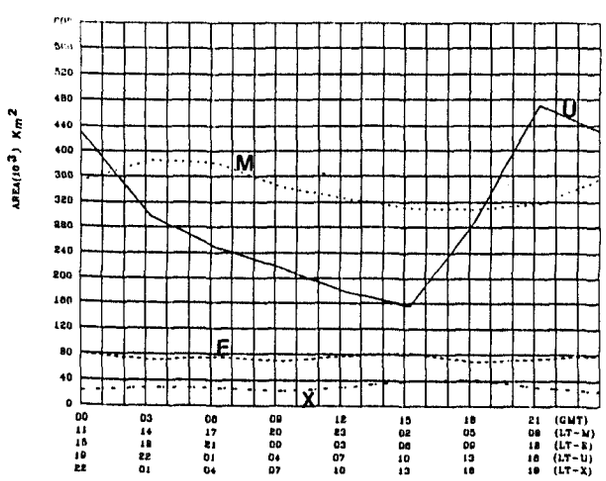

Figure 3. As Figure 2, for the temperature range -41 to -60.

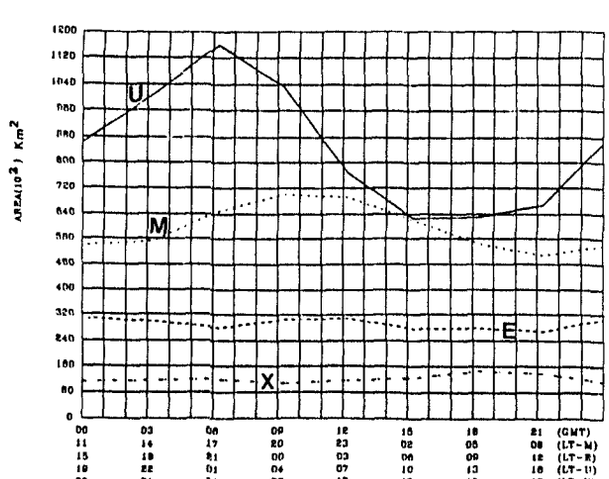

Figure 4. As Figure 2, for the temperature range -11 to -40.

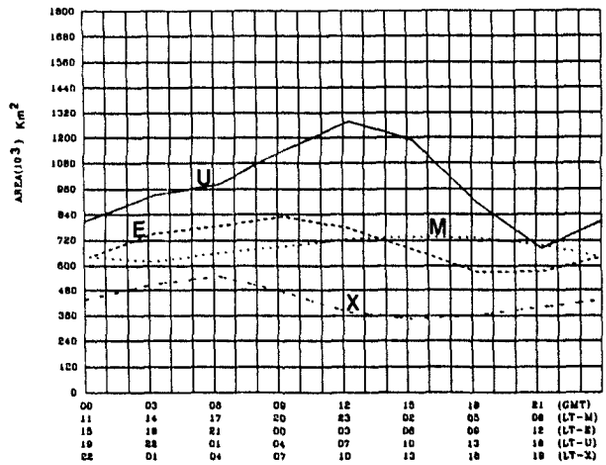

Figure 5. As Figure 2, for the temperature range +10 to -10.

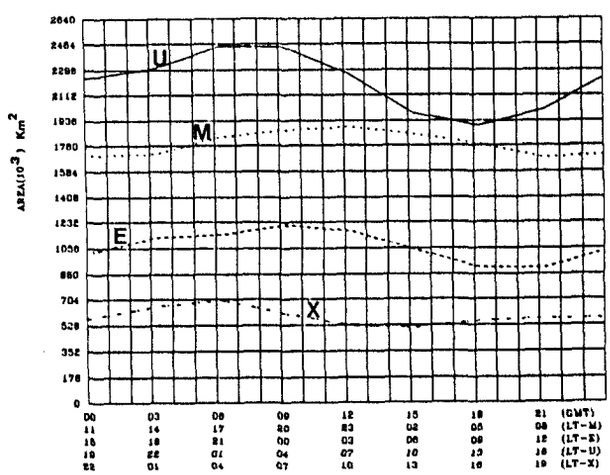

Figure 6. As Figure 2, for all temperatures colder than +10.

a broad maxima, as in subregion M as seen in Figure 5. While the mechanism proposed for this warmer cloud in subregions U and M was deep convective debris, that is apparently not the case for subregions E and X (although some of that cloudiness may have been advected into those subregions). It is interesting to note that the maximum cloudiness observed at any time in subregions E and X was in this warmest range. Both subregions E and X exhibit the same diurnal characteristics, with the very early morning maxima followed by a late morning to early afternoon minima approximately 12 hours later. This requires further investigation.

As a part of this study, the common area of view for the two GOES satellites, bounded by the box 15 N to 15 S and 90 W to 120 W were compared. There were a number of reasons for this comparison, however with the loss of GOES-West we will not go into detail here. It is sufficient to say that cloudiness in the temperature ranges specified above compared favorably on both a daily and monthly basis. It was felt that the minor differences that were observed could be explained as a result of the different viewing perspective of the two satellites.

4.0 CONCLUSIONS AND FUTURE PLANS

The results for the diurnal variation of deep convective activity over the study region was similar to that shown earlier by Zehr (1987) and inferred from rainfall by Gray and Jacobsen (1977). The debris cycle, described by Zehr (1987) for tropical cyclones was also evident in the stronger convective regions. A very early morning peak in cloudiness in the +10 to -10 range was detected in all areas but one, noted above. This peaking of cloudiness was evident in every subregion for at least one of the months studied, and in all but three subregions for both months. This very early morning increase in warm cloudiness was in many cases not related to deep convective activity; indeed, associating such cloudiness with the deeper convective cloudiness at all may be a mistake - this cloudiness and its formation and maintenance mechanism is a point for further investigation, and as mentioned earlier cloudiness in this temperature range should be above the trade inversion. We plan to include cloudiness with top temperatures between +20 and +15 Celsius into this study to assess the diurnal characteristics of cloudiness beneath the trade inversion: our main interest here are those regions with more persistent stratus and stratocumulus cloudiness. We also plan to include a sector to investigate the diurnal character of California coastal stratus.

This study is ongoing, but is now limited to a smaller area due to only one GOES satellite. The infrared resolution for the study was 16 km due to storage area limitations on VDUC (with two GOES satellites), with a single GOES operation we plan to use full resolution of the IR data.

5.0 ACKNOWLEDGMENTS

This study was supported by NOAA grant NA-85-RAH-0545. The authors appreciate Ray Zehr's helpful comments concerning the manuscript, and Debbie Eckdahl's help in its preparation.

6.0 REFERENCES

Gray, W.M. and R.W. Jacobsen, 1977: The diurnal variation of deep cumulus convection. Mon. Wea. Rev., 105, 1171-1188.

Zehr, R.M., 1987: The diurnal variation of deep convective clouds and cirrus with tropical cyclones. Preprints, 17th Conf. on Hurricanes and Tropical Meteorology, Amer. Meteor. Soc., April 7-10, Miami.

ESTIMATES OF GATE CONVECTIVE AND STRATIFORM RAINFALL DERIVED FROM RADAR AND SATELLITE DATA

9.1

Andrew J. Negri
Robert F. Adler

NASA/Goddard Space Flight Center
Severe Storms Branch/Code 612
Greenbelt, MD 20771

1. INTRODUCTION

The objective of this work is to examine the statistics of tropical rain system structure, primarily the division between convective and stratiform (C/S) rainfall, over the GATE B-scale array. Phases I and II are examined using the composite radar data described by Hudlow and Patterson (1979). Using the satellite infrared (IR) based Convective-Stratiform Technique (CST) (Adler and Negri, 1988) hourly estimates were made on the first two days of GATE, and verified against the radar data. The potential exists for the calibration of the satellite technique within the B-scale, and subsequent application to larger, tropical areas. The results of the C/S partitioning are compared to the results of Houze and Rappaport (1984) and Cheng and Houze (1979). Results are potentially applicable to the estimation of the vertical profile of latent heating.

2. ANALYSIS TECHNIQUES

The low-level reflectivity data were processed hourly for the 36 days of GATE phases I and II. Two objective techniques were used: a threshold technique where rain is considered convective when its rate is equal to or greater than a given threshold (in this case 7 mm/h); the other is the technique of Churchill and Houze (1984), henceforth CH, which defines convective rain as either 1) a fixed-size area surrounding a rainrate peak; or 2) a rainrate exceeding 20 mm/h. Figure 1a displays a contour plot of radar-derived rainrates at 1300 GMT 28 June 1974. A squall line is evident in the region of tight gradients. The division of C/S rainfall by CH is shown in Fig. 1b, and by a simple threshold method using a threshold of 7 mm/h in Fig. 1c. Compared subjectively to the radar data, the CH appears to under-estimate the convective component. This was true for not only for this image but for most days and times examined. The CH gave higher stratiform percentages and disagreed qualitatively with contoured and enhanced radar imagery. Subsequent results thus utilize only the threshold approach. In Fig. 1d, a satellite infrared estimate of the C/S partitioning from the CST, (Adler and Negri, 1988) is presented. These results are discussed in section 5.

3. RADAR RESULTS

Using a threshold of 7 mm/h, a value based on a subjective analysis of radar images, the Phase I and Phase II stratiform component of the total rain is estimated to be 37% and 38% respectively. Cheng and Houze (1979) estimate (subjectively, and using only data at 1200 GMT), values of 50% and 40% respectively. To compare more directly with the results of Cheng and Houze, the 1100, 1200 and 1300 GMT values were averaged. Results are summarized in Table 1. Although indications are that our lower values may be a truer representation of the actual stratiform percentage, it is clear that the results are sensitive to the technique or to the parameters used. For example, the methodology of Churchill and Houze (1984) gave values of 50-55% with little diurnal variation.

In Fig. 2, the results of compositing the hourly radar data are presented. Figure 2a is for Phase I (14-19 observations per hour) and presents the average volume rainrate (kg/h x 10^{10}) as a function of time. Maximums were attained at 1600 GMT. The percent of the total due to the stratiform component in Phase I is shown in Fig. 2b. The 1200 GMT results are affected by missing observations.Results for Phase II (14-19 observations per hour) show peak amounts of total and convective rain around 0900 GMT (Fig. 2c). The stratiform amount is fairly constant, though in relative terms there is a minimum at 1200 GMT and a maximum at 1500 GMT (Fig. 2d). Results for the combined Phase I and Phase II (30-35 observations per hour) are shown in Fig. 2 e,f. Again, four missing observations at 1200 GMT may affect the results, but there is a broad maximum from 1000 to 1500 GMT in the convective regime, followed by at peak in the stratiform regime at 1600 GMT.It is difficult to generalize about the diurnal variation of C/S rainfall because of the small sample size in each phase. Futhermore, 9 of the 36 days accounted for 63% of the total rainfall.

4. SATELLITE RESULTS

The satellite technique (in exactly the same form as published in Adler and Negri, 1988) is applied to two GATE days (Days 179 and 180). The rainrate and rain area coefficients were set for the Florida environment of the original study. The technique attempts to define convective areas as those with relative minima in the IR temperature field, and attempts to screen out thin cirrus. It also computes an anvil background (or tropopause) temperature directly from the data. This is used in the determination of the stratiform raining area.

Results for day 179 (28 June 1974) are presented in Fig. 3a, with verification from the radar in Fig. 3b. The CST underestimated the total rain, but captured the diurnal variation, particularly in the stratiform component. It failed, however to catch the significant rain after 1600 GMT, which was mostly stratiform. Table 2 presents a summary of the CST's application on two days. It grossly underestimated the total rainfall on Day 180, and on both days under-estimated the stratiform percentage compared to the radar. A potential reason for this is that the stratiform rainrate in the CST is fixed at 2 mm/h. Actual stratiform rainrates ranged from 1.87 to 3.94 on day 179 with an average of 3.35. On Day 180 the range was 2.00 to 3.04, with an average of 2.54. Once properly calibrated, (or at least initialized with a non-Florida sounding), the CST could be applied to other areas of the tropical Atlantic to investigate if this C/S percentage is unique to the GATE region. This remains to be done.

Finally, the C/S threshold of 7 mm/h was applied to estimates of precipitation made with an SSM/I 86 GHz data (see the companion paper, Adler et al., 1989, figure 5). Application to data coincident with radar datafrom the Wallops Island radar yielded a stratiform percentage of 61%, identical to the radar estimate. The C/S division in a Pacific tropical cyclone and a mid-latitude (U.S.) squall line are presented in Fig. 4. 89% of the rainfall in the tropical cyclone was determined to be stratiform, while 40% of the squall line rain was stratiform. There is no radar verification for these numbers however.

5. CONCLUSIONS

The statistics of tropical rain system structure, specifically the division between convective and stratiform rainfall over the GATE B-scale array was examined. It was found that a simple threshold technique applied to the radar data yielded C/S results which were in agreement with a subjective evaluation of the radar imagery. The objective method of Churchill and Houze (1984) produced (it seemed) too little convective rain.

Applying this threshold technique to all the data yielded stratiform contributions to the total rain of 37-38%. Cheng and Houze (1979) subjectively examined only 12 GMT data and found 43%. They found variations between the phases; we did not. Generalizations on the diurnalvariation were not possible due to the limited number of days on which significant rainfall occurred.

Results using a satellite technique were mixed: good estimates on Day 179, poor ones on Day 180. On both days the stratiform percentage was underestimated compared to the radar, possibly due to a bias in the stratiform rainrate. The potential exists to make C/S estimates using rain algorithms applied to SSM/I data.

TABLE 1
Comparison of percent stratiform rainfall estimated from the GATE radar.

	PHASES		
	I	II	I & II
Cheng & Houze (12Z only)	50%	40%	43%
Threshold (11,12,13Z)	36%	33%	34%
Threshold (all times)	38%	37%	37%

TABLE 2
Comparison of satellite and radar estimated rain parameters.

	VOLUME RAINRATE (10^{10} kg/h)		% STRATIFORM		
	CST	RADAR	CST	RADAR	H & R[1]
DAY 179[2]	175	228	19%	29%	40%
DAY 180[3]	71	144	31%	38%	---

[1] Houze and Rappaport (1984) squall line only
[2] 01-20 GMT except 12,18,19 GMT
[3] 00-23 GMT except 6,12,13,16,20 GMT

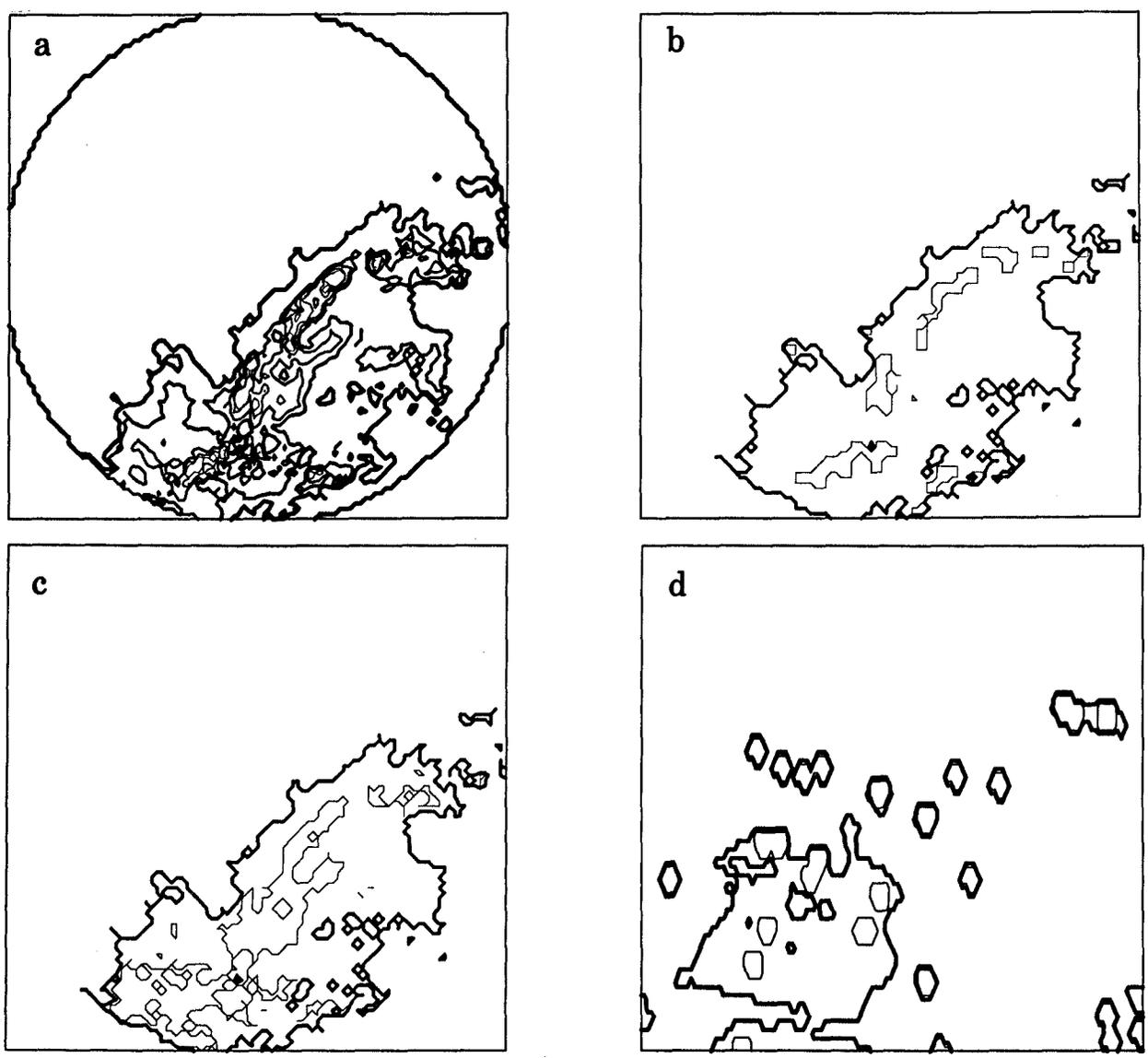

Figure 1. *a) GATE radar-derived rainrate field at 1300 GMT 28 June 1974. Contours are 1, 5, 10, 20, and 30 mm/h.*
b) Convective (thin contour) and stratiform (thick contour) rain areas defined by the Churchill-Houze technique.
c) Same as (b) except convective rain areas are defined by the 7 mm/h threshold.
d) Satellite-derived convective/stratiform partitioning. Note: coordinate system for this image is satellite, not radar.

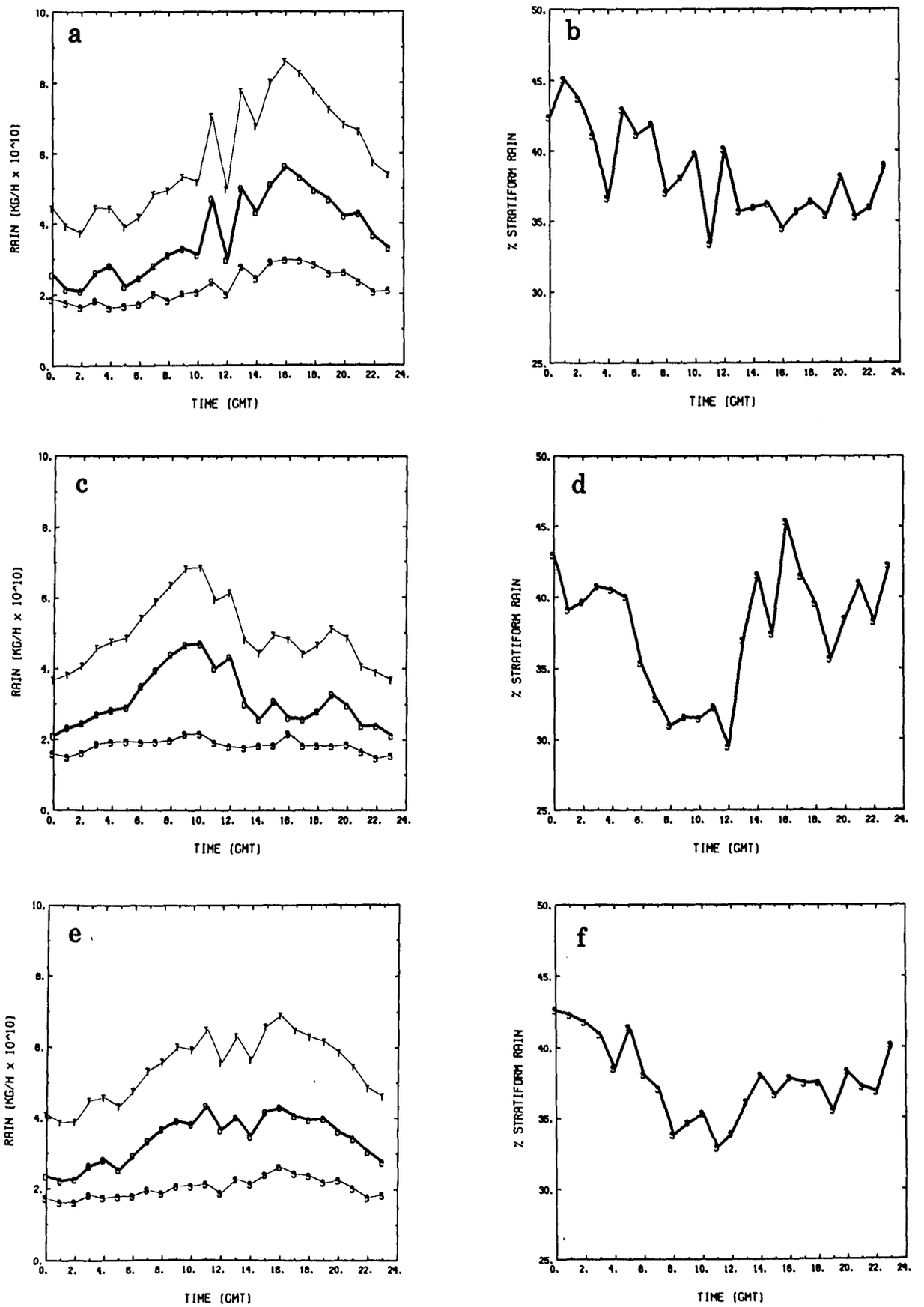

Figure 2. *a) Total, convective and stratiform rain from the Phase I hourly radar data, using a threshold of 7 mm/h.*
b) Percentage of the total volume rainrate due to stratiform component.
c,d) Same as (a,b) except GATE Phase II.
e,f) Same as (a,b) except GATE Phases I and II combined.

REFERENCES

Adler, R. A. and A. J. Negri, 1988: A satellite infrared technique to estimate tropical convective and stratiform rainfall. J. Appl. Meteor., 27, 30-51.

Adler, R. A., A. J. Negri, N. Prasad, and W.-K. Tao,1989: Cloud model-based simulations of satellite microwave data and their application to an SSM/I rain algorithm. Preprints, 4th Conf. on Satellite Meteorology and Oceanography, AMS, Boston, MA, 4 pp.

Cheng, C. P. and R. A. Houze, 1979: The distribution of convective and meso- scale precipitation in GATE radar echo patterns. Mon. Wea. Rev., 107, 1370-1381.

Churchill, D. D. and R. A. Houze, 1984: Development and structure of winter monsoon cloud clusters on 10 December 1978. J. Atmos. Sci., 41, 933-960.

Houze, R. A. Jr and E. N. Rappaport, 1984: Air motions and precipitation structure of an early summer squall line over the eastern tropical Atlantic. J. Atmos. Sci., 41, 553-574.

Hudlow, M. D. and V. L. Patterson, 1979: GATE Radar Rainfall Atlas, NOAA Spec. Rep., Center for Environmental Assessment Services, NOAA, 155 pp.

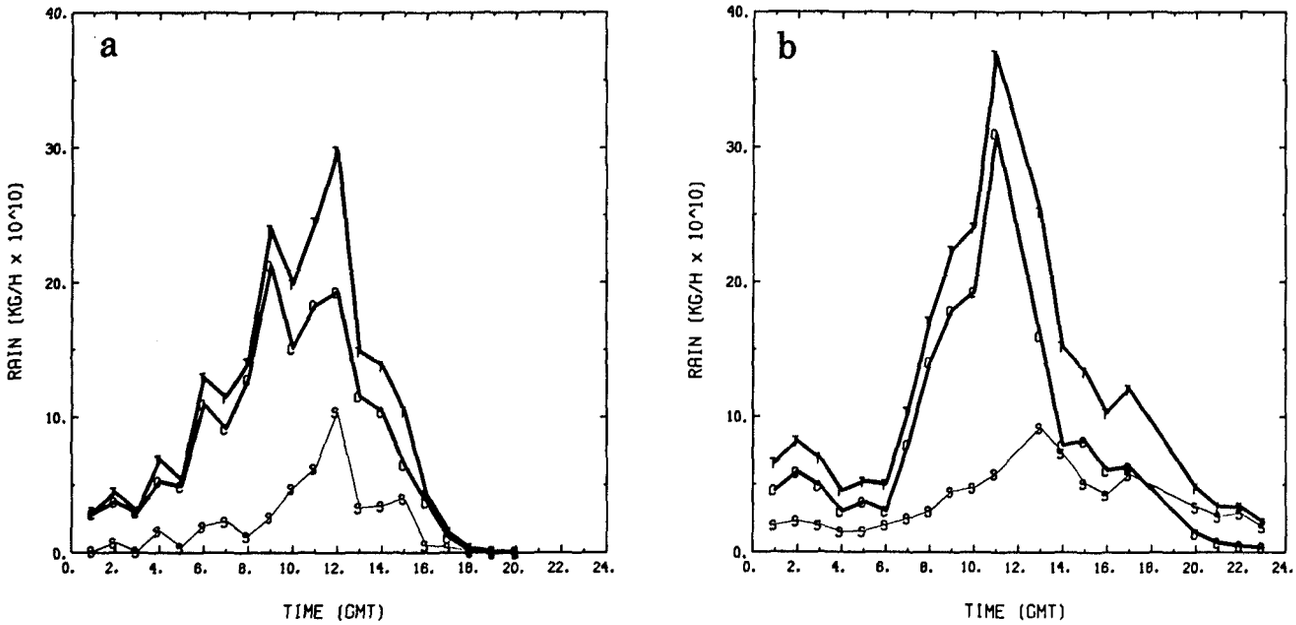

Figure 3. *a) Estimates of the total, convective and stratiform rainfall from satellite infrared data on Day 179 (28 June 1974). b) Same as (a) except from the thresholded radar data.*

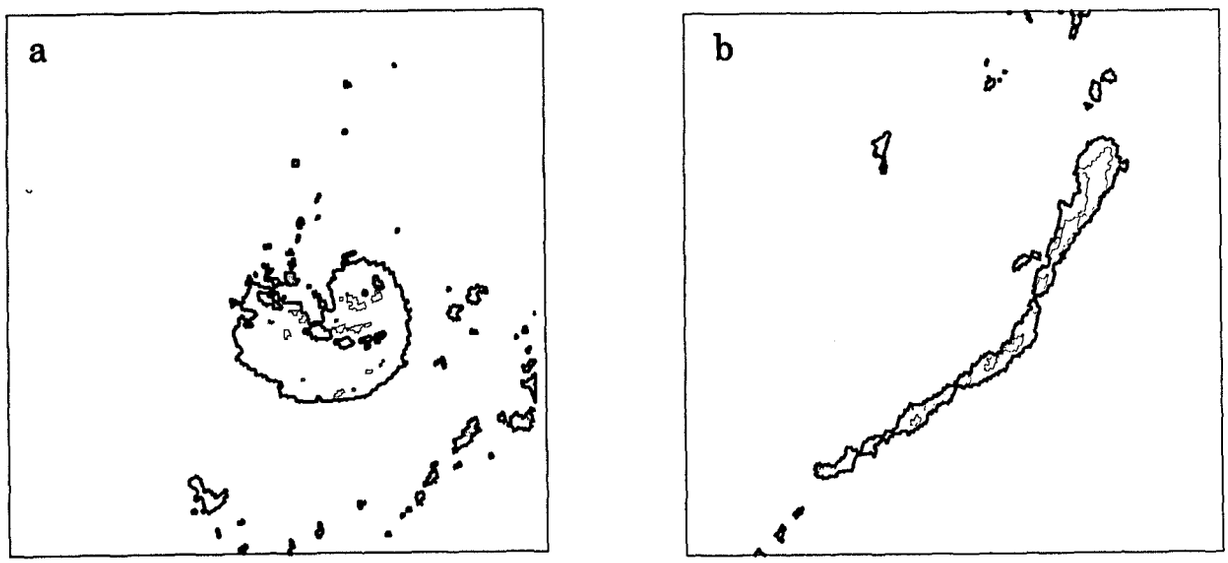

Figure 4. *Convective/stratiform partioning of rainrates derived from the SSM/I 86 GHz algorithm of Adler et al. (1989). a) A tropical cyclone off Taiwan at 2130 GMT 11 July 1987. b) A squall line in the central United States at 0052 GMT 17 August 1987.*

How Universal are the GATE Rainfall Statistics?

Kyung-Sup Shin*, Phil E. Riba, Yoo-Shin Ahn, and Gerald R. North

Climate System Research Program
Department of Meteorology
Texas A&M University, College Station, Texas

1. Introduction

The area-time averaged rainrates in the tropics are measure of latent heat release which is vital in the study of general circulation and short term climate change. However, due to the large fraction of earth covered by ocean and lack of a proper data acquision system over the ocean, tropical precipitation data over the oceans is notoriously poor. Perhaps, the only possible solution is to rely on the measurements from space. But measurements from satellites produce different types of problems which are related to the temporal and spatial scales of rainrates.

Two well documented sources of error, the sampling error (North 1987) due to discrete observations in time on a given area and the beam filling error (Chiu et al. 1988, Short 1988) due to the non-homogeneous distribution of rainrate inside a field-of-view (FOV) and the non-linear relationship between the rainrates and the radiant intensity, make present-day satellite measurements of rainfall uncertain even with the assumptions of perfect instrument and retrieval algorithms. Present efforts to identify the characteristics of these errors are being hampered by a lack of real measurements (ground truth) of precipitation data over the oceans. Therefore, the required parameter values rely heavily on the GATE rainfall statistics. Naturally, the question, "How universal are the GATE rainfall statistics?" is inevitable.

The objective of this study is to provide some qualitative evidence toward answering this question. In the absence of ground truth, our strategy is to compare some statistics of satellite data over the tropical ocean. We concentrate on parameters related to the time scale of area averaged rainfall, the intensity of the diurnal and semi-diurnal cycles of area averaged rainfall, and the spatial scale of rainfall in anticipation of the sampling error for precipitation measurements from scanning instruments on low orbiting satellites.

2. Time scale of area averaged rainfall

The GOES-W infrared cloud top temperatures were used in this study. The data were recorded at 3-hour intervals during December 19, 1987 to March 31, 1988 over the central and eastern tropical Pacific bounded at 20°N to 20°S with 2.5° × 2.5° resolution. The brightness temperatures were classified to a histogram of 16 classes (see Meisner and Arkin 1987). From the histogram, GOES Precipitation Index (GPI) (Arkin 1983) was calculated by counting the number of pixels colder than 235K out of the totals at each $2.5^{\circ 2}$ and $5^{\circ 2}$ grid.

Spectral analyses were performed on time series of the GPI to estimate the lagged autocorrelation time scale of the area averaged rainrate and the power spectrum near the diurnal and semi-diurnal frequencies over the tropical Pacific. The analyses have been conducted on $2.5^{\circ 2}$ and $5^{\circ 2}$ grid boxes, separately.

a) Lagged autocorrelation time scale

It is suggested that the time series of area averaged rainrate is composed of the sum of a first order Markov process and a few discrete sinusoidal frequencies. Using the autocorrelation coefficient of lag 1 (α), the autocorrelation time (τ_0) are estimated by $e^{-1} = \alpha^{\tau_0}$. Figure 1 illustrates the dependence of τ_0 over the domain for the $2.5^{\circ 2}$ grid (thin arrow) and for the $5^{\circ 2}$ grid (thick arrow). The direction of the arrow represents the time (hour) from the north as indicated at the upper left corner. To get meaningful interpretation, only the regions of strong variation of GPI are presented.

At any location, τ_0 of 5° grid has a longer time scale than that of 2.5° grid as expected. At ITCZ region, the time scale is about 12 hours for 2.5° area, and for the 5° area it is slightly longer, generally. But SPCZ regions exhibit much a longer time scale than that associated with the ITCZ and the time scale of larger area is much different to the smaller area. Direct comparison of these results to the same statistics at GATE area (about 8 hours for 2.5° area) suggests that Pacific ITCZ has a little longer or comparable time scale to the GATE region, but SPCZ region has a significantly longer time scale. However, it should be mentioned that actual comparison is impossible because of uncertainty of the GPI as a indicator of real rainfall and the difference of season for comparison. It is also suggested that the convection in the ITCZ and SPCZ are certainly driven by different mechanisms because of large time scale differences of the small and large areas.

b) Characteristics of diurnal and semi-diurnal cycles

The existance of diurnal and semi-diurnal cycles of precipitation is very important in sampling design (North and Nakamoto 1988), and the semi-diurnal cycle will add additional sampling error on precipitation measurements from low earth orbiting satellite. From

* *Current affiliation:* Korea Advanced Institute of Science and Technology, Seoul, Korea.

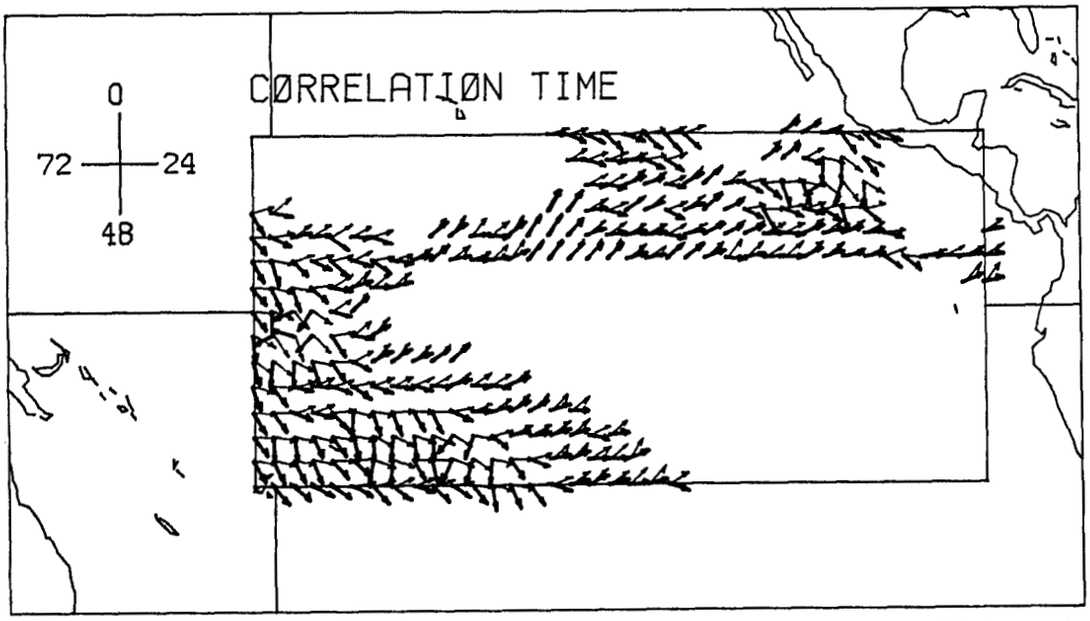

Fig. 1 Lagged autocorrelation time (hour) for 2.5° × 2.5° (thin arrow) and 5° × 5° (thick arrow) grid boxes. The direction of arrow from the north to clockwise represent autocorrelation time as indicated upper right corner.

the GPI time series of 100 days with 3 hour interval, the power spectrum is calculated at each $2.5°^2$ and $5°^2$ grid, respectively. Using the τ_0 estimated from the previous section, the background red noise spectra are also calculated. The power at the diurnal and semi-diurnal frequencies are estimated by subtracting background red noise spectrum from the power spectrum. Figure 2 illustrates the results of 5° ×5° grid area over the tropical Pacific.

In Fig. 2, the thin arrows indicate the amplitudes over 80% of statistical significance and the thick arrows indicate them over 95% significance. The length is proportional to the amplitude and the direction of arrow indicates the time of maximum in a 24 hour clock as shown in lower left corner.

In the region of the Pacific ITCZ, the diurnal variations are basically composed of the first harmonic which has noon maximum, however, they are only marginally significant statistically. Strong and statistically significant diurnal and semi-diurnal cycles exist in the region of SPCZ. The maximum of the diurnal cycle occurs noon to early afternoon, and that of semi-diurnal cycle occurs at dawn and mid-afternoon in this region, generally (note two maximums of semi-diurnal cycle). Therefore, the afternoon maximum is pronounced and midnight minimum is depressed by the sum of the two harmonics. This agrees well with the results of previous studies.

The diurnal variation in the GATE region is composed of mostly the first harmonic (Albright et al. 1981) which is similar to the Pacific ITCZ region. Therefore, it is suggested that the diurnal variation of the Pacific and Atlantic ITCZ looks similar and mostly first harmonic. But that of SPCZ looks different to the ITCZ and the amplitude is stronger than the ITCZ. From the satellite

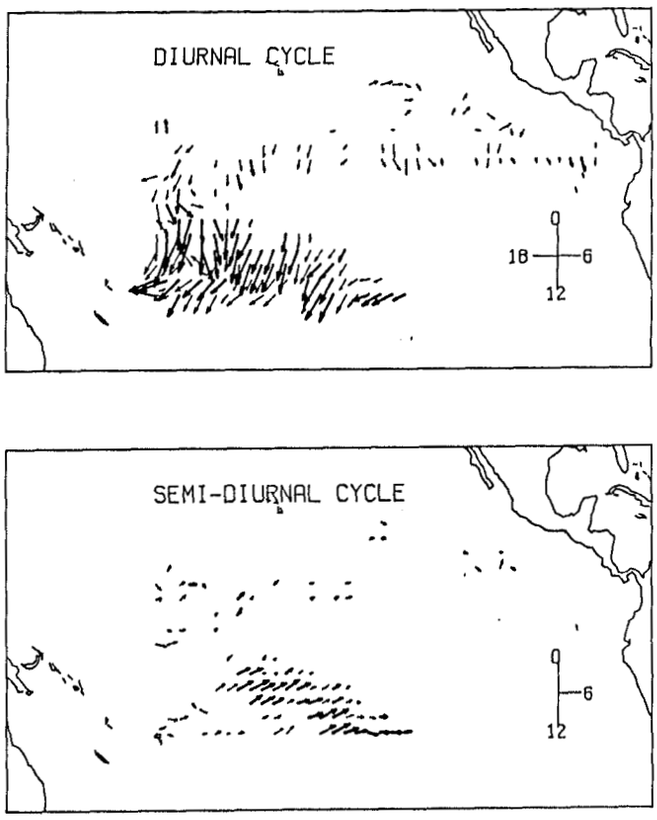

Fig. 2 The amplitude of the diurnal cycle and semi-diurnal cycle of area averaged rainrate for 5° × 5° grid box. The thin arrow indicates over 80% statistical significance and the thick arrow indicates those over 95% significance. The length is proportional to amplitude and the direction of arrow indicates the time of maximum in a clock as shown in lower left corner.

sampling point of view, the existence of semi-diurnal cycle over SPCZ region may add an additional sampling error of 5 to 10 percentage points for sun-synchronous satellites. Sampling errors without the diurnal errors are expected to be about 10% (Shin and North 1988).

3. Spatial scale of tropical rainfall

Nimbus-5 Electrically Scanning Microwave Radiometer (ESMR-5) brightness temperatures during the year of 1974 were analyzed over the tropical Atlantic and Pacific bounded 30°N to 30°S to estimate the statistics of the spatial autocorrelation of brightness temperatures at each $5° \times 5°$ grid box for each season. Because of non-linear relationship of brightness temperature to rainrate, we cannot relate the results directly to rainfall, however, the comparison of the statistics between grid boxes may give some insight into the homogeniety of spatial statistics of rainfall in the tropics in a relative sense. To avoid bias of brightness temperatures with scan angle, only 21 pixels near nadir ($\pm 12°$ corresponding to $\pm 250km$ in ground scan) are analyzed. This will also give the same spatial resolution for each FOV (25 km).

For each strip of 21 pixels, the autocorrelation function with pixel separations, $R(i)$, (distance $= i \times 25$ km) are calculated. The statistics are assigned to the grid box of nadir location. Then statistics are collected and averaged over a season at each grid box. The maps of $R(1)$ (not shown) shows some irregularity but generally the ITCZ and SPCZ regions show that $R(1)$ is between 0.3 and 0.4 including the GATE area, and that in the major dry regions are between 0.1 and 0.2. However, we have found that the autocorrelations at all grid boxes decrease quite regularly with almost the same rate after $R(1)$. This is illustrated in Fig. 3.

In Fig. 3, we plot scatter diagrams of $R(1)$ vs. $R(2)$, $R(2)$ vs. $R(3)$, and $R(3)$ vs. $R(4)$ of the entire grid box. They show a remarkably linear relationship with almost the same slope (β) with spatial lag. The results indicate that $R(2) \simeq \beta R(1)$, etc, and $R(n) \simeq \beta^{n-1} R(1)$. Therefore, once the $R(1)$ is known, other coefficients can reasonably be determined from β. But $R(1)$ differs with geographic region. The results of a linear regression fit of each season are summarized in Table 1. The slopes are slightly different for seasons and lag, however, they are suggested to be quite regular within the uncertainty of data quality. Same analyses were conducted for the subgroups of area such as ITCZ or SPCZ regions only, but we have not found any serious differences.

Our interpretation of these results is as follow. Consider two random variables, X which is spatial white noise with variance σ_x^2 and Y which is red noise with variance σ_y^2. If X and Y are independent, the autocorrelation function of $X + Y$ will be

$$R_{x+y}(d) = \frac{\sigma_x^2 \delta(0-d) + \sigma_y^2 R_y(d)}{\sigma_x^2 + \sigma_y^2}$$

where d is the distance. For $d = 0$, $R(0) = 1$. But for $d \neq 0$,

$$R_{x+y}(d) = \frac{\sigma_y^2}{\sigma_x^2 + \sigma_y^2} \beta^d = const \times \beta^d$$

since, $R_y(d) = \beta^d$ for red noise. Therefore, $R(1)$ is determined by the ratio of the variances of white and red noises, but higher order coefficients will decrease regularly by β.

It is suggested that the ESMR has some instrumental noise possibly a white noise. It is also suggested that the meteorological signal that ESMR senses could be a red noise within a 100 km scale. If the variance of instrumental error is constant, then the variance of a signal will determine the $R(1)$. Small spatial variance of signal in a dry region will give small $R(1)$. This will be reversed in convective regions. We cannot say that the variance of signal is solely contributed by the variation of rain in space. Obviously, the signal that ESMR senses would be a mixture of upwelling radiation due mainly to rain, cloud, and water vapor. Rain contributes the biggest variation but may be rare. Instead we would like to say that the atmospheric backgrounds that ESMR senses including rain have the same spatial scale over the entire tropical ocean. Therefore, we cannot unequivocally answer question of homogeniety of spatial statistics of tropical rainfall at this stage. But we cannot reject the hypothesis that the spatial statistics are homogeneous throughout oceanic ITCZ regions.

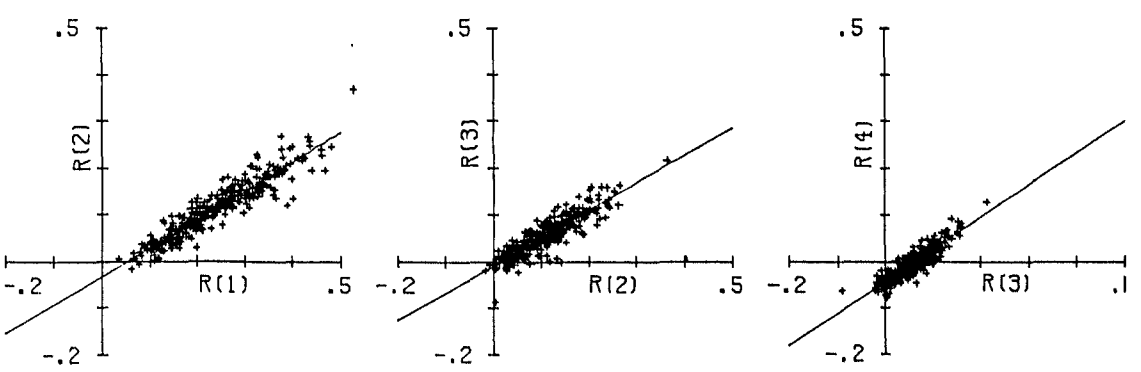

Fig. 3 Scatter diagrams of spatial autocorrelation and the best fit by linear regression at the winter of 1974.

4. Summary

An investigation has been conducted to address the representativeness of the GATE rainfall statistics in other parts of the tropics in anticipation of the sampling error on precipitation measurements from space. The GOES Precipitation Index was used to investigate the time scale of area-averaged rainrate, and the ESMR-5 data were used to examine the spatial scale of tropical rainfall. Due to the inherent limitation, it is difficult to give a clear interpretation, however, following suggestions are summarized.

The time scales of area-averaged rainfall in tropical oceanic ITCZ regions are different to those at SPCZ. SPCZ shows longer time scale than in the ITCZ. The SPCZ shows significant diurnal and semi-diurnal cycles but ITCZ shows only a marginally significant diurnal cycle. The rainfall characteristics in the Pacific ITCZ suggest similar ones at the Atlantic ITCZ in both time scale and diurnal variation. It should be emphasized, however, that these suggestions are dependent upon ability of the GPI to represent tropical oceanic rainfall. It is not clear whether the spatial scale of tropical rainfall is the same throughout the tropical ocean. But the likelihood of horizontally homogeneous statistics along the ITCZ is strengthened by the microwave data used here.

Table 1 Fitted regression coefficient of scatter diagram, for each season.

	Slope(R^2)		
	R(1) vs R(2)	R(2) vs R(3)	R(3) vs R(4)
Winter	.610(.877)	.587(.784)	.694(.798)
Spring	.603(.814)	.567(.720)	.600(.618)
Summer	.566(.853)	.552(.754)	.645(.686)
Fall	.634(.916)	.590(.844)	.640(.770)

References

Albright, M. D., D. R. Mock, E. E. Recker and R. J. Reed, 1981: A diagnostic study of the diurnal rainfall variation in the GATE B-scale area. *J. Atmos. Sci.*, 38, 1429-1445.

Arkin, P. A., 1983: A diagnostic precipitation index from IR satellite satellite imagery. *Tropical Ocean-Atmosphere Newsletter No. 17, 5-7*

Chiu, L., G. North, A. McConnell and D. Short, 1988: Estimation of rainrate from satellite: Finite field of view effect. Submitted to *J. Appl. Meteor.*

Meisner B., and P. A. Arkin, 1987: The relationship between large scale convective rainfall and cold cloud over the western hemisphere during 1982-1984. *Mon. Wea. Rev*, 115,51-74.

North, G. R., 1987: Sampling studies for satellite estimation of rain, *Preprints 10th Conf. on Probability and Statistics in Atmospheric Science, Edmonton*, Amer. Meteor. Soc., 129-135.

North, G. R., and S. Nakamoto, 1989: Formalism for comparing rain estimation designs, *to be published in J. Atmos. Ocean. Tech.*

Shin, K.-S., and G. R. North, 1988: Sampling error study for rainfall estimate by satellite using a stochastic model, *J. Appl. Meteor.*, 27, 1218-1231.

Short, D. A., 1988: Remote sensing of oceanic rainrates by passive microwave sensors: a statistical-physical approach, Ph.D dissertation, Texas A&M University, College Station, TX.

9.3

TROPICAL OCEANIC RAINFALL: ESTIMATION FROM SMMR AND SSM/I

C. Prabhakara , Guiseppe Dalu *, and B. E. Vollmer **

NASA/Goddard Space Flight Center
Greenbelt, Md

1. INTRODUCTION

Rainfall is highly variable in space and time. For this reason passive microwave radiometers flown on orbiting satellites with a fairly large field of view, about 25 to 100 km, would appear to be ill suited to measure rainfall. However based on recent studies, such as that of Doneaud et al, (1984), it appears that one could take advantage of the inherent statistical properties of rain over a mesoscale to estimate area-time-integrated rainfall. Basically these studies indicate that the average intensity of rain increases as the areal extent of the rain grows. Previous investigation by Prabhakara et al, (1986) incorporated some of these ideas to infer rainfall over the oceans utilizing Nimbus 7 Scanning Multichannel Microwave Radiometer (SMMR) data that ranged in frequency from 6.6 GHz to 37 GHz. In order to improve the earlier method the present study takes advantage of the data from the Special Sensor Microwave Imager (SSM/I) flown on DMSP satellite that has a finer spatial resolution and a channel at a higher frequency near 85 GHz.

2. ANALYSIS OF MICROWAVE DATA

Over the global oceans dual polarization measurements at 18 and 37 GHz made by Nimbus 7 SMMR with a resolution of 60 km indicate two important characteristics. (1) The brightness temperature in these two channels bears nearly a linear relationship up to the saturation level of about 265 K. (2) The difference in the V and H polarization temperatures, V-H, in each one of these channels decreases almost monotonically as brightness temperature increases. These characteristics are further reinforced by the measurements made at 19 and 37 GHz by SSM/I at a resolution of 25 km. The scattering due to ice hydrometeors is not strong at these wavelengths. On the basis of the above findings, we infer that the microwave brightness at frequencies below about 37 GHz depends strongly on the effective area of optically thick precipitation within the field of view (fov) of the instrument. In addition, in the area that is not covered by optically thick precipitation, light rain, liquid water in the clouds, and wind-induced perturbations in the surface emissivity play a secondary role in increasing the microwave brightness. These properties of microwave observations are illustrated in Fig. 1, panels a, d and e, with the help of SSM/I data taken during July 1987 in a small rainy region of the tropical Pacific Ocean centered at 7.5 N and 92.5 W. The data taken at the same time in a rainy region in the mid-latitudes centered at 43.5 N and 167.5 W, illustrated in Fig. 2, panels a, d and e, show similar behavior.

Contrasting with the nature of microwave observations at low frequencies described above, SSM/I measurements near 85 GHz reveal vividly the scattering effect due to ice associated with convective rain. Scattering leads to a marked decrease in brightness. Over the rain belts of the tropics and mid-latitudes this scattering effect varies substantially, highlighting the variations in ice hydrometeors in the upper levels of the convective clouds. This is vividly brought out when the brightness at 85 GHz is compared with that at 37 GHz (see Figs. 1 and 2, panel b). The polarization difference V-H at 85 GHz does not decrease monotonically with an increase in 85 GHz brightness (Figs. 1 and 2, panel f) due to scattering effects. Hence the idea of an effective area of optically thick precipitation that could account for, in a gross fashion, the behavior of brightness at low frequency measurements apparently does not hold at the high frequency measurements due to scattering effects.

* C. N. R., Instituto di Fisica del Atmosfera
Rome, Italy

** Applied Research Corporation
Landover, MD

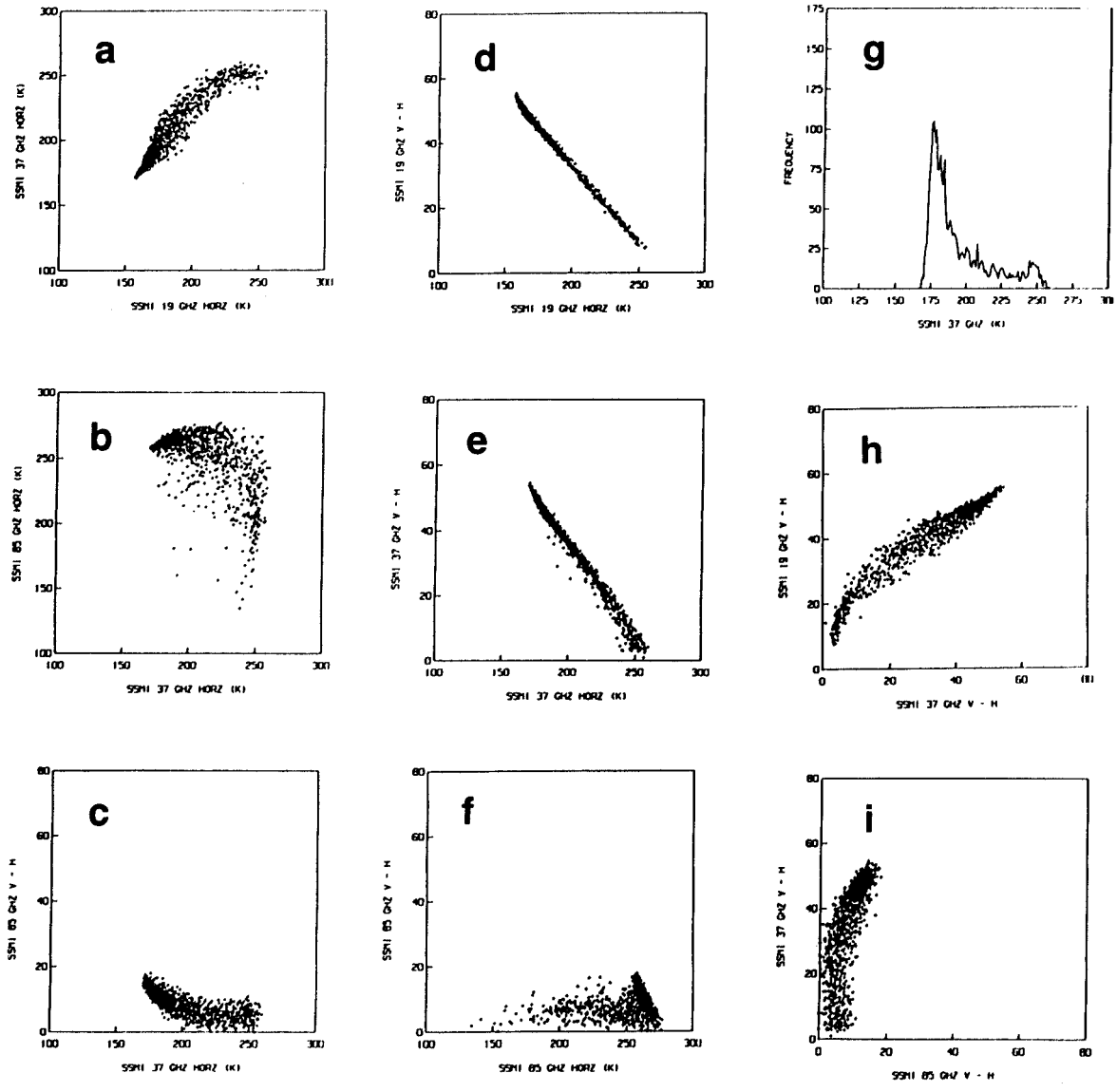

Fig 1. Multispectral dual polarization information contained in the SSM/I data of July 1987 over a rainy region of the tropical Pacific (3-6°N, 90-95°W). Number of observations is nearly 2200. Field of view is 25 km.

a. Comparison of brightness temperature (K) T37 vs T19
b. Comparison of brightness temperature (K) T85 vs T37
c. Polarization difference (K) between V and H components, V-H, at 85 GHz vs T37 (K)
d. V-H (K) at 19 GHz vs T19 (K)
e. V-H (K) at 37 GHz vs T37 (K)
f. V-H (K) at 85 GHz vs T85 (K)
g. Frequency of observations per 1 K interval vs T37 (K)
h. V-H (K) at 19 GHz vs V-H at 37 GHz
i. V-H (K) at 37 GHz vs V-H at 85 GHz

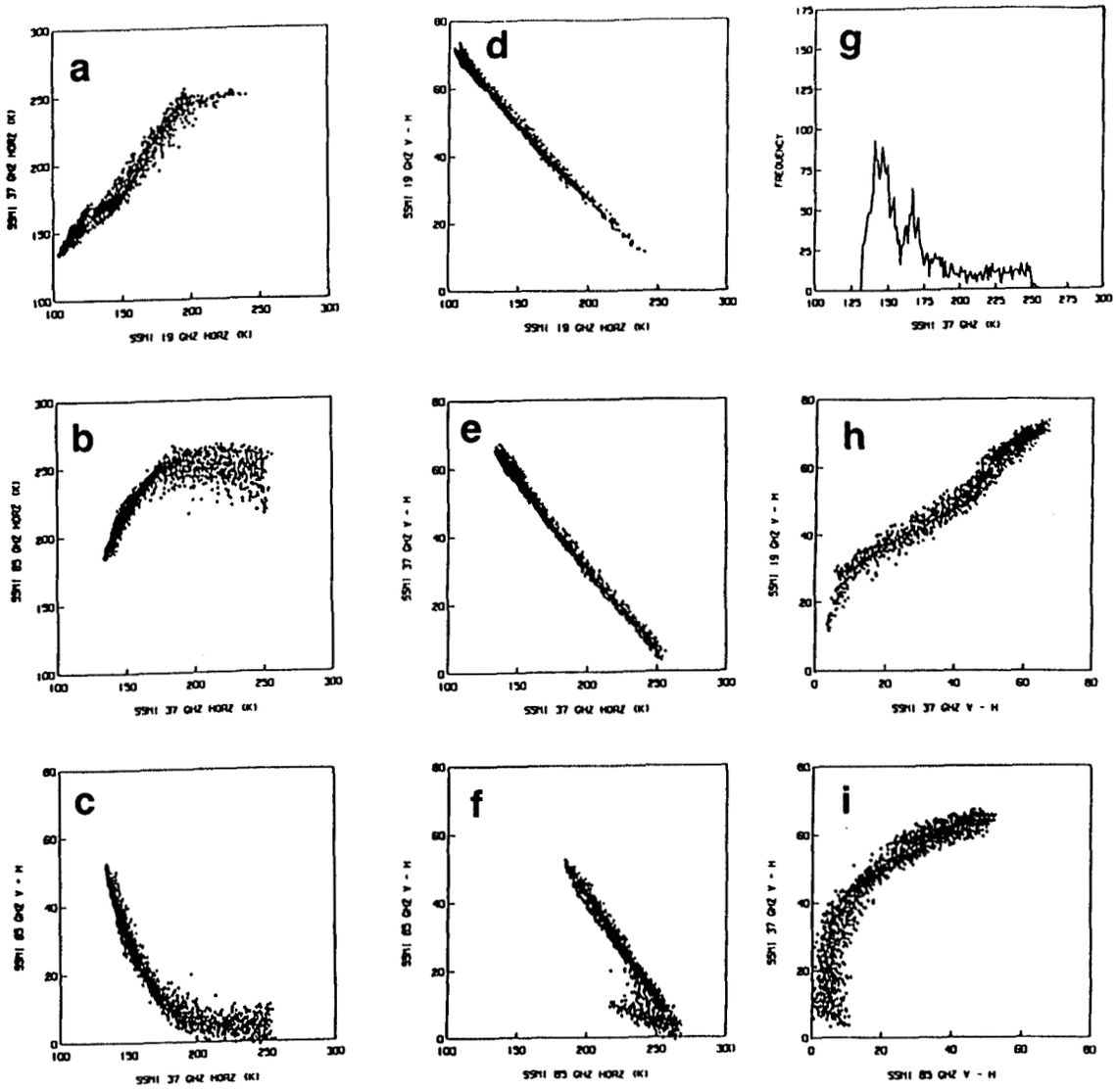

Fig 2. Same as Fig 1 except over a rainy region in the mid-latitude north Pacific Ocean (42-45°N, 160-165°W)

A close examination of the polarization effects at 85 GHz reveals further that the ice hydrometeors above the raining area lead to a small difference in V-H. As a result, we infer that the observed difference between V & H is coming mainly from the sea surface that is not affected by rain. A plot of 85 GHz V-H vs brightness at 37 GHz (Figs. 1 and 2, panel c) leads to this inference.

Yet another information that can be gained comes from a cross comparison of V-H at 19, 37 and 85 GHz as shown in Figs. 1 and 2, panels h and i. The inference from these figures is that the effective area of optically thick rain in the fov of the instrument is increasing as the frequency, and hence the extinction, increases.

3. RETRIEVAL TECHNIQUE

From the discussion presented above, it is preferable to estimate the area averaged precipitation in the fov of the instrument from the lower frequencies at 18, 19, or 37 GHz. With these considerations, a technique that depends on the population distribution in a month of T37, the brightness temperature measured by SSM/I at 37 GHz, is developed to estimate monthly mean precipitation over global oceans. This population distribution resembles the shape of a Gaussian curve at low brightness temperatures with a long tail

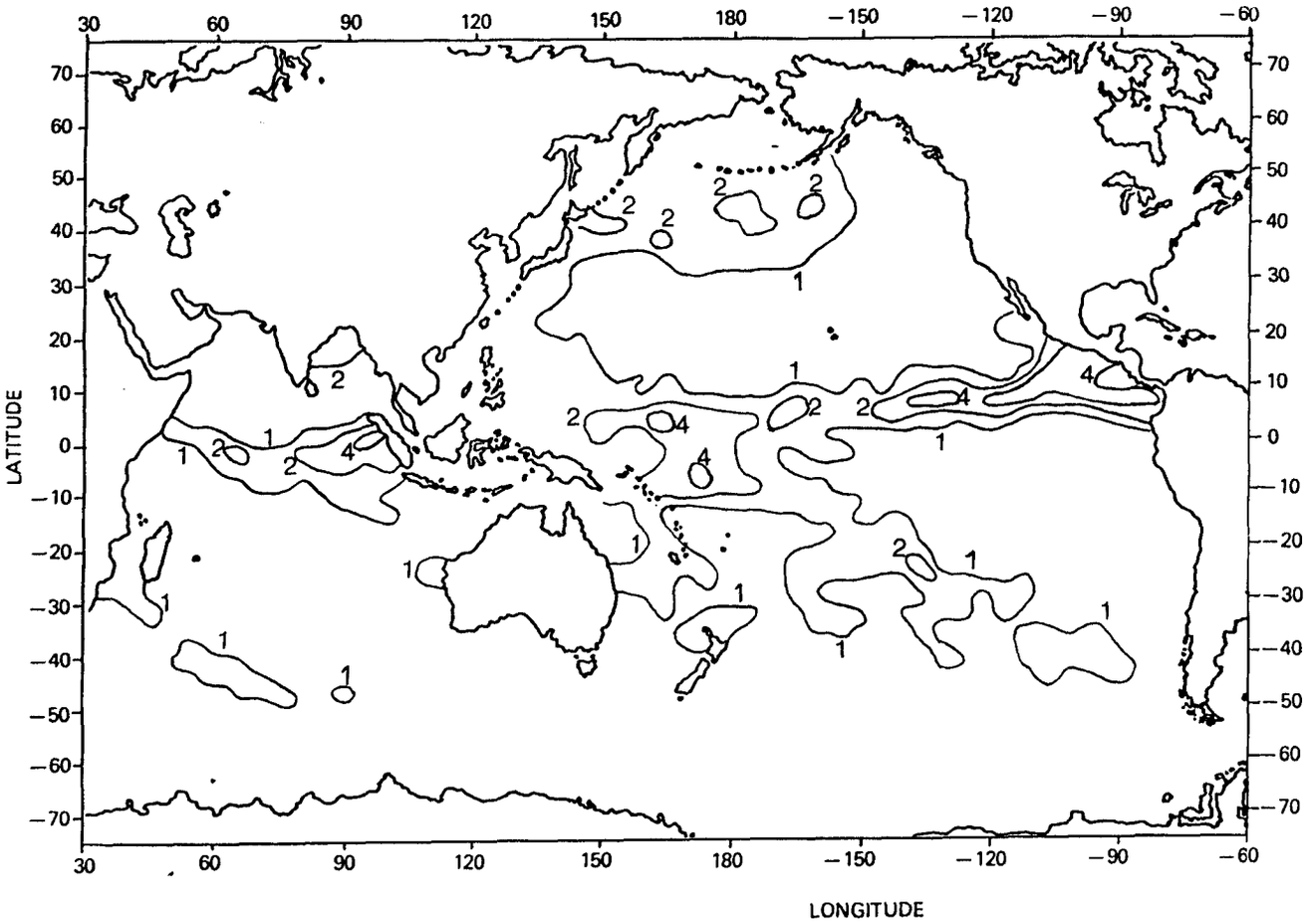

Fig 3. Mean rainfall rate (mm/hr) derived from SSM/I 37 GHz data for July 1987 in grid boxes of 3° lat X 5° long over the north and south Pacific Ocean

toward the high end (Figs. 1 and 2, panel g). The most probable value of T37 is close to the mean $\overline{T37}$ of the distribution. Based on this we hypothesize that the brightness temperature less than or equal to $\overline{T37}$ is primarily dependent on water vapor, sea surface temperature, surface winds, and cloud liquid water. It is postulated that rain starts when T37 exceeds $\overline{T37}$. Furthermore, it is observed that T37 has a significant latitudinal dependence and tends to be relatively large in the rain belts of low and mid-latitudes. This enables us to use $\overline{T37}$ as a parameter in our rain model to simulate the beam-filling effect over global oceans. The GEOSAT altimeter radar measurements over global oceans, which have a resolution of about 600 meters, lend credibility to this modelling of the beam-filling effect.

Utilizing the mean and intensity distribution of rainfall obtained from radar in the GATE experiment as guiding informations, an equation that makes use of $\overline{T37}$ and T37 is developed to estimate rainfall. The distribution of rainfall over tropical oceans deduced from this equation for different seasons agrees well with climatolgical patterns.

A map of the monthly mean rainfall rate derived from SSM/I for July 1987 over the North and South Pacific Oceans is shown in Fig. 3 to illustrate the technique.

REFERENCES

Doneaud, A.A., S.I. Niscov, D.L. Priegnitz and P.L.Smith, 1984: The area time integral as an indicator for convective rain volumes. J. Clim. Appl. Meteor., 23, 555-561.

Prabhakara, C., D.A. Short, W. Wiscombe, R.S. Fraser and B.E. Vollmer, 1986: Rainfall over oceans inferred from Nimbus 7 SMMR: Application to 1982-83 El Nino. J. Clim. Appl. Meteor., 25, 1464-1474.

SSM/I RADIANCES CORRELATED WITH 15 MINUTE RAIN GAUGE DATA

Roy W. Spencer

and

Robbie E. Hood

Earth Science and Applications Division/ES43
NASA/Marshall Space Flight Center
Huntsville, Alabama 35812

1. INTRODUCTION

Precipitation size ice over land produces significant brightness temperature (T_B) depressions at microwave frequencies near and above 30 GHz observed passively from space (Savage, 1976; Weinman and Guetter, 1977; Spencer et al., 1983). Here, the relationship of the 85.5 and 37 GHz T_B observations of the SSM/I (Special Sensor Microwave/Imager) with rain rate are explored. The ultimate intent of this work is the development of a T_B - rain rate relationship which can be applied to the SSM/I data base for the quantitative mapping of global precipitation.

While weather radar, due to its instantaneous and spatially continuous sampling characteristics, provides a better source of data for high-correlation comparisons with the satellite radiometer (Spencer, 1984), accurate (i.e. minimum bias) calibration of such a satellite technique with radar would require a significant number of rain gauge calibration points for the radar. Thus, calibration might best be performed with rain gauge data alone. Even though we would not expect a high correlation between the satellite and gauge reports (due to the high spatial variability of rainfall, see Vogel, 1981), gauges still represent the best way of calibration in the sense that they probably have the least bias of any method for measuring the amount of rain reaching the ground. Here we present preliminary results of a limited number of gauge comparisons to SSM/I 37 and 85.5 GHz T_B.

2. METHOD

Digitized rain gauge data from the National Climate Data Center (NCDC) were compared to SSM/I observations of a long-lived rain event over the south-central United States. Three SSM/I observations (0055 UTC 16 November, 1215 UTC 16 November, and 0042 UTC 17 November, 1987) of a squall line were utilized. This precipitation system had both isolated deep convective elements and widespread stratiform rainfall. The rain system T_B were compared to rain gauge totals for 15 minute intervals surrounding the SSM/I observation time. Fig. 1 shows the SSM/I 85.5 GHz polarization corrected T_B (Spencer et al., 1989) defined as

$$PCT_{85.5} = 1.818*T_{Bv} - 0.818*T_{Bh} \qquad (1)$$

for these three SSM/I passes. The PCT is an upward-adjusted T_B based upon the degree of polarization (i.e. the difference between T_v and T_h). This polarization difference is mostly the result of low emissivity water bodies. A correction based upon the polarization magnitude resolves the ambiguity between low T_B resulting from water surfaces and volume scattering by frozen precipitation. This not only allows discrimination *between* water bodies and precipitation, but even discrimination of light precipitation *over* water. The coefficients in Eq. 1 are empirically chosen so that the PCT computed over a cloud free water surface results in the effective radiating temperature of the lower troposphere (typically near the 80 kPa level). This brightness temperature is always higher than that which results from scattering by precipitation.

Also shown in Fig. 1 are the locations of gauges reporting non-zero 15 minute rain gauge amounts approximately 15 minutes after the SSM/I observation time. The gauge totals are derived from strip chart records by NCDC and digitized to 0.01 inch and 0.10 inch precision, depending upon the gauge type. Because some of these gauges were noted to be reporting only hourly totals, only those gauges which were obviously reporting 15 min. totals were accepted for comparison. No gauges were accepted that showed rain totals only on the hour, even though a few of these might have indeed been reporting 15 min. amounts. Most gauges in high T_B areas that were reporting no rainfall were excluded from the analysis. However, any gauges whose locations showed any evidence for rain activity, either from the gauge alone or from low SSM/I T_B, were retained.

In addition to the 85.5 GHz PCT, gauge totals were also compared to SSM/I 37 GHz PCT, defined as

$$PCT_{37} = 2.4*T_{Bv} - 1.4*T_{Bh}. \qquad (2)$$

These SSM/I data were area averaged over 40 km^2 square areas centered on each gauge. This was done separately for gauges reporting hundredths of an inch precision, and tenths of an inch precision.

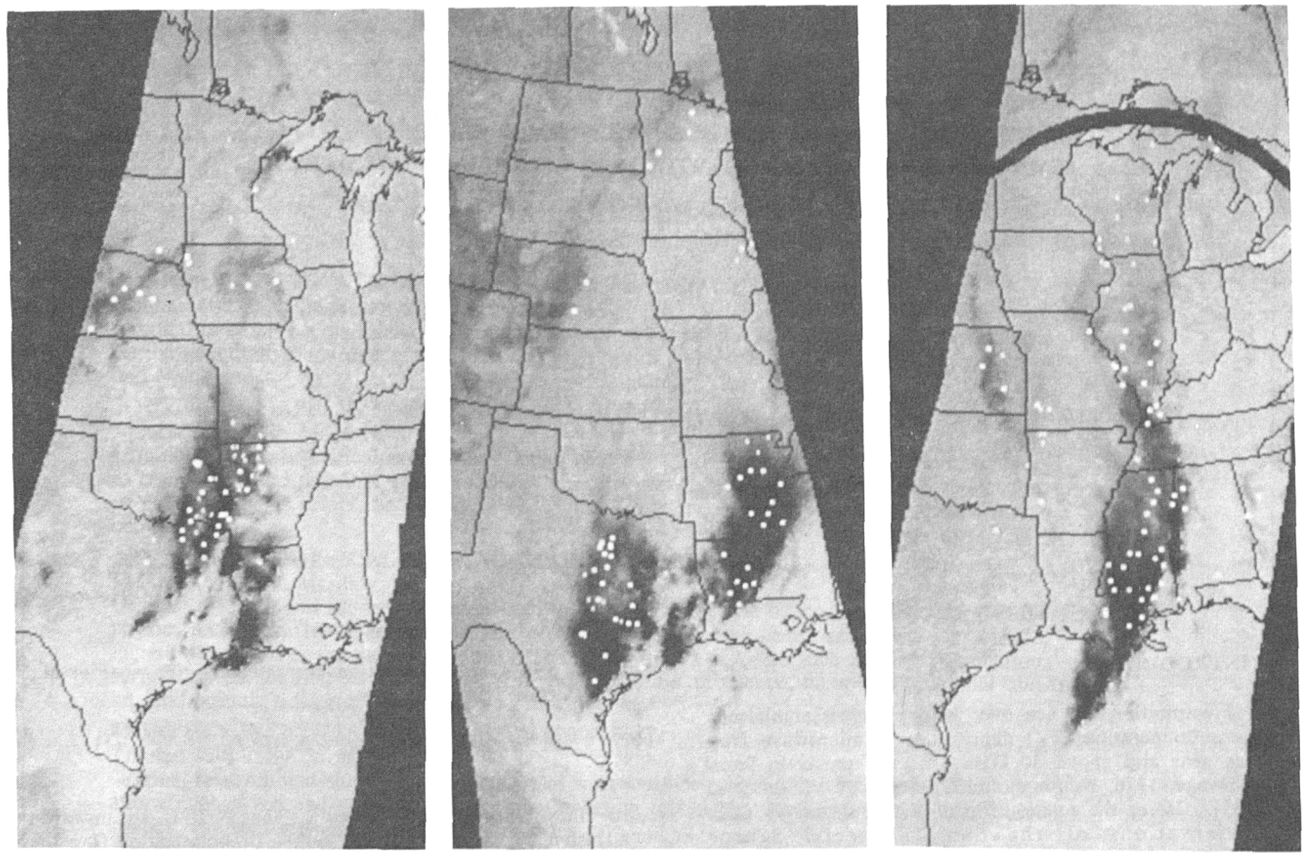

Fig. 1 Three SSM/I 85.5 GHz PCT images of a squall line at twelve hour intervals (0055 UTC [left] and 1215 UTC [center] 16 November, and 0042 UTC [right] 17 November, 1987) over the southern United States. White spots show the locations of rain gauges reporting non-zero 15 minute rain amounts at approximately 15 minutes after the SSM/I observation time.

3. RESULTS

a. squall line

Correlations between the PCT and various gauge amounts are summarized in Table 1. The gauges used in this analysis were for the squall line system shown in Fig. 1, and did not include the gauges in the weaker and spotty rain signals in the northern plains states. These rain systems will be discussed later. Several results are obvious from the data in Table 1. First, the correlations with the hundredths reports are considerably higher than with the tenths reports. This difference is generally a factor of two in explained variance. This is to be expected due to the lower precision inherent in estimating rain totals to the nearest tenth of an inch. Second, the time of highest correlation is the 15 minute period following the SSM/I observation time. This is also to be expected because the SSM/I observes the total attenuation integrated over the depth of the precipitation (primarily, ice) layer as it is falling. The precipitation observed by the SSM/I would generally take about 5 to 20 minutes to reach the ground, depending upon the altitude, phase, and habit of the hydrometeors. Thirdly, the 85.5 GHz correlations are slightly higher than the 37 GHz correlations, resulting in about 5% higher explained variances. This is probably a reflection of the fact that the 85.5 GHz channels are more sensitive to the ice scattering process at low rain rates than are the 37 GHz channels (Spencer et al. 1989).

Table 1 Correlations between SSM/I PCT and 15 minute rain gauge amounts (.01 inch reports/.10 inch reports) for the 16-17 November 1987 squall line system in Fig. 1. The 15 minute gauge integration time ending at the SSM/I overpass time is designated by "t"; the 15 minute period following the SSM/I overpass time is "t+15"; etc.

	t-15	t	t+15	t+30
$PCT_{85.5}$	.48/.22	.64/.36	.70/.35	.48/.24
PCT_{37}	.42/.12	.60/.32	.65/.34	.51/.20

Based upon the results in Table 1, a stepwise regression procedure was used to evaluate whether any additional variance of the gauge totals could be explained by more than the 85.5 GHz PCT alone. The two additional independent variables used were the 37 GHz PCT, and the standard deviation of the 85.5 GHz PCT within the 40 km^2 averaging area. Regression against the .01 inch data at t+15 revealed that, after selection of the 85.5 GHz PCT with a 0.70 correlation coefficient, only the 85.5 GHz standard deviation was selected, with the multiple correlation coefficient increasing to 0.74 (55% explained variance). The 85.5 PCT term was negative (because as the PCT decreases, the rain rate increases) and its coefficient was approximately 0.1, indicating that every ten degree depression in PCT results from an average increase of 1 mm h^{-1} in rain rate. The

standard deviation term's coefficient, however, was positive. This indicates that, given similarly low 85.5 GHz PCT, the more convective (more spatially inhomogeneous) portions of the rain system were producing more rainfall than the stratiform regions. In fact, for every 10 degrees of additional 85.5 GHz PCT standard deviation, the rain rate increased by an average of 2.3 mm h^{-1}. Stepwise regression against the .10 inch data did not produce any additional explained variance over the 85.5 PCT alone.

These SSM/I results have considerably higher correlations than similar comparisons made with Nimbus-7 Scanning Multichannel Microwave Radiometer (SMMR) data reported by Spencer (1984). In that study, hourly gauge amounts led to a multiple correlation of only 0.29 with single polarization 37 and 10.7 GHz data, whereas correlations with WRS-57 radar data yielded multiple correlations of 0.80.

b. northern stratiform rain areas

Non-zero rain gauge amounts are seen in areas north of the southern squall line system in Fig. 1. Some of these correspond to 85.5 GHz PCT depressions, but significantly, others do not. Of special interest is the third SSM/I time (Fig. 1, right image) where rain is being reported over western Missouri and northwest Arkansas, but where there was no indication of volume scattering in either the 85.5 GHz or 37 GHz T_B. This is evidence of probable warm rain conditions, where rain is initiated with little or no ice phase. This result is very significant, and if validated indicates that a certain amount of precipitation will not be observable over radiometrically warm backgrounds (primarily land) by passive microwave methods.

4. CONCLUSIONS

For the squall line system addressed here, 15 minute rain gauge amounts correlated quite well with SSM/I polarization corrected 85.5 GHz T_B. Regression against the .01 inch data set resulted in a correlation coefficient of 0.70, and an average 1 mm h^{-1} increase in rain rate for every 10 degree decrease in brightness temperature. Inclusion of the standard deviation of the 85.5 GHz PCT within the 40 km^2 averaging area as a predictor led to a higher correlation (0.74) and higher rain rates when the standard deviation was high representing convective signatures. While these correlations (.70 for a single predictor, 0.74 for two predictors) were not high in an absolute sense, they were surprisingly high considering the very different sampling characteristics of the SSM/I and individual rain gauges, combined with the very short integration time of the gauges (15 minutes). This is substantiated by Vogel (1981), who reported gauge totals in a dense Illinois network of gauges showed significant decorrelation with neighboring gauges as gauge separation increased from 3 to 32 km. This is a reflection of the extreme variability that can exist in point rainfall over short distances, and thus the unrepresentative nature of single gauge measurements for the 40 km^2 areas addressed here. Nevertheless, because the gauge is a direct measure of the amount or rain reaching the ground, rain gauge comparisons should allow calibration of the satellite technique with the least amount of bias.

Portions of a rain system adjacent to the squall line addressed here had little or no scattering signature in either the 85.5 or 37 GHz data. This is assumed to be due to little or no ice phase present to result in a significant T_B depression. This appears to indicate an inability of passive microwave methods to discern warm rain over land. Regional and seasonal upward adjustments of satellite passive microwave retrievals might therefore be necessary to correct for this shortcoming.

5. REFERENCES

Savage, R.C., 1976: *The Transfer of Thermal Microwaves through Hydrometeors*. Ph.D. Thesis, University of Wisconsin, Madison, Wisconsin 53706

Spencer, R.W., W.S. Olson, W. Rongzhang, D.W. Martin, J.A. Weinman, and D.A. Santek, 1983: Heavy thunderstorms observed over land by the Nimbus 7 Scanning Multichannel Microwave Radiometer. *J. Climate Appl. Meteor.*, **22**, 1041-1046.

Spencer, R.W., 1984: Satellite passive microwave rain rate measurement over croplands during spring, summer, and fall. *J. Climate Appl. Meteor.*, **23**, 1553-1562.

Spencer, R.W., H.M. Goodman, and R.E. Hood, 1989: Precipitation retrieval over land and ocean with the SSM/I: Identification and characteristics of the scattering signal. To appear *J. Atmos. Ocean. Tech.*

Vogel, J.L., 1981: Raingage network sampling statistics. *Precipitation measurements from Space*. NASA Workshop Report, Goddard Space Flight Center, Greenbelt, Maryland 20771.

Weinman, J.A., and P.J. Guetter, 1977: Determination of rainfall distributions from microwave radiation measured by the Nimbus-6 ESMR. *J. Appl. Meteor.*, **16**, 437-442.

6. ACKNOWLEDGMENTS

This work was supported by the NASA Headquarters Mesoscale Atmospheric Processes Research Program. The authors are grateful to Mr. Frank Wentz for supplying the reformatted SSM/I data.

10.1

SSM/I LIQUID AND FROZEN PRECIPITATION PATTERNS IN HURRICANE GILBERT

by

Roy W. Spencer

and

Robbie E. Hood

Earth Science and Applications Division/ES43
NASA/Marshall Space Flight Center
Huntsville, Alabama 35812

1. INTRODUCTION

The passive microwave radiances measured by the Special Sensor Microwave/Imager (SSM/I), the first copy of which was launched in June 1987 aboard the DMSP F8 satellite, have allowed our best opportunity yet to derive both liquid and frozen precipitation patterns over the ocean.

The lowest frequency SSM/I channels (19.35 GHz) observe radiometrically cold brightness temperatures (T_B) over the highly reflective ocean background (about 160 K for the horizontally polarized T_B, and 220 K for the vertically polarized T_B). Rain over the ocean causes the T_B to increase up to nearly the thermometric temperature of the rain if the precipitation is intense and widespread (Wilheit et al., 1977).

In contrast, the highest frequency SSM/I channels (85.5 GHz) respond readily to volume scattering by precipitation size ice (Savage, 1976; Weinman and Guetter, 1977; Wilheit et al., 1982; Spencer et al., 1983; Spencer et al., 1989), causing T_B decreases of up to 200° C in widespread deep convection. The weaker T_B depressions over the ocean are not unambiguous, however, because a dry atmosphere can result in T_B considerably lower than many stratiform precipitation systems produce. Fortunately, because the SSM/I has dual polarization at 85.5 GHz, and because the low T_B due to ocean reflection are much more polarized than the volume scattering induced T_B depressions by precipitation, we can correct the T_B for the degree of ocean surface influence. In effect, this changes the background from low emissivity to high emissivity.

Here we will explore the rain and ice signatures of tropical oceanic precipitation systems, including Hurricane Gilbert. A method for polarization correction without the F8 SSM/I V85.5 channel, which has experienced a severe degradation in quality, will also be presented. Liquid precipitation imagery at 19.35 GHz presented at the conference will also include deconvolution to approximately the 37 GHz spatial resolution.

2. METHOD

a. 85.5 GHz ice signatures with and without V85.5

The correction for any depression of 85.5 GHz T_B by the ocean surface is accomplished by the computation of a polarization corrected temperature,

$$PCT_{85.5} = 1.818*T_{Bv} - 0.818*T_{Bh}. \qquad (1)$$

The derivation of this expression is covered more fully by Spencer et al., 1989. Use of the PCT allows the identification of T_B depressions due to volume scattering by precipitation over the ocean with no ambiguity from dry airmasses.

After the failure of the V85.5 channel, it became necessary to derive a new expression for $PCT_{85.5}$ to be used with the F8 SSM/I. Because the other five SSM/I channels (V37, H37, V22.235, V19.35, H19.35) also have information on the water vapor content of the atmosphere, as well as other geophysical processes, it should be possible to substitute them for the V85.5 channel. Stepwise linear regression was applied to a carefully chosen SSM/I data set which included tropical and polar air masses over the ocean with and without clouds and precipitation, storms over land, warm land, cold land, and wet ground. A total of over 10,000 footprint locations were used, each having a 3 footprint by 3 footprint area averaged H85.5 T_B as well as all lower frequency channels T_B. These were regressed against $PCT_{85.5}$, as defined in Eq. 1. The results are summarized in Table 1.

Table 1. Results of stepwise regression of all SSM/I channels T_B (except V85.5) against $PCT_{85.5}$ for a training data set of 10,332 records involving a wide variety of atmospheric conditions over land and ocean. Shown are the regression step number; which term was chosen for explaining the most additional variance of $PCT_{85.5}$; the multiple correlation coefficient (R) of the model at that step; the fraction of the variance (R^2) of $PCT_{85.5}$ explained by the model at that step; and the resulting standard deviation (^{o}C) of the model error for that step.

Step #	Term	Corr. Coeff.(R)	Expl. Var.(R^2)	S.D.
1	V37	0.399	0.159	9.7^o
2	H85	0.654	0.428	8.0^o
3	H37	0.899	0.808	4.6^o
4	V22	0.940	0.883	3.6^o
5	V19	0.953	0.907	3.2^o
6	H19	0.962	0.925	2.9^o

It should be noted that the correlations in Table 1 can be made significantly higher by using a more restricted set of SSM/I data in the regression. However, the desire for the model to reveal the most subtle oceanic precipitation scattering signatures (snow, without rain below), and still be robust enough to not fail in a wide variety of atmospheric and surface situations, required a training data containing diverse phenomena. It is also significant that separate regressions for ocean and land data sets were no more successful than regression with land and ocean data combined.

The model equation at step six for the regression derived $PCT_{85.5R}$ is

$$PCT_{85.5R} = 0.391*H85 + 3.281*V37 - 2.039*V22 - 0.636*V19 + 0.627*H19 - 34. \qquad (2)$$

This equation was then applied to the Hurricane Gilbert cases, since at that point in time the V85 channel was very noisy.

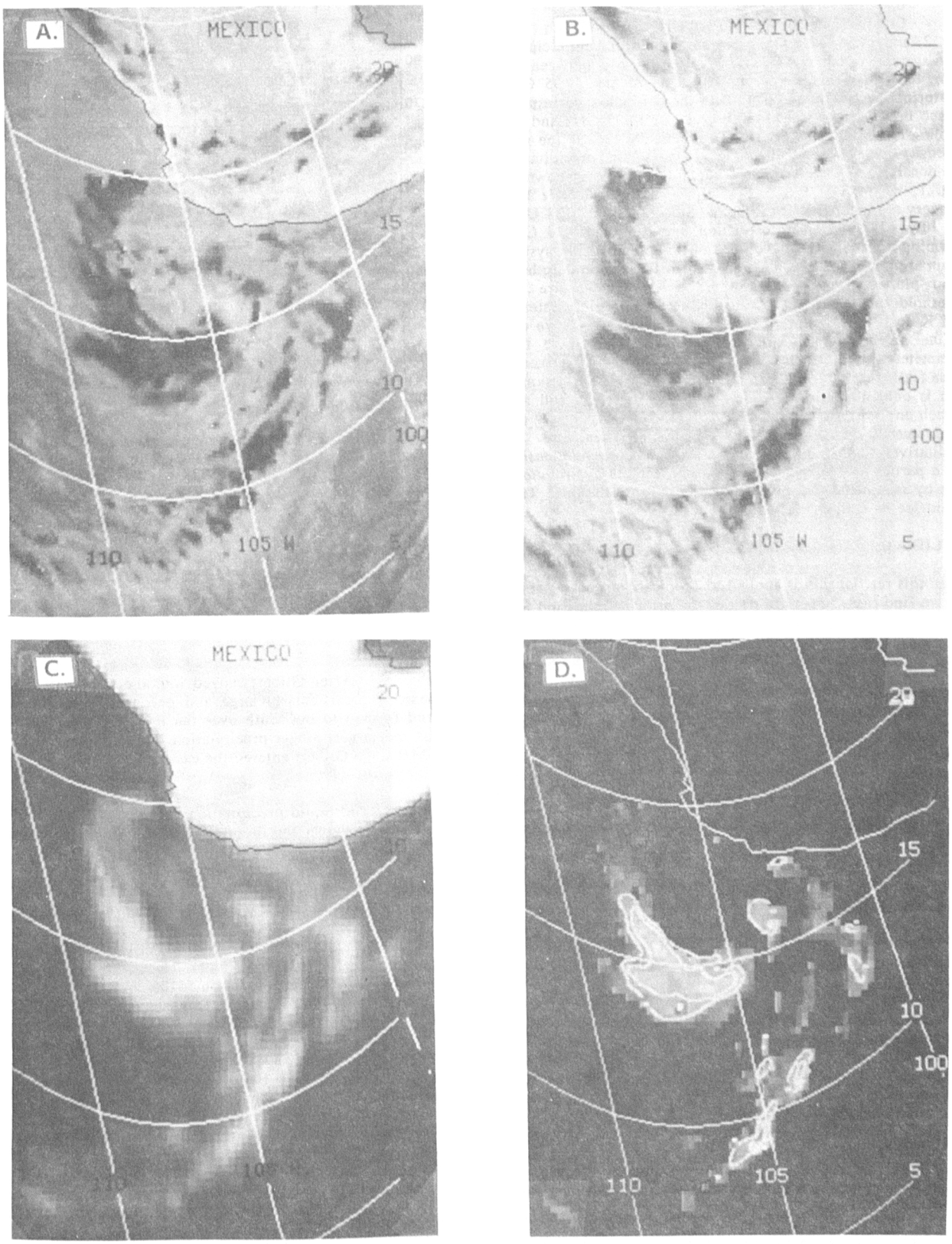

Fig. 1 SSM/I imagery of Tropical Storm Greg at approx. 0138 UTC 30 July 1987: a) 85.5 GHz T_{Bh}; b) $PCT_{85.5}$; c) 19.35 GHz T_{Bh}; and d) the liquid/ice deviation (LID) from average conditions (see text for details).

b. Rain versus ice signatures

Comparisons between 85.5 GHz PCT (using Eq. 1 or Eq. 2) and 19.35 GHz T_B for a number of tropical precipitation systems usually revealed a good correlation between the rain and ice signatures. On the scale of the 19.35 GHz footprints (approximately 50 km) there is good correspondence between the warming observed at 19.35 GHz and the cooling observed at 85.5 GHz. This indicates that as the rain intensity and coverage increases, so does the precipitation ice density and coverage. An example of this is shown in Fig. 1, where SSM/I H85.5, $PCT_{85.5}$, and 19.35 GHz T_{Bh} imagery are compared for Tropical Storm Greg at 0138 UTC 30 July 1987. The correlation between the 19.35 GHz warming and 85.5 GHz cooling for this precipitation system is apparent in Fig. 2, where the data in Figs. 1b and 1c have been plotted against each other. Also shown are the thresholds used in this study to isolate precipitating systems, 265 K for $PCT_{85.5}$ and 201 K for the H19.35 T_B. We can define an average linear relationship between these two parameters (the diagonal line in Fig. 2) when their T_B exceed these (rather arbitrary) threshold values. The linear assumption is only an approximation, since the H19 T_B will approach an asymptotic value near 265 K, somewhat below the thermometric temperature of the rain. Then, we can qualitatively determine *how much the liquid/ice relationship for a particular footprint deviates from this average relationship* by measuring the distance of any point to the line. This liquid/ice deviation (LID) is expressed as

$$LID = 0.568*H19 + 0.823*PCT_{85.5R} - 333.3 \qquad (3)$$

When this relationship is applied to Tropical Storm Greg (Fig. 1d) we find that the central part of the primary rain band has relatively more rain than ice (positive LID) whereas the periphery has relatively more ice than rain (negative LID). Also, the northern end of this rainband is dominated by ice precipitation, which might be a result of drier continental and mid-latitude air being drawn into the system from the north, causing relatively more evaporation of the raindrops. The small rainband to the south shows some evidence of directional shearing toward the storm center, with ice domination toward the center, and rain domination away from the center.

3.HURRICANE GILBERT RESULTS AND CONCLUSIONS

Hurricane Gilbert was imaged by the SSM/I several times during its traverse of the Caribbean Sea and Gulf of Mexico. Unfortunately, the V85.5 channel was very noisy, and so Eq. 2 (instead of Eq. 1) was used to compute $PCT_{85.5}$. The emissive signal of rain at 19.35 GHz can only be discriminated over a water surface, so the method for average liquid/ice ratio deviation (LID) outlined in the previous section can not be applied over and very near land. Thus, liquid portions of Gilbert's rainbands were sometimes not visible due to the proximity of land masses. However, some of the Gilbert LID patterns were observable (e.g. Fig. 3) where the precipitation was sufficiently far from land. While most Gilbert imagery will be presented at the conference, several conclusions follow which were made from inspection of the SSM/I T_B fields at eight different times.

1) The area of precipitation covered by the eyewall always represented a small portion of the total hurricane precipitation coverage.

2) Outer rainbands in Gilbert were usually dominated by ice (negative LID), with a significant directional shear causing the ice layer to be displaced away from the storm center, and rain domination (positive LID) in a thin zone on the inward side of the rainband. This is consistent with the strongly sheared environment of a mature hurricane.

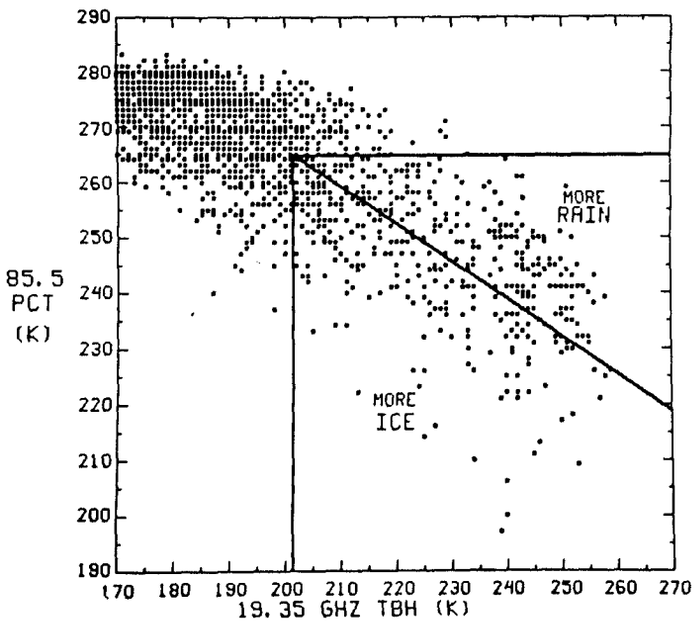

Fig. 2 Scatterplot of Tropical Storm Greg 19.35 GHz T_{Bh} versus 85.5 GHz PCT, showing the average relationship between the rain and ice signals (respectively).

3) After Gilbert moved into the southwest Gulf of Mexico, a particularly large and persistent rain-dominated band formed to the south over the Bay of Campeche. This was the largest single precipitation feature observed by the SSM/I since Gilbert entered the eastern Caribbean.

Other ice and liquid precipitation features of Hurricane Gilbert will be shown and discussed at the conference.

4. REFERENCES

Savage, R.C., 1976: *The Transfer of Thermal Microwaves through Hydrometeors.* Ph.D. Thesis, University of Wisconsin, Madison, Wisconsin 53706

Spencer, R.W., W.S. Olson, W. Rongzhang, D.W. Martin, J.A. Weinman, and D.A. Santek, 1983: Heavy thunderstorms observed over land by the Nimbus 7 Scanning Multichannel Microwave Radiometer. *J. Climate Appl. Meteor.*, **22**, 1041-1046.

Spencer, R.W., H.M. Goodman, and R.E. Hood, 1989: Precipitation retrieval over land and ocean with the SSM/I: Identification and characteristics of the scattering signal. To appear *J. Atmos. Ocean. Tech.*

Weinman, J.A., and P.J. Guetter, 1977: Determination of rainfall distributions from microwave radiation measured by the Nimbus-6 ESMR. *J. Appl. Meteor.*, **16**, 437-442.

Wilheit, T.T., A.T.C. Chang, M.S.V. Rao, E.B. Rodgers, andJ.S. Theon, 1977: A satellite technique for quantitatively mapping rainfall rates over the oceans. *J. Appl. Meteor.*, **16**, 551-560.

Wilheit, T.T., A.T.C. Chang, J.L. King, E.B. Rodgers, R.A. Nieman, B.M. Krupp, A.S. Milman, J.S. Stratigos, and H. Siddalingaiah, 1982: Microwave radiometric observations near 19.35, 92, and 183 GHz of precipitation in Tropical Storm Cora. *J. Appl. Meteor.*, **21**, 1137-1145.

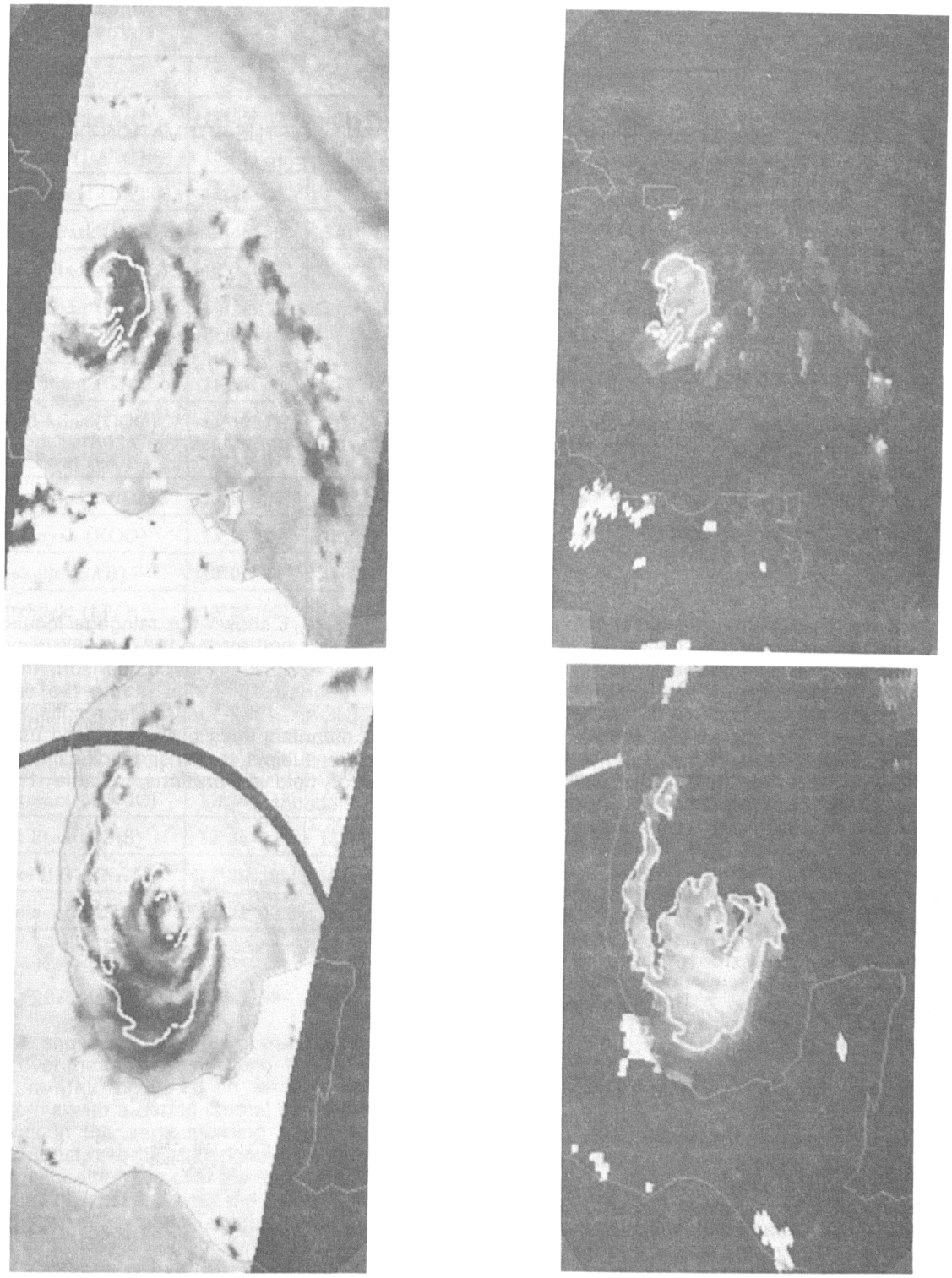

Fig. 3 Hurricane Gilbert 85.5 GHz T_{Bh} and LID images for 2215 UTC 10 September 1988 over the Eastern Caribbean (top), and 0045 UTC 16 September 1988 over the southwest Gulf of Mexico (bottom). Low 85.5 GHz T_{Bh} (left) in rainbands appear dark. LID imagery (right) have brighter areas (within contours) representing relatively greater liquid than ice precipitation; darker areas (outside contours) represent greater ice than liquid precipitation.

A RAINGAGE, RADAR AND SATELLITE SIMULATION STUDY OF THE ESTIMATION OF CONVECTIVE RAINFALL BY AREA - TIME INTEGRALS

David A. Short

Goddard Laboratory for Atmospheres
NASA/GSFC, Greenbelt, MD 20771

David B. Wolff

Applied Research Corporation
8201 Corporate Drive,Landover, MD 20785

Daniel Rosenfeld

Department of Atmospheric Sciences
Hebrew University, Jerusalem, Israel

David Atlas

Consultant
7420 Westlake Terrace, Bethesda, MD 20817

1. INTRODUCTION

A recent survey of radar observations of convective rain by Rosenfeld et al. (1988) has shown remarkably high correlations between area averaged rainrates, <R>, and the areal fraction of rainrates exceeding a preset threshold, F(T). These findings hold great promise for our ability to infer area averaged rainrates from satellite by measuring accurately at an optimal threshold (T), provided that we know the coefficient of the <R>, F(T) regression, S(T). Atlas et al. (1988) have shown how S(T) is related to the probability density function (pdf) of rainrates when R is averaged over space and time (the area-time integral of Doneaud et al., 1984, and Lopez et al., 1988), or space only (the area integral used by Chiu, 1988 and Rosenfeld et al., 1988). Because these studies have been based on radar reflectivity data (Z) there is some uncertainty in S(T) related to uncertainties in the Z, R relation. In this study we have examined <R> and F(T) with data from a network of raingages.

2. THE DARWIN AREA RAINFALL NETWORK

The rainfall data presented here come from a network of 22 tipping bucket raingages located within 120 km of the National Oceanic and Atmospheric Administration (NOAA) / Tropical Ocean - Global Atmosphere (TOGA) C-band meteorological radar at Darwin, Australia. Six of the gages and the radar were used during the Bureau of Meteorology Research Centre (BMRC) Australian Monsoon Experiment (AMEX, Holland et al., 1986)). Radar and raingage observations have been continued for the 1987-1988 and 1988-1989 rainy seasons in a joint effort by NOAA/BMRC/NASA to investigate temporal and spatial statistics of tropical rainfall. These studies will be useful in developing rainfall climatologies, defining sampling requirements and developing ground truth strategies for the Global Energy and Water Cycle Experiment (GEWEX), TOGA and the proposed Tropical Rainfall Measuring Mission (TRMM, Simpson et al., 1988).

Figure 1 shows the raingage locations and rainfall totals (mm) for the 1987 - 1988 rainy season (November - April). For comparison, the Darwin Airport reported 1508 mm during the same time interval (NOAA, 1987-1988). Our results, in which a uniform manufacturer's calibration was used for all gages, are subject to minor modification, pending reports of field calibrations. Table 1 lists the raingage locations.

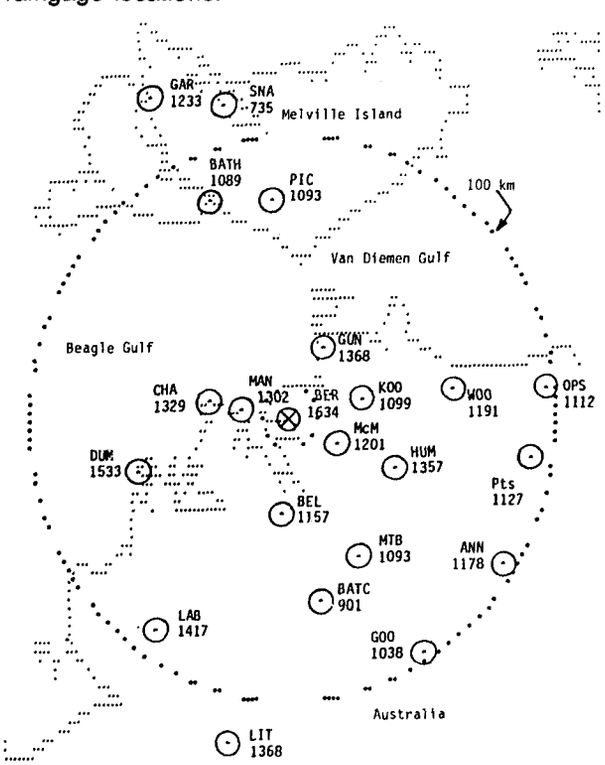

Fig.1. The Darwin area raingage network. Rainfall totals (mm) are for November 1987 - April 1988.

Table1. Locations of the Darwin area raingages. The radar is at Berrimah.

Station	Latitude	Longitude
Annaburro (ANN)	12°55' 00"	131°40' 08"
Batchelor (BATC)	13°03' 12"	131°01' 36"
Bathurst Island (BATH)	11°45' 30"	130°38' 06"
Belleville Park (BEL)	12°45' 30"	130°52' 48"
Berrimah Radar (BER)	12°27' 26"	130°55' 31"
Charles Point (CHA)	12°24' 48"	130°37' 30"
Dum In Mirrie (DUM)	12°38' 18"	130°22' 18"
Garden Point (GAR)	11°24' 30"	130°25' 00"
Goodall Mine (GOO)	13°12' 17"	131°21' 42"
Gunn Point (GUN)	12°14' 34"	131°02' 34"
Humpty Doo (HUM)	12°37' 00"	131°17' 12"
Koolpinyah (KOO)	13°23' 24"	131°10' 30"
Labelle (LAB)	13°07' 24"	130°28' 48"
Litchfield (LIT)	13°26' 00"	133°28' 00"
Mandorah Jetty (MAN)	12°26' 36"	130°45' 48"
McMinns Lagoon (McM)	12°32' 00"	131°04' 55"
Mount Bundey (MTB)	13°13' 50"	131°07' 46"
Old Point Stuart (OPS)	12°21' 30"	131°48' 48"
Pickertaramoor (PIC)	11°46' 11"	130°52' 30"
Point Stuart (PtS)	12°35' 12"	131°45' 30"
Snake Bay (SNA)	11°25' 18"	130°40' 18"
Woolner (WOO)	12°22' 00"	131°28' 00"

3. THE 1987 - 1988 WET SEASON

Figure 2 shows a time series of daily rainfall totals averaged over the raingage network. From day 304 - 349 the rainfall occurred in widely scattered thunderstorms with a strong diurnal variation. Peak rainfall was in the early morning hours near the Australian coast, shortly after noon over the islands and during late afternoon over the continent. On day 350 a squall line passed over the network from the south. The average rainfall depth for the 22 gages was 39.8 mm. Day 352 coincides with the onset of summer monsoon westerly winds at 850 mb (Keenan,1988). The monsoon rains were widespread, having a weaker diurnal cycle with a significant increase in the occurrence of stratiform rain. The daily rainfall record in fig. 3 shows high network average rainrates just after day 350, just after day 400 and around day 450. This behavior is suggestive of the influence of the tropical 40 - 60 day oscillation on Darwin area rainfall. An analysis of large scale wind and pressure fields would be required for verification.

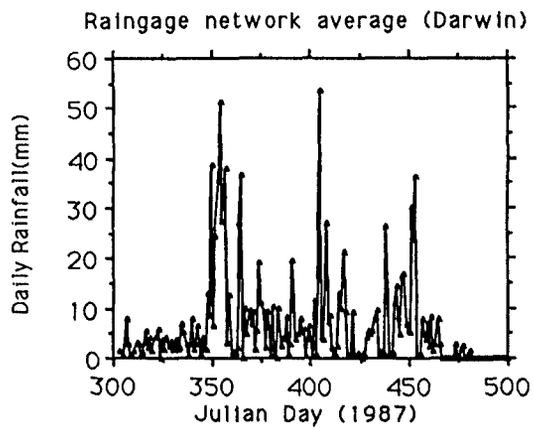

Fig. 2. Daily rainfall totals (mm) averaged over the raingage network. Julian day 1 of 1988 is given as Julian day 366 of 1987.

3.1 Pre-monsoon

In Fig. 3 the running sum of daily rainfall totals shows that the network average rainfall was accumulating at a rate of about 3 mm/day for 46 days in the pre-monsoon environment. For the purposes of further discussion it is useful to break this average rainrate down into the mean rainrate for the time that it was actually raining, [R], and the fraction of time that rain was observed, F(0). For the pre-monsoon we find [R] = 12 mm/hr, and F(0) = 1 %. Thus the "average" raingage reported about 15 minutes of rain per day (1 % of 1 day) at a mean rainrate of 12 mm/hr.

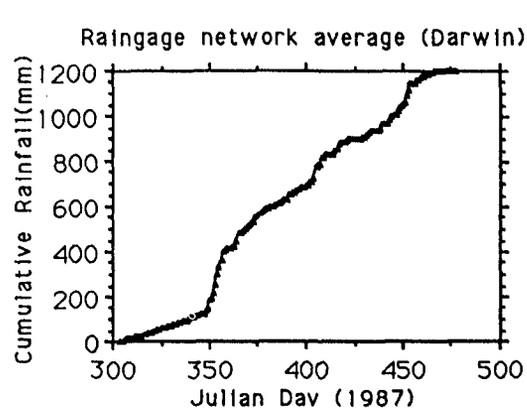

Fig. 3. Cumulative rainfall totals (mm) from Fig. 2 .

3.2 Active monsoon

Figure 3 also shows that in 8 days of active monsoon rainfall (352 - 357, and 364 - 365) the rainfall accumulation rate was 30 mm/day, ten times greater than the pre-monsoon rate. The increase is attributed to a higher F(0) of 16 % and a lower [R] of 8 mm/hr. The "average" raingage reported about 3.8 hours of rain per day at a mean rainrate of 8 mm/hr.

The tipping bucket gages recorded the time of each tip to the nearest second. One-minute rainrates were derived from these records and rainrate pdfs were tabulated as in Jones and Sims (1978). Figure 4 contrasts the normalized distributions of cumulative rain depth and number of observations versus rainrate for the pre-monsoon and active monsoon time intervals. The percentage of rainrates observed above T mm/hr is denoted by f(T). Note that f(10) was 30 % for the pre-monsoon and 20 % for the active monsoon. Rainrates below 10 mm/hr accounted for 15 % of the pre-monsoon rain depth and 30 % of the monsoon rain depth.

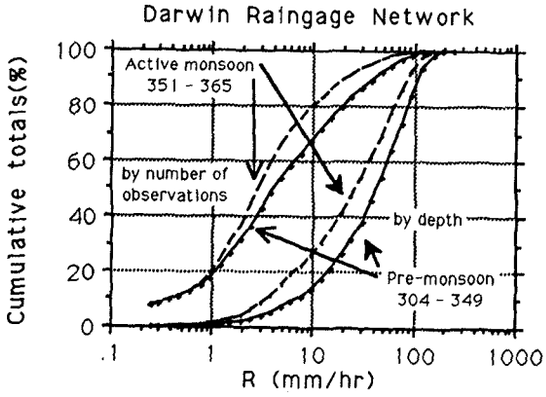

Fig. 4. Normalized distributions of the cumulative rainfall by depth and by number of observations versus rainrate for the pre-monsoon and active monsoon periods.

4. CORRELATIONS BETWEEN <R> AND F(T)

In order to examine the <R>, F(T) relation we have used the raingage network data to estimate statistics of rainrate within a space (Darwin area network) - time (one day) volume. The daily rainfall totals shown in fig. 2 were divided by 24 hr to provide a space - time averaged rainrate, <R>. Error bars on <R> are about ±30% for the pre-monsoon, and ±15% afterwards, based on covariance statistics of the daily totals and the average spacing of the gauges (Zawadski, 1973). The fraction of the space - time volume having rainrates that exceed a given threshold, F(T), was estimated by examining the gage records individually. Errors in F(T) may be difficult to determine, but are likely to be highly correlated with errors in <R>.

4.1 Pre-monsoon

Figure 5 shows F(10 mm/hr) versus <R> for the first 46 days of the record shown in fig. 2. A linear regression analysis gives a correlation and slope that are with 10% of the values found by Rosenfeld et al. (1988) for radar data from South Africa, Texas, the tropical eastern Atlantic Ocean (GATE) and a small sample at Darwin. The slope, as predicted from the rainrate pdfs (Atlas et al. (1988) and Kedem et al., 1989) is given by the following:
S(10) =100 x [R] / f(10) = 12 mm/hr / 0.3 = 40 mm/hr.

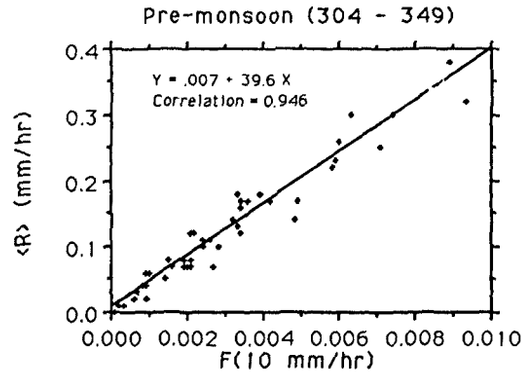

Fig. 5. Network averaged daily rainrates, <R>, versus the fraction of rainrates greater than 10 mm/hr (F(10 mm/hr)), for the pre-monsoon period (days 304 - 349). The correlation is similar for thresholds from 5 - 15 mm/hr. The slope varies systematically with threshold.

4.2 Monsoon

Figure 6 shows F(10 mm/hr) versus <R> for days 352 - 467. The slope predicted from the monsoon rainrate pdf is [R] / f(10) = 8 mm/hr / 0.2 = 40 mm/hr, again in good agreement with the regression slope. Note that the predicted pre-monsoon and monsoon slopes are identical even though the rainrate distributions are different (fig. 4). This is because the ratio [R] / f(10) is constant for the two cases. Atlas et al. (1988) present evidence for natural variations in [R] and f(T) that result in a nearly constant ratio for the correct choice of T.

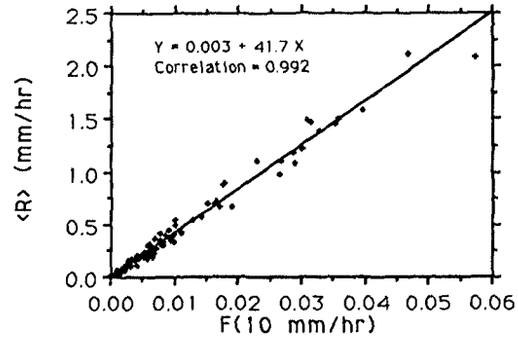

Fig. 6. As in Fig. 5 but for days 352 - 467, including the active monsoon period and the majority of the wet season. Day 350 is not included in this analysis, but would fall at X = 0.0313, Y = 1.47 mm/hr, close to the regression line.

4.3 A satellite simulation

In order to simulate the use of the <R>, F(T) relation to obtain space - time averaged rainrates from a satellite sensor the NOAA/TOGA radar observations were used to estimate F(T) using a reflectivity threshold. This procedure may be analogous to a thresholding method applied to infrared (IR) observations from a geostationary satellite, although a reflectivity contour is probably a better estimator of a rainrate threshold than an IR contour. By choosing a Z,R relation for the pre-monsoon and monsoon separately the accuracy of the simulation was improved, but we could not avoid the problems associated with Z,R variations that are known to occur naturally from day to day and within storms (Battan, 1973).

The radar scans are available at 5-minute intervals, providing a dense sampling of the space - time volume. For days 341 - 349, 1% of the reflectivities exceeded 36 dBZ in the range interval 30 - 100 km. For days 350 - 355, 16 % of the reflectivities exceeded 30 dBZ. $F(10\ mm/hr)_{radar}$ was estimated from these dBZ thresholds for each of the 15 days from 341 - 355.

Figure 7 shows <R> versus $F(10mm/hr)_{radar}$ for days 341 - 355. The slope is within 5 % of 40 mm/hr indicating that <R> could have been accurately predicted from the threshold measurements of Z with prior knowledge of S(10). An analysis of the errors in <R>, F(T), S(T) and $F(T)_{radar}$ will be reported later.

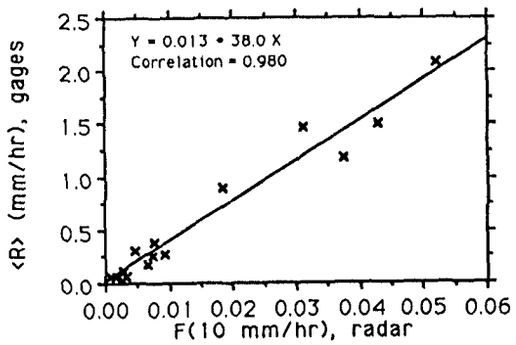

Fig. 7. <R> from the gages versus F(10 mm/hr) estimated from radar reflectivity thresholds for days 341 - 355.

5. DISCUSSION

The present study of raingage data from the Darwin, Australia network has shown that area averages of convective rainfall are highly correlated with the fraction of rainrates exceeding a preset threshold, corroborating numerous previous studies that used radar derived rainrates from Darwin and other parts of the world. These area - time integral methods have the potential for improving our ability to infer area averaged rainrates from spaceborne instruments as the methods require accurate measurements of rainrate only at a specified, moderate rainrate threshold. Radar and raingage data from several tropical sites are being collected at NASA/GSFC for TRMM definition studies. These data will be examined to determine the spatial, temporal and threshold limitations of area - time integral methods.

6. REFERENCES

Atlas, D., D. Rosenfeld and D. A. Short, 1988: The estimation of convective rainfall by area integrals. Part I: The theoretical and empirical basis. Conf. on Mesoscale Precipitation: Analysis, Simulation and Forecasting, MIT, Cambridge, MA, Sept. 13-17, 1988. (Submitted to J. Geophys. Res.)

Battan, L. J., 1973: *Radar Observation of the Atmosphere*. University of Chicago Press, Chicago and London, 324 pp.

Chiu, L.S., 1988: Rain estimation from satellites: Areal rainfall - rain area relations. 3rd Conf. on Satellite Meteorology and Oceanography, Amer. Met. Soc., Jan. 31 - Feb 4, 1988, Anaheim, CA.

Doneaud, A. A., S. I. Niscov, D. L. Priegnitz and P. L. Smith, 1984: The area-time integral as an indicator for convective rain volumes. *J. Appl. Meteor.*, **23**, 555 - 561.

Holland, G. J., 1986: Interannual variability of the Australian summer monsoon at Darwin: 1952-82. *Mon. Wea. Rev.*, **114**, 594-604.

Holland, G. J., J. L. McBride, R. K. Smith, D. Jasper and T. D. Keenan, 1986: The BMRC Australian Monsoon Experiment: AMEX. *Bull. Amer. Met .Soc.*, **67**, 1466 - 1472.

Jones, D. M. A., and A. L. Sims, 1978: Climatology of instantaneous rainfall rates, *J. Appl. Meteor.*, **17**, 1135 - 1140.

Kedem, B., Chiu, L. S., and G. R. North, 1989: Estimation of mean rainrate: Application to satellite observations.. *J. Geophys. Res.*, (to appear).

Keenan, T. D., 1988, (personal communication).

Lopez, R. E., D. Atlas, D. Rosenfeld, J. L. Thomas, D. O. Blanchard and R. L. Holle, 1989: Estimation of rainfall using the radar echo area time integral. *J. Appl. Meteor.*, (to appear).

NOAA (National Oceanic and Atmospheric Administration), *Monthly Climatic Data for the World*, November 1987 - April 1988, National Climatic Data Center, Asheville, NC.

Rosenfeld, D., D. Atlas and D. A. Short, 1988: The estimation of convective rainfall by area integrals. Part II: The height area rainfall threshold (HART) method. Conf. on Mesoscale Precipitation: Analysis, Simulation and Forecasting, MIT, Cambridge, Sept. 13-17,1988. (Submitted to J. Geophys. Res.)

Simpson, J., R. F. Adler and G. R. North, 1988: A proposed tropical rainfall measuring mission (TRMM) satellite. *Bull. Amer. Met. Soc.*, **69**, 278 - 295.

Zawadski, I. I., 1973: Errors and fluctuations of raingauge estimates of areal rainfall. *J. Hydrol.*, **18**, 243 -255.

IR SATELLITE ESTIMATIONS OF RAIN IN SAHELIAN AFRICA : STUDY OF DIFFERENT SPATIAL AND TEMPORAL RESOLUTIONS.

Isabelle JOBARD & Michel DESBOIS

Laboratoire de Météorologie Dynamique du CNRS
Ecole Polytechnique, 91128 Palaiseau Cedex, France

1. INTRODUCTION

The aim of this work is to study the influence of the spatial and temporal resolutions of the Meteosat data on the estimation of cumulated precipitations over the Sahel region. It is already well known that the estimation of rain by a simple method relating the convective cloud analyses retrieved from satellite IR data to the precipitation recorded at the surface at local scale, is not accurate below the monthly period ; so that only climatic amounts must be considered.

2. DATA SETS

Three sets of Meteosat images of the window covering West Africa for July 86 are used with different spatial and temporal resolutions : 5 km - 1/2 hour ; 5 km - 3 hours ; 30 km - 3 hours (ISCCP-B2 resolution). Moreover the ISCCP images for the whole season 86 (May to September) are considered in the study of the spatial structure of the convective cloudiness.

Cold cloud occurrence frequencies are computed from the IR images by using a temperature threshold of -40°C.

Since there are no radar measurements available in the Sahel region, the precipitation data set is made of the daily rainfall collected by rain-gauges. They are located in the six countries of the Sahel situated between 10°N and 20°N, and between 25°E and 20°W. The 425 stations of this network are not uniformely distributed : most of them (375) are gathered in Mali, Burkina-Faso and Niger.

3. CORRELATION FOR VARIOUS SATELLITE DATA RESOLUTIONS AND TIME PERIODS

A simple statistical analysis is carried out to correlate the cold cloud occurrence frequency for the pixel corresponding to a station, to the precipitation cumulated at this station. The linear correlation coefficients computed for different periods of time (day to 6 months) are given in Table 1, with the error, function of the sample size, associated to each value. It is verified that the correlation improves with increasing period of time and that it is satisfactory only for the season. (The correlations for the day period are significantly larger than the values that would be obtained if the no-rain cases were ignored).

It is noticeable that, for a given time period, the correlations obtained for different satellite data resolutions are more or less similar : the more degraded resolution leads to values which are slightly smaller than the values obtained with higher resolutions. But it is important to observe that for the month period the departures between the correlation coefficients are not significant if the errors are taken into account. Thus, the correlations are not degraded when the spatial and temporal resolution of satellite data are reduced, as far as monthly values are concerned and therefore, the ISCCP B2 resolution is suitable for the estimation of climatic rain amounts from IR imagery.

4. CORRELATION FOR DIFFERENT COUNTRIES

Several tests were carried out to assess the coherence of the precipitation data set for each country separately. It appears that for Burkina-Faso, for example, there is no correlation at all for at least 2 months. This is difficult to understand when considering the correlation obtained for the neighbouring countries (Mali, Niger). One explanation can be the poor quality of some raingauge measurements : it is well-known that there are many causes of errors, such as errors of reading, of transcription, shifting the d-day value at date d±1, etc... Actually, it is evident that the quality of the network is not homogeneous and one must be aware of the fact that the precipitation data set is not quite reliable.

5. COMPARISON OF SPATIAL STRUCTURES

The spatial structures of the fields of cumulated precipitation and cold cloud occurrence are compared on Figs. 1 for different months [July (a) and September (b) and for the Season (c)] for a set of 375 stations. They show the spatial correlation functions (called variogram) given by :

$$V(d) = \sum_{i=1}^{N_d} \left[X_i(z)-X_i(z+d)\right]^2 \Big/ 2 \sum_{i=1}^{N_d} \left[X_i(z)-\bar{X}\right]^2$$

where N_d is the number of pairs of raingauge stations separated by a distance d. Actually, these functions are computed for classes of distance of chosen width. The minimum width allowing to contain a large enough number N_d of pairs of stations was found to be at least 3 pixels (about 15 km).

Both "curves" on each figure show the same increase with increasing distance : they are roughly parallel. It indicates that the precipitation field and cold cloud field are related to the same spatial phenomenon corresponding to the climate regime ; it is characterized by a long range (greater than 250 km).

Moreover the spatial functions computed for specific directions (East-West or North-South) show also similar spatial structure at large scale, for both cold clouds and precipitation fields and present the same anisotropy : as a matter of fact, the "East-West" correlations are better.

At short scales, one must notice that the behaviour of the cold cloud curve, near the origin, is linearly and close to zero ; it indicates that the variable has a high continuity and regular variations. While the precipitation curve is characterized by a large discontinuity which means that the variable present a high variability at a scale which is shorter than the minimum distance considered (i.e. 15 km). Thus the field of monthly values of precipitation is not homogeneous at short scale contrary to the cold cloud field.

The local variability of cumulated rain is smoothed only when the number of rainy events is sufficiently large and periods of several months have to be considered, as it can be observed on Fig. 1(c). The variogram functions are plotted for the season (May to September 1986) : the discontinuity of the precipitation curve is small and probably this remaining discontinuity accounts only for the variability due to the measurement errors which are not negligible as it is said previously.

The spatial structures of the cold cloud field corresponding to the three different data sets described in Section 3, are compared on Fig. 1(d). They show the same good homogeneity for short distances, which is indicated by the similar linear behaviour of the curves near the origin. This indicates that the cold cloud field, whatever the satellite data resolution, cannot be well correlated to the precipitation field, which presents a high local variability.

The amelioration of the correlation (and as a result, of the estimation of rain in the Sahel) must come from the improvement of the precipitation field ; it is necessary to get rid of the short range variability due to point measurements by using radar data or by determining the precipitation field by a Kriging method associated to a dense network of raingauges, such as the set of gauges recently implemented in the square degree of Niamey.

6. REFERENCE

LAHUEC, J.P., GUILLOT B. (1986). Convection et pluviométrie en Afrique de l'Ouest. Bilan provisoire pour la saison 1986. Veille Climatique Satellitaire n° 15, pp. 19-23.

Table 1 Linear correlation coefficients for different time periods and satellite data resolution (* : May to October, 6 images/day ; 61 synoptic stations ; value taken from Lahuec, 1986).

r±dr	Full resolution 1/2 hour	Full resolution 3 hours	B2 resolution 3 hours	Sample size
Day	.42 ±.02	.40 ±.02	.37 ±.02	12 750
Decade	.46 ±.04	.44 ±.04	.41 ±.05	1 275
Month (July)	.60 ±.06	.60 ±.06	.56 ±.07	425
Season	-	*.89 ±.05	.82 ±.04	358

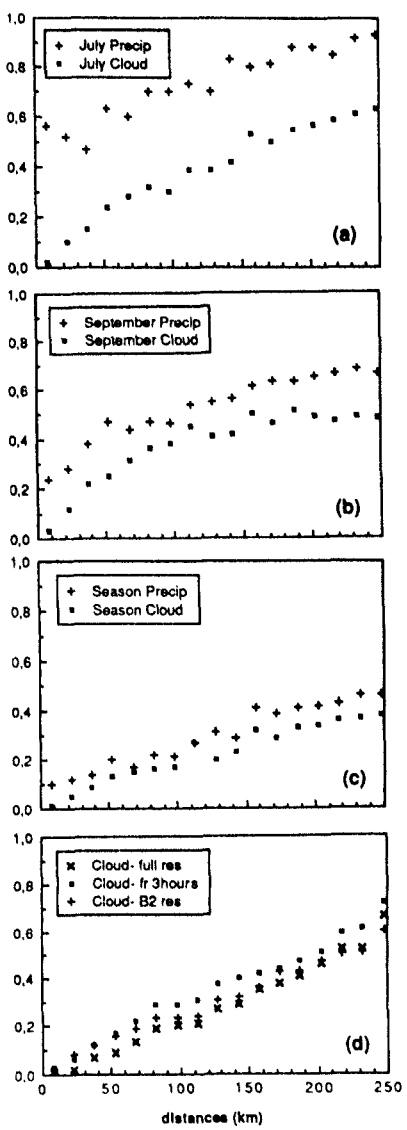

Figure 1

Variograms for cold cloud occurrence and for precipitation.

a) July 1986

b) September 1986

c) Season 86

d) July 86 : three different satellite data resolutions.

10.4

THE COLD CORE LOW ANALYSIS DURING TAMEX

Koung-Ying Liu Tian-Yow Shyu

Weather Wing, CAF
the Republic of China

1. INTRODUCTION

During the summer time, over the tropical ocean, one of the important weather system is the so-called upper level cold core low. Although the data are very limited in the related region of their sources and/or tracks, Palmen (1949) and Palmer (1953) found two (one by each other) types of these upper tropospheric phenomena. The Palmen type is a cut-off low style. He pointed out that under certain favorable circumstances the southern part of a cold trough in the upper troposphere would be broken from it and formed a low with the lowest tempreture near its center. On the other hand Palmer investigated the same phenomena in the lower latitude area and found that an upper level cold low can be born over the saddle point of an eastly trough. The Palmen type, generally, moves toward east or southeast and the Palmer one moves in an opposite way.

In this study we analyzed two cases which occured in the TAMEX (Taiwan Area Mesoscale EXpriment) period (a Sino-American field experiment which was carried out from May to June, 1987). One of the cold core lows generated over the north part of Mainland China moved toward Taiwan in a northwest to southeast direction. The other one occured in the upper tropospheric level over the East China Sea and also, moved toward Taiwan but in an opposite way. Both of them brought a large amount of rainfall in a certain area of Taiwan.

2. SATELLITE IMAGERY ANALISIS

Kelley et al (1982) and Shimamura (1981, 1982) had been investigated the upper level cold core low over the West Pacific area through satellite imagery analysis. In this study conventional rawinsonde data as well as the satellite imageries will first be used to analyze our two cases.

Fig.1 was the GMS-3 satellite maps from 3 to 5 June, 1987. It was very obvious that a cloud system was formed on the Northern China, moved southeastward, and dissipated as it passed over the sea near Taiwan.

Fig.2 showed the same materials as Fig.1. But for case 2. the upper level cold core low was organized on 6th of June, then, from its source region, moved very slowly northwestward. Finally, it merged with the cold front near Taiwan on 7th of June.

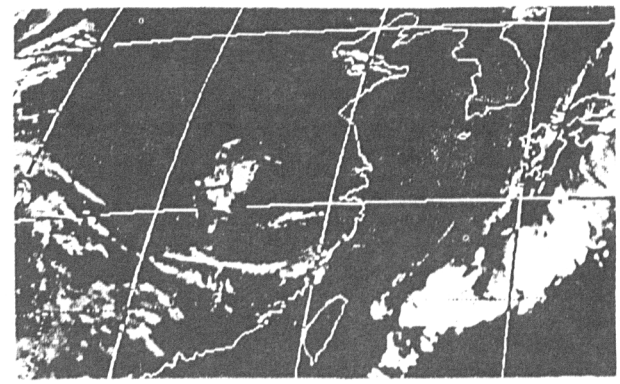

Fig. 1.a 0000UTC 3 June 1987

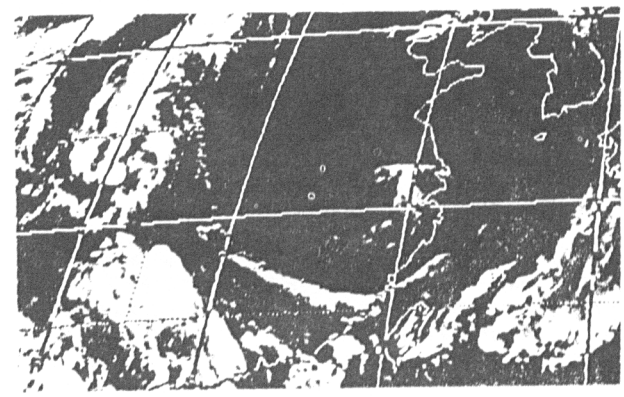

Fig. 1.b 1200UTC 3 June 1987

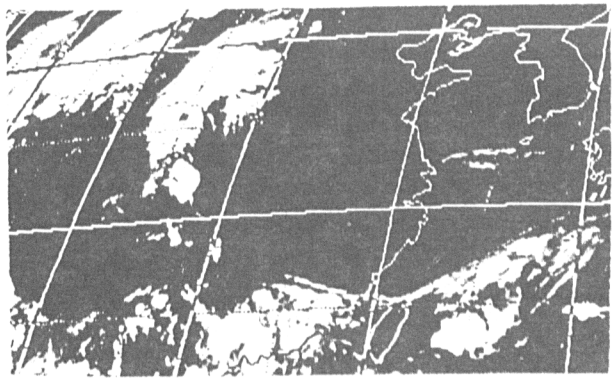

Fig. 1.c 0000UTC 4 June 1987

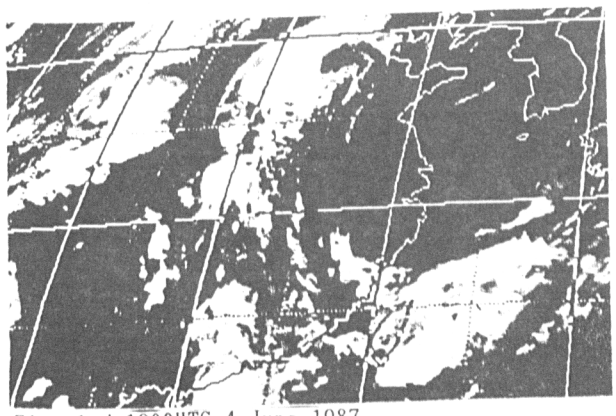

Fig. 1.d 1200UTC 4 June 1987

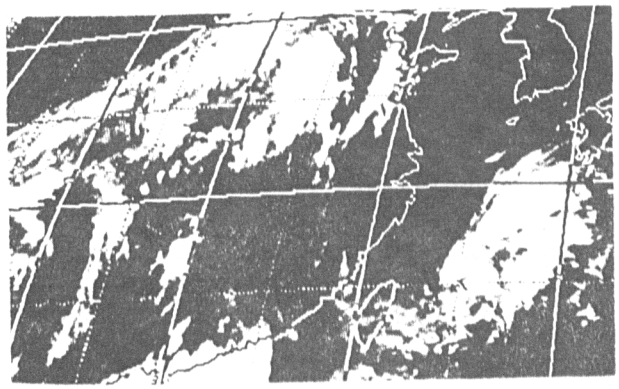

Fig. 1.e 0000UTC 5 June 1987

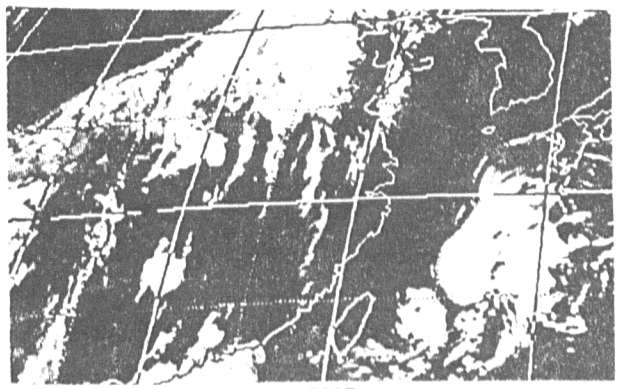

Fig. 1.f 0300UTC 5 June 1987

Fig.1 The sattelite image from 3 to 5 June 1987.

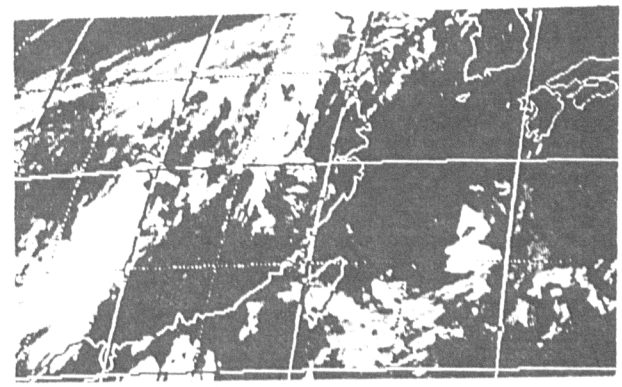

Fig. 2.a 0000UTC 6 June 1987

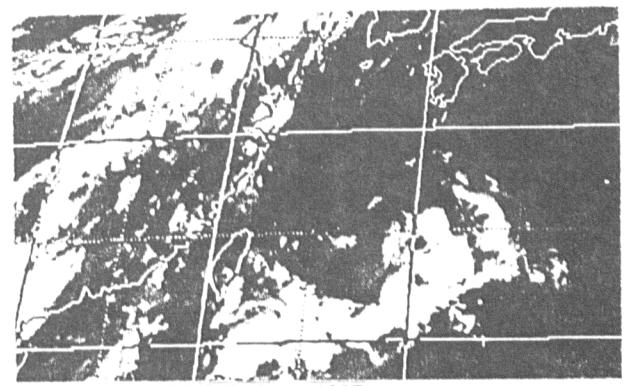

Fig. 2.b 1200UTC 6 June 1987

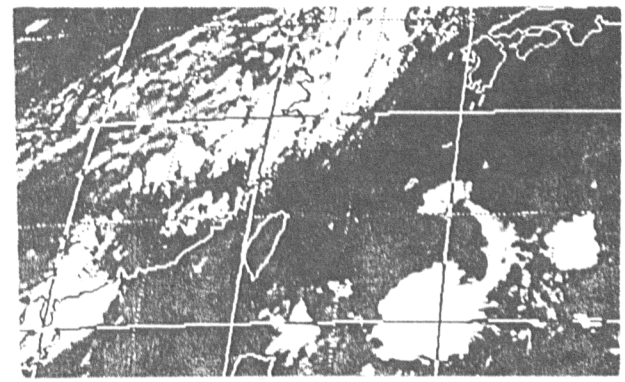

Fig. 2.c 0000UTC 7 June 1987

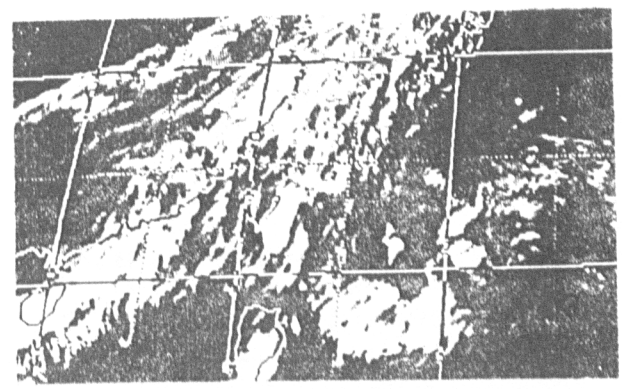

Fig. 2.d 1200UTC 7 June 1987

Fig.2 The sattelite image from 6 to 7 June 1987.

3. CONVENTIONAL DATA ANALYSIS

By using the conventional rawinsonde data the temperature as well as the wind fields of the two systems were analyzed. The tracks of those low centers were also constructed by connect their centers day by day. Fig.3 to Fig.4 and Fig.5 to Fig.6 show our results for case one and two, respectively.

Tables 1 and 2 show the rainfall amount of several stations in Taiwan during the related periods of our two cases. From rainfall amount and/or its distribution we find that the rainfall amounts of those stations in the east side of the Central Mountain Range (leeward side of cold front) are very large. In Hwalien station the rainfall amount within 9 hrs is 138.9 mm. This gives the indication that the upper level cold core system may be an important factor which enhances the precipitation.

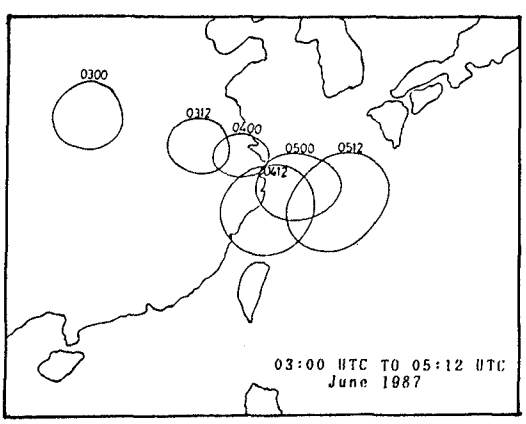

Fig.3 The cold core low teacks (500 Hpa) of wind field analysis from 3 to 5 June 1987.

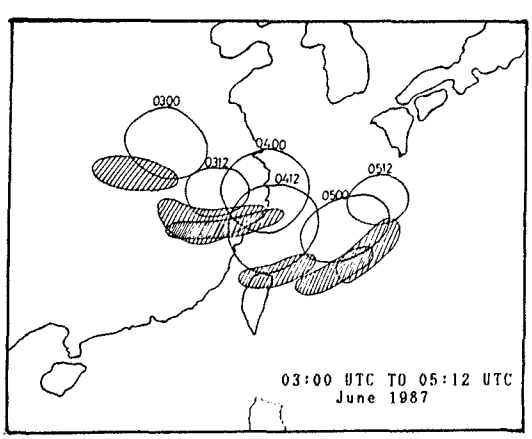

Fig.4 The cold core low tracks (500 Hpa) of temperature field analysis from 3 to 5 June 1987. The maximum wind part of cold core low was hatched during its period.

4. WEATHER CONDITIONS

Table 3 and 4 show the time periods of precipitation and thunderstorm of several related stations in Taiwan. There were thunderstorms in all those stations. This kind of weather condition is consistent with previous studies(Wu, 1976).

5. CONCLUSION AND REMARKS

According to the foregoing analysis we know that both the two cold core lows did not pass over Taiwan directly, but they influence the weather condition in that area. The major contribution arises from the cold core lows triggers and/or enhances the upward motion in certain related area. In the Mei-Yu (plume rain) seasons of Taiwan many similar cases may be there. Therefore further investigation will be carried out in the near future.

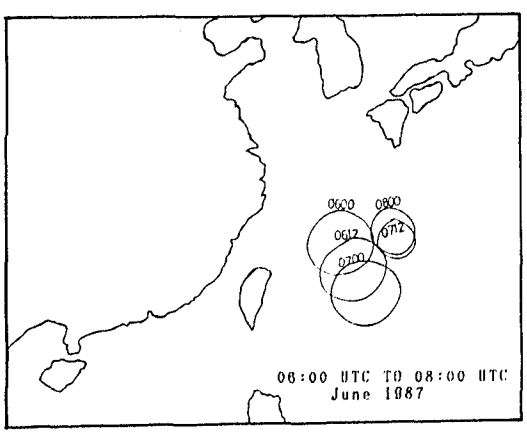

Fig.5 The cold core low tracks (300 Hpa) of geopotential field analysis from 6 to 8 June 1987.

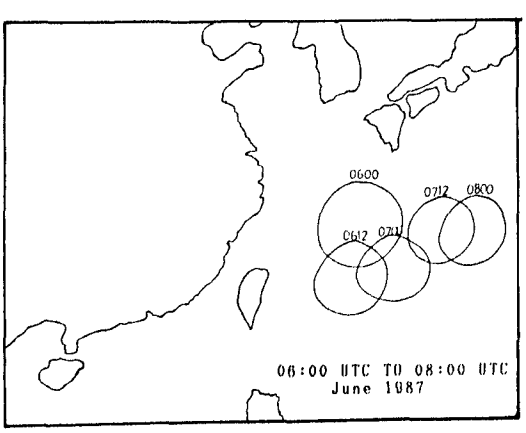

Fig.6 The cold core low tracks (300 Hpa) of wind field analysis from 6 to 8 June 1987.

Table 1. The rainfall and thunderstorm time (LST) of June 4.

Period (LST) / Station / Category	Shunshan	Taoyuan	Ilan	Hwalien	Tainan	Kangshan	Pingtung	Hengchung	Taitung
Rain	14 to 15		16 to 20	17		19	23 to 24		18 to 20
Thunderstorm	16	16 to 17	13 to 16	14 to 16 18 to 23	19 to 23	20 to 24	18 to 22	12 to 16 24 to 20	16 to 17 21 to 22

Table 2. The rainfall and thunderstorm time (LST) of June 7.

Period (LST) / Station / Category	Shunshan	Ilan	Hwalien	Taichung	Chiayi	Kangshan	Pingtung	Taitung
Rain	13 16 to 18	18 to 19	15 19 to 21	14		15 to 16	17 to 20	12 to 15
Thunderstorm	14 to 15	15 to 17	17	21	14	15 to 16 18 to 19		16 to 19

Table 3: The stations of major large precipitation from 4 to 5 June 1987.

Station	Hwalien	Taitung	Taipei	Nitou	Yonagunijima	Ishigakijima	Miyakojima
Date (June)	4	4	4	4	5	5	4
Precipitation (m,m)	138.9	59	34	84	22	30	32

Table 4: The stations of major large precipitation from 6 to 7 June 1987.

Station	Naha	Keelung	Taipei	Hwalien	Tachienshun	Sun-moon Lake
Date (June)	6	7	7	7	7	7
Precipitation (m,m)	55.5	59	31	94	52	32

ACKNOWLEGEMENT :

The work was partly supported by the National Science Concile of the Republic of China under the grant NSC77-0414-P072-03B. Thanks are also due those who interesting in the paper.

REFERENCES

Kelley, W. E., and D. R. Mock, 1982: A diagnostic study of upper tropospheric cold lows over the Western North Pacific. Mon. Wea. Rev., 110, 471-480.

Palmen, E., 1949: Origin and structure of high-level cyclones south of the maxinum westerlies. Tellus, 1, 22-31.

Palmer, C. E., 1953: The impulsive generation of certain changes in the tropospheric circulation. J. Meteor., 10, 1-9.

Shimamura, Masaru, 1981: The upper-tropospheric cold lows in the northwestern Pacific as revealed in the GMS satellite data. Geophy. Mag., 39, 119-156.

Shimamura, Masaru, 1982: An application of GMS satellite data in analysis of the upper cold low in the western north Pacific. Geophys. Mag., 40, 113-152.

Wu, T. Y., 1976:An observational study of the cold core low in the upper troposphere in Far East in summer. Atmospheric Sciences, Vol. 3, 1-11.(in chinese)

10.5

ESTIMATING TROPICAL RAINFALL FROM MULTIPLE SOURCES OF INFORMATION

Phillip A. Arkin
John E. Janowiak

Climate Analysis Center, NMC/NWS/NOAA
Washington, DC 20233

1. INTRODUCTION

Estimation of tropical rainfall on climatic space and time scales has been attempted frequently over the past 20 years, often with significant apparent success. Qualitative estimates based on polar orbiting satellite data (Garcia, 1981; Lau and Chan, 1983) have been used in climate studies, while a great variety of estimates with superior diurnal resolution have been derived from geostationary satellite data (see Arkin and Ardanuy, 1989, for references). Passive microwave observations from both the Nimbus-7 SMMR and the DMSP SSM/I instruments have also served as the basis for estimates of oceanic precipitation (Prabhakara et al., 1986; Spencer et al., 1989). The distinguishing characteristic of the vast majority of such work has been the reliance on a single source of data in the production of the estimates. In this paper, we have two objectives. We will begin with the description of an effort to produce analyses of monthly global precipitation using several sources of satellite and conventional data. We will then propose a method through which a wide variety of information regarding precipitation distribution and intensity might be used to generate an optimum analysis of the temporal and spatial distribution of large-scale precipitation.

2. THE GLOBAL PRECIPITATION CLIMATOLOGY PROJECT

2.1 Background

The need for analyses of large-scale areally averaged precipitation for periods of 5 days to monthly covering at least the tropics to satisfy the requirements of the World Climate Research Programme (WCRP) became clear in early 1985 as the Tropical Ocean-Global Atmosphere (TOGA) Programme was beginning. A Workshop on Global Large-Scale Precipitation Data Sets for the WCRP was held in Camp Springs, MD, USA in July 1985. It recommended (WCRP, 1986) that a Global Precipitation Climatology Project (GPCP) be instituted to use available algorithms and data to produce these analyses. Its objectives include:

a. the production of estimates of tropical precipitation for areas of 2.5^{0} latitude x 2.5^{0} longitude for periods of 5 days using geostationary satellite data;

b. the derivation of rainfall estimates for similar spatial scales and for months from passive microwave radiometric data;

c. the use of these data together with conventional rainfall data to produce analyses of monthly rainfall on a near-global scale; and

d. the development of a capability to validate and calibrate the various satellite estimates.

2.2 Organization

The GPCP is organized into several centers. The production of rainfall estimates from geostationary data requires the routine production of statistics, including histograms, means and spatial variances, of IR brightness temperatures for 5-day periods from each of the available satellites. This activity is carried out at Geostationary Satellite Data Processing Centres (GSDPCs) for Meteosat, GMS, GOES and INSAT. The integration of these data into rainfall estimates for the global tropics is performed by the Geostationary Satellite Precipitation Data Centre (GSPDC). Data from the SSM/I (Special Sensor Microwave/Imager) instrument on the U.S. Defense Meteorological Satellite Program polar orbiting satellite is processed at the Polar Satellite Data Processing Centre (PSDPC) and sent to the Polar Satellite Precipitation Data Centre (PSPDC), where it is used to obtain estimates of monthly oceanic precipitation. Both of the Precipitation Data Centres use calibration and validation information provided by the Surface Reference Data Centre (SRDC), where developmental work on new methods of measuring rainfall over the oceans is also coordinated. The Global Precipitation Climatology Centre (GPCC) receives the various satellite estimates and, by combining them with conventional rainfall measurements, produces monthly analyses of near-global rainfall.

2.3 Current Status

a. Geostationary Component

The GSDPCs for each of the geostationary satellites are currently producing the statistics required by the GPCP, and, with the exception of that for INSAT, are regularly delivering data. Figure 1 shows the status of geostationary data for the GPCP as of January 1989. The GSDPC for GOES is co-located with the GSPDC and has been producing data routinely for both satellites

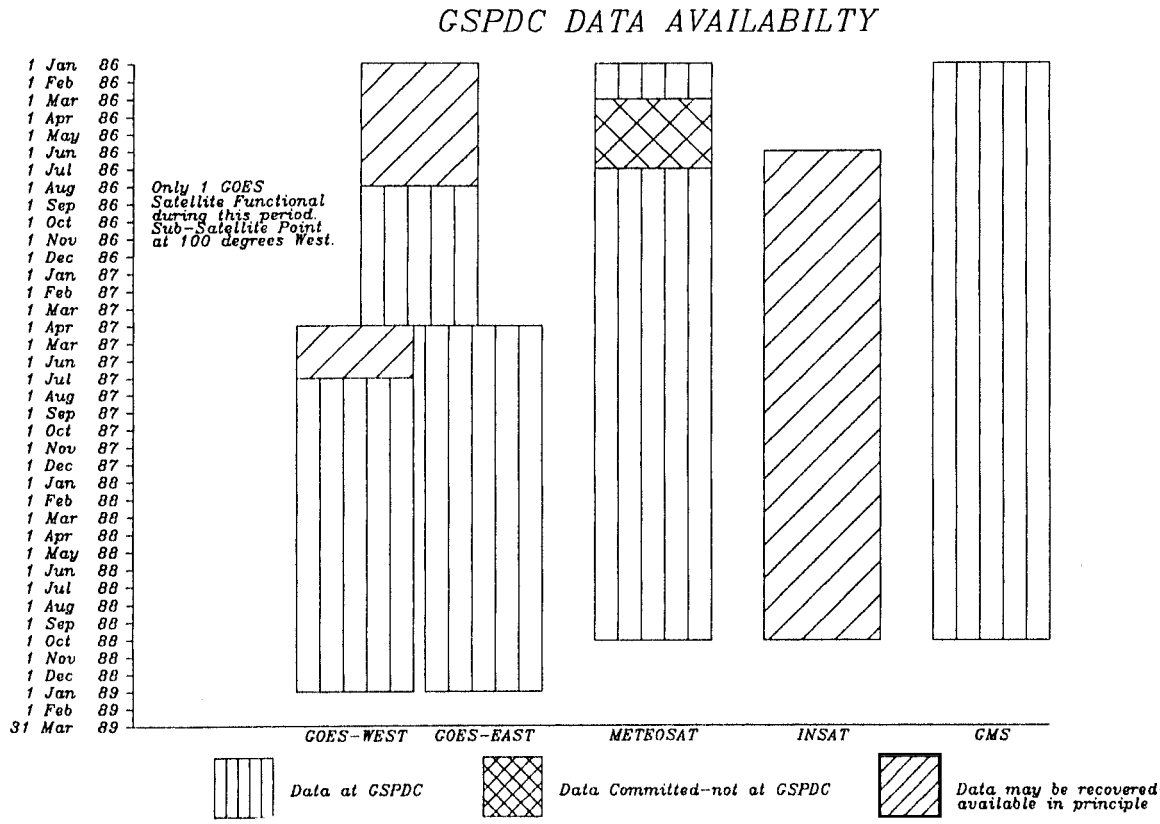

Figure 1. Availability of geostationary satellite data at the Geostationary Satellite Precipitation Data Center as of October 1988.

since July 1987. The GSDPCs for Meteosat and GMS, operated by the European Space Agency under contract from Eumetsat and by the Japan Meteorological Agency (JMA), respectively, have been delivering data since late 1987. JMA has completed post-processing and delivery of older data as well, while retrospective processing of Meteosat data is complete, except for part of 1986. India has not yet agreed to participate in the GPCP. However, the functional duties of an INSAT GSDPC have been carried out since June 1, 1986, by the India Meteorological Department as a result of a collaborative effort under a joint Indo-U.S. research program.

The GSPDC has been staffed and has begun processing data. A microcomputer workstation has been obtained to make the development of merging and quality control algorithms feasible, and preliminary results have been obtained for all pentads from November 1987 through June 1988. Rainfall estimates are computed from each satellite for each 5-day period and then merged into an analysis covering the global tropics. Various merging algorithms are being tested, and the experience gained by the Global Processing Center of the International Satellite Cloud Climatology Project is being utilized. In an attempt to avoid gaps due to the lack of geostationary data from one or more satellites, the use of estimates based on histograms of outgoing longwave radiation derived from IR window channel observations on the NOAA polar orbiting satellites is being tested. Figure 2 shows an example of estimated tropical rainfall for a 30-day period during June 1988 in which data from GOES West, GOES East, Meteosat, GMS, NOAA-9 and NOAA-10 were used.

b. Polar Orbiting Component

Estimates of rainfall based on passive microwave observations from the SSM/I (Special Sensor Microwave/Imager) instrument on a polar orbiting satellite of the Defense Meteorological Satellite Program offer considerable potential for supplementing and improving the geostationary estimates. The satellite was launched on June 19, 1987, and data began to be produced near the end of that month. No formal commitments for either the PSDPC or the PSPDC have been received, although initial data processing as well as development and testing of estimation algorithms, is under way.

SSM/I data will be archived at NOAA/NESDIS, and the possibility that the Satellite Data Services Division of NESDIS could provide the PSDPC is being explored. In the interim, data for a period of up to one year from launch are being supplied by a NASA/NESDIS contractor to a group headed by T. Wilheit at NASA/Goddard Space Flight Center. This group has agreed to provide the PSPDC if a satisfactory arrangement for supply of the data can be made. They have presently received data for about 9 months and have applied the preliminary estimation algorithm to data for August 1987. This algorithm, which uses 18 GHz data and a physically-based model of the absorption due to raindrops, appears to yield good results over the tropical oceans, but systematically overestimates

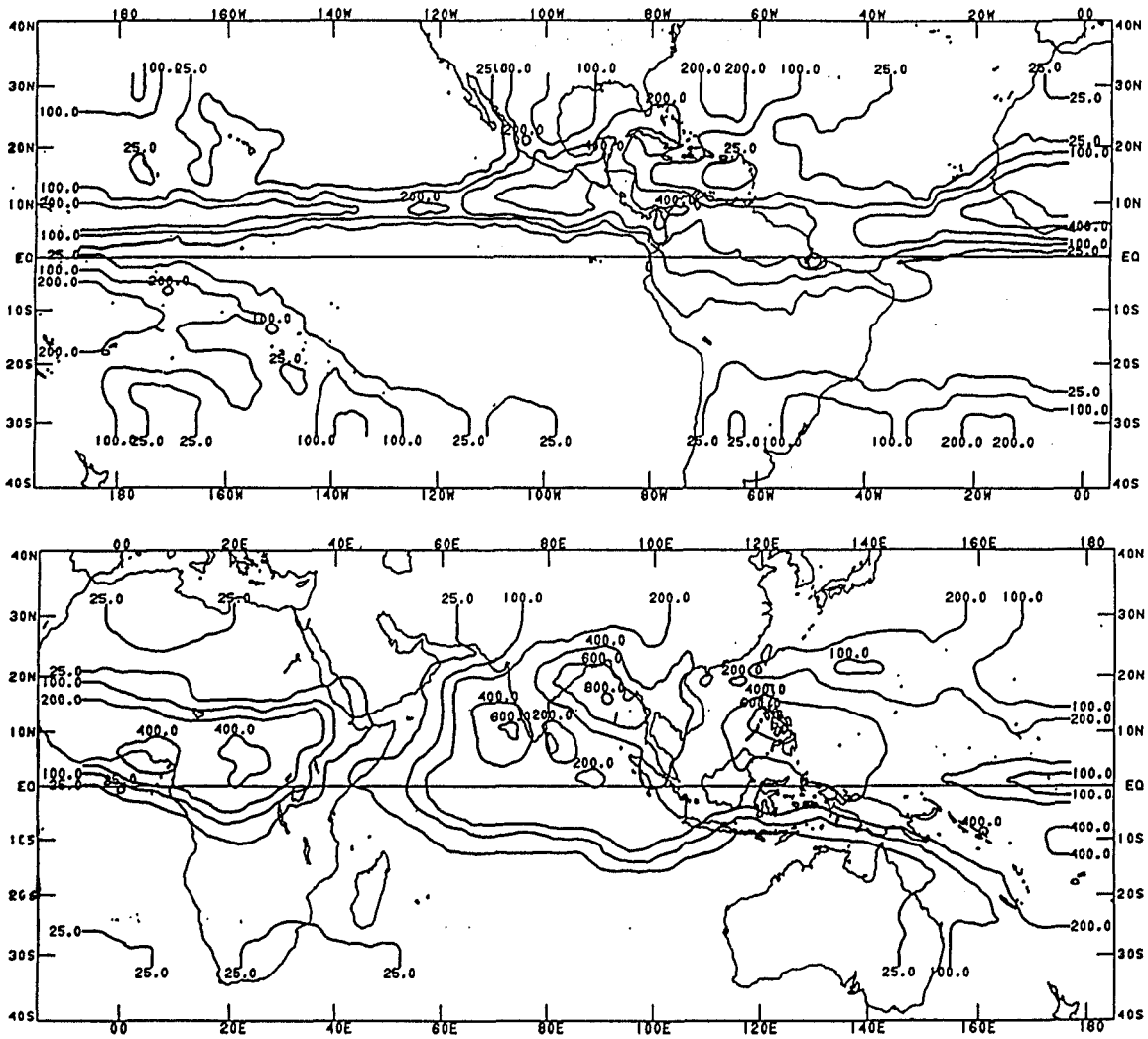

Figure 2. Merged IR-based estimates for May 31-June 29, 1988, using data from GOES-E, GOES-W, GMS, Meteosat, NOAA-9 and NOAA-10. Contours at 200 mm intervals beginning from 200 mm and at 25 and 100 mm.

rainfall in higher latitudes. Another algorithm, based on scattering due to ice at 86 GHz, is being developed by R. Spencer of NASA/Marshall Space Flight Center.

c. Calibration and Validation

The use of indirect estimates of rainfall (such as those based on observations of clouds or ice particles) requires calibration and validation in order to be usable with confidence. The Calibration/Validation (Cal/Val) Program of the GPCP consists of two principle efforts: the aquisition and organization of surface observations of rainfall from areas representing different climatic regimes; and the sponsorship and coordination of efforts to develop new methods of observing rainfall over the oceans.

A Workshop of the Validation of Satellite-Based Precipitation Estimates for the GPCP (WCRP, 1988) was held in November 1986. One of its principal recommendations was that a Surface Reference Data Center (SRDC) be established to coordinate this effort. The National Climatic Data Center of NOAA/NESDIS has expressed interest in providing the SRDC, and initial development is under way. Figure 3 shows the distribution of primary and secondary sites from which calibration/validation might be obtained. Current efforts to acquire and format these data have begun.

The Cal/Val Project has arranged for an experiment in the application of new rainfall measurement techniques to oceanic rainfall to be conducted during the June-September 1989 period. A subsurface acoustic sensor and an optical rain gage are to be mounted on a buoy in the Atlantic Ocean near Kennedy Space Center (KSC) and within range of the KSC rain-measuring radar. If usable rainfall measurements can be obtained, the possiblity of mounting such instruments on buoys in the tropical Pacific will be explored.

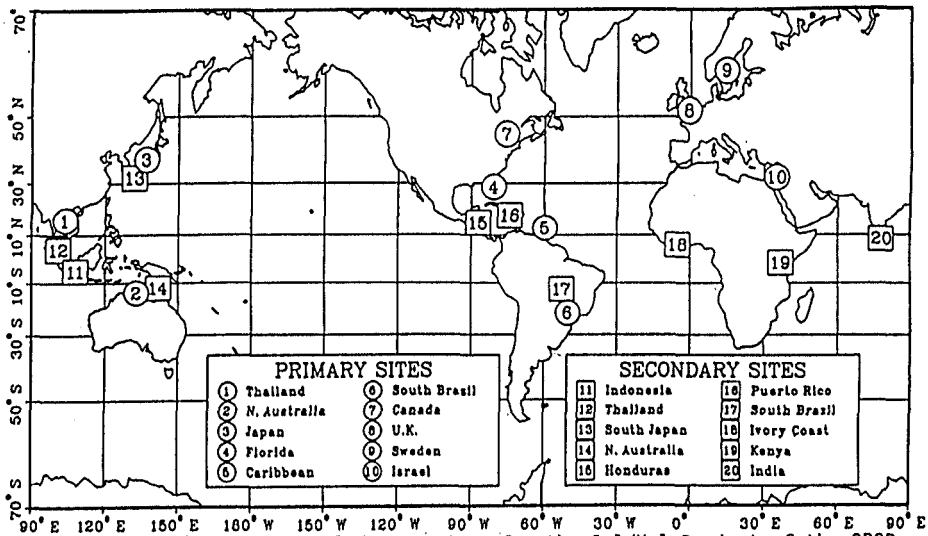

Figure 3. Primary and secondary validation sites for the Cal/Val Project of the GPCP. Primary sites are those where a precipitation radar is or could be available along with a dense network of rain gages; secondary sites are those for which only gage data will be available.

3. FUTURE DIRECTIONS

A critical component of the GPCP not mentioned above is the Global Precipitation Climatology Center (GPCC). The Federal Republic of Germany has offered to provide the GPCC, and it began operations on October 1, 1988. Its principal task is the integration of the satellite-based estimates with station observations of rainfall into global analyses of monthly precipitation over the globe. In the early stages, this operation will be carried out in quite a simple manner, by using satellite data only where surface data are unavailable. In the long run, however, the GPCC will require a method of optimally merging all the observations.

This is the most critical research task facing the GPCP, and one which will be critical to the future of such WCRP programs as GEWEX. The development of methods of analyzing rainfall which can make optimal use of multiple sources of information, such as station observations, radars, various satellite estimates, circulation data and model forecasts of precipitation is clearly a challenging task. However, all of these data contain (or at least will in the future contain) information on the distribution and intensity of large-scale rainfall.

One can see in this problem an analogy to the solution achieved by numerical weather prediction centers to the problem of generating optimal initial conditions for their models given a wide variety of data sources. The global data assimilation systems which have evolved are not perfect, but they do succeed to a remarkable extent. In the case of precipitation, one can envision the use of a model forecast of precipitation as a first guess, with corrections generated from estimates and observations of rainfall obtained both from satellite and surface observations. One fundamental difficulty with this approach is that the first guess must have sufficient skill to contribute to the analysis. In our oral presentation, we hope to present some results of comparisons between satellite derived rainfall estimates and precipitation forecasts from NMC and/or ECMWF.

4. REFERENCES

Arkin, P. A., and P. E. Ardanuy, 1989: Estimating climatic-scale precipitation from space: A review. J. Clim., 2, (in press).

Garcia, O., 1981: A comparison of two satellite rainfall estimates for GATE. J. Appl. Meteor., 20, 430-438.

Lau, K. M., and P. H. Chan, 1983: Short-term climate variability and atmospheric teleconnections from satellite-observed outgoing longwave radiation. Part 1: Simultaneous relationships, J. Atmos. Sci., 40, 2735-2750.

Prabhakara, C., D. A. Short, W. Wiscombe, R. S. Fraser, and B. E. Vollmer, 1986: Rainfall over oceans inferred from Nimbus 7 SMMR: application to 1982-83 El Niño, J. of Climate and Appl. Meteor., 25, 1464-1474.

Spencer, R. W., H. M. Goodman, and R. E. Hood, 1989: Precipitation retrieval over land and ocean with the SSM/I: Identification and characteristics of the scattering signal. J. of Atmos. and Ocean. Tech., (in press).

World Climate Research Programme, 1986: Global Large-Scale Precipitation Data Sets for the WCRP. Report of the workshop held July 24-26, 1985, Camp Springs, MD, USA, WCP-111, WMO/TD - No. 94, 50 pp.

World Climate Research Programme, 1988: Validation of Satellite-Derived Precipitation Estimates for the Global Precipitation Climatology Project of the WCRP. Report of the workshop held November 17-20, 1987, Washington, DC, USA, (in press).

JP8A.1

COMPARISON OF SSM/I RAINRATES AND SURFACE WINDS WITH THE CORRESPONDING CONVENTIONAL DATA IN THE *NORTH WEST PACIFIC TYPHOONS*

G. V. Rao, E. J. Ciardi, and D. K. Rhudy

St. Louis University

St. Louis, Missouri

1. INTRODUCTION

Microwave radiation would reveal the surface characteristics faithfully because the radiation emanating from the surface does not suffer much attenuation from absorption from any gas in the atmosphere. In several comprehensive review articles (e.g., Rao, 1984) the advantage of microwave radiometry in the measurement of rainfall over the oceans has been documented. Bunting and Hardy (1984) discussed how the brightness temperature of the earth's surface depends on surface type and condition. For example the ocean emissivity depends on wind speed and land emissivity on the soil temperature. They further commented how the Special Sensor Microwave Imager (SSM/I) aboard the DMSP satellite would remotely sense the surface wind speed and rainrates over the vast expanse of the oceans.

The SSM/I launched in June 1987 has vertical and *horizontal polarization detection capability.* The chief objective of this imagery was to provide surface wind and precipitation patterns over the oceans.

The primary objective of this study is to compare the microwave derived precipitation and surface wind fields pertaining to some typhoons with radar derived precipitation and conventional wind fields of the corresponding typhoons. The demonstration that the SSM/I data are reasonably accurate encourages the employment of the data for the prediction of typhoon intensity and track speed.

2. SOME CHIEF CHARACTERISTICS OF SSM/I

Hollinger et al (1987) discussed the SSM/I's footprint geometry. The SSM/I is a seven channel four frequency linearly polarized passive microwave radiometric system. It appears that 35-40 km is the scale of a resolution of the wind and precipitation fields of the SSM/I. The 85 GHz channel registers on a finer scale (15 km) but the registered data are available only in terms of brightness temperatures and not (customarily) in terms of precipitation rate or wind speed. The scale of resolution is important to remember when a comparison of the radar rainrate and the satellite rainrates is made.

3. RADAR RAINRATES

Most investigators of radar rainrates consider an empirically derived relationship of the form

$$Z = A R^{b} \qquad (1)$$

relating the reflectivity factor Z to the rainrate R. A well known relationship called the Marshall-Palmer (see Rogers, 1976) is written as

$$Z = 200 R^{1.6} \qquad (2)$$

Recently Jorgensen and Willis (1982) established a Z-R relationship

$$Z = 300 R^{1.35} \qquad (3)$$

based on aircraft data from four flights into three storms at three levels. This Z-R relationship was shown to be good both for convective and stratiform rain regions. Jorgensen and Willis reviewed various Z-R relationships and found the MP relationship (Eq. 2) to yield higher rainrates in the lower Z's than what JW (Eq. 3) would give. In the following study the spatial distribution of rainrates is displayed using the JW formulation. While developing correlation coefficients and regression estimates both formulations are used.

4. COMPARISON OF THE SSM/I AND RADAR RAINRATES

The precipitation associated with mature typhoons *as inferred by the SSM/I is compared with the radar* derived precipitation. The radar is stationed in Kaohsiung, Republic of China. The important specifications of this radar are: Wavelength, 11.1 cm; Frequency 2900 MHz; and beam width, 2.25 degrees.

For the comparison of the rainrates typhoon Lynn was chosen. This typhoon traveled slowly about 300 km south of Taiwan on October 24, 25 and 26, 1987, experienced some decay and was under the surveillance of the Kaohsiung radar.

Fig. 1 shows the SSM/I rainrates for 1035 UTC 25 October. Most of the rain is concentrated in bands east and south east of the storm center. The 8 mm h^{-1} isopleth covers an elliptical area of 50 km (major

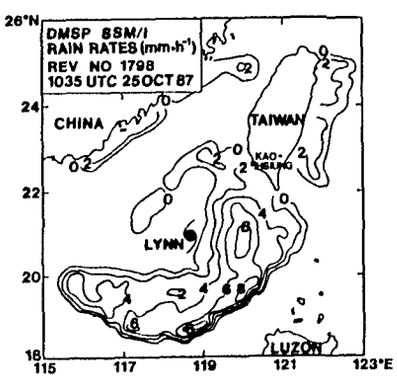

Fig. 1. The SSM/I rainrates (mm h^{-1}) for 1035 UTC 25 October 1987. Notice the extreme rainrates in south east of the typhoon center.

axis) and 15 km (minor axis). Gradients of precipitation are packed south east of Lynn.

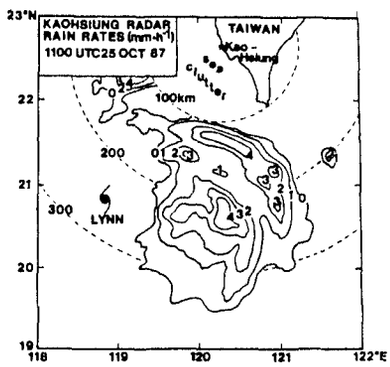

Fig. 2. Rainrates derived under the Jorgensen and Willis (1982) formulation from the reflectivity values of the Kaohsiung radar. Note the superior resolution of the rainbands.

Fig. 2 shows the radar precipitation for 1100 UTC 25 October. A circular area of radius 100 km with Kaohsiung as center is blocked. This was interpreted as sea clutter. Three prominent rainbands are noticed. It is noteworthy that the SSM/I rainrates (e.g., 8 mm h^{-1}) are north-south oriented while the radar rainrates have a southeast northwest orientation. Unlike the twin maxima in Fig. 2 only one maximum near 21 N and 120 E is shown by the SSM/I. On the other hand, the other two maxima facing Luzon in SSM/I are not captured by radar. This lack of agreement between the two figures is likely due to the differences in time and space scales of measurement. Similar figures for other maptimes are not shown.

Fig. 3 shows the linear regression line between the SSM/I and radar rainrates for the composite of three maptimes. From the regression it is found that when the radar is showing a rainrate of 2 mm h^{-1} the SSM/I is producing 3.6 mm h^{-1}. As the radar rate goes up this overestimate decreases. With the MP formulation the correlation improved slightly (not shown).

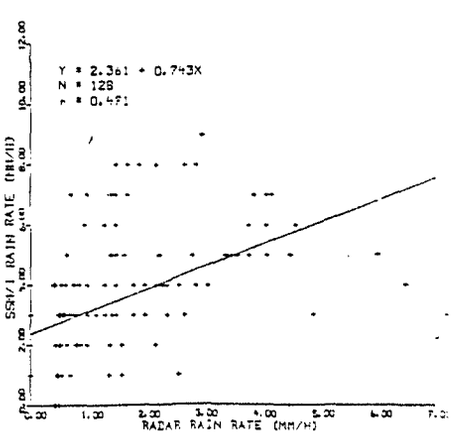

Fig. 3. Regression equation and correlation coefficient (r = 0.49) between the SSM/I rainrates and radar rainrates under the JW formulation.

5. COMPARISON OF THE SSM/I AND CONVENTIONAL WINDS

Fig. 4 shows the surface winds as inferred by the SSM/I for 2200 UTC 24 October 1987. An envelope of 30 m s^{-1} surrounds the typhoon center. In general strong winds (15 m s^{-1}) are observed over the map. Fig. 5 shows the surface winds as observed by ships (+ or - 3h of SSM/I time) and some islands. The island and coastal winds are converted to the equivalent winds over the sea following Hsu (1986). A fair comparison is seen between these two figures. Winds north east of Taiwan are shown in Fig. 4 stronger than what the surface truth was indicating (Fig. 5).

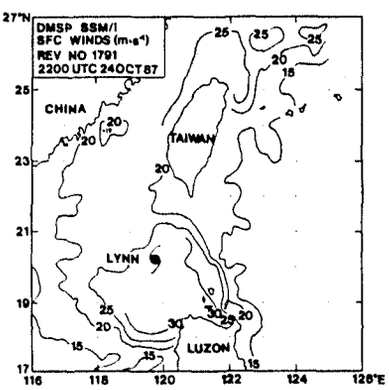

Fig. 4. The SSM/I winds. Note the 30 m s^{-1} envelope surrounding the center.

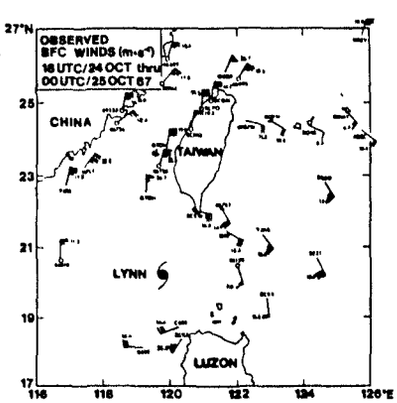

Fig. 5. Sea level winds + or - 3h centered on 2200 UTC (SSM/I time) 24 October 1987.

Fig. 6 shows the correlation coefficient and linear regression estimates between the SSM/I winds and all winds. Since satellite winds are representative of an area of 850 sq. km the conventional wind in such an area closest to the subtrack point is selected and compared. A good correlation of 0.75 resulted. From Fig. 6 it is clear that the SSM/I overestimated winds in the lower range up to 15 m s^{-1} and underestimated above 22 m s^{-1}. These results are similar to those of Black et al. (1986). Similar findings was also made by Holliday and Waters (1988).

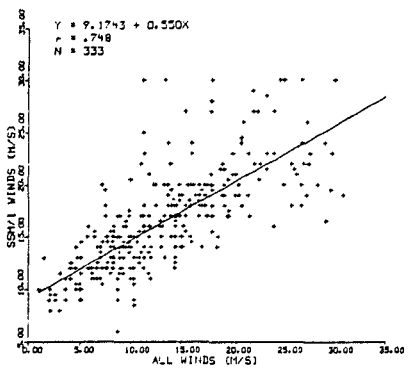

Fig. 6. A linear regression analysis of the SSM/I and all winds (ship, coastal, island and reconnaissance).

6. WIND FIELD COMPARISON WITH AN ENLARGED SAMPLE AND WITH REVISED COEFFICIENTS

In the following data from more maptimes (satellite passes over several typhoons) are assembled. A set of revised regression coefficients were employed to rederive the SSM/I winds and rainrates.

The resulting wind fields, were analyzed for a total of 11 SSM/I passes over tropical storms in the North West Pacific under various spatial and temporal criteria. The results are shown in the Table below.

Because of the inherent problem in comparing the SSM/I data to an in situ wind measurement, a stricter temporal criteria of 1 hour was applied in column B which showed improved results for the nonlinear (semi-log) fit. Because most of the data occurred at wind speeds of less than 17 m s^{-1}, it is not appropriate to draw any hard conclusions for wind speeds greater than this value.

One problem in using the SSM/I wind data is the accurate measurement of wind speeds in the presence of rainfall. This problem is due to impaction of rain drops on the surface of the ocean, which will increase the roughness of the surface, therefore, increasing the surface emissivity and measured brightness temperatures. Olson (1987) suggested that although this may have a significant impact, in tropical storms the formation of foam by the high winds, and its associated increase in emissivity, will predominate. This seems to hold true in the evaluation of the SSM/I data when precipitation was present (210 cases). The results in columns C and D showed a very large overestimation at low speeds (0-10 m s^{-1}) due to the effect of the raindrops impacting the ocean surface. But as the wind speeds increased, the effect of the precipitation impacting the ocean surface was secondary to the roughness caused by the wind. Above 14 m s^{-1} both the linear and semi-log fits showed a 3-5 m s^{-1} low bias.

WIND SPEED	COL A		COL B		COL C		COL D	
(M/S)	LIN	NLIN	LIN	NLIN	LIN	NLIN	LIN	NLIN
4	6.98	6.63	7.93	6.90	13.74	13.20	14.73	14.04
8	8.99	8.11	9.48	8.61	15.79	14.56	16.63	15.35
12	11.01	9.91	11.04	11.01	17.85	16.06	18.54	16.78
16	13.02	12.12	12.59	13.41	19.91	17.71	20.45	18.35
20	15.03	14.81	14.15	16.74	21.97	19.53	22.36	20.06
24	17.04	18.10	15.70	20.89	24.02	21.54	24.27	21.93
28	19.05	22.13	17.25	26.07	26.08	23.76	26.18	23.98
32	21.07	27.05	18.81	32.54	28.13	26.21	28.09	26.21

The formats for the curves are:

Linear: Y=A + Bx

Nonlinear: Y=aexp(bx)

Column

A: SSM/I winds within ±3 hours and ±30 Nm. (n=799)
A= 4.9675 B= 0.5032 r= 0.6248
a= 5.4265 b= 0.0502 r= 0.5721

B: SSM/I winds within ±1 hour and ±30 Nm. (n=258)
A= 6.3740 B= 0.3886 r= 0.4063
a= 5.5270 b= 0.0554 r= 0.4202

C: Same criteria as column A, however rain was indicated by the verifying observation. (n=210)
A= 11.6796 B= 0.5143 r= 0.3207
a= 11.9661 b= 0.0245 r= 0.2765

D: Same as column C, but the time criteria is ±1 hour. (n=156)
A= 12.8155 B= 0.4774 r= 0.2886
a= 12.8412 b= 0.0223 r= 0.2418

7. CALCULATION OF LATENT HEAT RELEASE USING SSM/I RAINFALL DATA.

The SSM/I measured rainrates were used to calculate the latent heat release (LHR) in 23 storm cases. The procedure used was similar to that presented by Rodgers and Adler (1981) in their calculation of LHR derived from ESMR-5 data. The average rain rate for all 23 cases, with an area of 444 km radii, was 1.5 mm h^{-1} For the 18 mature storms (wind speeds $\geq$ 32.5 m s^{-1}) the average rainrate was 1.7 mm h^{-1}. Rainrates calculated at 111 and 222 km radii showed results comparable to Rodgers and Adler. The average LHR within 444 km radii for all cases was 6.5×10^{14} W and 7.3×10^{14} W for the 18 mature storms. Once again, these values compare favorably to the work of Rodgers and Adler, as well as other authors who measured LHR using different schemes.

The LHR was related to the storms maximum wind speed with a linear correlation of 0.62. This is close to the 0.71 correlation found by Rodgers and Adler. The storm maximum wind speeds were obtained from the current intensity number (CI) derived from the Dvorak technique.

ACKNOWLEDGMENTS

This research was sponsored by the Air Force Office of Scientific Research Under Contract F49620-85-C-0013 through the Universal Energy system. Captains Edward J. Ciardi and Don K. Rhudy were Air Force AFIT sponsored students. Various suggestions were made by Dr. Ken Hardy and Morton Glass of the AFGL in the course of this research. Mr. Gerald Felde of AFGL supplied us with the SSM/I data. The radar data were supplied by Mr. Tsung Yao Wu, Director of the Central Weather Bureau and his colleagues Dr. Tai-Chi Wang of the National Central University and Mr. Lai-Fa Chen. Messers Keith Nieman, and Mark Baricevic of the computing center of St. Louis University helped us in the computations.

REFERENCES

Black, P. G., R. C. Gentry, V. J. Cardone, and J. D. Hawkins, 1986: SEASAT microwave wind and rain observations in severe tropical and mid-latitude marine storms. Advances in Geophysics, 21, 197-277.

Bunting, J. T., and K. R. Hardy, 1984: Cloud identification and characterization from satellites, in a Satellite Sensing of a Cloudy Atmosphere: Observing the Third Planet, Edited by A. Henderson-Sellers, 203-240, Taylor and Francis, London.

Holliday, C., and K. Waters, 1988: SSM/I wind alogrithm evaluation; late winter-spring buoydata. Unpublished manuscript. AFGWC/WFMP, 8 pp. Available from Col. R. P. Wright, AFGWC, Offutt AFB, Nebraska.

Hollinger, J., R. Lo, G. Poe, R. Savage, and and J. Pierce, 1987: Special Sensor Microwave/Imagery, *User's Guide*. Naval Research Laboratory, Washington, DC.

Hsu, S. A., 1986: Correction of land based wind data for offshore applications. A further evaluation. *J. Phys. Ocean*, *16*, 390-394.

Jorgensen, D. P., and P. T. Willis, 1982: A Z-R relationship for hurricanes. *J. Appd. Meteor.*, *21*, 356-366.

Olson, W. S., 1987: Estimation of rainfall rates in tropical cyclones by passive microwave radiometry. Ph.D. Dissertation, Univ. of Wisconsin, 282 pp.

Rao, M. S. V., 1984: Retrieval of world wide precipitation and allied parameters from satellite microwave observations. Advances in Geophysics, 26, 237-336.

Rodgers, E. B., and R. F. Adler, 1981: Tropical cyclone rainfall characteristics as determined from a satellite passive microwave radiometer. *Mon. Wea. Rev.*, *109*, 506-521.

Rogers, R. R., 1976: A short course in *Cloud Physics*. Pergamon Press, 227 pp.

JP8A.2

TROPICAL STORM UPPER LEVEL FLOW PATTERNS DETERMINED FROM MESOSCALE CLOUD MOTION VECTORS

Gary Ellrod

Satellite Applications Laboratory (NOAA/NESDIS)
Washington, DC

1. INTRODUCTION

The development and movement of tropical storms over mainly oceanic regions require the use of remote sensing techniques in monitoring trends in storm evolution. While aircraft reconnaisance has been used to a large extent in the past, the current trend is toward a reduction of such monitoring, except when the storms are threatening land. Data from weather satellites are now being employed in a number of ways: Infrared (IR) and visible imagery is used to estimate the location of the surface center (Jixi and Dvorak, 1987); IR temperature patterns are used to derive "T-numbers", an indication of tropical storm intensity (Dvorak, 1984); composite wind sets derived from cloud and water vapor motion and VAS (VISSR Atmospheric Sounder) height gradients are used to produce the Deep Layer Mean (DLM) flow field (Velden and Smith, 1982). The DLM is believed to be useful in determining the steering current for future cyclone motion (Chan and Gray, 1982).

In the near storm environment, however, satellite-derived winds are limited primarily to the upper levels (above 200mb) because of extensive cirrus and deep convective clouds. This wind data can be useful in monitoring the critical outflow region of storms. Outflow analyses using satellite motion were accomplished as early as 1971 (Black and Anthes) for 5 cases using ATS-III data. More recently, composited wind data from a variety of sources revealed differences in the characteristics of developing vs non-developing systems (McBride and Zehr, 1981). This paper will describe preliminary results of an ongoing study of mesoscale, high level cloud motion winds and analyses derived from GOES cloud motion vectors. The objective is to determine if such data sets would be useful for short range, operational forecasts of tropical storms.

2. WIND DERIVATION

Cloud motion winds were derived on the VAS Data Utilization Center (VDUC) image analysis system located at the World Weather Building at Camp Springs, Md. Wind data were produced by the Windco program, part of the core software for the McIDAS (Man-computer Interactive Data Analysis System).

Wind vectors were determined manually using the "single pixel" technique from three consecutive 4 km scale IR images. In the tropics, this imagery covers an areas approximately 1000 nm on a side. In the single pixel technique, the analyst selects the targets to be tracked, and manually moves the cursor to follow the cloud element. Cloud targets were identified as cirrus based on cloud top temperature, texture or motion. Two wind vectors are determined; one for the first 30 min interval, another wind for the second 30 min period. Differences in wind speeds of greater than 5 m sec^{-1} or wind directions differing by more than 30° between consecutive vectors were considered excessive and the resulting wind was deleted.

Maximum cloud top heights determined from IR temperatures were usually in the range from 100 to 200mb. Upper level winds were determined as close to the surface center as possible. This was sometimes difficult because of the lack of suitable targets, especially for storms with uniform convective cloud top cores, often referred to as Central Cold Covers (Dvorak, 1984). Another difficulty often encountered was motion (propagation) of cold convective cells against the upper level flow. Where the presence of convective clouds was suspected, the downwind portion of any anvil debris was used to determine cloud drift winds.

TABLE 1.

Summary of Tropical Storm Cases

Type	Name	Date/Time	Flow Type	Trend
TS	Javier	8/26/86-19Z	ITR	NC
TS	Frances	11/19/86-14Z	TR	S
TS	Calvin	7/7/87-13Z	ITR	NC
TS	Calvin	7/8/87-13Z	AO	W
TS	Eugene	7/23/87-13Z	SO	S
TS	Emily	9/21/87-19Z	SO	SR
TD	22-E	11/24/87-13Z	SO	S
TS	Daniel	7/19/88-16Z	SO	S
H	Fabio	8/3/88-16Z	TR	W
TS	Kristy	8/20/88-14Z	ITR	S
TS	Florence	9/7/88- 14Z	SO	S
TS	Florence	9/9/88	SO	S
TS	Joan	10/14/88	SO	S
TS	Keith	11/22/88-12z	AO	NC

Key:
TS=Tropical Storm
H=Hurricane
TD=Tropical Depression

SO=Symmetric outflow
TR=Trough-ridge couplet
ITR=Inverted trough-ridge couplet
AO=Asymmetric outflow

S=Strengthened
SR=Strengthen rapidly
NC=No change
W=Weaken

A total of 14 days was analyzed for 12 separate storms between November, 1986 and November, 1988. The cases are summarized in Table 1. Most were tropical storms, although two were hurricanes and one was a depression. While the storms were observed during various stages of evolution, the main emphasis was to determine conditions present just prior to a change in intensity, either weakening or strengthening, in the following 12 hours. The trend was determined from bulletins issued by the National Hurricane Center (NHC) in Miami and/or by an assessment of cloud pattern changes observed in GOES imagery. Examples of the latter are the development or dissipation of an eye, or organization of convection into persistent, curved bands.

Objective analyses produced on the VDUC were streamlines, divergence and, in a few cases, vorticity. The VDUC employs a Barnes objective analysis scheme.

3. FLOW PATTERN TYPES

Four basic types of upper level flow patterns were observed for the 14 cases. They are shown in Figure 1 along with the number of occurrences of each. Table 1 lists the flow type for each storm on an individual basis.

3.1 Symmetric Outflow (SO)

The most common type (7 cases) was the symmetric outflow (SO) pattern. In this flow pattern, streamlines diverge outward from a singular point, with anticyclonic curvature near the periphery of the storm (Figure 1a). This is the classic upper flow commonly associated with tropical storms.

All of the seven SO pattern storms intensified in the following 12 hours. In six of the seven cases, the surface center was located downstream (with

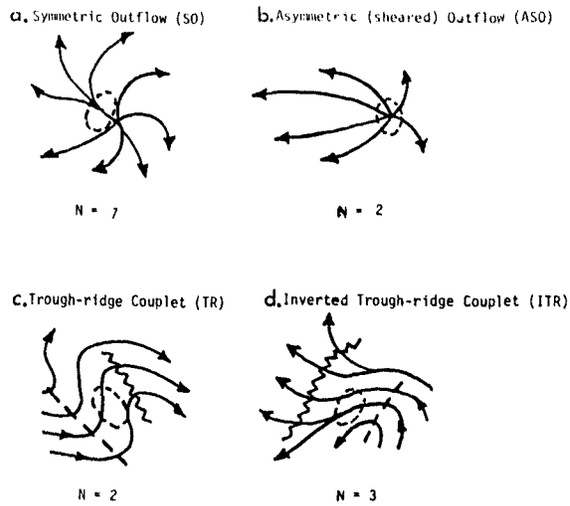

Figure 1. Four main types of upper level flow for the cases listed in Table 1. The dashed areas outline the most likely location of the surface center.

respect to storm motion) from the upper level outflow singular point, as shown in Figure 1a. Thus, for a storm moving to the west, the upper level outflow origin will be east of the surface center position. For the single case that apparently did not strengthen (Florence - 7 Sept 88), the singular point was in advance (North) of the surface position. Previous studies seem to confirm the above results. Black and Anthes (1971) and McBride and Zehr (1981) both found that the upper level anticyclone center was east of the surface center for developing Atlantic and Pacific tropical systems.

A dramatic example of an SO type storm was T.S. Emily on 21 September, 1987. Wind vectors and streamlines for this case are shown in Figure 2. The winds clearly locate the outflow center about 3-4 degrees longitude east of the surface center. A strong outflow jet of 50-55 kt was present in the northwest quadrant, near Puerto Rico. This storm intensified rapidly and became a major hurricane in 24 hours.

3.2 Asymmetric Outflow (AO)

The asymmetric outflow (AO) type is strongly sheared, with a weak component (if any) away from the direction of motion (Fig. 1b). Two such cases were observed: T.S. Calvin and T.S. Keith. In both instances, a subsequent weakening trend was observed in storm strength. It was also noted in visible images that the surface center of each storm was located on the upstream side of the convective cloud mass, near or just to the right (looking downstream) of the outflow singular point. This relationship could be a useful application of upper flow analyses for

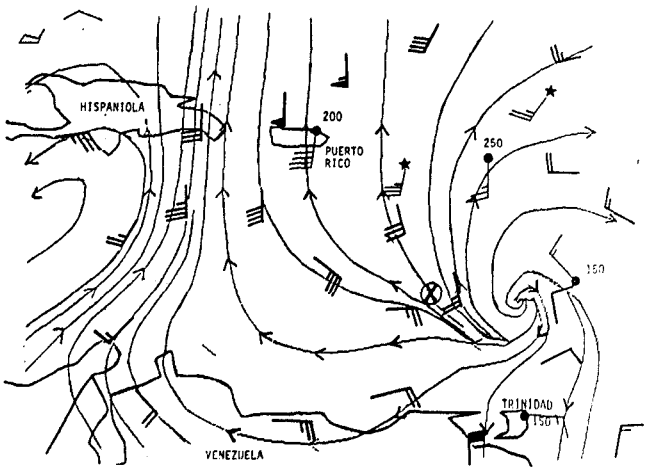

Figure 2. Satellite-derived high level winds and objective streamlines for T.S. Emily on 21 September, 1987. Radiosonde winds and pressure levels are shown for 0000 UTC, 22 September (solid circles). Operational satellite winds (★'s) are for 0000 UTC. The surface center is located near the circled "X".

locating surface centers which are not being monitored by aircraft reconnaissance.

3.3 Trough-ridge Couplet (TR)

The trough-ridge couplet (TR) type (Fig. 1c) was observed in two cases. This pattern is similar to that associated with the development of mid-latitude, extratropical cyclones. For the tropical cases, one occurred with slow intensification, while the other resulted in the weakening of a small but strong hurricane (Fabio) in the east Pacific. The location of the surface center with respect to the upper trough may be an important factor in determining whether or not weakening will occur. In the weakening case, the trough was relatively close (<2 degrees latitude/longitude) to the surface center (Figure 3). In the following 12 hours, the eye of Fabio was observed to disappear. The storm that strengthened (Frances) was well east of the trough, under the axis of maximum diffluence.

3.4 Inverted Trough-ridge Couplet (ITR)

In three cases, the trough-ridge pattern was inverted (ITR) as shown in Figure 1d. The trough was normally open to the south, while the upper ridge arched across the northern semicircle of the storm. The surface center was typically midway between trough and ridge, as with the TR pattern. Once again, the location of the trough with respect to the surface center may be an important factor, as the only storm that strengthened appreciably (Kristy) was located midway between the trough and ridge axes.

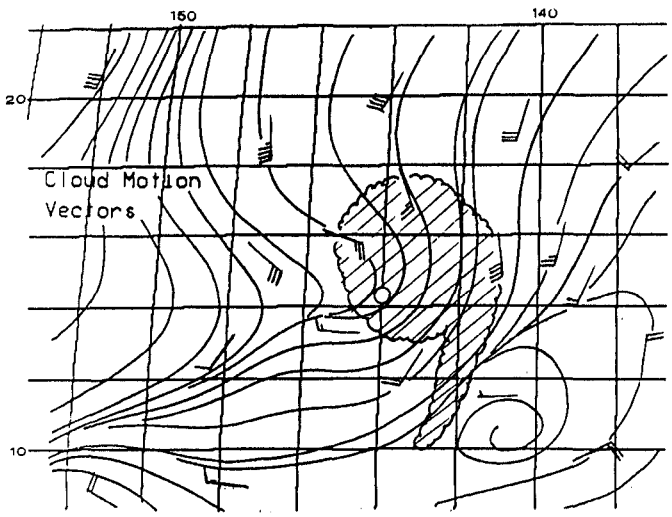

Figure 3. Winds and objectively-drawn streamlines for Hurricane Fabio on 3 August, 1988. Hatched area enclosed by scallops is outline of cold cirrus and convection. The eye, shown by the small circle, disappeared within 12 hours.

4. DIVERGENCE

4.1 Divergence versus Strengthening

There appeared to be no significant relationship between the magnitude of divergence and storm intensification. This finding is supported by previous studies (e.g., McBride and Zehr, 1981). All cases had rather large divergence, except for Hurricane Javier, a small storm which was steady state during the analysis period. The magnitude of divergence ranged from 5 to 14 x 10^{-5} sec^{-1}. While all developing storms had significant divergence aloft near the center, so did many of the non-developers.

For weakening cases, the pattern of divergence may be significant. In those instances (Fabio and Calvin) a region of upper convergence or very weak divergence was analyzed near the surface center, resulting in a divergence gradient over the surface center. It is possible that sinking motion was occurring that acted to weaken convection near the cyclone center, leading to a decrease in storm intensity.

4.2 Divergence versus Convection

The relationship between divergence and the location of deep convection was generally good. Strong divergence was usually associated with clusters of convection having high, cold IR tops. Strong convergence, on the other hand, usually occurred in areas of minimal convective cloudiness.

4.3 Divergence versus Movement

Recent studies (e.g., Lajoie, 1988) have indicated that the Direction of Divergence Asymmetry (DDA) at 200 mb may serve as a useful predictor for tropical storm motion 24 to 36 hours later. The DDA is the orientation of the zero divergence isopleth in the poleward semicircle. The DDA is required to be at least 500 km long and must lie between 400 and 1200 km from the cyclone center.

In the cases described here, the DDA was clearly defined in only a few storms. The inability to analyze this feature is likely due to: (1) the presence of multiple centers of divergence and convergence, (2) the relatively small area in which the objective analyses were produced and (3) the lack of sufficient wind data in cloud-free peripheral regions of the storm. In the cases for which the DDA was determined, the future storm motion agreed well with the DDA orientation. To determine if the DDA concept will be useful using satellite-derived winds, it will be necessary to (1) add more wind data in cloud-free areas, probably using the 6.7μ water vapor channel and (2) produce the objective analyses at a slightly larger scale. The latter will have the effect of smoothing out some of the small scale features and will extend the analyses farther from the center. Divergence derived from composite wind data now produced for NHC during the hurricane season may be useful for this purpose.

5. SUMMARY AND CONCLUSIONS

Objective analyses of cloud motion vectors derived from GOES IR images at high levels of tropical storms have revealed several types of flow patterns. The most common is the classic anticyclonic, spiraling outflow which produces strengthening if the outflow origin is east of the surface center. Three other types were also observed. One type is sheared anticyclonic outflow, with the strongest isotachs in the downstream direction. This pattern was related to steady state or weakening conditions, with the surface center upstream from the convection. The other two were variations of a trough-ridge couplet arrangement. Strengthening storms occurred if the surface center was midway between trough and ridge. If the trough was near (<2 degrees latitude/longitude) the cyclone center, weakening occurred. The latter condition was reflected by a strong gradient in the divergence analysis. Also, while the magnitude of divergence had little relationship to trends in storm strength, it accurately reflected the pattern of convection.

6. FUTURE PLANS

Further cloud motion data sets will be produced to increase confidence in some of the preliminary findings described here. It is expected that in the Summer of 1989, operational, mesoscale wind sets and, possibly some derived analyses, will be provided to the NHC on a test basis. Although manually derived winds are time consuming, software now exists for automatic wind generation from a sequence of images. Considerable editing of such automated wind sets is likely, but the increased volume of wind vectors will make frequent, mesoscale analyses of the tropical storm environment a real possibility.

7. REFERENCES

Black, P. G. and R. A. Anthes, 1971: On the asymmetric structure of the tropical storm outflow layer. J. Atmos. Sci., 28, 1348-1366.

Chan, J. C. L. and W. M. Gray, 1982: Tropical storm movement and surrounding flow relationships. Mon. Wea. Rev., 110, 1354-1374.

Dvorak, V. F., 1984: Tropical storm intensity analysis using satellite data. NOAA Tech. Report NESDIS 11, Satellite Applications Laboratory, Washington, D.C., 47 pp.

Jixi, J. and V. F. Dvorak, 1987: Tropical cyclone center locations from enhanced infrared satellite imagery. NOAA Tech. Memo. NESDIS 18, Sat. Appl. Lab., Wash., D.C., 10 pp.

Lajoie, F. A., 1988: Circulation asymmetries around a tropical cyclone and its future direction of motion. BMRC Research Report No. 10, Bureau of Meteorology Research Centre, Melbourne, Australia, 34 pp.

McBride, J. L. and R. Zehr, 1981: Observational analysis of tropical cyclone formation, Part II: Comparison of non-developing versus developing systems. J. Atmos. Sci., 38, 1132-1151.

Velden, C. S. and W. L. Smith, 1984: Quantitative satellite applications-tropical cyclone intensity monitoring and track forecasting. Proc. 15th Conf. on Hurricances and Tropical Meteor. Jan 9-13, 1984, Miami, FL, 159-162.

JP8A.3

MOISTURE RETRIEVALS FROM THE GOES VAS

Christopher M. Hayden

NOAA/NESDIS, University of Wisconsin-Madison
Madison, Wisconsin

Anthony J. Schreiner

Cooperative Institute for Satellite Studies
University of Wisconsin-Madison
Madison, Wisconsin

1. INTRODUCTION

The VISSR Atmospheric Sounder (VAS) has been included in the GOES instrumentation since September, 1980. The principal use of the VAS has been to provide frequent and timely images of water vapor and two derived products, lifted index and total precipitable water, to the National Severe Storm Forecast Center during the severe weather season to assist in assessing severe weather potential. The VAS has also been used successfully to provide wind estimates from tracers in 6.7 and 7.2 micrometer images of water vapor, helping to define the deep-layer-mean steering flow used by the National Hurricane Center to forecast tropical storm movement. Finally, temperature soundings from the VAS have been used in defining the initial state in experimental forecasts made by the National Meteorological Center (NMC). In this application they have been least successful. A number of tests introducing VAS temperature profiles over the North Pacific could not be shown to give a consistent, positive effect on forecasts over the U.S. (O'Lenic, 1986). It was concluded that the VAS temperature profiles, derived from 11 measurements with relatively poor vertical resolution, could not improve on the synoptic scale representation of the temperature field already contained in the forecast. Efforts to include the VAS data on a routine basis were discontinued.

Subsequent to the temperature impact studies, the CIMSS and the NMC have cooperated on a study of VAS moisture definition, with the intention of carrying out VAS Model Impact Studies (VMIS) of this parameter. The area of concentration has shifted from the eastern Pacific to the Gulf of Mexico. The purpose is to evaluate the VAS capability in defining the moisture in this important source region. Initial results of the VMIS were given by Mostek et al. (1987), reporting on a study of the VAS moisture retrievals for a case study of 3 September 1986. The study examined level dewpoints retrieved with the VAS as compared to the NMC analysis. Several deficiencies were noted, among them the fact that the VAS made only slight improvements on forecasts used to provide a first guess profile (several forecasts were used); was quite dependent on the first guess; and showed little skill at low levels. Based on these findings the retrieval algorithm was modified, and the updated version has been run, unchanged, since March 1988. This paper briefly discusses the retrieval method currently used and assesses the quality of the moisture retrievals now produced.

2. RETRIEVAL METHOD

The VAS retrieval method is described in detail in Hayden (1988). We shall give here a brief qualitative description of the method and also note the changes which have been instituted since that publication. The radiative transfer equation, which describes the outgoing radiation measured by the satellite in the sounding instruments spectral channels (12 for VAS) is linearized into three contributions; that portion arising from surface skin temperature; that portion arising from the atmospheric temperature distribution, and that portion arising from the atmospheric water vapor distribution. A part of the linearization process is to express the relationship as a perturbation to a first guess. That is to say, the incremental difference between the measurement and a radiance calculated from the first guess is equated to an incremental change from the first guesses of the skin temperature, the temperature, and the moisture. The last three "retrievals" are accomplished simultaneously.

In order to stabilize the solution, to realistically represent the vertical resolution of the instrument, and to economize, the perturbation profiles are represented in terms of pressure-dependent basis functions. Prior to the March 1988 modifications, the functions chosen were all transmittance "weighting functions" (normalized) chosen from the VAS channels. Four basis functions were used for the temperature profile and three for the moisture profile retrieval. In March, 1988, the selection for moisture was changed to a set of four Gaussian curves designed to better represent the lower atmosphere. Figure 1 gives an example of the previous and current basis functions. A second change introduced in March was to include band 11, the 4.4 micrometer measurement peaking

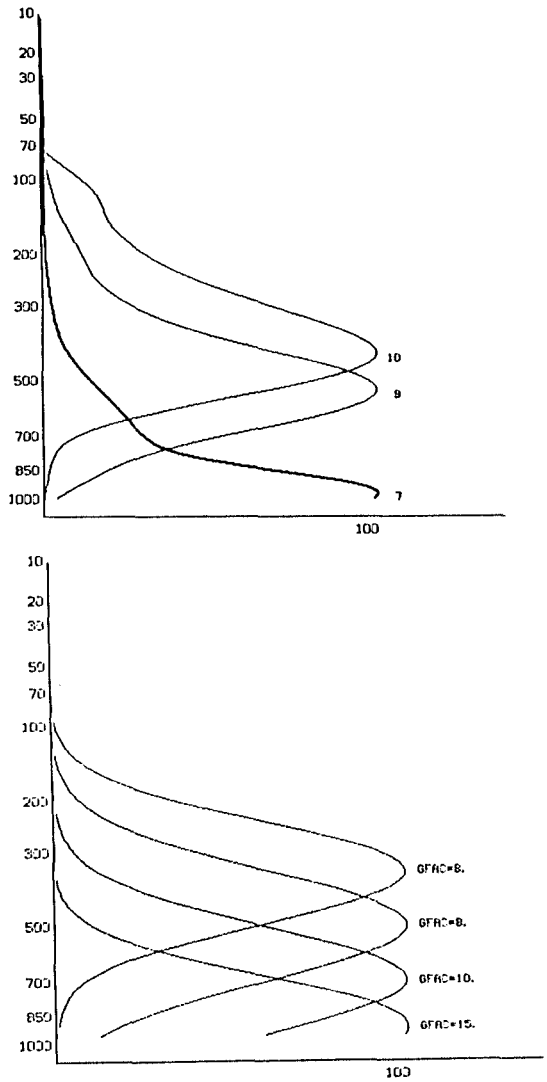

Fig. 1. Top: Moisture basis functions derived from VAS channels 7, 9 and 10. Used prior to March 1988. Bottom: Gaussian moisture basis functions used subsequent to March 1988.

near 300 mb in the retrieval. Previously, this measurement was considered too noisy to use, but improved performance on GOES 7 permits its use. It is desirable to use this channel because it has very little sensitivity to moisture and therefore helps to distinguish between temperature and moisture errors in the first guess.

3. METHOD OF EVALUATION

It has been our practice in the past to evaluate moisture retrievals by the comparison of level dewpoints with coincident radiosondes. This has not been very satisfactory. The dewpoint as measured by the radiosonde can vary rapidly in the vertical, on a scale well below that sensed by the satellite, leading to large, apparent errors in the satellite estimate. For the VMIS we have changed the standard from level dewpoints to layered precipitable water. The latter is the quantity which actually affects the radiation sensed by the satellite. The layers we have used are sigma= 0.9, 0.7, and 0.3 where

$$\text{sigma} = p / ps$$

and ps is the surface pressure. The layers are thus, approximately, the lowest 100, the lowest 300, and the lowest 700 mb of the atmosphere.

The radiosonde again serves as the standard, though for evaluating the Gulf of Mexico this is necessarily imperfect. The layered precipitable water is calculated from the radiosonde (with the requirement that the radiosonde report at significant as well as mandatory levels), and compared to an analysis of the satellite data. The analysis is accomplished on a latitude/longitude grid with a 1.5 degree grid length using a three-dimensional recursive filter analysis method (Hayden and Purser, 1988) in sigma coordinates.

4. COMPARISONS

Satellite temperature and moisture retrievals have been made daily, five days a week, data permitting, since March 1988 from two dwell soundings beginning at 12:48 and 13:18 UTC. The two soundings cover approximately 17 to 50N and 70 to 105W. The principal area of comparison has been the Gulf of Mexico, 17 to 31N and 70 to 98W, although the complete area has also been examined. Particular attention has been given to verifying the Regional Analysis and Forecast System (RAFS) 12 hour forecast (which serves as a first guess for the retrievals) and the analysis from the VAS retrievals. In addition, however, we have also considered the "moisture bogus" data which is supplied by the NESDIS to NMC at each synoptic analysis time. Moisture bogus is provided in oceanic cloudy areas, based on synoptic interpretation, as a selection of one of 13 relative humidity profiles. It should be added that the RAFS forecast acts as a background for both the retrieval and moisture bogus analyses. Examples of the analyses are shown in Figs. 2 and 3 (for a typical case rather than a selected, spectacular success). The contours are mm of precipitable water. The top, middle and bottom figures show the RAFS forecast, the retrieval analysis, and the moisture bogus analysis, respectively. The analyses are for the surface to sigma = 0.9 and surface to sigma = 0.7 layer. Radiosonde values are plotted on the RAFS forecast; the locations of the satellite retrievals and the moisture bogus values are shown on their respective analyses. Several features of these figures are notable:

- Despite the fact that we are dealing with a layered quantity, the precipitable water measured by the radiosonde is still, spatially, highly variable. Examples are the "33" and "18" along the Gulf coast and the "30" in Georgia shown in Fig. 3. The mountains of Mexico also lead to strong gradients which test the analysis scheme.
- The RAFS forecast seems to underestimate the moisture in both layers, especially at higher values. This tendency is corroborated in monthly statistics as shown in Fig. 4 below.
- The VAS data usually removes the dry bias of the forecast, strengthens gradients, and increases detail. If one were to edit on the basis of satellite data the radiosonde reports of "30" in Georgia, and of "18" in Mississippi are suspect. However, in compiling the statistics given below we have not edited in this manner.

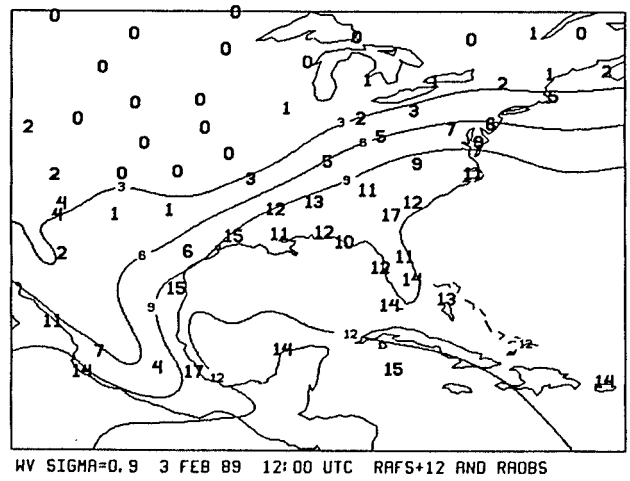

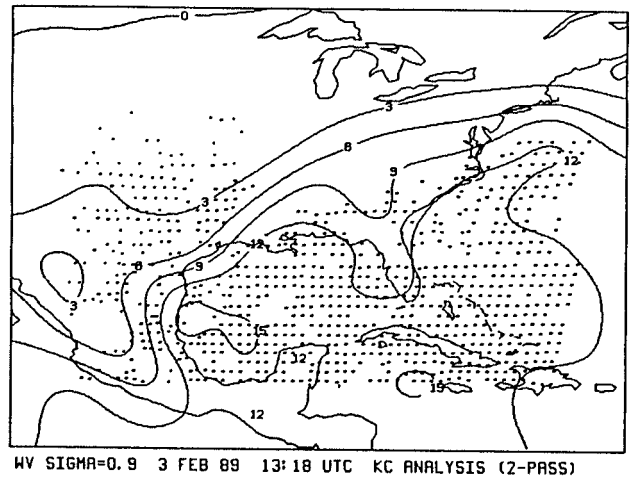

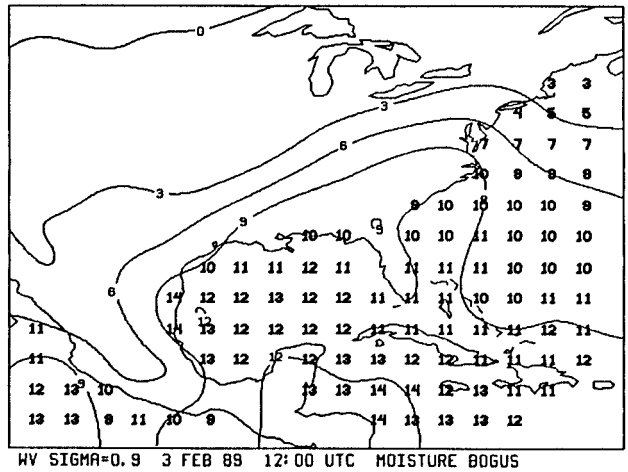

Fig. 2. Top: RAFS +12 hr analysis with radiosonde values superimposed. Middle: VAS analysis with retrieval locations. Bottom: Moisture bogus analysis with data superimposed. Analysis and values are layered precipitable water, mm, from surface to sigma = 0.9.

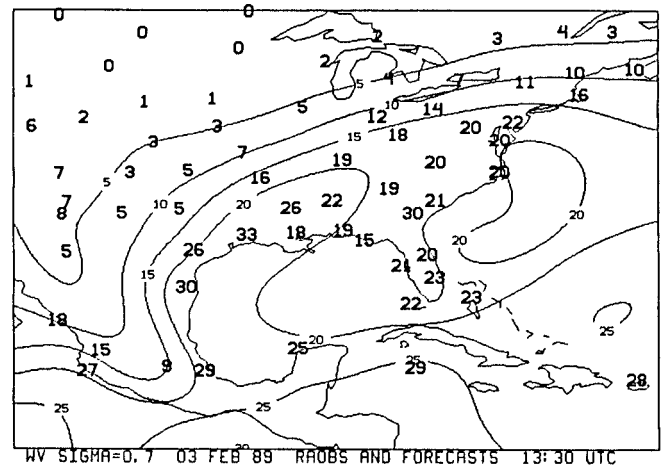

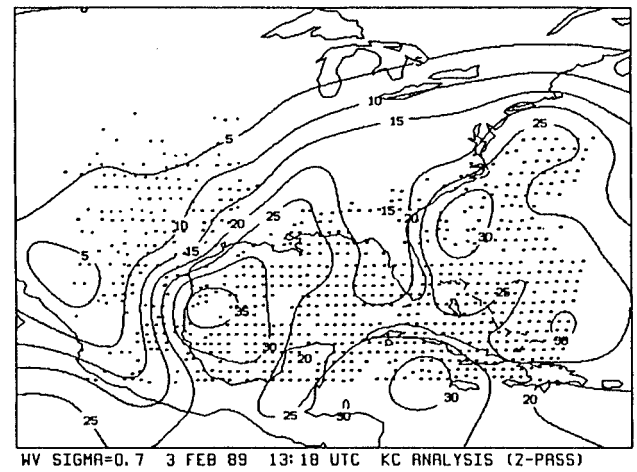

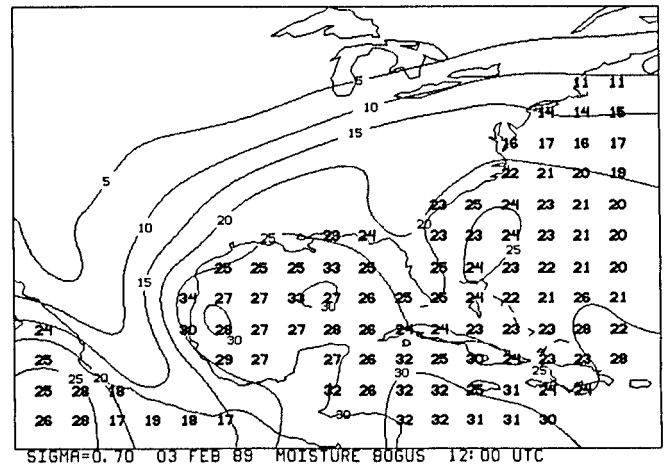

Fig. 3. Same as Fig. 2, but for surface to sigma = 0.7 layer.

- The RAFS and VAS analyses agree more closely over the U.S. than over the oceanic areas. This has been a persistent feature of the comparisons.
- The analysis resulting from the moisture bogus is generally less detailed than even the forecast. Part of the reason is that the analysis system has difficulty fitting some of the larger discontinuities which frequently appear (note the 34 near Brownsville, TX in Fig. 3). Also, the moisture bogus analysis is very bland in the lower layer.

Fig. 4 shows scatter diagrams for the sigma = 0.9 and sigma = 0.7 layers comparing the radiosonde values with the analyses of the RAFS and the VAS. This sample was collected

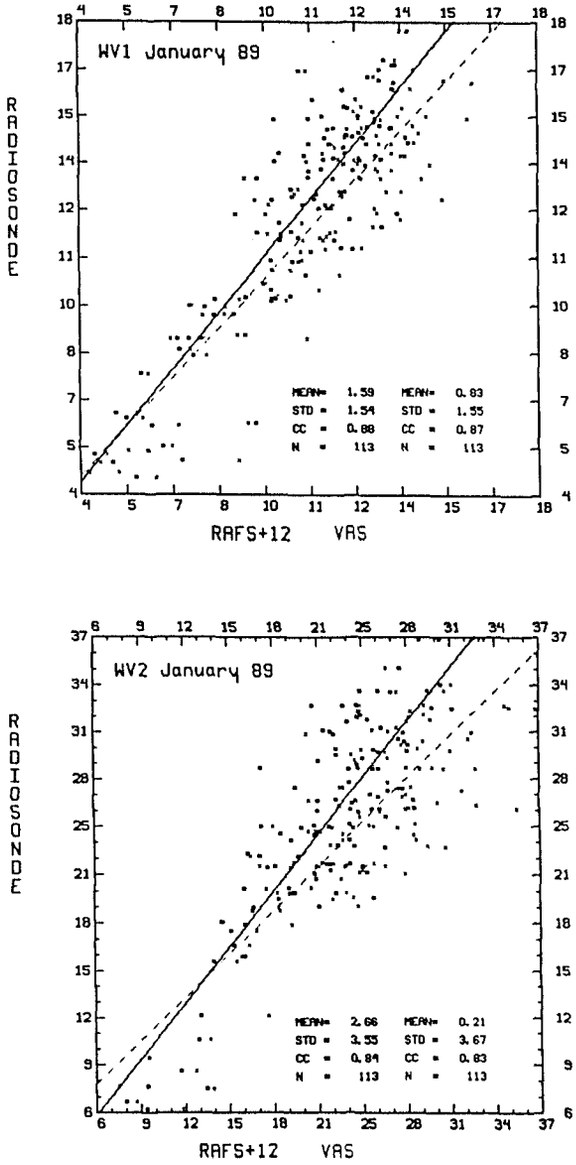

Fig. 4. Scatter plot of precipitable water estimates. Radiosonde vs. RAFS +12 forecast (rectangle, solid) and radiosonde vs. VAS (cross, dash). Units are mm. Top: Layer from surface to sigma = 0.9. Bottom: Layer from surface to sigma = 0.7.

during January 1989 for the Gulf zone. Statistics of the samples are also given in the figure. In terms of the correlation between radiosonde and analysis or the standard deviation of the differences (STD), there is little to choose between the RAFS and the VAS. The mean difference, however, and the lines-of-best-fit show that the VAS is correcting the dry bias of the RAFS for both layers. The January sample is fairly typical of the results for other months, though the statistics slightly favor the VAS in the wetter seasons.

Fig. 5 is a plot of the standard deviation of the daily data for November 1988, again taken over the Gulf zone. The figure shows that the analyzed VAS data contain approximately the same variance as the radiosondes whereas the RAFS (GUESS) and especially the moisture bogus are considerably smoother. This result is one reason why the VAS analyses usually give approximate statistical parity with the RAFS even though, visually, they almost always appear to be superior. In general, higher variance penalizes statistical comparisons of RMS or correlation.

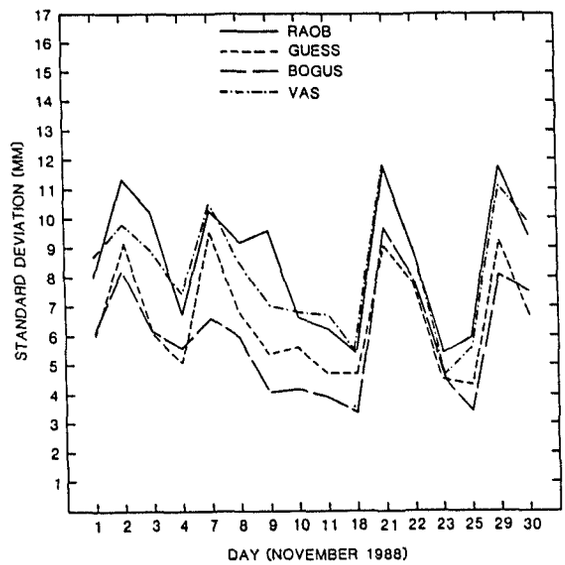

Fig. 5. Standard deviation of precipitable water in layer from surface to sigma = 0.7, November 1988, Gulf of Mexico zone. Values are given for radiosonde, RAFS +12 forecast (GUESS), moisture bogus, and VAS.

Figs. 6 and 7 look at middle and upper layer precipitable water layers for the same case shown in Figs. 1 and 2. The gradient detail is maximized in the VAS analysis for the sigma = (0.7 - 0.9) layer. This field does not exactly fit the radiosonde data, but it is not seriously discrepant and is very coherent. The local maximum off the Carolina coast which is not contained in the RAFS forecast is the type of feature which might influence a precipitation forecast. This feature extends into the upper layer as well. For the upper layer in general, the VAS analysis has only modestly changed the RAFS forecast. One apparent improvement is over the western Gulf where the southward extent of the moisture maximum has been limited.

The moisture bogus analyses of Figs. 6 and 7 are unsatisfying. Whereas the moisture in the lower layer has been improved over the western

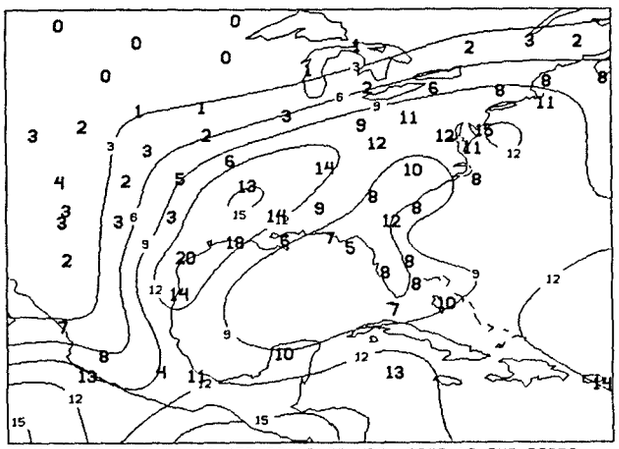

WV SIGMA=(.7-.9) 3 FEB 89 12:00 UTC RAFS+12 AND RAOBS

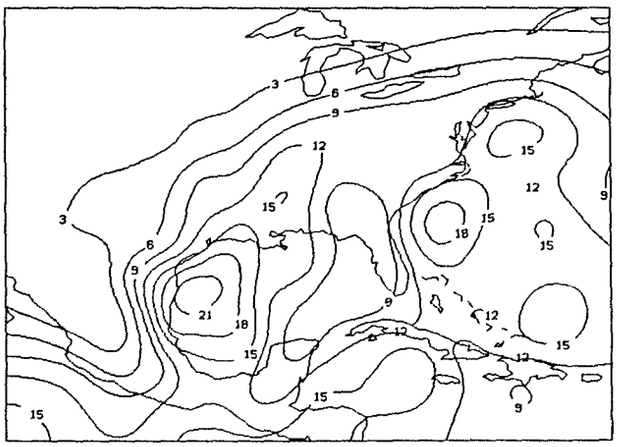

WV SIGMA=(.7-.9) 3 FEB 89 13:18 UTC KC ANALYSIS (2-PASS)

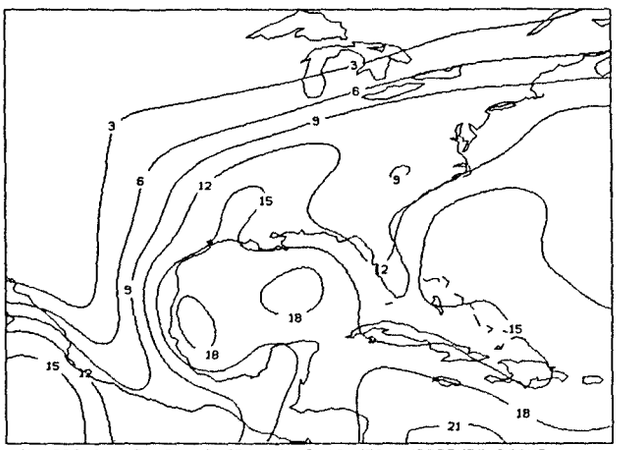

WV SIGMA=(.7-.9) 3 FEB 89 12:00 UTC MOISTURE BOGUS

Fig. 6. Like Fig. 2, except for layer sigma = 0.7 to sigma = 0.9.

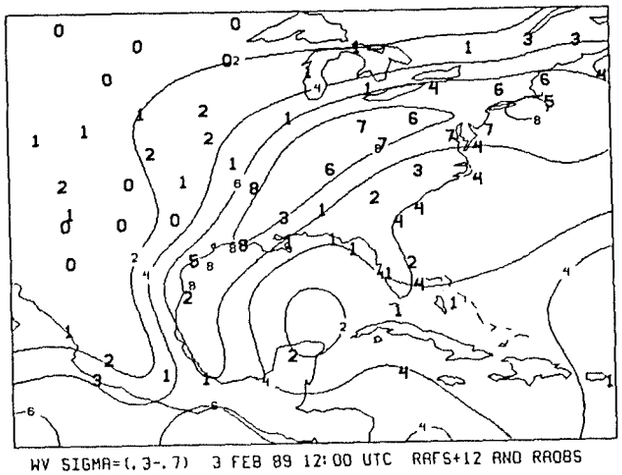

WV SIGMA=(.3-.7) 3 FEB 89 12:00 UTC RAFS+12 AND RAOBS

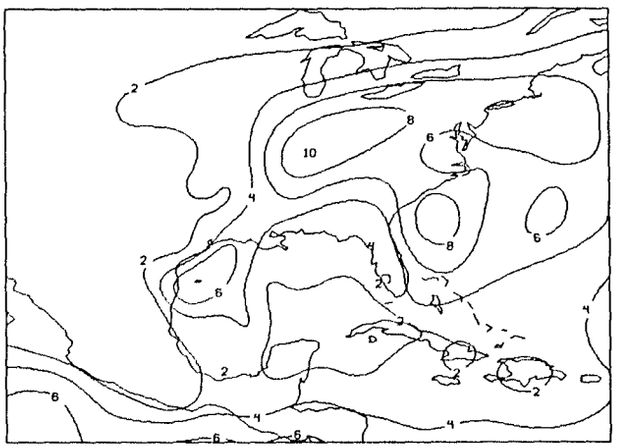

WV SIGMA=(.3-.7) 3 FEB 89 13:18 UTC KC ANALYSIS (2-PASS)

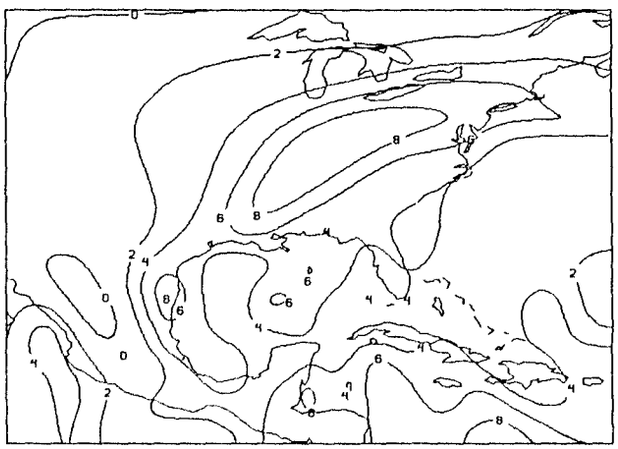

WV SIGMA=(.3-.7) 3 FEB 89 12:00 UTC MOISTURE BOGUS

Fig. 7. Like Fig. 2, except for layer sigma = 0.3 to sigma = 0.7.

Gulf, a seemingly spurious second maximum over the central Gulf has destroyed the moist-dry couplet clearly shown in the VAS and RAFS analyses. In the upper layer the pattern given by the moisture bogus seems almost random.

5. CONCLUSIONS AND FUTURE PLANS

The VAS retrievals have demonstrated a capability to improve on the RAFS forecast of layered precipitable water for an extended period of comparison. In terms of statistical correlation and RMS, the improvement is slight, but in terms of the mean value and total variance, the VAS analyses are clearly closer to the radiosonde. There is evidence that the VAS can make appropriate adjustments to three layers from the surface to 300 mb.

While it appears that the VAS can be of benefit to the NWS forecast mission, it is not yet clear how the data should be introduced. Individual moisture retrievals are quite noisy. For this reason we have chosen the objective analysis route for evaluation. It may be that a grid of values, similar to the moisture bogus program, would be appropriate. The NWS is also not prepared to accept layered precipitable water as data. Perhaps this can be converted to profiles of relative humidity, again like the moisture bogus.

The CIMSS is pursuing the question of using the VAS moisture data in the GUFMEX experiment. In this application, full resolution images of two layers of precipitable water are being assimilated. Progress in this experiment is discussed in a companion paper (Aune, 1989).

6. REFERENCES

Aune, R., 1989: Impact of VAS retrievals on a simulation of return flow in the Gulf of Mexico. Preprints, 4th Conference on Satellite Meteorology and Oceanography, May 16-19, 1989, San Diego, CA.

Chesters, D., L. W. Uccellini and W. D. Robinson, 1983: Low-level water vapor fields from the VISSR Atmospheric Sounder (VAS) "split window" channels. J. Clim. Appl. Meteor., 22, 725-743.

Hayden, C. M., and R. J. Purser, 1988: Three-dimensional recursive filter objective analysis of meteorological fields. Preprints, 8th Conference on Numerical Weather Prediction, February 22-26, 1988, Baltimore, MD, 185-190.

Hayden, C. M., 1988: GOES-VAS simultaneous temperature-moisture retrieval algorithm. J. Appl. Meteor., 27, 705-733.

Mostek, A., A. Siebers, R. Petersen, D. Keyser, C. Hayden, W. Menzel, and A. Schreiner, 1988: VAS Model Impact Studies at NMC. Preprints, 8th Conference on Numerical Weather Prediction, February 22-26, 1988, Baltimore, MD, 277-284.

O'Lenic, E. A., 1986: The effect of VISSR Atmospheric Sounder (VAS) data on some LFM analyses and forecasts. Mon. Wea. Rev., 114, 1832-1846.

GROUND TRUTH OBSERVATIONS FOR TRMM

Otto W. Thiele

Goddard Space Flight Center
Greenbelt, Maryland

INTRODUCTION

Because of the extreme variability of rainfall both in time and space and the sampling limitations inherent with a single satellite, the Tropical Rainfall Measuring Mission (TRMM) Science Steering Group has mandated a substantial surface based validation program. Given the state-of-the-art for areal rain measurements, however, it was clear that a strong pre-mission research effort would have to be initiated, not only to be able to provide reliable "ground truth" data for the mission, but also to support instrumentation and algorithm development beforehand. An early objective in the TRMM "ground truth" strategy was to pursue fundamental rain measurement research for developing a transfer standard so that consistent observational data could be acquired from the various rain regimes in the tropics. Also, it was determined that physical processes and statistical properties of rainfall must be studied to better understand regional characteristics of rainfall. Furthermore, data sets representing tropical ocean regimes, continental regimes, monsoon regimes, etc., would have to be collected to support sampling and statistical studies. Then, data assimilation techniques tailored to the available data sources would have to be developed. These early efforts also will provide the source for long-term climatologies of these regions, another key objective of the pre-mission program.

The "ground truth" effort will begin with established techniques, i.e., rain gauges and radar. Rain gauges, even if substantially improved, will not be sufficient by themselves. We must rely on radar for large area coverage. Furthermore, radar is crucial for validating the vertical structure of raining systems. Without reliable information on this parameter, we cannot detect the levels of latent heat release which is an objective of GCM's in determining the heating impact on global circulation and thus climate variability. The "ground truth" program, already underway, involves several new measurement techniques and radar applications. Data are presently being collected with radar and rain gauges from central Florida, Kwajalein (Marshall Islands), and Darwin, Australia. Soon, tropical continental data will be collected from northern Thailand. How to cope with the formidable task of developing useful data sets and products from these sources is the most pressing problem now facing us.

STRATEGY

There are two main components of the validation (often referred to as "ground truth") program envisioned for TRMM, i.e., pre-mission and mission (Thiele, 1987). The ultimate objective is to provide reliable comparative data during the mission for area and time averaged rainfall representative of tropical or near tropical regions. Of course, instantaneous comparisons will be attempted as well. To achieve the end objective, however, a strong pre-mission program is critical. Elements of the validation program are outlined in Figure 1.

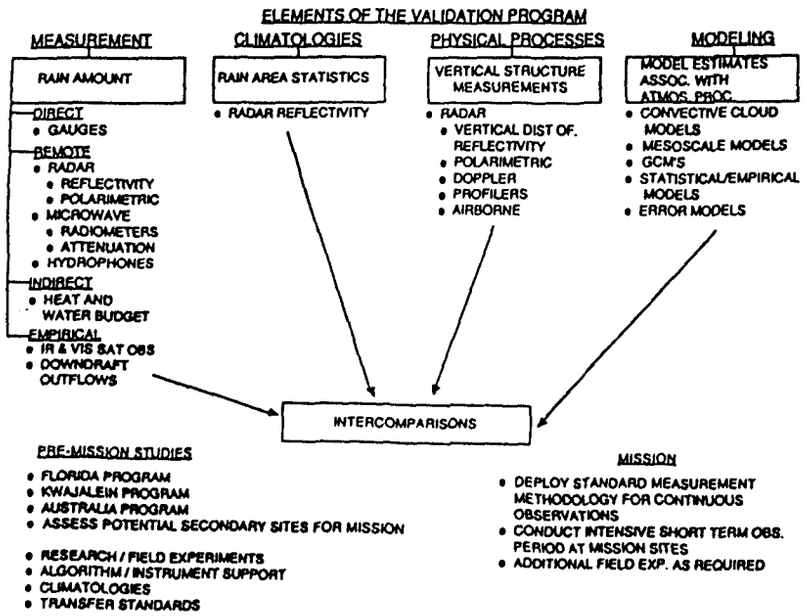

Fig. 1. Hierarchy of activities necessary to validate TRMM observations

An early aim of the pre-mission strategy is to seek more accurate rainfall measurements both from direct and indirect methods. While regional climatologies of rainfall have already begun using available radar and rain gauge data, extensive research is underway to investigate new observational techniques, or where feasible, to improve conventional ones. A number of experimental techniques are currently under study (Table 1).

Table 1. Experimental Rainfall Methods

Device	Advantages
1) Optical Rain Gauge	Fast response, wide dynamic range
2) Zenith pointing VHF-UHF Doppler rain gauge	Explicit vertical velocity, drop size distribution, rainfall rate, level of diabatic heating
3) Scanning Doppler radar	Mesoscale vertical motion, profiles of condensate production and fallout
4) Multiple frequency/polarization radar	Observations over water, semi-independent estimates of rainfall
5) Microwave attenuation with alternating horizontal and vertical polarization	Calibration of radar statistics over land and observations over water
6) Satellite beacon attenuation	Sampling over remote (ocean) areas
7) Airborne Doppler radar	Sampling over oceans/remote areas
8) Underwater hydrophones	Sampling over oceans, integration of rainfall over a surface area
9) Profilers	Vertical structure in convective cloud systems

For improving surface measurement techniques, a small scale experimental rain measurement research facility, Fig. 2, is being developed to determine the best methods and equipment to deploy at the primary test site. A polarized multi-frequency microwave attenuation link will be the key component of the facility. Attenuation of horizontally propagating microwave radiation is strongly related to the intensity of intervening precipitation and less sensitive than radar Z-R to rain drop size distribution (Crane, 1985; Ulbrich and Atlas, 1985). If this technique can be successfully developed, it will provide an accurate way of determining mean rain rates over large areas.

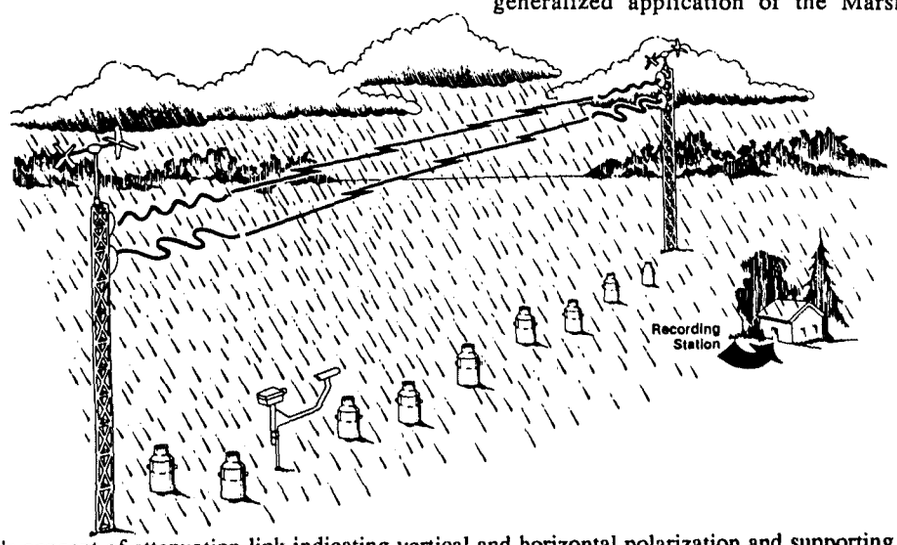

Fig. 2. Artist's concept of attenuation link indicating vertical and horizontal polarization and supporting rain gauges. Planned frequencies are 8, 25, 38, 80 and 240 GHz. CRL Japan plans to furnish the 80 and 240 GHz systems.

Under the microwave transmission path will be two distrometers and a number of state-of-the-art rain gauges for calibration. Also, at least two new "gauge" techniques will be investigated, i.e., an optical rain gauge and an upward looking Doppler rain gauge. The Communications Research Laboratory (CRL) of Japan is participating in this research.

Two other methods of obtaining corroborative rain data is through inference from mass, heat and moisture budgets derived from surface wind measurements or rawinsonde data. In one technique, convective outflow at the surface is related to rainfall (Ulanski and Garstang, 1978a, 1978b, 1978c). The downward vertical velocities are integrated over time and space to estimate downward mass transport which in turn can be directly related to rainfall. Over much larger areas, surface fluxes of precipitation are inferred from heat and moisture budgets calculated from upper air soundings describing a large volume of the atmosphere (See, for example, Brummer, 1978). This budget method is one of the few techniques that can provide an estimate of rainfall amount on the largest scales of interest to TRMM.

Improving direct measurements of rainfall intensity is expected to substantially increase our confidence in areal estimates of rainfall derived from radar reflectivity observations. This is particularly so now since recent studies (Atlas et al., 1989) show that substantial improvement in such estimates can be achieved with reliable rain rate measurements. In the past, most approaches to rainfall estimates from radar have depended on the generalized application of the Marshall-Palmer Z-R relationship. However, current investigations have verified that there is an extremely high correlation between the fraction of rain rate above a certain threshold and rain rate averaged over a large area. For convective rain, this threshold has been found to be in the approximate range of 5 to 10 mm/hr. This correlation is based on relatively stable probability density functions (PDF's) of rain intensities for wide area rain cloud systems having similar depths. The Height-Area-Threshold-Technique (HART), as it is called by Atlas and his co-workers, makes use of this relationship to

provide more precise Z-R functions tailored to varying convective characteristics as may occur in different regions and/or different seasons. The necessary PDF's for an area can be obtained from a few well calibrated rain rate gauges within the area covered by the radar.

If the pre-mission objectives are satisfactorily accomplished, there will be at least 3 or 4 key ground truth sites already in place and functional to begin providing validation data when the mission begins. However, it is intended to pursue cooperative efforts to obtain "ground truth" observations from other representative areas as well. The TRMM program will depend heavily on contributions from other countries and their institutions for additional "ground truth" data. Figure 3 illustrates the expected TRMM coverage and both current and potential verification sites.

As indicated earlier, data is being collected regularly from three tropical sites using calibrated radars with digital recording systems in association with recording rain rate gauges. At the present time, the radars in Florida and the west Pacific (Kwajalein) provide only reflectivity data. However, the radar in Darwin, Australia, includes Doppler capability. During this past rainy season at Darwin (1988-1989), dual Doppler observations were made with a second Doppler radar in connection with an NSF grant to MIT. Through a U.S. Bureau of Reclamation cooperative program in Thailand, a new higher precision 10 cm Doppler radar with recording capability, supported by approximately 40 recording rain gauges, will provide continental tropical rainfall data beginning in approximately 1990. Data from the three initial sites are being collected continuously for processing at NASA's Goddard Space Flight Center. While the raw data will remain the basic archive, a number of rainfall data products are planned, including a variety of statistical and phenomenological analyses. Resources are limited at this time, but every effort will be undertaken to make these data accessible to serious researchers over and above those directly supported by NASA.

TRMM Ground Track for 35° Orbit with Ground Truth Verification Sites; 1 Day--16 Orbits

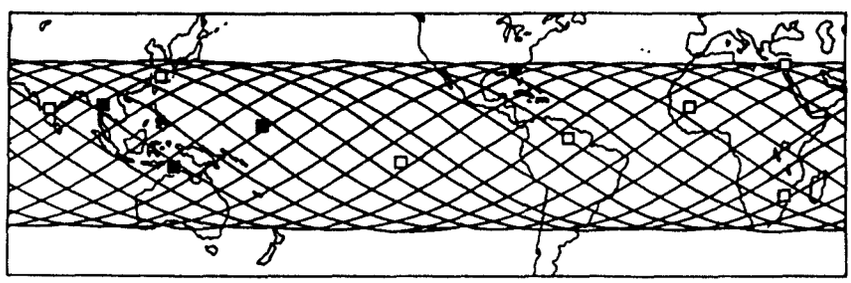

Fig. 3. The black squares show the locations of the primary test facility (Central Florida) and the secondary test sites. Radar and rain gauge data are already being collected at the Florida, Australia, and Kwajalein sites and observations are expected to begin in Thailand during 1989. The white areas indicate potential sites of other representative rain regimes.

Validation of the TRMM observations is expected to be accomplished in two ways: (1) average the TRMM rainfall data over time periods of a month or more for large areas (500 x 500 km) and compare with similarly averaged ground truth measurements. (2) compare both the rainfall and height distribution data from TRMM with the instantaneous values observed at one or more "ground truth" stations.

To be successful, the mission is dependent on high quality "ground truth" data. The averaged TRMM rainfall data could conceivably be validated with rain gauge data alone, but instantaneous calibration will require four dimensional precipitation data from at least one location in the tropics. The second strategy must have priority early in the mission because verification would be more rapid than with the climatological approach.

CONCLUSION

While the TRMM satellite project provided the impetus for this rather extensive program to validate the space observations, the potential for contributing to a broad field of precipitation research is enormous. Indeed, it was hoped that these efforts would encourage new interest and stimulate a wide range of investigations in an area of research that is perhaps one of natures least understood atmospheric phenomenon. The TRMM project and the related "ground truth" program cannot support all of the studies that may contribute, but the unique data sets being acquired offer great opportunity for the study of rainfall characteristics, associated physical processes, data assimilation techniques, etc.

REFERENCES

Atlas, D., D. Rosenfeld, and D. A. Short, 1989: The estimation of convective rainfall by area integrals. Part I: The theoretical and empirical basis. Submitted, J. Geophys. Res.

Brummer, B., 1978: Mass and energy budgets of a 1 kilometer high atmospheric box over the GATE C-scale triangle during undisturbed weather conditions. J. Atmos. Sci., 35, 997-1011.

Crane, R. K., 1985: Comparative evaluation of several rain attenuation prediction models. Radio Science, 20, 843-863.

Thiele, O. W., Ed., 1987: On requirements for a satellite mission to measure tropical rainfall. NASA Ref. Pub. 1183, 49 pp.

Ulanski, S. L., and M. Garstang, 1978a: The role of surface divergence and vorticity in the life cycle of convective rainfall, Part I: Observations and analysis. J. Atmos. Sci., 35, 1047-1062.

Ulanski, S. L., and M. Garstang, 1978b: The role of surface divergence and vorticity in the life cycle of convective rainfall, Part II: Descriptive model. J. Atmos. Sci., 35, 1063-1069.

Ulanski, S. L., and M. Garstang, 1978c: Some aspects of Florida convective rainfall. Water Resour. Res., 14, 1133-1139.

Ulbrich, C., and D. Atlas, 1985: Extinction of visible and infrared radiation in rain: comparison of theory and experiment. J. Atmos. and Oceanic Tech., 2, 331-339.

JP8A.6

THE GROUND TRUTH ANALYSIS OF RAIN GAUGE DATA FOR THE TRMM PROJECT

Karen J. Kowalewsky
Applied Research Corporation
8201 Corporate Drive
Landover, MD. 20785

Otto Thiele
Code 613.0
NASA Goddard Space Flight Center
Greenbelt, MD. 20771

1. INTRODUCTION

Several area integral methods used to infer the instantaneous area averaged rain rates, <R>, have been examined by Chiu (1988 a , b), Atlas et al., (1988), Rosenfeld et al., (1988), and Doneaud et al., (1981; 1984). Their methods could be used to accurately estimate area averaged rain rates from satellites if the observations provide a good estimate of the areal coverage of rain rates greater than a specified threshold, and the coefficients of the area integral algorithm are appropriate for the rain regime being investigated. It has been shown that these methods depend on consistent probability density functions (PDF's) of the rain rates. For regions which have a strong diurnal rainfall cycle, the area integral methods may contain serious errors if the rain rate PDF's experience diurnal variations.

As part of the TRMM Ground Truth program, rain rate data have been collected, beginning in September, 1987, from a network of tipping gauges located near the Cape Canaveral and Kennedy Space Center area. A statistical analysis was performed on the rain gauge data set to determine the diurnal variability of the area wide rain rates, the rain rate PDF's, and their effect on the area integral algorithms.

2. RAIN GAUGE DATA

The data we used in this study are rain rates derived from 27 digitally recording tipping rain gauges scattered over an approximate 10 km by 6 km area near Cape Canaveral and the Kennedy Space Center (KSC). A preliminary analysis has been performed on the eleven gauges located near the Kennedy Space Center. The analysis including data from the sixteen gauges at the St. John's rain collection site is in progress. These gauge networks are located within 100 Km of the Patrick Air Force radar site and will be useful in the development of a rainfall climatology study for the TRMM project. A map of the KSC rain gauge network is given in Figure 1. The data used in this study covers the period between February 16, 1988 and August 31, 1988.

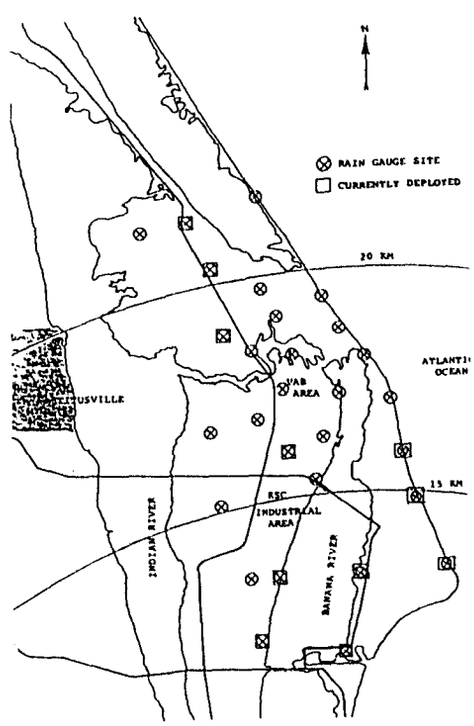

Fig. 1. Cape Canaveral/Kennedy Space Center rain gauge network. The curved lines indicate the distance from the radar located at the Patrick Air Force Base, Florida.

3. DATA ANALYSIS

The first step of the data analysis is to determine the hourly and daily rain accumulations and rain rates. The rain gauge recorder system records gauge tips only during rain events, and the time of these gauge tips are variable. Therefore, the rain rate is the rain amount (r, in mm) that falls during the period of time between tips (ΔT, in hours). Then, the hourly rain accumulations for all the gauges are used to determine the network averaged hourly and daily rain rates for the time it actually rained (conditional average). The network averaged hourly (instantaneous area averaged) rain rate (mm/hr), $\langle R \rangle$, is defined as:

$$\langle R \rangle = \frac{1}{G\ \Delta T} \sum r(I) \qquad (1)$$

where G is the total number of rain gauges, ΔT is equal to one hour, and the index I correspond to the number of measurements for a particular hour. The network averaged daily rain rate (mm/day) is the sum of the network averaged hourly rain rates for the day.

The next step is to compute the fraction ($F(\tau)$) of hourly and daily rain rates that exceed a particular threshold, τ, and analyze the hourly and daily rain rate probability density function for the network. The value of the rain rate threshold will be varied (τ = 0, 1, 5, 10, 20 mm/hr), and comparisons of $\langle R \rangle$ and $F(\tau)$ will be made for each value of τ. The approach for this part of the analysis is similar to that used by Atlas et al., (1988).

4. PRELIMINARY ANALYSIS

In this preliminary analysis, the seasonal diurnal rainfall and network averaged rain rates were determined using the data from the eleven gauges at the KSC site. Figures 2-4 illustrate a sample of the spring and summer network averaged rainfall as a function of time (local standard time). Note that the maximum network averaged rainfall occurs at 2000 LST for the spring, and at 1400 LST for the summer. The spring maximum shown in Fig. 2 was caused by squall line activity which occurred between 1900 LST and 2000 LST on March 19, 1988. In Fig. 3, the 2000 LST maximum was reduced by nearly 66% when the squall line activity was removed from the distribution. The summer rainfall maximum found in Fig. 4 was caused by persistent afternoon thunderstorm activity.

Figure 5 shows the summer network averaged diurnal rain rate, $\langle R \rangle$. The highest value of $\langle R \rangle$ (~7.6 mm/hr) occurs at the same time of the maximum network averaged rainfall (1400 LST), indicating a period of heavy convective rainfall. The network averaged rain rates and accumulations gradually decrease after 1400 LST, as the afternoon thunderstorms dissipate and the rain type changes from convective to stratiform. The high percentage of rainy hours (Fig. 6) found between 1200 LST and 1600 LST confirms the presence of the afternoon thunderstorms. The maximum percentage of rainy hours occur during the time of predominantly convective rain, and gradually decreases during the stratiform rain stage of the storm.

The results from this preliminary analysis indicate that there are diurnal, as well as seasonal, variations in the components that determine the network rain rate PDF's. The analysis of $\langle R \rangle$ as a function of $F(\tau)$ is in progress, and from these results it will be possible to determine the magnitude of the diurnal and seasonal variations on the PDF's and the area integral algorithms.

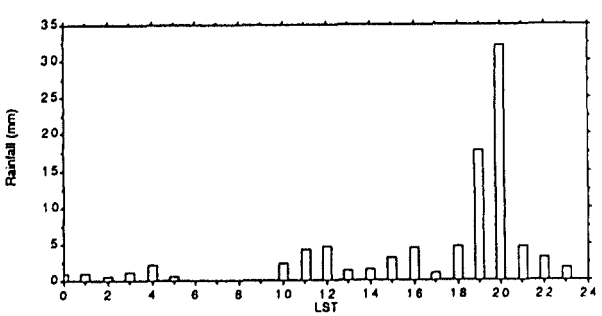

Fig. 2. The KSC network averaged rain rate, $\langle R \rangle$, as a function of time for March 18 through May 2, 1988.

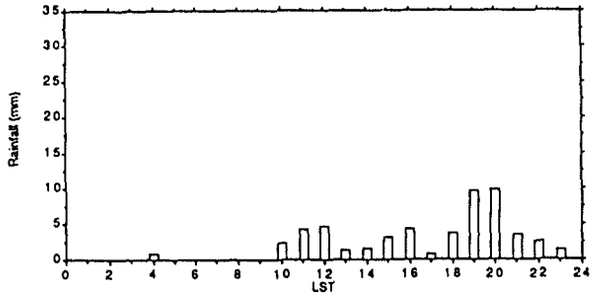

Fig. 3. Same as Fig. 2 except for March 26 through May 2, 1988.

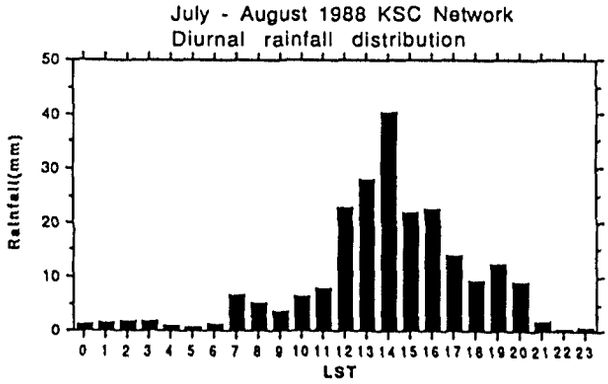

Fig. 4. The July-August 1988 KSC network diurnal rainfall distribution.

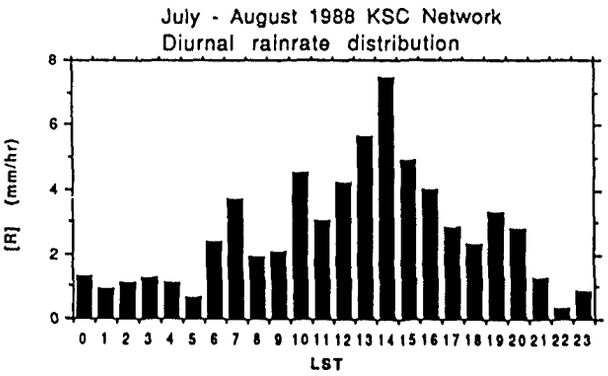

Fig. 5. The July-August 1988 KSC network diurnal rain rate distribution.

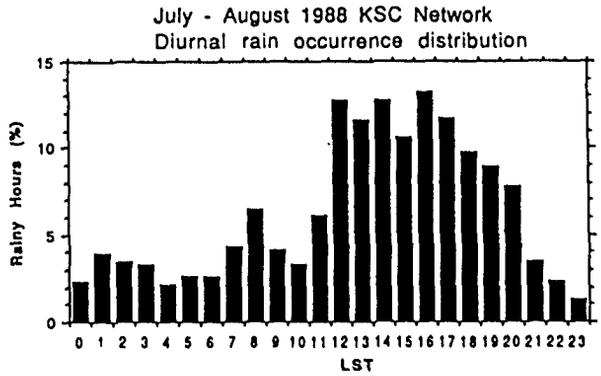

Fig. 6. The July-August 1988 KSC network diurnal rain occurrence distribution.

5. REFERENCES

Atlas, D., D. Rosenfeld, and D. A. Short, 1988: The estimation of convective rainfall by area integral. Part I: The theoretical and empirical basis. Conference on Mesoscale Precipitation: Forecasting. Mass. Inst. of Tech., Cambridge, Massachusetts, Sept. 13-16, 1988.

Chiu, L. S., 1988a: Estimating areal rainfall from rain area. Proceedings, International Symposium on Tropical Precipitation Measurements, October 28-30, 1987, Tokyo. A. Deepak Publishing, Hampton, VA (in press).

Chiu, L. S., 1988b: Rain estimation from satellites: Areal rainfall-rain area relation. 3rd Conference on Satellite Meteorology and Oceanography, Amer. Meteor. Soc., January 31-February 4, 1988, Anaheim, CA.

Doneaud, A. A., P. L. Smith, A. S. Dennis, and S. Sengupta, 1981: A simple method for estimating convective rain volume over an area. Water Resour. Res., 17, 1676-1682.

Doneaud, A. A., S. I. Niscov, D. L. Prienitz, and P. L. Smith, 1984: The area-time integral as an indicator for convective rain volumes. J. Clim. Appl. Meteor., 23, 555-561.

Rosenfeld, D., D. Atlas, D. Short, 1988: The estimation on convective rainfall by area integrals. Part II: The height area rainfall threshold (HART) method. Conference on Mesoscale Precipitation: Analysis, Simulation, and Forecasting. Mass. Inst. of Tech., Cambridge, MA, Sept. 13-16, 1988.

INTERDIURNAL VARIABILITY OF DEEP CONVECTION OVER TROPICAL AFRICA DURING THE SUMMER OF 1983

Adel F. Hanna
and
B. W. Crissman

Research Triangle Institute
Research Triangle Park, North Carolina 27709

1. INTRODUCTION

The African atmosphere in the tropics exhibit different multi-day periods of variability. The easterly waves, for example, with 5-day period and 4000 km wavelength is the most characteristic synoptic disturbance in tropical Africa. Such waves propagate westward off the coast of Africa through the Atlantic region during summer. On the other hand mesoscale systems in the area of the Inter-Tropical Convergence Zone (ITCZ) exhibit shorter time periodicities. Orlanski and Polinsky (1977), using NOAA-4 satellite imagery found that periods of 1 to 3.25 days dominate the variance of the cloud cover of March-May season of the year 1975 over the tropical African continent. In contrast, the interdiurnal variability of IR radiances over the Atlantic Ocean is dominated by longer periods of variability (2.6 - 8.4 day) (Duvel, 1988). While the origin of the easterly waves is related to the shear instability of the mean easterly flow, the origin of the multi-day cloud cover periodicities is not clear. One suggested mechanism for such periodicities considers the excitation of the large-scale internal gravity waves by the diurnal variability of atmospheric stability (Orlanski, 1976).

The purpose of this research is to provide an analysis of the interdiurnal variability of deep convection during Summer, 1983. A target area in West Africa is used to study this variability. This area is characterized by below average rainfall during the Summer of 1983.

2. DATA AND METHOD OF ANALYSIS

The data used in this study were derived from the IR (10.5-12.5 μm) METEOSAT ISCCP-B3 measurements for the months of July and August, 1983. The analyzed area is between latitudes 6.4°N - 7.7°N and longitudes 0° to 15W. The area is divided into 1.3° latitude x .8° longitude regions. IR temperatures as revealed by the counts of channel 2 for different pixels are averaged for each of the regions. The daily values are represented by the 1800 GMT observations which are representative to the diurnal maximum of tropical convection. Missing data are substituted by the 2100 GMT measurement during the same day. Only four 1800 GMT data records are missing during the 62 days of the analysis. Deep convection associated with high cloud cover and low IR temperature is isolated using a threshold temperature of 270° k. Such temperature is typical of the atmosphere at about 5 km heights during Summer in tropical Africa. To exclude the effects of the low cloud cover, values larger than the threshold temperature are considered threshold. Normalized departures from the threshold temperature are calculated. Spectral analysis are applied to regions with more than 50% of non-zero elements in order to examine the dominant periodicities in the data with variations longer than one day.

3. ANALYSIS AND DISCUSSION

Figure 1 represents a typical power spectra for the deep convection time series for two regions within the analyzed area. The short periods of variability (2.7 - 3.2 days) is quite pronounced in the cold cloud temperatures. A secondary peak also exists around 5 days for region 2. At the edge of the analyzed area (7.7°N), which is more close to the core of the ITCZ, Figure 2 reveals similar spectral features to the regional analyses.

The seasonal rainfall during the summer, 1983 in the region of the analysis was less than average. To relate that anomaly feature to the

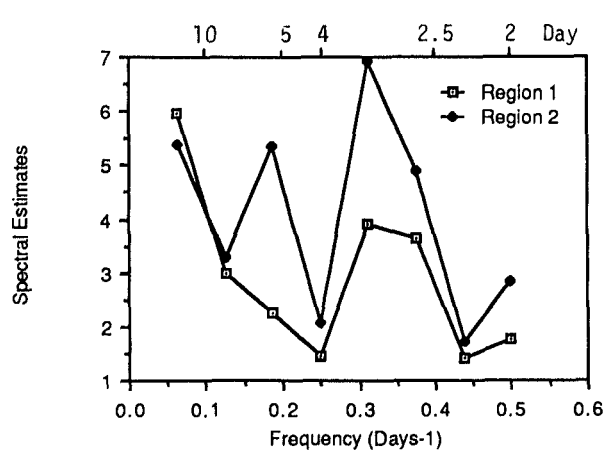

Figure 1. Spectral Analysis of Normalized Cold Cloud Tops Anomaly Time Series Belt (6.4°N - 7.7°N) for the period 1 July 1983 - August 31, 1983.

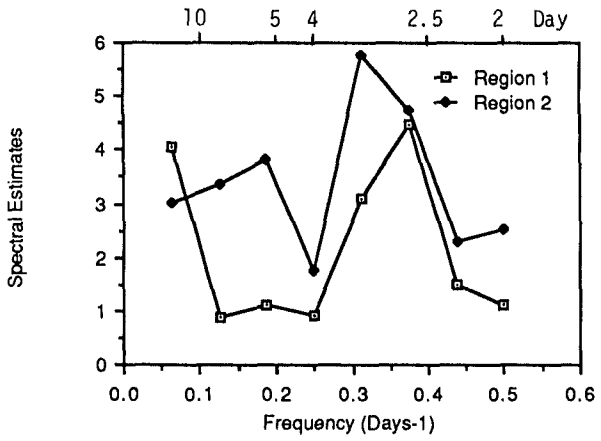

Figure 2. The same as Figure 1 except for cold cloud tops centered at 7.7°N.

interdiurnal variability of the convective and mesoscale systems certain possibilities arise. One might expect less frequent mesoscale and deep convective systems in such a way that the seasonal rainfall is less than average. The other possibility is that such convective systems with the 2 to 3.2 day periods are not capable or vigorous enough to produce the normal amounts of rainfall. The results of this research tends to support either possibility however the analysis is not comprehensive enough to confirm the answers. Seasonal characteristics of the deep convective systems during different years using ISCCP-C1 data over Africa and the Atlantic are subject of future research.

4. ACKNOWLEDGEMENT

The authors are indebted to Lola Olsen, Task Leader, NASA Climate Data System (NCDS) for her enthusiastic technical assistance with the ISCCP Data Set.

5. REFERENCES

Duvel, J.P. (1988). Analysis of Diurnal, Interdiurnal and Interannual variations during Northern Hemisphere Summers using METEOSAT Infrared Channels. J. Climate, 1, 471-484.

Orlanski, I., and L. J. Polinsky (1977). Spectral distribution of cloud cover over Africa. J. Met. Soc. Japan, 55, 483-493.

Orlanski, I. (1976). The trapeze instability in equatorial β plane. J. Atmos. Sci., 30, 1007-1016

JP8A.8

RAINFALL ESTIMATION USING T.I.R METEOSAT IMAGERY OVER THE WESTERN SAHEL (1986-87). Interest of the Maximum Radiative Temperature Technique.

M. Carn-J.P. Lahuec-D. Dagorne-B. Guillot
Antenne ORSTOM, CMS, BP.147, 22302 Lannion (France)

1. INTRODUCTION

Since 1984, the ORSTOM research team based in Lannion, in the premices of the "Centre de Meteorologie Spatiale" (French receiving station for environmental satellites) has been developing a tropical research program called "Veille Climatique Satellitaire" (Climatic Monitoring using satellite Remote Sensing).

Among several tasks dealing with climatic parameters monitoring in Africa, attention has been paid to the development of a rainfall estimation scheme lying on the use of three variables which are related to observed rainfall by means of a multiple linear regression :

- the number of cold clouds, by the pixel resolution which is inferred for a given period from Meteosat TIR channel using a simple thresholding technique ;
- the soil surface maximum radiative temperature called hereafter T°Max, derived also from thermal infrared analysis ;
- the latitude.

2. THE METHODOLOGY

2.1 Background

Most of rain in Sahelian countries come from convective clouds (isolated storms, squall lines, convective clusters... etc). Consequently, a threshold at -40°C was choosen by the nephanalysts from CMS, after numerous tests combining visible and infrared imagery, to discriminate rain bearing clouds over the western Sahel.

However, this method is not perfect :
- thick cold cirrus and, sometimes, non precipitating altocumulus are improperly taken in account,
- clouds with top warmer than -40°C, which can produce some significant rains are not included in the accounting.

The use of surface maximum radiative temperature was suggested from previous works by INRA and IRAT researchers (1). They found that cumulative rainfall amounts were closely related to corresponding cumulative values of T° Max. More recently, SAVANE and SEGUIN (2) have proved that T°Max is useful for assessing evaporation patterns not only in Africa, but also in mid-latitude countries.

The use of latitude is a practical mean to take in account the differences in the physical environment of clouds over West Africa, eventhough it can be judged imperfect or too empiricist. However, as far as the rainfall field is closely related to the latitude in continental western Sahel, this process allows to correct the overestimation of rainfall north of 400 mm. isohyete mean position and, on the contrary, the underestimation which occurs south of this position when using only cold clouds and T°Max parameters.

2.2 Observed rainfall vs cold cloud occurrences (occ), T°Max, Latitude

In 86 and 87, 6 images were processed every day. Files of cold clouds and T°Max were created on a five-day rythm. From this initial process, ten-day, monthly, plurimonthly and seasonal fields of cold clouds and T°Max values were computed all along the rainy season (May to October).

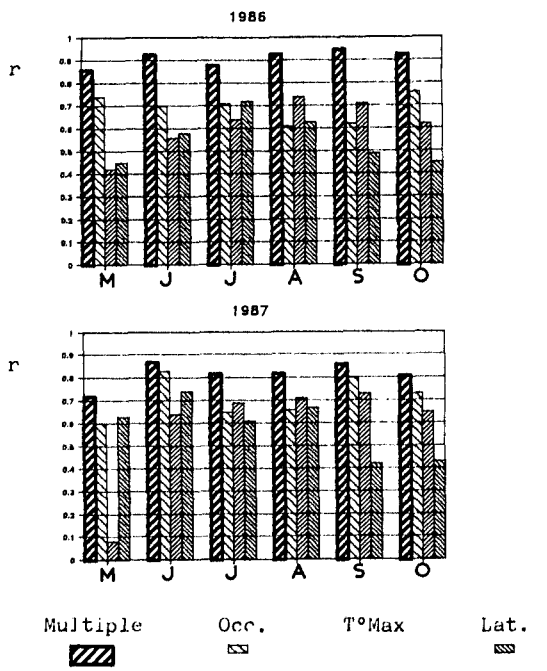

Fig.1. Evolution of simple and global correlation coefficients (r), for monthly periods. Actual Rainfall vs three variables (Occ., T°Max, Latitude) in 1986 and 1987 rainy seasons.

---

(1) INRA : Institut National de Recherche Agronomique - Avignon - (France)
IRAT : Institut de Recherche d'Agronomie Tropicale - Montpellier - (France)

(2) Citation from the summary of a proposed contribution to the next Barcelone meeting (personal communication from SAVANE ane SEGUIN - INRA).

Fig.1 shows the correlation coefficients between observed rainfall and each of the three variables on one hand (simple linear regression), between rainfall and the three variables acting together, on the other hand (multiple linear regression), for monthly periods.

Correlation patterns for both rainy seasons 1986 and 1987 are very similar :

- rain vs cold cloud occurrences : this relationship is quite stable from one month to another over the two years ; the correlation coefficient varies from .60 to .80 ;
- the relationship rain vs T°Max shows a well marked evolution during the season ; poor results are obtained at the beginning and at the end of the season (mainly due to the scarcity of rainy events and to dust and atmospheric pollution) while it works as well as the previous one during the rainy months.
- the multiple linear regression improves the monthly correlation coefficient in a significant manner : .86 is the lower one in 86, .72 is the lower one in 87, both for the month of May.

Valuable results are obtained since the multiple linear regression is computed over a two-month period. The lower correlation coefficient reaches 0.90 for May and June in both cases, and it increases as and when the studied period becomes longer.

In the same way, we notice that the separate correlation coefficients significantly increase since the period is longer.

2.3 Presentation of the algorithm

It occurs that the use of a multiple regression is the best way to obtain suitable estimates :

$$Rain = a\ Occ + b\ T°Max + c\ Lat + Cte \qquad (1)$$

Where :

- Occ. = Number of cold clouds for a given station and a given period of time.
- T°Max = Surface maximum temperature for the same location (and the same period of time).
- lat. = Latitude of the station.

3. RAINFALL ESTIMATES VALIDATION

Validation attempts have been undertaken at the synoptical level for cumulative monthly periods.

Our ground data sets (2) were separated in two sets from which coastal stations were eliminated due to the lack of significancy of T°Max values.

Then the equation was applied to an independant set of 25 (1986) and 22 raingauge locations (1987) in order to match estimated and observed rainfall. (Fig.2).

---

(1) Carn and al. (1987).

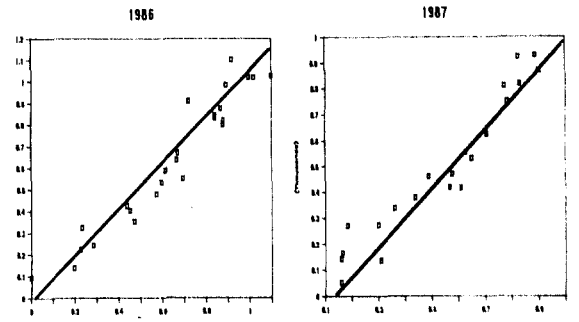

Fig.2. Seasonal Validation Test - 1986 and 1987 -
x axis : Estimated Rainfall
y axis : Actual Rainfall

Scattered diagrams were done to check the accuracy of the method for cumulative monthly periods. The correlation coefficients become significant since the studied period reaches two months (r = 0.77) ; for the whole rainy season, estimates and actual rainfall are strongly correlated (r=.97 in 1986, r=.96 in 1987).(Fig.2)

The spatial distribution of differences between estimates and actual rainfall was checked as well, and it occured that most of the area of our concern enterred the category within ± 10 % error.

Taking in account the results of these validation attempts, we allowed ourselves to generate a rainfall precipitation field derived from the multiple linear regression. Then it was possible to view this field on an image processing system and to draw it on a printing device.

4. INTERANNUAL REPRODUCIBILITY OF COLD CLOUD OCCURRENCES FIELD AND THERMAL FIELD, RELATED TO RAINFALL

In order to know whether or not the thermal field and the cold cloud occurrences field related to rainfall reproduce the same patterns from one year to another, and therefore are relevant to be used in an automatic rainfall estimation process, two indexes have been designed at each station for ten-day and cumulative periods :

PcB= Rainfall per Cold Cloud (3)
PvT= Rainfall per Maximum Temperature (mm/°)

Zones	Areas(km2)	stations
District of Niamey	120 000	16
Republic of MALI	1 250 000	34
Countries of CILSS	5 300 000	71

Table 1. The three zones of the study.

---

(2) Ground data were collected in various ways from National Meteorological Boards, AGRHYMET Center (Niamey), ASECNA (Dakar).
Seventy raingauge locations were used in 86 and 87 to calculate the equation of the regression straight line.

(3) LAHUEC and al. (1986)

Correlation studies have been achieved between 1986 and 1987 PcB on one hand, between 1986 and 1987 PvT on the other hand, at different scales of space (table 1 and fig.3) and time (with ten-day period as a basic increment) from the beginning to the end of the rainy season (May,1 - October,31).

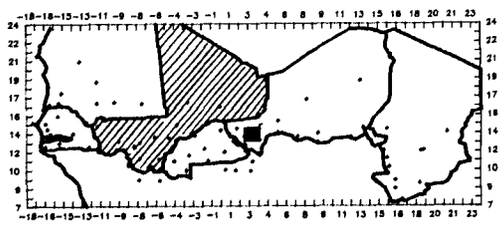

Fig.3. The three scales of the study

CILSS countries Mali Niamey area

4.1 86 PVT vs 87 PvT

Zones	Slope	Intercept	r**	rms
Niamey	0.93	-0.08	0.75	0.10
MALI	1.15	+0.21	0.93	0.15
CILSS	0.99	-0.10	0.91	0.59

Table 2. Results of the linear regression between 86 PvT and 87 PvT

For the whole rainy season and at the three scales of space, PvT are well correlated (table 2) eventhough the correlation coefficient is slightly lower at the local scale than at the synoptic or regional ones.

This result is of a particular interest especially if we consider that in the area of Niamey, isohyetes and PvT fields show a meridian structure, either in 1986 or 1987, which is different from the zonal pattern encountered at the regional and synoptic scales.

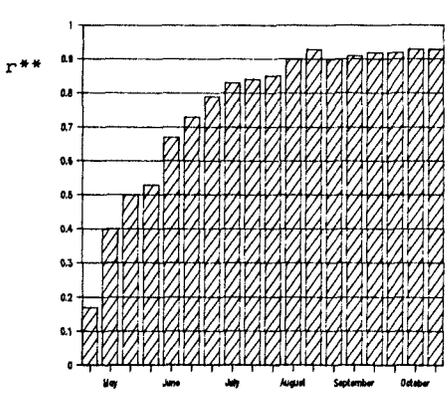

Fig.4.
Correlation between 86 PvT and 87 PvT in Mali
Evolution of r** per cumulative ten-day periods during the rainy season (May,1 to October,31).

For shorter periods as shown in fig.4 which describes the r** coefficient evolution for cumulative periods at the regional scale (MALI), the correlation reaches a satisfactory level since the onset of steady rains is general over the country, i.e at the beginning of July (r** = .80)

We have to point out that atmospheric dust and sand pollutions, which frequently occur in May, are also responsible for poor correlations observed at the beginning of the rainy season.

4.2 86 PcB vs 87 PcB

Zones	Slope	Intercept	r**	rms
Niamey	0.65	+0.85	0.23	1.11
MALI	0.42	+1.94	0.32	1.10
CILSS	0.74	+1.13	0.68	1.65

Table 3. Results of the linear regression between 86 PcB and 87 PcB.

Such good correlations are not found between 86 PcB and 87 PcB, whatever the scales of time and space may be (table 3). Perhaps, this is due to the fact that a single thresholding technique cannot account for the multiplicity of meteorological factors and dynamical processes which generate rainfall and which are obviously variable from a period to another, from a season to another,as well as from an area to another one.

5. CONCLUSIONS

In all cases, the use of three variables in the regression give overall better results than separate calibration in rainfall estimation using satellite data. In particular, surface maximum temperature significantly improves the relationship which would be obtained only from a simple linear regression between cold cloud occurrences (or cold cloud duration) and observed rainfall.

However, one major problem needs further investigations : how to get confident results for periods shorter than one month as far as the accuracy of the method is relevant to statistical means wherin the cumulative process takes a major part in terms of relationship assessment ?

It seems illusive to assess automatic rainfall estimates from a climatology based on a simple accounting of cold clouds, whatever the threshold may be. On another hand, the use of a rainfall index deduced from Soil Surface Radiative Temperature appears much more promising for cumulative periods (two months minimum), and probably for shorter periods provided the parasitic atmospheric effects can be corrected and the rainy season onset adjusted.

6. REFERENCES

Assad, E. and al., 1987 : Approche quantitative de la pluviométrie au Senegal à l'aide d'images IR thermique du satellite Meteosat. Veille Clim. Sat., 13, Lannion, 21-29.

Carn M., Dagorne D., Guillot B., and Lahuec J.P., 1987 : Estimation des précipitations par satellite au Sahel pour la période de mai à septembre 1987. Veille Clim. Sat., 20, Lannion, 26-30.

Lahuec J.P. and al., 1986 : Convection inter-tropicale et pluviométrie. Essai de mise en relation pour l'Afrique de l'Ouest du 11 mai au 20 août 1985. Veille Clim. Sat., 12, Lannion, 13-19.

ANALYSIS OF THE OPTICAL PROPERTIES OF HAWAIIAN CONVECTIVE WARM BAND CLOUDS

A. RIGAUD, C. PONTIKIS, S. BOUADJADJ

METEOROLOGIE NATIONALE, EERM/CRPA
78470 MAGNY LES HAMEAUX

1- Introduction

The visible satellite imagery allows the determination of some cloud characteristics related to cloud brightness. However no simple relationship exists between these parameters. Nevertheless cloud thickness and cloud surface-to-volume ratio are the main factors determining brightness. Their theoretical influence has been studied by many authors (McKee and Cox (1974), McKee and Klehr (1978), Mosher (1979), Reynolds et al. (1978)).

Comparisons between experimental results (aircraft in-cloud measurements) and the theoretical ones obtained with a radiative transfer model using Monte Carlo technics are necessary to define the influence of the different cloud parameters on the brightness. McKee et al. (1983) have used cloud droplet size distributions obtained with an instrumented aircraft as model input. However, the electrostatic disdrometer measuring size distributions had several problems, thus introducing incertitudes.

The Joint Hawaii Warm Rain Project (JHWRP 1985) collected dynamic, thermodynamic and microphysical data on warm band clouds. Along with these data, GOES West visible satellite data were also collected for this area and allowed the observation of cloud visible brightness. Preliminary results concerning this comparison are presented in this paper.

2- Data set

The JHWRP took place from 1 July to 15 August 1985. The characteristic properties of band clouds developing off the east coast of Hawaii have been collected. The University of Wyoming King Air aircraft was used. The cloud droplet size distributions were measured by the FSSP spectrometer for radii from 1.5 to 22.5 µm. Liquid water contents were simultaneously measured with a Johnson Williams probe and calculated according to the FSSP droplet distributions. Cloud studies started usually at 6 a.m. local time. Several traverses were made in each cloud at regular height intervals starting either at cloud base or cloud top.

Visible satellite images obtained at the same time and concerning 12 characteristic days during the JHWRP experiment have been studied. Two successive images are separated by half an hour. Every pixel represents 1Kmx1Km. The navigation program allows the localisation of aircraft penetrations on the corresponding image. The maximum observed brightness value was 255 (relative units) and the mean sea brightness value in the same time was 64.

3- Mean characteristics of band clouds

The mean cloud features can be calculated for each cloud by using all samples. Table 1 shows the mean characteristics of some clouds sampled during July 10,12 and 19 : temperature, liquid water content, vertical velocity, droplet concentrations in FSSP, 1DC, 2DC and 2DP probes ranges, depth and optical thickness. The optical thickness of each layer is calculated according to the classical expression taking into account the mean droplet size distribution of each layer. The total optical thickness is then obtained by integrating the whole depth.

The differenciation between precipitating and non precipitating clouds is made with microphysical features: no signal is collected for 1DC, 2DC and 2DP probes in non precipitating clouds sampled on July 19. The liquid water contents and the optical thickness are lower than in precipitating clouds.

Figure 1 presents the mean FSSP droplet size distributions respectively for clouds N9 (July 10), N4 (July 12) and N10 (July 19). Distribution shapes for clouds N9 (July 10) and N4 (July 12), which have developed precipitation, are similar with a mean radius of 9 µm, while the non precipitating cloud N10 (July 19) has a distribution with a 3 µm mean radius. The droplet spectral distributions classically used for numerical simulation calculating satellite cloud brightness are the ones defined by Deirmendjian in 1969, referred as C1 and C3 (with mean radii respectively of 4 µm and 2 µm). Essential differences exist between them and the observed ones in the above mentionned Hawaiian band clouds. The shape of distribution C3 with a mean radius of 2 µm is close to the mean one calculated for N10 (July 19). However, droplet concentrations are very different. Further, for the precipitating clouds N9 (July 10) and N4 (July 12), the corresponding distributions are very different from C1 as well for concentrations as for radii. The corresponding liquid water contents are also very different from the ones used for theoretical calculations.

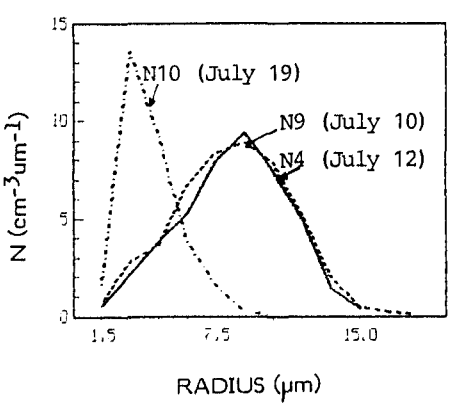

FIGURE 1

CLOUD	t (°C)	Q_L (gm^{-3})	WI (ms^{-1})	FSSP (cm^{-3})	1DC (l^{-1})	2DC (l^{-1})	2DP (l^{-1})	DEPTH (m)	OPTICAL THICKNESS
JULY 10									
N8	13.6	0.33	0.68	66.6	3.4	13.4	1.8	2500	95.8
N9	12.5	0.73	0.96	140.1	7.0	23.6	3.2	2300	161.4
N10	12.7	0.42	0.24	103.5	0.8	2.6	0.6	1500	73.3
JULY 12									
N4	14.0	0.56	1.07	130.0	1.4	6.5	1.0	1800	113.0
N5	14.6	0.71	1.07	140.0	1.2	5.8	1.2	1600	108.0
N6	14.9	0.28	0.52	97.0	1.8	7.8	2.0	1800	81.0
JULY 19									
N10	14.9	0.10	0.57	76.5				1000	20.0
N11	13.0	0.14	0.72	74.1				1200	21.3

TABLE 1

4- Comparison between satellite and aircraft data

Bands were oriented (NW-SE) perpendicular to the tradewind direction. The corresponding main horizontal axis measured roughly 25 to 50 Kms and the mean cloud width was about 15 Kms. Due to their geometric shape, the bands can be assimilated to semi-infinite slabs. Figures 2,3 and 4 represent the maximum brightness values observed along the main horizontal axis against the corresponding width, respectively for bands observed on July 10, 12 and 19. The circles represent the theoretical values calculated by Reynolds et al. (1978) by using the C1 distribution defined by Deirmendjian (1969).

For July 12, a partial overlap of two bands was observed, thus leading to an increase of maximum brightness values. The agreement between observed and

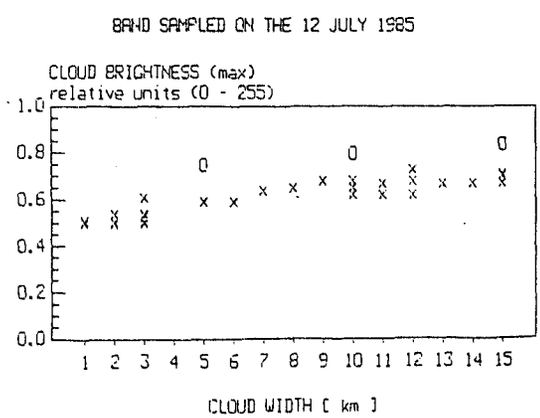

FIGURE 3

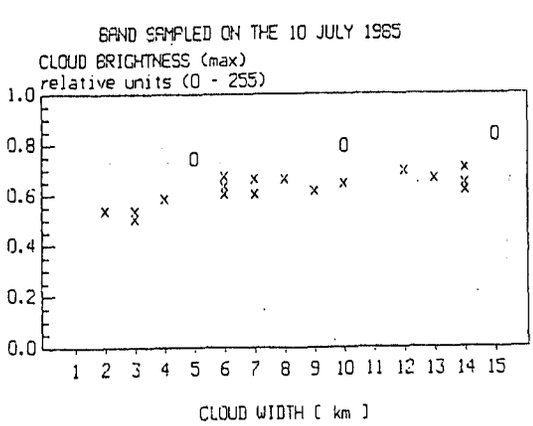

FIGURE 2

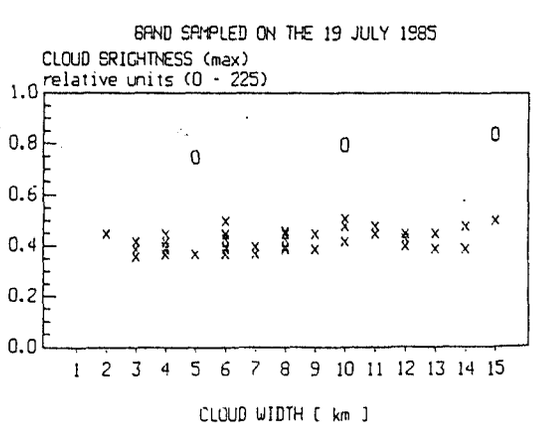

FIGURE 4

calculted values presented in Fig.3 is fair.
For July 10, the band was an isolated one. There is no satisfactory agreement between observed and calculated values presented in Fig.2. As mean droplet size distributions are similar for both bands (Fig.1), overlap is probably responsible for the observed differences.
Further for July 19, there is no agreement between observed and calculated values (Fig.4). This could be due to the differences between the real size distribution and C1 and corresponding liquid water contents used for theoretical calculations.

5- Conclusion

Theoretical and observed brightness for convective cloud bands sampled during JHWRP have been compared.
Although these bands can be assimilated to semi-infinite slabs, important differences appear. This behavior could be due to the differences between droplet size distributions and corresponding liquid water contents.
Further the oceanic character of these bands leading to lower concentrations than the ones used in calculations could also be related to this behavior. Overlap of bands can also lead to an increase of the brightness values.

References

MCKEE T.B. and S.K. COX (1974): Scattering of visible radiation by finite clouds. J. Atmos. Sci., 31, 1885-1891
MCKEE T.B. and J.T. KLEHR (1978): Effects of cloud shape on scattered solar radiation. Mon.Weather Rev.,106, 399-404
MCKEE T.B., M. DE MARIA, J.A. KUENNING and S. COX (1983): Comparison of Monte Carlo calculations with observations of light scattering in finite clouds. J. Atmos. Sci., 40, 1016-1023
MOSHER F.R. (1979): Visible flux variations across finite clouds. Ph.D. Univ. Wisconsin, Madison.
REYNOLDS D.W., T.B. MCKEE and K.S. DANIELSON (1978): Effects of cloud size and cloud particles on satellite-observed reflected brightness. J. Atmos. Sci., 35, 160-166.

TROPICAL APPLICATION OF TECHNIQUES TO MEASURE SURFACE EMITTANCE AND CLOUD LIQUID WATER CONTENT OVER LAND

Andrew S. Jones
Thomas H. Vonder Haar

U.S. Army Center for Geosciences
Cooperative Institute for Research in the Atmosphere (CIRA)

Colorado State University
Fort Collins, Colorado

1. INTRODUCTION

Satellite estimates of cloud liquid water have been largely limited to ocean regions due to the cold radiative background the ocean surface provides (Grody, 1976, Staelin *et al.*, 1976). An assumption made over ocean surfaces is that the atmospheric transmittance is large for the two channels which are generally used, the 22.235 GHz water vapor absorption line, and a window channel at approximately 31 GHz, which is generally a good assumption. However, the 85.5 GHz channels on the Special Sensor Microwave/Imager (SSM/I) have stronger attenuation due to cloud liquid water than the lower frequencies, which allows for the estimation of cloud liquid water over land surfaces which have surface emittances approaching unity (*i.e.* radiatively warm).

Since cloud attenuation is stronger at 85.5 GHz, the microwave brightness temperatures observed are depressed when clouds containing liquid water pass over the warm surface features due to the colder ambient temperatures of the clouds. Therefore assuming a uniform cloud liquid water distribution and given a temperature profile from which to calculate upwelling microwave emission from the the clouds, the integrated cloud liquid water amount can be estimated by comparing observed brightness temperatures with calculated brightness temperatures for varying cloud liquid water amounts. The calculations are performed assuming absorption processes dominate, which for 85.5 GHz means the technique is valid for non-precipitating clouds in which the water droplet size is small. Scattering effects become important for larger precipitating cloud liquid water and ice and has been used to relate the 85.5 GHz brightness temperature to a rainfall threshold (Spencer *et al.*, 1988).

Previous work using the technique over the northeast Colorado region during the Convective Initiation and Downburst Experiment (CINDE) in the summer of 1987 showed an ability to estimate integrated cloud liquid water with an approximate retrieval accuracy of 0.15 $kg{\cdot}m^{-2}$ from numerical error analysis (Jones, 1988). Validation data for that particular case study was sparse but the spatial distribution of cloud liquid water appeared reasonable. A new data set is currently being studied to perform the necessary validation.

In this paper I will briefly outline the procedure and data requirements for measurement of surface emittance and retrieval of integrated cloud liquid water over land. Applications and potential effects on the technique when used in the tropics are discussed in the later part of the paper with examples from Hurricane Gilbert.

2. THEORETICAL BACKGROUND

The integrated radiative transfer equation for a non-scattering, plane-parallel atmosphere with a non-blackbody surface boundary condition is

$$\begin{aligned} L_\nu(0) = {} & \epsilon_\nu B_\nu(T_s)\tau_\nu(p_s,0) \\ & + \int_{p_s}^{0} B_\nu[T(p)]\frac{\partial\tau_\nu(p,0)}{\partial p}dp \\ & + (1-\epsilon_\nu)[\tau_\nu(p_s,0)]^2 \int_{p_s}^{0} \frac{B_\nu[T(p)]}{[\tau_\nu(p,0)]^2}\frac{\partial\tau_\nu(p,0)}{\partial p}dp \\ & + (1-\epsilon_\nu)[\tau_\nu(p_s,0)]^2 B_\nu(T_{space}) \end{aligned}, \quad (1)$$

where $L_\nu(0)$ is the radiance at the top of the atmosphere at a frequency ν, ϵ is the surface emittance, B is the Planck function, τ is the transmittance, T, temperature, and p pressure, where the subscript s denotes surface values. T_{space} is the cosmic background microwave emission, and is small ($T_{space} \approx 2.7$ K). Calculation of the atmospheric transmittance $\tau_\nu(p_1,p_2)$ is based on the Millimeter-wave Propagation Model (MPM) developed by Liebe (1985). The MPM requires additional information about the atmospheric temperature and moisture profiles which in the Colorado case study was obtained from the high density network of CLASS soundings during CINDE.

2.1 Approximation of the RTE for frequencies < 50 GHz

Assuming a relatively transparent atmosphere at microwave wavelengths such that the atmosphere can be assumed to be isothermal and applying the Rayleigh-Jeans approximation, the apparent microwave brightness temperature is given by (Grody, 1976)

$$T_B = T_s[1-(1-\epsilon_\nu)\tau_\nu^2]. \quad (2)$$

The sensitivity of T_B from Equation 2 is,

$$\frac{\partial T_B}{\partial \tau_\nu} = -2T_s(1-\epsilon_\nu)\tau_\nu, \quad (3)$$

which is proportional to $(1-\epsilon_\nu)$. This implies that for high surface emittance values close to unity (such as land surface values) the radiometer is insensitive to atmospheric variations, thus explaining the limitation of determining cloud liquid water over land from previously flown microwave satellites which had lower frequency radiometers than the SSM/I.

2.2 Radiative Transfer Equation at 85.5 GHz

At 85.5 GHz the atmosphere is no longer transparent to cloud liquid water and can not be approximated as having an isothermal atmosphere as in Equation 2. The transmittance of the atmosphere decreases with increasing cloud liquid water which in turn decreases the observed brightness temperature due to the vertical thermal structure of the atmosphere. In Figure 1 (from Spencer *et al.*, 1988), the upwelling brightness temperature at 85.5 GHz is shown as a function of increasing cloud top height (and therefore colder cloud top temperatures) and cloud liquid water concentrations. Notice in Figure 1 that the brightness temperature depression is larger for high cloud tops and virtually non-existent for low level clouds. The ability of the retrieval process to measure cloud liquid water is dependent on a sufficiently large brightness temperature contrast from the surface brightness temperature and the contribution of the colder brightness temperature from the cloud.

3. PROCEDURE

3.1 Surface emittance measurement

A background surface emittance is calculated using coincident GOES infrared imagery with the SSM/I imagery during clear sky conditions previous to the cloud formation to determine the variability in the surface radiative properties. Results from a Colorado study showed significant differences between areas of irrigation and recent precipitation to dry land regions with values ranging from approximately 0.8 to 1.0 (Jones, 1988). Since the SSM/I 85.5 GHz channels have an effective-field-of-view (EFOV) of 13 × 15 km (Hollinger, *et al.*, 1987) this has possible applications for initialization of mesoscale models which need soil surface wetness information at a relatively high spatial resolution for developing mesoscale circulations between moist and dry regions.

In our Colorado case study, coincident GOES infrared data was used to determine the skin surface temperature, T_s, and was corrected for atmospheric effects (Jones *et al.*, 1987). Equation 1 is then solved for the surface emittance, ϵ_ν, using the observed microwave radiance, $L_\nu(0)$, in clear sky conditions which are determined for the EFOV at 85.5 GHz from available GOES visible and infrared data. Using GOES infrared data, the surface emittance retrieval absolute accuracies were estimated to be approximately 0.012.

A brief outline of the surface emittance retrieval method is given below.

1) Remap SSM/I microwave data into the GOES satellite projection.

2) Determine cloud/nocloud threshold using GOES infrared and visible data. If cloudy within the microwave EFOV, go on to the next microwave data point.

3) Calculate the surface skin temperature within the microwave EFOV.

4) Compute the microwave atmospheric transmittance using the Liebe MPM model and in-situ atmospheric soundings.

5) Calculate the surface emittance by solving the microwave radiative transfer equation for ϵ_ν.

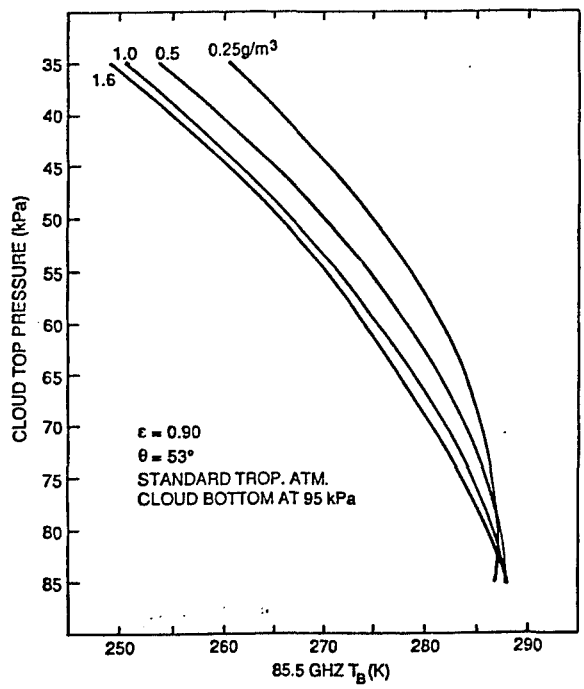

FIG. 1: Brightness temperature as a function of vertical extent and cloud water content at 85.5 GHz. Calculations assume Rayleigh absorption, a zenith angle of 53°, a surface emittance of 0.9, and a cloud base at 950 hPa (from Spencer *et al.*, 1988).

3.2 Cloud liquid water retrieval method

The cloud liquid water is retrieved by calculating theoretical brightness temperatures and comparing them to the observed brightness temperatures measured by the SSM/I radiometer for the 85.5 GHz channels. The surface emittance results from an earlier time period are used as an estimate of the current surface emittance values. The difference between the calculated and observed brightness temperatures is used to make a new estimate of the cloud liquid water content. The cloud liquid water iteration process ends once the calculated and observed brightness temperatures are within the instrument noise level. Retrieval of cloud liquid water is possible at any location over the land which has an estimate of ϵ_ν and SSM/I 85.5 GHz coverage.

To summarize the cloud liquid water retrieval method:

1) Calculate the theoretical brightness temperature T_B for clear sky conditions given the in-situ atmospheric sounding, surface temperature, and estimated surface emittance.

2) Find the difference between calculated and observed brightness temperatures.

3) Add cloud liquid water to the sounding and continue adding cloud liquid water iteratively until the observed and measured brightness temperatures agree to within the noise level of the instrument.

4) Sum cloud liquid water throughout the depth of the cloud to produce the integrated cloud liquid water amount of the cloud.

3.3 Data Requirements

The method requires some a priori knowledge of the surface emittance characteristics for the land area under study. The land surface emittance values vary depending on the surface composition, wetness, and roughness, among other variables. This makes it necessary to determine the spatial surface emittance features from a recent data sample before the cloud retrieval time period. The surface emittance measurement requires coincident microwave and infrared data with in-situ sounding data for the microwave transmittance calculations. The cloud liquid water retrieval process needs only the 85 GHz microwave data, in-situ sounding data for the transmittance calculations, and the previous estimates of the surface emittance.

4. DISCUSSION

GOES channel 8 infrared imagery of Hurricane Gilbert on 1203 UTC 15 September 1988 in Figure 2 contrasts sharply with the SSM/I 85.5 GHz horizontal polarization imagery in Figure 3 which has been remapped to match the GOES imagery. The difference between image times is small (approximately 5 minutes) and in both images white represents colder effective brightness temperatures. The most noticeable feature is the lack of obscuring high level cloudiness of the most active rain bands of the Hurricane in the 85.5 GHz SSM/I imagery. Since heavy precipitation is occurring in association with the Hurricane, scattering processes are also occurring in addition to the absorption processes which the cloud liquid water retrieval method assumes. This means that precipitating clouds would need to be flagged before processing the SSM/I data so that erroneous cloud liquid water amounts would not be retrieved. This was done in the Colorado CINDE case study using the 255 K threshold suggested by Spencer *et al.* (1988). For the Hurricane Gilbert example, cloud liquid water information over the land surface such as the Yucatan Peninsula could be retrieved for clouds which were determined to be non-precipitating.

Retrieval of cloud liquid water in the tropics should also be more accurate due to the higher freezing level of the clouds which means more of the cloud water is in liquid form. As Figures 2 and 3 showed, non-precipitating ice is generally transparent at 85.5 GHz and therefore it is not possible to measure the water in ice form as well as in liquid form.

The tropics also have warm surface temperatures as well which is necessary to produce a significant brightness temperature signal to retrieve cloud liquid water. If surface temperatures are cold, the brightness temperatures of the clouds may approach or exceed the surface brightness temperature depending on the surface emittance value. This means that for a cold surface, several cloud liquid water amounts may satisfy the observed brightness temperature within the instrument noise level. Therefore the higher the brightness temperature contrast between the surface and the cloud, the larger the cloud liquid water signal.

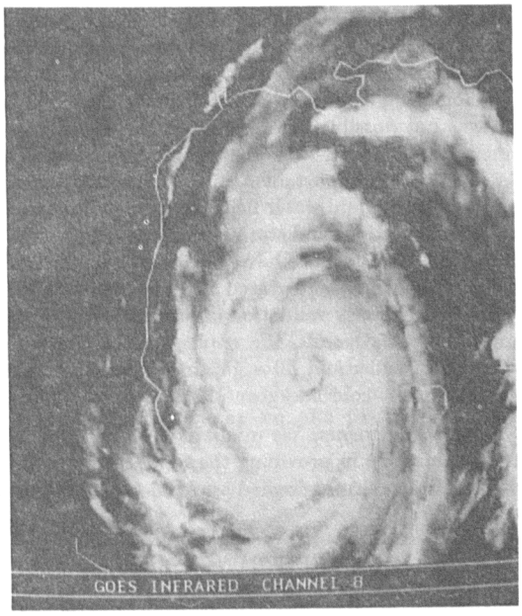

FIG. 2: GOES channel 8 infrared imagery of Hurricane Gilbert 1203 UTC 15 September.

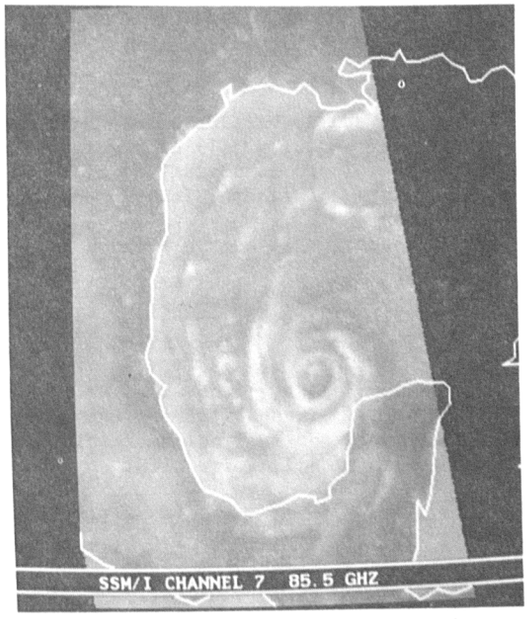

FIG. 3: Image of SSM/I 85.5 GHz (horizontal polarization) brightness temperatures for Hurricane Gilbert 1208 UTC 15 September.

5. CONCLUSIONS

By being selective in the type of cloud from which cloud liquid water can be retrieved (*i.e.* non-precipitating) the method offers a preliminary step in finding more about integrated cloud liquid water budgets in the tropical atmosphere which was not possible before without the higher frequency channels of the SSM/I. Also, the techniques discussed are capable of detecting important surface emittance features and integrated cloud liquid water fields which may influence later mesoscale circulations and storm system development. While the data sets used to date have had limited validation data, spatial distributions of integrated cloud liquid water appeared reasonable. Necessary validation is currently under way with a new data set. Overall, the application of this technique to areas over land could fill a gap in current methodologies which rely on the cold background signature of the ocean.

Acknowledgements. We would like to thank Dr. Richard Savage for his help in providing the SSM/I data used in this work. This research was funded by ARO Grant DAAL03-86-G-0190.

REFERENCES

Grody, N. C., 1976: Remote sensing of atmospheric water content from satellites using microwave radiometery. *IEEE Trans. on Antennas and Propag.*, **AP-24**, 155–162.

Hollinger, J., R. Lo, G. Poe, R. Savage, and J. Peirce, 1987: *Special Sensor Microwave/Imager user's guide.* Naval Research Laboratory, Washington, D. C., 120 pp.

Jones, A. S., Microwave remote sensing of cloud liquid water and surface emittance over land regions, M.S. Thesis, Colo. State Univ., 1988.

Jones, A. S., D. W. Hillger, J. F. W. Purdom, and T. H. Vonder Haar, 1988: Enhanced image products by limb-correction and smoothing of VAS radiance measurements. *Preprint Volume, Third Conf. on Sat. Meteor. and Ocean.*, 31 January - 5 February, Anaheim, CA (AMS), 105–108.

Liebe, H. J., 1985: An updated model for millimeter wave propagation in moist air. *Radio Sci.*, **20**, 1069–1089.

Spencer, R. D., H. M. Goodman, and R. E. Hood, 1988: Precipitation retrieval over land and ocean with the SSM/I, Part 1: identification and characteristics of the scattering signal. *submitted to J. Atmos. and Oceanic Tech.*

Staelin, D. H., K. F. Kunzi, R. L. Pettyjohn, K. L. Poon, R. W. Wilcox, and J. W. Waters, 1976: Remote sensing of atmospheric water vapor and liquid water with the Nimbus 5 Microwave Spectrometer. *J. Applied Meteor.*, **15**, 1204–1214.

THE INFLUENCE OF ATMOSPHERIC STRATIFICATION ON SCATTEROMETER DATA

Jean-François Louis and Ross N. Hoffman

Atmospheric & Environmental Res., Inc.
Cambridge, MA 02139

1. INTRODUCTION.

Scatterometer data have been proposed as a way of measuring surface winds over the ocean. A scatterometer is an active radar which emits in a wavelength scattered by the centimeter length waves of the ocean. The strength of the signal can be related to the amplitude of the waves, and thus to the wind. Such an instrument was flown on the SEASAT satellite. Other scatterometers are planned both by NASA and ESA, to be flown in the 1990's.

Since the surface winds are not measured directly by the scatterometer, but are inferred from the scattering cross-section of the underlying surface, they are subject to several ambiguities. First of all, there is a directional ambiguity. Each measurement is usually compatible with two or more wind directions. These are assigned different probabilities, but the direction with the largest assigned probability is not always the correct one. This problem has been extensively studied (Wurtele et al., 1982) and algorithms have been designed to minimize the errors associated with the directional ambiguity.

The second source of ambiguity is the fact that the scattering cross-section of the surface is more closely related to the surface stress than to the wind, and that the stress depends on the stability of the atmospheric stratification as well as on the wind. That is why the scatterometer measurements are reported as "neutral stability winds" at a certain height above the surface rather than as true winds.

For oceanographic applications this second type of ambiguity is generally not important since the neutral stability wind is a direct measure of the stress and, thus, is sufficient to provide the forcing to drive ocean models. In meteorology however, the distinction between true wind and neutral stability wind may be quite important, for example if these data are to be used to provide initial conditions for numerical weather prediction (NWP).

This paper quantifies the problems associated with the stability ambiguity, using a simple boundary layer model. A variational analysis method is suggested, which allows direct assimilation of scatterometer data.

2. BOUNDARY LAYER AND SURFACE STRESS.

The influence of atmospheric stratification on wind stress is well known. The now classical Monin-Obukhov similarity theory, which relates momentum and heat fluxes to the profiles of wind and temperature, has been verified by observations (e.g. Businger et al., 1971) and used extensively as a basis for boundary layer models.

In this work we use the boundary layer model developed by Louis (1979), as used in the ECMWF model. It is based on the Businger flux-profile relationships, integrated over a layer typical of the lowest layer of a forecast model. The resulting relationships between the surface stress $\underset{\sim}{\tau}$ the wind at the lowest model level $\underset{\sim}{V}$ and the potential temperature difference $\Delta\theta$ between the surface and the model level are expressed in terms of the Richardson number

$$Ri = \frac{gz\,\Delta\theta}{\theta\,|V|^2} \tag{1}$$

which defines the stability of the atmospheric stratification. In (1), g is the acceleration of gravity, z is the height of the lowest model level and θ is the virtual potential

The surface stress is expressed by the formula:

$$\underset{\sim}{\tau} = -\rho \left(\frac{k}{\ln \frac{z}{z_0}}\right)^2 f(Ri)\ |\underset{\sim}{V}|\ \underset{\sim}{V} \tag{2}$$

where ρ is the air density, k the von Karman constant (0.4) and z_0 the roughness length of the surface. The function f of the Richardson number is defined as follows. In stable cases (Ri>0):

$$f(Ri) = \frac{1}{1 + \frac{b\,Ri}{\sqrt{1+dRi}}} \tag{3a}$$

and in unstable cases:

$$f(Ri) = 1 - \frac{b\,Ri}{1 + c\left(\frac{k}{\ln \frac{z}{z_0}}\right)^2 \sqrt{\frac{z}{z_0}\,|Ri|}} \tag{3b}$$

The constants b, c and d have the values 10, 75 and 5 respectively.

Over the oceans the problem is somewhat more complicated than over land since the roughness length z_0 itself depends on the stress. We use the Charnock (1955) formula:

$$z_0 = a\,\frac{|\underset{\sim}{\tau}|}{\rho g}, \tag{4}$$

with a = 0.032. This means that (2) is actually an implicit formulation for $\underset{\sim}{\tau}$.

We now define a neutral stability wind. It is the wind that would produce the same stress as the true wind if the stratification were neutral.- From (3) it can be seen that, in neutral stability (Ri = 0), f(0) = 1. Hence if we call $\underset{\sim}{U}$ the neutral stability wind, (2) can be written:

$$\underset{\sim}{\tau} = -\rho \left(\frac{k}{\ln \frac{z}{z_0}} \right)^2 |\underset{\sim}{U}| \; \underset{\sim}{U} \qquad (5)$$

It can be seen, from (4) and (5), that there is a one to one relationship between $\underset{\sim}{\tau}$ and $\underset{\sim}{U}$, while the relationship between τ and the true wind $\underset{\sim}{V}$ is not unique. Figure 1 shows how $\underset{\sim}{\tau}$ varies with $|\underset{\sim}{V}|$ and $\Delta\theta$ when these values are taken at 30 m. It can be seen that the stress is most sensitive to stratification for slightly stable situations. This sensitivity is amplified when the height z becomes greater.

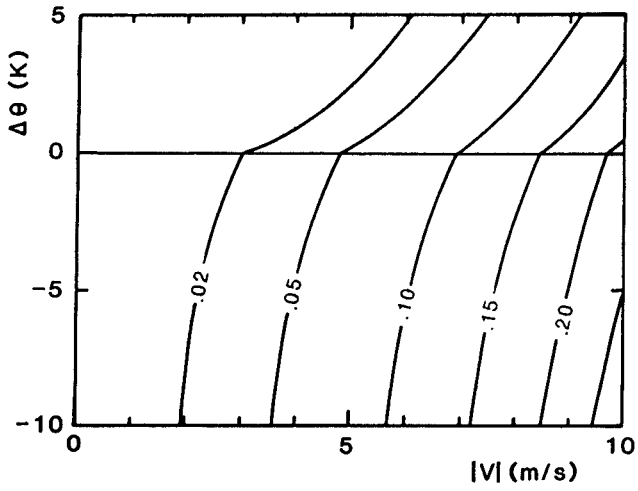

Fig.1. Surface stress in terms of the wind magnitude at 30m. and the potential temperature difference between 30m and the surface.

3. VARIATIONAL ANALYSIS OF SCATTEROMETER DATA.

The representation of the scatterometer measurement as a neutral stability wind obscures the true nature of the measurement, namely, surface stress. Since the stress depends on both the wind and the temperature profile, the information obtained from the scatterometer could be applied to either quantity, or both. If we already knew the wind field exactly over a region observed by the scatterometer, we could deduce the drag coefficient, and thus use the scatterometer to define the surface layer stability. In practice we do not know the true wind speed, nor do we know the true boundary layer temperature, specific humidity and sea surface temperature T_s. Generally we would have a background (or first guess) field for these variables from a NWP assimilation system either in the form of a short (6h) forecast, an analysis performed independently of the scatterometer data, or climate values. For the sake of discussion we will assume that T_s and q are to be held fixed, i.e. not analyzed.

Given the scatterometer measurements of neutral stability wind U^o and the background fields of V^B and T^B, the question then is: is it appropriate to use the scatterometer neutral stability winds directly to update V^B or must we consider a multivariate analysis scheme to update both V^B and T^B. The answer to this depends on the relative uncertainties of V^B and T^B and the relative sensitivity of neutral stability wind $\underset{\sim}{U}$ to V and T. The uncertainties on V^B and T^B may be estimated by considering the size of the errors made by misplacing the location of a front. Very roughly, the scales are 10 m/s and 10°K. Figure 1 already suggests that |U| is almost uniformly sensitive to |V|. The sensitivity of |U| to T varies widely with |V| and T; at low values of $|\underset{\sim}{V}|$ and for neutral and slightly stable conditions the sensitivity of |U| to T is as important as the sensitivity to $|\underset{\sim}{V}|$.

We conclude that special objective analysis methods are required for scatterometer data. Our techniques deal directly with the stability ambiguity. We assume the directional ambiguity has been already resolved. We will use a variational approach which will allow adjustments to T as well as V. We favor the variational approach over the conventional OI approach when non-standard data is available because of the flexibility and ease of adding additional data and other information within the variational formulation. In fact the variational approach has been used to remove the ambiguity of the SASS scatterometer winds (Hoffman, 1982, 1984).

The variational analysis approach (Sasaki, 1970) finds the smallest possible adjustments to the model variables which give good agreement with the data. In the case where the errors are Gaussian, this approach is formally equivalent to a Bayesian estimator

Our point of departure for this work is the neutral stability winds at anemometer height. These data are not model prognostic variables. An observation of U^o should affect (virtual) temperature as well as velocity in the boundary layer. That is, we wish to make small changes to T^B and $\underset{\sim}{V}^B$ so that, when the new analyzed values T^A and $\underset{\sim}{V}^A$. are used to calculate neutral stability winds, better agreement with the observation U^o is obtained. That is, using a squared difference norm [$\|a-b\| = (a-b)^2$] we wish to minimize

$$S = \gamma_T \|T-T^B\| + \gamma_V \|\underset{\sim}{V}-\underset{\sim}{V}^B\| + \|\underset{\sim}{U}(\underset{\sim}{V},T)-\underset{\sim}{U}^o\| \qquad (6)$$

where U is the neutral stability wind depending on V and T and where γ_T and γ_V are parameters controlling the tradeoff between fidelity to the background fields and fidelity to the data. These parameters might vary geographically and temporally. If errors in T^B and V^B are correlated, then the lack of fit to the background should be measured by $X^T C^{-1} X$ where $X^T = (T, u, v)$ and C is the error covariance matrix of X. The T and $\underset{\sim}{V}$ which minimize S are then the analysis T^A and $\underset{\sim}{V}^A$.

The simplest implementation for a scatterometer analysis system is the following: (1) Interpolate (i.e., analyze) the neutral stability anemometer height SCAT winds to the model grid using as a first guess the values of $\underset{\sim}{U}$ diagnosed

from the model (6 h) forecast. (2) Interpolate (analyze) all other available data in the conventional way. This yields a preliminary analysis of V and T which does not depend on the scatterometer data. (3) Combine the results of (1) and (2) gridpoint by gridpoint by minimizing S defined above. For this purpose the preliminary analyses of step (2) become the background fields T^B and V^B defined above. This paper is concerned primarily with step (3).

Some extensions to the above are possible. For example, horizontal consistency can be enforced by minimizing a global measure of S and adding some smoothness constraints. Other indirect measurements of boundary layer properties can also be included easily. If the boundary layer model diagnoses surface stress, this in turn could be used to compute radar backscatter for comparison with the σ^0 values themselves. Cloud drift winds at the top of the boundary layer could also be used to advantage.

There are a variety of techniques for minimizing functions like S. These range from Newton methods to searching methods. The more efficient methods require derivatives of S to be calculated; thus derivatives of $\underset{\sim}{U}$ with respect to $\underset{\sim}{V}$ and T are required.

It remains to specify $\underset{\sim}{U}$. This is done by using the model described in section 2. Equating the two expressions (2) and (5) implicitly defines $\underset{\sim}{U}$ as a function of $\underset{\sim}{V}$ and T.

The derivatives of |U| with respect to |V| and T are shown on Fig. 2a and 2b, as functions of the wind speed and temperature difference between the height z and the sea surface. These plots were computed for a height of 50 m. It can be seen that $\partial U/\partial T$ is close to unity over a wide range of wind speeds and atmospheric stability. difference between 50m and the surface. On the other hand $\partial U/\partial T$ is uniformly small for unstable conditions but can be large in slightly stable cases, especially at low wind speeds, where the sensitivity of U to T becomes larger than to V. Note that this sensitivity to stability also increases with the height of the analysis level.

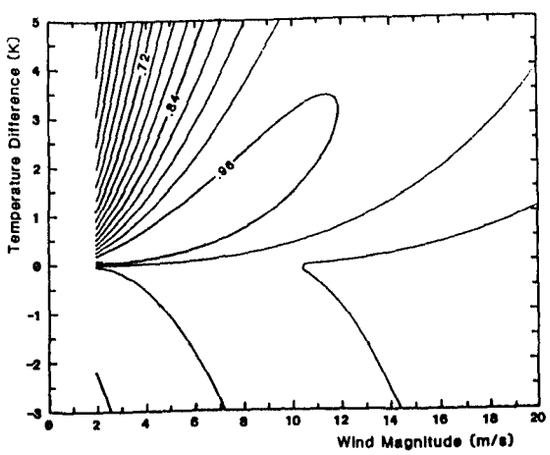

Fig. 2a. Derivative of the 19m neutral stability wind to the 50m true wind magnitude ($\partial U/\partial|\underset{\sim}{V}|$), as a function of that wind and the temperature

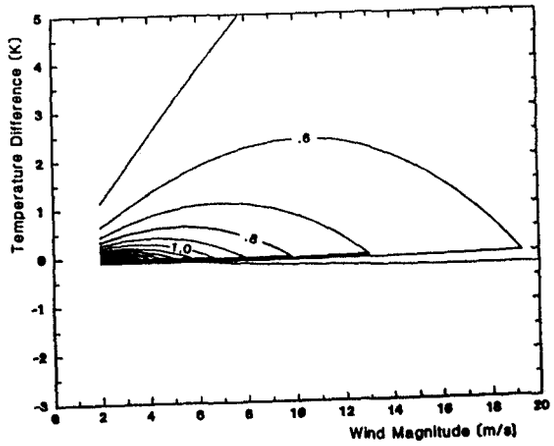

Fig. 2b. Same as 2a, but for $\partial U/\partial T$.

We next consider the sensitivity of the objective function S to the parameters γ_T and γ_V. This is illustrated in Fig. 3 for a single case in which $|\underset{\sim}{V}^B| = 6$m/s, $T^B - T_S = 2$K, Z = 50m and $|\underset{\sim}{U}^0| = 8$m/s. The only difference between the panels is that $\gamma = \gamma_T = \gamma_V$ varies from 10 to 1 to 0.1. In each panel, the location of the observation (O), background (B) and analysis (A) is shown in the space of the analysis parameters $T - T_S$ and $|\underset{\sim}{V}|$. The analysis point is at the minimum of S. For large γ the observation creates only a small perturbation to the quadratic function measuring the difference between analysis and background. For $\gamma = 1$, the variational analysis strikes an approximate balance between data and background. For small γ, the analysis matches the data more closely, but the analyzed point A does not necessarily approach point O where V = U and $T = T_S$. Instead, it approaches the line of constant stress corresponding to the neutral stability wind U^0. For $\gamma = 0$, the locus of the minimum of S would be that same line. All the points on that line would satisfy $U(V,T) = U^0$. It should be noted that, even though one may not have much confidence in

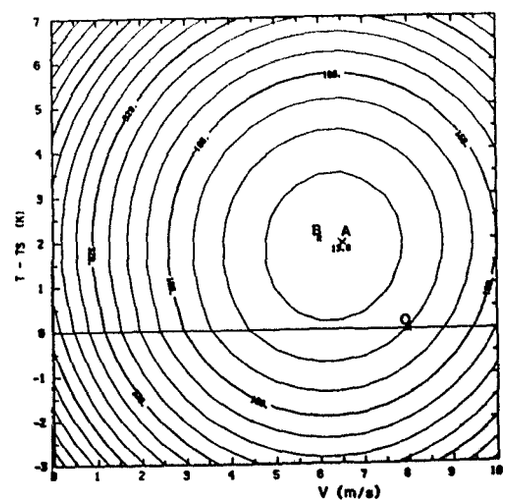

Fig. 3a. Cost function S in terms of wind magnitude and temperature difference at 50 m for γ=10.

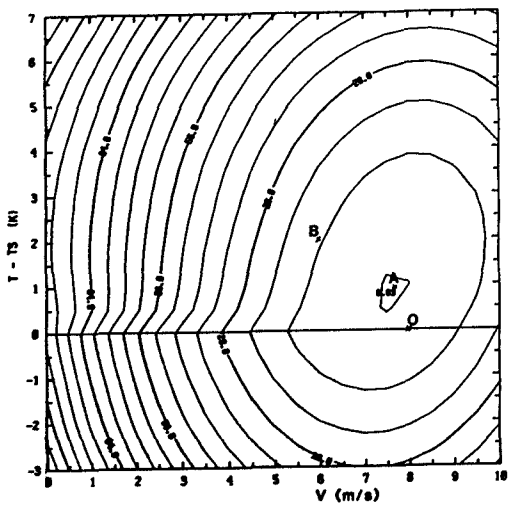

Fig. 3b. Same as 3a, with γ=1.

the background field, some weight must be given to it (i. e. γ must be $\neq$ 0), otherwise there is no unique solution to the analysis problem.

Finally, figure 4 shows the magnitude of the analysis increments that would be obtained for different values of the background field. The observed neutral stability wind is 8m/s, and the background field is given as much weight as the observation, i.e. $\gamma_V = \gamma_T = 1$. As expected the effect of stability on the wind velocity increment is felt mainly in the stable region. The kink in the curves of fig. 4a corresponds to the point at which the analyzed profile switches from stable to Although the effect of stability on the wind increment may seem relatively small, it should be remembered that it is a systematic effect. Neglecting it would consistently underestimate the winds in the stable regions.

4. ACKNOWLEDGEMENT

This work was performed under NASA (JPL) contract No. 957644.

5. REFERENCES

Brown, R.A., 1983: On a Satellite scatterometer as an anemometer. J. Geophys. Res., 88(C3), 1663-1673.

Businger, J.A., J.C. Wyngaard, Y. Izumi & E.F. Bradley, 1971: Flux-profile relationship in the atmospheric surface layer. J. Atmos. Sci., 28, 181-189.

Charnock, H., 1955: Wind stress on a water surface. Q.J.R. Meteorol. Soc., 81, 639-640.

Hoffman, R., 1982: SASS wind ambiguity removal by direct minimization. Mon. Weather Rev., 110, 434-445.

Hoffman, R. N., 1984: SASS wind ambiguity removal by direct minimization. II. Use of smoothness and dynamical constraints. Mon. Weather Rev., 112, 1829-1852.

Hoffman, R. N., 1985: Using smoothness constraints in retrievals. In Advances in Remote Sensing Retrieval Methods, edited by A. Deepak.

Louis, J.-F., 1979: A parametric model of vertical eddy fluxes in the atmosphere. Boundary-Layer Meteor., 17, 187-202.

Sasaki, Y., 1970: Some basic formalisms in numerical variational analysis. Mon. Weather Rev., 98, 875-883.

Wurtele, M.G., P.M. Woiceshyn, S. Peteherych, M. Barowski, and W.S. Appleby, 1982: Wind direction alias removal studies of SEASAT scatterometer derived winds, J. Geophys. Res., (87(C5), 3365-3377.

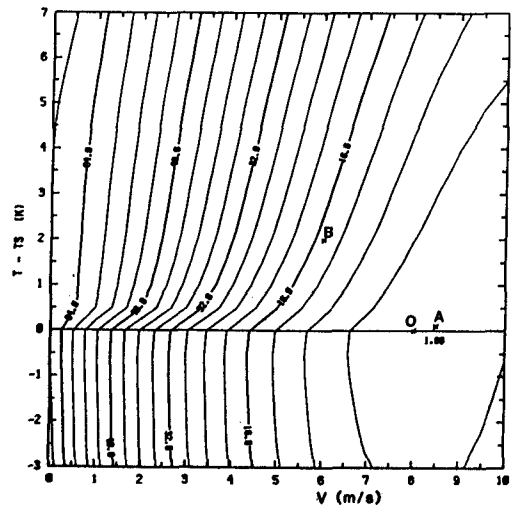

Fig. 3c. Same as 3a, with γ=0.1.

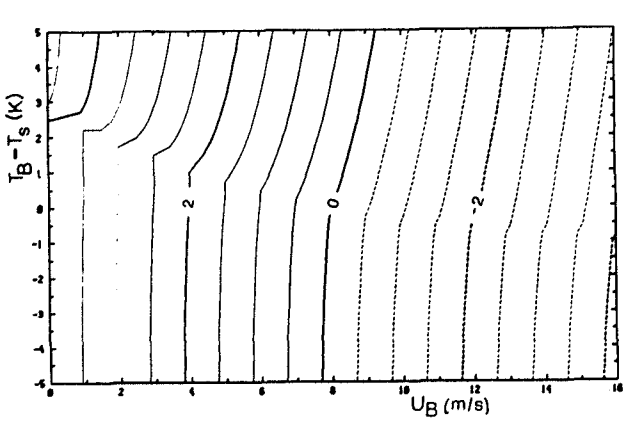

Fig. 4a. Analyzed 50m wind increment, in terms of background wind and temperature difference.

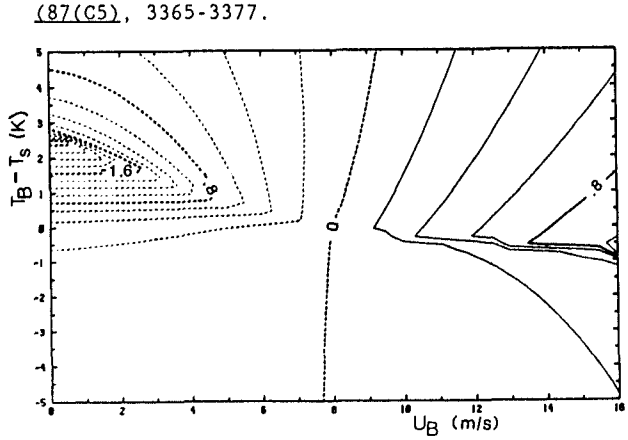

Fig. 4b. As 4a, but for analyzed 50m temperature increment.

A COMPARISON OF VAS AND ODW DATA AROUND A SUBTROPICAL COLD LOW

James L. Franklin[1], Christopher S. Velden[2]
Christopher M. Hayden[3], and John Kaplan[1]

[1] NOAA/AOML/Hurricane Research Division
Miami, Florida
[2] University of Wisconsin
Cooperative Institute for Meteorological Satellite Studies
Madison, Wisconsin
[3] NOAA/National Environmental Satellite Data and Information Service
Madison, Wisconsin

1. INTRODUCTION

A study by Neumann (1985) has shown that the rate of improvement of tropical cyclone track forecasts has decreased in recent years. Many believe that an important limitation of track forecast accuracy is the poor quality of the anaylsis of the hurricane environment, and that the potential of new dynamical and statistical tropical cyclone models will not be fully realized until the quantity and quality of observations over the oceans is increased (Burpee, 1984). Since 1982 the Hurricane Research Division (HRD) of the NOAA/Atlantic Oceanographic and Meteorological Laboratory has conducted several experiments in which Omega dropwindsondes (ODW's) were deployed to measure the wind and thermodynamic fields within about 1000 km of the centers of tropical cyclones. Efforts are ongoing at HRD to produce three-dimensional analyses of the hurricane environment for these cases (e.g., Lord and Franklin, 1987) using data from the ODW's and all other available sources, including satellite products, and to assess the impact of these data on hurricane track forecasts.

A qualitative study by Franklin and Lord (1988) compared data obtained from ODW's in the environment of Hurricane Debby (1982) with soundings obtained by the VAS (Visible Infrared Spin Scan Radiometer Atmospheric Sounder) instrument onboard the GOES satellite. They found that the quality of the VAS retrievals was mixed, leading to differences of 5-12 ms^{-1} in 400 mb gradient winds between estimates computed from ODW and VAS thermodynamics. A statistical analysis of this case was also done by Velden et al. (1984).

The areal coverage of the Franklin and Lord comparison was limited somewhat by the distribution of clouds around Hurricane Debby. On 1-2 Sept. 1988, HRD conducted a dedicated "clear-air" field experiment to collect an additional ODW data set to compare with data from the VAS. The flight tracks and locations of the ODW's are shown in Fig. 1. The experiment was coordinated with the Cooperative Institute for Meteorological Satellite Studies (CIMSS) at the University of Wisconsin. Water-vapor satellite imagery clearly showed that a mid-tropospheric subtropical cold low was moving westward through the region at this time. The low was not characterized by heavy convection during the experiment, allowing VAS retrievals to be made by CIMSS throughout the entire domain.

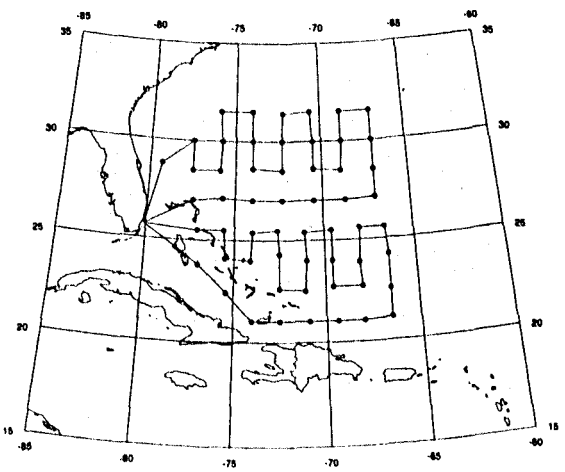

Fig 1. Flight tracks of the two NOAA WP-3D aircraft during the ODW field experiment, 1830 UTC 1 Sept. to 0430 UTC 2 Sept. 1988. ODW drop locations are indicated by the closed circles.

2. DATA AND ANALYSIS PROCEDURES

A data set consisting of in-situ (INS) observations was collected, consisting of data from the 55 ODW's deployed during the experiment, flight-level data from the 2 NOAA P-3 aircraft used to deploy the ODW's, and reports from surface ships. The ODW's and flight-level data were collected over a 10-hour period from 1830 UTC 1 Sept. 1988 to about 0430 UTC 2 Sept. Most of the ODW's were released from between 400 and 500 mb. The ODW soundings were postprocessed as described by Franklin (1987), run through a low-pass filter with a cutoff wavelength of 100 mb, and then sampled at 50 mb intervals for analysis. Flight level data were filtered horizontally with a filter cutoff of 15 minutes (the approximate spacing of the ODW's). Flight-level temperatures were adjusted to the nearest even 50 mb level using a lapse rate determined from the top 50 mb of the two nearest

ODW soundings. Flight-level data from one of the two flights were not included in the INS data set due to an inconsistency between the flight-level temperatures and the ODW's.

VAS retrievals were produced using the "simultaneous" retrieval algorithm (Hayden, 1988). The retrievals were taken between 2218 and 2258 UTC 1 Sept. The first guess for the soundings was provided by a 12 hour forecast from the RAFS (Regional Analysis and Forecast System). Values from the first guess fields at the locations of the retrievals make up the data set identified by "FGS" below. The VAS soundings were quality controlled using a combination of automated and manual techniques. The ODW's were not used in the quality control process.

Three sets of temperature and mixing ratio analyses were made using the HRD Spline Analysis (Lord and Franklin, 1987). Sounding data from the VAS retrievals ("VAS", below) were analyzed objectively at the mandatory pressure surfaces at and below 500 mb. Similar analyses were also produced for the first guess soundings ("FGS"). Finally, the in-situ ("INS") data set was analyzed at 50 mb levels from the surface to 500 mb. Other quantities as described below were computed from the temperature and moisture analyses.

The HRD Spline Analysis contains a low-pass filter, enabling both VAS and ODW data to be analyzed on the same horizontal scale. The cutoff wavelength for this filter was set to 5° lat/lon. This ensures that both the INS and VAS analyses will depict the same scales of motion, and nearly eliminates the influence of data density from the analyses. The distribution of both VAS and INS data points at 700 mb (the distribution is very similar at other levels) over the domain analyzed is shown in Fig. 2. The overlapping distribution of data is seen to be excellent. (By definition, the distribution of FGS points is identical to VAS.)

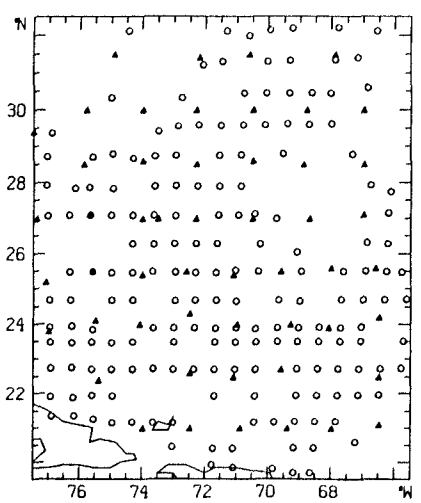

Fig 2. Location of INS (▲) and VAS (○) observations at 700 mb used as input to the objective analyses.

3. RESULTS AND DISCUSSION

Analyses of 850 mb temperature for INS, VAS, and FGS data are shown in Fig. 3a-c. The INS analysis is seen to be fairly flat, while the VAS analysis indicates a moderate east/west temperature gradient, particularly in the northern part of the domain. A similar but considerably weaker gradient can be seen in the FGS analysis. Instead of acting to weaken this FGS gradient to be more in line with the INS data, the VAS data have acted to increase the gradient. The FGS surface temperature analysis (not shown) contains very similar gradients to the 850 mb VAS analysis in the northwest corner of the domain, and may be responsible for some of the 850 mb VAS error. The effect of the surface first guess will be evaluated in future work. The statistics in Table 1 show that the VAS analysis compares less favorably with INS than does the FGS analysis, in terms of mean error (bias), standard error, and root-mean-square error. The VAS/INS correlation, however, is somewhat better than the FGS/INS correlation.

Analyses of 500 mb temperature for INS, VAS, and FGS data are shown in Fig. 3d-f. The mid-level cold low is easily identified in the INS analysis by the -8°C contour. A weak minimum in approximately the proper location can also be identified in the VAS analysis. Both analyses show strong gradients to the southwest of the cold low, and weak gradients to the north and northwest. It is seen immediately that the VAS analysis is much improved over the FGS analysis, which places the cold center off the analysis domain and indicates similar gradients to the northwest and southwest of the low. Statistics in Table 1 show that the VAS improved the standard and root-mean-square error, as well as improved the correlation with INS.

INS, VAS, and FGS analyses of 700 mb mixing ratio are shown in Fig. 3g-i. The VAS improves the depiction of the moisture minimum centered near 28°N, 74°W, relative to FGS. A dry bias in FGS is reduced, particularly in the northern third of the domain. These improvements are quantified in Table 1.

Inspection of Table 1 reveals some interesting items. It is seen that temperature biases in the VAS were always warmer than those of the FGS. Algebraic increases in the bias ranged from 0.7-1.1°C. It is also seen that the FGS has a strong dry bias at low levels, and that this bias is significantly reduced by the VAS. This dry bias has been previously observed by Schreiner and Hayden (1988). Examination of the standard errors suggests that VAS has improved the analyses at 500 mb, and degraded them at 850 mb. Results for 700 mb are mixed. Curiously, correlations with INS are better for the VAS than FGS at all levels for both temperature and mixing ratio. This suggests that the general effect of VAS modifications to the first guess is to improve the phase, but not necessarily the magnitude of the horizontal variations.

The quality of the horizontal gradients from the VAS can be evaluated in a number of ways. Here we use the temperature and moisture analyses and their derivatives (which are also a direct product of the HRD Spline Analysis; no finite differencing is involved) to compute gradient winds at 500 mb. Winds are computed using INS, VAS, and FGS thermodynamic data, but all start out from an identical surface pressure analysis. Comparison of these wind fields (Fig. 3j-l) shows similar features in the INS and VAS analyses, but the amplitudes of the features are much stronger in the VAS analyses. The RMS vector error of the VAS gradient winds is 7.4 ms^{-1}; errors for the INS and FGS gradient winds are 5.0 and 6.0 ms^{-1}, respectively. (These

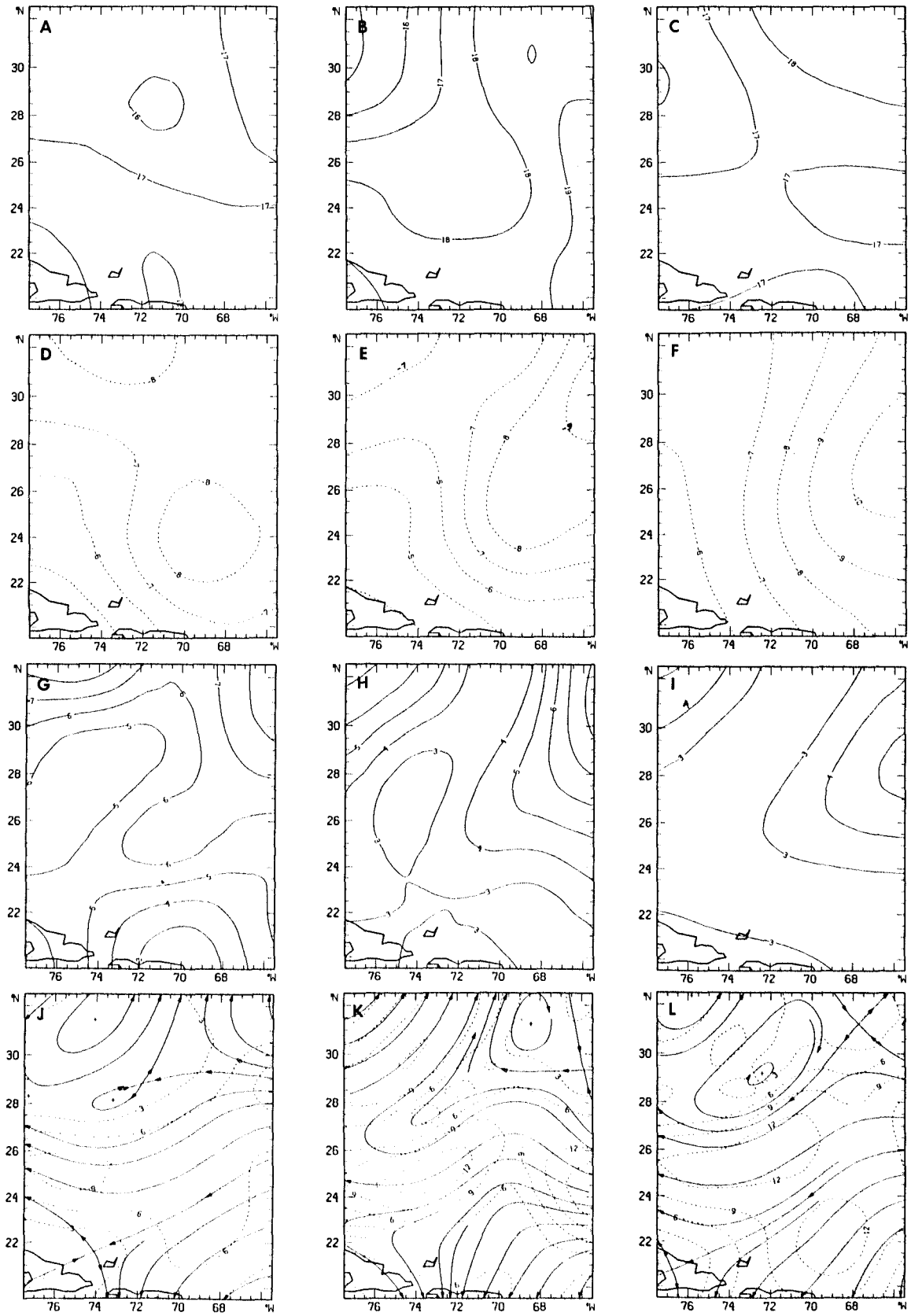

Fig. 3. Objective analyses of 850 mb temperature (°C) for INS (a), VAS (b), and FGS (c); 500 mb temperature for INS (d), VAS (e), and FGS (f); 700 mb mixing ratio (gkg^{-1}) for INS (g), VAS (h), FGS (i); and 500 mb gradient wind (ms^{-1}) for INS (j), VAS (k), and FGS (l). Nominal time of analyses is 0000 UTC 2 Sept. 1988. Filter cutoff was 5° latitude for all analyses.

Table 1

Error statistics for the VAS and FGS analyses. The error E is defined as the difference from the INS analysis: (VAS-INS) or (FGS-INS). The error is evaluated on a regular 1° lat/lon grid of points. The statistics shown are E, the mean error (or bias), S, the standard deviation of the errors E (standard error), RMSE, the root-mean-square error, and R, the correlation coefficient with the INS analysis. Statistics are given for temperature (T) and mixing ratio (Q) for the levels indicated. Units are °C and g/kg, where appropriate.

STATISTIC:	E		S		RMSE		R	
LEVEL/VARIABLE	VAS	FGS	VAS	FGS	VAS	FGS	VAS	FGS
850 MB T	0.9	0.2	1.1	0.8	1.4	0.8	0.26	-.07
700 MB T	1.6	0.8	0.8	0.8	1.8	1.1	0.59	0.40
500 MB T	0.5	-.6	0.8	1.1	1.0	1.3	0.85	0.65
850 MB Q	-0.6	-2.6	2.4	1.9	2.5	3.2	0.11	-.22
700 MB Q	-1.5	-2.4	0.9	1.1	1.7	2.6	0.78	0.64
500 MB Q	-0.5	-0.7	0.3	0.5	0.5	0.8	0.91	0.68

errors are determined as the differences from an analysis of actual wind observations from the NOAA P-3's and the ODW's.) Although the VAS gradient winds at 500 mb are not as accurate as those of the first guess, the general tendency of VAS performance to improve with altitude suggests that a mid-level VAS wind shear or thickness product might be useful.

4. CONCLUDING REMARKS

The comparisons identified several areas where the VAS performed poorly (i.e., worse than the first guess), as well as areas where the VAS performed well (better than the first guess). It should be noted, however, that the first guess used in this study was quite good, and may have limited the ability of the VAS to demonstrate improvements. Many of these results are consistent with those of previous ODW/VAS comparisons. They suggest that as optimum ways of using VAS data in the analysis of the hurricane environment and the tropics are explored, the most useful products may be mid-tropospheric wind shear or thickness products, as well as low level moisture. In the hurricane environment, VAS data may turn out to be extremely valuable in estimating winds in layers above where ODW's can be dropped by the P-3's.

We have only had a short period of time for the analysis of data from the experiment on 1-2 Sept. 1988. We expect to complete several additional investigations by the time of the conference, including tests of various quality control techniques on the sounding set, evaluations of some integrated quantities such as precipitable water, wind shear, and thickness, and estimates of the relationship of errors in the first guess to errors in the final soundings.

5. REFERENCES

Burpee, R. W., D.G. Marks and R.T. Merrill, 1984: An assessment of dropwindsonde data in track forecasts of Hurricane Debby (1982). Bull. Amer. Meteor. Soc, **65**, 1050-1058.

Franklin, J.L., 1987: Reduction of errors in Omega dropwindsonde data through postprocessing. NOAA Tech. Memo., ERL AOML-65, Miami, 22pp.

——, and S.J. Lord, 1988: Comparisons of VAS and Omega dropwindsonde thermodynamic data in the environment of Hurricane Debby (1982). Mon. Wea. Rev., **116**, 1690-1701.

Hayden, C.M., 1988: GOES-VAS simultaneous temperature/moisture retrieval algorithm. J. Clim. Appl. Meteor., **27**, 705-733.

Lord, S.J., and J.L. Franklin, 1987: The environment of Hurricane Debby (1982). Part I: Winds. Mon. Wea. Rev., **115**, 2760-2780.

Neumann, C. J., 1985: Trends in forecasting the tracks of Atlantic tropical cyclones: An update through 1984. Preprints, Ninth Conf. Probability and Statistics in Atmospheric Science, Virginia Beach, Amer. Meteor. Soc., 109-115.

Ooyama, K.V., 1987: Scale controlled objective analysis. Mon. Wea. Rev., **115**, 2479-2506.

Schreiner, A.J., and C.M. Hayden, 1988: An evaluation of VAS satellite moisture retrievals and moisture bogus data in the Gulf of Mexico. Report from the Cooperative Institute for Meteorological Satellite Studies, Madison, 16pp.

Velden, C.S., W.L. Smith and M. Mayfield, 1984: Application of VAS and TOVS to tropical cyclones. Bull. Amer. Meteor. Soc., **65**, 1059-1067.

SATELLITE OBSERVATIONS OF HURRICANE GILBERT

Eugene Kratz, Ralph Ferraro, Martha E. Maiden, and Deborah Carr

S M Systems and Research Corporation
Landover, Maryland

John Alishouse
Henry F. Drahos, Jr.

National Environmental Satellite,
Data and Information Service
Suitland, Maryland

1. INTRODUCTION

Hurricane Gilbert, one of the most powerful storms of the 20th century, began as an easterly wave off the coast of Africa in late August of 1988 and assumed hurricane status upon reaching the Caribbean where it terrorized Gulf Coast residents and awed the meteorological community. As Gilbert approached the Cayman Islands, its winds were estimated to be in excess of 160 mph (258 km/hr). The only other storm in this century to boast such a threatening force was Hurricane Camille. Camille's winds were estimated at 190 mph (306 km/hr) as it converged on the Gulf Shore of Mississippi, August 17, 1969. Gilbert's most notable feature was its record low central pressure of 26.13 inches (88.5 kPa), observed as the hurricane approached Mexico's Yucatan Peninsula, September 13. No lower barometric pressure has ever been recorded in the Atlantic-Gulf of Mexico-Caribbean region of tropical storm activity. The lowest pressure on record previous to Gilbert was 26.35 inches (89.2 kPa) during the 1935 Labor Day hurricane off the coast of Long Key, Florida (Ludlum, 1988).

Gilbert was observed by several satellite sensors during its passage through the Caribbean. Among the sensors were the Special Sensor Microwave/Imager (SSM/I), and the Special Sensor Microwave/Temperature (SSM/T). Measurements from these instruments when combined with visible and infrared satellite images from the Advanced Very High Resolution Radiometer (AVHRR) lead to a unique depiction of the storm and far more useful information about Gilbert than can be inferred from the sparse surface and upper level observations that presently exist for the storm.

2. SENSOR DESCRIPTIONS AND CAPABILITIES

2.1 SSM/I

The SSM/I is a passive microwave radiometer system (Hollinger, et al, 1987). The radiometer travels in sun-synchronous near-polar orbit and has an ascending equatorial crossing of 0612 LST (local standard time). The SSM/I instrument operates at four frequencies: 19.3, 22.2, 37.0 ,and 85.5 GHz. Vertical and horizontal polarizations are provided for each frequency except the 22.2 GHz channel, which has only vertical polarization. The 19.3, 22.2, and 37.0 GHz channels are sampled every 25 km in the along-scan and across-scan directions and the 85.5 GHz channel is sampled every 12.5 km. The SSM/I scans the earth with a conical pattern and an earth incidence angle of 53 degrees. The effective fields of view (EFOV) of the channels are 45x70, 40x60, 30x38 and 14x16 km for the channels in ascending order of frequency. The 22.2 GHz channel is at the center of a weak water vapor absorption band. This channel, when combined with the other channels, permits the depiction of total precipitable water (TPW) and cloud liquid water (CLW) (Alishouse, et al, 1989a, 1989b). The 85 GHz and 37 GHz channels can be utilized to detect precipitation (Spencer, et al, 1988) while other channels can be used to infer surface winds over ocean (Wilheit, 1979).

2.2 SSM/T

The SSM/T is a 7 channel and frequency microwave radiometer that makes vertical temperature profiles of the atmosphere (Drahos, et, al, 1987). The SSM/T measures brightness temperatures in the 50-60 GHz oxygen complex. Each scan comprises seven cross-track earth views with a horizontal swath width of 1595 km. The field of view at nadir is 175 km. (Maiden, et al, 1989) The SSM/T can yield significant temperature structure and detect heavy cloud and precipitation areas (Piepgrass, et al, 1987).

2.3 AVHRR

The AVHRR on board the NOAA 10 spacecraft provides data in the following five spectral intervals: 0.58-0.68 μm, 0.725-1.10 μm, 3.55-3.93 μm, 10.3-11.3 μm, and 11.5-12.5 μm (Kidwell, 1986). The AVHRR has an instantaneous field of view (IFOV) of 1.4 milliradians which yields a nadir resolution of 1.1 km. It scans the earth spanning an angle of ± 56 degrees from nadir. The purely visible spectral interval can provide data on cloud structure, cloud amount, and upper level winds. The IR spectral intervals can provide significant information on cloud top heights and cloud temperatures.

3. SUMMARY

The data provided by the previously discussed satellite sensors can greatly enhance sparse surface and upper level observations of Gilbert and further our understanding of this gigantic storm. In this poster paper, color enhanced images from all four sensors are presented along with concurrent surface and upper level data. Combining results from these spectrally diverse sensors conveys a unique and full representation of this historic storm.

4. REFERENCES

Alishouse, J.C., S. Snyder, and J. Vongsathorn, 1989a: Determinations of Total Precipitable Water in the Tropics from the SSM/I. Fourth AMS Conference on Satellite Meteorology and Oceanography, San Diego, CA.

Alishouse, J.C., C. Ruf, C. Swift, S. Snyder, and J. Vongsathorn, 1989b: Determinations of Cloud Liquid Water in the Tropics from SSM/I. Fourth AMS Conference on Satellite Meteorology and Oceanography, San Diego, CA.

Drahos, H.F., D. Gray, and M. V. Piepgrass 1987: NESDIS Shared Processing Microwave Temperature Sounding Experience, Conference on Passive Microwave Observing from Environmental Satellites, Williamsburg, VA.

Hollinger, J. R. Lo, O. Poe, R. Savage, and J. Pierce, 1987: Special Sensor Microwave/Imager User's Guide. Naval Research Laboratory, Washington, D.C., 122 pp.

Kidwell, K.B., 1986: NOAA Polar Orbiter Data (TIROS-N, NOAA-6, NOAA-7, NOAA-8, NOAA-9, and NOAA-10) User's Guide, U.S. Dept. of Commerce, NOAA/NESDIS, Washington, D.C.

Ludlum, P.M, 1987: September Weather Watch, Weatherwise, December, Vol. 41, No.6, p.354.

Maiden, M. E., M. Piepgrass, D. Donahue, M. Sylva, and H. Drahos, 1989: Atmospheric Temperature Retrieval from Satellite Microwave Measurements, Fourth AMS Conference on Satellite Meteorology and Oceanography, San Diego, CA.

Piepgrass, M.V., and M. E. Maiden, 1987: SSM/T Temperature Soundings, Conference on Passive Microwave Observing from Environmental satellites, Williamsburg, VA.

Spencer, R.W., H.M. Goodman and R.E. Hood, 1988: Precipitation Retrieval Over Land and Ocean with the SSM/I, Part I : Identification and Characteristics of the Scattering Signal. In press.

Wilheit, T.T., 1979: A Model For the Microwave Emissivity of the Ocean's Surface as a Function of Wind Speed. NASA TM 80278.

WATER VAPOR RETRIEVAL FROM NOAA SATELLITES

APPLICATION TO TROPOSPHERIC WET CORRECTION ON TROPICAL AREAS

Y. TAHANI, A. CHEDIN, N. A. SCOTT

Laboratoire de Meteorologie Dynamique du CNRS
Ecole Polytechnique, 91128 Palaiseau Cedex, France.

1. INTRODUCTION

An altimeter measures the distance between the ocean and the satellite by determining the path followed by a signal emitted by a radar aboard the satellite and reflected on the sea surface. The objective of futur altimetry programmes (TOPEX-Poseidon, ERS1) is to map sea level variations with an accuracy of a few centimeters. Altimeter measurements must be corrected for several atmospheric effects and, in particular, for the path delay due to the presence of water vapor in the troposphere. Determination of the so called "tropospheric wet correction", which can reach 40cm (equivalent to a total water vapor content of 6-7 cm), requires developing and validating an accurate method of computation of total water vapor content.

The "3I" (Improved Initialization Inversion) algorithm has been designed with the purpose of retrieving geophysical parameters from space radiometric measurements and oriented towards the processing of the TIROS-N series observations made by TOVS (Tiros-N Operational Vertical Sounder) instruments : HIRS-2, a 20-channel infrared radiometer, and MSU, a 4-channel microwave radiometer.

This procedure is a physico-statistical method which relies on a "pattern recognition" type approach. Inversion of the radiative transfer equation is splitted into two steps, both of which take satellite measurements as their source of data. The first step "inverts" these measurements according to the principle of "best initial profile" from among a vast selection of atmospheric situations archived in advance and classified in groups according to air mass type. This "library" of atmospheric situations, "TIGR" (TOVS Initial Guess Retrieval data set), consists at present of about 1200 situations carefully sampled by statistical analysis methods . The selected set of brigthness temperatures serves to initialize the inversion algorithm in a second step.

Retrievals of water vapor quantities (relative humidities, integrated precipitable water vapor) is made for 3 layers delimited by the levels 1000, 800, 500 and 300 mb. Following the temperature profile inversion, the brigthness temperatures associated with the initial guess are corrected for the deviations between the initial temperature profile and the final solution giving rise to the initial guess for water vapor and surface temperature retrievals. The method used is based upon a simultaneous physical inversion of the water vapor amounts and of the surface temperature.

Four HIRS-2 channels are presently used : 8, 10, 11, 12 for day-time observations and 18, 10, 11, 12 for nigth-time observations. A ridge type estimation is used :

$$\Delta\beta = (X'X + \gamma I)^{-1} X' \Delta Y$$

where X (X' transpose of X) is the matrix of the partial derivatives of the brigthness temperatures with respect to relative humidities and surface temperature. ΔY is the difference between observed (cleared) brigthness temperatures and the initial corresponding values; γ is a smoothing parameter (Lagrangian parameter).

2. A METHOD TO OBTAIN CONTINUOUS FIELD OF WATER VAPOR

"3I" algorithm has been applied to derive water vapor from space observations under various meteorological conditions and for various geographical areas. Some difficulties complicate the water vapor retrieval procedure when the cloud coverage becomes too large (more than 60%), and in these cases, "holes", due to rejection by the algorithm, appear in the retrieved water vapor field.

However, altimetry requires space-continuity of data. Aiming at solving the problem resulting from the occurence of clouds, use is made of the ECMWF (European Center for Medium-range Weather Forecasts) analyses as a complementary source of data.

ECMWF analyses are first interpolated in time and space. Statistics are then performed separately for three classes of air mass type to detect eventual biases against "3I" retrievals, available on clear or partly cloudy areas. The analyses, corrected for these biases, finally serve to fill the "holes". A continuous field of water vapor total content is thus obtained by mixing "3I" retrievals and ECMWF corrected analyses.

3. APPLICATION TO NOAA-9 PASSES OVER TROPICAL AREAS

The method described here has been applied to two satellite passes over tropical oceanic areas :

- orbit nº 10202 of NOAA 9 for december 5th, 1986 at 15:36Z, over western Africa and partly Atlantic Ocean.

- orbit nº 10273 of NOAA 9 for december 10th, 1986 at 16:24Z, over Atlantic Ocean off western Africa down to latitude 3º.

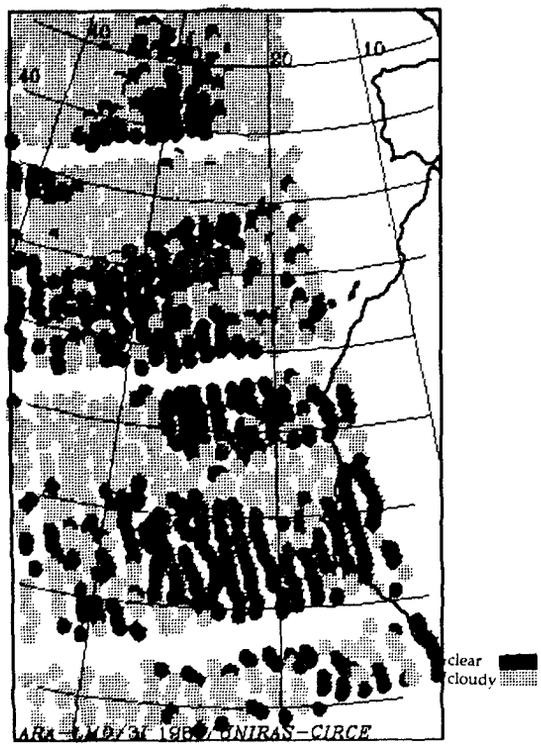

figure 1 :
Results of the cloud detection algorithm for the orbit nº 10273

Figure 1 represents a map of "3I" retrieved cloud coverage for orbit nº 10273, resulting from the cloud detection algorithm. A comparison of this product with AVHRR (Advanced Very High Resolution Radiometer) image was carried out and showed a great coherence.

On figure 2, water vapor content retrieved from satellite observations is shown (same orbit as above).

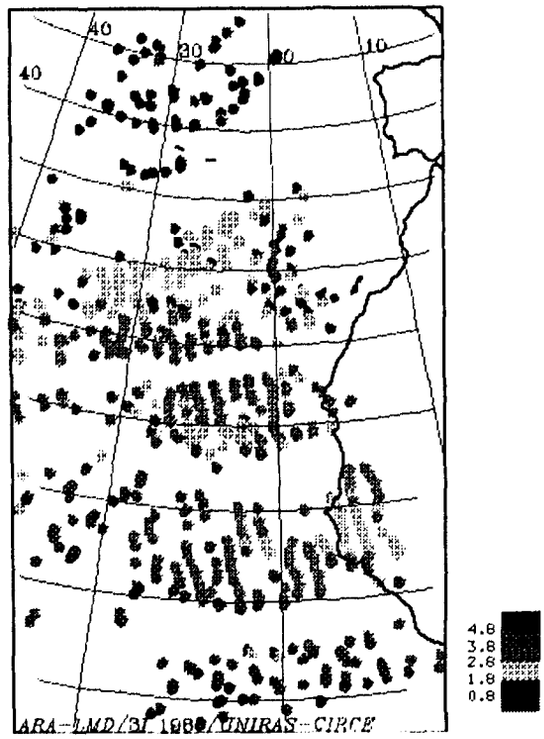

figure 2 :
Integrated precipitable water vapor field retrieved through "3I" algorithm, in cm (orbit nº 10273)

Lack of data correspond either to calibration periods of the radiometers or to areas where the percentage of cloud cover (effective cloud amount) is larger than 60%. Similar results are observed for orbit nº10202.

Before attempting to fill the holes observed in the "3I" retrievals field, statistics between available "3I" water vapor retrievals and matched ECMWF analyses have been performed. Results of the differences "3I - ECMWF" are on figures 3 and 4, for the two satellite passes : 10202 and 10273.

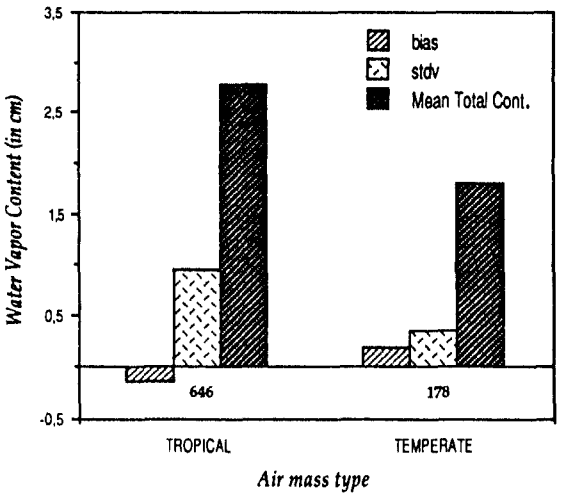

figure 3 :
"3I-ECMWF" total water vapor content statistics for the orbit n° 10202

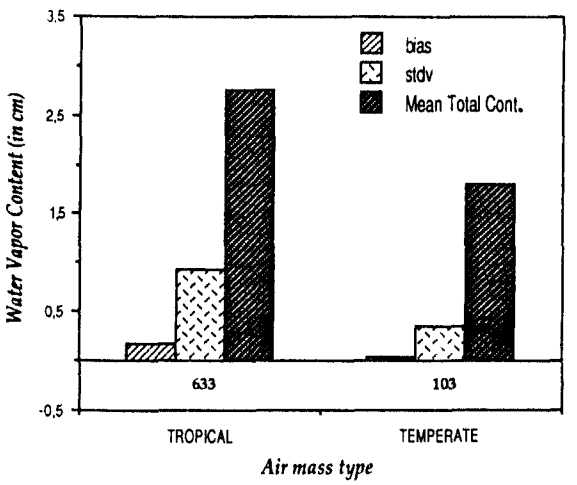

figure 4 :
Same as figure 3 for the orbit n° 10273

These diagrams show weak biases and satisfactory standard deviations.

Water vapor field from ECMWF analysis (expressed in mm) is presented on figure 5.a for orbit n°10202. The corresponding chart resulting from the mixing of "3I" values and corrected ECMWF analysis is displayed on figure 5.b . Qualitatively, a good coherence between the two maps is observed; however, the higher resolution of "3I" retrievals results in more detailed information on areas where they are available. Particularly, between latitudes 4° and 9° north and longitudes -12° west and 0° (south of the map) the gradient observed on figure 5.b (about 20 mm) is stronger than the one appearing over the same area on figure 5.a (about 10 mm).

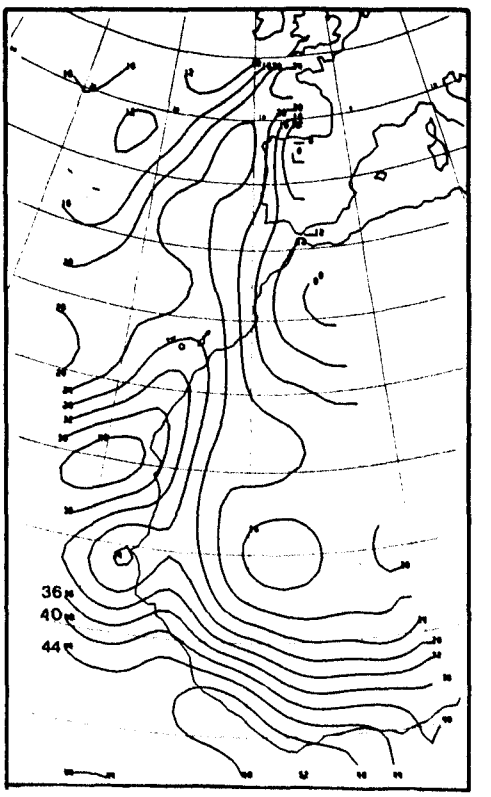

figure 5.a :
Water vapor total content isolines resulting from ECMWF analyses, in mm (orbit n° 10202)

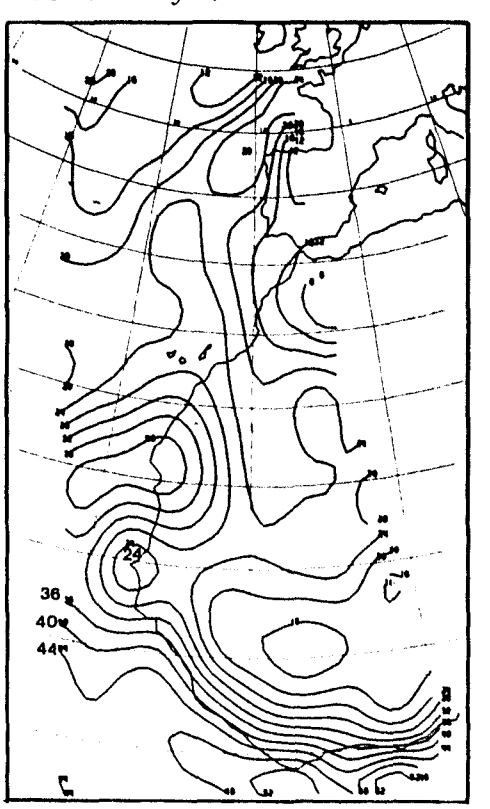

figure 5.b :
Water vapor total content isolines resulting from the mixing of "3I" retrievals and ECMWF corrected analyses, in mm (orbit n° 10202)

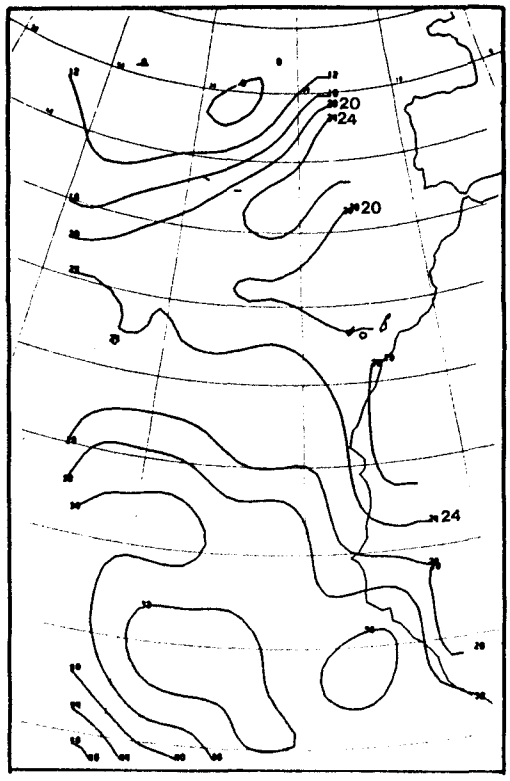

figure 6.a :
Water vapor total content isolines resulting from ECMWF analyses, in mm (orbit nº 10273)

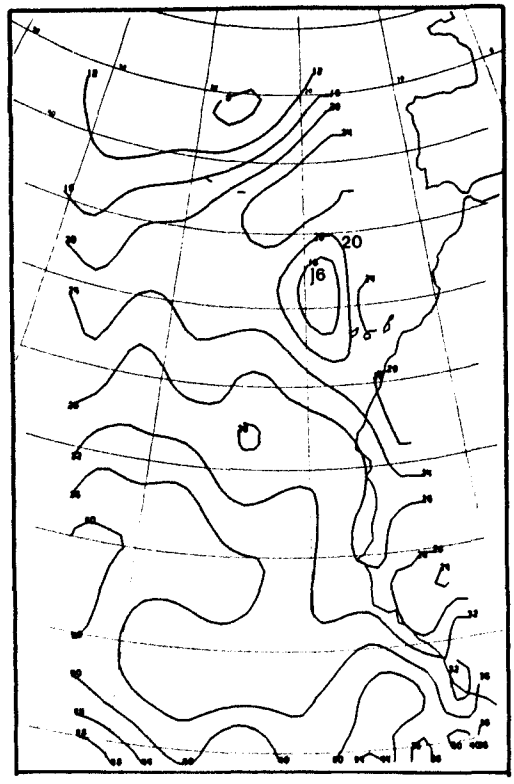

figure 6.b :
Water vapor total content isolines resulting from the mixing of "3I" retrievals and ECMWF corrected analyses, in mm (orbit nº 10273)

Figures 6.a and 6.b show the same type of results as figures 5.a and 5.b, for orbit nº 10273. On the meridian -20º west, between latitudes 25º and 30º north, "3I" retrievals present greater variability than ECMWF analysis. Moreover, several structures appear with more details on the "mixing map" (figure 6.b) than on the ECMWF analysis map (figure 6.a), particularly on the western coast of Africa.

In the absence of a sufficiently dense and reliable network of in-situ measurements on the one hand, and of a higher spatial resolution model analysis on the other,validation of the method remains difficult.

In cooperation with the CNES/GRGS (Centre National d'Etudes Spatiales-Groupe de Recherche de Géodésie Spatiale) a study has been undertaken on GEOSAT altimeter measurements. Such data will be corrected for tropospheric wet delay derived from total water vapor content obtained by the method described above, in order to check its repercussion on altimetric product quality.

4. CONCLUSION

Radiometers calibration periods and heavy cloudiness preclude satellite retrievals from producing continuous fields of total water vapor content that are necessary to correct altimeter data for the "wet tropospheric delay". Combining retrievals and ECMWF analyses, a method has been developed in order to solve this problem. An application to NOAA-9 passes over tropical atlantic shows encouraging results. This study is developing towards application to GEOSAT altimeter.

4.REFERENCES

- A. Chedin, N.A. Scott, C. Wahiche and P. Moulinier (1985)
The Improved Initialisation Inversion Method : A High Resolution Physical Method for Temperature Retrievals from Satellites of the TIROS-N Series.
J. Clim. Appl. Meteor. Vol. 24, n°2.

- C. Wahiche (1984)
Contribution au Problème de la Détermination de Paramètres Météorologiques et Climatologiques à Partir de Données Fournies par les Satellites de la Série TIROS-N, Impact de la Couverture Nuageuse.
Thèse de Doctorat.

- C. Wahiche, N.A. Scott and A. Chedin (1985)
Cloud detection and cloud parameters retrieval from the satellites of the TIROS-N series
Annales Geophysicae, 1986, 4B, 2, 207-222.

- G. Elgered, B. Ronnang, E. Winberg, J. Askne (1985)
Satellite Earth Range Measurements
I. Correction of excess path length due to atmospheric water vapor by ground based microwave radiometry - Research Report
ESA Contract nº 5910/84/NL/MD

JP8A.16

MOISTURE STRUCTURE OF TROPICAL CLOUD SYSTEMS AS INFERRED FROM SSM/I

Franklin R. Robertson
Earth Science and Applications Division, ES42
NASA/ Marshall Space Flight Center
Huntsville, AL 35812

1. INTRODUCTION

One of the more urgent requirements for advancing our understanding atmospheric predictability and climate is a better knowledge of the distribution of tropical precipitation and the processes which modulate it. It is well established that organized precipitation systems in the tropics are predominantly convective in origin and typically evolve a stratiform rain and cloud component that may contribute significantly to the total rain production (Cheng and Houze, 1979). Several intensive field programs, starting with GATE (GARP Atlantic Tropical Experiment) and more recently EMEX (Equatorial Mesoscale Experiment), have documented specific systems for case study analysis. Yet, there still exists a lack of reliable statistics concerning the bulk microphysical characteristics of tropical cloud systems and an understanding of how these properties relate to large scale controls such as moist static stability, surface energy fluxes and SST patterns. It is necessary to quantify these relationships since they form the basis of subgrid-scale cloud parameterizations in numerical models.

The SSM/I (Special Sensor Microwave Imager) launched in mid-1987 has frequencies (19.35, 22.2, 37 and 85.5 GHz) which allow detection of vertically-integrated vapor, liquid and ice. In this investigation, we will use these data to examine the structure of tropical cloud systems. In particular, the relative amounts of ice and liquid water present in extensive anvil systems is studied. Because the 85 GHz channel is sensitive to scattering of upwelling radiation by precipitation size ice, a discrimination is possible between active, precipitating anvils and cirrus debris. The latter, while not producing rainfall, may produce diabatic effects through longwave radiative flux convergence. The volume scattering by ice has been explored by Weinman and Guetter (1977), Spencer *et al*, (1983) and Spencer *et al*, (1989). In the latter paper a polarization corrected temperature ($PCT_{85.5}$) is formulated which removes ambiguities arising from observing the radiaometrically-cold, highly polarized ocean surface. $PCT_{85.5}$ values can then be regarded largely as a signal of precipitation size ice. The 19 GHz channel which is more sensitive to liquid water drops is used as an indicator of rainfall. Over oceans microwave emission by liquid water at 19H appears as a warm signal against the radiometrically cold sea surface. However, cloud water can often contribute significantly to elevating 19H temperatures. Sequences of infrared geostationary imagery are also used to monitor the life cycle of convective systems since the SSM/I sensor flies aboard a polar orbiting spacecraft and does not provide continuous coverage over a geographical region.

2. CASE STUDY OF A CENTRAL PACIFIC CLOUD CLUSTER

As an example of the correspondence between cloud morphology provided by IR imager and the inferrences on microphysical structure available through SSM/I data we consider a cloud cluster associated with a Pacific easterly wave. Figure 1 shows a sequence of three GOES West IR images at intervals of 90 minutes. The cloud cluster in this sequence (apparent as cold high clouds) traversed the central Pacific during September 1987. SSM/I data shown in Figs. 2-4 was available coincident with the middle time (1645 UTC 14 September). Apparent in the IR data are T_b minima presumably associated with cores of deep convection. The cores are embedded within warmer connecting stratiform anvils and cirrus debris. The cold cores near points A and B show relatively small changes over this 3h period; however, near point C the IR temperatures show a distinct warming trend. The $PCT_{85.5}$ signature in Fig 2. indicates maxima of precipitation size ice that correspond quite well to the IR T_b minima at 1645 UTC. The ice signatures are prominent as $PCT_{85.5}$ minima near locations A and B where IR T_b minima are also found. Between A and B there is another, weaker, ice signature which also is associated with cold IR cloud tops. The H19 channel in Fig. 3 shows maxima in emission as a result of liquid water. Although cloud water can produce significant warming at this frequency, the maxima are greater that 40 K warmer than the background 19H temperatures, strongly suggesting the presence of rainfall. At points A and B the centers of 19H maximuum warming correspond well to the presence of ice indicated by the $PCT_{85.5}$ minima. A significant 19H maximum is also found near point C, but there the $PCT_{85.5}$ values indicate much less ice that near A or B. The larger fraction of liquid to frozen precipitation implied at point C is not inconsistent with idealized models of mature or decaying stratiform anvils. Such systems would have lost their source of ice production either by weakened upward vertical motions or the lack of transfer of frozen condensate from active convective cells.

In addition to liquid and ice signatures, SSM/I is able to provide quantitative measurements of precipitable water. In rain free, areas these values are accurate to within $\pm$ .3 cm. Fig. 4 shows precipitable water extracted from the Ocean Products Tapes data produced using a modification of the Wentz (1983) algorithm. The very moist region northwest of the cloud cluster has precipitable water amounts in excess of 5.0 g cm^{-2} and contrasts with the relatively dry region near the equator where values are between 2.0 and 3.0 g cm^{-2}. Sea surface temperatures for both locations are in excess of 301 K, emphasizing that for convection to be sustained, some convergence mechanism is needed in addition to warm SSTs (Gadgil, 1984). It is apparent that in and close to the raining portions of the cluster the precipitable water amounts are unrealistic.

3. DISCUSSION

The case study of this cloud cluster provides a sample of the varying signatures of bulk microphysical processes in organized tropical convection. In order to interpret this variability and its significance in terms of the response of

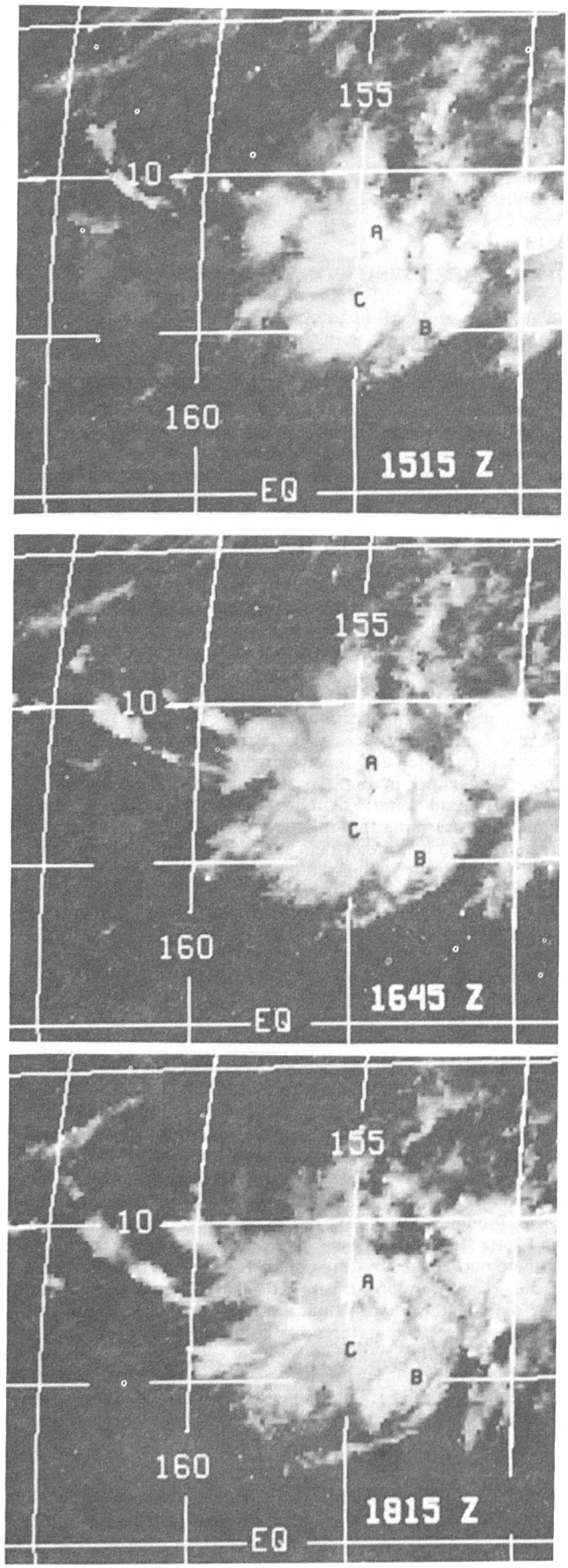

Figure 1. GOES W infrared imagery for 1515 (top) 1645 (middle) and 1815 (bottom) UTC September 14, 1987.

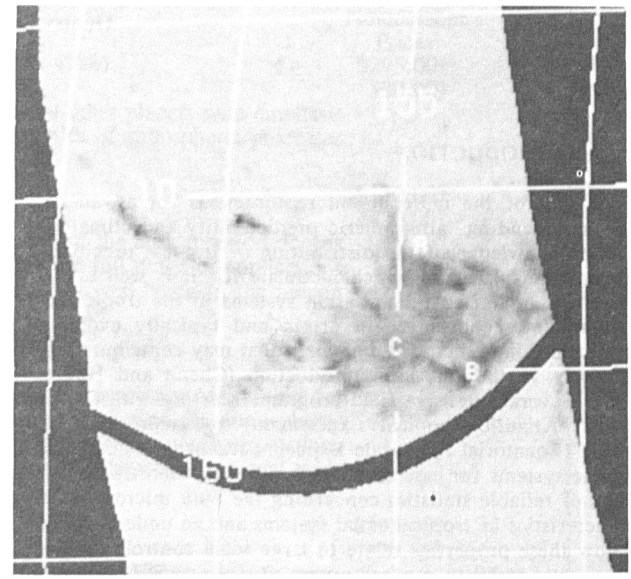

Figure 2. SSM/I $PCT_{85.5}$ for 1645 UTC 14 September 1987. Darker regions have lower values implying the presence of precipitation size ice.

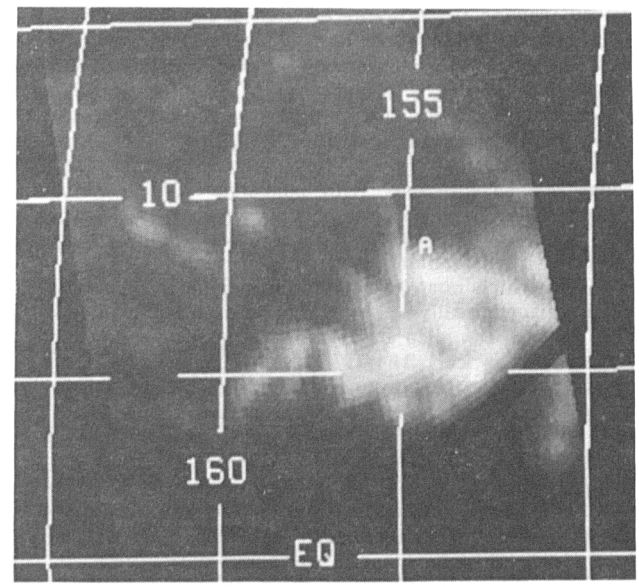

Figure 3. SSM/I 19H imagery for same time as Figure 2. Lighter areas are warmer, implying higher liquid water amounts.

convection to its thermodynamic environment, compositing techniques are being employed. We are currently using IR data to interpret the life cycle stage of tropical mesoscale convective systems and to partition them into convective cores and associated stratiform anvils. The relative intensities of ice and liquid water signatures should provide insight on the relative contribution of stratiform vs. convective rain and the characteristics of the water budgets of mesoscale convective systems. Results of this compositing procedure will be discussed at the conference.

4. ACKNOWLEDGEMENTS

This research is supported under the NASA Global Scale Atmospheric Processes Research Program. Dr. Frank Wentz, Remote Sensing Systems, Sausalito, CA provided the SSM/I calibrated temperatures and Ocean Products Tapes.

5. REFERENCES

Cheng. C.-P., and R. A. Houze, Jr., 1979: The distribution of convective and mesoscale precipitation in GATE radar echo patterns. *Mon. Wea. Rev.*, 107, 1370-1381.

Gadgil, S. P. V. Joseph and N. V. Joshi, 1984: Ocean-atmosphere coupling over monsoon regions. *Nature*, 312, 141-143.

Spencer, R. W., W. S. Olson, W. Rongzhang, D. W. Martin, J. A. Weinman, and D. A. Santek, 1983: Heavy thunderstorms observed over land by the Nimbus 7 Scanning Multichannel Microwave Radiometer. *J. Climate Appl. Meteor.*, 22, 1041-1046.

Spencer, R. W., H. M. Goodman, and R. E. Hood, 1989: Precipitation retrieval over land and ocean with the SSM/I: Identification and characteristics of the scattering signal. Accepted, *J. Atmos. Ocean. Tech.*

Weinman, J. A. and P. J. Guetter, 1977: Determination of rainfall distributions from microwave radiation measured by the Nimbus-6 ESMR. *J. Appl. Meteor.*, 16, 437-442.

Wentz, F. J., 1983: A model function for ocean microwave brightness temperatures. *J. Geophys. Res.*, 88, 1892-1908.

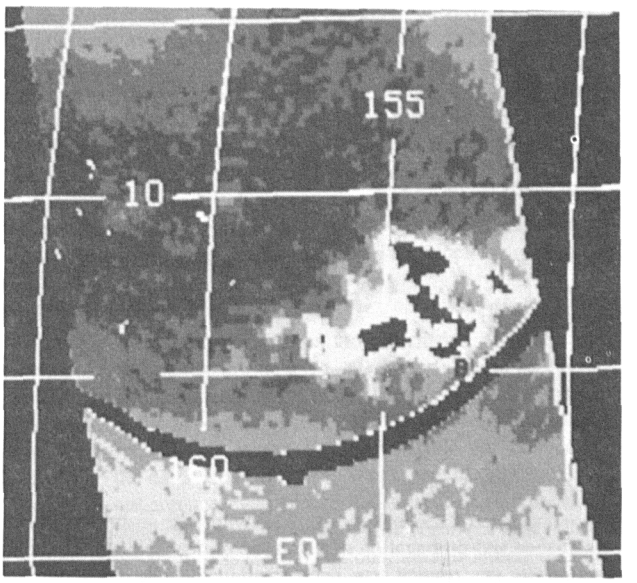

Figure 4. SSM/I precipitable water from Wentz (1983) algorithm. Gray shades (light --> dark) correspond to amounts greater than 1.0, 2.0, 3.0, 4.0, and 5.0 g cm^{-2}. Black regions within data swath have no retrieved values.

MOISTURE CONVERGENCE DURING A CONVECTIVE FLARE-UP IN THE TROPICS

Ellen J. Steiner
Cooperative Institute for Research in Environmental Sciences
University of Colorado
Boulder, Colorado 80309

1. INTRODUCTION

The role of 850 mb moisture convergence in the possible sustenance and propagation of a flare-up of near- equatorial convection in the tropics has been examined. The convection, which occurred in the context of a 30 - 60 day oscillation of tropical convection and circulation, shifted from the eastern Indian to western Pacific ocean in November to December, 1981. Weickmann et al. (1989) have described some of the dynamical and thermodynamical aspects of this event. The case was initially selected from one of the Knutson and Weickmann (1987) 30 - 60 day filtered 250 mb velocity potential events, because of its strong equatorial signal and because strong surface westerlies accompanied the eastward shift of convection. Theory, in particular the wave - CISK formulations, has suggested that moisture convergence leads the convective maximum, thus providing a means for the convection to propagate eastward. Moisture divergence to the west suppresses convection. These assumptions will be examined with the present data.

Moisture convergence is an appropriate variable with which to study the occurrence and distribution of deep tropical convection. Ardanuy et al. (1987) estimated vertically integrated water vapor flux convergence from NIMBUS-7 observations, and related the convergence to rainfall on monthly time scales. Steiner and Khalsa (1987) have shown that the correlation between convection and moisture alone is poor in the normally warm, moist, and convective western tropical Pacific. The combination of the dynamics and moisture fields presumably results in a closer relationship to convection than either the wind convergence or moisture alone. This presumption will be discussed. Although surface moisture convergence would be more closely related to convection than 850 mb convergence, the data sets described in the following section limit themselves to computation at 850 mb. The aim of this study differs from that of Chen et al. (1988) who examined water vapor transport during the FGGE year and concluded that a 30 - 50 day oscillation of water vapor transport modulates the East Asian monsoon.

2. DATA AND ANALYSIS METHODS

Three data sets were used in this analysis. They were:

1. Satellite derived outgoing longwave radiation (OLR)
2. NMC 850 mb winds
3. Low-level precipitable water (LLPW) in the 1000-700 mb layer from the TIROS operational vertical sounder (TOVS).

Low values of OLR denote large scale tropical convection. A comparison of 3-day averaged OLR (such as used in this study) with daily satellite mosaics has shown that the brightest and most convective clouds correspond to OLR of about 200 W/m^2.

The NMC 850 mb winds are a mixture of satellite cloud drift wind vectors, station observations, and model analysis. The 850 mb winds are better than the surface winds, which is one reason for the computation of moisture convergence at 850 mb. West of Indonesia (about 100°E) the NMC winds are admittedly poor, since no cloud drift vectors were available there in 1981 and there were few surface observations. East of 100°E, the number of observations and quality of the analysis improve. The twice daily data were averaged into daily values. A data gap existed from 17 December to 19 December.

LLPW from TOVS has been found to provide good quality information on the moisture content of the tropical atmosphere on intraseasonal and shorter time scales. (Khalsa and Steiner, 1988). One drawback of the TOVS data is that no precipitable water observations can be made under completely cloudy conditions. This results in a dry bias in the presence of heavy convection. However, Khalsa and Steiner found that regions surrounding cloudy data gaps had higher precipitable water than nearby areas, so that interpolation across the data gaps preserved relative maxima of LLPW in those areas. The TOVS data were gridded, 5° latitude by longitude daily averages.

Moisture convergence is defined as:

$$\nabla \cdot q \vec{v} = q \nabla \cdot \vec{v} + \vec{v} \cdot \nabla q \qquad (1)$$

where q in this case is precipitable water and $\vec{v}$ is wind velocity. Daily values were computed from the NMC winds and TOVS LLPW, from which 3 - day averages were taken for the period 5 November 1981 through 28 December 1981.

3. DISCUSSION

Figure 1, taken from Weickmann et al. (1989), is a time-longitude diagram of 3 - day averaged OLR from 40°E to 80°W, and 5 - 7 November to 26 - 28 December 1981, averaged in latitude from 5°N to 5° S. The longitudes range from Somalia in the west to South America in the east. The shaded values indicating OLR less than 180 W/m^2 illustrate the convective flare-up. Pairs of vertical lines indicate the presence of land: Sumatra and the Malay peninsula between 95°E and 105°E, Borneo between 110°E and almost 120°E, and New Guinea between 135°E and 145°E. Other islands of Indonesia also intervene. There was persistent convection (<200 W/m^2) centered near 105°E from about 11 - 13 November. Beginning 26 - 28 November, there was an intensification and eastward expansion of convection in a major convective "burst". The burst decayed around 8 - 10 December at about the time 2 smaller convective maxima appeared centered near 130°E and 150°E. These maxima were separated by New Guinea. By 17 - 19 December, the center of convection had shifted to 155°E, well to the east of the major burst.

Figure 2 is a time-longitude diagram of LLPW with the convective flare-up superimposed. The influence of Indonesia and New Guinea on the moisture field is evident in the observed moisture minima. The beginning of the flare-up followed a period of high moisture (> 38 mm) by a few days. Following the onset of the convective burst, high values of moisture expanded to the east. There was also a lesser westward increase of moisture at the time of the burst, extending from at least 160°W (shown by the dashed line on figure 2). The increase of moisture at the dateline on 5-7 December most likely resulted from both perturbations. A sequence of maps of 3-day averaged LLPW shows the increase of moisture in the Pacific more distinctly (not shown). There was also an increase of moisture north of the equator in the central and eastern Pacific simultaneous with the expansion of the convective burst but presumably independent of it.

The main convective burst did not occur in a region of maximum low-level moisture, probably "because" of the dry bias of LLPW in the presence of heavy convection. Following the main burst, an intense moisture minimum occurred in the area where the burst had been. High values of moisture remained on the equator east of New Guinea until 14-16 December. The remaining convective maxima occurred where moisture was still relatively high. At the end of the final convective event on 20-22 December, there was another shortlived moisture increase in the western Pacific.

Figure 3 is a time-longitude diagram of moisture convergence with the convective flare-up superimposed. The entire flare-up occurred within a broad region of moisture convergence interrupted by patches of divergence. Eastward propagation of strong convergence was evident from the beginning of the period, prior to the convective flare-up. The flare-up did not appear to have affected the propagation speed of the moisture convergence. A convergence maximum centered at 130°E which directly followed the greatest eastward extent of the convective burst also moved eastward with the general flow. Weickmann et al. (1989) claimed that an eastward shift of westerly winds along with an increase in Pacific ocean trades at 175°W resulted in strong wind convergence (as well as the observed increase in moisture) to the east following the burst. That may well have resulted in the intense moisture convergence maximum seen there, but the general eastward propagation remains unexplained. Strong equatorial moisture divergence abutted the intense convergence at the dateline from about 5-7 through 11-13 December. Moisture convergence also intensified between 5°-10°S, east of the dateline during this time (not shown).

The main convective burst did not occur at a time of maximum, or even persistent, moisture convergence. This cannot be attributed to a dry bias in LLPW since it will be shown that the moisture convergence is dominated by the wind divergence. Although moisture divergence followed the burst in the area where the convection had been, this divergence was a continuation of that which had presumably existed during the burst itself. This divergence may have reflected small scale effects due to islands or have resulted from errors in the wind data. Three-day average maps of the moisture convergence show this divergence consistently in time and space and would not alone be suspect except for their poor match-up with OLR.

Figure 4 is a time-longitude diagram of the mean moisture times the wind divergence (the first term on the right hand side of equation 1), with the convective flare-up superimposed. The pattern is nearly identical to that of the moisture convergence, and for that matter, to the wind divergence alone. The reason why is shown in figure 5, which is a plot of the moisture advection term (second term on the right of equation 1). The gradient of moisture is much smaller than the divergence over the region in question, even over land and between land and ocean. Moisture advection is negative over land and mostly positive over the equatorial Pacific due to a combination of easterlies and decreasing moisture to the east. Patches of negative advection in the western Pacific may result from westerlies there. While there may be situations where the moisture advection and wind divergence terms on a 5° scale are of comparable magnitude, in this study the wind divergence alone would have been sufficient to show the major features of moisture convergence.

4. CONCLUSIONS

This case study has given no conclusive evidence that moisture convergence during a 30 - 60 day oscillation leads convection in the manner proposed by theory. In examining the same case study, Weickmann et al. (1989) proposed that the convective burst resulted in conditions favorable for convection moving to the east. However, there was eastward propagation of moisture convergence even before the most intense convection began. In addition, while maxima of LLPW moved east following the burst, there was a simultaneous, though lesser, increase of moisture from the east. These factors make it difficult to ascribe cause and effect. K. Weickmann (personal communication) has suggested that individual cold surges may have lent an appearance of eastward propagation to the moisture convergence maxima. The intense convergence to the east of the convective burst may still have been induced by it, if it is regarded as a single event rather than part of a general trend. This possibility needs further testing. Another factor which could influence convection in this region is the presence of the maritime continent itself. New Guinea was probably the reason for the "split" of the 2 convective maxima following the main burst. The presence of moisture divergence during the main convective burst was possibly the result of errors in the wind analysis or of the effects of islands, and should be regarded with caution. There was moisture divergence following the main burst, if the wind data are to be believed.

Moisture convergence is dominated by the wind divergence except in situations where the moisture gradient is large. For purposes of this study, it would have been sufficient to use the wind divergence and moisture fields independently.

It hardly needs to be stated that generalizations cannot be inferred from a single case study. To confirm the conclusions of this report other cases should be examined, preferably in later years when the wind data were of better quality.

5. REFERENCES

Ardanuy, P.E., P. Cuddapah, and H.L. Kyle, 1987: Remote sensing of water vapor convergence, deep convection, and precipitation over the tropical Pacific ocean during the 1982-83 El Nino. *J. Geophys. Res.*, *92*, 14,204-14,216.

Chen, T.- C., M.- C. Yen, and M. Murakami, 1988: The water vapor transport associated with the 30 - 50 day oscillation over the Asian monsoon regions during 1979 summer. *Mon. Wea. Rev.*, *116*, 1983 - 2002.

Khalsa, S.J.S., and E.J. Steiner, 1988: A TOVS dataset for study of the tropical atmosphere. *J. Appl. Meteor.*, *27*, 851 - 862.

Knutson, T.R. and K.M. Weickmann, 1987: 30- 60 day oscillations: composite life cycles of convection and circulation anomalies. *Mon. Wea. Rev.*, *115*, 1407 - 1436.

Steiner, E.J., and S.J.S. Khalsa, 1987: Sea surface temperature, low-level moisture, and convection in the tropical Pacific, 1982 - 1985. *J. Geophys. Res.*, *92*, 14,217 - 14,224.

Weickmann, K.M., S.J.S. Khalsa, and E.J. Steiner, 1989: The dynamics and thermodynamics of a 30 - 60 day tropical oscillation. *Mon. Wea. Rev.*, in review.

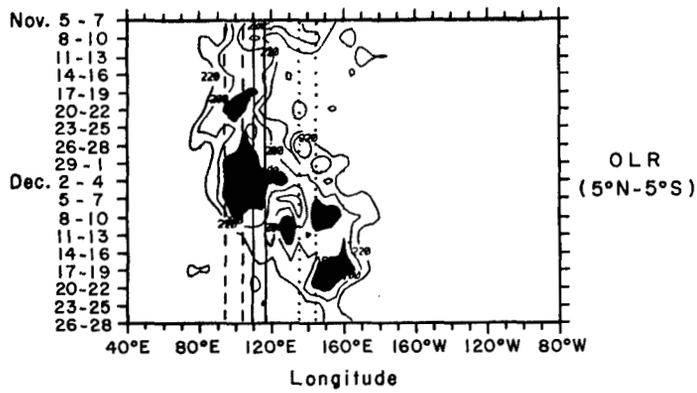

Figure 1: Time-longitude diagram (5°N-5°S) of 3-day averaged OLR for 5-7 November 1981 through 26-28 December 1981. Values less than 220 W/m^2 are contoured and values less than 180 W/m^2 are shaded. Contour interval is 20 W/m^2. Pairs of vertical lines indicate land identified in the text.

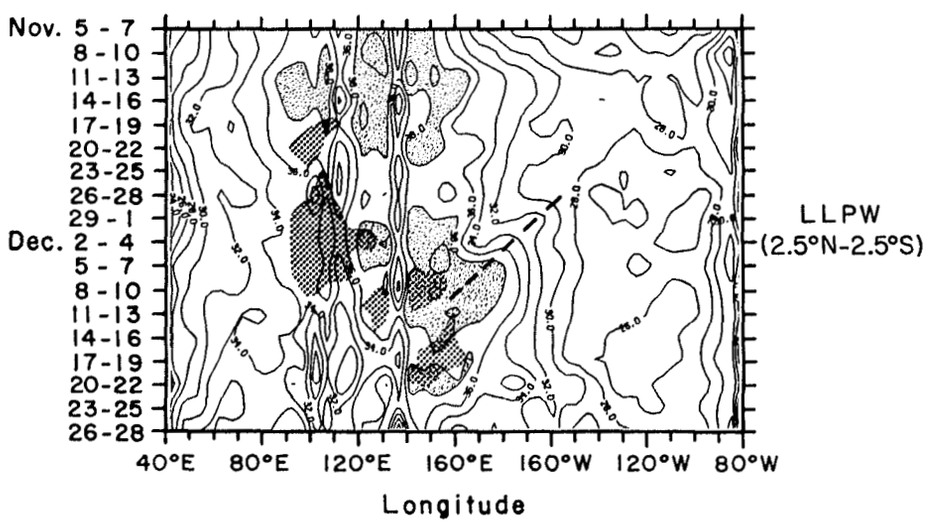

Figure 2: Time-longitude diagram as in figure 1 but for low-level precipitable water averaged from 2.5°N-2.5°S. The convective flare-up is superimposed. Contour interval is 2 mm precipitable water and values greater than 38 mm PW are stippled. The dashed line is an axis of increasing precipitable water.

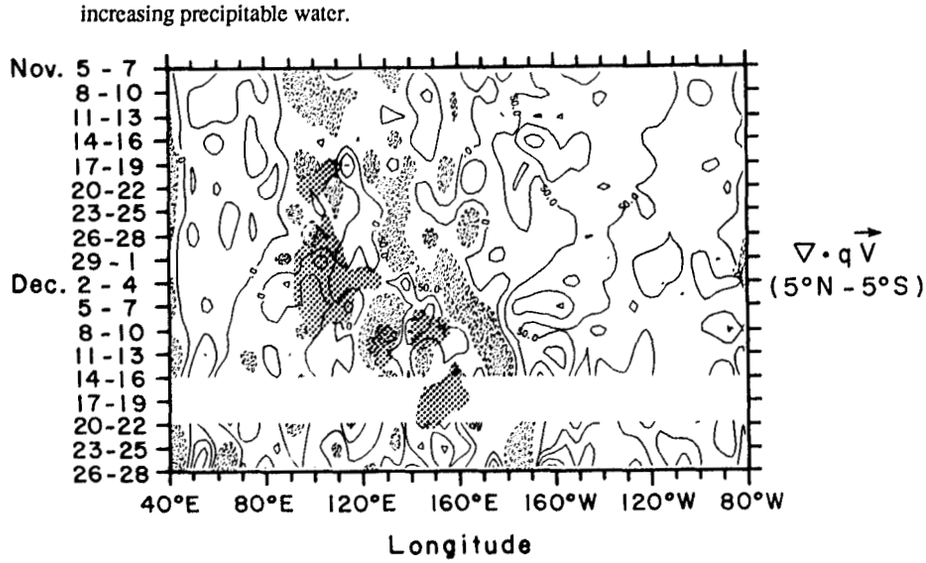

Figure 3: Time-longitude diagram as in figure 1 for moisture convergence with the convective flare-up superimposed. Contour interval is 50 X 10^{-6} mm PW/sec and values less than -50 X 10^{-6} are stippled.

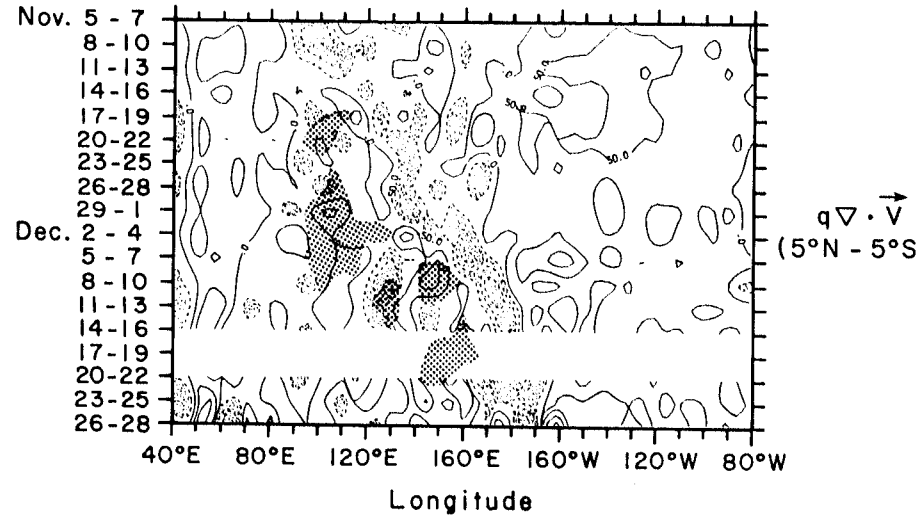

Figure 4: Time-longitude diagram as in figure 1 for mean precipitable water times wind divergence with the convective flare-up superimposed. Contour interval is 50 X 10^{-6} mm PW/sec and values less than -50 X 10^{-6} are stippled.

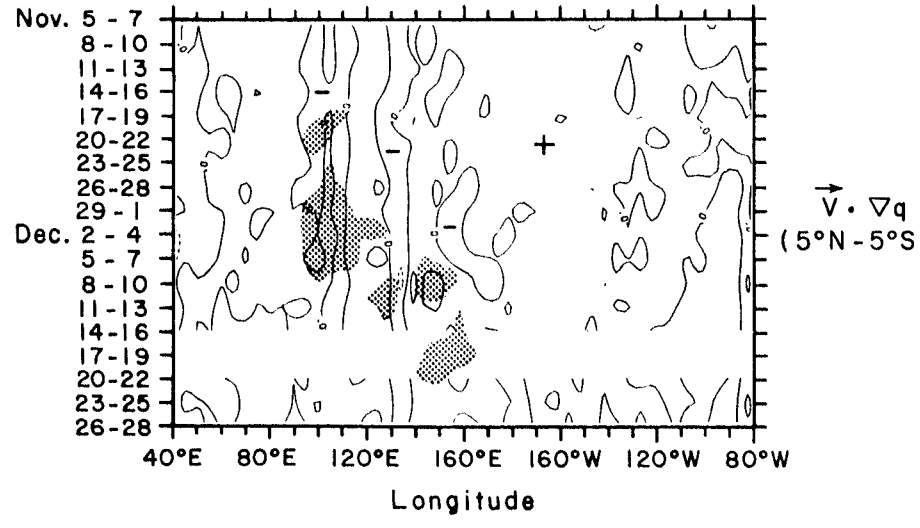

Figure 5: Time-longitude diagram as in figure 1 for moisture advection with the convective flare-up superimposed. Contour interval is 50 X 10^{-6} mm PW/sec.

JP8A.18

SIMULATED APPEARANCE OF AN EVOLVING SUPERCELL HAIL STORM AT SSM/I MICROWAVE FREQUENCIES

Eric A. Smith [1]
Harry J. Cooper [1]
Alberto Mugnai [2]
Gregory J. Tripoli [3]

[1] Dept. of Meteorology and
Supercomputer Computations Research Institute
Florida State University
Tallahassee, FL 32306
904-644-4253

[2] Istituto di Fisica dell'Atmosfera
Consiglio Nazionale delle Ricerche
Frascati 00044, Italy

[3] Dept. of Meteorology
University of Wisconsin
Madison, WI 53706

1. INTRODUCTION

This investigation examines the contribution by distinct classes of hydrometeors generated from a cloud model to top-of-atmosphere microwave brightness temperatures at the four separate frequencies of the Air Force Special Sensor Microwave Imager (SSM/I) instrument. The objective of this research is to help understand the relative radiative roles of individual modes of hydrometeors during the evolution of a severe thunderstorm, particularly in conjunction with their horizontal and vertical distribution. For this study we have coupled a microwave radiative transfer model with a 3-D cloud model capable of simulating the essential dynamical and microphysical features of an intense hail storm.

The microwave RTE model has been described by Mugnai and Smith (1988a); it is based on extensive modifications to Wiscombe's (1982) original adding-doubling ATRAD model designed for the solar and infrared spectrums. It has been used to explore the influence of detailed microphysical phenomena within an evolving convective cloud on passive microwave brightness temperatures at the top-of-atmosphere -- see Smith and Mugnai (1988a). The model has recently been augmented to calculate generalized emission/scattering vertical weighting functions which can be decomposed in terms of purely emissive and purely scattering parts -- see Mugnai and Smith (1988b). In addition, the weighting functions are further divided into relative weighting functions by the individual hydrometeor components. This makes it possible to determine, layer by layer, how radiation reaches the satellite instrument and how much can be attributed to the separate hydrometeor classes, the atmospheric gases, and the surface.

The cloud model was configured from the CSU RAMS model [Tripoli and Cotton (1982) and Cotton et al. (1986)] to simulate the growth of a hail storm based on environmental conditions preceding a severe storm outbreak that took place during the NASA COHMEX experiment [11 July, 1986]. The cloud model simulation was integrated over a four hour period. During the first two hours a multicell storm complex was generated; in the later half of the simulation, a supercell class hail storm developed whose passive microwave radiative properties are consistent with aircraft measurements of an actual severe storm that developed during the evening of July 11 near Eldridge, Alabama--see Smith and Mugnai (1988b) for a discussion of this storm. The classes of hydrometeors produced by the version of the RAMS model utilized for this project consist of cloud drops, rain drops, ice crystals, ice aggregates, and graupel particles. These are the hydrometeors that are examined vis-a-vis their role on top-of-atmosphere brightness temperatures at the SSM/I frequencies of 19, 22, 37, and 85 GHz.

2. RESULTS OF SIMULATION STUDY

The basic means for examining the model calculations are various time series of color graphic motifs which contain information on both the cloud model microphysics and the multi-frequency microwave signatures; the black-white diagram given in Figure 1 helps illustrate. In this diagram, which represents an instantaneous time step at hour 3/minute 40 during the simulation, the upper 3 panels portray a top-down plan view of the model microphysics along with x-z/y-z microphysical cross-sections showing the vertical structures along east-west and north-south transects through the storm core. The plan view (upper left panel) uses shading to express the vertically integrated equivalent liquid water content given in $gm \bullet m^{-2}$ for four of the hydrometeor classes (cloud, rain, aggregate, graupel).

The contours are used to represent the vertically integrated concentration of ice crystals also in $gm \bullet m^{-2}$. High ice crystal concentrations can develop within the anvil away from the main concentrations of the other hydrometeors. Since we will show that model generated ice crystals can significantly attenuate radiation at the higher SSM/I frequency (85 GHz), we give the ice crystals special attention.

The lower panels are used to help understand the origins of top-of-atmosphere brightness temperature information. The 5 left most panels show the vertical distribution of the separate hydrometeor concentrations (in $gm \bullet m^{-3}$) for a particular target region of the cloud model domain. That region is highlighted with the black cursor box seen in the upper left hand plan view panel -- in this case directly over the storm core. The model generated surface rain rate at this time is numerically indicated at $\approx 34\ mm \bullet hr^{-1}$.

The 4 rightmost panels provide the relevant information on the radiative contributions by surface and atmosphere for each frequency. The TOA flux equivalent brightness temperatures (in Kelvin) associated with the selected target are indicated above the frequency labels. The relative contributions by the surface (in %) to the total TOA brightness temperatures are indicated below the 4 individual frequency panels. Within the panels are the vertically distributed total emission/scattering weighting functions in ($deg \bullet km^{-1}$) which indicate the fractional contribution by a given level to a total brightness temperature. Note that the vertical coordinate at which the weighting functions peak increases with increasing frequency. This feature of the brightness temperature points out the possibilities of using multispectral information from SSM/I for recovering precipitation information in the framework of classic inversion methods.

In conference we will demonstrate the time dependence of these processes over the lifetime of the hail storm. Included in the presentation will be the detailed contributions by the individual hydrometeor classes, vis-a-vis both their emission contributions and their scattering contributions.

3. APPLICATIONS TO SSM/I

The results of the model simulations are intended for application with actual multi-channel measurements from SSM/I instruments to provide a framework for multispectral precipitation retrieval algorithms. The basic averaging area we are currently using for constructing the model generated hydrometeor profiles for RTE model input is a 10 x 10 km grid box, however, this factor can be varied. The choice of our spatial resolution is based on matching resolutions to the highest resolution channel on SSM/I, i.e. 85 GHz. The RTE calculations thus provide brightness temperatures at a spatial scale of 10 km from a nadir view of 53° (the SSM/I conical scan angle). Since each independent frequency provides information on the radiative contributions by different depths in the cloud, it is possible to devise precipitation retrieval algorithms which provide the profile of hydrometeor concentration as opposed to the vertically integrated concentrations (or vertically integrated rain rate). At this stage of the research we are experimenting with deconvolution methods (to bring low resolution channels into conjunction with the highest resolution 85 GHz channel) and low pass filtering methods (to bring high resolution channels into conjunction with the lowest resolution 19 GHz channel). This issues will be discused in conference.

4. ACKNOWLEDGEMENTS

Support for this research has been provided by NASA Grant NAGW-991 and the FSU Supercomputer Research Institute under DOE contract DE-FCO5-85ER250000. Travel support for Dr. Mugnai has been provided by the Gruppo Nazionale per la Difesadalle Catastrofi Idrogeologiche and Piano Spaziale Nazionale of Italy.

5. REFERENCES

Cotton, W.R., G.J. Tripoli, R.M. Rauber, and E.A. Mulvihill, 1986: Numerical simulation of the effects of varying ice crystal nucleation rates and aggregation processes on orographic snowfall. J. Clim. Appl. Meteor., **25**, 1658-1680.

Mugnai, A., and E.A. Smith, 1988a: Radiative transfer to space through a precipitating cloud at multiple microwave frequencies. Part I: Model description. J. Appl. Meteor., **27**, 1055-1073.

Mugnai, A., and E.A. Smith, 1988b: Passive microwave remote sensing of precipitation from space: Impact of cloud microphysics. To appear in Microwave Radiometry and Remote Sensing Applications, VNU Science Press, Zeist-Netherlands, 10p.

Smith, E.A., and A. Mugnai, 1988a: Radiative transfer to space through a precipitating cloud at multiple microwave frequencies. Part II: Results and analysis. J. Appl. Meteor., **27**, 1074-1091.

Smith, E.A., and A. Mugnai, 1988b: The influence of ice microphysics on microwave radiation transfer through an evolving rain cloud. To appear in Current Problems in Atmospheric Radiation, A. Deepak Pub., Hampton, VA, 4p.

Tripoli, G.J., and W.R. Cotton, 1982: The Colorado State University three dimensional cloud/mesoscale model 1982. Part I: General theoretical framework and sensitivity experiments. J. Rech. Atmos., **16**, 185-200.

Wiscombe, W.J., 1982: The ATRAD model. Tech. Rep., Dept. of Appl. Sci., New York Univ., 26p.

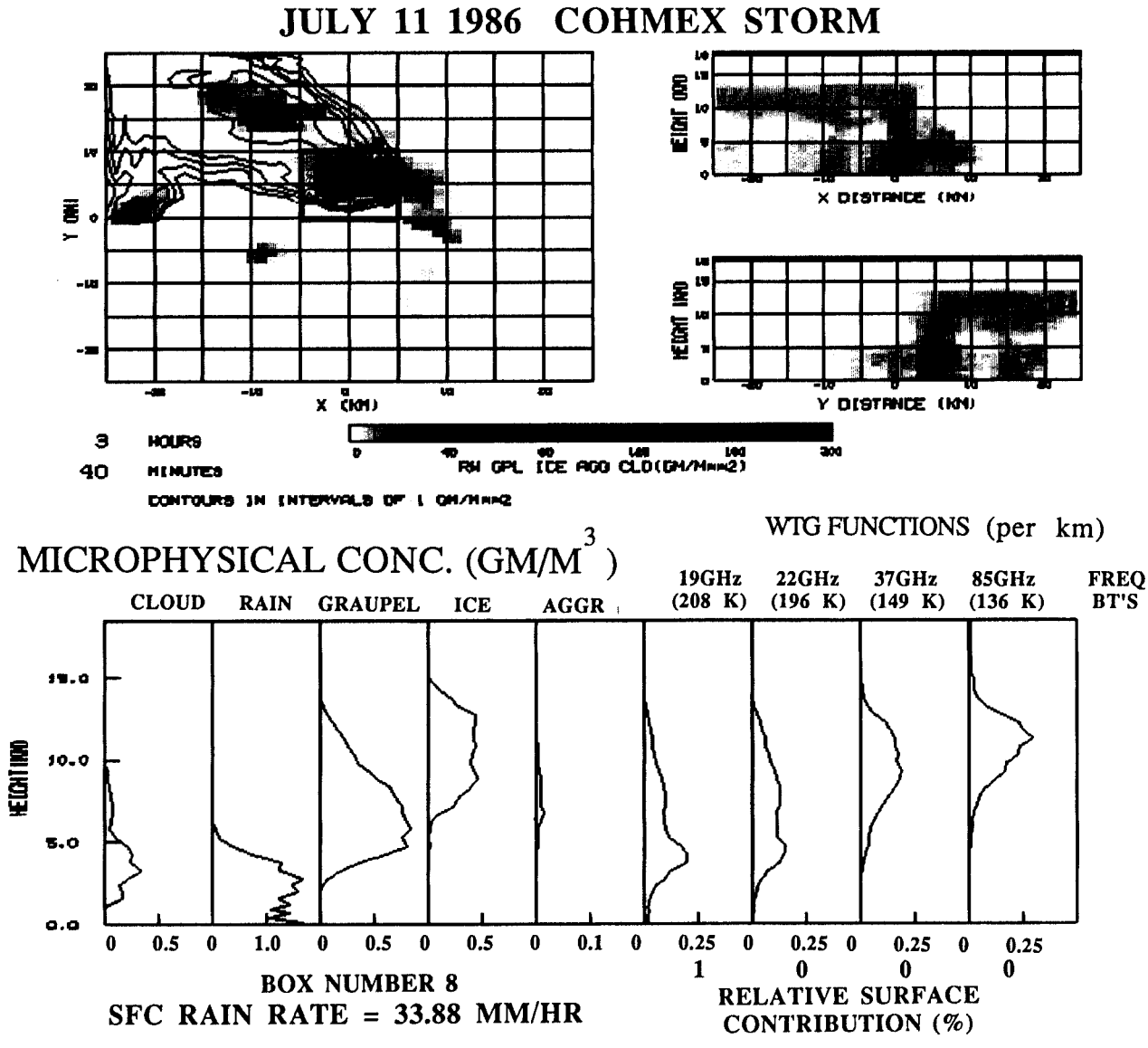

Fig. 1: Composite summary of model simulation at one time step (3 hour, 40 minutes) along with vertical profiles of hydrometeor concentrations and microwave weighting functions at SSM/I frequencies for an individual target. The upper 3 panels provide a top-down plan view, and x-z/y-z cross-sectional views of the microphysical structure of the storm. The five left-hand bottom panels show the vertical profiles of concentration for the five individual hydrometeor components of cloud, rain, graupel, ice crystals and ice aggregates for the target region outlined by the cursor given in the plan view. The four right hand bottom panels show the vertical temperature weighting functions for each SSM/I frequency associated with the target region considering contributions by all five modes of hydrometeors. The relative surface contribution to top-of-atmosphere brightness temperature is indicated below each weighting function panel; the frequency dependent top-of-atmosphere brightness temperatures are shown above each panel.

Time evolution of cloud fields from ISCCP observations.

G.G. Campbell and T.H. Vonder Haar

CIRA/CSU
Ft. Collins, CO. 80523

1. INTRODUCTION

One of the largest problems facing large scale model of the atmosphere is the difficulty of simulating clouds and cloud changes. New observations from the International Satellite Cloud Climatology Project (ISCCP) allow use to attack this problem from purely an empirical approach. Hear we discuss the time evolution of 280 km regional cloud amounts.

2. DATA

The ISCCP data are available every three hours on a 280 km by 280 km grid. Narrow band 11 um infrared and reflected visible observations are included from Meteosat, GOES 5, GOES 6, GMS and AVHRR. The original 10km X 10km pixel satellite data have been classified as cloudy or clear based upon a threshold comparison to the clear sky conditions (Rossow et al. 1988). The clear sky values were derived from the warmest or darkest satellite data in the region. Suitable tests were performed for bad data which is especially important in the clear sky derivation. A large number of parameters including cloud pressure and optical properties were saved onto the C1 archive tape. The primary data used in this study was the ratio of the number of cloudy pixels to the total number of analysed pixels in data grid. This we call cloud amount. It is a slight over estimate of cloud amount because it does not fully account for partly cloudy pixels.

Most of the observations in the middle latitudes and tropics come from the geosynchronous satellites with the polar orbiter filling in the nearest three hour bin if the geosynchronous data is not available. Figure 1 shows the zonal mean cloud amount from ISCCP for July 1983 and January 1984. This shows the expected features of high cloudiness near the equator, cloud minima in the subsidence zones and higher cloud amounts in the midlatitudes especially in the winter hemisphere.

3. METHODS

The time series of cloud amounts were analysed in several ways. Our primary interest in this study was to use the time series to characterize the evolution of the cloud fields. Now with the 3 hour ISCCP resolution, one cannot track individual cloud elements, but we see continuity in the regional average cloud amounts. The simplest thing to do is to calculate the lag correlations and look for the shape and length of the memory of cloud amount. Equation 1 defines the calculation:

$$1.\ \mathrm{Cor}(L) = \frac{\sum (f(T)-F)(f(T+L)-F)}{\sum (f(T)-F)(f(T)-F)}$$

where f is the cloud amount and F is the time mean amount.

One would expect cloud to be a first order Markov process and that Cor(T) would show an exponential decay. These correlations were then fit with an exponential, equation 2:

$$2.\ \mathrm{Cor}(L) = \mathrm{Exp}\ (\ L\ /\ t\ )$$

where t is minus the efolding time and the halflife is tln(.5).

This model of decay is reasonable if there are primarily local causes for cloud changes. External forcings confuse the issue with negative correlations and even periodic correlations driven by diurnal cycles.

There is a difficulty with this statistical method because it measures changes in fluctuations around the mean. But it would give zero corelation and undefined life time if the cloud amount were 100% for the entire time series. To measure this we also counted the longest string of hours with mostly cloudy conditions (greater than 75%) called persistence below.

4. TIME SERIES

Figures 2 shows a sample time series of cloud amount for July, 1983. In addition to the 3 ten day time series, a diurnal composite and a Fourier spectra a plotted. Over land areas where there are significant diurnal cycles, a peak will occur in the spectra at period 24 hours. This particular region shows an insignificant diurnal cycle. The top two plots show the lag corelation of the data and second the time series minus the diurnal mean. Superimposed are the exponential fit lines. For this particular region, the cloud halflife was calculated to be 29 hours. In addition there was one period of 141 hours in which the cloud amount never dropped below 75%. One sees in this series two kinds of cloud regimes, one with cloudiness continuously present for several days, and the other with short term fluctuations over a few days. The rise and fall rate of the clouds look to have time scales of about one day, indicating that the halflife time estimate of 29 days is too long for the short term events and too short for the persistent event.

5. LIFETIMES AND PERSISTENCE

Figure 3 shows the large scale view of the persistence. Long periods of continuous cloudiness occurs in the north and south Pacific. At the margin of these regions, long cloud halflife times occur beyond 40 hours, figure 4. The stratus regions west of North and South America and Africa also show long persistence. Most of the equatorial Pacific show halflives of between 6 and 12 hours. Most the continental areas show shorter life times and short persistences, because of diurnal forcing. For instance South America shows a halflife of

less than 6 hours. Distinct anomalies occur over the India ocean and central Asia. This is because no geosynchronous satellite data was available around 75 East. Figure 5 shows that the zonal mean halflife times are concentrated at 25 north in July and 25 south in January. The winter cloud persistences and lifetimes are generally longer than the summer situations.

Figure 6 expands the halflife plot from figure 4 to make details more evident. The maxima of halflife east of Asia at 30 north is the boundary between the very long persistence cloud north of 37.5 and the middle Pacific. This represents two climate regimes, the locally controlled cloud systems of the equatorial regions and the traveling wave regimes of the midlatitudes. There is a longer life time area associated with the south Pacific convergence zone seen in the plot at 195 east and 15 south.

6. LAGRANGIAN VIEW

In the real world cloud systems move with the motion of dynamical disturbances in the atmosphere. A time latitude plot of cloud amount at one latitude shows diurnal changes over the continent as well as semipermanent cloud systems at particular locations (Figure 7). One can track moving individual storm systems as diagonal stripes in the plots. Some of these persist for the entire length of the 30 day record. This implies that a Lagrangian view of the problem would show different cloud lifetime if one followed the storm systems.

To test this we moved the cloud data with the monthly mean climatological wind (Oort, 1983) and recalculated the correlations and lifetimes. Figure 8 shows longer lifetimes in some areas of the Pacific (as compared to figure 6) when the data is drifted with the mean wind. The patterns are distinctly different, depending upon the presence or absence of cloud systems. Adjustments in the speeds by direct measurements from the time latitude plots was considered, but then we would have run into the persistence problem. Basically if one tracks the clouds, then the cloud amount would be 100% all through the time series.

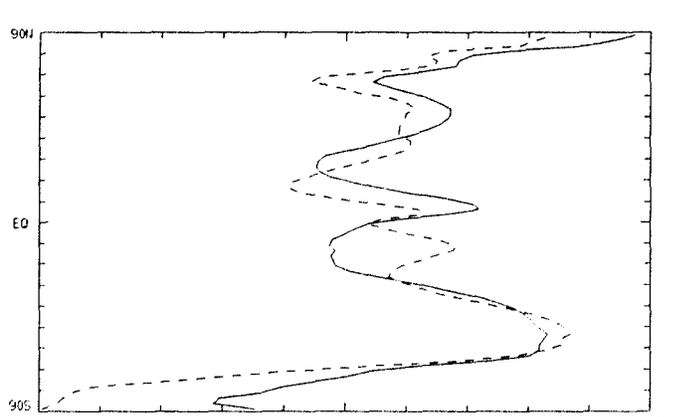

Figure 1, Zonal mean cloudiness for July 1983 and January 1984 (dashed). (%)

7. DISCUSSION

One of the most difficult problems for general circulation modeling is the transport and rain out of liquid water. These results imply that the cloud scheme utilized in these models must maintain clouds for several hours at the minimum and for 40 hours or more in the midlatitude ocean areas. Notice that we measured the regional cloudiness and the model attempts to simulate the regional average condition. The cloud physics problem of individual convective elements is not the whole story. These models generally suffer from cloud blinking (on/off clouds from one time step to the next) and too many extreme rain events (Thompson, 1989). One would like the cloud scheme to smoothly go from no cloud to partly cloudy to 100% cloudy with rise and fall times of many hours.

Taking the other view of following the air masses will produce longer lifetimes as shown in figure 8. This is fact is an alternative method being used for liquid water processes in GCM's.

8. CONCLUSIONS

We have shown of both persistence of cloud and cloud lifetimes show very long times scales to 40 hours for lifetime and weeks for persistent cloud systems. The simulation of these effects in GCM's requires more than attempting to simulate the variations of individual cloud elements. The tropical regions over the oceans show shorter lifetimes because there are basically local controls to the presence of clouds.

9. Acknowledgements

This research was supported under NOAA project NA85 RAH05045 and NASA project NAG-1-865.

10. REFERENCES

Oort, A., 1983: Global Atmospheric Circulation Statistics 1958-1973, NOAA Professional Paper 14, Rockville, Md.

Rossow, W., 1988: International Satellite Cloud Climatology Project, Documentation of Cloud Data, WMO.

Thompson, S., 1989, personal communication.

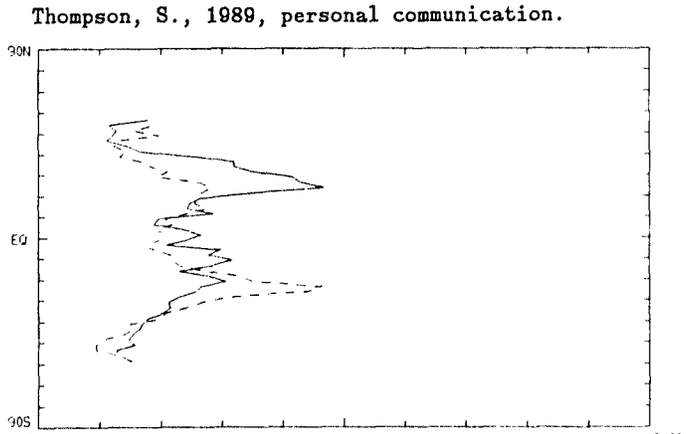

Figure 5, Zonal mean halflife over ocean for July 1983 (solid) and January 1984 (dashed). (hours)

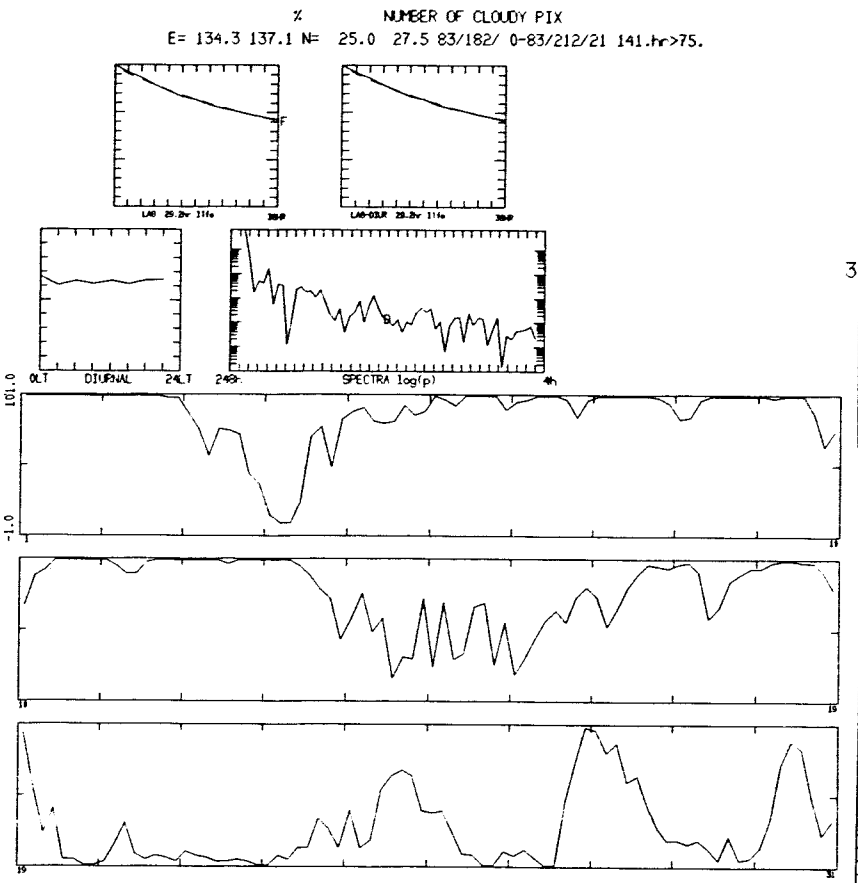

Figure 2, Time series of cloud amount for one ISCCP grid bin. (%)

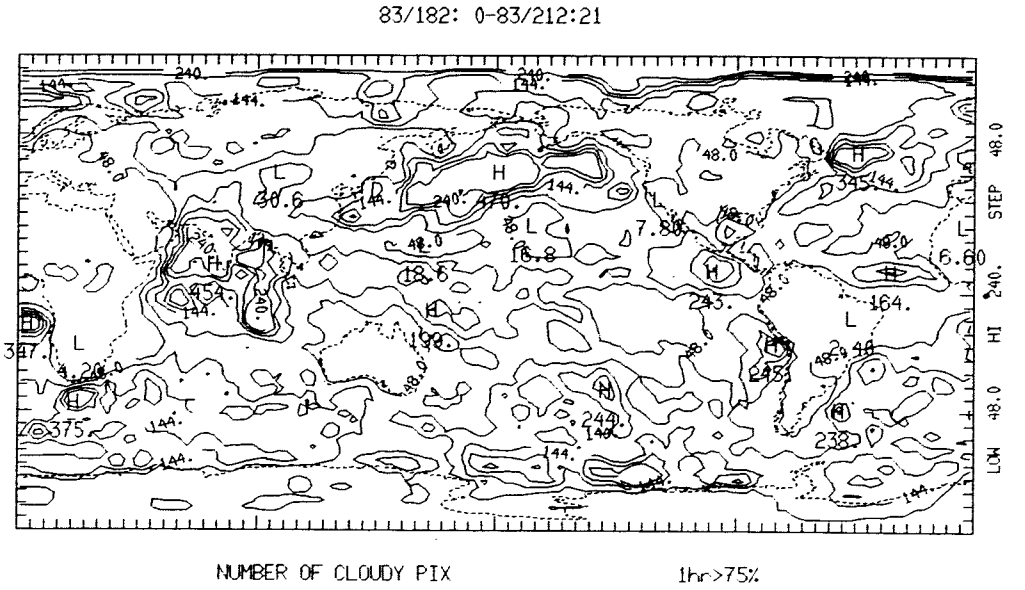

Figure 3, Longest string of cloudiness greater than 75%, persistence, for July, 1983. (hours)

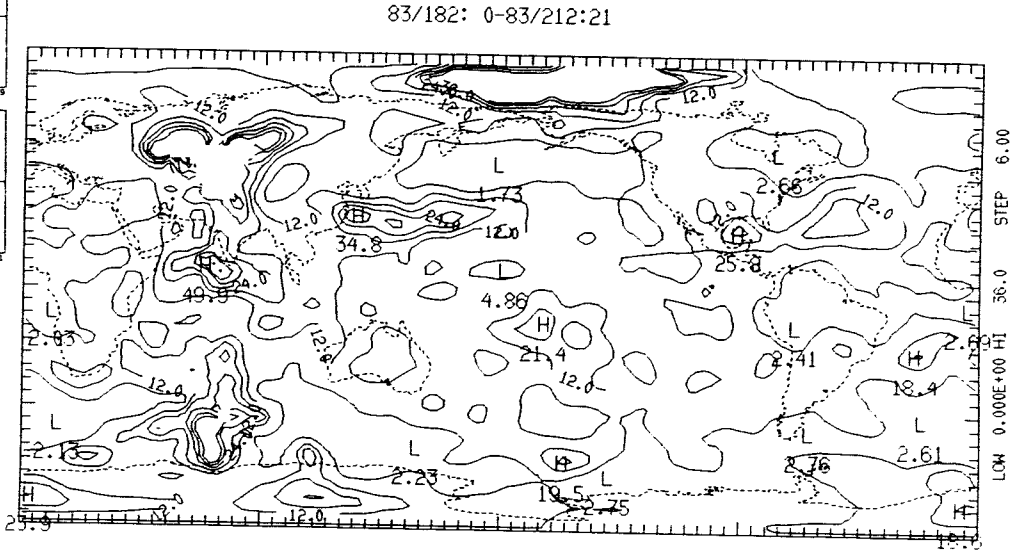

Figure 4, Cloud halflife for July 1983. (hours)

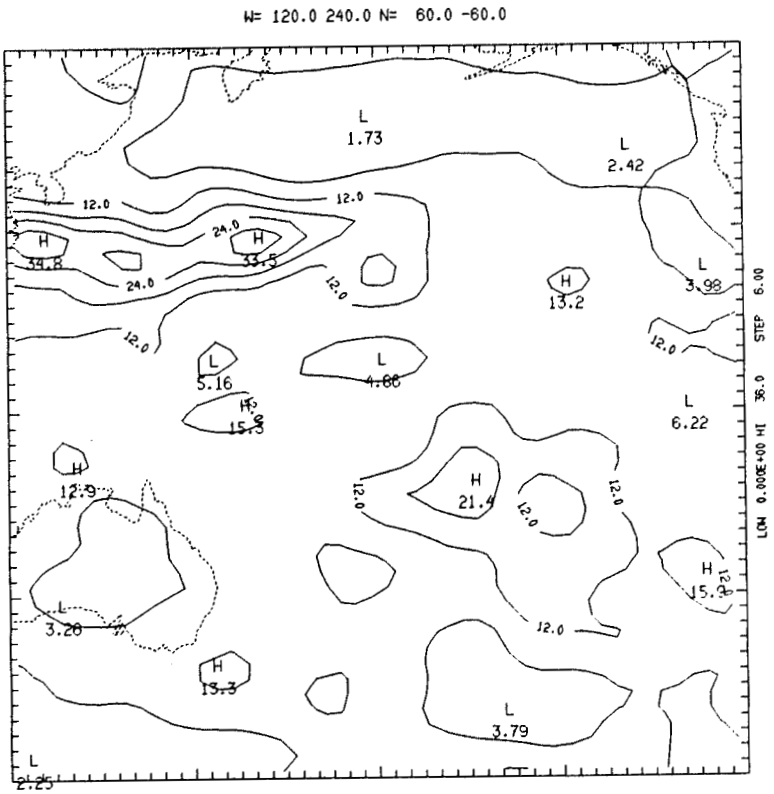

Figure 6, Expanded view of halflife for July 1983, 60 North to 60 South and 120 East to 240 East. (hours)

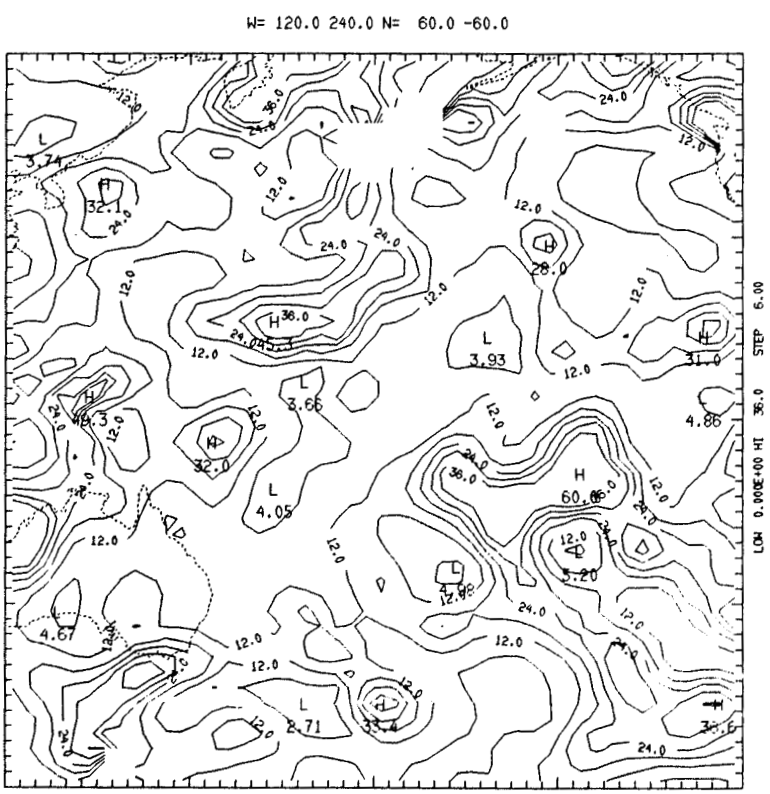

Figure 8, Cloud halflife with the movement of clouds with the mean wind added, for July 1983, 60 North to 60 South and 120 East to 240 East.

Figure 7, Time latitude plot of cloud amount for 0 to 2.5 north. (%)

SHORT-TIME-SCALE FLUCTUATION OF TROPICAL CONVECTION ABOVE AFRICA AND THE ATLANTIC OCEAN

J. Ph. DUVEL

Laboratoire de Météorologie Dynamique
Ecole Polytechnique - F91128 - Palaiseau cedex - France.

1. Introduction

A major characteristic of tropical convection is its strong response to the diurnal forcing not only over land but also over ocean (Minnis and Harrison, 1984; Duvel and Kandel, 1985; Albright et al, 1985). In addition, above Africa and many other tropical areas of the Earth, interdiurnal fluctuations of cloudiness appear to be mainly at short time scales (a few days) in relation with synoptic-scale tropospheric wave disturbances (Nitta, 1985; Duvel, 1988). The study of the modulation of the convection by both solar and wave forcings gives then a basis for a better understanding of the processes of generation and dissipation of tropical cloudiness. Such a study is also important for the validation of General Circulation Models because if they are to represent mean states correctly, they should also describe the fluctuations more directly related to physical processes. Such a description is needed not only for the good representation of the present climate but also to increase the credibility of sensitivity studies. For example, Wilson and Mitchell (1986) have shown that inclusion of the diurnal cycle has a large influence on climate simulations.

For such studies, data from geosynchronous satellites are adapted because only they are able to resolve the diurnal cycle homogeneously at a relatively large scale. In relation with the International Satellite Cloud Climatology Project (ISCCP) (Schiffer and Rossow, 1983), manageable geosynchronous satellites datasets are available for a relatively long period. It is therefore now possible to study diurnal modulation of cloudiness with the more climatological approach needed for validation of GCMs. The aim of the present study is also to analyse the relationship between convective clouds and African Easterly Wave disturbances. For this, we study summer 1985 which represents a new and larger dataset, previous studies being based for the most part on Phase III of GATE. The wind data set comes from analysed fields of the ECMWF which appear to well describe the African wave disturbances (Reed et al., 1986) over West Africa and adjacent Atlantic Ocean.

2. Data and analysis

The radiance data for the present study consists of three-hourly sampling of IR (10.5-12.5 μm) Meteosat ISCCP B2 data for summer (June to September) 1985. The area of investigation is the large area between 25°N and 5°S and 50°W and 50°E (fig.1). This area is divided into 533 regions of 2.5°x 2.5°. Wind fields, temperature and humidity profiles come from ECMWF analyses with horizontal resolution of 2.5° and 7 pressure levels between 1000 and 100 mb.

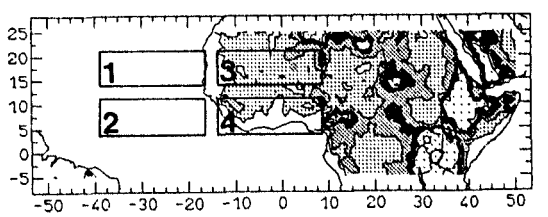

Figure 1 : Definition of regions 1-4.

The diurnal variation is defined here as the coherent diurnal variation (Duvel, 1988) obtained by computing the mean value of the considered quantity for each available hour. The wave modulation is also defined by a composite method. For this, the 850 mb meridional wind at the reference latitude (20°N for regions 1 and 3 of figure 1; 10°N for regions 2 and 4) is filtered using a Kaiser-Bessel filter centered at 4 days and with an attenu-ation of 20db at 7.7 and 2.7 days. At a *given longitude* the dates τ_i of maximum northerly wind are detected, defining the beginning of each oscillation i. Each wave, defined as the period between two northerly wind maxima (τ_i τ_{i+1}), is divided into 8 categories. Category 1 corresponds then to the maximum northerly wind at 850 mb for the reference latitude, category 5 to the maximum southerly wind, categories 3 and 7 correspond respectively to the trough and the ridge of the wave, other categories represent intermediate positions. The different quanti ties are averaged in each category.

In order to show in detail the response of cloudiness to the different forcings it is possible to compute the mean diurnal or wave modulation of the histograms over selected nearly homogeneous regions (Duvel and Kandel, 1985; Albright et al, 1985). For the wave modulation, each histogram has been initially computed (averaged for each category) on the

basis of the wave position relative to the individual 2.5°x 2.5° region. Results are presented on the average over each of the 4 nearly homogeneous regions defined on figure 1. The surface percentage (figure 2 and 3) is the number of pixels emitting in a radiance interval expressed as a percentage of the total number of pixel of the considered region. For clarity, the radiance scale is converted into a pressure scale computed for each region using LOWTRAN with the mean summer temperature and water vapor profiles and assuming that a cloud with top at a given pressure level emits as a black body at the temperature of this level. White areas under 700 mb must be considered with care since these levels may be contaminated by surface emission especially over land. Note that the following figures must not be interpreted in terms of multi-layered cloud but in terms of clouds at different altitudes distributed over the whole considered area and with varying coverage from one day (or wave) to another. The evolution of the population of each radiance level may then be interpreted - independently of other radiance levels - as the modulation of the probability of presence of clouds with top emitting this radiance.

3. Diurnal variation of cloudiness

Over Subsaharan and Sahelian regions (region 3) and over the land portion of the active ITCZ (region 4), high and mid-level clouds appear to be concentrated mainly at 2 pressure levels around respectively 200 and 500 mb (fig.2). This figure exhibits clearly the well known maximum of deep convection at the end of the afternoon. Over region 3, mid-level clouds have a very strong diurnal modulation with maximum coverage between 0200 LST and 0500 LST and a rapid decrease until local noon. These clouds are mainly concentrated south and west of the region. The diurnal amplitude is around 11% of the total surface of the region (80% of the mean cloud cover). For regions further south (region 4) the diurnal variation of the effective mid-level cloud coverage is around 15% (50% of the mean cloud cover).

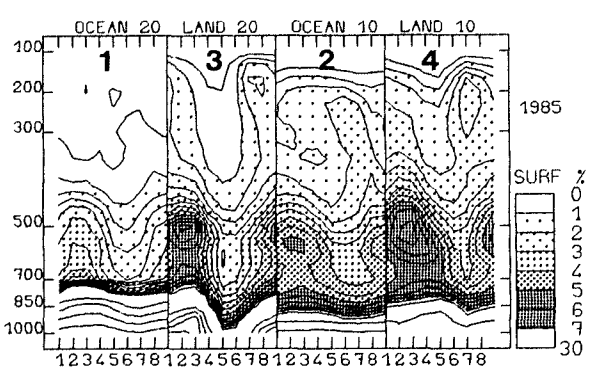

Figure 2: Diurnal histogram evolution of regions 1-4 for summer 1985 (see text). Abscissas are time steps (3 h) the fisrt time step being 00 GMT. Ordinates are pressure levels. The percentage of surface is multiplied by a factor 2 for regions 1 and 3.

While the shape of the diurnal variation of mid-level clouds over ocean is very close to that over land, deep convection has a different diurnal behavior. Over the oceanic part of the ITCZ (region 2), the highest cloudiness (around 200 mb) presents a very weak maximum around 0400 LST. The time of maximum occurs progressively later with decreasing height giving a maximum cloud amount around 1900 LST above 500 mb. The largest high cloud concentration occurs between 1300 and 1600 LST consistently with the diurnal variation of rainfall activity found by Albright et al (1981) on the basis of GATE data and showing maximum precipitation around 1500 LST. This maximum may be a consequence of the large scale land-induced subsidence inhibiting convection in the late afternoon and during the night in the absence of large clusters. In the early morning, there is a large maximum of mid-level clouds and also a weak maximum of the highest clouds. These maxima in the early morning may be attributed to enhancement of low-level convergence by the radiational cooling difference at night between the ITCZ and the stratocumulus regions to the North.

4. Wave modulation of the cloudiness

The composite analysis reveals that the phase of the wave modulation of the cloudiness depends only on the geographical location and therefore on the mean atmospheric state. This phase is nearly homogeneous over 4 large areas (fig.1) for which the modulation of the atmospheric state and of the moisture fluxes have been computed.

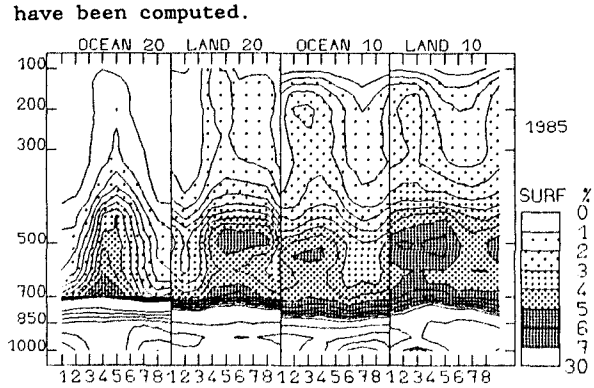

Figure 3 : As in figure 2 but for the wave modulation. Abscissas are wave categories.

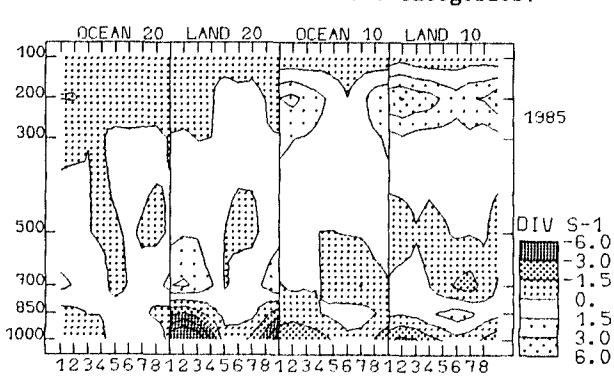

Figure 4 : Wave modulation of the divergence (10^{-6} s^{-1})

Over oceanic regions around 7.5°N, deep convection is maximum at and ahead of the trough and minimum on the ridge (fig.3) with a mean amplitude of effective cloud cover greater than 10% (75% of the mean high cloud cover). Mid-level clouds have a weaker wave modulation (24% of the mean mid-level cloud cover). The maximum cloud development at and ahead of the trough corresponds to maximum low-level convergence and to maximum high-level (200 mb) divergence (fig.4). The net moisture flux is convergent in the mean with maximum values ahead of the trough due to strong meridional convergence (fig.5). There is slight moisture divergence on the ridge. The storage rate is nearly in phase with the divergence and the resulting difference Evaporation-Precipitation (E_o-P_o) is minimum just ahead of the trough (Table I). For the strong convective activity at and ahead of the trough, the direct water vapor supply from surrounding regions is mainly from the north at low and mid-levels. At mid-levels (around 700 mb), this flow certainly contributes to the convective activity by injection of moisture into the boundary layer by downdraft. The net zonal flux is slightly convergent on the ridge due to horizontal convergence around 700 mb which increases the storage rate.

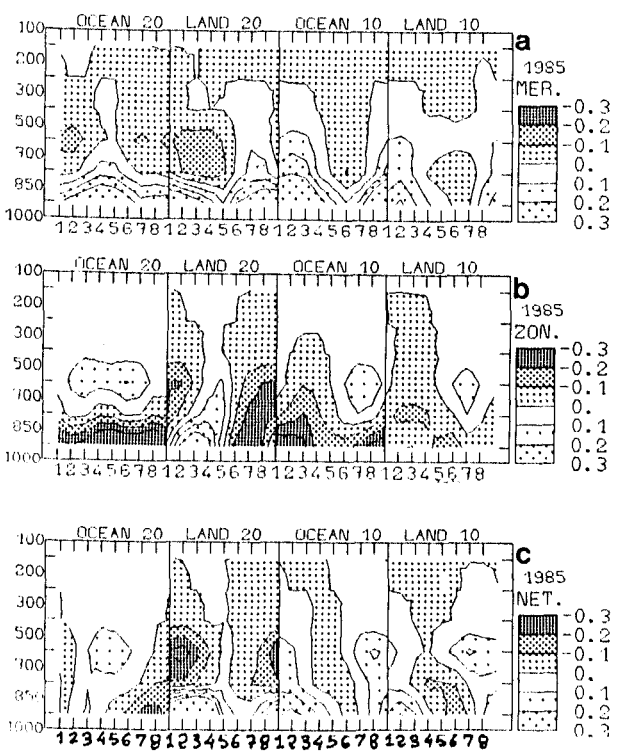

Figure 5 : Wave modulation of the moisture convergence for a mean 2.5x2.5° region belonging to each large region 1-4. (a) meridional convergence; (b) zonal convergence; (c) total convergence. (10^7 kg s^{-1}/2.5°).

Categories		N	2	T	4	S	6	R	8	Mean
	D_q^i	3.4	-1.0	-4.4	-4.0	-2.8	-0.8	2.0	4.3	-0.4
Reg. 1	A_q^i	-2.6	2.2	3.8	2.5	0.7	-0.4	-2.0	-4.2	0.
	E_o-P_o	0.8	1.2	-0.6	-1.5	-2.1	-1.2	0.	0.1	-0.4
	D_q^i	-7.3	-7.0	-4.1	-1.4	0.5	0.5	-3.0	-6.2	-3.5
Reg. 2	A_q^i	2.6	1.5	-0.5	-1.7	-2.5	-2.4	0.5	2.5	0.
	E_o-P_o	-4.7	-5.5	-4.6	-3.1	-2.0	-1.9	-2.5	-3.7	-3.5
	D_q^i	-0.2	-2.5	-6.0	-5.8	-2.7	0.0	1.0	0.5	-2.
Reg. 3	A_q^i	-3.0	-0.5	2.4	4.5	1.5	-1.4	-1.0	-2.5	0.
	E_o-P_o	-3.2	-3.0	-3.6	-1.3	-1.2	-1.4	0.	-2.0	-2.
	D_q^i	-5.1	-5.1	-2.3	1.2	1.2	1.7	-2.0	-4.1	-1.8
Reg. 4	A_q^i	1.9	1.3	-0.5	-1.8	-1.7	-1.1	0.3	1.6	0.
	E_o-P_o	-3.2	-3.8	-2.8	-0.6	-0.5	0.6	-1.7	-2.5	-1.8

Table I : Wave modulation of the accumulation rate (A_q), the moisture divergence (D_q+D_q^W) and the difference between evaporation and precipitation E_o-P_o (expressed in mm day^{-1}).

There are only small differences between the wave perturbations over oceanic and land regions around 7.5°N. Over land regions, deep convection is also maximum on the trough and minimum on the ridge with a mean amplitude of effective cloud cover greater than 9% (60% of the mean high cloud cover). The mid-level cloud modulation is stronger during the dryest year (55% for 1983 instead of 14% for 1985 presented here). Net moisture flux is convergent in the mean with maximum values ahead of the trough and there is slight divergence ahead of the ridge. The storage rate and E_o-P_o have nearly the same phase in good agreement with the phase of the convection. Net moisture flux convergence ahead of the trough is due to net meridional flux convergence resulting from equal contributions of a low-level southerly inflow and a mid-level northerly inflow. This leads to the conclusion that, for the maximum convective activity on the trough, half of the direct moisture supply from surrounding regions is from Sahelian regions at mid-levels. As for the oceanic regions, a part of this mid-level flow is certainly injected into the boundary layer by downdraft and then contributes directly to the convective development. In addition, there is an effective although weak water vapor supply from the AEJ which contributes to the moisture storage east of the ridge (fig.5).

The wave modulation of the convection over Sahelian regions is not directly related to synoptic scale dynamical forcing. Sahelian convection has a primary maximum 1/4 wavelength east of the trough and a secondary maximum east of the ridge consistent with the divergence pattern above 500 mb (fig.4). On the basis of a relatively small sample (June months) of active squall lines, only the secondary maximum appears to be related to squall episodes. Modulation of effective cloud cover related to deep convection has a mean amplitude of the order of 4% (77% of the mean high cloud cover). Mid-level clouds have a wave modulation representing 51% of the mean cover. Ahead of the trough, there is shallow dry convection (fig.4) characterised by : strong low-level convergence and mid-level (700 mb) divergence; subsidence

above 500 mb; maximum cyclonic vorticity and highly suppressed conditions. This is certainly the main mechanism for dust injection into the troposphere over the Sahel. The direct low-level moisture supply from surrounding regions appears to be mainly due to zonal convergence for the maximum convection east of the trough and to meridional convergence and moisture storage for the secondary convective maximum east of the ridge (fig.5). The term E_o-P_o has 3 minima in categories 1, 3 and 6. This phase does not agree well with the phase of the cloudiness (Fig.3) which is maximum in categories 4 and 7. A part of this disagreement may be related to the computation of the storage rate on the basis of centered finite differences with a large time step. Examination of the cloud behavior does show indeed strong gradients around cat.2. Over Sahelian regions, the net *wave* moisture divergence is slightly positive suggesting that the wave leads to increased evaporation compared to precipitation. This *wave* divergence is due to an unbalanced northward *wave* humidity flux.

5. Discussion

The large concentration of cloud with top around 500 mb and with a maximum horizontal extension near sunrise appears over all the studied regions. Previous results - over Brazil and West Africa in August and January 1979 (Duvel and Kandel, 1985) or for the GATE region in summer 1974 and Central Pacific in winter 1979 (Albright et al, 1985) - also show the presence of this type of cloud. This tends to show that these clouds are typical of tropical regions. However, their nature and their origin have not yet been well documented. The diurnal cycle of the mid-level cloud appears to be directly related to the higher-level cloudiness and suggests a horizontal spreading of altocumulus or altostratus at night when the higher cloudiness dissipates. Especially over Ocean, this behavior may be however related to a nighttime development of cumulus congestus. The diurnal phase, the large amount and the relatively high altitude (around 5 km) of these mid-level clouds give an enhancement of their greenhouse effect at the expense of their albedo effect. This diurnal behavior is then an important factor for the radiative forcing of these clouds and contributes to the warming of the tropical regions. Over land regions, this is also valid for the higher cloudiness which has a maximum horizontal extension between 1700 LST and 2000 LST and a minimum around local noon.

The mean structure of the wave and the associated cloud modulation, derived by a composite method, reveal a very good consistency between the Meteosat observed cloudiness and ECMWF analyses. These results lead to the conclusion that only land and oceanic regions around 7.5°N may be subject to wave-CISK (Lindzen, 1974). For these regions, there is effectively a synoptic-scale organisation of the convective cells consistent with the synoptic-scale dynamical forcing. Over Sahelian regions, the large-scale dynamical forcing of the wave gives shallow dry convection which may be in part a consequence of subsidence from regions further south. The deep convection develops in contradiction with the wave forcing and must have then a damping effect on the wave. In addition, because of the different responses of the cloudiness to the wave forcing, the longitudinal and the latitudinal variations of the phase of the cloudiness modulation must be considered for a correct estimation of the wave characteristics (wavelength, phase speed) on the basis of satellite observations alone.

References

Albright, M.D., D.R. Mock, E.E. Recker, and R.J. Reed, 1981 : A diagnostic study of the diurnal rainfall variation in the GATE B-scale area. *J. Atmos. Sci.*, **38**, 1429-1445.

Albright , M.D., E.E. Recker, R.J. Reed and R. Dang, 1985 : The diurnal variation of deep convection and inferred precipitation in the central tropical Pacific during January-February 1979. *Mon. Wea. Rev.*, 113, 1663-1680.

Duvel, J.P., and R.S. Kandel, 1985 : Regional-scale diurnal variations of outgoing infrared radiation observed by Meteosat. *J. Climate Appl. Meteor.*, **24**, 335-349.

Duvel, J.P., 1988 : Analysis of diurnal, interdiurnal and interannual variations during Northern Hemisphere summers Using Meteosat Infrared Channels. *J. Climate*, 1, 471-484.

Lindzen, R.S., 1974 : Wave-CISK in the tropics. *J. Atmos. Sci.*, **31**, 156-179.

Minnis, P., and E.F. Harrison, 1984 : Diurnal variability of regional cloud and clear-sky radiative parameters derived from GOES data. Part I : analysis method ; part II : November 1978 cloud distributions ; part III : November 1978 radiative parameters. *J.Climate Appl. Meteor.*, 23, 993-1051.

Nitta, T., Y. Nakagomi, Y. Suzuki, N. Hasegawa and A. Kadokura, 1985 : Global analysis of the lower tropospheric disturbances in the Tropics during Northern Summer of the FGGE year. Part I: Global features of the disturbances. *J. Meteor. Soc. Japan*, **63**, 1-18.

Reed, R.J, A. Hollingsworth, W.A. Heckley and F. Delsol, 1986 : An evaluation of the performance of the ECMWF operational forecasting system in analysing and forecasting tropical Easterly waves disturbances. Part 1 : Synoptic investigation. ECMWF Tech. Rep. 58.

Schiffer, R.A., and W.B. Rossow, 1983 : The International Satellite Cloud Climatology Project (ISCCP) : The first project of the World Climate Research Program. *Bull. Amer. Meteor. Soc.*, 64, 779-784.

Wilson, C.A. and J.F.B. Mitchell, 1986 : Diurnal variation and cloud in a general circulation model. *Quart. J. Roy. Meteor. Soc.*, 112, 347-369.

JP8A.21

IMPACT OF VAS RETRIEVALS ON A SIMULATION OF RETURN FLOW IN THE GULF OF MEXICO

Robert M. Aune

NOAA/NESDIS Systems Design and Applications Branch
Madison, Wisconsin

1. INTRODUCTION

A major source of thermodynamic energy that fuels most of the precipitation-producing weather in the central and eastern United States is the Gulf of Mexico. Any dynamic situation that produces a southerly wind component in the lower troposphere along the Gulf Coast will almost invariably have a destabilizing effect on the surrounding atmosphere. The accurate specification of the temperature and moisture structure in the Gulf is crucial in producing numerical simulations of precipitation-producing events such as Gulf Coast sea-breeze convection, dry line disturbances, and cold-air outbreak/return flow events. Unfortunately, conventional temperature and moisture observations of sufficient temporal and spatial resolution to initialize numerical forecast models are not routinely taken in the volume of atmosphere bounded by the Gulf.

Retrievals from the VISSR Atmospheric Sounder (VAS) are a source of high horizontal and temporal resolution temperature and moisture data that are routinely available with excellent coverage over the Gulf. Wade et al. (1988) demonstrated the usefulness of VAS derived precipitable water and SST images for identifying features in the Gulf. Other studies have used VAS data, with limited success, to augment conventional data networks for analysis studies (Mostek et al. 1986) and numerical forecast experiments (Gal-Chen et al. 1986; Aune et al. 1987; and Benjamin et al. 1988). Temperature and moisture retrievals can be generated as often as every 3 hours using all 12 channels from the VAS Dwell Soundings, with a horizontal resolution down to the satellite FOV of approximately 8 km. Needless to say, conventional data with this kind of resolution are not usually available in the Gulf.

During February and March of 1988, comprehensive observational data sets were collected during the Gulf of Mexico Experiment (GUFMEX) to examine two Gulf phenomena:

(1) Airmass modification over the Loop Current, and
(2) the origin and characteristics of the return flow that follows a cold-air outbreak over the Gulf.

A complete overview of GUFMEX is presented by Lewis et al. (1989). Data sets from GUFMEX can be used to identify the impact VAS retrievals might have on a numerical simulation of a return flow event.

The purpose of this study is to determine if thickness and precipitable water retrievals from VAS can have a positive impact on a numerical simulation of return flow in the Gulf. VAS thickness data will be inserted into a numerical simulation of two cases documented in GUFMEX: 20-24 February and 6-10 March, 1988, using a variational technique. In addition, a similar technique for assimilating VAS precipitable water will be developed. The technique used for assimilating VAS thickness data is that described by Aune et al. (1987). As such only a discussion of assimilating precipitable water is presented in Section 2. A series of impact experiments are proposed in Section 3.

2. ASSIMILATION TECHNIQUE

Studies have shown that temperature and moisture profiles derived from VAS radiances can have a positive impact on an analysis of the preconvective environment. Mostek et al. (1986) demonstrated a positive impact when using VAS retrievals to enhance the conventional observing network in an analysis of one case over the central United States. Their results were particularly promising when vertically integrated quantities were analyzed, such as precipitable water, mainly because such a parameter is physically representative of what the instrument senses. Retrieving temperature and moisture profiles from VAS in the form of 10 or 15 level pseudo-RAOBs certainly exceeds the instrument's vertical

resolving capabilities. This might be one cause for the less-than-spectacular impact found by Cram and Kaplan (1985) and O'Lenic (1986) when they assimilated VAS pseudo-RAOBs in their respective numerical model impact studies. To eliminate these resolution restrictions, Gal-Chen (1983) proposed using a calculus of variations approach that would assimilate vertically integrated quantities, such as thickness and precipitable water from geostationary satellites into mesoscale numerical models. The advantage of this technique is that it allows for the insertion of timely satellite information with high horizontal resolution, while simultaneously preserving the significant solutions generated by the forecast model, in particular, the evolving vertical structure. Gal-Chen et al. (1986), and more recently Aune et al. (1987), have obtained favorable results using similar forms of this technique to assimilate VAS thickness data into a mesoscale model without moisture. By using a dry model, i.e. no predictive equation for moisture and no moist physics, they were able to clearly trace the impact of the VAS data throughout their simulations. The impact would have been less obvious with moist processes present.

The assimilation of a vertically integrated moisture parameter, such as precipitable water from VAS, is not as straight forward as inserting thicknesses. In the atmosphere, and in most numerical models, temperature maintains a fairly intimate relationship with other state variables, i.e. with momentum through the geostrophic and thermal wind equations and with pressure through the hydrostatic approximation, hypsometric equation, and ideal gas law. One or all of these relationships can be used to constrain the vertical distribution of incremental temperatures that result when a layer-average temperature at a model grid point location is in disagreement with a colocated thickness retrieval. Moisture, on the other hand, is a quasi-passive contaminant. It is free to advect about the atmosphere and only interacts with temperature when saturation is reached or through evaporation (to a lesser extent it is linked to the virtual temperature). The vertical distribution of moisture in the atmosphere can display a wide range of variability with the only restriction being the upper limit of saturation. Consequently, where a VAS precipitable water retrieval disagrees with a colocated model precipitable water, it is not intuitively obvious how to distribute the resulting moisture adjustment in the vertical.

A first attempt has been made to devise a scheme to analytically adjust model mixing ratio profiles to reflect precipitable water retrievals from VAS. Adjustments to the mixing ratio profile are distributed as a function of the pre-adjusted mixing ratio values. In other words, where VAS precipitable water retrievals showed an increase over the computed model value, mixing ratio adjustments are added to the model profile, with moist layers receiving proportionally more adjustment than dry layers. This approach was adopted for two reasons: 1) It preserves the original vertical gradient of mixing ratio, with only slight deviations, and 2) it inherently inserts more moisture in the lower levels and reduces the chances of accidently saturating a layer, which contradicts the presence of a cloud-free VAS retrieval at that location. If saturation is encountered moisture is then iteratively redistributed to adjacent layers above and below until a clear-air criteria is met.

This scheme was tested on hundreds of mixing ratio profiles taken from the 20 July, 1981 case used by Aune et al. (1987). Figure 1 shows a typical mixing ratio profile before and after adjustment. The solid line is the original model profile and the dashed line is the profile after it has been adjusted to reflect a slight increase in precipitable water. The increased departure from the original profile at sigma level 8 is a result of assimilating two precipitable water layers: 920-600mb and 600-100mb at this grid point. The majority of the moisture correction ended up in the lowest level of the upper precipitable water layer because the mixing ratio values in the upper sigma layers were two orders of magnitude drier than the lower. This phenomena also occured when moist layers were present, such as might be found in a stable boundary layer. On a few occasions at certain grid points the mois-

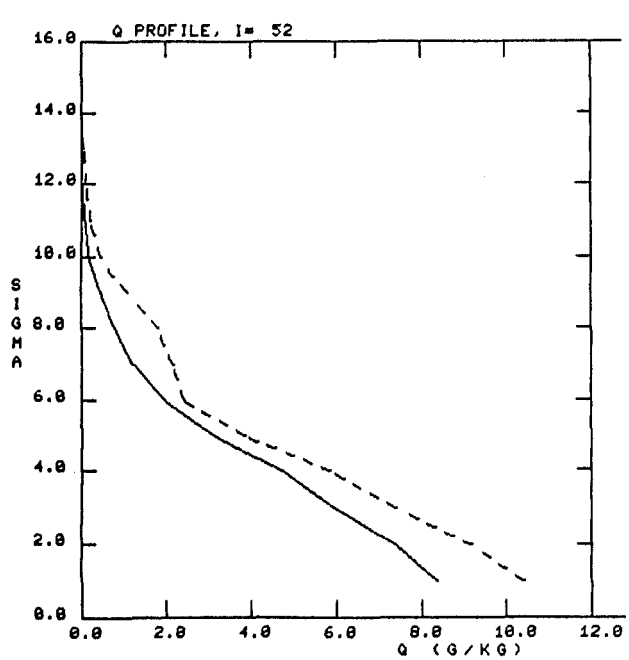

Fig 1. A typical vertical profile (sigma) of mixing ratio (g/kg): Solid, before adjustment; Dashed, after adjustment, reflecting an increase in the column precipitable water.

ture adjustment completely saturated the precipitable water column. This infers that the corresponding temperature profile may be evolving unrealistically (suggesting the need for the simultaneous assimilation of temperature). Efforts to resolve inconsistencies in the above scheme are continuing. In addition, a variational approach similar to that used by Aune et al. (1987) to assimilate thicknesses is being investigated.

3. EXPERIMENT DESIGN

A series of data assimilation impact studies are planned to determine if VAS retrievals can positively influence a numerical simulation of return flow in the Gulf of Mexico. The sub-synoptic scale primitive equation model at the Cooperative Institute for Meteorological Satellite Studies (CIMSS) will be used to produce a series of data/no data simulations of the 20-24 February and 6-10 March cases. The model is a version of the Austrailian Meteorological Bureau's operational forecast model (Leslie et al. 1985). VAS retrievals for two layers bounded by specified model sigma layers were generated by Hayden and Schriener (1989). The VAS radiances are converted to thickness and precipitable water directly from the imagery which allows the data to be matched directly to the model resolution. Results of the simulations will be presented at the conference.

4. REFERENCES

Aune, R. M., L. W. Uccellini, R. A. Petersen, and J. J. Tuccillo, 1987: A VAS numerical model impact study using the Gal-Chen variational approach. Mon. Wea. Rev., 115, 1009-1035.

Benjamin, S. G., D. L. Birkenheuer, R. D. McPherson, T. L. Smith, and J. S. Snook, 1988: Experiments in the assimilation of radiance observations from VAS. Preprints, 4th Conf on Sat Meteor and Oceano, San Diego, AMS.

Cram, J. M. and M. L. Kaplan, 1985: Variational assimilation of VAS data into a mesoscale model: Assimilation method and sensitivity experiments. Mon. Wea. Rev., 113, 467-484.

Gal-Chen, T., 1983: Initialization of mesoscale models: The possible impact of remotely sensed data. Mesoscale Meteorology: Theories, Observations and Models, D. K. Lilly and T. Gal-Chen, Eds., Reidel, 157-171.

Gal-Chen, T., B. D. Schmidt, and L. W. Uccellini, 1986: Simulation experiments for testing the assimilation of geostationary satellite temperature retrievals into a numerical prediction model. Mon. Wea. Rev., 114, 1213-1230.

Hayden, C. M. and A. J. Schriener, 1989: Moisture retrievals from GOES VAS. Preprints, 4th Conf on Sat Meteor and Oceano, San Diego, AMS.

Lewis, J. M., C. M. Hayden, R. T Merrill, and J. M. Schneider, 1989: GUFMEX: A study of return flow in the Gulf of Mexico. Bull. Amer. Met. Soc., 68, 24-29.

Leslie, L. M., G. A. Mills, L. W. Logan, D. J. Gauntlett, G. A. Kelly, M. J. Manton, J. L. McGregor and J. M. Sardie, 1985: A high-resolution primative equations model for operations and research. Aust. Meteor. Mag., 33, 11-35.

Mostek, A., L. W. Uccellini, R. A. Petersen, and D. Chesters, 1986: Assessment of VAS soundings in the analysis of a preconvective environment. Mon. Wea. Rev., 114, 62-87.

O'Lenic, E. A., 1986: The effect of VISSR atmospheric sounder data on some LFM analyses and forecasts. Mon. Wea. Rev., 114, 1832-1846.

Wade, G. S., C. M. Hayden, J. M. Lewis, and R. T. Merrill, 1988: Modification of air masses over the Gulf of Mexico - Progress report from a VAS viewpoint. Preprints, 15th Conf on Severe Local Storms, Baltimore, AMS, 484-487.

ESTIMATION OF FREQUENCY-WAVE NUMBER SPECTRUM IN GATE RAIN DATA

Shoichiro Nakamoto, J. B. Valdes+, G. R. North
Climate System Research Program
College of Geosciences, Texas A&M University
College Station, Texas 77843-3146

+Civil Engineering Department
College of Engineering, Texas A&M University
College Station, Texas 77843-3146

1. INTRODUCTION

Since rainfall is a spatial and temporal phenomenon the space-time correlation and its associated frequency-wave number spectrum are needed to model the processes. Satellite observations of rainfall provide information on the space-time structure of rainfall but they are limited by their intermittent visits.

In this study GATE(GARP Atlantic Tropical Experiment) radar data were used to obtain the frequency-wave number spectrum and its associated space-time correlation. In section 2, we describe the data set used and the method of analysis is explained. In section 3, we use a simple space-time Markov model to explain the observed spectrum and propose the applicability of the model. In section 4, we use the spectrum to estimate the mean square sampling error of an imaginary satellite flying over the GATE area.

2. THE GATE RADAR DATA

2.1 Data Description

The GATE experiment was conducted during the summer of 1974. During the GATE experiment measurements from raingages and radars were made in a 400 km diameter hexagon. Patterson et al. (1979) calculated rainfall rate from the observations, given mean equivalent rainfall in 4 km x 4 km bins. The data used in this study is the GATE Phase I covering from 28 July to 16 July.

We are interested in the space-time structure of the rainfall process at all possible resolutions. Thus equally spaced data in space and in time are needed in our analysis. In the GATE Phase I data set, however, we found that there exist several gaps in the observations and an interpolation procedure was used to fill or reject these gaps. Two subsets whose total observation time interval exceeded 4 days were selected (data set #5 and data set #11).

In order to obtain the frequency-wave number spectrum three-dimensional fast Fourier transforms of the two data sets were generated. To smooth the results, a Tukey-Hanning filter which has a 3-term weighted moving average with weights equal to 1/4, 1/2, 1/4 is applied. This filter has the equivalent lag window $\lambda(t) = \frac{1}{2}\left(1+\cos\left(\frac{\pi t}{M}\right)\right)$ for $|t|<M$ and zero for $|t|>M$, where t denotes the center point of the filtering and M denotes the total data length. In the wave number domain two dimensional Tukey-Hanning filter having an equivalent lag window was used. The spectral bandwidth for the frequency domain was defined as

$$W = \frac{1}{2M(1-2a+1.5a^2)}$$

where a=0.5 for Tukey-Hanning filter case (Blackman and Tukey, 1985). Thus the frequency increment becomes $\Delta f = \frac{4}{3M}$. A similar approach was followed for the two dimensional wave number domain. The ratio of the magnitude of the spectral estimate to the local magnitude of the true spectrum was defined as 95% chi-square divided by the degree of freedom of the spectral estimate used as the 95% confidence limit (Mitchell, 1966).

The space-time correlation was computed by taking the inverse fast Fourier transform of the observed frequency-wave number spectrum. The resulting space correlation function was compared with the one calculated by taking all products of the rainfall intensity for all discrete time and for random sampling in space (Bell et al., 1988).

2.2 Results

In Fig. 1 the estimated frequency-wave number spectrum is shown. The low frequency-low wave number region was matched to the following empirical formula

$$P(f, \upsilon) = \frac{1}{A^2 f^2 + \left(1+B^2\upsilon^2\right)^2} \quad , \qquad (1)$$

where A=0.67, B=0.82 for data set #5 and A=0.91, B=0.70 for data set #11. The dashed-lines in Fig. 1 show the model frequency wave number spectrum. Fig. 2 the frequency spectrum for different wave numbers is shown in log-log graph. Notice that the power in the lower frequency region (f<1/day) is approximate-

ly -2 but the power in the higher frequency region drops to -4. Also the fourth power becomes dominant for frequencies larger than 3/day. A significant interrelation between frequency and wave number up to the frequency 3/day and wave number 2/280 km is observed. In contrast to this, the slope is independent of wave number in the frequency region higher than 3/day. The diurnal and semi-diurnal cycles are noticeable only for the very low wave number case. In Fig. 3 the wave number spectrum for data sets #5 and #11 are shown. In Fig. 4 the observed wave number spectrum for the zero frequency case and the model spectrum are shown.

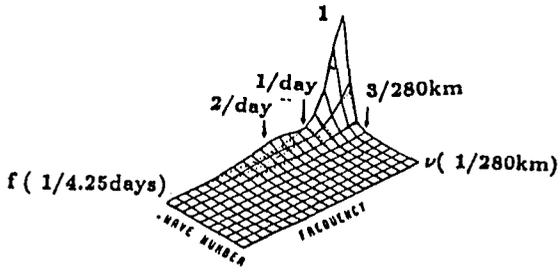

Fig. 1 Frequency wave number spectrum

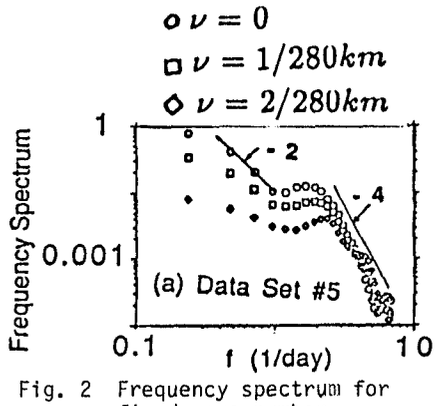

Fig. 2 Frequency spectrum for fixed wave number

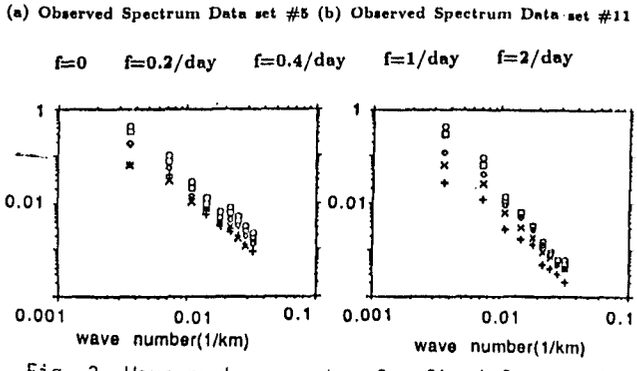

Fig. 3 Wave number spectra for fixed frequencies for data set #5 and #11

The space-time correlation function obtained by fast Fourier transform of the observed spectrum had a propagation of a wave with speed estimated to be 29km/hour. The observed auto-correlation has a longer tail than exponential for time lags larger than 1 hour. Zawadzki (1973) found similar results. In Fig. 5 the observed spatial correlation functions are compared with the empirically obtained spatial correlation function (Bell, 1988). Notice that the observed space correlation has a longer tail than exponential for space lag larger than 40 km.

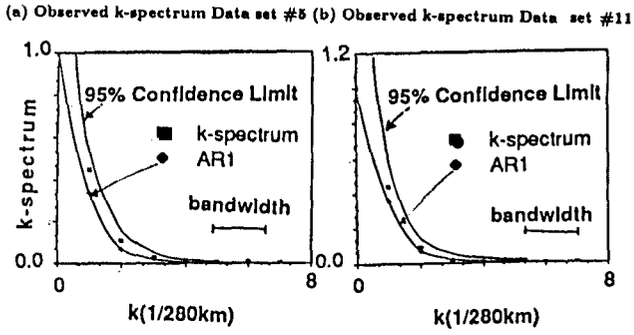

Fig. 4 Wave number spectra for zero-frequency case for data set #5 and #11

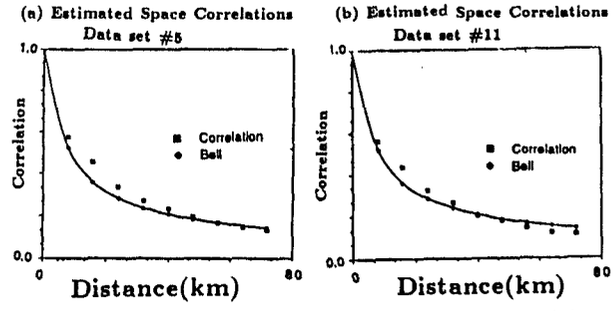

Fig. 5 Space correlation function obtained by Fast Fourier transform of the observed frequency-wave number spectrum

3. SPACE-TIME AR(1) MODEL

North and Nakamoto (1989) proposed a simple random field model of rainfall. Consider a random variable Ψ governed by

$$\tau_0 \frac{\partial}{\partial t}\Psi - \lambda_0^2 \nabla^2 \Psi + \Psi = F(t, x, y), \qquad (2)$$

where τ_0 and λ_0 are inherent time and length scales and F is a noise forcing function which is white noise in both space and time up to a cutoff frequency and wave number.

The power spectrum may be expressed as:

$$P(f, \upsilon) = \frac{P_F}{4\pi^2 f^2 \tau_0^2 + \left(1 + 4\pi^2 \upsilon^2 \lambda_0^2\right)^2} \qquad (3)$$

where P_F is the spectrum of the noise forcing, f is the frequency and υ is the wave number. If the spectrum of the noise is constant, the above spectrum for the random process is a well behaved function, smooth and maximum at origin and tapering off in all directions in f and υ.

Comparing the above formula with that fitted from GATE data, the inherent time and space scales are determined to be 10.3 hours and 36.4 km for data set #5 and to be 15.8 hours and 36.5 km for data set #11.

4. SATELLITE SAMPLING ERROR

North and Nakamoto (1989) proposed a formalism to estimate a mean square error of the rainfall

measurement by satellite for large area averaging. The mean square for the satellite measurement is written as

$$\varepsilon^2 = \sigma_A^2 \frac{2\tau_0}{T} \int df \sum_{n \neq 0} \delta(f - \frac{n}{\Delta t}) P(f, 0) \quad , \qquad (4)$$

where T is the total observation interval. The integrand is the contribution of frequency spectrum of zero-wave number. If we assume the satellite visits the same area every 12 hours, the first contribution of the spectrum is at semi-diurnal cycle and the next contribution may be negligible since the power spectrum shows one order smaller magnitude.

If we use the empirical spectrum which excludes diurnal and semi-diurnal cycles, we obtain the root mean square error to be 0.044 times areal variance for data set #5 and 0.033 times areal standard deviation for data set #11. These values are close to that obtained by North and Nakamoto (1989). Using the empirical value 1.3 as the ratio of the standard deviation and the mean rainfall value estimated by Laughlin (1984), the root mean square error may be scaled as to be 5.8% of the mean rainfall for data set #5 and 4.3% of the mean rainfall for data set #11.

Since the actual data showed a significant semi-diurnal cycle in the observed spectrum, we estimated the contribution from the semi-diurnal cycle to the sampling error. Comparing the magnitude of the observed power spectrum and the empirical spectrum which omits semi-diurnal cycle, we found that the semi-diurnal cycle enhances the sampling error estimate 1.9 times for data set #5 and 1.72 times for data set #11. Thus the resulting error may be estimated to be 10.8% for data set #5 and 7.3% for data set #11.

REFERENCES

Bell, T. L., 1987: A Space-Time Stochastic Model of Rainfall for Satellite Remote Sensing Studies. J. Geophys. Res., 92D8.

____, A. Abdullah, R. Martin and G. North, 1989: Monte Carlo Study Sampling Errors for Satellite-derived Tropical Rainfall Using Space-Time Stochastic Model. Submitted to J. Geophys. Res.

Blackmon, R. B. and J. W. Tukey, 1958: The Measurement of Power Spectra. Dover Publications, New York.

Laughlin, C., 1981: On the Effect of Temporal Sampling on the Observation of Mean Rainfall, Precipitation Measurements from Space. Workshop Report., Ed. by D. Atlas and O. Thiele. Available from Goddard Space Flight Center, Greenbelt, MD. 20771.

Mitchell, J. M. Jr., 1966: Climate Change. Tech Note No. 79. 36-62, World Meteorological Organization, Geneva, Switzerland.

North, G. R. and S. Nakamoto, 1989: Formalism for Comparing Rain Estimation Designs. Submitted to J. Atmos. Oceanic Tech.

A MODEL FOR ATMOSPHERIC BRIGHTNESS TEMPERATURES OBSERVED BY THE SPECIAL SENSOR MICROWAVE IMAGER (SSM/I)

Grant W. Petty and Kristina B. Katsaros

University of Washington
Seattle, Washington

1. INTRODUCTION

The first Special Sensor Microwave Imager (SSM/I), on board the Defense Meteorological Satellite Program's F-8 Satellite, has been operational since July, 1987. Like its predecessor, the Scanning Multichannel Microwave Radiometer (SMMR) on board the Nimbus-7 and Seasat satellites (1978-1987), this microwave radiometer operates at frequencies for which the atmosphere is relatively transparent. It is capable of providing estimates of a number of surface and atmospheric parameters not readily obtainable from other sources.

Over the ocean, these parameters include integrated water vapor, integrated cloud liquid water, surface wind stress, and locations and intensities of precipitation. Although the data from the SSM/I are not presently available to civilian meteorologists in real time, the unique view of the ocean-atmosphere system afforded by microwave radiometers neverthless continues to arouse a great deal of interest in the research community, particularly for the study of atmospheric water distributions (vapor and liquid) in midlatitude cyclones and for the mapping of rainfall at all latitudes. It has been found, for example, that distributions of water vapor and liquid water may be used to reliably infer surface frontal locations over data-sparse regions of the ocean (McMurdie and Katsaros, 1985; Katsaros and Lewis, 1986) and to provide verification of atmospheric water parameterizations in numerical forecast models (Katsaros et al., 1988). Microwave radiometer-derived maps of surface wind stress and vapor over the ocean are also being examined for possible insight into surface energy flux distributions (e.g., Liu, 1988).

Perhaps because of the relative newness of the instrument, there continues to be a shortage of published theoretical and empirical guidance for quantitatively interpreting microwave images obtained from the set of channels available on the SSM/I (19.35, 22.235, 37 and 85.5 GHz, all except 22.235 GHz in dual polarization). In particular, the 85 GHz channels have not been available on any earlier sensor. As a result, their potential for quantitative atmospheric applications has not yet been fully explored.

Simple statistical retrieval algorithms (Lo, 1983), developed years prior to the launch of the SSM/I have been found to be adequate for applications requiring only qualitative maps of the various retrievables, but appear to exhibit significant biases and cross-parameter contamination (e.g., Alishouse and Vongsathorn, 1988) which limit their usefulness for more demanding research applications.

In order to contribute to improved quantitative interpretation of microwave imagery from the SSM/I, we have developed a closed-form mathematical model for the atmospheric contribution to microwave absorption and emission at SSM/I frequencies. The present model is similar in purpose to an earlier model developed by Wentz (1983) for SMMR frequencies, but is based on a considerably more comprehensive treatment of the relevant physics. This additional rigor was necessitated by the higher atmospheric opacities encountered at certain SSM/I frequencies, notably 22.235 and 85.5 GHz, by the absence of low frequency channels (e.g., the SMMR's 6.6 and 10.7 GHz channels) for accurately measuring surface parameters without significant atmospheric interference, and by the need to assess the impact of the variability of non-retrievable parameters, such as vapor scale height and cloud layer height, on the accuracy of retrievals.

For the atmospheric model to have direct practical application in SSM/I retrievals over the ocean, one must, of course, couple it with a suitable model for sea surface emission and scattering, including accurate dependences on wind-induced roughening and sea surface temperature. Unfortunately, a sea surface model of demonstrated accuracy at SSM/I frequencies has proven elusive, due to the complex nature of microwave interaction with surface waves and sea foam and the lack of high-quality in situ data over much of the world's oceans. However, the availability of an accurate model for the atmospheric contribution to microwave radiances can potentially contribute to more reliable direct observations of the variability of sea surface emissivity, using a suitably chosen set of SSM/I data.

No attempt is made to include precipitation in the model, due to the fundamentally different character of a problem entailing multiple scattering effects and non-plane-parallel geometry. However, empirical and theoretical studies of the microwave response to rain are being conducted by a number of workers, including the authors (Petty and Katsaros, 1989)

2. ATMOSPHERIC MODEL

2.1 Mathematical Development

For reasons of space, a detailed derivation and presentation of the model function is not attempted here. Instead, a brief description of the characteristics of the model is given, along with a discussion of some relevant results. A floppy diskette (MS-DOS format) containing FORTRAN routines implementing the model may be requested from the authors.

The starting point is the integral form of the radiative transfer equation appropriate to microwave transfer in a plane-parallel, non-scattering atmosphere:

$$T_B^{\uparrow} = \frac{1}{\cos\theta}\int_0^{\infty} T(z)\,k(z)\,\exp\left[\frac{-1}{\cos\theta}\int_0^{z} k(z')\,dz'\right]dz \qquad (1a)$$

$$T_B^{\uparrow} = \frac{1}{\cos\theta}\int_0^{\infty} T(z)\,k(z)\exp\left[\frac{-1}{\cos\theta}\int_z^{\infty} k(z')\,dz'\right]dz \qquad (1b)$$

where $T_B^{\downarrow}$ and $T_B^{\uparrow}$ are the downwelling and upwelling brightness temperature at the surface and top of the atmosphere, respectively; T(z) is the temperature as a function of height, z; k(z) is the absorption coefficient; and θ is the zenith/nadir angle.

Several simplifying assumptions are made to reduce the number of degrees of freedom in (1) and to permit the integral to be reduced to a closed-form mathematical expression. It is first assumed that the temperature profile T(z) may be approximated as linear, with an effective surface temperature T_A and lapse rate Γ. Gaseous absorption in the atmosphere is modeled as the sum of two exponentially decaying functions of height, with separate scale heights H_V and H_o corresponding to water vapor absorption and dry air (mostly oxygen) absorption, respectively. Thus

$$k(z) = \frac{\sigma_o}{H_o}e^{-z/H_o} + \frac{\sigma_V}{H_V}e^{-z/H_V} \qquad (2)$$

where σ_V and σ_o are the total atmospheric optical depth (in Nepers) of each constituent. These, together with H_V and H_o, are found to depend on frequency, water vapor content (V), vapor scale height (H_{WV}), surface pressure (p_o), temperature (T_A) and lapse rate (Γ).

A single cloud layer of arbitrary water content (L) but negligible geometric thickness is assumed at a height Z_L above the surface. The total atmospheric contribution to the microwave emission/absorption is thus treated as being due to three distinct layers: the gaseous layer between the surface and the cloud, the liquid water in the cloud layer, and the gaseous layer extending from the top of the cloud to infinity. Accordingly, (1a) and (1b) are each broken up into three integral terms which are separately reduced to closed-form expressions and then recombined to give the desired result.

Since the total optical path due to gaseous absorbers is generally less than one Np at SSM/I frequencies and viewing angles, the exponential terms in (1) involving σ_V and σ_o may be approximated by truncated Taylor series expansions including only quadratic and lower-order terms. The resulting expressions are integrated to yield fairly simple rational functions (quotients of polynomials) expressing the dependence of the "effective emitting height" of each layer on the various optical depths and scale heights and on the simplified temperature profile.

2.2 Frequency-dependent model coefficients

Earlier microwave radiative transfer calculations for remote sensing purposes have usually relied on absorption data published by Barrett and Chung (1962) or Waters (1976) for water vapor, and Meeks and Lilly (1959) or Rosenkranz (1975) for oxygen. Recently, Liebe (1985, 1988) has collected the latest empirical and theoretical data on water vapor and dry air absorption into a unified Millimeter-wave Propagation Model (MPM), which calculates microwave attenuation as a function of temperature, humidity, pressure, and hydrosol content, over a wide range of atmospheric conditions. Notable improvements over the earlier models include new empirically-derived formulations for both water vapor and dry air continuum absorption, that is, absorption not accounted for by the wings of nearby absorption lines, as well as improved line parameters obtained from recent measurements.

Comparisons between water vapor attenuation values calculated using the MPM model and those obtained from earlier formulations revealed differences of up to 20% at some frequencies, primarily in spectral regions where continuum absorption dominates. As the new MPM model benefits from a more extensive base of empirical measurements than was available at the time the earlier models were developed, we chose to adapt the gaseous absorption routines in MPM for the radiative transfer calculations of the present study. Nevertheless, continuum absorption probably remains the greatest single source of uncertainty in the model presented below, especially since the exact physical basis for this component of the microwave spectrum has not been definitely established.

A calendar year's worth of radiosonde-derived profiles of atmospheric temperature and humidity were obtained for each of 29 island, coastal, and ship weather stations (Table 1). The stations were chosen to be representative of maritime conditions in all latitude belts. After discarding soundings which failed to pass a number of quality checks, explicit radiative transfer calculations were performed for each sounding (under the assumption of clear sky) in order to obtain the corresponding upwelling and downwelling atmospheric microwave brightness temperatures and optical depths at the four SSM/I frequencies. In addition, total water vapor content and vapor scale height were computed, along with effective lapse rate and surface temperature. A total of 16,893 soundings were processed in this manner. Algebraic models relating water vapor and dry air optical depths and absorption scale heights to water vapor content, water vapor scale height, temperature and surface pressure were then fitted to the numerically integrated values.

TABLE 1
Source of radiosonde soundings used to evaluate model coefficients

Station	Year	Soundings	lat.	lon.
Thule	1969	632	76.5N	68.8W
Barter Isl.	1978	669	70.1N	143.6W
Keflavik	1980	714	64.0N	22.6W
OWS B	1971	690	56.5N	51.0W
OWS C	1971	643	52.8N	35.5W
St. Paul	1979	719	57.2N	170.2W
OWS D	1971	670	44.0N	41.0W
Terceira	1970	721	38.8N	27.1W
OWS E	1971	655	35.0N	48.0W
Pt. Mugu	1978	715	34.1N	119.1W
St. George	1970	539	32.4N	64.7W
Midway	1979	569	28.2N	177.4W
Key West	1978	725	24.6N	81.8W
Lihue	1979	725	22.0N	159.4W
Wake Isl.	1979	701	19.3N	162.7E
Johnston Isl.	1979	724	16.7N	169.5W
Guam	1979	741	13.6N	144.8E
Yap	1979	494	9.5N	138.1E
Truk	1979	487	7.5N	151.9E
Majuro	1979	483	7.1N	171.4E
Diego Garcia	1978	312	7.3S	72.4E
Ascension Isl.	1969	509	8.4S	14.4W
EMEX ship	1987	130	14 S	140 E
Pago Pago	1979	716	14.3S	170.7W
Easter Isl.	1979	207	27.2S	109.4W
Quintero	1980	443	32.8S	71.6W
Punta Arenas	1980	298	53.0S	70.9W
Macquarie Isl.	1975	522	54.5S	159.0E
Argentine Isl.	1955	349	65.3S	64.3W
Casey	1975	391	66.3S	110.6E
Total		16893		

The mass extinction coefficient of cloud liquid water (for droplet radii << wavelength) is readily calculated from the complex index of refraction of water (Van de Hulst, 1957). The index of refraction, in turn, depends on both temperature and frequency (Gunn and East, 1954). Third-order polynomials in temperature were fitted to the calculated mass extinction coefficient at each frequency over the range -20 to +30 C.

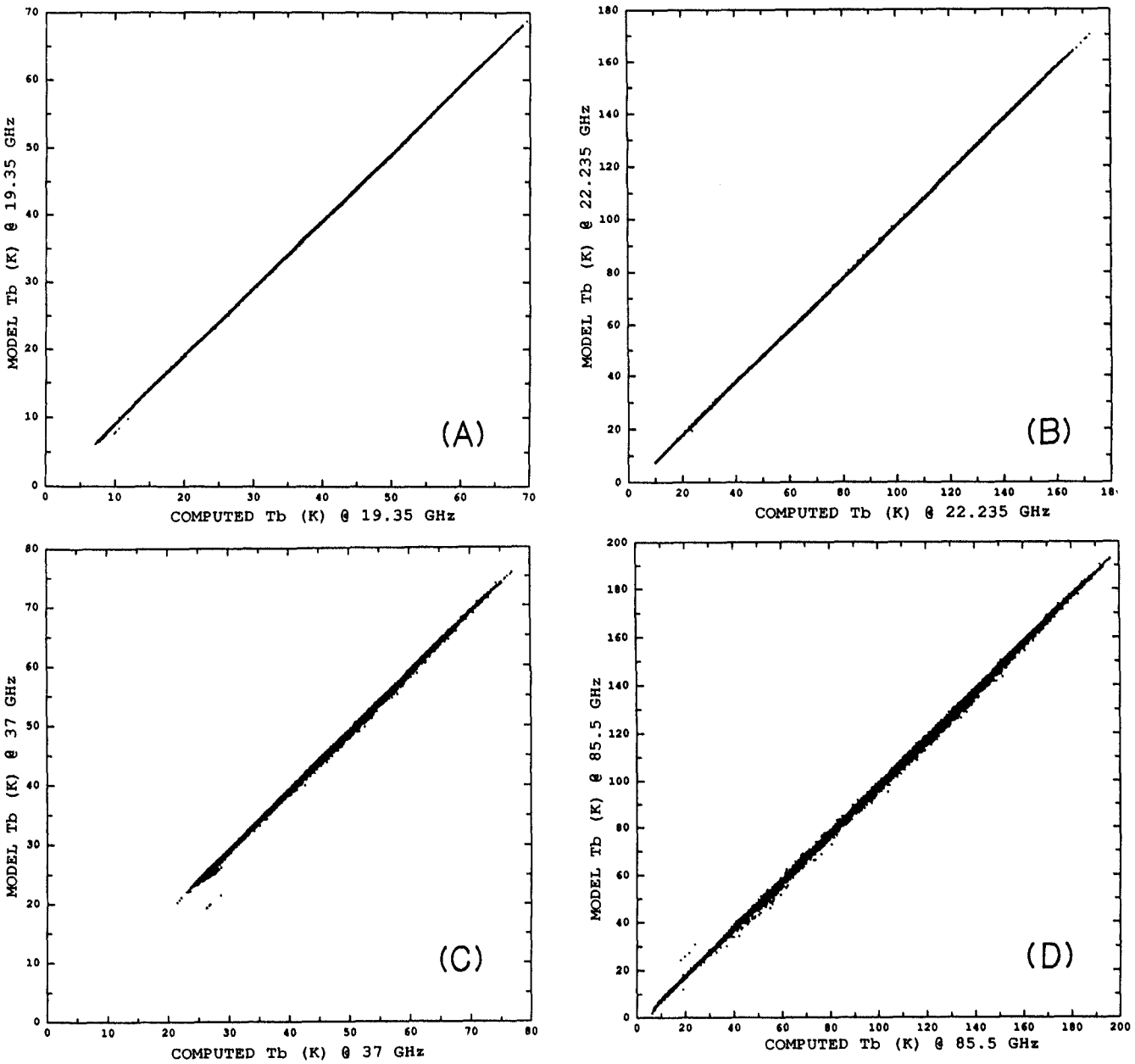

Figure 1. Comparison between model-predicted and numerically integrated downwelling brightness temperatures for 16,893 radiosonde soundings: a) 19.35 GHz b) 22.235 GHz c) 37 GHz d) 85.5 GHz

Combining the fitted models of liquid water, water vapor and dry air absorption and absorption scale height with the mathematical model yields a complete set of parameterizations of atmospheric emission and absorption at SSM/I frequencies having the following form:

$$T_B^{\uparrow} \cong f^{\uparrow}(\theta, T_A, \Gamma, V, H_{WV}, L, z_L, p_s) \quad (3a)$$

$$T_B^{\downarrow} \cong f^{\downarrow}(\theta, T_A, \Gamma, V, H_{WV}, L, z_L, p_s) \quad (3b)$$

3. RESULTS

Scatter plots of downwelling brightness temperatures as computed explicitly from the soundings versus those obtained from the final model are depicted in Fig. 1 for a viewing angle of 53° from zenith. Similar results (not shown) are obtained for upwelling brightness temperatures. R.M.S. error of the fit ranges from about 0.1 K at 19.35 GHz to about 0.7 K at 85.5 GHz.

The good fit we obtained for the model would have been impossible without including variability in atmospheric opacity and emission due to differences in temperature profile, vapor scale height, and surface pressure. Vapor scale height changes, in particular, imply changes in effective pressure acting on the vapor column, in turn inducing opacity changes via the pressure dependence of the absorption line width. Such effects are particularly important at 22.235 GHz, since this is at the peak of a weak water vapor resonance line.

As a byproduct of the radiosonde integrations, a number of statistics were generated relating to the frequency of appearance of various combinations of values of model input variables, for different regions and seasons. Since the frequency dependent coefficients of the model were derived by statistical regression, it is important to ensure that input values are both statistically and physically realizable, else the model may give meaningless results. Note that the availability

of a priori information concerning variances and covariances of atmospheric variables in a given region may be used in constraints to reduce retrieval errors for that region.

4. CONCLUSIONS

A model has been developed which is intended to accurately predict upwelling and downwelling atmospheric brightness temperatures at SSM/I frequencies, as functions of eight input parameters: zenith (nadir) angle, integrated water vapor and vapor scale height, integrated cloud water and cloud height, effective surface temperature and atmospheric lapse rate, and surface pressure.

It was shown that the model accurately reproduces clear sky brightness temperatures computed by explicit integration of a large number of radiosonde soundings representing all maritime climate zones and seasons. Though not demonstrated here, we expect that the model should also perform well for the case of a cloudy sky containing a horizontally homogeneous layer of non-precipitating cloud water at an arbitrary height in the atmosphere.

Given the excellent agreement between the model brightness temperatures and the numerically integrated brightness temperatures, it may be concluded that at least the mathematical form of the model is valid for the range of atmospheric opacities encountered at SSM/I frequencies. The validity of the frequency-dependent coefficients, however, depends entirely on the accuracy of the microwave propagation model of Liebe (1985, 1988). At the time of this writing, we can say only that observed SSM/I brightness temperatures over the ocean appear to behave approximately as predicted by the model; detailed verification will ultimately depend both on access to high quality in situ measurements and on the availability of an accurate sea surface emissivity model.

The model may be employed directly in physically-based retrieval algorithms for the SSM/I, or it may simply serve as an accurate "benchmark" for developing and/or evaluating simpler models and algorithms. The potential impact on geophysical parameter estimates by variations in "non-retrievable" parameters, such as water vapor scale height and cloud layer height, may be readily examined with this model. Although it does not attempt to predict brightness temperature response to precipitation, scattering-based algorithms for rain rate estimation (e.g., Spencer, 1986) depend on reasonable estimates of the "pure emission" component of brightness temperature variations, which this model, in combination with a sea surface model, can contribute.

ACKNOWLEDGEMENTS: We are grateful to Dr. H.J Liebe of the National Telecommunications and Information Administration for providing us with his Millimeter-wave Propagation Model. Radiosonde soundings were obtained from the Data Support Section of the Scientific Computing Division, National Center for Atmospheric Research. This work was supported by NASA grant NAG-943.

REFERENCES:

Alishouse, J.C., and J. Vongsathorn 1988: Total precipitable water measurements from the SSM/I. Preprints, Third Conference on Satellite Meteorology and Oceanography, Feb. 1-5, 1988, Anaheim CA, Amer. Meteor. Soc., 74-75

Barrett, A.H., and V.K. Chung 1962: A method for the determination of high-altitude water vapor abundance from ground-based microwave observations. J. Geophys. Res., 67, 4259-4266

Gunn, K.L.S, and T.W.R. East 1954: The microwave properties of precipitation particles, Quart. J. Royal Meteor. Soc., 80, 522-545

Liebe, H.J. 1985: An updated model for millimeter wave propagation in moist air. Radio Science, 20, 1069-1089

Liebe, H.J. 1988: new MPM coefficients, personal communication

Liu, W.T., 1988: Moisture and latent heat flux variabilities in the tropical Pacific derived from satellite data. J. Geophys. Res., 93, 6749-6760.

Lo, R.C. 1983: A Comprehensive Description of the Mission Sensor Microwave Imager (SSM/I) Environmental Parameter Extraction Algorithm. NRL Memorandum Report 5199, Naval Research Laboratory, Washington, D.C.

Katsaros, K.B., and R.M. Lewis, 1986: Mesoscale and synoptic scale features of North Pacific weather systems observed with the Scanning Multichannel Microwave Radiometer on Nimbus 7. J. Geophys. Res., 91, 2321-2330

Katsaros, K.B., G.W. Petty and U. Hammarstrand 1988: Liquid water and water vapor in mid-latitude cyclones observed by microwave radiometry and compared to model calculations. Proceedings of Palmen Memorial Symposium, Aug. 29-Sept. 2, 1988, Helsinki, Finland

McMurdie, L.A., and K.B. Katsaros, 1985: Atmospheric water distribution in a mid-latitude cyclone observed by the Seasat Scanning Multichannel Microwave Radiometer. Mon. Wea. Rev., 115, 1281-1294

Meeks, M.L., and A.E. Lilly 1963: The microwave spectrum of oxygen in the earth's atmosphere. J. Geophys. Res., 68, 1683-1703

Petty, G.W., and K.B. Katsaros 1989: Empirical studies of the microwave radiometric response to rain in the tropics and midlatitudes. This volume.

Rosenkranz, P.W. 1975: Shape of the 5 mm oxygen band in the atmosphere. Trans. IEEE (AP), 23, 498-506

Spencer, R.W. 1986: A satellite passive 37 GHz scattering based method for measuring oceanic rain rates. J. Climate Appl. Meteor., 25, 754-766

Van de Hulst, H.C., 1957: Light Scattering by Small Particles, John Wiley and Sons, Inc., New York

Waters, J.W. 1976: Absorption and emission of microwave radiation by atmospheric gases, in Methods of Experimental Physics, M.L. Meeks, ed., 12, Part B, Radio Astronomy, Academic Press

Wentz, F.J 1983: A model function for ocean microwave brightness temperatures, J. Geophys. Res., 88, 1892-1908

CHARACTERISTICS OF THE GOES I-M IMAGER AND SOUNDER

Edward W. Koenig

ITT Aerospace/Optical Division
Fort Wayne, Indiana

1. INTRODUCTION

The next generation Geostationary Operational Environmental Satellite (GOES I-M) is to be a three axis, body stabilized spacecraft. Included as part of its instrument complement are improved thermal imaging and sounding instruments. These instruments have been improved over the combined imager and sounder on the present spin stabilized GOES in sensitivity, scan flexibility, and pointing accuracy.

Moreover, the new Imager and Sounder are designed to be integral parts of the on-board stabilization and pointing determination system to maintain accurate (within 4 km) pointing of both instruments. Each instrument is capable of utilizing a visible detector array to sense fourth magnitude stars to assist in location and pointing accuracy determination.

The spacecraft layout (Figure 1) provides for the mounting of the instruments on the earth facing side of the spacecraft, with their optical ports pointing to the Earth and their passive coolers pointing North.

The instruments share a significant amount of design commonality. The sensor modules are shown in Figure 2. Both instruments have 31 cm optical systems. The telescope configurations are nearly identical, except for the prescription of their secondary mirrors. The scanners have identical scan mirrors, driven by DC torquers and controlled by Inductosyn derived digital-controlled servo systems. The combination of louvers and an electrical thermal control system is designed to limit diurnal temperature excursions of both sensor modules to 18°C±5°C. The electrical systems of both instruments also share near identical designs for power conversion, telemetry, and command circuitry.

Although the instruments share these common designs, they operate completely independent of each other. The instruments simultaneously perform their varied and unique tasks without compromise to either instrument's performance or data. A list of features of the two instruments is given in Table 1.

The instruments' designs incorporate many features to enhance reliability over previous GOES radiometric instruments: independent Sounder and Imager, redundancy, and more reliable position sensors and lubricant methods. Design life is for over 5 years in orbit.

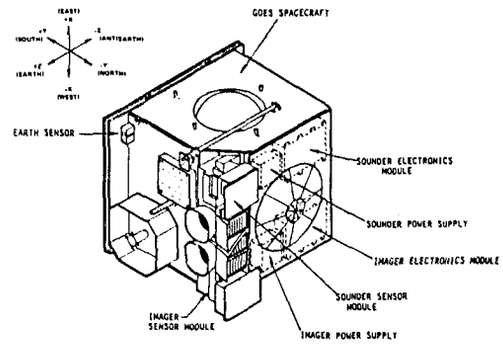

Figure 1. GOES I Spacecraft, Launch Configuration

Table 1. Instrument Parameters

FEATURE	IMAGER	SOUNDER
OPTICAL APERTURE	31 CM (12.25 IN)	31 CM (12.25 IN)
TOTAL STEP & SAMPLE TIME	NA	0.1 SEC (0.2 SEC & 0.4 SEC OPTIONAL)
METHODS OF SCAN	2-AXIS, LINEAR E-W STEP N-S ALTERNATE E-W AND W-E	2-AXIS; STEP & DWELL E/W 280 URAD STEPS N/S 1120 URAD STEPS (OPTIONAL 2240 URAD STEPS, 0.2 SEC DWELL)
SCAN RATE	20°/SEC OPTICAL	40 SOUNDING/SEC
SLEW RATE	10°/SEC MECHANICAL	10°/SEC MECHANICAL
SPATIAL RESOLUTION (URAD)	CHANNEL VIS / 2,4 & 5 / 3	ALL CHANNELS
SPEC MAX	28 / 112 / 224	224
NOMINAL	27 / 96 / 196	242 (ROUND)
SAMPLING	1.75/IGFOV VIS, 2,4 & 5 3.5/IGFOV CHANNEL 3	4 IGFOVS SAMPLED SIMULTANEOUSLY
SAMPLING RATE	183.3 US/PIXEL (IR) 45.8 US/PIXEL (VIS)	0.1 SEC
EARTH LOCATION ACCURACY	± 42 URAD-3 SIGMA	± 42 URAD-3 SIGMA
PIXEL-TO-PIXEL REGISTRATION ACCURACY (LINE-TO-LINE, ALONG A LINE, FRAME-TO-FRAME)	± 29.7 URAD-3 SIGMA	± 29.7 URAD-3 SIGMA
CHANNEL CO-REGISTRATION	± 28 URAD	WITHIN 22 URAD OF CH 8
STAR SENSING	USES VISIBLE ARRAY; S/N 3 FOR 4TH MAG (400 SAMPLES)	SEPARATE VISIBLE ARRAY; S/N 3 FOR 4TH MAG (EACH SAMPLE)
DATA OUTPUT	10 BIT QUANTIZATION	13 BIT QUANTIZATION
DATA RATE	2.6208 MB/SEC	40 KB/SEC
DATA FORMAT	NRZ-S, PN CODE	NRZ-S, PN CODE
PATCH TEMPERATURE	REGULATED TO 105K 5K MARGIN AT 5 YRS BACKUP 110K	REGULATED TO 92K 8 MONTHS 102K, 4 MONTHS
TIME BETWEEN SPACE LOOKS	2 MIN	2 MIN
TIME BETWEEN B/B CALIBRATIONS (NOMINAL)	10 TO 30 MIN (CAN OVERRIDE OR INHIBIT)	20 MIN (CAN OVERRIDE OR INHIBIT)
PRIORITY FRAME SELECT	1 LEVEL NORMAL 2 LEVELS PRIORITY 1 LEVEL STAR SENSE	1 LEVEL NORMAL 2 LEVELS PRIORITY 1 LEVEL STAR SENSE

2. IMAGER DESCRIPTION

The GOES Imager is a multispectral imaging radiometer that has the following key features: 1) improved sensitivity, which on a 3 axis body stabilized platform makes it possible for the Imager to achieve a scan efficiency of approximately 80%, resulting in a dwell time approximately 15 times greater than the previous GOES Imager. 2) digital scan flexibility, which can rapidly accommodate commands to change the scan field from a normal full earth disc scan of 18° to a chosen location within the total scan. 3) pointing accuracy, to define a location within 4 km. 4) absolute pointing determination which is enhanced by ability to sense stars using the complete optics and detector system. 5) calibration using both a space look and an on-board 290 K full-aperture blackbody to provide a two-point radiometric calibration every 10 to 25 minutes. 6) expanded signal quantization to 10 bit level for all data channels.

3. IMAGER SIGNAL FLOW

Input radiation from the earth scene is reflected from the scan mirror into a telescope. The aft optics split the radiation into five spectral channels. The detectors for the infrared channels are located within the passive radiative cooler. The visible detectors are not cooled and are located on the visible optics subassembly. The detectors convert the scene radiation to electrical signals which go to a pre-amplifier, post amplifier, filters, and to a 10 bit A to D converter. A sample and hold circuit samples all data channels simultaneously prior to digitization. The digitized data is then stored in registers and read serially to the S/C data transmission system.

4. DETAIL DESCRIPTION

The Imager sensor module is shown in Figure 2 and its 5 spectral channels listed in Table 2. The visible resolution is 28 microradians (1 km at nadir). IR channels 2, 4, and 5 have resolutions of 112 microradians (4 km) and channel 3, the water vapor channel, is 224 microradians (8 km).

The detector configuration is shown in Figure 3. The IR detectors are completely redundant as are all of their respective electronics. The eight element visible channel array is located symmetrically about the optic axis. IR channels have two detectors for each redundant side. Channel 3 has one active 8km detector and one redundant. The active channels sweep a swath of 8 km as the mirror scans East to West or West to East.

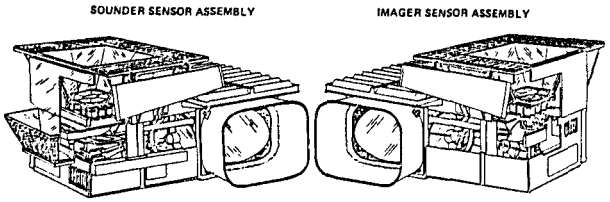

OVERALL CHARACTERISTICS

137 X 80 X 75	SENSOR ASSEMBLY SIZE (CM)	115 X 80 X 75
67 X 43 X 19	ELECTRONICS MODULE SIZE (CM)	67 X 43 X 19
29 X 20 X 16	POWER SUPPLY MODULE SIZE (CM)	29 X 20 X 16
24	STANDBY POWER (WATTS)	20
110	AVG POWER WITH THERMAL CONTROL (WATTS)	134
126	WEIGHT OF ALL THREE COMPONENTS (KG)	118

Figure 2. Sounder and Imager Characteristics

Table 2. Imager Sensing Performance

SPECTRAL CHANNELS	1	2	3	4	5
PURPOSE	CLOUD COVER	NIGHTTIME CLOUDS	WATER VAPOR	SURFACE TEMP	SEA SURFACE TEMP AND WATER VAPOR
1) WAVELENGTH (UM)	0.55 TO 0.75	3.80 TO 4.00	6.50 TO 7.00	10.20 TO 11.20	11.50 TO 12.50
SN OR NEAT SPEC	150:1	1.4K AT 300K	1.0K AT 230K	0.35K TO 300K	0.35K AT 300K
SN OR NEAT PRE-DICTED	420:1	0.09K	0.34K	0.12K	0.15K
DETECTOR TYPE	SILICON	InSb	HgCdTe	HgCdTe	HgCdTe
SPATIAL RESOLUTION SPEC IN MICRORADIANS	28+0%-10%	112+0%-10% (N-S)-25%	224+0%-25%	112+0%-25%	112+0%-25%
STAR SENSE:	4TH MAGNITUDE STARS 3:1 SN				

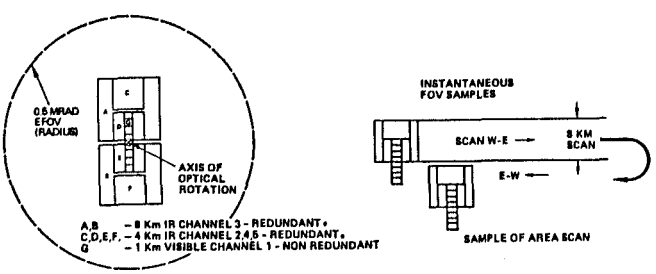

*A, C & D CHANNELIZED REDUNDANCY TO B, E & F

Figure 3. Imager Field and Scan Pattern

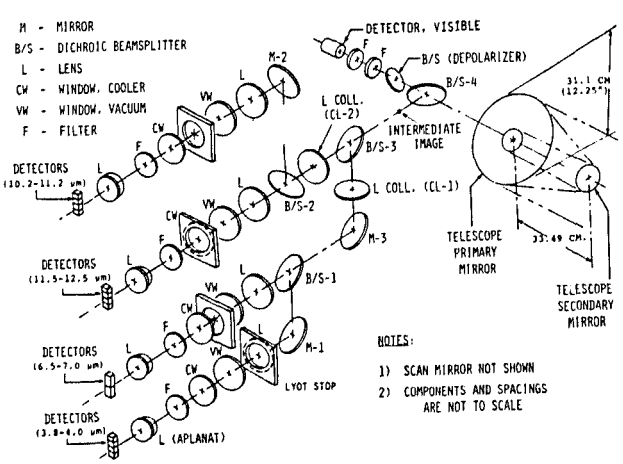

Figure 4. Imager Optic Parts

The Imager Optical System divides the scene radiation into 5 spectral bands by means of dichroic beamsplitters and registers all spectral channels to permit simultaneous viewing of the scene. Figure 4 schematically describes the optical system. Windows serve to isolate the passive radiative cooler from the sensor module. The telescope is an F 12.25 Cassegrain with a focal length of 381 cm. The obscuration is 22% (linear) of the clear aperture. The extended field of view at the detectors is 1.0 milliradian diameter.

The IR detectors are located on the third stage (patch) of a radiant cooler shown in Figure 5. A deployable cover protects the cooler prior to, during, and for approximately two weeks after launch. When the IR detectors reach 105K the IR channels are operative.

The Imager Scan Subsystem uses an Inductosyn as the servo error generator. When given a digital address, Sin/Cos signals are impressed on the winding of the Inductosyn stator. Induced in the rotor of the inductosyn is a voltage caused by the phase/amplitude difference of the stator windings. The position control drives a brushless DC motor to scan to a zero error condition. Compensating signals are added to the drive to offset internal systematic errors and both spacecraft and orbit induced errors.

The fields seen by the Imager and Sounder are shown in Figure 6. Combinations of scan size and locations may be selected.

5. SOUNDER DESCRIPTION

The Sounder is a nineteen-channel discrete-filter radiometer. Key features of the system design include: 1) high sensitivity for each channel sample permitting high quality soundings from each atmospheric column, 2) a small instantaneous geometric field of view to provide increased capability for clear column sounding, 3) multiple simultaneous samples and a high sampling rate which combine to provide rapid areal coverage and, 4) full aperture blackbody calibration, thermal control, space reference and 13-bit quantization.

The background of the GOES Sounder is that of the HIRS/2, providing familiarity with instrument operation and performance. A filter wheel rotating 10 times per second provides for data sampling at 10 steps per second. The filter complement is much like HIRS/2 in the selection of filter spectrum and bandwidth. The NEΔN values are slightly higher than in HIRS as a trade-off for faster sounding coverage. Provision is made in the instrument for increased dwell-time which improves the NEΔN of each area sample at the expense of sounding rate.

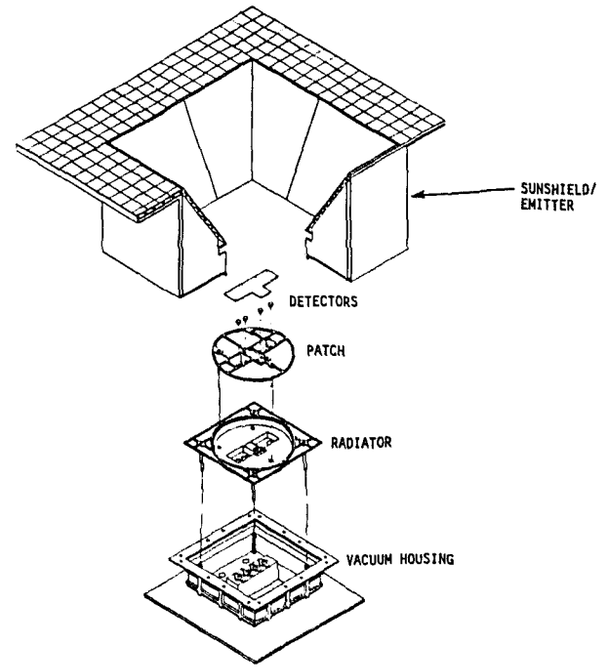

Figure 5. Radiant Cooler Parts

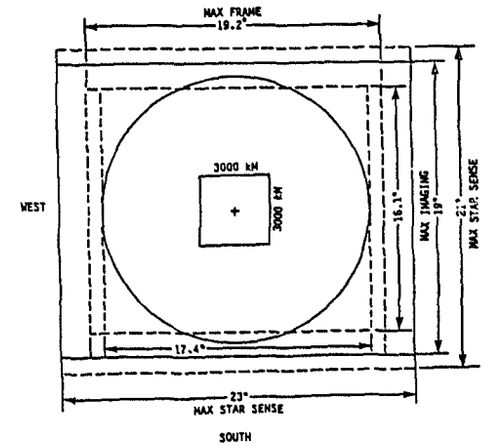

MAXIMUM FRAME FIELD 23°
MAXIMUM STAR SENSE AREA 23°
E-W BY 21° N-S

FULL EARTH IMAGE (17.4° x 17.4°) (Includes space, star and cal)	26.5 min
FULL EARTH SOUNDING (16.1° x 16.1°) (Includes space, star and cal)	454 min
3000 KM BY 3000 KM IMAGE	3.0 min
3000 KM BY 3000 KM SOUNDING	42 min
1000 KM BY 1000 KM IMAGER	40 sec
1000 KM BY 1000 KM SOUNDING	5.3 min

Figure 6. Imager and Sounder Scan Times

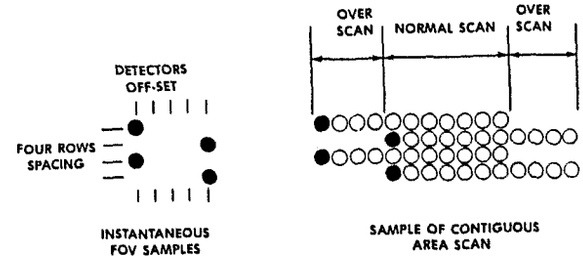

Figure 7. Sounder Field and Scan Pattern

6. SOUNDER CHARACTERISTICS

Characteristics of the GOES Sounder are given in Table 1. The detector and filter arrangement makes use of four spectral bands: longwave, midwave, shortwave and visible. Four detectors are simultaneously irradiated in each band, providing output from four IGFOV. In this manner, the system can sample four 8km IGFOV each 0.1 seconds. A step of 10km (at nadir) provides for adjacent pixel separation, providing nearly independent atmospheric samples of each column. Figure 7 shows the relative location of the four fields sampled simultaneously at each step location.

The complement of filters and their general characteristics is given in Table 3. It may be noted that the predicted NEΔN exceeds the requirements for the Sounder.

7. OPERATIONAL FEATURES

Scan control of the Sounder permits a fully-commandable set of coordinates at any time as shown in Figure 6. System design include flexibility to permit selective area and time, provide high location accuracy, and permit increased dwell for sensitivity improvement. The scan system is totally digitally controlled, permitting any start and stop locations to be selected.

The scan is basically West-East in 10km steps, dropping 40km at the end of a line and returning East-West, continuing this pattern until the desired frame is completed. Provision is made for stopping at one location, for 0.1, 0.2 or 0.4 seconds in normal scan. A skip-line mode provides a faster large area coverage at the expense of missing alternate lines. In this mode the dwell is always 0.2 seconds. The control system permits repeating frames and various combinations of normal and priority frames and star sensing.

The Sounder has the same motion control system as the Imager, reducing location errors to very low values.

8. DATA OUTPUT

The Sounder data is a complete set for each 0.1 second sample. Radiometric data from the four IGFOVs, each sampling 19 channels, is sent to the ground in a serial data stream with 13 bit precision. Included with the radiometric data are housekeeping telemetry, reference blackbody temperatures, and location information. Periodic views of space and IR blackbody provide radiometric calibration. Electronic calibration signals provide for monitoring of amplifier and data system quality.

The initial down-link is not for the end user, but goes to the NOAA Control and Data Acquisition Station at Wallops Island. This data is checked and tagged with ground coordinates, then merged with the Imager data in a single data format for retransmission. The end user has the raw radiometric data, calibration information, and ground location information for his purposes.

Acknowledgment:

The GOES I-M Imager and Sounder are being developed on Subcontract SC-922800-AZ to Ford Aerospace Corporation, Space Systems Division, Palo Alto, CA, and prime contract NAS-5-29500 to NASA.

Table 3. Sounder Sensing Performance

DETECTOR (BAND)	CHANNEL	CENTRAL WAVELENGTH [micrometers (cm^{-1})]	NE(DELTA)N (at 92K) ($mW/m^2/sr/cm^{-1}$) SPEC	PRED	PURPOSE
HgCdTe (LONGWAVE)	1	14.71 (680)	0.66	0.52	TEMPERATURE SOUNDING
	2	14.37 (696)	0.58	0.27	
	3	14.06 (711)	0.54	0.19	
	4	13.96 (733)	0.45	0.19	
	5	13.37 (748)	0.44	0.14	
	6	12.66 (790)	0.25	0.067	
	7	12.02 (832)	0.16	0.059	
HgCdTe (MIDWAVE)	8	11.03 (907)	0.16	0.024	SURFACE TEMP
	9	9.71 (1030)	0.33	0.040	TOTAL OZONE
	10	7.43 (1345)	0.16	0.024	WATER VAPOR
	11	7.02 (1425)	0.12	0.019	SOUNDING
	12	6.51 (1535)	0.15	0.034	
InSb (SHORTWAVE)	13	4.57 (2188)	0.013	0.0021	TEMPERATURE SOUNDING
	14	4.52 (2210)	0.013	0.0019	
	15	4.45 (2245)	0.013	0.0018	
	16	4.13 (2420)	0.008	0.0013	
	17	3.98 (2513)	0.0082	0.0012	SURFACE TEMPERATURE
	18	3.74 (2671)	0.0036	0.0005	
SILICON (VISIBLE)	19	0.969 (14367)	0.10%A	0.0057%	CLOUD
SILICON (STAR SENSE)		0.8		11.5:1	4TH MAGNITUDE STARS

CHARACTERISTICS OF THE AVHRR/3 AND HIRS/3 FOR NOAA-K,L,M

Larry Owens
Donald Ceckowski
Alan J. Ames

ITT Aerospace/Optical Division
P.O. Box 3700
Fort Wayne, IN, 46801

1. INTRODUCTION

Both the AVHRR and HIRS are optical instruments built by ITT Aerospace/ Optical Division for the third generation NOAA TIROS-N polar-orbiting meteorological satellite systems to provide multispectral imaging and sounding data. These low earth orbiting satellites which are placed in sun synchronous orbits, and are utilized in pairs with equatorial crossings at about 7:30 A.M. and 1:30 P.M. local time. Figure 1 illustrates the Advanced TIROS-N (ATN) configuration. The ATN spacecraft has an added payload capability that does not change the basic environmental mission of the series. During the ATN series, operational instruments were incrementally added. These include a Search and Rescue (SAR) Demonstration System, an Earth Radiation Budget Experiment (ERBE), and an operational Solar Backscatter Ultraviolet Instrument (SBUV).

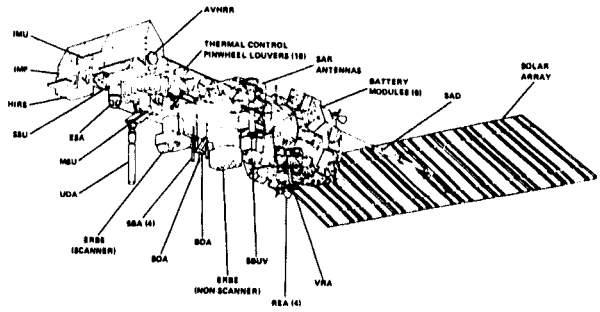

FIGURE 1. ADVANCED TRIOS-N SPACECRAFT

The Advanced Very High Resolution Radiometer (AVHRR/2) is a five channel imaging radiometer, sensing reflected sunlight and thermal emissions in five spectral bands from 0.58 to 12.5 microns. This version of the radiometer has been flying on the National Oceanographic and Atmospheric Administrative (NOAA) polar orbiting satellites since 1981. The last remaining AVHRR/1, a four channel sensor, is scheduled to be replaced in December 1989. The AVHRR/3 represents a six channel version of the basic instrument. The new 1.6 micron channel has a goal of improving snow/cloud discrimination.

HIRS/3, High Resolution Infrared Radiation Sounder, is the latest version of the highly successful multispectral optical sounding instrument first flown on TIROS-N. Including the protoflight model flown on TIROS-N, seven instruments have been providing operational sounding data since October 1978. The HIRS/2 was used through NOAA-9/F. FM-5 on NOAA-10/G has improved IFOV and cooler performance with the HIRS/2 spectral channel assignments. HIRS/2I has two different channels, #10 and #17. The first HIRS/2I is flying on NOAA-11/H with two more scheduled to fly on NOAA-I and J. HIRS/3 are scheduled for the NOAA-K,L, and M satellites, with a launch date projected between 1993 and 1995.

2. AVHRR DESCRIPTION

The AVHRR belongs to a class of instruments known as an imaging radiometer used for quantitative remote measurements of surface temperatures coupled with high spatial and thermal resolution. The infrared detectors are cooled to cryogenic temperatures to improve their sensitivity over the 3 to 12 micron wavelength bands. The strong atmospheric attenuation in the 5 to 8 micron band due to water vapor and carbon dioxide typically separate the infrared, therefore, into two distinct spectral regions of 3-5 and 8-12 microns. Both are utilized by the AVHRR for typical meteorological data, in addition to the visible channels which also measure Albedo, Cloud/Snow/Water/Ice cover, earth radiation, vegetation canopy moisture and index, and water vapor correction.

The AVHRR is an imaging system in which a small field of view (1.3 milliradians by 1.3 milliradians) is scanned across the earth from one horizon to the other by the continuous 360 degree rotation of a flat scanning mirror. The orientation of the scan lines is perpendicular to the spacecraft orbit track and the speed of rotation of the scan mirror is selected so that adjacent scan lines are contiguous at the subsatellite (nadir) position. Complete strip maps of the earth from pole to pole are thus obtained as the spacecraft travels in orbit at an altitude of 450 nautical miles. All the spectral channels of the AVHRR are registered so that they all measure energy from the same spot on the earth at the same time. All five channels are also calibrated so that the signal amplitude in each channel is a measure of the scene radiance. The solar channels are initially calibrated against an NBS - traceable

integrating sphere, while the thermal channels are calibrated against a laboratory blackbody source during thermal/vacuum testing. An passive blackbody mounted on the baseplate assists in-flight calibration.

The radiometers are designed to operate within specifications for a period of two years in orbit, and the data is processed by over 400 known receiving stations.

3. DETAILED DESCRIPTION

The AVHRR is comprised of several modules which are assembled together into a single unit instrument. These modules, as shown in Figure 2, are: the scanner module, the electronics module, the radiant cooler module, the optical subsystem module, and the base plate module. The base plate module is the common structure in which all other modules are secured. Dowel pins are used to establish and maintain alignment of the scanner and optics modules. Alignment of the cooler to the optics is established by shims.

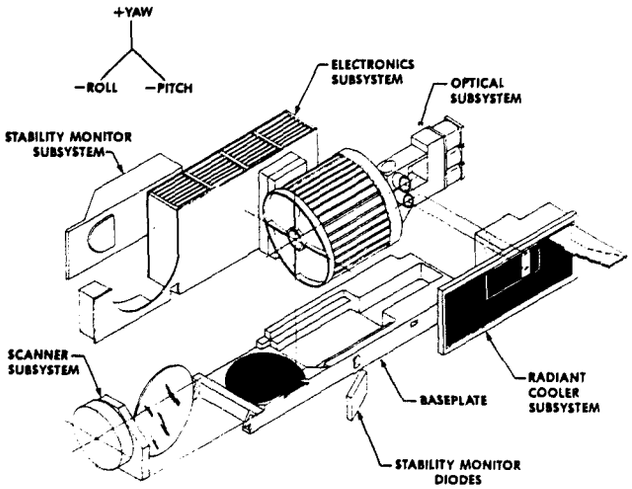

FIGURE 2. AVHRR/3 EXPLODED VIEW

The optical subsystem consists of two separate optical subassemblies, the collecting telescope and the relay optics unit as illustrated in Figure 3. The telescope is an 8.0 inch reflective Cassegrain design based on coaxial confocal paraboloids, and produces a collimated output beam which then feeds into the relay optics unit. The AVHRR relay optics unit consists of beamsplitters, fold mirrors, and imaging relay lenses which are designed, assembled, and aligned by ITT. In the newer AVHRR/3 configuration, the M4 mirror will be replaced with a beamsplitter to accommodate the new sixth channel.

Instrument polarization effects have been minimized by orientating the sensitive elements such that some elements compensate for others, resulting in less than seven percent residual polarization sensitivity in channels 1 and 2.

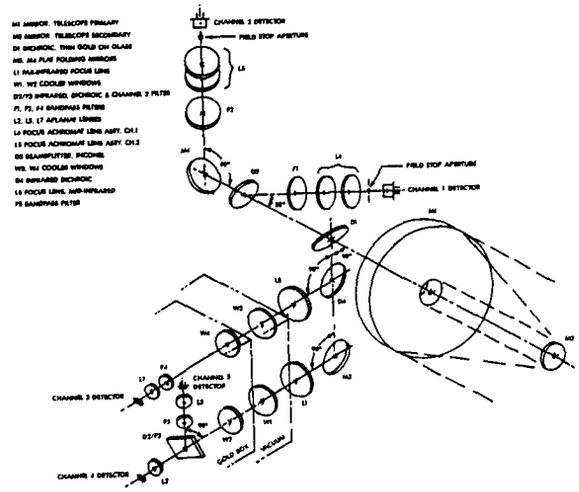

FIGURE 3. AVHRR/2 OPTICAL CONFIGURATION

4. IMAGING RADIOMETER PERFORMANCE

The overall instrument design is based upon the specific spectral channels, and meeting specified radiometer performance criteria. The key thermal resolution criteria for this sensor is the Noise Equivalent Temperature Difference (NETD). The NETD is defined as the specific temperature difference where the change in signal output equals the RMS system noise at a specific target temperature, typically at 300 degrees Kelvin. This parameter, in essence, is one limit to the system performance, based on a signal to noise figure, which can be measured and also is independent of output device, observer, and imaging capabilities. The AVHRR has a minimum NETD of 0.12 degrees Kelvin in channels 3, 4, and 5. In the visible channels, 1 and 2, a signal to noise ratio of 3:1 is specified at 0.5% Albedo for the performance requirement.

5. AVHRR/3 IMPROVEMENTS

The five channel AVHRR/2 continues to meet the needs of the weather service, yet a new six channel sensor is being introduced into the future AVHRR/3 for added capability. The AVHRR spectral bands, specified by NOAA, are listed in Table 1 in microns.

TABLE 1. AVHRR SPECTRAL CHANNELS

CHANNEL	AVHRR/1	AVHRR/2	AVHRR/3
1	0.58-0.68*	0.58-0.68	0.58-0.68
2	0.72-1.00	0.72-1.00	0.72-1.00
3	3.55-3.93	3.55-3.93	3.55-3.93
3A			1.58-1.64
4	10.5-11.5	10.3-11.3	10.3-11.3
5		11.5-12.5	11.5-12.5

*Protoflight AVHRR/1 had a spectral response of 0.55 to 0.90 microns in this channel.

This new channel, 3A, will provide better discrimination between snow and clouds and also provides the ability to monitor moisture of plants and leaf water content. It is a reflective sunlight channel using an uncooled Indium Gallium Arsenide photodiode detector. In order to maintain the same data rate to the spacecraft, this channel will be time-shared with the 3.7 micron channel. This 3.7 micron channel will be transmitted during the night portion of the orbit and the 1.6 micron channel during the day portion. Loss of the day time portion of the 3.7 micron data will not diminish the meteorological usefulness of the AVHRR. Ruff and Gruber (1988) note that daylight measurements are difficult to interpret because it is responsive to both reflected solar radiation and emitted terrestrial radiation. Figure 4 is adapted from their graphical data, indicating the solar flux and earth radiant flux along with the various AVHRR channels. The nature of data from this channel would appear to be strongly influenced by some threshold value of the earth's Albedo. Nevertheless, several researchers are reporting successful use of this channel during daylight hours.

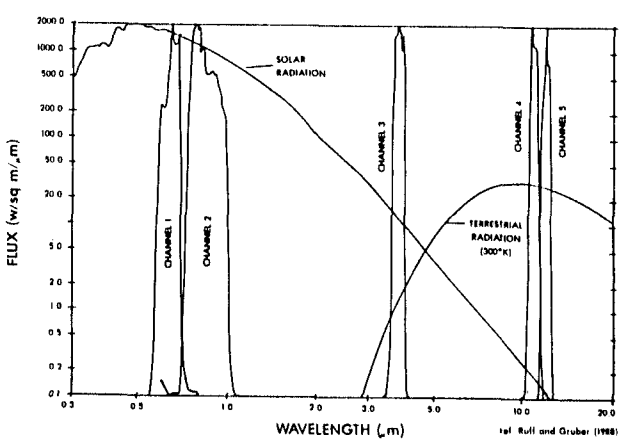

FIGURE 4. AVHRR/2 SPECTRAL RESPONSE

The 3.7 micron channel is being redesigned to eliminate the slow increase in noise level exhibited by several units in orbit. This redesign involves changes to the Indium Antimonide detector and its circuity. Another change is improved spectral response performance in channels 1 and 2, making them more symmetrical. The specified signal to noise ratio will be increased by a factor of three to 9:1, at a 0.5% Albedo, but the designed values are expected to closer to 20:1.

Finally, these channels will introduce a dual slope characteristic in the electronic gain function. The new gain curve will increase signal levels of scenes having albedos less than 25 percent. This will improve the usefulness of AVHRR data for land and sea surface analyses. The longwave thermal channels, 4 and 5, will have modified gain functions to allow maximum scene temperatures of 335K to be measured. Figure 5 indicates the change in the gain function. Curve #1 is the present output function in channels 1 and 2.

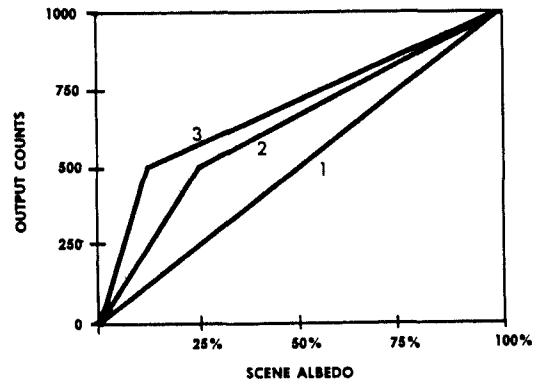

FIGURE 5. OUTPUT FUNCTIONS FOR AVHRR ALBEDO CHANNELS

6. HIRS

The design and function of the HIRS instrument has been described by various authors, e.g., Schwalb (1979, 1982), Henderson-Sellers (1984), Houghton et al. (1984), and Chen (1985). The NASA GSFC HIRS/3 specification S-480-28.2 gives this capsule description of the instrument: The HIRS/3 is a discrete stepping, linescan instrument designed to measure scene radiance in 20 spectral bands to permit the calculation of the vertical temperature from the Earth's surface to about 40km with particular emphasis on the troposphere and to detect clouds. The radiometer has a minimum field of view nominally 1.40 degrees, at the half power points; the scan mirror steps in increments of 1.80 degrees transverse to the sub-orbital track between 49.5 degrees from nadir for a total of 56 scan steps per line. Spacecraft orbital motion provides the forward along-orbital- track dimension to the scan pattern. The scan mirror dwells on each field of view for a period of 100 milliseconds, less step and settle time, and retrace in 800 milliseconds, taking a total time of 6.4 seconds per scan line. Primary infrared calibration is provided by two onboard blackbody targets and cold space.

Table 2 shows the central wavelengths for the spectral channels used in the HIRS/2 and HIRS/2I instruments, as well as the new HIRS/3 units. In addition to the spectral channel changes, the HIRS/3 is being designed for a three year design life and 100K detector operating temperature.

7. HIRS Performance

Table 3 presents the radiometric performance parameters for the earlier HIRS/2 and HIRS/2I instruments, and the specification for the HIRS/3. These data were taken during thermal vacuum test at ITT Aerospace/ Optical Division and from a sample of FM1T orbital data accumulated soon after the NOAA-11 launch. NEDT performance of the HIRS/2I instruments has been greatly improved over the HIRS/2 models in the longer wavelength channels due to cooler improvements which reduced microphonic effects on the detector induced by the spacecraft.

This cooler redesign also improved thermal performance resulting in more margin which will allow the operating point to be lowered to 100K from 105K.

TABLE 2. SPECTRAL CHANNELS AND DETECTORS

DETECTOR	CHANNEL	HIRS/2 WAVELENGTH (microns)	HIRS/2I WAVELENGTH (microns)	HIRS/3 WAVELENGTH (microns)
	1	14.95	14.95	14.95
	2	14.71	14.71	14.71
	3	14.49	14.49	14.49
	4	14.22	14.22	14.22
	5	13.97	13.97	13.97
	6	13.64	13.64	13.64
HgCdTe	7	13.35	13.35	13.35
(Longwave IR)	8	11.11	11.11	11.11
	9	9.71	9.71	9.71
	10	8.16	12.55	12.47
	11	7.33	7.33	7.33
	12	6.72	6.72	6.52
	13	4.57	4.57	4.57
	14	4.52	4.52	4.52
	15	4.46	4.46	4.47
InSb	16	4.40	4.40	4.45
(Shortwave IR)	17	4.24	4.13	4.13
	18	4.00	4.00	4.00
	19	3.76	3.76	3.76
Silicon (Visible)	20	0.69	0.69	0.69

TABLE 3. HIRS/2I RADIOMETRIC PERFORMANCE AND HIRS/3 SPECIFICATION

CHANNEL	SPECIFIED NEDT (DESIGN GOAL)	FM1I NEDT T/V DATA	ORBITAL NEDT DATA	FM2I NEDT T/V DATA	FM3I NEDT T/V DATA	HIRS/3 NEDT (SPECIFIED)	EXPECTED MAX. SCENE TEMP (K)
1	3.00/.75	0.876	0.970	0.646	1.747	3.00	280
2	0.67/.25	0.251	0.280	0.148	0.401	0.67	265
3	0.50/.25	0.190	0.260	0.118	0.274	0.50	240
4	0.31/.20	0.090	0.120	0.055	0.124	0.31	250
5	0.21/.20	0.088	0.100	0.050	0.101	0.21	265
6	0.24/.20	0.109	0.120	0.059	0.083	0.24	280
7	0.20	0.054	0.090	0.032	0.060	0.20	290
8	0.10	0.019	0.030	0.025	0.022	0.10	330
9	0.15	0.028	0.045	0.023	0.032	0.15	270
10	0.20/1.5	0.069	0.087	0.036	0.061	0.15	300
11	0.20	0.052	0.080	0.034	0.053	0.20	275
12	0.19/.10	0.055	0.069	0.035	0.065	0.20	255
13	0.006/.002	0.0011	0.0014	0.0009	0.0015	0.006	300
14	0.003/.002	0.0011	0.0018	0.0011	0.0014	0.003	290
15	0.004/.002	0.0011	0.0015	0.0009	0.0012	0.004	280
16	0.002	0.0007	0.0010	0.0007	0.0011	0.004	270
17	0.002	0.0010	0.0020	0.0009	0.0010	0.002	330
18	0.002	0.0006	0.0010	0.0004	0.0007	0.002	340
19	0.001	0.0002	0.0002	0.0004	0.0003	0.001	340
20	0.1% Albedo	0.005%	-	0.009%	0.006%	0.1% Albedo	100% Albedo

(NEDT measured in mW/M^2Str^2cm)

8. HIRS/3 Design Modifications

As mentioned, the HIRS/3 design changes are:

- Five spectral channel changes
- Three year design life
- Lower cooler operating temperature.

Four of the five spectral changes are slight central wavelength adjustments within the present spectral bands. The fifth, however, moves the lower boundary of the LW band from 6.72 microns to 6.52 microns. This affects the specification of the LW/SW beamsplitter in the telescope and the aplanatic lenses at the LW detectors.

Design activities for filter wheel lifetime improvements are concerned with bearing specifications and reduction of lubricant loss by decreasing the filter wheel motor venting to the minimum required to prevent excessive internal pressure during launch. Lower temperature operation of the cooler will result in less control power needs and increase in LW channel signals.

9. SUMMARY

Many of these changes to AVHRR/3 and HIRS/3 are the result of an continuous effort by NOAA to increase the performance of the instruments and refine the original mission of the AVHRR and HIRS to provide the operational collection of meteorological data. Today, other users are finding the moderate ground resolution data and high return viewing capability, not to mention easy access to the data, beneficial in a wide range of operational and research functions. This has expanded the broad based support of these systems and has helped to avoid funding problems which exist in other programs.

Acknowledgments

The AVHRR and HIRS instruments are produced directly for NASA/GSFC. AVHRR/1 were delivered under contracts NAS5-21900, NAS5-23400, and NAS5-22497. HIRS/2 and HIRS/2I were delivered under contracts NAS5-23567, NAS5-24179 and NAS5-26954. AVHRR/2 was delivered under contracts NAS5-26771 and NAS5-25143. AVHRR/3 and HIRS/3 are presently being designed and built under contract NAS5-30384.

REFERENCES

Chen, H.S., 1985, Space Remote Sensing Systems, Academic Press, Inc.

Colwell, R.N., ed., 1983, Manual of Remote Sensing, American Society of Photogrammetry.

Henderson-Sellers, Ann, 1984, Satellite Sensing of a Cloudy Atmosphere: Observing the Third Planet, Taylor & Francis.

Houghton, J.T., Taylor, F.W., and Rogers, C.D., 1984, Remote Sounding of Atmosphere, Cambridge University Press

ITT Aerospace/Optical Division, September 1982, AVHRR/2, Advanced Very High Resolution Radiometer, Technical Description.

ITT Aerospace/Optical Division, July, 1986, AVHRR/2 and HIRS/2I Improvement Study, Final Report.

ITT Aerospace/Optical Division, October 31, 1988, Monthly Program Status Report for the Advanced Very High Resolution Radiometer/3 (AVHRR/3) and High Resolution Infrared Radiation Sounder/3 (HIRS3) for the NOAA-K, L, and M Spacecraft, Report Number 1.

Koczor, R.J. and Comeyne, G.J., Jr., October 21, 1985, "Present and Future Uses of AVHRR Multispectral Data", Nineteenth International Symposium on Remote Sensing of Environment.

Ruff, I. and Gruber, A., General Determination of Earth Surface Type and Cloud Amount Using Multispectral AVHRR Data, NOAA Technical Report NESDIS 39, February, 1988.

Schwalb, A., 1979, The TIROS-N/NOAA A-G Satellite Series, NOAA Technical Memorandum NESS95.

Schwalb, A., 1982, Modified Version of the TIROS-N/NOAA-G Satellite Series (NOAA E-J)- Advanced TIROS-N (ATN), NOAA Technical Memorandum NESS 116.

Weinreb, M.P., Hamilton, G., Brown, S., and Koczor, R.J., publication pending, "Non-linearity Corrections in Calibration of AVHRR Infrared Channels", Journal of Geophysical Research.

DETERMINATIONS OF CLOUD LIQUID WATER IN THE TROPICS FROM THE SSM/I

John C. Alishouse

Satellite Research Laboratory
NOAA/NESDIS
Washington, D.C.

Calvin Swift
Christopher Ruf*

University of Massachusetts
Amherst, Massachusetts

Sheila Snyder
Jennifer Vongsathorn

S. M. Systems Research and Research Corporation
Landover, Maryland

*Present Affiliation: Jet Propulsion Laboratory
Pasadena, California

1. INTRODUCTION

1.1 Background

A companion measurement to the determination of total water vapor is the measurement of cloud liquid water content. Both liquid water and water vapor in the atmosphere contribute to the brightness temperatures measured by a microwave radiometer. Thus to solve for the water vapor from the SSM/I brightness temperatures it is necessary to correct for the contribution of liquid water. To adequately correct for the liquid water contribution requires sufficient information to derive the amount of cloud liquid water present.

Cloud liquid water content is important for the earth's radiation balance, precipitation formation, and dynamics of the atmosphere. Despite the importance of cloud liquid water content, previous experiments have provided almost no quantitative comparisons between surface and satellite determinations. A great deal of this is due to the difficulty in obtaining surface determinations of cloud liquid water on a spatial and temporal scale commensurate with a satellite radiometer.

This investigation was able to arrange for special upward looking microwave radiometric observations which were used to validate the SSM/I determinations and as a basis for the determination of new coefficients.

1.2 The SSM/I

The SSM/I (Hollinger et al, 1987) is a seven channel, four frequency linearly polarized microwave radiometer that was launched into a near polar orbit in June 1987. The satellite has an altitude of about 833 kilometers, a period of 102 minutes, and an approximately 0615 LST ascending node. The salient characteristics of the SSM/I are presented in Table 1. The last column in Table 1 is the Noise Equivalent Temperature Difference (NETD) of the instrument or its rms noise. The vertical polarization channel noise is given first in the NETD column. There was a significant increase in the 85 V channel noise in January 1988. This has caused the 85 V to be less useful than planned.

Table 1. SSM/I Characteristics

FREQUENCY (GHz)	POL.	EFOV (KM)	NETD (K)
19.35	V,H	45X70	0.43,0.41
22.235	V	40X60	0.67
37.0	V,H	30X38	0.33,0.37
85.5	V,H	14X16	1.70,0.72

2. SURFACE MEASUREMENTS

2.1 The UMASS Radiometer

Microwave autocorrelation radiometry synthesizes techniques developed for correlation radiometry and Fourier transform spectroscopy. The autocorrelation function, R(t), and the power spectral density function, S(f), are related by the Fourier transform. The autocorrelation function can be generated by correlating the voltage time series, x(t), with a time delayed voltage time series, x(t+T). The brightness temperature spectrum is related to the spectral density function by a simple linear relationship. In other words, a microwave autocorrelation radiometer will

produce samples of the brightness temperature spectrum by a Fourier transformation of measure ments of the cross-correlation of a signal with a time-delayed version of itself.

The upward looking cloud liquid water measurements were made using the University of Massachusetts autocorrelation radiometer (CORRAD) (Ruf and Swift, 1988) and an auxiliary single frequency radiometer at 37 GHz. The CORRAD operates between 20.5 and 23.5 GHz spanning the water vapor line at 22.235 GHz and permitting the deduction of water vapor profiles and cloud liquid water amounts.

The operating characteristics of the CORRAD are presented in Table 2. The radiometer is steerable and is calibrated by the "tipping curve" technique.

Table 2. CORRAD Characteristics

RF BANDPASS	20.5-23.5 GHz
TIME DELAYS	-0.2 TO 6.1 NS (0.1 NS STEPS)
FREQUENCY RESOLUTION	160 MHz/100 MHz (3 dB)
RECEIVER NOISE TEMP.	2000K
NOISE FLOOR (ΔT)	0.5 K/(SEC)1/2
EFOV	2 DEGREES

2.3 Data Reduction

The CORRAD puts out a brightness temperature spectrum every ten minutes, thus permitting the retrieval of a cloud liquid water value every ten minutes. These values were then used to derive coefficients for the SSM/I brightness temperatures to predict the cloud liquid water.

The CORRAD has an EFOV of 2 degrees, which means a footprint of about 30 meters at an altitude of 1 km, when operated at zenith viewing. By contrast the SSM/I has a 45 x 70 km at the earth's surface. This disparity lead us to investigate ways of compensation. One possibility was averaging the CORRAD data for a period of time.

3. INITIAL ALGORITHM

3.1 Structure

The initial algorithm (Hollinger et al, 1987) used to retrieve cloud liquid water was a linear, four channel algorithm that was generated by regression using brightness temperatures calculated from simulated clouds and a radiative transfer model. The algorithm was divided into latitudinal and seasonal segments called climate codes. There were eleven climate codes per hemisphere. Over the ocean there were nine distinct sets of coefficients that used the 19H, 22V, 37V, and 37H channels. Over land there was one set of coefficients per climate code which used the 19V, 19H, 37V, and 85V channels. Another set of coefficients was used to retrieve cloud water over snow. This set of coefficients was used for all climate codes and utilized the 22V, 37H, 85V, and 85H channels.

Globally the latitude zones were: 60-90, the polar zone; 55-60, a transition zone; 25-55, the temperate zone; 20-25, a transition zone; and 0-20, the tropical zone.

Data for our study were taken from Kwajalein Island between March 24 and April 7, 1988.

3.2 Problems

We found that more than 90% of all retrieved values of cloud liquid water were either out-of-limits or indeterminate values. This same percentage was also found at our extra-tropical test sites and before and after the SSM/I's shutdown during Dec. and Jan., 1987-8. As a result of this finding, it was decided to attempt to improve the algorithm.

4. IMPROVED ALGORITHM

4.1 Structure

The improved algorithm was derived from the CORRAD measurements of cloud liquid water and the matching SSM/I brightness temperatures by standard linear regression techniques. Various four channel combinations of the six SSM/I channels (85 V was excluded for noise reasons) were used in the regression. All six channels were also used as predictors. All algorithms are linear and have the form:

$$CLW = a_0 + \sum a_i T_{Bi} \qquad (1)$$

As a means of compensating for the disparity in the fields-of-view of the two radiometers averaging the data was investigated. It was discovered that with one exception the averages and the closest values differed only by minor amounts, except for one overpass. Accordingly, we used the coincident values and required a very close match in latitude and longitude between the island the pixels used in the retrieval.

4.2 Results

The initial algorithms for cloud liquid water were linear four channel algorithms. It would be most economical to utilize as much of the existing software structure as possible. For this reason we investigated four channel combinations to retrieve cloud liquid water. There are 15 possible channel combinations. The correlation coefficients ranged from 0.886 to 0.706 for the possible four channel combinations. The best combination is 19V, 22V, 37H, and 85H. The worst combination is 22V, 37V, 37H, and 85H. This was slightly surprising as the higher frequency channels are more sensitive to cloud liquid water. For all six channels the correlation coefficient is 0.973.

4.3 Statistics

The best four channel combination has an error of 14%. The sample mean is 0.168 Kg/m^2 with a mean square error (mse) of 0.024. The best six channel has the sample mean and a mse of 0.016 for an error of 9.5%.

The SSM/I also shows promise for discriminating between water and ice clouds.

Table 3. Channel Correlations

CHANNEL COMBINATIONS	CORRELATION COEFFICIENTS
ALL	.973
19V,22V,37H,85H	.886
19V,19H,22V,85H	.875
19V,22V,37V,85H	.840
19V,19H,22V,37V	.830
19V,22V,37V,37H	.823
19H,22V,37V,85H	.817
19H,22V,37H,85H	.807
19V,19H,37V,85H	.794
19V,19H,37H,85H	.791
19V,37V,37H,85H	.781
19H,37V,37H,85H	.779
19V,19H,22V,37H	.770
19V,19H,37V,37H	.764
19H,22V,37V,37H	.731
22V,37V,37H,85H	.706

5. REFERENCES

Ruf, C.S., and C.T. Swift, 1988: Atmospheric Profiling of Water Vapor Density with a 20.5-23.5 GHz Autocorrelation Radiometer. J. Atmos. Ocean. Tech., 5, 539-546.

Hollinger, J., R. Lo, G. Poe, R. Savage, and J. Peirce, 1987: Special Sensor Microwave/Imager Users Guide, Naval Research Laboratory, Wash., DC, 120pp.

SPACE-TIME VARIABILITY OF TROPICAL CONVECTION

by

Harry H. Hendon

Murry Salby

Ken Tanaka

Karen Woodberry

Pat Callaghan

University of Colorado

Boulder, Colorado

1. INTRODUCTION

As a major element of the World Climate Research Program, the operational phase of the International Satellite Cloud Climatology Project (ISCCP) began on 1 July 1983. The major objective of ISCCP was to produce, on an ongoing basis, a global, calibrated, infrared and visible radiance data set. From these data various properties of clouds, such as average cloud amount, cloud type etc, can be derived. Furthermore ISCCP hoped to encourage a variety of studies that could make use of their global, calibrated, radiance data.

The ISCCP radiance data consists of processed infrared and visible images from the four operational geostationary satellites (GOES-E, GOES-W, METEOSAT, and GMS) and the polar orbiting satellites (NOAA/TIROS-N). The original raw data, of horizontal resolution between 1 and 12 km and image frequency between 48 and 14 per day, were reduced to horizontal resolution of about 30 km and frequency 8 per day. The radiance measurements from the four geostationary satellites were cross calibrated to that of the polar orbiter, thus providing coherent and consistent global data. This reduced resolution, calibrated set is referred to as ISCCP B3. The original volume of about 50,000 tapes per year was reduced to about 114 tapes. (see Rossow et al, 1985 for full details)

At the Center for Atmospheric Theory and Analysis, the task of combining the individual infrared B3 images into single global images, 8 times per day has begun. While the temporal and meridional (20 km) resolution of the original B3 data is retained, computer limitations have forced a reduction in the zonal resolution (about 60 km). Still the resulting zonal resolution, combined with the temporal and meridional resolution yields an unsurpassed global radiance data set.

The major purpose for producing these synoptic, global, radiance images is to study the temporal and spatial variability of tropical convection and how this convection interacts with the global circulation. It is becoming increasingly apparent that the interaction of tropical convection, on scales of cloud clusters (10's of km) that last on order of hours, with the larger scale circulation must be understood in order to fully understand the global scale climate. These interactions need to be studied both to increase our theoretical and observational understanding of climate but also to improve convective parameterizations in climate models. The synoptic, global, radiance data compiled at CATA provides a unique tool with which to define and study these interactions.

One scale of variability that will be easily studied is the diurnal cycle throughout the tropics. Local phase and relative amplitude of the diurnal cycle can be determined. How and where the diurnal cycle interacts with the synoptic- and larger-scale will also be studied.

Another interesting scale interaction is that of the 40-50 day oscillation with convection on the synoptic and sub-synoptic scale. Recent observational and modelling studies of the 40-50 day oscillation suggest that the organization of convective complexes by the larger-scale circulation is crucial for the resulting slow eastward propagation. With this global, synoptic, radiance data set, these interactions throughout the tropics can be studied.

2. ASSIMILATION OF GLOBAL IMAGES

The initial task undertaken at CATA was to produce global infrared radiance images, 8 times per day, from the ISCCP B3 data. Full details of this assimilation process are given in Tanaka (1988). At a given time, say 12GMT, the four geostationary images at this time and the polar orbiting scans within $\pm$ 90 minutes are assimilated into a single image. To make use of the image processing and FFTs on the CATA computers, the final images are constrained to be 512x512 pixels. These 512 square pixels are projected onto a cylindrical equidistant projection. The raw pixels from the individual satellites are thus binned into this final grid. Where more than one raw pixel falls into the final bin, the pixel values are simply averaged together. In low latitudes on the order of 4-8 raw pixels are averaged to produce the final pixel. Unfortunately at longitudes around 70E, where METEOSAT and GMS barely overlap, this number is often less than this and actually falls to zero in some places. Special techniques are employed to alleviate this problem (discussed below).

To account for the inaccuracies of the data at the limb of the geostationary images, a combination of weighting and rejection of limb data is employed. All data values whose cosine of satellite zenith angle is less than 0.01 are rejected. This effects the extreme limb. Equatorward of 45 the geostationary data are weighted by their cosine of zenith angle prior to the averaging process described above. Poleward of 45 a further rejection of data whose cosine of zenith angle is less than 0.1 is employed. Because the geostationary images only give adequate coverage to about 60, this more stringent polar region rejection is used to eliminate as many spurious pixels as possible.

Figure 1 displays a typical synoptic image produced by the above procedure. This resulting image, with better than 95% filled pixels between 45N and 45S, forms the basis for producing global (in particular sub polar) synoptic images. As mentioned above, due to the lack of data from the Indian geostationary satellite, minor gaps are apparent around 70E. In every fourth image this gap is completely filled by an orbit of the NOAA satellite. Otherwise, an interpolation sequence described below adequately fills the voids.

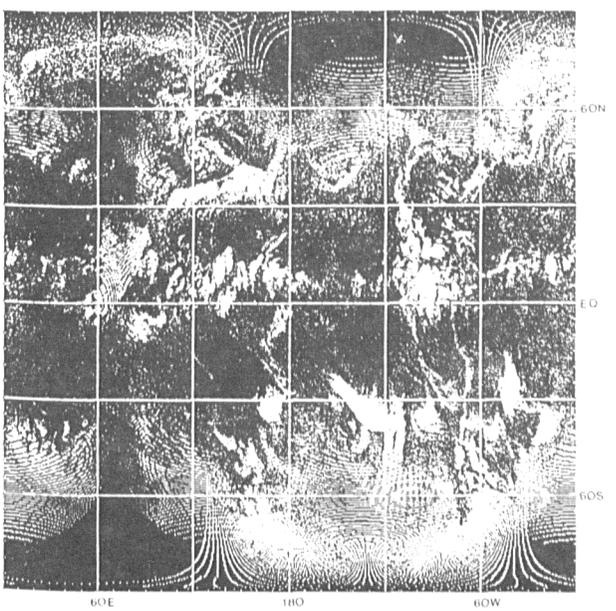

Figure 1 The initial assimilation of the global image for 6 GMT day 202 1983. Only data from the four geostationary satellites and the polar orbiter within 90 minutes of 6 GMT are used. No spatial interpolation has been performed.

Whereas the major intention of producing this data set is to study tropical cloud variability, we have spent considerable effort in filling in the large number of missing pixels poleward of 60. In reality this region represents a very small area. However for the sake of producing global images, it was decided to fill them to the best of our ability. Through a sequence of inclusion of polar orbiting data at wider time limits (up to ±200 minutes) and spatial interpolation on the polar gap projected onto a polar stereographic map, the polar region is readily filled.

Equatorward of 60 a series of 3× 3 and 5× 5 spatial interpolations are used to fill in missing pixels. To prevent propagation of purely interpolated data, pairs of opposing points along with at least half of the possible pixels in the interpolation grid must be present to fill a point. In general only a few passes of first the 3× 3 and then the 5× 5 interpolators are sufficient to fill the missing pixels due to bad scan lines, the Indian gap, and most minor satellite problems. If pixels are still missing after this process, linear interpolation in time between adjacent images is used.

Figure 2 displays the complete, interpolated image shown in figure 1. These assimilated images are stored as 512 × 512 pixel images, with each pixel as an eight bit integer ranging from 0-255. These integers represent a gray scale in brightness temperature ranging between 340-150K. To date, the month of July 1983 has been processed, though some bugs are still being worked out of the system. In the near future the entire first year of ISCCP data will be assimilated.

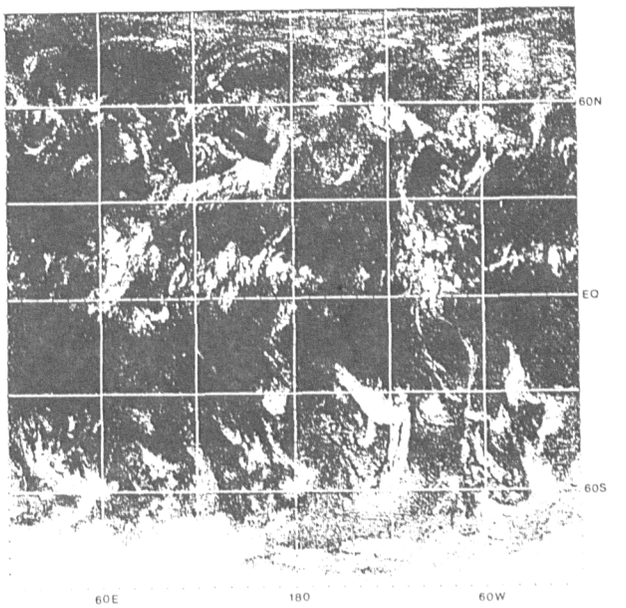

Figure 2 As in Figure 1 except the image is completely filled by the interpolation process.

3. SPACE-TIME VARIABILITY

Figure 3 is a demonstration of both the image processing capabilities at CATA and of the wide range of scales detectable in the data. Figure 3 is a classic Hovmoller diagram, along 10N, for the month of July 1983. Pixel values for the 10 scan lines about 10N are averaged together; the resulting array is reconstructed as an image, retaining the original gray scale for brightness temperature.

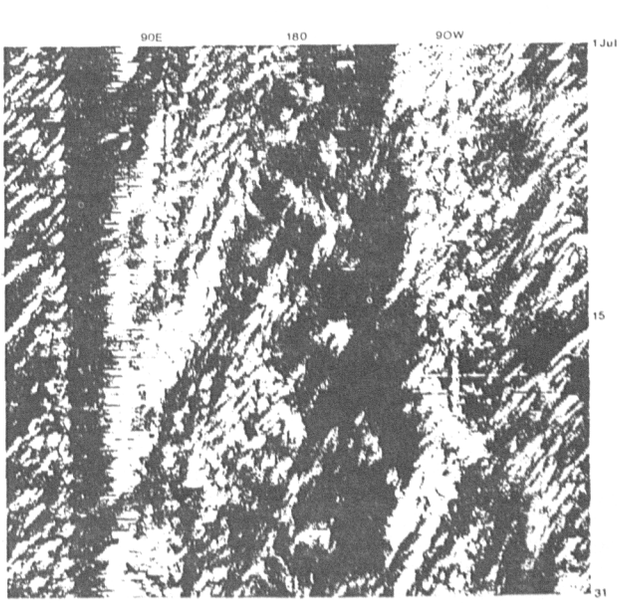

Figure 3 Hovmoller image along 10N for the month of July.

The immediate impression is that, at 10N, westward moving cloud clusters and wave forms dominate the variability. Over central Africa a pronounced diurnal fluctuation is seen. However, this convection is continually blown off to the west, giving the appearance of an easterly wave. Presumably the upper level easterlies are responsible for the westward blow off. Now and then this diurnally forced convection lasts for multiple days and propagates well into the Atlantic Ocean. The interaction with a true easterly wave is indicated, though this phenomena needs to be studied further.

In the western Pacific, much less diurnal signal is seen and the scale of the westward moving clouds is much bigger. The phase speed is about half that over Africa (5m/s as compared to about 10-15m/s). Intermediate in scale and phase speed between the western Pacific and Africa are the westward moving clouds over northern South America. Now and then a cloud cluster, which has its roots over central Africa, appears to propagate across the Atlantic, into the South American region.

The dominance of the westward propagation of clouds is confirmed by the w-k representation of power along 10N (Figure 4). Substantially more power exists in westward moving clouds than eastward. A dominant period of around 4 days is evident. Wavenumbers from 4-20 exhibit this 4 day period. The diurnal cycle shows up as predominantly westward wavenumber 1, though a stationary component in wavenumber 1 does exists. Furthermore, power in other wavenumbers at the diurnal period is also detectable, thus implying either wave or advective modulation of the diurnal forcing.

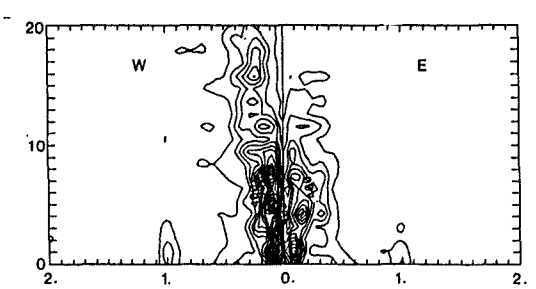

Figure 4 Power as a function of frequency and wavenumber along 10N for July 1983. The abscissa is cycles per day and the ordinate is zonal wavenumber.

Individual temporal spectra, for selected regions, demonstrate the dramatically different variability between ocean and land. Over central Africa (10N 22E), the spectra is predominantly diurnal (Figure 5). A secondary peak occurs at around 2.5 days, presumably due to westward blow-off. Off the west coast of Central America (10N 93W, Figure 6) a substantial diurnal modulation is felt, despite being over ocean. The proximity of the Central American coast is probably responsible for the strong diurnal peak. This modulation is then advected westward. Far away from land masses, however, the diurnal cycle is difficult to detect. In the central Pacific ITCZ (10N 180W, Figure 7), a predominantly red spectra is observed. Still substantial power exists in the sub (2 day) frequency range.

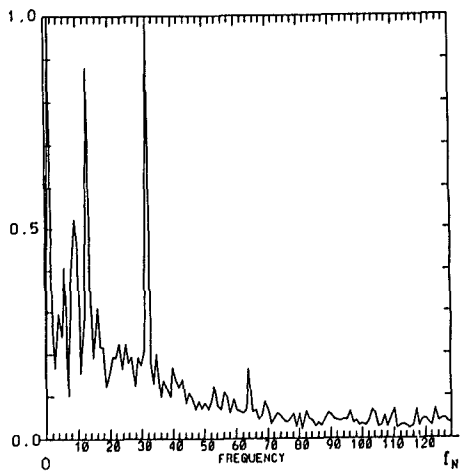

Figure 5 Temporal spectra at 22E 10N. Abscissa is cycles per 32 days. Power units are arbitrary.

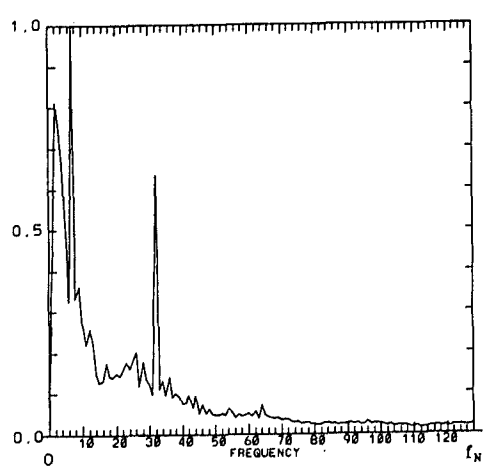

Figure 6 As in Figure 5 except at 93W 10N.

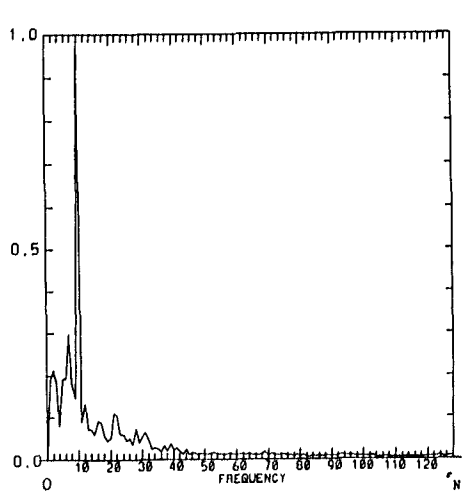

Figure 7 As in Figure 5 except at 180W 10N.

The total variance, percentage variance occurring in the diurnal range (21-27hours) and percent variance for frequencies greater than (2 days) is displayed in Figure 8. The variance estimates were made along 10N for the month of July. Large total variance in convection exists over Indonesia (90-140E), northern South America (60-100W) and western Africa (10W-20E). In general, the percentage variance at high frequencies (ie greater than (2 days), which is not resolved in traditional global OLR data) is about 40and suggest that much remains to be learned about how it interacts with the more well known lower frequencies. Only over tropical land masses does the diurnal band have large amplitude. It is interesting that where the diurnal band is large, the total variance is small. One explanation is that over land, diurnal forcing is great but there is insufficient available moisture to support continuous convection.

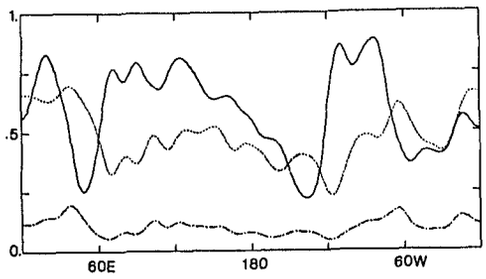

Figure 8 Total normalized variance (solid line), percent variance in the sub 2 day period range (dotted line), and percent variance in the diurnal range (dashed line), along 10N for July 1983.

4. SUMMARY

At the Center for Atmospheric Theory and Analysis, global-synoptic radiance images are being produced from the ISCCP B3 archives. Assimilation of these global images is possible because of the careful cross calibration of the individual satellites in the B3 archive. To date, 8 images per day, for July 1983, have been produced. Though this project is still in its infancy and problems still exist with the assimilated data, initial results are very promising.

The temporal and spatial resolution of the data are more than adequate to study tropical convection on the sub 2 day time scale. For the month of July 1983, the percentage variance for sub 2 day periods was shown to be large, especially over land areas. Upwards of 40of tropical convection operates on time scales less than 2 days. The structure and coherence of this high frequency convection is the subject of current study.

5. REFERENCES

Rossow, W.B., E. Kinsella, A. Wolf, and L. Gardner, 1985: ISCCP Description of Reduced Resolution Radiance Data. Available from ISCCP Global Processing Center, NASA Goddard, New York, NY 10025.

Tanaka, K, 1988: ASSIM: Maintenance Manual. CATA Technical Note 001a. Available from CATA, Campus Box 391, University of Colorado, Boulder CO 80303.

12.2

TEMPORAL CHARACTERISTICS OF TROPICAL CONVECTION

Lorraine A. Remer and Bryan C. Weare

Atmospheric Science Group, Dept. of Land, Air & Water Resources
University of California
Davis, California 95616

1. INTRODUCTION

The large-scale dynamical properties of the tropical atmosphere are strongly related to tropical convection. In addition, the meso-scale cloud systems produced by tropical convection dominate the radiative fluxes perceived by a satellite at the top of the tropical atmosphere. Thus a satellite can detect some of the important characteristics of convective systems in the tropics. The spatial and temporal characteristics of convection in the tropics are both important to the subsequent tropical circulation, and likewise both spatial and temporal characteristics of the convection can be measured by satellite.

Besides satellite data, other important tools for understanding atmospheric circulation and convection are the general circulation models (GCMs). These models are used extensively to study and predict variations in weather and climate. Initially, these models were validated with comparisons of model and observed zonally average statistics of traditionally measured values such as winds, geopotential heights and temperatures. Recent studies have begun to evaluate model radiative fluxes in terms of satellite data. These studies have concentrated on the spatial characteristics of the radiative fluxes. The temporal characteristics of tropical convection and thus the radiative fluxes above the tropical atmosphere are also important in determining the subsequent tropical circulation. The models must simulate the correct temporal periodicities of the convection in order to properly simulate the correct dynamical response. It is the purpose of this study to continue the validation process of one particular GCM by concentrating on a comparison of the temporal properties of the outgoing longwave radiation (OLR) of the model with satellite measured data.

2. THE MODEL VARIABLES

The GCM investigated in this study is the one developed by Arakawa and his coworkers at the University of California at Los Angeles (UCLA). The model used in this study is the 9 level coarse resolution (4° lat by 5°) UCLA GCM. The model which we analyze was initialized with NMC 12 UTC analyses for October 1, 1982 and run with actual sea surface temperatures measured during the 1982-83 period. It should simulate the approximate atmospheric circulation for the same period. This model output, recorded hourly, during July 1983 is sampled at three hour intervals.

3. SATELLITE DATA

We use outgoing longwave radiation (OLR) data as measured by the geostationary meteorological satellite (GMS) during July 1983

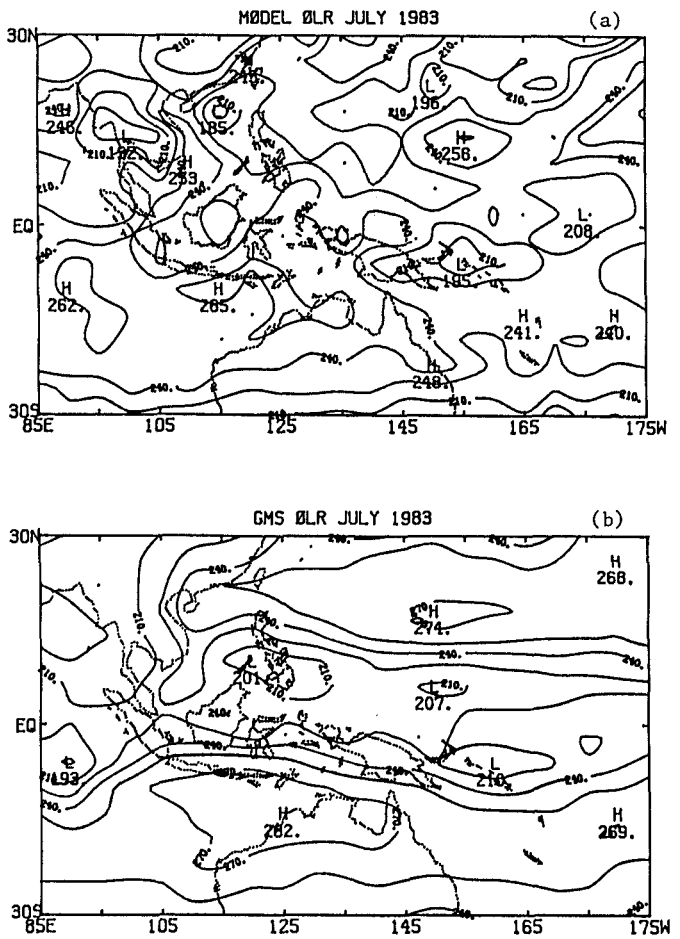

Fig. 1(a) Outgoing longwave radiation of the model output averaged for July 1983. (b) Same as (a) but for GMS data.

as a comparison data set for the model output. These satellite data were made available by the International Satellite Cloud Climatology Project (ISCCP). The ISCCP B3 product comes as narrowband radiances concentrated near the center of the 12 um window. The GMS data have been normallized to the radiances measured by the NOAA-7 polar orbiting satellite. The original resolution of the OLR data were roughly 30 km sampled at 3 hour intervals. The GMS satellite centered at the equator at 140°E longitude gives a good view of the western tropical and subtropical Pacific Ocean. To avoid extreme adjustments for limb darkening, we narrowed the area of interest to the latitude bands between 30°S and 30°N and the longitudes between 85°E and 175°W.

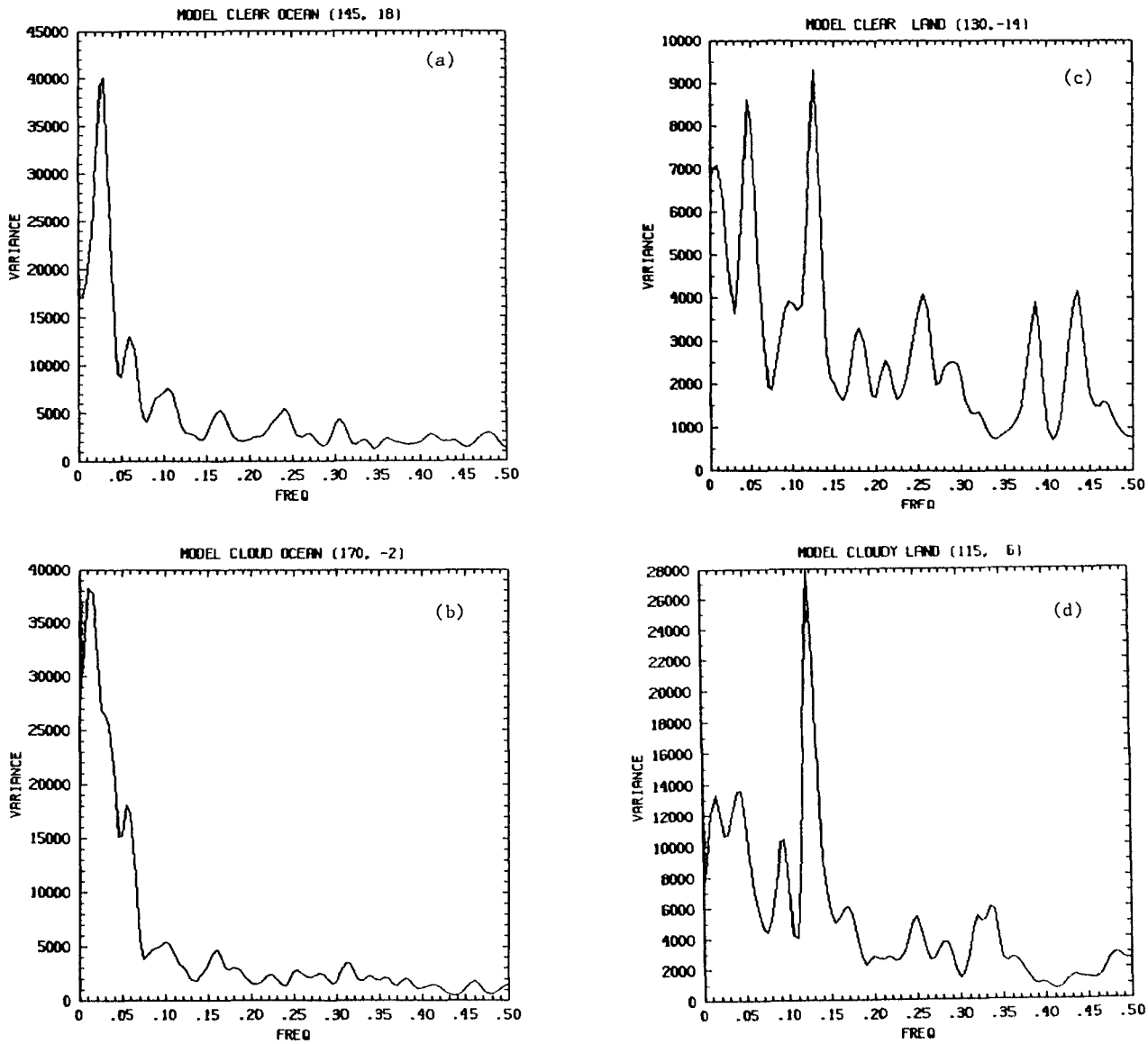

Fig. 2(a) Power spectra for OLR of the model output at a clear ocean square. The frequency .125 corresponds to a period of 24 hours. The frequency .04 corresponds to a period of roughly 3 days. (b) Same as (a) but for a convective ocean square. (c) Same as (a) but for a clear land grid square. (d) Same as (a) but for a convective land grid square.

The data were adjusted in two ways in order to be more comparable to the model output. Firstly the 30km resolution data were spatially averaged in order to conform to the 4° lat by 5° long model grid. Secondly, the longwave narrow band radiance was converted to full spectrum irradiance which is the model's output variable. This was done empirically. A number of errors in these estimates of OLR are possible. The most important of these probable errors are associated with transforming narrow band measurements to full spectrum. However, since this study will focus on a comparison of the time domain characteristics and not the absolute values of the OLR, the errors introduced by converting to full spectrum irradiance will have minimum impact on the results.

4. COMPARISONS OF MONTHLY MEANS.

The July 1983 monthly mean OLR for the model output and the GMS satellite data are plotted in Fig. 1a and 1b, respectively. The two plots are qualitatively similar. There are two broad highs in the subtropical regions, north and south of the equator. Between the two highs, there exists a region of relatively low OLR, the ITCZ, which runs in an east-west band over the maritime continent then turns northward over the mainland of Asia. The values of the two plots are not identical. The GMS data shows values roughly 20 W/m^2 greater than the model output in the regions of the subtropical highs. In the ITCZ region, the GMS data tend to be higher than the model output by 10-20 W/m^2.

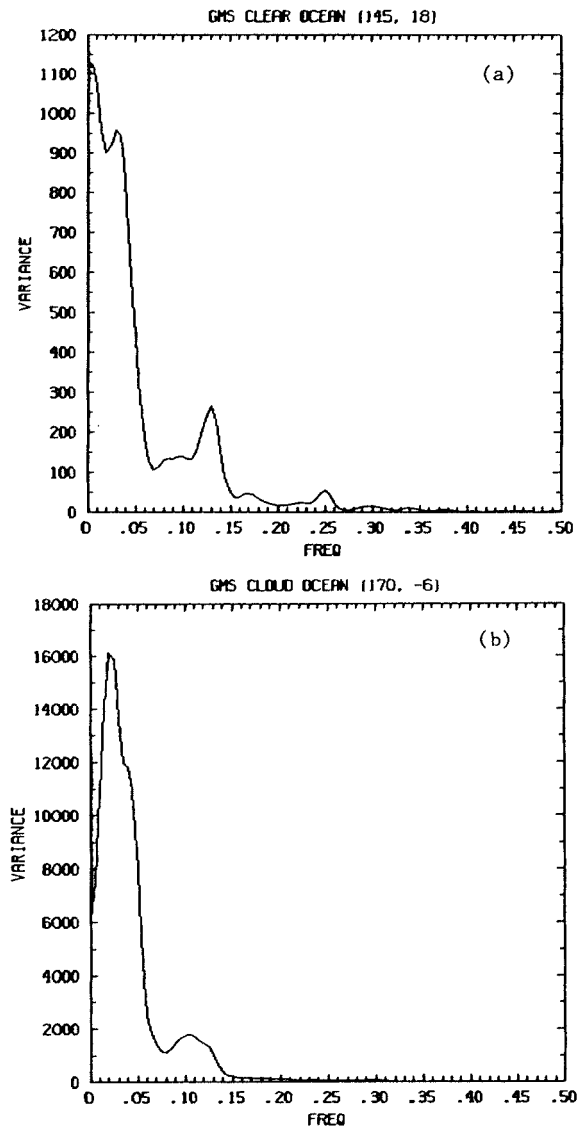

Fig. 3. Same as Fig. 2 but for the GMS data.

The most conspicuous difference in the two plots is how noisy the model output is compared to the GMS data. The GMS data clearly show an organized structure, the two subtropical highs separated by an ITCZ. These structures do exist in the model output, but they are much more difficult to discern. The GMS data have the advantage of being spatially smoothed since the 30km resolution values have been averaged to 4° lat by 5° long grid squares. The model on the other hand is attempting to mimic at each grid square the physical processes occurring on the much smaller cumulus scale. The model never undergoes a spatial average. It is expected that a time average of the model output will smooth out both the spatial and temporal variability caused by the model performing a cumulus-scale process on a full grid square. The long-term statistics of the model output should resemble the long-term statistics of the GMS data. Evidently, one month is not long enough. The high degree of variability apparent in the spatial plots also occurs in the time domain.

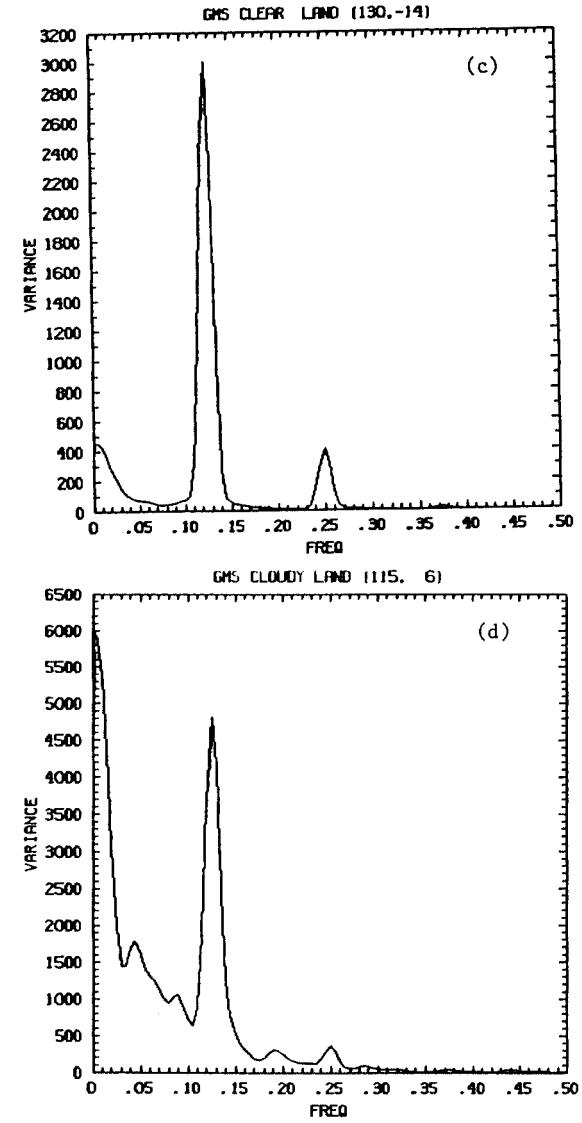

5. COMPARISONS OF POWER SPECTRA

For the purpose of comparing the power spectra of model output with that of GMS data, we choose several grid squares in each data set representative of four different climatic regions: convective over land, convective over ocean, clear over land and clear over ocean. Convective and clear zones were identified by low and high OLR values identified from Fig. 1. Figure 2 shows one example of power spectra from each of the four climatic regions for the model data. Figure 3 does the same for the GMS data. The power spectra were calculated by a method which fourier transforms the autocorreclation function and employs Parzen windows. The effective degrees of freedom for each plot is 12. The band width of each plot is .042. The bottom axis is labeled in frequency of data samples. Data is sampled every 3 hours.

The power spectra of the model output resembles that of the GMS data for low frequencies. Both the model output and the GMS data show strong peaks at the diurnal cycle for those climatic regions over land. These land areas show a mean diurnal cycle with a diurnal

range of 50 to 95 W/m^2 in the model output and roughly 30 W/m^2 in the GMS. Both model output and GMS data exhibit maximum OLR in the afternoon for clear regions and maximum OLR around noon in the cloudy regions. This indicates clearing during midday and convective activity in the late afternoon and evening. See Figure 4. In addition both data sets indicate another periodicity in the 2-6 day region which corresponds to the passage of cloud clusters and other synoptic variables.

The obvious difference between the model output and the GMS data again is the high degree of variability in the model data, especially at high frequencies. The model shows substantial signal across much of the high frequency end of the spectrum. The GMS data show nearly no signal at frequencies higher than 12 hours. In addition, the overall variability of the model output in each of the four climatic regions is from 2 to 5 times higher than the GMS data. One reason for the high degree of temporal variability in the model is that again, the model is attempting to mimic at each grid square the physical processes occurring at the much smaller cumulus square while the GMS data have already undergone a spatial average.

Even so, the model simulation suffers further from the binary nature of its cloud parameterization. A cloud is either on or off, and its existence is the primary determination of the OLR in the model. Physically, there is nothing inconsistent with the cloud in the grid square determining the OLR. The physically inconsistent property of the model output is that the change from clear sky to cloud and back again occurs on the order of hours rather than days.

6. DISCUSSION

In general the model tends to simulate the dominant periodicities which are evident in the GMS data. The major difference between the data sets is the high degree of variability in the model. The magnitude of the major spectral peaks can be an order of magnitude greater in the model than in the GMS data for the same region. The clear ocean regions of Fig. 2a and 3a present a good example. The difference in overall variability may be due in part to the fact that the GMS data has already been spatially averaged. However, the difference is so great that further evaluation of the models parameterizations are in order.

In the high frequency range of the spectrum the cloud and convective parameterizations of the model produce variability which does not exist in the GMS data. See Fig. 2 and 3. One factor is that clouds in the model unrealistically turn on and off on time scales which are on the order of hours. At low frequencies there is some discrepancy in the exact location of the peaks and occasionally the model produces a major periodicity which does not exist in the GMS data. For example in the clear land region the model shows a peak at 0.04 (3 days) and at 0.125 (24 hours) while the GMS data show only the 24 hour peak. See Fig. 2c and 3c. This spurious peak in the clear region may be due to the energy balance parameterization at the ground.

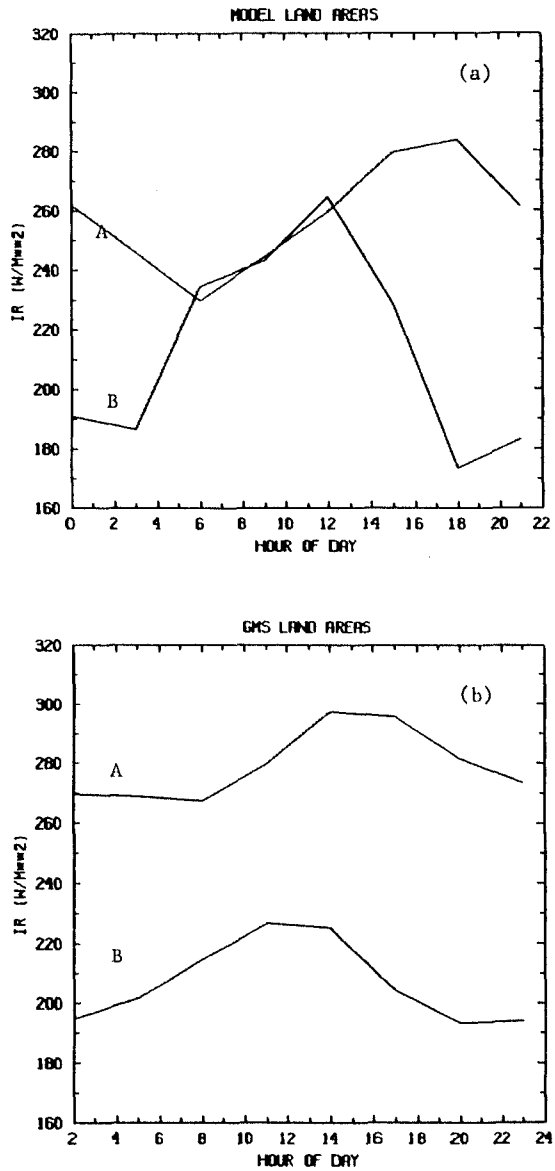

Fig. 4(a) Mean diurnal cycle for the OLR of the model at two selected land areas. Curve A is for the clear land area and curve B is for the convective land grid square. (b) Same as (a) but for the GMS data.

The discrepancies between the model output and observations in overall variability and in the high frequency range may affect short term or medium range forecasting using the model. These discrepancies may also affect long range and climate statistics if the errors are not eliminated by temporal averaging. The spurious low frequency peaks over land regions indicate that the climate statistics of the model should be thoroughly evaluated in these regions.

12.3

THE CLOUD AND SURFACE CONTRIBUTIONS TO THE NET RADIATION BALANCE DURING THE 1982-83 EL NIÑO

Byung-Ju Sohn
Eric A. Smith

Department of Meteorology and
Supercompter Computations Research Institute
Florida State University
Tallahassee, FL 32306

1. INTRODUCTION

Although satellite radiation budget measurements at the top of the atmosphere during the last two decades have improved our understanding of the global climate system of the earth there have been relatively few studies of the interannual variability of net radiation balance and in particular the sources and forcing mechanisms of the variations. Stephens et al. (1981) first drew attention to the significance of isolated regional variability in radiation budget parameters by the use of a dispersion index. In a more recent earth radiation budget study based on a 5-year Nimbus 7 ERB data set, it has been shown that significant interannual variability is largely confined to three epicenters; two associated within the ascending and descending branches of the Walker Cell and a third extending over the equatorial Indian Ocean and onto continental North Africa -- see Smith and Smith (1987). Among these regions, the North African sector was the only continental region to exhibit significant year-to-year perturbations in the five year period of study. In a recent North African study (Smith and Sohn, 1989) it was shown that precipitation anomalies can play a major role giving rise to net radiation perturbations because of their overriding influence on radiative boundary conditions at the surface.

In contrast to fluctuations over the arid and semi-arid continental North African energy sink, fluctuations in the radiation balance over oceanic regions are presumed to arise mainly from imbalances between the greenhouse and albedo effects of extended cloud systems that can force large changes in the top-of-atmosphere net radiation flux. With these factors in mind this research focuses on the impact of regionally confined interannual perturbations in the net radiation balance and the sources and mechanisms of these perturbations vis-a-vis land surface and cloudiness variability. It is our further intent to investigate the interannual fluctuations in terms of cloud and surface forcing associated with the unusually intense 1982-1983 ENSO event.

2. DATA

This analysis has been done over a 6-year period for which global radiation budget (RADBUD) and cloudiness measurements from the Nimbus-7 experiments are available simultaneously. Monthly averaged RADBUD quantities from ERB wide-field-of-view (WFOV) channels (Jacobowitz et al., 1984) and the data based on THIR/TOMS measurements (Stowe et al., 1988) are utilized for the analysis period of April 1979 to March 1985 during which the intense 1982-1983 ENSO phenomenon took place. Thus the period of this analysis encompasses a complete ENSO cycle.

The ERB and THIR/TOMS data sets represent the first lengthy time series of well calibrated and continuous measurements of RADBUD/cloudiness parameters and thus permit detailed interannual analysis. In order to understand how interannual perturbations in the net radiation balance arise from a combination of cloud forced and surface forced feedbacks, it is essential to combine cloudiness data with the RADBUD quantities. The Nimbus 7 cloud climatology permits us to study in detail cloud sensitivity and cloud impact on radiation balance processes.

3. ANALYSIS PROCEDURE

In order to obtain the perturbation in the net radiation balance due to cloud forced and surface forced feedbacks, the partitioning of the two terms is required. The basic approach is to first determine the cloud portion of the forcing; the residual from the total net radiation is then defined as the surface plus atmosphere forcing. In the following discussion we use a notation developed by Ramanathan (1987). In order to obtain the cloud forcing we first consider the outgoing longwave flux (L^*) covered with a cloud fraction (A_c) along with the definition of clear sky longwave flux (L_s) and cloud area flux (L_c):

$$L^* = L_s(1 - A_c) + L_c A_c$$
$$= L_s + C_f(L) \quad (1)$$

where longwave cloud-radiative forcing $C_f(L)$ is given by $A_c(L_c - L_s)$. Differentiating (1) with respect to cloud amount:

$$\frac{\partial L^*}{\partial A_c} = L_c - L_s \quad (2)$$

because L_s and L_c are not functions of cloud amount. Integrating (2) for changes in cloud amount we find $C_f(L)$:

$$C_f(L) = (L_c - L_s) A_c = \int_0^{A_c} \frac{\partial L^*}{\partial A_c} dA_c \quad (3)$$

Equations similar to (1) can be written for the solar term, i.e.:

$$K^* = K_o(1 - \alpha_s) + C_f(K) \quad (4)$$

where:

$$C_f(K) = K_o(\alpha_s - \alpha_c) A_c \quad (5)$$

and K_o is the available solar radiation at the top of the atmosphere; $C_f(K)$ is short-wave cloud-radiation forcing; α_s is the albedo of cloud free sky and α_c is cloud albedo. In the same manner we differentiate (4) with respect to cloudiness A_c:

$$\frac{\partial K^*}{\partial A_c} = -K_o(1 - \alpha_s) + K_o(1 - \alpha_c)$$
$$= K_o(\alpha_s - \alpha_c) \quad (6)$$

From (6), $C_f(K)$ can be written in the form:

$$C_f(K) = K_o(\alpha_s - \alpha_c) A_c$$
$$= \int_0^{A_c} \frac{\partial K^*}{\partial A_c} dA_c \quad (7)$$

The net radiative cloud forcing $C_f(N)$ can be written as:

$$C_f(N) = C_f(K) - C_f(L) \quad (8)$$

It is important to recognize that reliable estimates of cloud-radiation forcing (C_f) are the key to examining the influence of radiative cloud and surface variability on the atmospheric general circulation. For the given outgoing longwave radiation, incoming solar radiation at the top of atmosphere and cloud amount, we can obtain $C_f(L)$, $C_f(K)$ and $C_f(N)$ through the calculations of the partial derivatives of L^* and K^* with respect to A_c. This approach is more dependable than retrieving cloud forcing from radiation budget data with methods requiring minimum albedo which can give improper results over areas exhibiting semi-permanent cloud features such as the ITCZ and the SPCZ. In order to determine the values of the partial derivatives from the RADBUD and cloud data, we first adopt a methodology developed by Cess et al. (1982) in which we define the fluctuations of emitted infrared flux (ΔL_δ) and of reflected solar flux (ΔK_δ) solely due to cloudiness changes (ΔA_c). These terms can be obtained by linear regression, ie:

$$\Delta L_\delta = a + b\,\Delta A_c \quad (9)$$

$$\Delta K_\delta = c + d\,\Delta A_c \quad (10)$$

where we interpret b and d as the partial derivatives of L^* and K^* with respect to A_c. The ratio $\Delta L_\delta / \Delta K_\delta$ is Cess's (1976) climate sensitivity parameter ε.

The removal of cloud forcing from the net solar and infrared terms ($K^*$and L^*) generates residuals which we call the surface plus clear atmosphere forcing which for brevity we call surface forcing (this presumes that most of the atmosphere induced variability aries from variations in PBL moisture which is strongly coupled with surface variations). The distribution of surface induced forcing can then be examined for its role in maintaining the tropical radiation balance.

4. RESULTS AND DISCUSSION

The distribution of the climatic sensitivity parameter ε is presented in Figure 1. At low latitude it generally shows that the greenhouse effect is dominant, which can be associated with the large amount of high cloudiness produced in the tropics. The dominance of the albedo effect is in the subtropical oceans, associated with extensive regions of low cloud amount and corresponding to the locations of subtropical highs. The western Sub-Sahara/Sahel zone, which has experienced extensive drought conditions and fluctuations in seasonal and annual rainfall, is part of a zonal regime which extends to the Amazon basin in which the albedo effect dominates. This zonal regime also contains a feature extending from southern Ethiopia into the western Indian Ocean at equatorial latitudes.

It is interesting to note that highly confined regions of negative ε are located in the cold oceanic areas near the western coasts of the southern hemisphere continents where low, stratocumulus cloud decks are persistent The physical explanation for negative ε is that the change of L^* with respect to the increasing A_c is negative, implying that a cloud amount increase must be correlated with a cloud top height decrease. The partial-global average (65°S to 65°N corresponding to 93% of global area) of $\partial Q^*/\partial Ac$ is -2.5 Wm^{-2}. This supports the finding by Cess (1976) that in a globally averaged sense, the greenhouse and albedo effects of clouds compensate one another.

On the other hand, even though the average global effect of cloud-radiation feedback is small, local imbalances between the greenhouse and albedo terms induce significant changes in the local radiation balance. In order to investigate the significance of local imbalances, the 1982-83 El Niño event was examined as a case in point. During that period significant fluctuations of geophysical parameters occurred (Gill and Rasmusson, 1983). Of particular interest in this study are the contributions of cloud and surface to the outgoing longwave radiation (OLR) and incoming shortwave (SW) radiation. Major anomalies in cloudiness, due mostly to shifts of major convective center in the Pacific Ocean associated with inactive or active ENSO

phase, are most notable over the equatorial central Pacific from the date line to the west coast of Peru, the maritime continent over the western Pacific, the SPCZ and the Indian Ocean. The outstanding feature in OLR and SW radiation anomalies is an east-west coupled dipole structure in which the cancellation between OLR and SW radiation effects within either node of dipole gives rise to somewhat smaller changes in the net radiation anomalies. We believe that cloud variation can be considered a major factor in maintaining the dipole pattern.

To facilitate the examination of cloud impact on the net radiation balance during the El Niño period, the variations of OLR and SW radiation due solely to cloud are presented in Figures 2a-b. The strong negative perturbation (energy gain) of OLR cloud forcing (Figure 2a) over the central Pacific at the equator and the corresponding strong positive perturbation (energy loss) over the maritime continent raise the spatial extent of the dipole structure; the corresponding SW perturbations (Figure 2b) are in the opposite sense energetically. Considering that the tropical area is greenhouse dominant, the interannual fluctuation in the net radiation balance largely depends upon the coupling of the greenhouse mechanism with increased or decreased convective activity.

Surface contributions to the OLR and SW radiation anomalies have been computed using (1) and (4) by removing the cloud component of the forcing from net anomalies. These are presented in Figures 3a-b. The pattern of OLR surface forcing over the equatorial central Pacific is in general agreement with the expected ENSO SST anomaly pattern; the location of the anomaly extreme lies in at approximately 7°N. There is negative OLR surface forcing over the central Pacific during the 1982-83 ENSO period; this is associated with overall infrared energy gain by the sea surface or an effective increase in SST. By the same token the positive OLR perturbations in the western Pacific are consistent with the negative SST anomalies in that region during an active ENSO phase. In other words, the surface contribution to OLR anomalies should negatively correlate with SST anomalies. SW surface forcing over the 1982-83 central Pacific is negative (energy loss) and thus consistent with cloud forcing over that region. However, the SW net anomaly for both cloud and surface does not fully compensate the anomalous infrared gains. Thus combined OLR and SW surface forcing shows net energy gain over the central Pacific during the 1982-83 ENSO. A similar analysis over the western Pacific shows opposite energetic processes in OLR and SW.

For the two positions within dipole [the equatorial western Pacific (5°S-5°N, 130°E-140°E) and the equatorial central Pacific (5°S-5°N, 145°W-155°W)], the retrieved radiative energetics of the cloud and surface forcing can be described in the form of a 'box diagram' (Figure 4). There are uncertainties in the estimates of cloud forcing from the satellite retrieved RADBUD and cloud data, and the analysis procedures. Nevertheless, the diagram is consistent with the expected ENSO SST anomalies as described by Cane(1983). The basic features of the energetics arise from a compensation between the greenhouse and albedo effects of clouds as well as the associated surface forcing in both the infrared and solar spectrums. The compensation process by both cloud and surface serves to minimize the responses to changing environments and to keep the system in near steady state. Thus, in some sense these relationships support Dutton's theory (1973) that the atmosphere serves to minimize entropic energy, which is simply the departure from an atmosphere at rest.

5. ACKNOWLEDGEMENTS

The authors extend their appreciation to Phil Ardanuy, Lee Kyle and Larry Stowe for their assistance in obtaining the radiation budget and cloudiness data. This research has been supported under NASA Grant NAG5-849. A portion of the computational support has been provided by the FSU Supercomputer Computations Research Institute under DOE Contract DE-FCO5-85ER250000.

6. REFERENCES

Cane, M. A., 1983: Oceanographic events during El Niño. Science, **222**, 1189-1195.

Cess, R. D., 1976: Climatic change: An appraisal of atmospheric feedback mechanisms employing zonal climatology. *J. Atmos. Sci.*, **33**, 1831-1843.

____ , B. P. Briegleb and M. S. Lian, 1982: Low latitude cloudiness and climate feedback: Comparative estimates from satellite data. *J. Atmos. Sci.*, **39**, 53-59.

Dutton, J. A., 1973: The global thermodynamics of atmospheric motion. *Tellus*, **25**, 89-110.

Gill, A. E. and E. M. Rasmusson, 1983: The 1982-83 climatic anomaly in the equatorial Pacific. *Nature*, **306**, 229-234.

Jacobowitz, H., R. J. Tighe and The Nimbus 7 ERB Experiment Team, 1984: The earth radiation budget derived from the Nimbus-7 ERB experiment. *J. Geophys. Res.*, **89**, 4997-5010.

Ramanathan, V., 1987: The role of earth radiation budget studies in climate and global circulation research. *J. Geophys. Res.*, **92(D4)**, 4075-4095.

Smith E. A. , and ____ , 1987: Interannual variability of the tropical radiation balance and the role of extended cloud system. *J. Atmos. Sci.*, **44**, 3210-3224.

____ , and B. J. Sohn, 1988: The mechanism for net radiation anomalies over North Africa. To appear in *Current Problems in Atmospheric Radiation*, A. Deepak Pub., Hampton, VA, 4 pp.

Stephens, G. L., G. G. Campbell and T. H. Vonder Haar, 1981: Earth radiation budgets. *J. Geophys. Res.*, **86**, 9739-9760.

Stowe, L. L., C. G. Wellemeyer, T. F. Eck, H. Y. M. Yeh and The Nimbus 7 Cloud Data Processing Team, 1988a: Nimbus 7 global cloud climatology. Part I: Algorithms and validation. *J. Clim.*, **1**, 445-470.

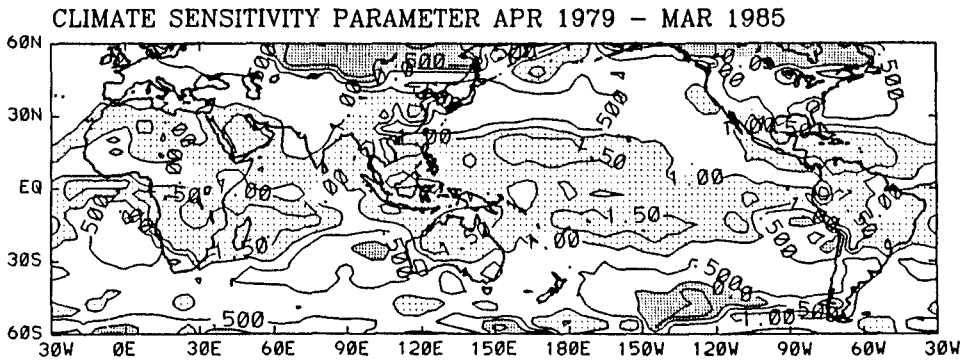

Fig. 1: Global distribution of sensitivity parameter ε for six year period. Areas with values larger than 1 (greenhouse-effect dominant region) are shown as a sparse dot pattern. Areas with values between 0 and 1 (albedo-effect dominant region) are shown as blank. Areas of negative ε are shown as a dense dot pattern.

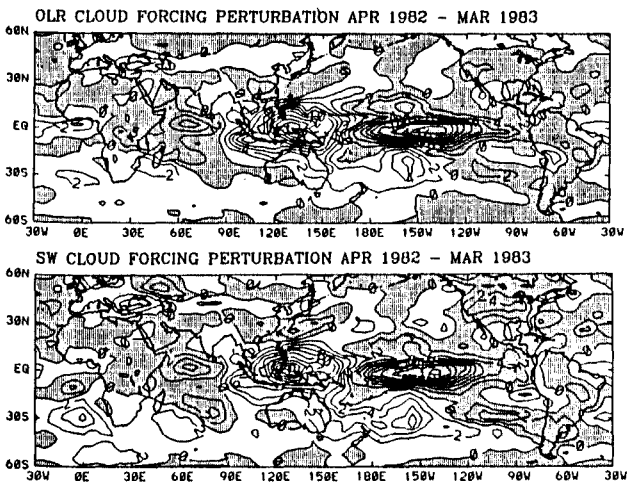

Fig. 2: Cloud forcing perturbation for April 1982 to March 1983 for (a) OLR and (b) SW. Contour interval is 2 Wm^{-2}. Negative perturbations are shaded.

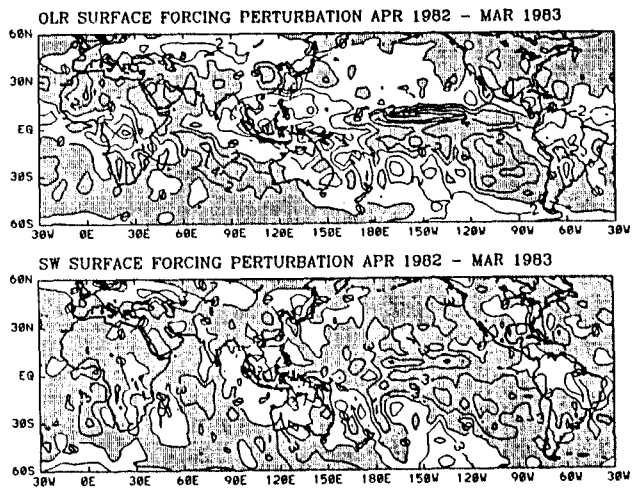

Fig. 3: Same as Fig. 2 for the (a) OLR and (b) SW surface forcing. Contour interval is 2 Wm^{-2} for OLR; 3 Wm^{-2} for SW.

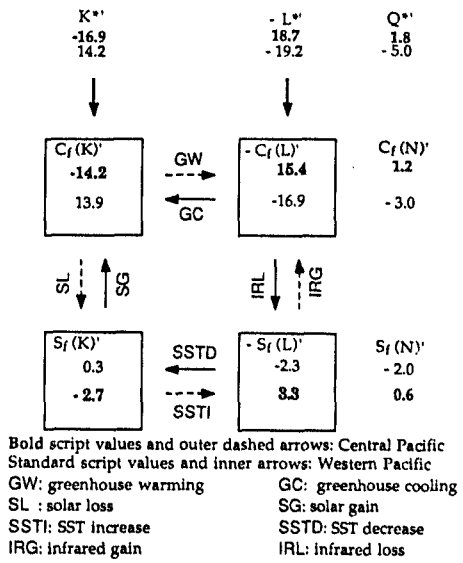

Fig. 4: Radiative energetics (Wm^{-2}) for two regions [Western Pacific (5°S-5°N, 130°E-140°E), Central Pacific (5°S-5°N, 145°W-155°W)] where C denotes cloud; S denotes surface; sub f denotes forcing; prime(') denotes perturbation.

COMPARISONS BETWEEN METEOSAT WATER VAPOUR RADIANCE AND ECMWF ANALYSED FIELDS FOR JULY 1985

Laurence Picon

LMD/CNRS, Palaiseau, France

1. INTRODUCTION

The atmospheric motions over Africa can be represented by cellular motions called Hadley-Walker circulations. The position and intensity of these cells are subject to strong interannual variations. The study of these climatic variations of the circulation is very difficult with conventional data. In the present paper, the interpretation of water-vapour radiances in terms of circulation parameters is examined. For this study, statistical relationships between radiances and some meteorological parameters have been established. Because of the scarcity of upper air data in the Africa-Atlantic area, ECMWF analyses are used.

2. THE WATER VAPOUR (WV) CHANNEL

Meteosat has two long wave radiometers, the IR radiometer is centered in the atmospheric window near 11.5 μm, the WV one is centered in a water vapour band around 6.3 μm. No signal from ground is detectable in a WV image, because it is absorbed in these wavelengths by the very humid low layers. Structures of middle and high troposphere essentially can be studied.

The altitude of the observable phenomena is located between 550 hPa and 300 hPa (Poc et al., 1981).

Many authors have used data from the WV channel of Nimbus-4 to perform case studies of the dynamic of the troposphere (Martin & Salomonson, 1970 ; Steranka, 1973, Rodgers et al., 1976). Ramond et al. (1981) study the dynamic of polar Jet Stream with the WV channel of Meteosat. A theoretical study based on an approximation of the radiative transfer equation is performed and they show that the altitude of weighting function peak is located on an isohumidity surface.

3. THE DATA

The satellite data used here are Meteosat ISCCP images : the spatial resolution is 30 km at subsatellite point (sampling of 1 pixel each 6) and one image is available every 3 hours.

A composite image (Fig. 1) has been computed by averaging the 240 images available between July 1 and 30, 1985. The missing data have been replaced by the ones of the July 31 at the same hour. Comparisons have been made with the 12h initialized analyses for the same time period provided by the ECMWF archives. These analysed have been also averaged over the same period of July 1985.

4. SPATIAL CORRELATION STUDIES

As previously shown (Desbois et al., 1988) the spatial structures of the mean WV images present strong interannual variations. We tried to understand these spatial structures.

4.1 Comparisons of patterns

The phenomena tracked in the WV channel are located in the middle troposphere. For this reason we present the relative humidity patterns at 500 hPa (Fig. 2). The relative humidity is the parameter which compares the best to radiances because, as the WV radiances, it takes into account the temperature and water vapour content. The spatial structure observed is very close to the radiance patterns. Over the Eastern Mediterranean a strong radiance maximum corresponds to an humidity minimum. Along the Canary Islands a weaker radiance maximum is associated with a less pronounced humidity minimum. A large strong radiances area related with a weak relative humidity is located at 20°S over Atlantic Ocean and African continent. This area is divided into two parts by weaker radiances identified from images animations as cirrus motions characterizing a NW-SW frontal zone. The same division occurs on the humidity patterns. The ITCZ weak radiances area is associated with a strong humidity.

Comparing water vapour radiances to vertical motions (Fig. 3), we can see that the strong positive vertical velocity over the Eastern Mediterranean is slightly shifted eastward relaive to the maximum of WV radiances. Over North Atlantic, subsidence is located over the reinforcement of the trade winds. This region corresponds also to a maximum of WV radiances. In the Southern Hemisphere, the situation is more complicated. Subsidence over the western part of South Atlantic corresponds with a WV radiance maximum. But the maximum of subsidence at 500 hPa over South Africa is shifted south-eastward relative to the radiance maximum.

The divergence is a very sensible parameter. We have computed divergence with the finite differences method without filtering, producing noisy results. But the strong radiance areas are almost always associated with convergence in altitude. Large divergence areas are present in the ITCZ. These areas correspond generally to very convective zones. From previous African convection studies, performed with satellite data (Desbois et al., 1988), divergence and vertical velocity maximum are correctly located eastward of Chad Lake. But the strong divergence along the Guinea Gulf is never observed in the satellite studies.

4.2 Results of quantitative comparisons

A regional study has been performed. Four regions are chosen : three are associated to strong radiances in subtropical regions, the fourth one is located in the ITCZ. The vertical repartition of spatial correlations between WV radiances fields and analysed fields are computed. The analysed parameters are the temperature, the relative humidity, the vertical velocity, the divergence and the geopotential. The level where the correlation is the strongest indicates the best fit level of two fields. For this kind of comparisons, temporal averages are more adapted. The study of instanteneous fields correlation is non convincing.

The mean relative humidity presents the best correlation with the mean WV radiances. But the levels of the maximum correlation is different from the levels which have been established by the previous case studies. These differences can be explained by an effect of temporal averaging or by the fact that the correlation has been computed at fixed levels.

The mean dynamic fields show that the strong WV radiance areas are almost always subsidence zone in the middle troposphere, divergence zone near the surface and convergence zone at top of the atmosphere.

But the results present a strong regional variability. Over maritime anticyclones the temperature and pressure effect is dominating while over the Eastern Mediterranean the humidity and vertical velocity effect are more important. The drying of the atmosphere and the subsidence in this region are more local phenomena related to a thermal surface effect. In the ITCZ relations between analysed fields and radiance field are not so clear. A shift between the convection areas identified by the WV radiances and by the analyses is observed.

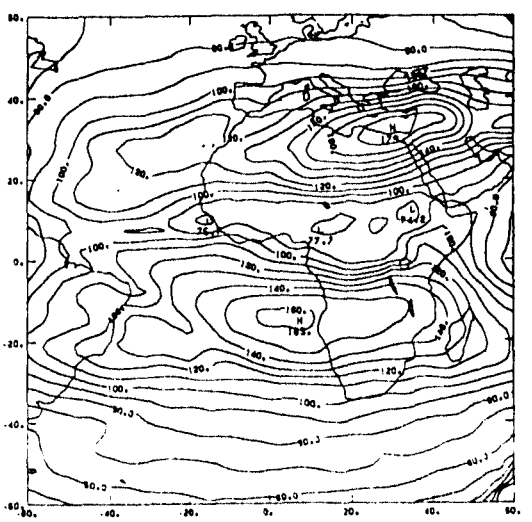

Fig. 1 Mean Meteosat WV radiance field, July 85.

Fig. 2 Mean relative humidity at 500 hPa from ECMWF analyses, July 1985.

Fig. 3 Mean vertical velocities at 500 hPa from ECMWF analyses, July 1985.

References :

Desbois M., T. Kayiranga, B. Gnamien, S. Guessous, L. Picon, 1988 : Characterization of some elements of the sahelian climate and their inter-annual variations for July 1983, 1984 and 1985 from the analysis of Meteosat ISCCP data. *J. of Climate* 1, 867-904.

Martin F.L., V.V. Salomonson, 1970 : Statistical characteristics of subtropical jet-stream features in terms of MRIR observations from Nimbus-II. *J. Appl. Meteor.* 9, 508-520.

Poc M.M., M. Roulleau, N.A. Scott, A. Chedin, 1981: Quantitative studies of Meteosat water vapor channel data. *J. Appl. Meteor.* 19, 868-876.

Ramond D., H. Corbin, M. Desbois, G. Szejwach, P. Waldteufel, 1981 : The dynamics of polar jet streams as depicted by the Meteosat WV channel radiance field. *Mon. Wea. Rev.* 109, 2164-2176.

Rodgers E.B., V.V. Salomonson, H. Lee Kyle, 1976 : Upper tropospheric dynamics as reflected in Nimbus-4 THIR 6.7 µm data. *J. Geophys. Res.* 81, 5749-5758.

Steranka J., L.J. Allison, V.V. Salomonson, 1973: Application of Nimbus-4 THIR 6.7 µm observations to regional and global moisture and wind field analyses. *J. Appl. Meteor.*, 12, 386-395.

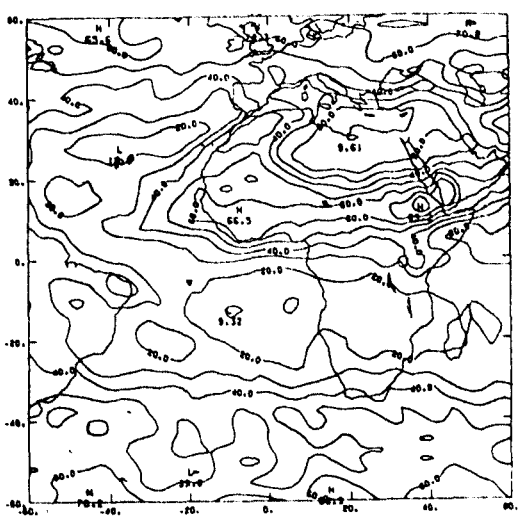

2

1

3

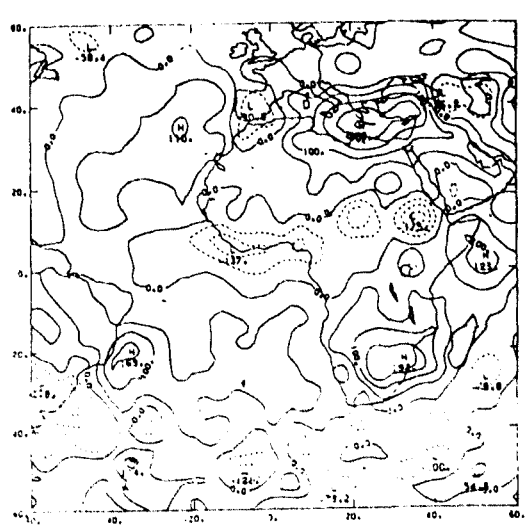

13.1

ATMOSPHERIC TEMPERATURE RETRIEVAL FROM SATELLITE MICROWAVE MEASUREMENTS

Martha E. Maiden, Michelle V. Piepgrass,
David R. Donahue and Mojgan Sylva

S M Systems and Research Corporation
Landover, Maryland

Henry F. Drahos, Jr.

National Environmental Satellite,
Data and Information Service
Suitland, Maryland

1. INTRODUCTION

Polar-orbiting, spacecraft-borne microwave temperature sounders sensing in the 50-60 GHz oxygen band have now operated for almost seventeen years. The primary advantage of using microwaves is that the atmospheric profiles can be obtained even under cloudy conditions. In the Defense Meteorological Satellite Program (DMSP), the U.S. Air Force launched the Special Sensor Microwave Temperature sounder (SSM/T) in June 1979. This was the first exclusively microwave sounder intended for operational use. The SSM/T has more channels than any microwave sounder launched previously, and provides both tropospheric and stratospheric soundings.

The two current SSM/T instruments were launched in June 1987 and February 1988. As with the previous instruments, both the hardware and software were developed by Aerojet ElectroSystems Company for use by Air Force Global Weather Central (AFGWC).

Due to a Shared Processing agreement between the Air Force, the Navy and NOAA, an extensive data processing and evaluation program was begun at the National Environmental Satellite, Data and Information Service (NESDIS) of NOAA in 1983. Under this agreement, NESDIS has the responsibility for producing and archiving the atmospheric temperature soundings from the SSM/T data.

1.1 Shared Processing Link

The Shared Processing Link is planned to make virtual temperature products available to FNOC, AFGWC, and NAVO in Bay St. Louis, Louisiana. At present a product formatter on the NMC/NESDIS main frame computer prepares a data file to be sent by the Shared Processing Link, and also to be the product archive, in the form of mean layer virtual temperatures. A program to change the share database to a CIDE (Committee on Interface Data Exchange) format transmission control file was successfully tested at NESDIS in September 1988. This format is planned to be sent by communications over the SATCOM link when it becomes operational in the fall of 1989.

1.2 Instrument Description

The SSM/T is a seven channel microwave sounder (Aerojet, 1977; Rigone and Stogryn, 1977), designed to provide global, synoptic scale soundings of temperature throughout the troposphere and lower stratosphere. All channels are within the 50-60 GHz oxygen band. A single cross-track reflecting antenna is used to direct the upwelling atmospheric radiation through a fixed circular horn which is coupled to the Dicke radiometers. The incoming broad band signal is first split into two bands having orthogonal polarization, and then filtered into seven discrete channels. The weighting functions of the SSM/T channels are shown in Figure 1 (for surface emissivity of one).

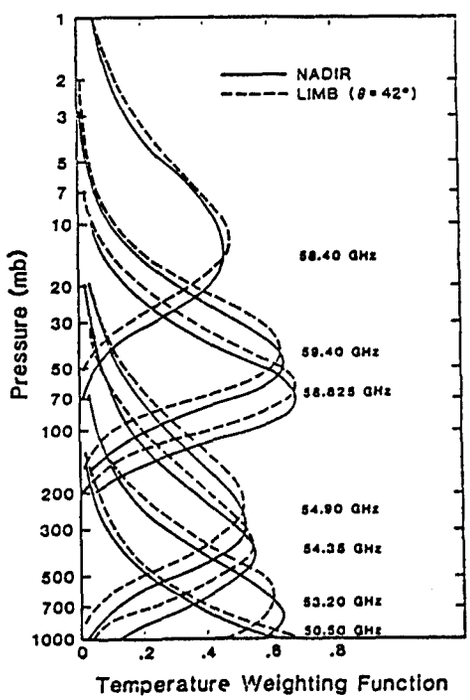

Fig. 1. Weighting functions calculated for the nadir and scan limit positions for a unity emissivity surface (Grody, et al, 1985).

The spatial resolution and scan coverage are defined by the antenna reflector, which is rotated perpendicular to the satellite flight path. A reflector dimension of about four cm produces an antenna beamwidth (3dB half power) of 12 degrees for all channels. This results in a footprint (half power on Earth) of 175 km at nadir for the Block 5D nominal orbiting altitude of 833 km. The reflector is rotated in seven equal angular increments of 12 degrees to scan the Earth. The resulting scan line has a swath width of 1595 km. Note that as the beam position scans from nadir, the footprint becomes elliptical, increasing to 304 x 228 km for the largest scan angle. Dwell time for each of the positions is 2.7 seconds. The total scan period is 32 seconds.

1.3 NESDIS Operational Environment

The processing of DMSP SSM/T data involves the performance of steps at several facilities, in the following sequence: The two operational spacecraft transmit recorded orbital data (readouts) to several receiving stations on the ground. These data are then transmitted to Offutt Air Force Base where the ephemeris data is appended, and the SSM/T data are processed into the MTPREP format. The readout is then transmitted to NESDIS via SATCOM link, at which time NESDIS begins processing.

The Ingest Processing Division receives the SSM/T data in MTPREP format and reformats and sorts the data into a NESDIS Level 1A data set (internal use only). Level 1A data sets are next converted to Level 1B data sets (archived). This processing step includes computation of calibration parameters for each scan and channel, and the appending of both earth location information and a complete time for each field of view. The ingest processing is done on an IBM 4381 series computer, using the MVS processing system. As each 1B data set is created, it is loaded onto the oldest of 14 data sets on 3380 disk packs connected to the NMC/NESDIS NAS 9000 series computer.

The DMSP product processing is performed entirely on the NAS 9000 series computer, using the MVS processing system. Permanent disk data sets are used to store necessary DMSP data and software. The operational libraries occupy 1850 tracks, or 88 Mbytes. The close to 100 permanent data files occupy about 6100 tracks, or 290 Mbytes, for a three spacecraft system. In addition to DMSP permanent disk data sets, the DMSP operational processing accesses TOVS and NMC data sets. Magnetic tapes are used only for backing up the software library, the critical operational data sets and the retrieval/radiosonde match data.

Two product formatters prepare data files for dissemination to users. One is the EDS format, which is picked up by NMC and sent on to the European Center for Medium Range Weather Forecasting (ECMWF). The other is the GTS format, which now is utilized by the Navy via the Carswell link. A third formatter produces the Shared Processing format (see Section 1.1), now archived for both current satellites.

2. RETRIEVAL OF SOUNDINGS

DMSP SSM/T operational processing is performed routinely at NESDIS, centering around the retrieval of global atmospheric temperature profiles. Each profile, or predictand, is composed of 30 temperatures at pressure levels between 1000 and 10 mb, 14 geopotential thicknesses at atmospheric layers also between 1000 and 10 mb, 15 water vapor mixing ratios at pressure levels between 1000 and 300 mb, and tropopause temperature and pressure. Each predictor consists of satellite measurements made by the SSM/T instrument at 6 frequency bands in the microwave region. These are corrected for surface and terrain elevation effects using a seventh, or window channel. Over sea, the SSM/T predictor is augmented by a seventh element, when available, between 50N and 50S: an independently measured sea surface temperature obtained from NMC.

The operational processing system is composed of four major components: orbital data preprocessing, retrieving, and product formatting; radiosonde match processing, regression coefficient updating, and DMSP processing system monitoring.

The synthetic regression Alpha, Beta Retrieval Method, originally implemented by Aerojet, has been replaced with a simple multiple linear regression retrieval scheme at NESDIS. The regression covariance matrices are updated weekly, using matched radiosonde and measured SSM/T brightness temperature data collected during the previous two weeks. The latitudinal breakdown for computing these coefficients is into twelve bands, each consisting of 15 degrees with an additional 7 1/2 degree overlap at each boundary to smooth boundary discontinuities. In addition, the surface and terrain height correction coefficients are updated weekly in order to maintain the internal consistency of all coefficients. NESDIS uses terrain information in a one-eighth mesh polar stereographic grid supplied by the Air Force.

3. EXPECTED IMPROVEMENTS

3.1 Employment of SSM/I Data

Soon NESDIS expects to have available SSM/I data in a mapped format. Plans are underway to convolute the image data to SSM/T footprints, and to test algorithms now under development for both precipitation and cloud liquid water identification and screening, and for surface correction. NESDIS hopes to employ SSM/I data to better remove surface emission effects from the lower sounding channel data. SSM/I data could also be useful in the definition of terrain type, such as the location of changing sea/ice boundaries. In the event that the evaluation of these algorithms show improvement, they will be implemented into the primary SSM/T retrieval path. The SSM/T-Only retrieval method will be used when the SSM/I instrument is not available.

3.2 Precipitation Filter

In order to supply SSM/T users with high quality DMSP sounding data over non-precipitating cloudy ocean areas, NESDIS has recently implemented (February, 1989) a precipitation algorithm to remove partially precipitating as well as heavily precipitating footprints. Since it is cloud liquid water which ultimately interrupts the path of microwave radiation, NESDIS has implemented an approach suggested by N. Grody (Grody, 1979) for the MSU. In this method, a simple regression equation with weighted brightness temperatures provides an estimate of cloud liquid water.

$$Q(\text{liquid water}) = C_0 + C_1 * TB_1 + C_2 * TB_2$$

C_0, C_1, and C_2 were previously determined by N. Grody for MSU and for SSM/T for each view angle. This procedure has dramatically improved the filtering of precipitation-contaminated retrievals in the tropics. The Q method is also planned for use in the NOAA KLM system. It is possible that use of the SSM/I may provide even more accurate screening (See Section 3.1). After limb correction is in place (see Section 3.3), a median filter can also be investigated.

3.3 Limb Correction

Retrieval products based on the present regression method suffer if a robust sample of retrieval/radiosonde matches cannot be obtained to regularly update regression coefficients. In certain radiosonde-poor areas, such as the extreme southern hemisphere and high in the atmosphere, this situation is encountered frequently. NESDIS has been attempting for several years to normalize the measurements

of the three non-nadir viewing angles to nadir, so that all seven beam positions can be combined, thus increasing the bin populations. A new method by D. Q. Wark (Wark, 1988) is now being tested, and is very promising. Preliminary evaluation results show virtually no degradation in the final retrieved product using this method. Once in place, a continued availability of increased sample size should improve the product. If, after completion of further evaluation, results remain favorable, this procedure will certainly be implemented at NESDIS.

3.4 Physical Retrieval

Regression is a very conservative method of retrieval production. In areas of high meteorological activity, valuable features may be mitigated or lost by being pulled toward a mean profile. A physical retrieval method has been implemented for the NOAA TOVS series, and a microwave method is now being developed (Fleming, 1987) as well, which may be implemented for the DMSP satellite series. The smoother character of the microwave data should lend itself well to such a method. Surface corrections and physical retrieval may be computed simultaneously for microwave instruments.

4. EVALUATION OF PRODUCTS

For evaluating DMSP retrievals, the capability exists to reprocess archive data which have been collocated with radiosondes using either alternative regression coefficients or a new procedure for processing the data. Retrieval values are then produced either from brightness temperatures computed from raw counts or the existing brightness temperatures in the so-called Match Archive. These subsequent "NEW" retrievals are compared with the on-line or "OLD" retrieval values in the Match Archive using numerous statistical output tables. In addition, the capability exists (called The 3-Way Match System) for evaluating retrievals against TOVS retrievals. The existing DMSP retrieval parameters are replaced by matched TOVS retrieval values and the DMSP retrieval is recomputed at the time of evaluation.

As retrievals are computed in the evaluation module, sums, averages, standard deviations, and root mean square statistics are compiled and collected in 30 and 15 degree latitude zone bins for the lowest 30 temperature levels, 14 thicknesses, tropopause temperature and thickness, and 15 mixing ratios. Statistics for NEW and/or OLD retrieval minus radiosonde differences can then be written to a holding file from which plots are made.

4.1 Performance in the Tropics

For most levels, the DMSP average retrieved temperature is generally within a degree Kelvin of the average radiosonde temperature and often less than 0.5 K (see Figure 2). The exceptions are near the surface, where emissivity effects are great and ground observations are extremely accurate, and at upper levels (above 100 mb) where the number of radiosonde observations are small. The RMS for temperature is generally around 2.0 K at mid levels and 3.0 K at the surface (see also Figure 2).

In comparison against TOVS, DMSP generally performs about equally well. At higher levels, particularly stratospheric, TOVS has the advantage of multiple HIRS channels. DMSP is, however, superior to TOVS for retrieving near the surface in cloudy regions, since TOVS uses MSU only, a four-channel instrument, in these situations (see Figure 3).

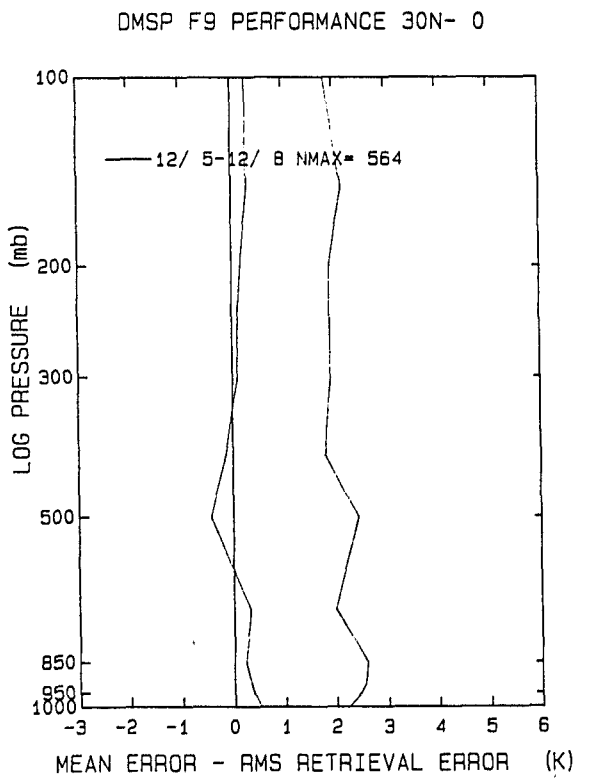

Fig. 2. DMSP F9 performance 30N-0, for the period of December 5-8, 1988.

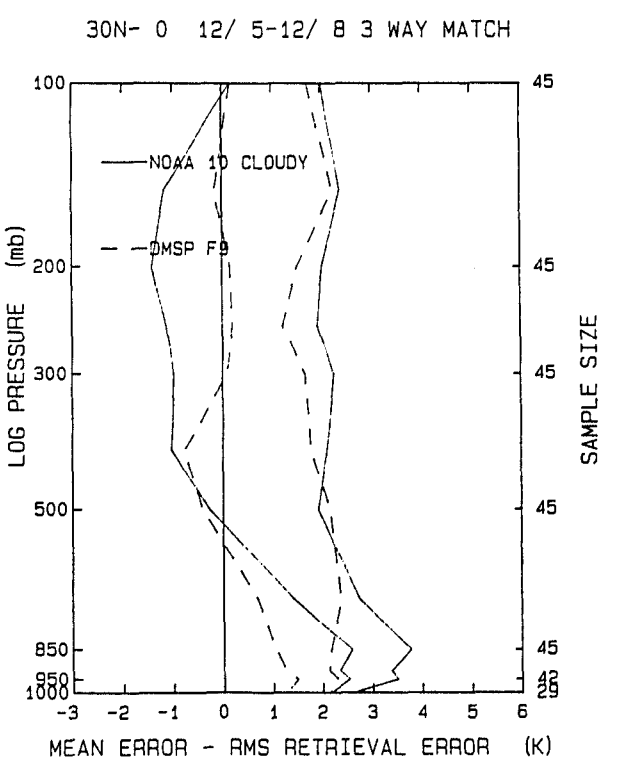

Fig. 3. 30N-0 12/5-12/8 3 Way Match, between the DMSP F9 and NOAA 10 cloudy-only retrievals.

5. SUMMARY

This paper summarizes the current state and near future plans of SSM/T product processing at NESDIS. Sample evaluative results in tropical latitudes are also presented.

6. REFERENCES

Aerojet ElectroSystems Company, 1977: System Summary Report on Passive Microwave Sounder (SSM/T), Report No. 5542 for the U.S.A.F. Space and Missile Systems Organization.

Fleming, H. E., 1987: A Physical Retrieval Algorithm for Obtaining Microwave Soundings, Conference on Passive Microwave Observing from Environmental Satellites, Williamsburg, VA.

Grody, N. C., 1979: Liquid Water Determination Over The Oceans from MSU Measurements, NOAA Internal Memorandum.

Grody, N. C., D. Gray, C. Novak, J. Prasad, M. Piepgrass, and C. Dean, 1985: "Temperature Soundings from the DMSP Microwave Sounder", Advances in Remote Sensing Retrieval Methods, pp. 249-264.

Grody, N. C., 1988: "Surface Identification Using Satellite Microwave Radiometers", IEEE Transactions on Geoscience and Remote Sensing, Vol. 26, No. 6.

Rigone, J. L., and A. Stogryn, 1977: Data Processing for the DMSP Microwave System, Proc. Eleventh International Symposium on Remote Sensing of the Environment, pp.1599-1608.

Wark, D. Q., 1988: Adjustment of Microwave Spectral Radiances of the Earth to a Fixed Angle of Propagation, NOAA Technical Report NESDIS 43.

HIGH RESOLUTION DEPICTION OF SST AND SSC FROM MAMS DATA

Christopher C. Moeller
Liam E. Gumley
Kathleen I. Strabala

Cooperative Institute for Meteorological Satellite Studies
University of Wisconsin
1225 West Dayton Street
Madison, Wisconsin 53706

W. Paul Menzel

NOAA/NESDIS Advanced Satellite Products Project
1225 West Dayton Street
Madison, Wisconsin 53706

1. INTRODUCTION

Monitoring the coastal environment is of great importance to the maintenance of the delicate balance that exists where water meets land. Coastal processes displace and deposit tons of material each year, with important implications on the physical and biological systems of these areas. The Gulf coast of Louisiana is a particularly dynamic area of coastal change. The presence of the Mississippi River Delta and the new Atchafalaya River Delta serve as sources of sediment rich fresh water. Roberts et al. (1987) have summarized various responses of portions of the Louisiana coastline depending on how this sediment is distributed. A need to monitor these responses is indicated.

Close monitoring of coastal (or ocean) environments is greatly enhanced through the use of high resolution remote sensing data. Instruments such as Landsat, Coastal Zone Color Scanner, and the Airborne Thematic Mapper have been used to obtain high resolution estimates of suspended sediment concentration (SSC), chlorophyll, and salinity in coastal environments (see, for example, Rimmer et al., 1987; Holligan et al., 1983; Khorram, 1982). The Multispectral Atmospheric Mapping Sensor (MAMS) is also well suited for water quality measurements. The aircraft mounted instrument carries eight visible/near infrared and three infrared channels, which sense upwelling radiance at 100m resolution. The visible/near infrared data can be used to determine estimates of SSC. Additionally, the MAMS infrared channels with their split window combination can be used to determine high resolution estimates of sea surface temperature (SST). High resolution SSC and SST estimates may be useful in determining water origin and identifying flows as well as inferring information about sea depth.

This paper presents MAMS high resolution estimates of SSC and SST and interprets these estimates to identify physical features and mechanisms of the coastal waters of Louisiana. MAMS data from a 27 January 1988 daytime flight along the Louisiana coastline is used in this study.

2. MAMS INSTRUMENT CHARACTERISTICS

The MAMS instrument is a 12 channel scanner which flies onboard high altitude aircraft at about 20 km. The MAMS scans across a total path width of about 36 km at 100m resolution.

The MAMS spectral bands are summarized in Table 1. Channels 1-8 are similar to those of the Airborne Thematic Mapper. Of the four infrared channels, two are used as redundant channels. The infrared data is collectable at 10 bit precision.

Table 1. - MAMS spectral channels

channel	bandwidth (@ 50% response)
1[a]	0.42 - 0.45
2	0.45 - 0.52
3	0.52 - 0.60
4	0.57 - 0.67
5	0.60 - 0.73
6	0.65 - 0.83
7	0.72 - 0.99
8	0.83 - 1.05
9	3.47 - 3.86
10	3.47 - 3.86
11	10.55 - 12.24
12	12.32 - 12.71

a) not available when 10 bit infrared data are collected

MAMS infrared data is calibrated by viewing two blackbodies of known temperature with the assumption that the detector response is linear with respect to radiance. The blackbodies are viewed on each scan. Visible calibration is accomplished in the laboratory with the use of an integrating sphere at periodic intervals throughout the year, often just prior to instrument deployments. Detailed information is available on the MAMS in Jedlovec et al. (1989), and Menzel et al. (1986).

3. DATA ALGORITHMS

3.1 SST

The MAMS 11μm and 12μm channels are used in a split window algorithm of the form:

$$SST = T11 + a(T11 - T12) + b$$

where T11 and T12 are the 11μm and 12μm brightness temperatures, a is a coefficient determined through regression, and b is a bias correction. This form of an SST algorithm has been used extensively with VAS data by Bates et al. (1987) and with NOAA AVHRR data by McClain et al. (1985), and has shown high correlation to NOAA fixed buoys.

The coefficients a and b can be determined by regressing in-situ ship and buoy SST against collocated T11 and T12 data. However, because of a lack of collocated in-situ points along the Louisiana coastline on 27 January, a value of a=1.4846 from a VAS SST algorithm was used here. This is acceptable because of the similarity of the VAS and MAMS 11μm and 12μm channels (see Jedlovec et al., 1988). The value of b could not be reliably determined using 27 January data, however a small number of ground truth SSTs were collected on 22 January. These were used as guidance for the value of b. In order to improve the application of the VAS coefficient, a radiance bias between the VAS and MAMS 11μm and 12μm channels was also applied. These were generated by collocating 74 VAS footprints (8 km resolution) over the MAMS data of 27 January; spectral and viewing angle differences were taken into account. The bias for each channel was applied to the MAMS data as a correction before the SST algorithm was applied.

3.2 SSC

The MAMS visible data are used to calculate an image that is closely related to the SSC. In order to accomplish this, the radiance signal scattered upward out of the water must be separated from an atmospheric solar scattering contribution and a direct ocean surface reflected contribution.

The atmospheric contribution, or path radiance, is due to scattering of photons into the sensor field of view by air molecules (Rayleigh scattering) and aerosols (Mie scattering). Radiance is also reflected into the sensor from the ocean surface (sun glint). Procedures for correction of these effects have been established for NIMBUS-7 Coastal Zone Color Scanner imagery (Gordon et al., 1983; Viollier et al., 1980). For this study, we have considered only the Rayleigh scattering component of the path radiance, and the sun glint radiance. Procedures for evaluating the aerosol scattered component are currently under development.

The total signal, L_t, received by the sensor at a particular wavelength is given by

$$L_t = L_r + L_a + L_g + t*L_w$$

where L_r : Rayleigh scattered path radiance
L_a : aerosol scattered radiance (presently neglected)
L_g : sun glint radiance
L_w : water leaving radiance
t : diffuse transmittance from sea to sensor

The Rayleigh path radiance L_r is given by (Gordon et al., 1983).

$$L_r = \{F_0 T_{o3}(\Theta_0,\Theta) t_r(\downarrow) P_r(\Theta_+)[r(\Theta_0) + r(\Theta)]\} / 4\pi\cos(\Theta) + \{F_0 T_{o3}(\Theta_0,\Theta) t_r(\uparrow) P_r(\Theta_-)\} / 4\pi\cos(\Theta)$$

where F_0 : Solar spectral irradiance incident at top of atmosphere
T_{o3} : Ozone transmittance $= \exp[-t_{o3}(1/\cos(\Theta) + 1/\cos(\Theta_0))]$
t_{o3} : Ozone optical depth
Θ_0 : Solar zenith angle
Θ : Sensor zenith (scan) angle
$t_r(\downarrow)$: Rayleigh optical depth for space to sea surface
$t_r(\uparrow)$: Rayleigh optical depth for sea surface to sensor
$P_r(\Theta)$: Rayleigh scattering phase function $= 0.7629[1 + 0.9324\cos(\Theta)]$
$\cos(\Theta_-) = -\cos(\Theta)\cos(\Theta_0) - \sin(\Theta)\sin(\Theta_0)\cos(\phi - \phi_0)$
$\cos(\Theta_+) = \cos\Theta_- + 2\cos\Theta\cos\Theta_0$
ϕ_0 : solar azimuth angle (east of north)
ϕ : sensor azimuth angle (defined as the azimuth of a vector from the point on the sea surface being examined to the sensor; east of north)
$r(\Theta)$: Fresnel reflectance of ocean surface at angle Θ (refractive index of sea water = 1.341)

The term containing Θ_- describes the path radiance due to photons which are scattered by the atmosphere into the sensor without interacting with the ocean surface. The term containing Θ_+ describes the path radiance due to photons which are scattered by the atmosphere towards the ocean surface, and then specularly reflect from the surface into the sensor, as well as photons which are specularly reflected from the surface, and then scattered by the atmosphere into the sensor. The ocean surface is assumed to be flat for this reflectance calculation. The sun glint radiance L_g is given by (Viollier et al., 1980).

$$L_g = F_0 T_{o3} T_r r(\Theta) p(\Theta)$$

where T_r : Molecular (and aerosol if known) transmittance $= \exp\{-[t_r(\downarrow)/\cos(\Theta_0) + t_r(\uparrow)/\cos(\Theta)]\}$
Θ : Sun glint reflection angle
$p(\Theta)$: Probability function for direct reflection of sun radiance at angle Θ depending on wind speed at the ocean surface (Cox and Munk, 1954).

The sun glint term takes into account the effect of surface wind causing capillary waves on the ocean which tend to reflect solar radiance in directions other than the specular direction. The water leaving radiance can thus be calculated by

$$L_w = (L_t - L_r - L_g)/t$$

where $t = \exp[-(t_r/2 + t_{o3})/\cos(\Theta)]*T_a$
T_a = aerosol transmittance (assumed to be 1.0 here)

Estimation of SSC requires regression of in-situ measured SSC's against collocated water leaving radiances. Previous studies (Collins and Pattiaratchi, 1984) have shown that a useful model is a linear multiple regression of the form

$$\log_e(SSC) = C_0 + C_1R_1 + C_2R_2 + C_3R_3$$

where C_i are regression coefficients and R_i represents water leaving radiances in visible channels. In practise, the C values are determined from the in-situ SSC data. However, no in-situ data were available for the 27 January flight. As a result, the three MAMS visible channels centered at 0.48μm, 0.56μm, and 0.62μm are given equal weight in this model. Regression using in-situ data may alter the scale of the SSC values obtained, but the spatial features in the imagery will not be significantly changed. The model used coefficients $C_0 = 0.3$, $C_1 = C_2 = C_3 = 0.2$. This produced unscaled SSC indicator values in the range 0.0-10.0; these may be related to in-situ measurements of SSC in the Atchafalaya Bay region which have been shown to range from about 50 mg/liter up to about 600 mg/liter (Egleme, 1985).

4. EVALUATION OF CAPABILITY AND INTER-COMPARISONS

On 27 January 1988, the MAMS instrument was flown along the Louisiana coastline. Figure 1 shows a portion of the flight and identifies locations along the route. The MAMS collected 10 bit data for channels 9-12. Clear skies with light northeasterly winds (~5 knots) prevailed along the entire coastline yielding excellent data collection conditions between 1400 and 1700 GMT. The flight came in the wake of a strong cold air outbreak on the morning of 25 January 1988. Although northerly winds had diminished, the coastline was still under the influence of cold high pressure which followed the cold front.

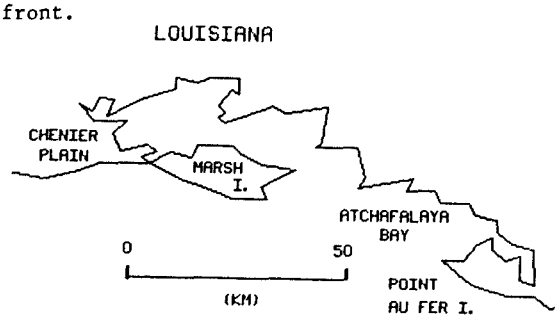

Fig. 1. Atchafalaya Bay region of Louisiana coastline.

In processing the MAMS data, corrections were applied to the infrared calibration when it deviated significantly from time averaged means (spike noise). The navigation was also checked against observable landmarks and corrected for biases, which produced accuracy to within about .5 km rms (Jedlovec et al., 1989).

Single sample noise was calculated for channels 11 and 12. Noise values in channels 11 and 12 were 0.10K and 0.13K, respectively. By applying these noise values to the SST algorithm the accuracy of the SST calculation was estimated to be on average about .25k. This SST error value is well within the error given by Bates et al. (1987) for various VAS algorithms. It is noted, however, that Bates' error estimates were for comparisons to actual SST and therefore may include significant ground truth measurement error.

As a further check on the MAMS infrared data, a comparison was performed between the MAMS 11μm data and collocated NOAA 10 AVHRR 11μm data (1 km resolution) for 27 January. In total 95 collocations were found. Corrections were made for spectral differences and viewing angle differences via a simulated radiance calculation. Results showed that the MAMS 11μm data was highly correlated (r=.91) with the AVHRR 11μm data. In a similar comparison with VAS (74 collocations), the correlation was significantly less (r=.55), probably owing to the large difference in resolution between the instruments. Near coastlines even a single pixel offset in the VAS navigation can make a large difference in the observed 11μm brightness temperature.

Images of SST and SSC were processed for the MAMS flight tracks of 27 January. The SST and SSC images for a flight track over the Atchafalaya Bay are shown together in Fig. 2. In both images, dark shades represent lowest values. Simulated radiance calculations indicated that no limb correction would be necessary for the 11μm and 12μm data. Sun glint was also found to be zero for the visible data.

Figure 2 shows a high degree of variability in both the SSC and SST products. SST variability is about 10K with each grey shade representing .25K of variability. Through the use of the sparse ground truth available from 22 January 1988 and that given by Egleme (1985), the SSC grey shades can be assigned a variability of about 50 mg/l for each grey shade in the image.

The SSC image indicates that high SSC water exists in the bay with significantly lower SSC values outside of the bay. High SSC water flows from the mouth of the Atchafalaya River and fans out into the bay. The low SSC water represents water originating from the gulf. As the high SSC water streams outward it is affected by prevailing currents. Roberts et al. (1987) have reported that this sediment can travel westward along the coast and be deposited as fluid mud on the face of the Chenier Plain. Evidence of this type of flow is present in the SSC depiction with an apparent wide band of relatively high SSC water flowing westward out of the bay past Marsh Island. Streamers of SSC within the bay are possibly tracers of flows within the bay. However no ground truth data was collected to verify these flows.

The contrast in SST from within the bay to gulf waters also acts as an indicator of the water origin, especially when coupled with the contrast in SSC values. It is expected that the bay waters would be cooler for two reasons. First, the river water flowing into the bay with its continental origin is cooler than the gulf water in the winter. Second, from simple heat

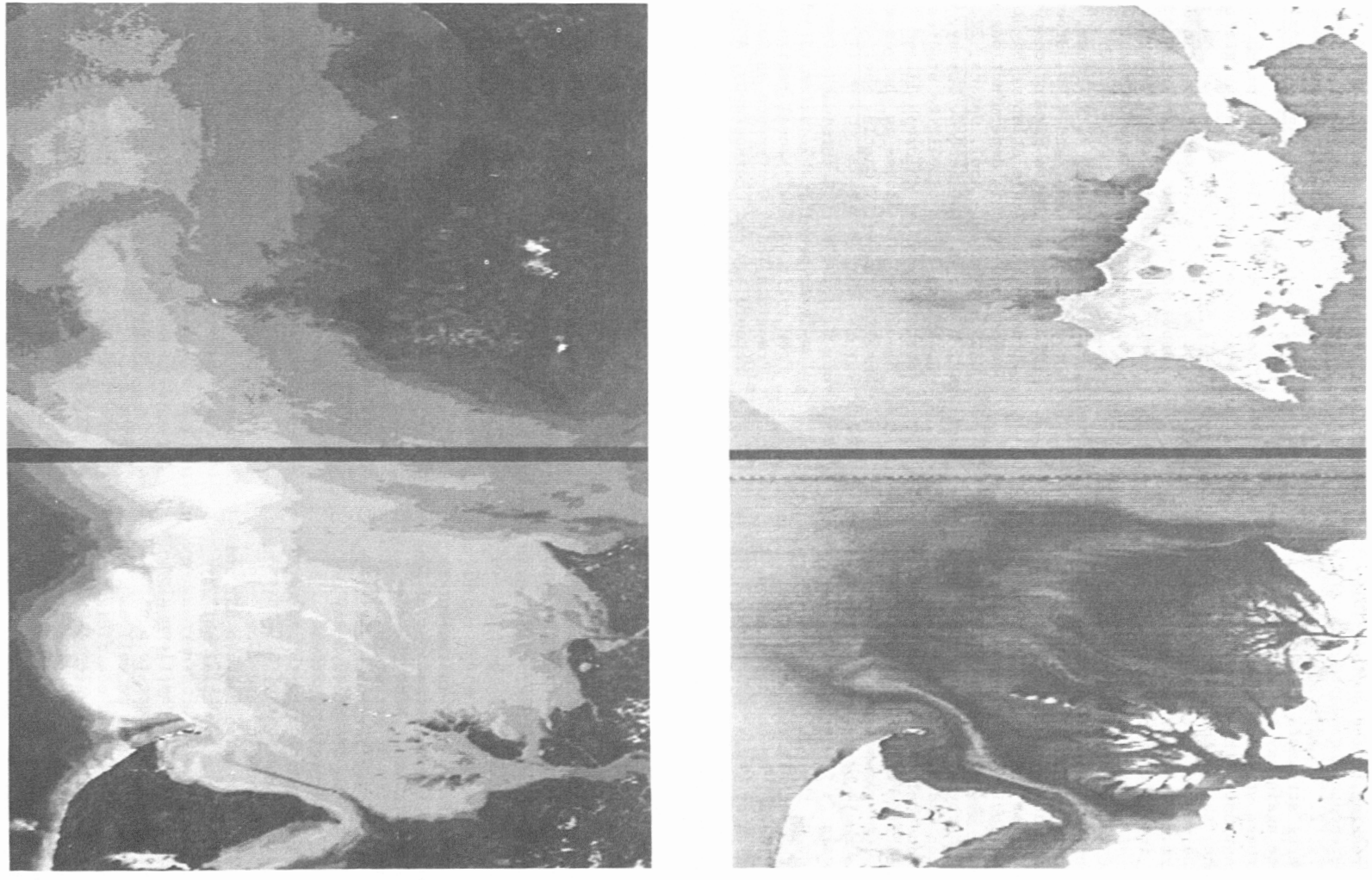

a b

Feb. 2. Images of MAMS 100 resolution (a) unscaled SSC, (b) SST in Atchafalaya Bay region. Each SST gray shade represents .25k. Each SSC gray shade is estimated to represent 50 mg/l. North is towards top of page. Images are compressed by factor of 2 in east-west direction. Black line is missing data.

capacity considerations, the shallowest waters would be cooled the most when cold air outbreaks occur. Bathymetry charts show the shallowest waters of the region to be in the Atchafalaya Bay with depth increasing to the south. This agrees with an inference of sea depth from the SST depiction of Fig. 2. In addition, as in the SSC depiction, several streamers are apparent in the bay. These once again may be indicators of flow. Several of these streamers show significant temperature contrast with surrounding water. For instance, the SW/NE oriented streamer just to the west of Point Au Fer Island shows a decided warm core. This may indicate a flow of gulf water into the bay and/or a greater water depth in the streamer. Interestingly, a streamer of low SSC water occurs at the same location, which lends credence to the idea that this streamer water is of a different nature than the surrounding water. Other streamers of both warm and cold water are evident throughout the bay; they may be indicating areas of deeper and shallower water. However, it is difficult to verify this with bathymetry charts in an area of dynamic deposition and erosion like the Atchafalaya Bay. Nonetheless, if depth information may be inferred from the SST depiction, then daily, weekly, or even seasonal high resolution SST data could be useful in tracking the shifting of shoals in these waters.

A correlation of the SSC and SST fields was calculated in the Atchafalaya Bay region. Land areas were excluded from the correlation. An inverse correlation of r=-.57 was found. Warm SSTs correlated to low SSCs. This is a good indication that the warm SST/low SSC water of the gulf and the cold SST/high SSC water of the Atchafalaya River maintain their characteristics as they are advected in the region. This would seem to underscore the possibility of tracking these different water types through time. It is noted that this correlation improved when data further out in the gulf (warm SST, low SSC) was added to the computation.

5. CONCLUSIONS

The capability of the MAMS instrument to produce high resolution (100m) depictions of SSC and SST has been demonstrated. MAMS SST displays a spatial variability of better than .5k while SSC fields display realistic variability. The high variability in the Atchafalaya Bay of the Louisiana coastline depicted in these products is a strong testimonial to the value of such data. There are indications of SSC advection, water depth, water origin, and flow. In addition, an inverse correlation between SST and SSC is observed indicating a potential ability to track these features.

The MAMS will continue to be flown along the Louisiana coastline. An effort to monitor temporal changes along the coast as well as improve the SSC and SST algorithm coefficients will be made. Daily as well as seasonal changes will be investigated with an emphasis on the relationship between weather patterns (such as cold front passages) and the geomorphology of the Louisiana coastline.

REFERENCES

Bates, J. J., W. L. Smith, G. S. Wade, and H. M. Woolf, 1987: An interactive method for processing and display of sea-surface temperature fields using VAS multispectral data. Bull. of Amer. Met. Soc., 68, 602-606.

Collins M., and C. Pattiaratchi, 1984: Identification of suspended sediment in coastal waters using airborne thematic mapper data. Int. J. Remote Sensing, 5, 635.

Cox C., and W. Munk, 1954: Statistics of the sea surface derived from sun glitter. J. Mar. Res., 14, 198.

Egleme, L. E., 1985: Landsat-4 based models for suspended sediment concentrations in central Louisiana coastal waters. M.S. Thesis, Louisiana State University, 124 pp.

Gordon, H. R., D. K. Clark, J. W. Brown, O. B. Brown, R. H. Evans, and W. W. Broenkow, 1983: Phytoplankton pigment concentrations in the Middle Atlantic Bight: comparison of ship determinations and CZCS estimates. Appl. Optics, 22, 20.

Holligan, P. M., M. Viollier, C. Dupouy, and J. Aiken, 1983: Satellite studies on the distributions of chlorophyll and dinoflagellate blooms in the western English Channel. Contin. Shelf Res., 2, 81.

Jedlovec, G. J., 1988: Determination of low-level precipitable water variability from split window channel radiance data. Preprints Third Conference on Satellite Meteorology and Oceanography, AMS, Boston, 89-94.

Jedlovec, G. J., K. B. Batson, R. J. Atkinson, C. C. Moeller, W. P. Menzel, and M. W. James, 1989: Improved capabilities of the Multispectral Atmospheric Mapping Sensor (MAMS). NASA Technical Memorandum (in print), Marshall Space Flight Center, Huntsville, AL, 71pp.

Khorram, S., 1982: Remote sensing of salinity in the San Francisco Bay delta. Remote Sensing Environ., 12, 15.

McClain, E. P., W. G. Pichel, and C. C. Walton, 1985: Comparative performance of AVHRR-based multichannel sea surface temperatures. J. Geophys. Res., 89(C6), 11587-11601.

Menzel, W. P., G. J. Jedlovec, and G. S. Wilson, 1986: Verification of small scale features in VAS imagery using high resolution MAMS imagery. Second Conference on Satellite Meteorology/ Remote Sensing and Applications, AMS, Boston, 108-111.

Rimmer, J. C., M. B. Collins, and C. B. Pattiaratchi, 1987: Mapping of water quality in coastal waters using Airborne Thematic Mapper data. Int. J. Remote Sensing, 8, No. 1, 85-102.

Roberts, H. H., O. K. Huh, S. A. Hsu, L. J. Rouse, Jr., and D. Rickman, 1987: Impact of cold-front passages on geomorphic evolution and sediment dynamics of the complex Louisiana coast. Coastal Sediments '87, WW Div./ASCE, New Orleans, 1950-1963.

Viollier, M., D. Tanré, and P. Y. Deschamps, 1980: An algorithm for remote sensing of water color from space. Boundary Layer Meteorol., 18, 247.

13.3

ESTIMATION OF SURFACE SKIN TEMPERATURES OVER THE TIBETAN PLATEAU FROM AVHRR SPLIT WINDOW MEASUREMENTS

Lei Shi
Eric A. Smith

Department of Meteorology and
Supercomputer Computations Research Institute
Florida State University
Tallahassee, FL 32306

1. INTRODUCTION

Tropical and subtropical climates are strongly influenced by the thermodynamic effects of the Tibetan Plateau (Gao et al, 1981). In a recent study of the infrared cooling rate structure over the Plateau, we have shown that the plateau surface plays an important role in modulating the gradient cooling pattern during the transition of the summer Asian Monsoon -- see Smith and Shi (1989) and Shi and Smith (1989). A critical factor constituting the surface effect is the discontinuity of skin temperature at high elevation.

The utility of satellite measurements for obtaining surface temperature estimates has been investigated by various authors. Anding and Kauth (1970) and Dalu (1985) have discussed the calculation of sea surface temperatures; Price (1984) and Becker (1987) have investigated the temperature measurement problem over land surfaces. A comparison of models which use different "windows" in calculating surface temperature was provided by McMillin and Crosby (1984). In their study, the models were examined based on one single window, a split 10-12.5 micron window, and a triple-window involving the addition of a weak window measurement at 3.7 microns. The physical interpretation of the coefficients was provided in a following paper (McMillin and Crosby, 1985).

After making comparisons among a number of algorithms developed by different authors, Dalu et al. (1985) concluded that although the results obtained from AVHRR split window data are slightly more accurate for a non-linear algorithm, a linear algorithm can give better results if it is optimized for a particular region and season. In this study we experiment with a surface temperature estimation technique based on Dalu's suggestions for a particular region of the Tibetan Plateau, during the summer monsoon transition season in 1986.

A field experiment entitled "The 1986 Tibetan Plateau Meteorology Experiment (TIPMEX-86)" (Reiter et al., 1987) was carried out at two sites [Naqu (92.0 E, 31.5 N) and Lasa (91.1 E, 29.6 N)] on the Tibetan Plateau during June-July, 1986. We have used the Naqu ground measurements to improve upon the operational AVHRR based, 2-channel linear surface temperature regression equation developed by NESDIS for sea surface temperature estimation -- P. McClain (personal communication, 1988). The Naqu site has been selected for the algorithm development because its flat open terrain region with homogeneous characteristics provide an unambiguous data set for a set of AVHRR-GAC measurements we have acquired for this study.

The satellite data used in this study cover the period from June 10 to June 24, 1986. The AVHRR split window measurements have been transformed into a standard $10^{o}x10^{o}$ map frame extending from 85 E to 95 E, and from 25 N to 35 N. The interval of the grid points is approximately 4 km in both latitude and longitude. For each pair of measurements from the AVHRR split window channels, a corresponding simultaneous surface skin temperature at the Naqu site (referred to as a "ground measurement" hereafter) is obtained from the soil temperature data base taken during TIPMEX-86.

2. ANALYSES AND RESULTS

The current operational split NESDIS window equation for SST retrieval is expressed as:

$$T_s=3.4317T_{11}-2.5062T_{12}-251.24$$

$$=0.9255T_{11}+2.5062(T_{11}-T_{12})-251.24 \quad (1)$$

where T_{11} and T_{12} are the 11 and 12 micron brightness temperatures obtained from AVHRR channels 4 and 5 (Kidwell, 1986).

Fig. 1 compares the satellite estimations calculated by eq. (1) with the Naqu ground measurements. In this figure, the X-axis denotes the ground measurement; the Y-axis denotes the satellite estimation. A unit correlation line is drawn to facilitate the comparison of the values from the two sources. The satellite estimations in Fig. 1 are obtained from eq. (1) in which T_{11} and T_{12} are the split window measurements over the Naqu site. The ground measurements are obtained from the corresponding simultaneous surface readings at that site. Fig. 1 shows that the asterisks are consistently too high with respect to the diagonal, indicating that the satellite estimations mostly give higher values than the ground measurements. On the average, the over-estimate in temperature by the split window method is approximately 3°C. Eq. (1) was developed for sea-surface temperature retrieval. The over-estimation of Naqu surface temperatures is due to the influence of different atmospheric transmission and surface emissivity conditions from a sea-surface and plateau-surface vis-a-vis the regression coefficients.

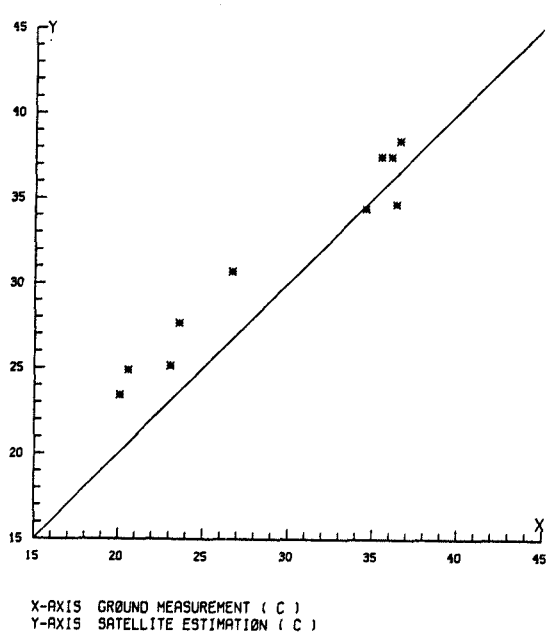

Fig. 1: Comparison of satellite derived skin temperature estimates to ground measurements. The satellite estimation is based on the regression equation developed by McClain (personal communication, 1988) for SST retrieval.

Equation (1) is obtained through a statistical procedure. The physical mechanisms influencing the retrieval of surface temperature is embodied in the coefficients of the equation. In order to obtain better coefficients for the plateau, an equation similar to eq. (1) but strictly based on the ground measurements of the Naqu site is developed here. This equation is derived by a linear regression method utilizing T_{11} and T_{12} as independent variables, and the ground measurement at the Naqu site as the dependent variable. The resultant equation is expressed as:

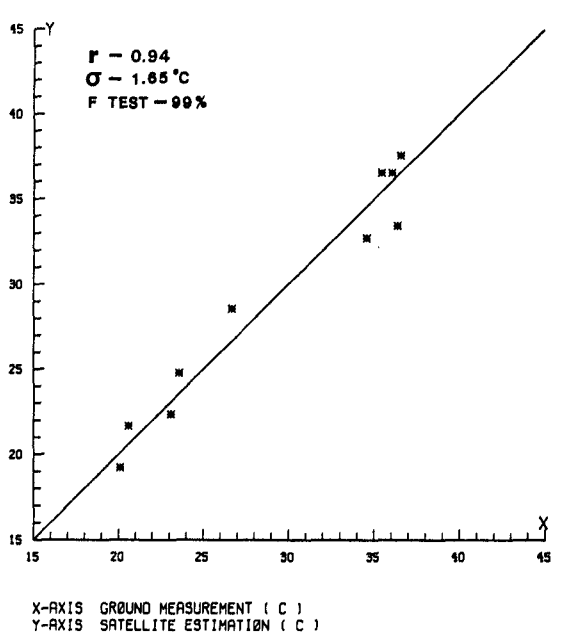

Fig. 2: Comparison of satellite derived skin temperature estimates to ground measurements. The satellite estimates are based on the regression coefficients developed in this study. The values of linear correlation (r), the standard deviation (σ) and F test significance level are shown in the upper left of the diagram.

$$T_s=3.4548T_{11}-2.4161T_{12}-287.44$$

$$=1.0387T_{11}+2.4161(T_{11}-T_{12})-287.44 \quad (2)$$

The fit of this regression equation to the data set is shown in Fig. 2. By comparing eq. (2) with eq. (1), it can be noted that the signs of the coefficients in eq. (2) are the same as those in eq. (1), however, the values of the coefficients are slightly altered.

The motive for deriving an equation suitable to the plateau conditions is to obtain the surface temperature distribution over a region where the topographical and biophysical features serve to impart a complicated pattern in the skin temperatures. The satellite estimations of surface temperature for June 22, 1986 are calculated by eq. (1) and eq. (2) and plotted in Figs. 3 and 4, respectively. This date was selected because of the relatively cloud free conditions that characterized that day. The basic temperature distribution patterns in Figs. 3 and 4 are similar, with high values centering around three locations: (88 E, 29 N), (87 E, 31 N) and (93 E, 32 N); and a low value belt aligned with 28 N. In the region analyzed, the variation of temperature is found to be more than 10°C within a distance of 100 km.

The main difference between Figs. 3 and 4 is in the magnitude of the temperature. The temperatures in Fig. 4 are consistently lower than those in Fig. 3, with each corresponding value in the two figures differing from between 0 to 5°C. It is noted that along the latitude of 28°N, the temperatures in Fig. 4 are approximately 4-5°C lower than those in Fig. 3 and in closer proximity to the freezing level. Considering that the Himalayas are located along 28°N and there are permanent ice and snow features on the high peaks all year round, the lower surface temperatures estimated for this sector seem to be more consistent with the real situation. This provides indirect evidence that eq. (2) is more applicable for the Tibetan area than eq. (1).

Comparing the large spatial variation of surface temperature which results from the extremely complicated orography and biophysical features, the operational stations over the Tibetan Plateau are very sparse. They are generally 200-500 km apart. Thus, the information on the detailed gradient pattern of surface cannot be provided by routine measurements. In order to obtain a reliable distribution pattern of surface temperature, a finer temperature scale is needed. This can only be done effectively by using the satellite measurements.

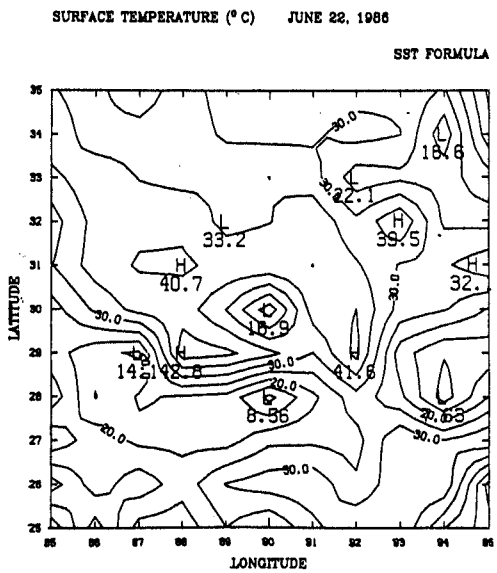

Fig. 3: Distribution of surface skin temperatures in the central Tibetan region of 85-95°E, 25-35°N on June 22, 1986, based on the SST equation.

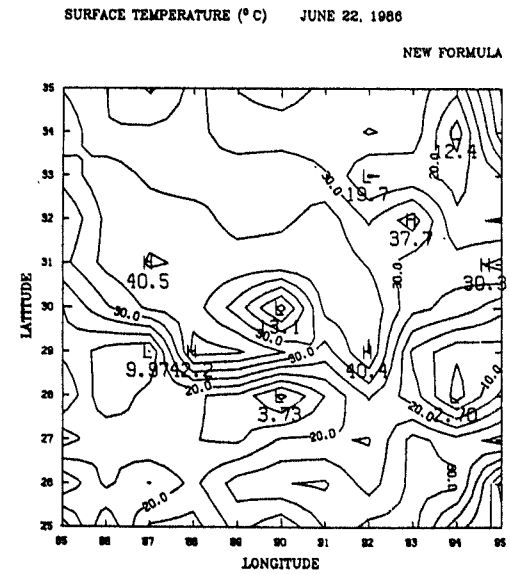

Fig. 4: Same as Fig. 3 for the regression coefficients developed in this study.

3. CONCLUSIONS

In order to obtain a reliable estimate of surface skin temperature distribution over the plateau, AVHRR split window measurements obtained from the operational NOAA satellite are employed in this study. Using the basic NESDIS operational SST regression equation as a guide, we develop a new 2-channel coefficient set applicable to high elevation flat terrain sites within the central Plateau. The use of split window measurements for estimating the distribution pattern of land surface skin temperature has shown promise for the Tibetan Plateau. In using the operational SST split window method the temperature estimates are consistently higher than the ground measurements. Better results of surface temperature estimates for the central Tibetan Plateau can be obtained by adopting new regression coefficients established strictly for plateau conditions.

The surface temperature distribution obtained by split window data reveals that the variations of skin temperature can be more than 10°C within a distance of 100 km in the central Tibetan region. This information cannot be adequately obtained by the sparsely distributed observational stations, and therefore bodes well for the application of AVHRR split window measurements for studies of the radiative flux divergence structure throughout the large scale Plateau region.

4. Acknowledgements

We wish to thank Dr. Kyung-Whan Oh for his assistance with the satellite data analysis and extend our appreciation to Mr. Byung-Ju Sohn for his assistance with checking the manuscript. This research has been supported by NSF Grant ATM-8812411.

5. REFERENCES

Anding, D. and R. Kauth. 1970: Estimation of sea surface temperature from space. Remote Sensing of Environment, 1, 217-220.

Becker, F., 1987: The impact of spectral emissivity on the measurement of land surface temperature from a satellite. Int. J. Remote Sensing, 8, 1509-1522.

Dalu, G., A. Viola and S. Marullo, 1985: Sea surface temperature from AVHRR-2 data. Il Nuovo Cimento, 8c, 793-803.

Gao, Y.X., M.C. Tang, S.W. Luo, Z.B. Shen and C. Li, 1981: Some aspects of recent research on the Qinghai-Xizang Plateau meteorology. Bull. Amer. Meteor. Soc., 62, 31-35.

Kidwell, K. B., 1986: NOAA polar orbiter data user's guide. Satellite Data Services Division, NOAA-NESDIS, Washington, DC.

McMillin, L. M. and D. S. Crosby, 1984: Theory and validation of the multiple window sea surface temperature. J. Geophys. Res., 89, 3655-3661.

McMillin, L. M. and D. S. Crosby, 1985: Some physical interpretations of statistically derived coefficients for split-window corrections to satellite-derived sea surface temperatures. Quart. J. R. Met. Soc., 111, 867-871.

Price, J. C., 1984: Land surface temperature measurements from the split window channels of the NOAA 7 Advanced Very High Resolution Radiometer. J. Geophys. Res., 89, 7231-7237.

Reiter, E. R., J. D. Sheaffer, J. E. Bossert, E. A. Smith, G. Stone, R. McBeth and Q. Zheng, 1987: Tibet Revisited - TIPMEX-86. Bull. Amer. Meteor. Soc., 68, 607-615.

Shi, L. and E. A. Smith, 1989: Surface forcing of the infrared cooling profile over Tibetan Plateau. Part II: Cooling rate structure over large-scale plateau domain during 1979 monsoon transition. Submitted to J. Atmos. Sci.

Smith, E. A. and L. Shi, 1989: Surface forcing of the infrared cooling profile over Tibetan Plateau. Part I: Influence of relative longwave heating at high altitude. Submitted to J. Atmos. Sci.

CLOUD TYPES AND SST OVER THE TROPICAL PACIFIC OCEAN DERIVED FROM NOAA-9 SPLIT WINDOW DATA

Toshiro Inoue

Meteorological Research Institute
1-1 Nagamine Tsukuba, Ibaraki, 305, JAPAN

1. INTRODUCTION

The International Satellite Cloud Climatology Project (ISCCP) was established to obtain an accurate global cloud climatology. The validation of the operational cloud climatology and the development of improved cloud analysis methods are two major elements of the ISCCP (Rossow *et al.* 1985). ISCCP cloud algorithm intercomparisons have been done several times by intercomparing cloud parameter results derived from various methods using full-resolution Geostationary Operational Environmental Satellite (GOES) visible and infrared data. It was found that all of the methods had some trouble in detecting thin cirrus clouds and small low-level cumulus clouds. Rossow *et al.* (1985) implied that visible data seems indispensable for a proper detection of the two important cloud types: cirrus and boundary layer cumulus. The usage of visible data limits accurate results to daylight hours. In order to get the uniform cloud climatology which resolves diurnal cloud variations, an infrared algorithm is desired. Inoue (1987) developed a method which can classify optically thin cirrus type clouds and optically thick cumulus type clouds using the split window data in 10μm region on board NOAA-7. This method uses only infrared data.

This technique developed by Inoue (1987) was applied for cloud cover determination over the tropical Pacific ocean between 20°N and 20°S latitude and 110°E and 80°W longitude. The $(4km)^2$ resolution data of split window channels on board NOAA-9 were used for the cloud cover retrieval. Six cloud types including optically thick and cold clouds (cumulonimbus type clouds), optically thick and warm clouds (cumulus and stratocumulus type clouds), optically thin and cold clouds (dense cirrus type clouds) and optically thin and warm clouds (cirrus type clouds) were classified in this study. The 30 day, during January 11-February 9, 1987, mean cloud cover features over the studied area were estimated from NOAA-9 day time orbits based on the cloud cover in each 2.5° x 2.5° latitude/longitude area for each cloud type.

2. DATA

Advanced very high resolution radiometer (AVHRR) global area coverage (GAC) data of NOAA-9 are used in this study. The spatial resolution of the GAC data is approximately 5 x 3 km^2 at the subsatellite point. The area covered by the scan spots increases away from nadir. Split window data(10.3-11.3μm and 11.5-12.5μm) are only used in cloud type classification and cloud cover retrieval.

The calibration of split window data was described by Lauritson *et al.* (1979). A non-linear correction was performed according to the table with zero radiance for the space (Rochard 1988, personal communication). This non-linearity correction was tabulated between 205°K and 320°K.

The alignment between the split window data and visible data was checked by computing cross correlation. The original AVHRR data extracted from HRPT received at Meteorological Satellite Center (MSC) in Tokyo were used in computing the cross correlation. Cross correlations were computed for 50 x 50 data over eastern and western side of scan swath. Highest correlation was seen at 0 lag point. Thus no misalignment (position and scanning direction angle) was found between the three channels in original non-sampled AVHRR data.

The 0.1° grid data between 20°N and 20°S latitude and 110°E and 80°W longitude was constructed by selecting the closest spot computed from the navigation data of the GAC.

3. METHODOLOGY

Based on the method of Inoue (1987), cloud types are classified with the information of both the brightness temperature (TBB) of 11 μm and the TBB difference between the split window data (DT) for every pixels. The DT is defined as the TBB of 11μm minus the TBB of 12μm ($DT = TBB_{11\mu m} - TBB_{12\mu m}$). The DT is a good indicator for distinguishing between optically thick clouds and optically thin clouds. Clouds which can be assumed to be black-body show small values of the DT, while optically thin clouds which consist of ice show large values of the DT due to the difference of emissivity in 11μm and 12μm (Inoue, 1985).

Cloud type classification is based on a threshold technique in the TBB - DT diagram. There are two threshold values for DT. One is the threshold value for optically thick clouds and the other is for optically thin clouds. In this study, the former is set to 1°C and the latter is set to the DT of clear-sky condition. There also are two threshold values for TBB. For high level clouds the threshold value for TBB is set to -20°C which corresponds to about the 400mb temperature at these latitudes. Another threshold value of TBB is set to the value which indicates cloudy or clear.

An example of cloud type classification diagram is shown in Fig.1. Since each pixel data on the 0.1° grid point has both TBB and DT, each data point is positioned somewhere in the diagram. Each box in Fig.1 represents a cloud type. Comparisons between cloud type and neph-analysis are shown in Inoue(1987). Cloud types are labeled as U, B, N, I_1, I_2, I_3 and Clear. Cloud types B and U represent optically thick clouds because DT is small.These two types are considered to consist mainly of cumulonimbus type clouds and of low level cumulus or stratocumulus type clouds, respectively. According to Inoue (1985), the DT becomes larger as the cloud emissivity becomes larger till it becomes about 0.5, then the DT becomes smaller as the cloud emissivity becomes larger. Therefore, cloud types I_1, I_2 and I_3 are regarded as optically thin cirrus type clouds. The cloud type I_3 and I_2 are considered to be thin cirrus clouds and relatively thick cirrus clouds ,respectively, because of the larger DT. The cloud type I_1 is considered to be very dense cirrus clouds, which is close to cumulonimbus type clouds. Clouds colder than 205°K are regarded as type B since calibration does not extend below 205°K.

In this study, we do not insist on the classification of clouds according to the International Cloud Atlas (1956) by World Meteorological Organization, using this TBB-DT diagram. The cloud type classified by this diagram introduce some radiative properties such as the optical thickness and temperature of clouds measured by 10μm window region. We believe this information is very useful although it is not necessarily real information of cloud types in a rigid sense.

We have to determine the two threshold values of TBB and DT for clear-sky in Fig.1 in advance for cloud type classification. The idea of spatial coherence (Coakley and Bretherton,1982) was applied for detecting clear-sky areas over the ocean. The standard deviation of TBB for 2 x 2 grid points are computed. The area whose standard deviation is less than 0.05°C and warmer than 18°C which is the air temperature at about 850 mb over the tropics, is regarded as cloud free area. We construct 30 day mean clear-sky TBB and corresponding DT within 1° x 1° area. The 10° x 10° areal mean of these mean values are used as threshold values of cloud type classification. Within the 10° x 10° area, the threshold values are fixed. The cloud type classification is processed for every pixel using these four threshold values.

4. RESULTS

4.1. Sea Surface Temperature

Since, in this study clear-sky TBB and clear-sky DT were determined in advance for cloud type classification, as a by-product, sea surface temperature (SST) was estimated using the clear-sky split window data. NOAA started the operational multichannel SST product from December 1981 using NOAA-7 AVHRR data. The following NOAA operational multichannel SST equation was used in this study;

$$SST(°C) = 3.6446 \times TBB_{11\mu m}(°K) - 2.6616 \times TBB_{12\mu m}(°K) - 267.96.$$

The SST can be retrieved over ~20 x 20 km^2 using the restricted clear-sky data defined in the earlier section: the standard deviation and mean of TBB for 2 x 2 grid points is less than 0.05°C and warmer than 18°C, respectively.

Fig.2.1 shows the 30-day mean SST smoothed over 5° x 5° area from 1° x 1° grid areal average SST. Since the analysis period in this study is during 11 Jan-9 Feb. 1987, we do not have the exact SST map to be compared. However, comparison between this map and the monthly mean SST of January (Fig.2.2) constructed by Japan Meteorological Agency (JMA) from ship observations show overall agreement in magnitude and patterns. Although, clear-sky data are selected under restrictive conditions in this study, during the thirty day period we can estimate SST as the 1°x 1° areal mean over 95% of the 1°x 1° ocean grids. Most of the area where SST could not be retrieved were seen in the western equatorial Pacific where convection was very active as shown in a later section.

4.2. Clear-sky TBB and Clear-sky DT

Fig.3.1 and Fig.3.2 represent the 30 day mean clear-sky TBB and clear-sky DT. These maps are retrieved by averaging clear-sky TBB and corresponding DT over the clear-sky area which satisfy the spatial coherence conditions stated earlier.The clear-sky TBB reflects both the sea surface temperature and water vapor content. The higher SST produces the higher TBB, while the larger amount of water vapor reduces the values of TBB more because of water vapor absorption. It is interesting the coldest contour of 21°C at the equator between 170°E and 165°W coincides with the warmest SST contour of 29°C, and with the largest DT contour of 3°C.

Differential absorption by vapor between 11μm and 12μm causes the larger DT where the larger amount of water vapor exist (Prabhakara *et al.* 1979). Therefore the clear-sky DT distribution shows water vapor amount qualitatively. Although quantitative water vapor retrieval has been done using split window data (Chester *et al.* 1983; Kleespies and McMillin, 1984, etc.), it is beyond the scope of this study. The large DT area is seen over the western equatorial Pacific where deep convective activity is significant (see Fig.6). Small DT areas are seen at higher latitudes in the northern hemisphere and in the south-eastern part of the analysis area, where high level clouds are very few and low level clouds are dominant (see Fig.6). Overall the pattern of water vapor content implied by DT distribution is similar to the results of Prabhakara et al. (1979) and Aoki and Inoue (1982).

Fig.4 shows the difference between derived SST and clear-sky TBB (SST-TBB). This difference represents the amount of absorption effect by water vapor in 11μm. The TBB in 11μm shows 8°C colder than SST at most over the western Pacific. This map introduce another perspective of water vapor distribution.The pattern of Fig.3.2 is similar to that of Fig.4 except for the magnitude.This SST and clear-sky TBB difference is more sensitive to water vapor content than DT.

4.3. Cloud Types and Visible Counts

Kaveney *et al.* (1977) showed brightness values can be used to infer cloud thickness more reliably for relatively stable clouds. Although Kaveney *et al.* (1977) exclude the clouds of tropical (or maritime) origin, here we check optical thickness of cloud types by comparing visible data (original 10-bit counts) with cloud types. The same threshold values stated above are used for cloud type classification. To avoid sun glitter in visible data, we used the data of the zenith angle between 0° and 30° from the nadir over the eastern part of the swath. The comparisons were performed for ten days for the orbits near the dateline. The mean values of visible data for each cloud type are shown in Fig.5 by darker printing. The higher values of visible data indicate higher reflectivity of sunlight. This figure assures us that the optical thickness of cloud type B and U classified by split window are greater than cloud type I_2 and I_3. The cloud type I_1 seems relatively thick and comparable to the optical thickness of cloud type U. The cloud type N is thicker than cloud type I_3 and thinner than cloud type U.

4.4. 30 Day Mean Cloud Cover

Zenith angle effect is one of the major problems in estimating cloud cover from satellite data. In order to minimize the effect of viewing angle in cloud cover retrieval, we select data whose satellite zenith angle is smaller than thirty degrees. In this case, about six satellite paths for one day cover only one-third of the analysis area. This method is based on threshold technique which has deficiency in the problem of partial cloudiness within field of view. As is usual in remote sensing method, the problem of multi-layered cloud system is another deficiency in this method.

The cloud cover is defined as the ratio of the number of cloud pixels to that of total pixels within a 2.5°x 2.5° area. The cloud cover is computed only when effective pixels cover more than 75% in the 2.5°x 2.5° area. The 30-day mean distributions of cloud cover for B, I_3, and U types classified by split window data are shown as percentage analysis in Fig.6. The number of observations are relatively small over the area west of 120°E and east of 90°W. The cloud cover over land area has some error caused by inappropriate threshold values in the cloud type classification diagram.We cannot determine clear-sky threshold values over land where spatial coherence is not seen.

4.4.1. *B Type Cloud Cover*

B type cloud cover represents well active convective areas. The average cloudiness of this cloud is 6% over the analysis area. The maximum of 39% cloud cover appears north of the Australia where Australian monsoon is active. A relatively active area is seen about 8 degrees south of the equator extending eastward to 170°W which splits into southeast and northeast branches. And other active regions over the eastern Pacific are seen north of 5°N between 135°W and 105°W, and around 5°N, 85°W. These active convection areas correspond well to the high SST (> 29°C) areas except the area of eastern part of the Pacific.

4.4.2. *I Type Cloud Cover*

The average coverage of I_1 type cloud over the studied area is 4%. The cloud cover distribution of this type is quite similar to B type cloud cover except for the area over the eastern Pacific where very small amounts of this type cloud is observed. The average cloudiness in the analysis area for I_2 and I_3 are 4% and 24%, respectively. Cloud type I_2 are usually surrounded by I_3. These clouds are often observed as anvil clouds expanding from core of cumulonimbus type clouds. Generally, their distribution patterns are similar to that of B type. Close examination shows the high cloud amount areas of I_3 are seen just off the cores of the B type high cloud cover region.

The maximum of total I type cloudiness (sum of I_1, I_2 and I_3) reaches 79% over the west of Arafura Sea.The mean cloudiness of this type cloud is 32% over the study area. Woodbury & McCormick (1986) determined the frequency of occurrence of cirrus clouds. They showed significantly large areas of high frequency (>60%) over the western tropical Pacific. Although the analyzed period and statistics are different, this study reveals cirrus type clouds are dominant over the western tropical Pacific, also.

4.4.3. *U Type Cloud Cover*

The average cloudiness of U type cloud is 9% over the area studied. The high cloud cover is seen north of 10°N latitude over the western Pacific, and a large part of the eastern Pacific except for south of Central America and the southwest Pacific. These areas agree well with the climatological areas where trade wind cumulus or marine stratocumulus clouds are dominant. And these areas coincide with relatively cold SST (<27°C) area (see Fig.2.1).

4.4.4. *Total Cloud Cover*

The average cloudiness of total cloud over the analysis area is 54%. While corresponding average total cloudiness estimated from ISCCP C1(January,1984) is 60%. In the computation, we selected the C1 data which cover the same analysis area and 00-06 GMT observations.

4.5. Cloud Top Temperature

Since the method can classify optically thick clouds, we can estimate cloud top temperature for these clouds with relatively good accuracy.Fig.7 demonstrates the 30-day mean cloud top temperature computed from cloud types U and B.

The coldest contour appears over the Arafura Sea of 220°K. The area where mean cloud top temperature is colder than 240°K shows a similar distribution pattern of B type cloud in the western part of the analysis area. The cloud top temperatures which correspond to high B type cloudiness over the eastern part of the study area are only 260°K. It is revealed that deep convection in the western Pacific along 8°S latitude is more active and prevalent than that in the northern part of the eastern Pacific.

Areas of warmer mean cloud top temperature are seen over both the northwestern Pacific and the southeastern Pacific. These area match well with the high cloud cover area of U type cloud. The cloud area over the northwestern quadrant agrees with the climatological location of prevailing trade wind cumulus. In addition, the area over southeastern quadrant agrees with the dominant marine stratocumulus area.

5. CONCLUDING REMARKS

The high cloud cover area of B type cloud over the western Pacific corresponds well to the high SST area (>29°C) derived in this study. The distribution of mean cloud top temperature of optically thick clouds reveals that deep convection is very active over the western Pacific (<240°K) especially over the Arafura Sea (220°K) during the analysis period. Meanwhile mean cloud top temperature off the Mexican coast where high B type cloudiness is analyzed, is only about 260°K. It is interesting to note that SST off the Mexican coast is less than 26°C. The high U type cloudiness (low level optically thick clouds) corresponds well to low SST area (<27°C) and to the climatological area where trade wind cumulus and stratocumulus are dominant. It is also found that optically thin cloud is a major cloud type over the tropical ocean. In addition SST and water vapor distribution over cloud free area can be estimated from the split window data.

6. REFERENCES

Aoki, T. and T. Inoue, 1982: Estimation of the precipitable water from the IR channel of the geostationary satellite, *Remote Sens. Environ.*, **12**, 219-22

Chesters, D., L.W. Uccellini and W.D. Robinson, 1983: Low level water vapor fields from the VISSR atmospheric sounder (VAS) "Split window" channels. *J. Clim. Appl. Met.*, **22**, 725-743.

Coakley, J.A., Jr., and F.P. Bretherton,1982: Cloud cover from high-resolution scanner data: Detecting and allowing for partially filled fields of view. J. Geophys. Res., 87, 4917-4932.

Inoue, T., 1985: On the temperature and effective emissivity determination of semi-transparent cirrus clouds by bi-spectral measurements in the 10μm window region., *J. Meteor. Soc. Japan*, **63**, 88-99.

Inoue, T., 1987: A cloud type classification with NOAA-7 split window measurements., *J. Geophys. Res.*, **92**, 3991-4000.

Kaveney, W.J., R.G. Feddes and K.N. Liou, 1977: Statistical inference of cloud thickness from NOAA 4 scanning radiometer data.*Mon.W.Rev.*, **105**, 99-107.

Kleespies, T.J. and L.M. McMillin,1984: Physical retrieval of precipitable water using the split window technique, Preprints of Conference on satellite meteorology/remote sensing and applications, Clearwater Beach FL., *Amer. Meteor. Soc.*

Lauritson, L., G.G. Nelson and R.W. Port, 1979: Data extraction and calibration of TIROS-N/NOAA A-G radiometer, *NOAA Tech. Memo., NESS 107*

Prabhakara,C., G. Dalu, R.C. Lo, and N.R. Nath, 1979: Remote sensing of seasonal distribution of precipitable water vapor over the oceans and the inference of boundary-layer structure, *Mon. Wea. Rev.*, **107**, 1388-1401.

Rossow, W.B. et al., 1985: ISCCP cloud algorithm inter-comparison.*J.Climate Appl. Meteor.*, **24**,877- 903

Woodbury, G.E. and M.P. McCormick, 1986: Zonal and geographical distributions of cirrus clouds determined from SAGE data, *J. Geophys. Res.*, **91**, 2775-2785.

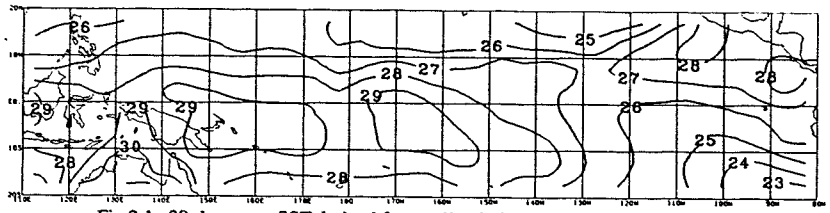

Fig.2.1 30-day mean SST derived from split window for 5°x 5° areal mean (°C).

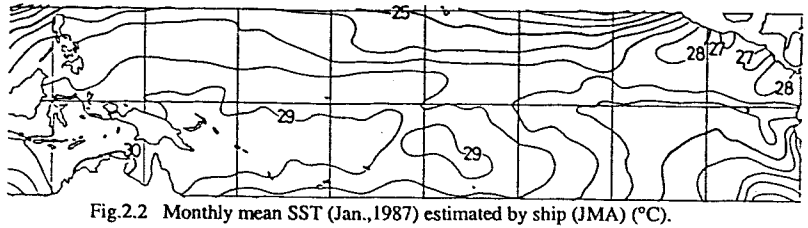

Fig.2.2 Monthly mean SST (Jan.,1987) estimated by ship (JMA) (°C).

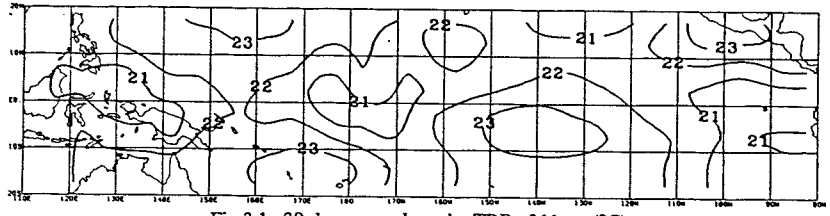

Fig.3.1 30-day mean clear-sky TBB of 11μm (°C).

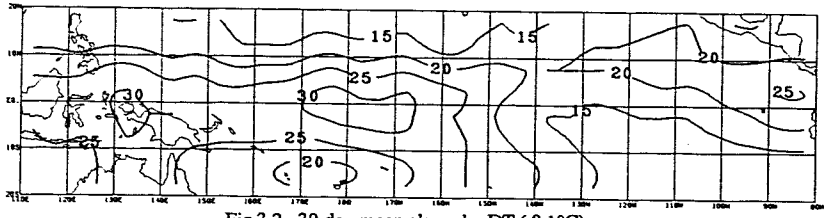

Fig.3.2 30-day mean clear-sky DT (0.1°C).

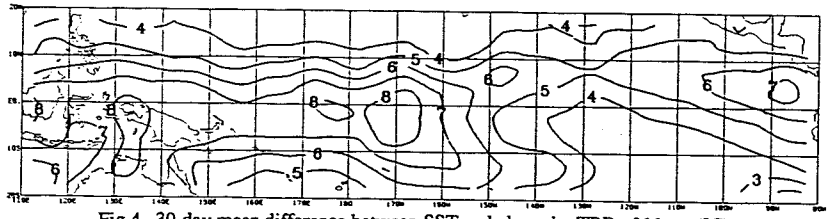

Fig.4 30-day mean difference between SST and clear-sky TBB of 11μm (°C).

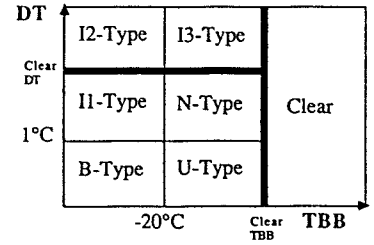

Fig.1 Cloud type classification diagram.

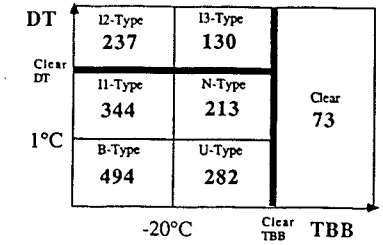

Fig.5 Mean visible counts in 10 bit and cloud types.

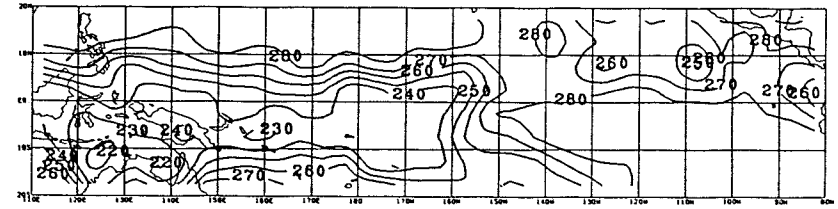

Fig.7 30-day mean cloud top temperature for optically thick clouds (°K).

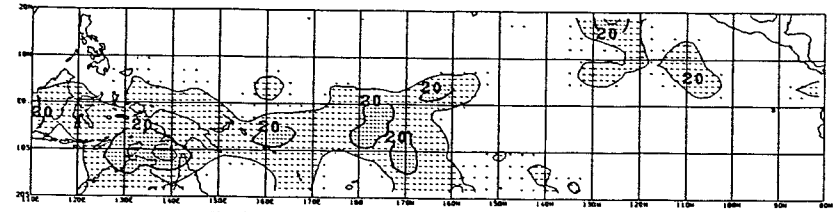

Fig.6.1 30-day mean cloud cover for B type cloud (%) .

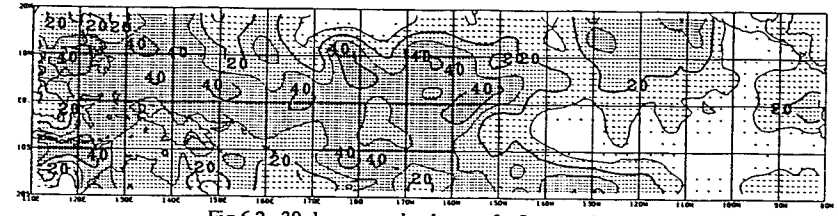

Fig.6.2 30-day mean cloud cover for I3 type cloud (%) .

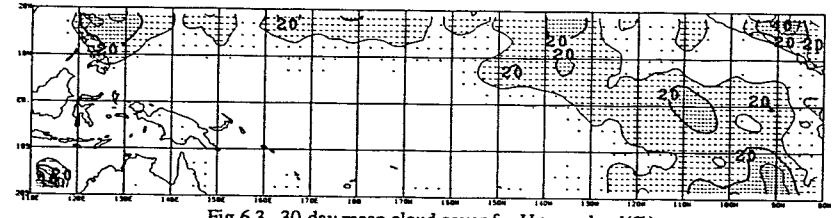

Fig.6.3 30-day mean cloud cover for U type cloud(%).

DETERMINATIONS OF TOTAL PRECIPITABLE WATER IN THE TROPICS FROM THE SSM/I

John C. Alishouse

Satellite Research Laboratory
NOAA/NESDIS
Washington, D.C.

Sheila Snyder
Jennifer Vongsathorn

S. M. Systems and Research Corporation
Landover, Maryland

1. INTRODUCTION

1.1 Background

Atmospheric water vapor is important for many facets of human life. The world's oceans are the major source of atmospheric water vapor. In particular the tropical oceans are an important source of atmospheric water vapor. Several previous experimental instruments have been used to make determinations of atmospheric water vapor. The results for these experiments have been presented by Gurvich and Demin (1970), for the radiometer on Cosmos 243; Staelin et al (1976), for the NEMS on Nimbus 5; Grody et al (1980), for the SCAMS on Nimbus 6; Alishouse (1983), for the SMMR on SeaSat and Gloersen et al (1984), for the SMMR on Nimbus 7. The SSM/I advances the state-of-the-art by being an operational instrument that can provide accurate real time measurements of total precipitable water over the world's oceans.

1.2 The SSM/I

The SSM/I is a seven channel, four frequency linearly polarized microwave radiometer that was launched into a near polar orbit in June 1987. The satellite has an altitude of about 833 kilometers, a period of 102 minutes, and an approximately 0615 LST ascending node. The salient characteristics of the SSM/I are presented in Table 1. The last column in Table 1 is the Noise Equivalent Temperature Difference of the instrument or its rms noise. The vertical polarization channel noise is given first in the NETD column. It is readily apparent that the 85.5 GHz vertical channel is of limited usefulness because of its large noise. The noise in this channel increased markedly in January 1988.

Table 1. SSM/I Characteristics

FREQUENCY (GHz)	POL.	EFOV (KM)	NETD (K)
19.35	V,H	45X70	0.43,0.41
22.235	V	40X60	0.67
37.0	V,H	30X38	0.33,0.37
85.5	V,H	14X16	1.70,0.72

2. SURFACE MEASUREMENTS

2.1 Raobs

To evaluate the system's ability to produce accurate determinations of total precipitable water, radiosonde observations (raobs) from selected stations were collected. It was required that the station be "small" in comparison with the SSM/I footprint. Initially, a list of 49 possible stations was compiled, however when our match-up criteria of 2 hours and 2 degrees of latitude and longitude between the SSM/I overpass and the raob are applied, match-ups from only 7 tropical stations were obtained. For our research the tropics are from 25 North to 25 South latitude. These stations are shown in Table 2. Latitudes are designated N and S for north and south. Longitudes are designated E and W for east and west. The station's WMO number is also given Table 2.

Table 2. Tropical Stations

STATION	NUMBER	LAT.	LONG.
COCOS IS.	96996	12.18S	96.83E
DIEGO GARCIA	61967	7.35S	72.48E
ISLA SAN ANDREAS	80001	12.58N	81.70W
BARBADOS	78954	13.07N	59.50W
SAN MAARTEN	78866	18.05N	63.12W
GRAND CAYMAN	78384	19.30N	81.37W
ISHIGAKIJIMA	47918	24.33N	124.17E

2.2 Data Handling

The radiosonde data were obtained from National Meteorological Center data files which are on computers shared with NESDIS. After the radiosonde files were obtained, they were integrated (Alishouse, 1983) to obtain the total precipitable water. This value of total precipitable water was used as a standard of comparison for retrievals by the initial algorithm and as a basis to derive new coefficients for the improved algorithm. The new coefficients were derived by standard regression techniques.

3. INITIAL ALGORITHMS

3.1 Structure

The initial algorithm (Hollinger et al, 1987) used to retrieve total precipitable water was a linear, four channel algorithm that was generated by regression using brightness temperatures calculated from raobs and a radiative transfer model. The four channels were 19H, 22V, 37V, and 37H. The algorithm was divided into latitudinal and seasonal segments called climate codes. There were eleven climate codes per hemisphere. Over the ocean there were three distinct sets of coefficients. Retrievals were not attempted over land.

Globally the latitude zones were: 60-90, the polar zone; 55-60, a transition zone; 25-55, the temperate zone; 20-25, a transition zone; and 0-20, the tropical zone. Two of the three sets of coefficients were used in the tropics. There were 235 match-ups for this data set.

3.2 Gradients

The boundaries between the latitudinal zones were "hard" in that the changes in coefficients occurred abruptly over an infinitesimal increment of latitude. The same was true for the seasonal changes. These types of algorithms frequently give rise to unnaturally large gradients at these boundaries. This was found to be the case.

3.3 Statistics

Table 3 is a summary of the results from the initial algorithm. The entries in Table 3 are in Kg/m^2 or precipitable millimeters. There were no match-ups in the southern lower latitude transition zone. The mean values are the sample means for the retrieval and the radiosondes (RAOB). The standard deviation (STD DEV) is the natural variance of the sample set. RMS DIFF is the rms difference between the retrieval and the corresponding raob. The BIAS is the difference in the sample means. A positive bias means an overestimate by the retrieval and a negative bias implies an underestimate.

The statistics presented in Table 3 show that the initial algorithm has a tendency to overestimate the amount of water vapor present in the tropics. It also shows comparatively large rms errors relative to the natural variance of the sample set.

Table 3. Initial ALGO Stats

LATITUDE ZONE	SAMPLE SIZE	MEAN RET	MEAN RAOB	STD DEV RET	STD DEV RAOB	RMS DIFF	BIAS
20-25 N	35	45.3	38.9	13.8	12.2	7.4	6.3
0 -20 N	134	44.2	39.8	11.7	9.0	6.7	4.4
0 -20 S	66	53.8	50.4	10.2	9.3	6.3	3.4
20-25 S	0						
TROPICAL	235	47.0	42.6	12.4	10.8	6.7	4.4

4. IMPROVED ALGORITHM

4.1 Structure

In devising the improved algorithm, we attempted to make the algorithm linear, global, use only four channels, and as accurate as possible. We were unable to find a linear, global four channel algorithm of sufficient accuracy. Our best linear algorithm tended to overestimate the amount of water vapor at mid-range values and underestimate at large values of water vapor. It was possible to devise a global, four channel algorithm that was not linear. By introducing the square of the 22 GHz brightness temperature, we were able to construct an algorithm. The other three predictors are the 19V, 22V, and 37V channels. Being global this algorithm does not introduce spurious gradients at the boundaries. The statistics for this algorithm for the tropics (25N-25S) are shown in Table 4. Also shown in Table 4 are statistics for a linear algorithm that is tailored to the tropics and a non-linear algorithm that uses the same channels as the global non-linear algorithm, but has coefficients derived just from the tropical data. Entries in Table 4 are in Kg/m^2 or precipitable millimeters.

4.2 Gradients

The global, non-linear algorithm does not produce spurious gradients.

Table 4. Improved ALGO Stats

LATITUDE ZONE	SAMPLE SIZE	MEAN RET	MEAN RAOB	STD DEV RET	STD DEV RAOB	RMS DIFF	BIAS
GLOBAL 25N-25S	235	42.7	42.6	9.9	10.8	3.8	0.1
TROPICAL 25N-25S	235	42.6	42.6	10.0	10.8	4.0	0.0
TROPICAL, NON-LINEAR 25N-25S	235	42.6	42.6	10.1	10.8	3.7	0.0

4.3 Statistics

The results presented in Table 4 are encouraging for the retrieval of total precipitable water in the tropics. The fact that a global algorithm, albeit non-linear, gives results that are as good or even better than algorithms based only on tropical data, is encouraging. A truly global algorithm will also eliminate the anomolous gradients found at the boundaries of a segmented algorithm. The fact that the global algorithm is non-linear need not be disconcerting. It was noted by Grody et al (1980) that the relationship between 22 GHz brightness temperatures and total water vapor was not linear. The SSM/I's water vapor channel works at the center of the water vapor line, 22.235 GHz. The large amount of water vapor and the greater vertical extent of water vapor in the tropics contribute to this non-linearity. The algorithms show little bias and are able to reproduce the range of values of total precipitable water in the tropics.

5. REFERENCES

Alishouse, J.C., 1983: Total Precipitable Water and Rainfall Determinations from the SEASAT Scanning Multichannel Microwave Radiometer. J. Geophys. Res., 88, 1929-1935.

Grody, N.C., A. Gruber, and W.C. Shen, 1980: Atmospheric Water Content over the Tropical Pacific Derived from the Nimbus-6 Scanning Microwave Spectrometer. J. Appl. Meteor., 19, 986-996.

Gloersen, P., D.J. Cavalieri, A.T.C. Chang, T.T. Wilheit, W.J. Campbell, O.M. Johannessen, K.B. Katsaros, K.F. Kunzi, D.B. Ross, D. Staelin, E.P.L. Windsor, F.T. Barath, P. Gudmandsen, E. Langham, and R.O. Ramsier, 1984: A Summary of Results from the First Nimbus 7 SMMR Observations. J. Geophys. Res., 89, 5335-5344.

Gurvich, A.S., and V.V. Demin, 1970: Determination of the Total Moisture Content in the Atmosphere from Measurements on the Cosmos 243 Satellite. Atmos. Ocean. Phys., 6, 453-457.

Hollinger, J., R. Lo, G. Poe, R. Savage, and J. Peirce, 1987: Special Sensor Microwave/Imager Users Guide. Naval Research Laboratory, Wash., DC, 120pp.

Staelin, D.H., K.F. Kunzi, R.L. Pettyjohn, R.K.L. Poon, R.W. Wilcox, and J.W. Waters, 1976: Remote Sensing of Atmospheric Water Vapor and Liquid Water with the Nimbus 5 Microwave Spectrometer. J. Appl. Meteor., 15, 1204-1214.

14.1

THE CLASSIFICATION OF ATMOSPHERIC PARAMETERS OVER THE OCEANS USING PRINCIPAL COMPONENT ANALYSIS OF SSM/I MEASUREMENTS

Russell A Ambroziak

Jane D'Aguanno

NOAA/NESDIS
Washington, DC 20233
(301)-763-8042

Ralph R Ferraro

S M Systems and Research Corporation
8401 Corporate Drive, Suite 510
Landover, MD 20785
(301)-459-3322

1. INTRODUCTION

An eigenvector approach to analysis of SSM/I data is currently being used to organize these data for target identification and measurement of water vapor over water surfaces. The approach uses 3-dimensional clustering of principal component scores to find and identify the major targets in the data. A sampled, plate carree (xy plot of latitude and longitude) image of 29 July 1987 was used to test the clustering methodology and then applied to the problems of measuring total precipitable water and cloud liquid water.

2. DATA

The SSM/I is a seven channel microwave radiometer measuring earth emitted radiation at 19, 22, 37 and 85 GHz. All measurements are dual-polarization except the 22 GHz which has only vertical polarization. More details of the SSM/I instrument is provided by Hollinger et al, 1987.

All available SSM/I passes for 29 July, 22 September and 12 November 1987 are mapped into three plate carree images, one for each day. The resolution of the images is 160km at the equator and extends from 120 degrees west longitude eastward through 180 degrees longitude and pole to pole. Each pixel contains the last data entry mapped to that location. No averaging or filtering was attempted. The final images are 200 by 200 pixels but less than half of these pixels contain data. The 29 July case was used for development and the result tested on the other two cases. The coverage for July includes Greenland, most of Antarctica, South America, Europe, Australia, and Africa. All of North America and South Asia are missing. Atlantic and western Pacific ocean coverage is nearly complete.

The data are whole degrees Kelvin minus 75 to scale them between 0 and 255. This allows the data sets to be stored as a 1-byte image plane on the Number-Nine graphics board which was used to process these data.

3. ANALYSIS, RESULTS AND DISCUSSION

The first three principal components contain most of the information in the data set (table 1). Visual inspection of simple RGB (red, green, blue) images of the first three eigenvectors show large differences between the major surface targets -- water, land, sea ice and continental ice and snow. On the RGB eigenvector image the colors for water range from dark blue where the air is dry to a medium magenta where the air contains large amounts of precipitable water. The color of land ranges from a bright peach over heavy vegetation to a bright magenta over desert regions. Ice over water ranges from cyan to magenta while ice over land is a bright green. Heavy precipitation is bright white.

Within each of these targets there is a considerable amount of texture. Weather patterns appear over the oceans and, to some extent, over land. Tropical water looks different than temperate and polar water. The deserts of the world are clearly visible and the degree or lack of vegetation seems to be visible on the RGB principal component score images.

EIGENVECTORS (All 7 SSM/I Channels)

EigenVectors

	SSM/I Channel	1	2	3
1	19 GHz-V	0.367	0.128	0.352
2	19 GHz-H	0.558	0.449	0.069
3	22 GHz-V	0.317	-0.183	0.693
4	37 GHz-V	0.306	-0.134	-0.131
5	37 GHz-H	0.476	0.198	-0.577
6	85 GHz-V	0.200	-0.631	-0.072
7	85 GHz-H	0.307	-0.541	-0.189

Table 1

Principal component MAXIMA AND MINIMA

p.c. score	Maximum	Minimum	Range
1	555.80	152.56	403.24
2	0.00	-212.07	212.07
3	101.48	5.22	96.26

Table 2

The principal components (E[i]) were scaled from 1 to 255 to create each principal component score image (e[i]).

$$e[i] = (E[i] - E[i](min))/R[i] * 255$$

where:

e[i] = principal component score
E[i] = principal component
E[i](min) = minimum principal component in image
R[i] = principal component range
= E[i]max - E[i]min (table 2)

It is always tempting to reduce eigenvectors to their major components and speak of them as being simpler than they are. They are not real physical things and never should be thought of as such. Having said that, the first eigenvector is very close to being the average of all channels. To be a true average all components would be 0.378 rather than those values listed on table 1 for eigenvector 1. Actually the 19-H and 37-H are favored at the expense of the 85-V, giving a slight frequency and polarization sensitivity. This is likely due to the high autocorrelation of the seven SSM/I channels and to the land/sea contrast in apparent brightness (figure 1a).

Principal Component Score Image Planes

First Principal Component Score

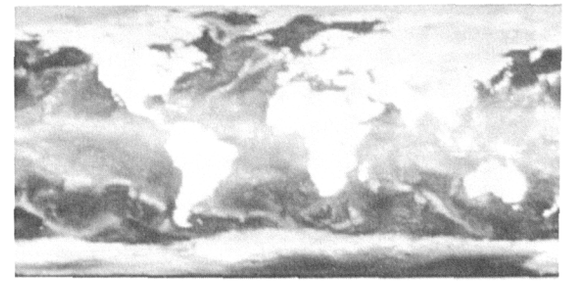

Figure 1a

Second Principal Component Score

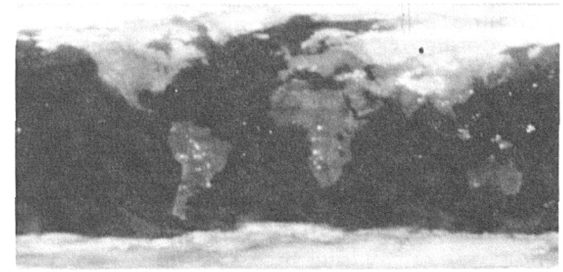

Figure 1b

Third Principal Component Score

Figure 1c

The second eigenvector is heavily influenced by frequency since the major contributions come from 19-H and the two 85 GHz channels. This appears to be caused by the separation of scattering targets (snow, multi-year ice and precipitation) from absorbing targets (land, ocean and first year ice) (Ferraro et al, 1986). Again it is well to remember that the other channels contribute so that this is not purely a frequency difference. The second principal component highlights snow, ice and precipitation (figure 1b).

The third is more confusing. It is heavily weighted by the difference between the 19-V and 22-V channels and the 37-H. The large weight at 22-V is most likely in response to variations

in water vapor over the oceans as 22-GHz is near the center of a strong water vapor absorbtion band at 22.235 GHz (Alishouse, 1983). This third principal component highlights the land vegetation cover. The third principal component is inversely related to vegetation cover being high over deserts and low over vegetation (figure 1c).

Regardless of the physical nature of these three vectors, they are useful in determining the nature of the target for a given pixel.

Linear regression of 587 ground truth points of total precipitable water and the 7 SSM/I channels explained 95.33 percent of the total variance while the first 3 principal components explained 95.21 percent. Channels 2, 3 and 5 alone explain 95.27 percent of the variance linearly, and 96.68 percent with a quadratic term on channel 3 (table 3). The first 3 principal components explain 96.01 percent of the variance using a quadratic fit but a linear fit of just the first and third principal component explains 95.21 percent of the variance.

Regression of channel values

	Coefficients			
	Regress.	Beta	error	t-value
B[0]	15.75048		1.60180	9.83
22-V	-0.17630	-2.393	0.01441	-12.24
22-V^2	0.00057	3.504	0.00003	17.93
37-H	-0.01672	-0.178	0.00114	-14.66

root mean square error = 0.3084 cm
explained variance = 0.9668
number of points = 587

Table 3

Regression of Principal Components

	Coefficients			
	Regress.	Beta	error	t-value
B[0]	-4.63808		0.07020	-66.07
P.C. 1	0.05237	0.708	0.00075	69.58
P.C. 3	0.03176	0.420	0.00077	41.31

root mean square error = 0.3705 cm
explained variance = 0.9521
number of points = 587

Table 4

The first and third principal components contain nearly all of the SSM/I information about total precipitable water. The same is true of cloud liquid water. For targets tested so far, including water, sea ice, land ice and snow, precipitation and vegetative cover over land the same first three principal components contain nearly all of the information contained in the full seven channel SSM/I data set (figure 2).

Estimate of Total Precipitable Water

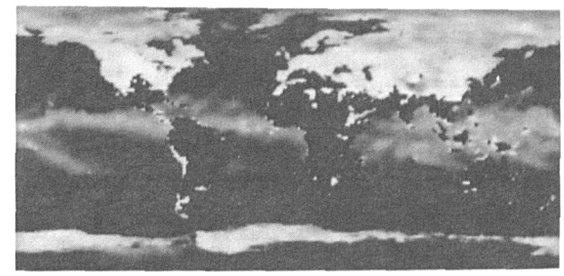

Figure 2

The ability to describe SSM/I targets in three dimensions simplifies processing of images. RGB images can be produced directly from SSM/I tape data sets on a PC based system and initial analysis can be done directly from these images. Color coordinate system rotations, pseudo color charts of algorithm outputs, and non-linear target coloring can be accomplished interactively to evaluate scenes for information content in a matter of minutes using these principal component images.

It is fully expected that not all of the useful information about the targets of interest is contained in just three principal components, but so much information is contained in them that more than a cursory analysis can be done. In the absence of ground truth it is possible to do a considerable amount of ordinal and relative classification of features using a global image and a knowledge of the geographic distribution of surface types and the shape and texture of atmospheric phenomenon.

Initial classification of the principal components over the oceans produced nearly the same model for precipitable water as the regression analysis. Units could not be accurately placed on the output of such a model but the vector direction of increasing atmospheric humidity was correctly measured from the initial global image alone. The procedure is to locate several pixels over dry polar air masses and another group of pixels over moist tropical air masses. The

equation of the line between these two points is then a crude model of the target being measured.

Vector Direction Model:

	Coefficient
intercept	-1.12245
Princ. Comp. 1	0.03680
Princ. Comp. 2	-0.03391
Princ. Comp. 3	0.02550

Knowing that dry air was near zero and very moist air was near 7 cm the range of the model could be estimated. This turned out to be close to the regression model. Regression of the values for the global image of the regression model output estimated by the vector direction model output yielded an r-squared of 0.977 with an intercept of -0.21 and a slope of 0.962.

The connection of targets produced a model which shows the second principal component to be as important as the first. This was not found to be the case in the regression analysis using ground data. The ratio of the coefficients for the first and third principal components are similar, 1.65 for the regression and 1.63 for the target connecting method.

4. APPLICATION TO HURRICANE GILBERT

Images of hurricane Gilbert show bands of precipitable water which are consistent with the structure of the storm (figure 3). Comparisons of the regression and target direction methods yield similar precipitable water fields over the ocean in all cases tested. The result over land is very different but the model does not work over land so this is of no consequence. The reason that the second principal component in the target direction model does not change the result is that the plot of precipitable water in principal component space is nearly 2-dimensional and cutting it in different directions can result in the same answer.

Estimate of Total Precipitable Water

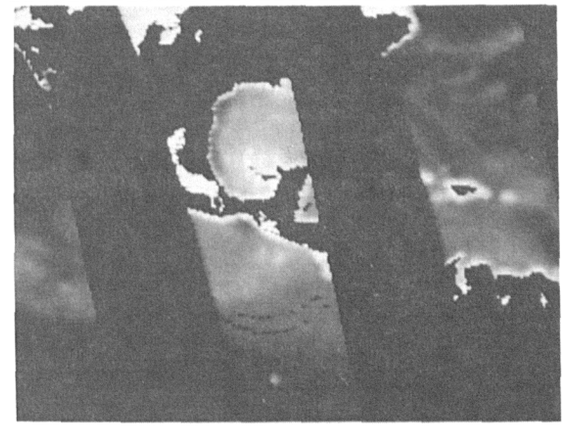

Figure 3

More data sets of SSM/I and ground truth are needed to test the true information content of these principal component images, but it is clear that they provide a way to view and organize SSM/I data in its entirety rather than a few channels at a time.

5. REFERENCES

Alishouse, J.C., 1983: Total precipitable water and rainfall determinations from Seasat scanning multichannel microwave radiometer. J. Geophys. Res., 83, 1929-1935.

Alishouse, J.C., S. Snyder and J. Vongsathorn, 1989: Determinations of total precipitable water in the tropics from the SSM/I. Fourth AMS Conference on Satellite Meteorology and Oceanography, San Diego, CA.

Ferraro, R.R., N.C. Grody and J.A. Kogut, 1986: Classification of geophysical parameters using passive microwave satellite measurements. IEEE Trans. Geosci. Remote Sensing, GE-24, 1008-1013.

Hollinger, J., R. Lo, G. Poe, R. Savage and J. Pierce, 1987: Special sensor microwave imager user's guide. Naval Research Laboratory, Washington, DC, 122pp.

CLUSTERING OF SATELLITE/SOUNDING RADIANCES TO MAXIMIZE MESOSCALE METEOROLOGICAL DETAIL

Donald W. Hillger and James F.W. Purdom

NOAA/NESDIS/RAMM Branch/CIRA
Colorado State University, Fort Collins, CO 80523-0033 USA

1. INTRODUCTION

Clustering is used to optimize the retrieval of mesoscale meteorological detail in satellite sounding radiances. By placing sounding fields-of-view (FOVs) into groups of similar radiances, the mesoscale details are maximized, compared to arbitrary blocking of FOVs into a fixed block size. Both methods reduce the number of retrievals that need to be performed, but clustering takes advantage of similarity among the radiances to strengthen gradient information compared to arbitrary blocking techniques.

2. VAS DATA

The area of concern is shown in Figure 1. The VISSR Atmospheric Sounder (VAS) FOVs are at 15 km resolution in the east-west direction and about 23 km resolution in the north-south direction (due to the large zenith angle at this latitude). There are 19 lines of 45 elements each, or 855 FOVs minus missing values, covering an area about 450 km by 650 km. All FOVs are cloud free with some possible minor exceptions. Clustering is used to distinguish variations in VAS radiances and, therefore, in the temperature and water vapor structure in the area of concern.

3. CLUSTERING VERSUS BLOCKING

The mechanics of clustering as applied to mesoscale VAS data are explained in a previous publication (Hillger and Purdom, 1988). This work compares the clustering technique to blocking techniques used for "operational" retrievals of soundings from satellite radiances.

The resolution of VAS large-field-of view sensors is approximately 15 km. To increase the signal-to-noise ratio of the VAS data, multiple FOVs are averaged together. The amount of horizontal averaging varies, depending on a tradeoff between the desire for high resolution and increased signal-to-noise. In mesoscale applications, a resolution of 20 to 75 km is typically used (Jedlovec, 1984 and 1985). Operational VAS retrievals on the VAS Data Utilization Center (VDUC) average together 11 x 11 small detector FOVs to achieve a resolution of about 75 km (Hayden, 1988). That is equivalent to about 5 x 5 large detector FOVs. So in this study retrievals using clustered FOVs are compared to retrievals using blocking of 5 x 5 large FOVs.

The clustering process utilizes principal component analysis to place the radiances into groups of similar radiances based on information in all the VAS channels, except channels 1 and 11 (Hillger and Purdom, 1988). VAS channel 1 was eliminated because of low signal-to-noise for that channel and VAS channel 11 was missing from the original dataset. Therefore, principal components (PCs) of the remaining 10 channels were clustered based on PCs 1 and 2. By using two PCs there were fewer clusters than the same data blocked into groups of 5 x 5 or 25 FOVs. (Results for three PCs are similar to those for two PCs with only a limited number of additional clusters.) The criteria for clustering the radiances are the noise levels in the various VAS channels. Each channel radiance is normalized by the noise level for that channel. Noise levels were determined by structure function analysis of the VAS channels (Hillger and Vonder Haar, 1988). Clustered radiances were allowed to vary by plus or minus the noise level. Variations within a cluster therefore are only those due to noise, and variations from cluster to cluster are due to signal-above-noise.

The clustering technique produced the clusters in Figure 2 as shown in principal-component space. Ellipses around the clusters show the cluster extent, based on noise levels in the VAS channels. The same clusters are shown in X-Y space in Figure 3. The cluster members are designated by the letters A-N (14 clusters). Most clusters contain more FOVs than the arbitrary blocks, but that is reasonable considering that the clustered radiances are similar and should be treated as a group. The cluster pattern gives an indication of predominantly east-west features in the field, with stronger gradients oriented in the north-south direction. In contrast all the equal-sized blocks in Figure 4 contain FOVs from more than one cluster. The blocked retrievals therefore are expected to vary more than the clustered retrievals, since he variability in the clusters is limited to the noise level in the radiances, while the variability within blocks is not limited.

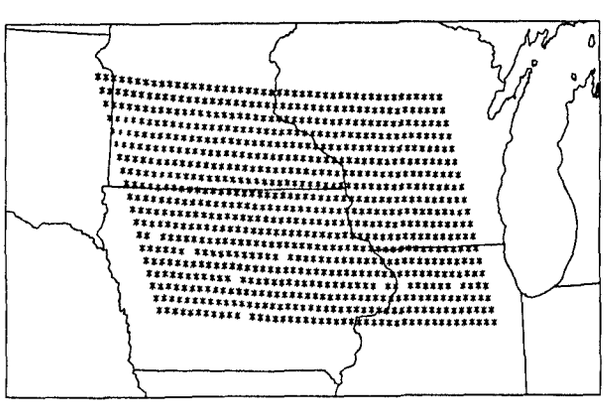

Figure 1: Selected VAS FOVs at 15 km (east-west) resolution for 7 September 1983 at approximately 14 UTC. Area is approximately 450 km by 650 km.

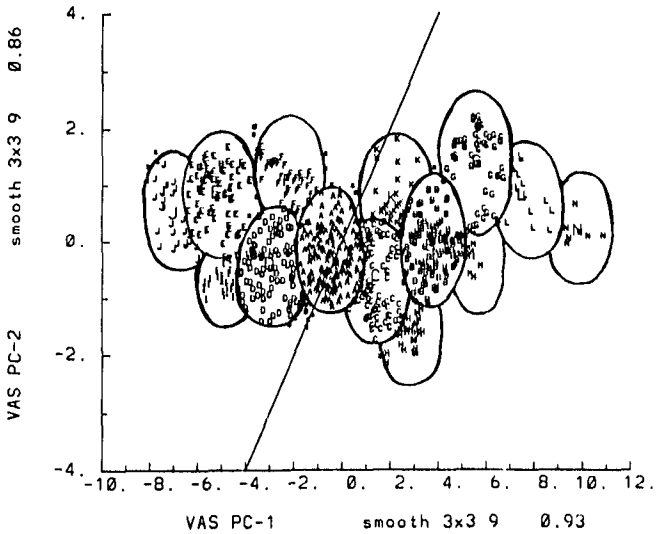

Figure 2: Clusters of VAS FOVs based on 2 principal components shown in principal-component space.

4. VAS RETRIEVALS

Retrievals are performed using the Smith, et. al., (1985) simultaneous temperature-moisture retrieval algorithm. Three retrievals are produced for each cluster, one representing the cluster means, and one each for the cluster minimum and the cluster maximum. Examples of retrievals for cluster A are shown on the skew T- log P plot in Figure 5. The thickest temperature and dew point temperature lines are for the cluster mean and the other lines show the spread in retrievals allowed by the variations due to noise. In contrast, a much larger spread in retrievals is evident in Figure 6 for block 12 (counting from upper-left, at the intersection of lines 6-10 and elements 11-15) which contains FOVs mostly, but not exclusively, from cluster A. The larger spread in retrievals is due to the arbitrary blocking picking values from more than one cluster (A, C, and K). Soundings for the adjacent block 11 (at the intersection of lines 6-11, and elements 6-10) are shown in Figure 7. There is much more variability in this block, because it contains FOVs from 6 clusters.

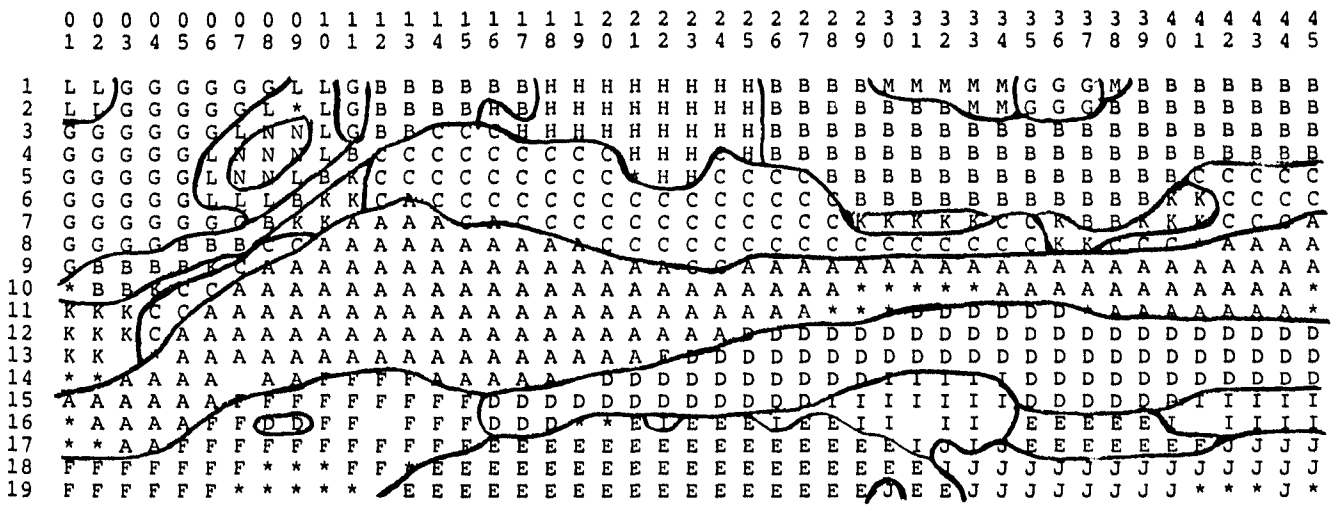

Figure 3: Clusters of VAS FOVs based on 2 principal components shown in X-Y space.

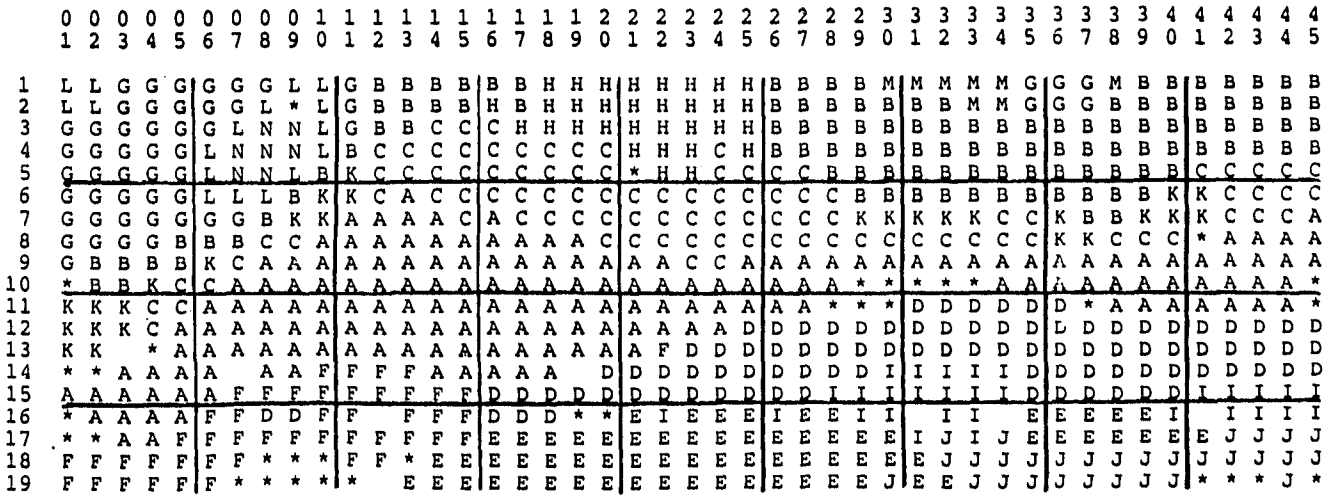

Figure 4: Blocks for "operational" 5 x 5 blocking of VAS FOVs shown over clusters in Figure 3.

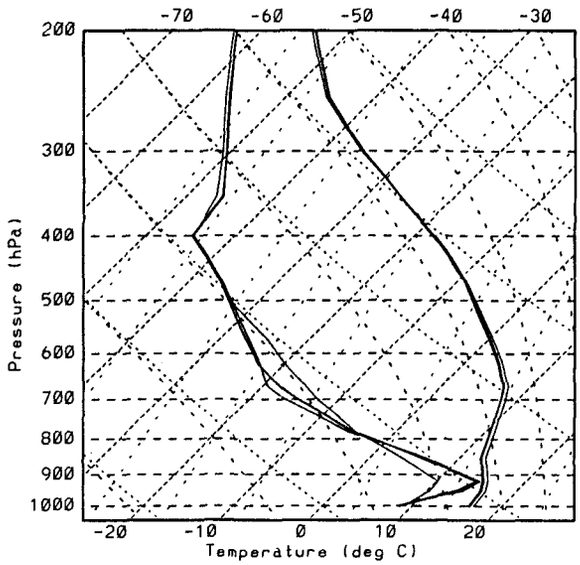

Figure 5: Examples of retrievals for cluster A. Shown are retrievals on the cluster mean, minimum, and maximum.

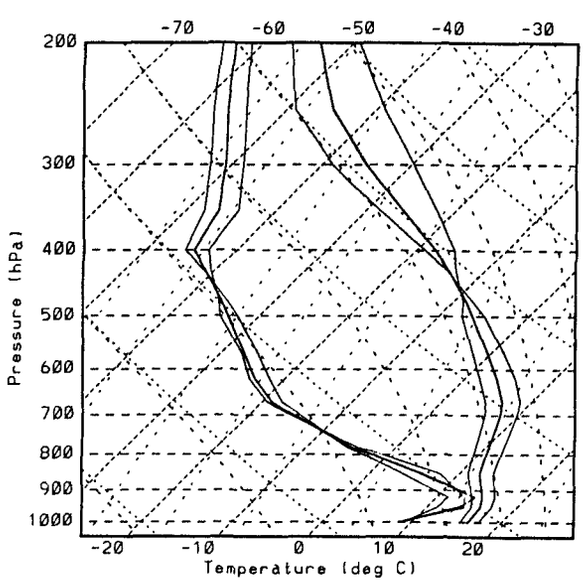

Figure 6: Examples of retrievals for block 12. Shown are retrievals on the block mean, minimum, and maximum. Note the larger variability in retrievals, due to FOVs from clusters A, C, and K.

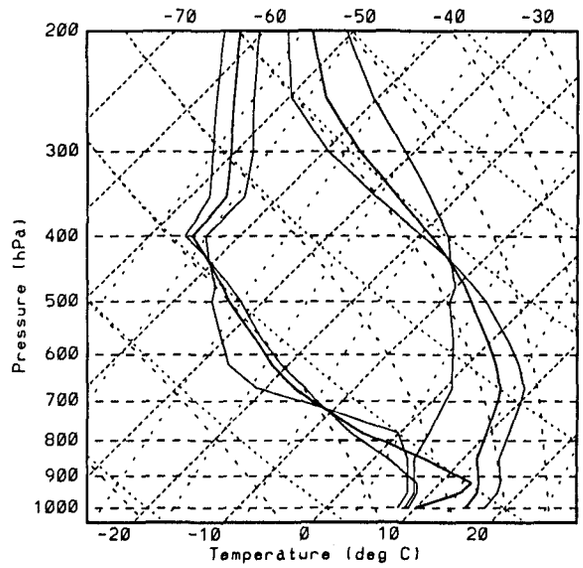

Figure 7: Same as Figure 6 but for block 11. Note the even larger variability in retrievals, due to FOVs from six clusters.

5. HORIZONTAL AND VERTICAL CROSS-SECTIONS

Horizontal and vertical cross-sections were produced from retrievals on both the clustered and blocked VAS data. In the case of the clustered retrievals only the cluster average profile is used, but that cluster-average retrieval was spread over the domain designated by that cluster. (For example, the A cluster retrieval was spread over all the FOVs labeled as A in Figure 3.) The method of spreading the influence over the cluster is based on the distance in radiance space from the cluster average (or center). FOVs closer in radiance space to the cluster center are weighed more and FOVs farther away are weighed less. Consideration was also given to adjacent clusters, with more than one cluster center considered in the weighting for the resulting profile at each FOV. Therefore, retrievals near cluster boundaries have characteristics of the cluster on each side of the boundary.

An example of a horizontal field based on clustered retrievals is shown in Figure 8. The 700 hPa temperature field shows mesoscale features which might not be expected on a small scale. The lower temperatures in the northwest corner of the field may be due to sub-resolution clouds in the VAS data. Fractional-FOV clouds can lower the temperatures, since the area was considered to be cloud free based on channel 8 (11 μm) VAS data. Clustering, therefore, may be useful for detecting and eliminating areas of sub-resolution cloudiness. The same field produced from blocked retrievals is shown in Figure 9. Note the smoother horizontal features, lacking mesoscale detail, with gradients not as strong as those in the clustered retrievals.

Some of the small-scale features in Figure 8 may or may not be real since high resolution conventional RAOB data are not available for verification. However, a previous publication showed some comparisons of VAS retrievals for this case with synoptic-scale RAOBs (Hillger and Purdom, 1988). Results of VAS/RAOB comparisons showed that the large-scale features are faithfully reproduced. Thus, it seems reasonable that smaller-scale features are similarly reproduced.

An example of a vertical cross-section is given in Figure 10. This is a north-south cross-section along element 22, about midway through the horizontal field. Shown is the temperature anomaly, with the horizontal mean subtracted to emphasize horizontal gradients. A cross-section of blocked-retrievals is similar and not shown. The main difference between the clustered and blocked retrievals is in the horizontal sections shown above.

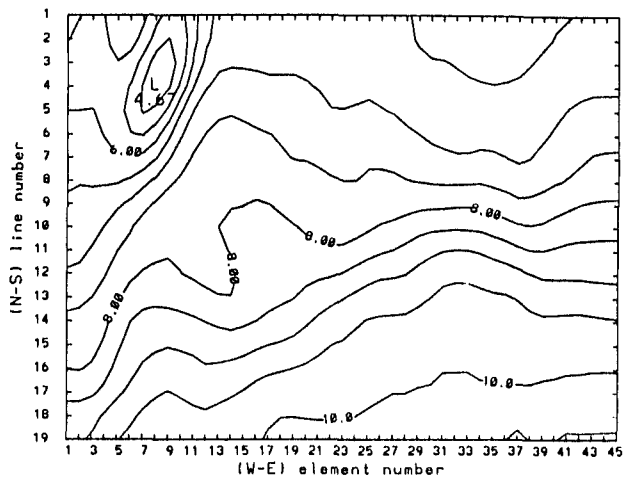

Figure 8: Horizontal field of 700 hPa temperatures derived from retrievals on blocked FOVs.

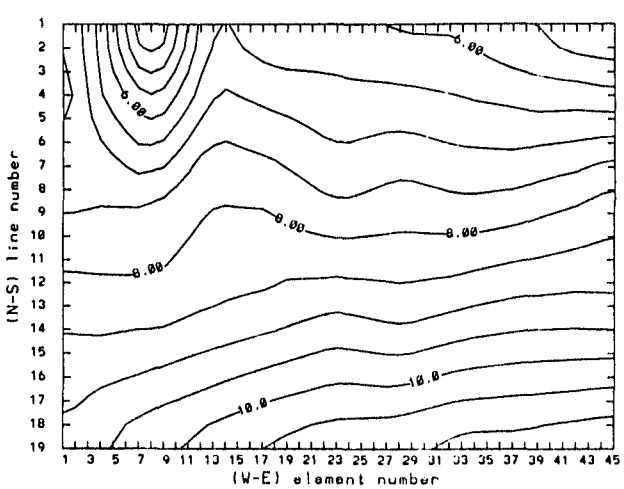

Figure 9: Horizontal field of 700 hPa temperatures derived from retrievals on blocked FOVs.

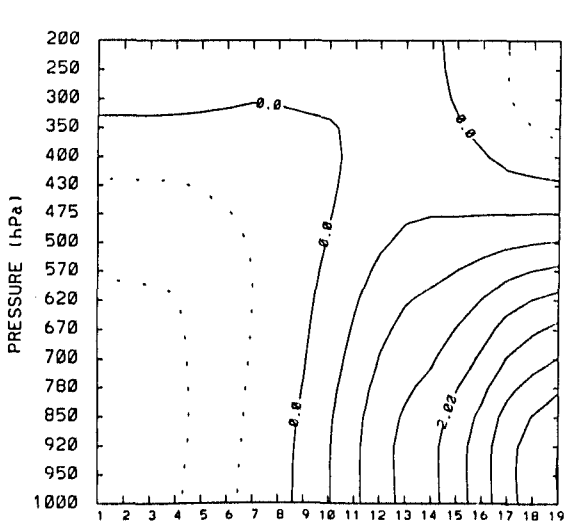

Figure 10: Vertical cross-section of temperature anomaly for a north-south section midway through the area of concern.

6. SUMMARY AND CONCLUSIONS

Comparisons were made of mesoscale satellite soundings based on VAS data treated two different ways. One way was by clustering the VAS data into groups of similar radiances with limits based on the noise levels of the VAS channels. The other way was by arbitrary blocking of VAS data into blocks with resolutions similar to that used for operational VAS retrievals. The clustered retrievals show more horizontal mesoscale detail due to the more natural grouping of the VAS data.

ACKNOWLEDGEMENTS

This work was supported by NOAA contract NA85RAH05045 (5-31208 and in part by 5-31209). Thanks to Mrs. Debbie Eckdahl for typing the manuscript.

REFERENCES

Hayden, C.M., 1988: GOES-VAS simultaneous temperature-moisture retrieval algorithm, J. Appl. Meteor., 27, 705-733.

Hillger, D.W. and J.F.W. Purdom, 1988: Clustering of VAS radiances to distinguish air mass characteristics, International Radiation Symposium, IAMAP, 18-24 August, Lille, France, 5 pp.

Hillger, D.W. and T.H. Vonder Haar, 1988: Estimating noise levels of remotely-sensed measurements from satellites using spatial structure analysis. J. Atmos. Ocean. Tech., 5, 206-214.

Jedlovec, 1984: A statistical evaluation and comparison of VISSR Atmospheric Sounder (VAS) data and corresponding rawinsonde measurements. NASA Technical Memorandum 82575, NASA/MSFC, 11 pp.

Jedlovec, 1985: An evaluation and comparison of vertical profile data from the VISSR Atmospheric Sounder (VAS). J. Atmos. Ocean. Technol. 2, 559-581.

Smith, W.L., H.M. Woolf and A.J. Schreiner, 1985: Simultaneous retrieval of surface atmospheric parameters: a physical and analytically direct approach. Advances in Remote Sensing, A. Deepak, H.E. Fleming and M.T. Chahine (Eds.), A. Deepak Pub., ISBN 0-937194-07-7, 221-232.

TOVS AND THERMODYNAMIC CONTROLS ON TROPICAL DEEP CONVECTION

Siri Jodha Singh Khalsa
Cooperative Institute for Research in Environmental Sciences
University of Colorado
Boulder, CO 80309-0449

1. MOTIVATION

The onset and maintenance of large-scale, organized deep convection in the tropics is controlled by two principal factors: thermodynamic instability and dynamical forcing. The former determines the energy in the atmospheric profile that can be released by the upward motion associated with the latter.

It has been noted that over the tropical oceans the climatological distribution of deep convection is largely coincident with surface water temperatures above 28°C. A warm surface can create instability by heating and moistening the air immediately above it. But organized convection, unlike sea surface temperature (SST), has a high spatial variability on subseasonal time scales.

Some of the variability in deep convection is tied to changes in atmospheric thermodynamics. If stability is parametrized as the buoyancy of a low-level parcel of air when lifted to midtroposphere, then we can examine separately the low-level and mid-level influences on stability. Over the oceans, lower tropospheric levels are affected by the SST as well as by low-level winds through evaporation and advection of temperature and moisture. Constraints to deep convection occur in the middle troposphere where variations arise mostly through advection or modifications of the atmospheric profile by deep convection. The effects of midlatitude disturbances on tropical stability are often manifest at this level.

The purpose of this work is to examine the relative importance of lower vs. middle tropospheric conditions in determining atmospheric static stability over the tropical oceans. We will examine these relationships for interannual, intraseasonal and higher frequency time scales. We will also examine the relationship of stability to deep convection as inferred from outgoing longwave radiation (OLR).

2. DATA AND METHODOLOGY

2.1 TOVS

The atmospheric temperature and moisture data that we used were derived from the NESDIS TOVS archive tapes. Slightly over 6 years of data (October 1981 through December 1987) have been interpolated onto daily 5° x 5° grids. Moisture variables at the temperature layers have been derived from the three available layers of precipitable water based on the assumption that relative humidity varies linearly with height (Khalsa and Steiner, 1988).

2.2 Stability Index

A stability index (SI) was defined as the difference between the value of saturated equivalent potential temperature at the third (500-700 hPa) TOVS level, θ_{es3}, and the value of equivalent potential temperature at the first (1000-850 hPa) level, θ_{e1}. Due to the coarse vertical resolution of the operational TOVS product this measure is not perfect. However, comparisons with *in situ* data from the tropics show that it is a good indicator of thermodynamic conditions relevant to static stability (Khalsa, 1989).

2.3 Filtering and analysis

To isolate variations on the time scales of interest, the following procedures were applied to the data. For interannual variability and intraseasonal variability, five day, non-overlapping averages were computed over the period of record. These time series then had the annual cycle removed by subtraction of the long-term (6 year) mean at each grid point. A 12 month (73 pentad) running mean was applied to determine interannual variability. A recursive digital filter was used to isolate fluctuations in the 28-72 day range. For identification of high frequency variability, the daily time series for each of 6 winter (Nov. - Mar.) seasons had a 5 day running mean removed.

The variance of SI can be expressed as

$$\sigma^2(SI) = \sigma^2(\theta_{e1}) + \sigma^2(\theta_{es3}) - 2 * COV(\theta_{e1},\theta_{es3})$$

where σ^2 is the variance and COV is the covariance. To the degree that θ_{e1} and θ_{es3} vary in unison, the variance in stability is reduced. The squares of the simple correlation coefficients $r(SI,\theta_{e1})$ and $r(SI,\theta_{es3})$ may be interpreted as the fraction of SI variance explained by θ_{e1} and θ_{es3}, respectively. The two terms will sum to one only where there is no correlation between θ_{e1} and θ_{es3}.

3. RESULTS

3.1 Time Series

Fig. 1a shows 5 day averages of SI at 2.5°S, 172.5°E for the period of record. The annual cycle has not been removed. Variations across a broad range of time scales are evident. In the latter half of 1982 stability is low with quasi-periodic fluctuations on a 40-50 day time scale. These oscillations are followed by a rapid change to stable conditions in early 1983. The cause of this abrupt change is the movement of the warmest waters and bulk of convection to east of the dateline during the El Niño/Southern Oscillation (ENSO). The oscillations at the end of 1984 and 1985 have periods of 30 days or less. Day-to-day variability of SI values are also substantial as shown by Fig. 1b.

3.2 Variances

The variances of θ_{e1}, θ_{es3} and SI for the period of record (no filtering other than 5 day averages and removal of the annual cycle has been done) are shown in Fig. 2. θ_{es3} variance (Fig. 2b) is at a minimum along the equator and maximum poleward of 20° where disturbances in the midlati-

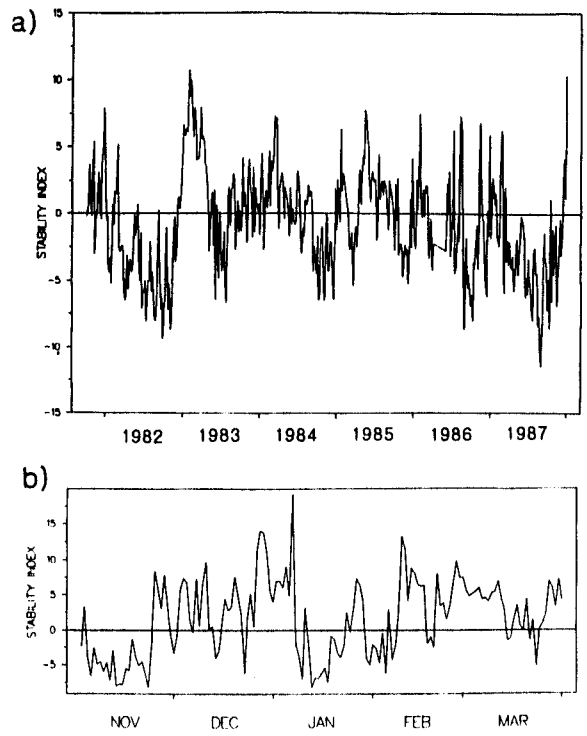

Fig. 1. Time series of the stability index at a) 2.5°S, 172.5°E for the period of record and at b) 7.5°N, 147.5°E for the northern hemisphere winter of 1981/82.

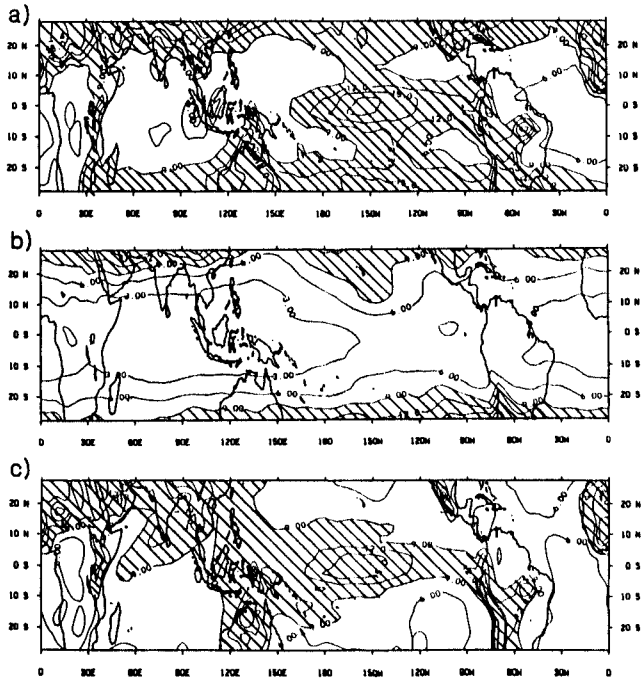

Fig. 2. Variance of a) θ_c (1000-850 hPa), b) θ_{cs} (700-500 hPa), and c) SI for October 1981 through December 1987. The annual cycle has been removed from the data. Values greater than 9 deg^2 are hatched.

tude circulation create large fluctuations in midtropospheric temperatures. Except for the equatorial central Pacific, where SST anomalies during ENSO increase θ_{e1}, the variance in θ_{e1} (Fig. 2a) is, for the most part, greater in the subtropics than in the tropics. Although the variances of both θ_{e1} and θ_{es3} are large in the subtropics, the variance in stability is small over most of the subtropical oceans (Fig. 2c). This is attributable to the high correlation between θ_{e1} and θ_{es3} at these latitudes. When midlatitude disturbances produce similar perturbations in both θ_{e1} and θ_{es3} there is only a small net affect on stability.

We wish to focus our attention on those regions where there is substantial variance in SI, which is equivalent to isolating areas where θ_{e1} and θ_{es3} act independently to affect atmospheric stability. Thus we will examine the magnitude of SI variance (rather than the fraction) explained by θ_{e1} and θ_{es3}.

3.2.1 Interannual Variations

On interannual time scales the variance in SI produced by θ_{e1} and θ_{es3} (Figs. 3a and 3b) is maximum for both variables over the equatorial Pacific and Indonesia. These are the regions where the largest anomalies in SST and convection occurred during the 1982-83 ENSO. The variance from θ_{es3} occurs in two distinct centers whereas the variance from θ_{e1} is continuous across the Pacific. Examination of the correlation coefficients reveals that θ_{es3} is negatively correlated with SI east of the dateline and positively correlated over Indonesia. During ENSO lower stability in the eastern Pacific is associated with higher θ_{es3} which suggests that persistent deep convection heated the middle and upper atmosphere in a region that is normally suppressed. The tendency for θ_{es3} to increase stability is apparently overwhelmed by the tendency for high SST and θ_{e1} to decrease it.

Stability increased over Indonesia during ENSO with contributions from low and middle levels being similar. Stabilization occurred through a decrease in θ_{e1}, mostly the result of a large decrease in humidity, and an increase in θ_{es3}. The latter may have been the result of subsidence heating as this region came under the descending branch of the Walker Circulation.

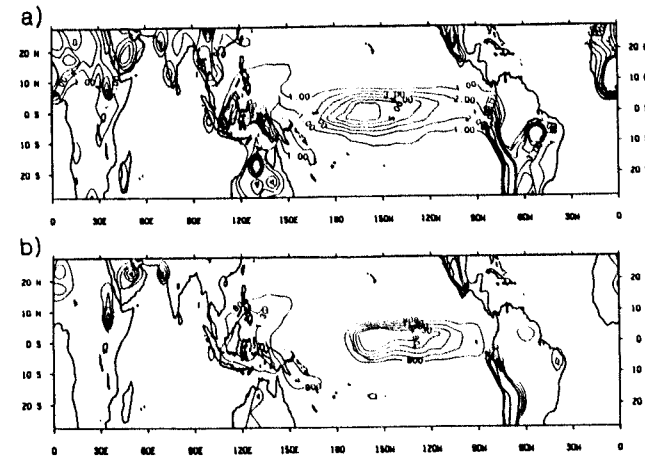

Fig. 3. Interannual variance in SI from a) θ_c (1000-850 hPa) and b) θ_{cs} (700-500 hPa).

3.2.2 Intraseasonal Variations

The intraseasonal variability in SI is manifest mainly in the Indian Ocean, off the Asian coast, and in the south Pacific convergence zone (Fig. 4). The contribution from θ_{e1} is roughly twice that from θ_{es3}. The pattern of θ_{es3} variance is very similar to the anomalous vertically integrated water vapor transport associated with the 30-60 oscillation during the Indian summer monsoon as shown by Chen et al. (1988).

3.2.3 High Frequency Variability

On the 1-5 day time scale during northern winter the variance in SI arising from θ_{e1} is broadly distributed over the Indian and western and central Pacific oceans (Fig. 5a). Higher values are also seen in the intertropical convergence zones over

the eastern Pacific and Atlantic oceans. The contribution from θ_{es3} has a roughly similar distribution (Fig. 5b) although magnitudes are one third to one fifth those associated with θ_{e1}. Maxima from both θ_{e1} and θ_{es3} occur in the vicinity of 140°E to the dateline between the equator and 10°N. This region exhibits low and even negative correlations between θ_{e1} and θ_{es3}.

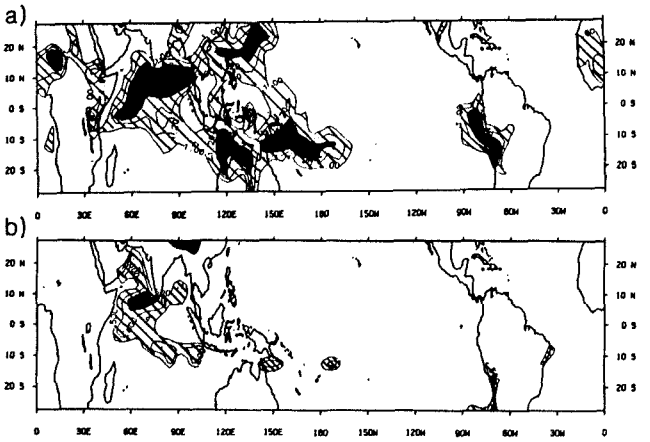

Fig. 4. As in Fig. 3, but for intraseasonal (30-60 day) variance. In a) values greater than 1.0 (1.4) deg^2 are hatched (solid). In b) values greater than 0.5 (0.7) deg^2 are hatched (solid).

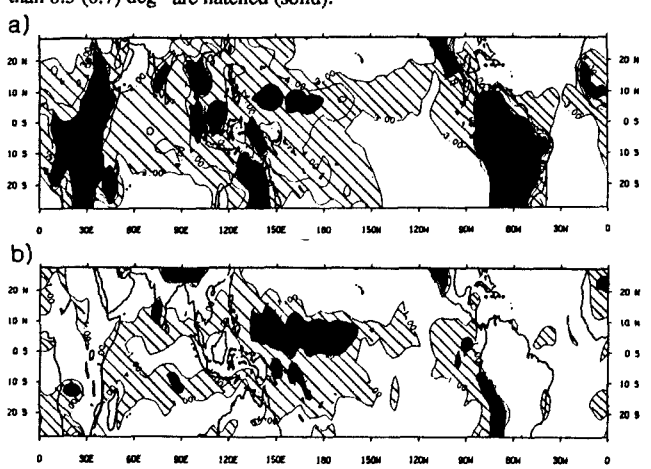

Fig. 5. As in Fig. 3, but for high frequency (periods of 5 days or less) variance. In a) values greater than 3.0 (5.0) deg^2 are hatched (solid). In b) values greater than 1.0 (1.5) deg^2 are hatched (solid).

3.3 Correlations between SI and OLR

In Khalsa and Steiner (1988) it was shown that on monthly time scales the distribution of lowest SI was largely coincident with highly reflective cloud, an index of deep convection. Here we examine correlations between SI and OLR, another measure of deep convection.

On interannual time scales the correlation of SI and OLR (Fig. 6a) is largest in the equatorial regions east of the dateline and over Indonesia and is similar to the pattern of interannual SI variance. Most of the changes in stability associated with ENSO were driven by the lower level which was warmed and moistened by increases in the sea surface temperature.

On the intraseasonal time scale, significant correlations (degrees of freedom > 100) occur in all ocean basins, principally between 10° and 20° latitude in both hemispheres (Fig. 6b). The largest values occur northwest of Australia, around the tip of India, and southeast of Hawaii. The latter region displays persistent circulation anomalies during certain phases of the zonally symmetric 30-60 day atmospheric angular momentum oscillation (Khalsa and Weickmann, 1988).

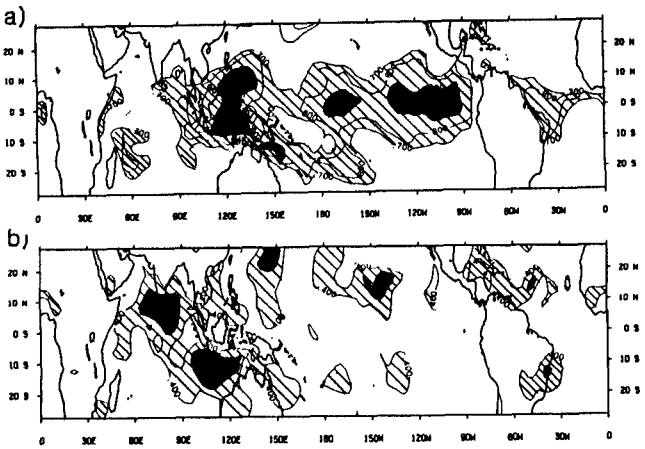

Fig. 6. Correlation between stability index and outgoing longwave radiation on a) interannual and b) intraseasonal time scales. In a) values greater than 0.7 (0.9) are hatched (solid). In b) values greater than 0.4 (0.5) are hatched (solid).

4. SUMMARY AND CONCLUSIONS

The interannual, intraseasonal and high frequency variations in SI each display distinctly different patterns. The largely ENSO-induced interannual changes in stability in the central and western Pacific were driven primarily by the low-level conditions in the atmosphere resulting from the anomalously high sea surface temperatures. Lower and middle tropospheric levels contributed equally to the secondary maximum in SI variance over Indonesia. The variance in stability on intraseasonal time scales from θ_{e1} was roughly twice that from θ_{es3}. For the high frequency variance in SI, the largest contributions from θ_{e1} are 3 to 5 times the largest from θ_{es3}.

The correlations between SI and OLR are high on interannual time scales where both are largely driven by changes in SST. On intraseasonal time scales the locations of the areas of high correlation between SI and OLR suggests that processes other than the direct influence of SST are responsible.

An improved understanding of the factors controlling atmospheric stability benefits diagnostic studies of variations in tropical convection. Atmospheric stability from TOVS is being used in investigations of the forcing mechanisms of the 30-60 day oscillation as discussed in Weickmann and Khalsa (1989) and Eischeid, Khalsa and Weickmann (1989).

5. ACKNOWLEDGEMENTS

This work was supported by the Equatorial Pacific Ocean Climate Studies (EPOCS) program of NOAA.

6. REFERENCES

Chen, T.-C., M.-C. Yen and M. Murakami, 1988: The water vapor transport associated with the 30-50 day oscillation over the Asian monsoon regions during 1979 summer. *Mon. Wea. Rev.*, **116**, 1983-2002.

Eischeid, J. K., S. J. S. Khalsa and K. M. Weickmann, 1989: Comparisons between the 30-60 day oscillations in the tropics and the varying frequency of atmospheric angular momentum oscillations. *Preprints 18th AMS Conference on Hurricanes and Tropical Meteorology*, May 16-19, 1989, San Diego, CA.

Khalsa, S. J. S., 1989: Atmospheric stability over the tropical oceans, derived from TOVS. *J. Appl. Meteor.* (in review)

Khalsa, S. J. S. and E. J. Steiner, 1988: A TOVS dataset for study of the tropical atmosphere. *J. Appl. Meteor.*, **27**, 851-862.

Khalsa, S. J. S. and E. J. Steiner, 1988: A climatology of atmospheric stability for the tropics derived from TOVS. *Preprints of the 3rd AMS Conference on Satellite Meteorology and Oceanography*, February 1-5, 1988, Anaheim, CA.

Khalsa, S. J. S. and K. M. Weickmann, 1988: A composite study of intraseasonal oscillations in atmospheric angular momentum and outgoing longwave radiation during northern hemisphere winter. *Proceedings of the 13th Annual Climate Diagnostics Workshop*, October 31 - November 4, 1988, Cambridge, MA.

Weickmann, K. M. and S. J. S. Khalsa, 1989: Observations of coupling between oscillations in northern hemispheric atmospheric angular momentum and the 30-60 day oscillations in the tropics. *Preprints of the 18th AMS Conference on Hurricanes and Tropical Meteorology*, May 16-19, 1989, San Diego, CA.

14.5

UNIQUE SIGNATURES OF SYNOPTIC FEATURES IN TIROS N SATELLITE DATA

G. A. White III and J. P. McGuirk

Department of Meteorology
Texas A&M University
College Station, Texas 77843-3146

1. INTRODUCTION

Observed tropical synoptic temperature variations are nearly absent from satellite derived temperature profiles. Enhanced information and increased resolution might be obtained through improved processing and analysis techniques using currently available data. White and McGuirk (1987) and White et al. (1988) described methods to extract meteorologically significant tropical synoptic features directly from satellite brightness temperatures. This research describes how these features can be quantified.

2. TECHNICAL CONSIDERATIONS

2.1 Radiative transfer model (RTM)

To develop analytical techniques a database of "satellite observed" synoptic features with known statistical properties was generated from a RTM. The RTM (Susskind et al., 1982) directly calculates satellite channel brightness temperatures that would have been measured from the TIROS N satellite had it viewed the atmosphere under study. The RTM supports 22 of the TIROS N's 27 channels.

2.2 Data

Nine tropical "seed" soundings of temperature and dew point, each containing a typical synoptic feature, were perturbed at each of 66 layers required by the RTM to generate a large set (50 each) of similar soundings. This random perturbation increased the sample size to one that is statistically meaningful given 22 satellite channels, while maintaining the integrity of the synoptic class. The perturbations of temperature and dew point in each sounding were introduced as white noise, highly correlated in the vertical, to simulate observed atmospheric variability. The nine seed soundings consisted of four inversions (frontal, radiation, turbulence and trade-wind), a warm-humid sounding, two observed island soundings, a warm anticyclone with a subsidence inversion, and the U.S. Standard Atmosphere to provide a baseline. The RTM produced 50 vectors of 22 brightness temperatures for each seed sounding.

2.3 Multivariate analysis

White and McGuirk (1987) demonstrated that such datasets can be partitioned, by variance, into two physically different portions: one explaining differences between synoptic sounding classes; the other detailing the fine structure within each sounding class. The former is

3.1 Sounding class (CDA)

CDA specifies the vertical structure functions by which the original soundings are sorted into their original classes. The first three structures are shown in Fig. 1. 58% of the between-class variance is contained in the first canonical variable. This variate senses tropospheric average temperature, even though the seeds possessed nearly identical mean temperatures. CAN2 explains 26% of the between-class variance, primarily in moisture and window channels. CAN3 accounts for 10% of the variance and is sensitive to mid tropospheric temperatures and surface temperatures of opposing signs. CAN2 and CAN3 together resemble a lapse rate signal with 2 being a moisture sensitive part and 3 being a moisture insensitive part. Rarely are more than three canonical variables required to explain most of the variance structure of satellite soundings.

3.2 Synoptic structure (RFA)

After classification, the synoptic characteristics of individual classes were quantified through their within-class variance. Factor analysis differentiates soundings from the same seed; the factors are rotated orthogonally to simplify structural information. Details of trade wind and frontal inversions are presented.

3.3 Specific inversion structures

Trade wind inversions are described by three factors (Fig. 2) explaining almost 90% of the total within-class variance. The first factor can be interpreted as a boundary layer lapse rate and average tropospheric temperature. Factor 2 contains the mid tropospheric water vapor channel and the near-surface temperature channels. Factor 3 shows surface contributions and a weak water vapor signal. Together they specify variations among trade wind inversions.

The frontal inversion is described by four factors (Fig. 3) which account for 94% of the variance within frontal soundings. Factor 1 describes lower tropospheric average temperature. Factor 2 relates temperature and moisture in the mid and upper troposphere. Factor 3 is a weak tropopause signal and is not shown. Factor 4 is a lapse rate signal.

4. CONCLUSIONS

The utility of satellite data depends, in part, on analysis methodology. This research describes splitting the variance of satellite observations into a portion which characterizes gross synoptic conditions, and a portion which quantifies details of the gross conditions. Factors identifying sounding types are different than those quantifying structural detail; structural factors vary between sounding types. Multivariate statistical techniques potentially can extend the use and information content of currently available satellite observations.

5. ACKNOWLEDGEMENTS

This research is supported by NASA's George C. Marshall Space Flight Center. GAW acknowledges the support of the U.S. Air Force Institute of Technology. Susskind and Reuter of the NASA Goddard Laboratory for Atmospheres provided the RTM.

6. REFERENCES

Susskind, J., J. Rosenfield, D. Reuter and M. T. Chahine, 1982: The GLAS physical inversion method for analysis of HIRS2/MSU sounding data. NASA Tech. Memo. 84936, Goddard Space Flight Center, Greenbelt, MD, 101 pp.

White, G. A. and J. P. McGuirk, 1987: Canonical discriminant analysis of synoptic signatures in satellite brightness temperature. Preprint from Tenth Conference on Probability and Statistics in Atmospheric Sciences, Edmonton, Alberta, Canada, Amer. Meteor. Soc.

_____, _____ and A. H. Thompson, 1988: Identification and recovery of discontinuous synoptic features in satellite-retrieved brightness temperatures using a radiative transfer model. Preprint from Third Conference on Satellite Meteorology and Oceanography, Anaheim, CA, Amer. Meteor. Soc.

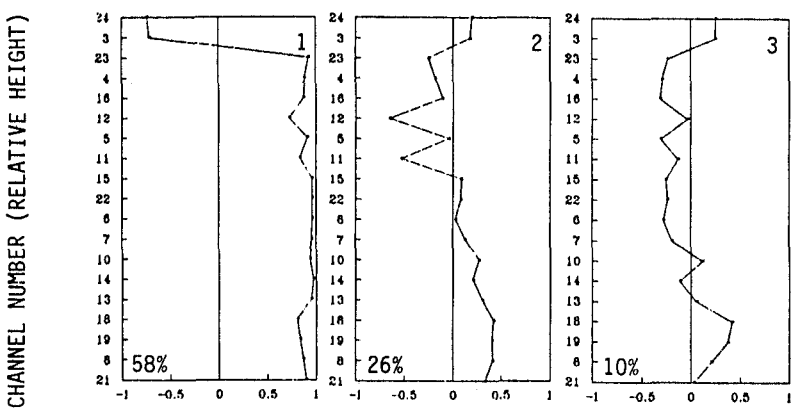

Fig. 1. Canonical variables identifying classes based on nine seed soundings. Channel numbers appear as the vertical axis according to each channel's weighting function maximum. Horizontal axis is the normalized channel amplitude. CAN1 represents tropospheric temperature; CAN2 represents water-vapor and surface window channels; CAN3 represents mid-tropospheric temperature and lapse rate. Per cent of explained between-class variance is given.

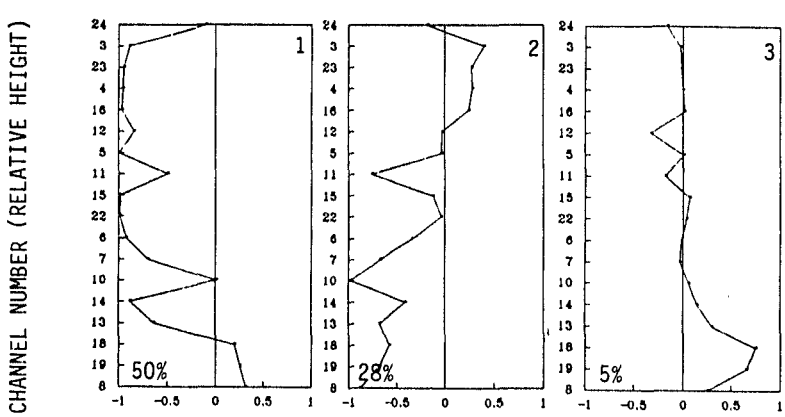

Fig. 2. Rotated factor loadings from a set of trade wind inversions. Axes as in Fig. 1. Factor 1 describes a near-surface inversion and tropospheric average temperature; factor 2 quantifies the amplitude of the trade wind inversion; factor 3 identifies low level moisture. Per cent of explained within-class variance is given.

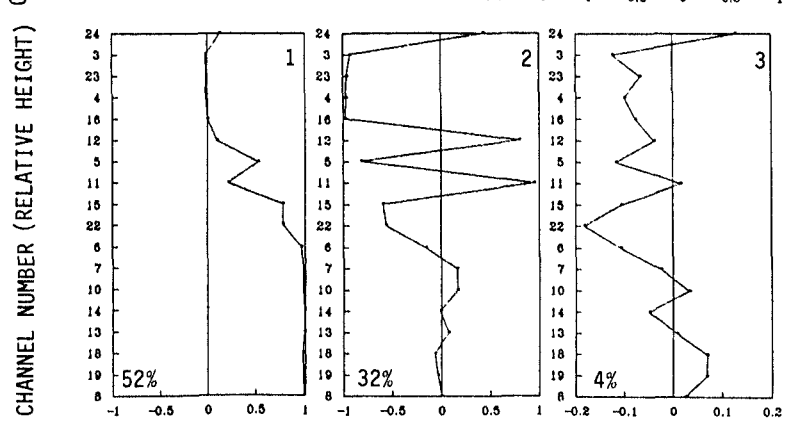

Fig. 3. As in Fig. 2, except for frontal inversions. Factor 1 quantifies lower tropospheric temperature; factor 2 is a mid and upper tropospheric temperature/moisture signal; factor 4 is a lapse rate signal (Note expanded scale).

15.1

GLOBAL DATA ASSIMILATION OF SSM/I WIND SPEED MEASUREMENTS

James S. Goerss
Naval Environmental Prediction Research Facility
Monterey, CA 93943-5006

1. INTRODUCTION

The SSM/I sensor is a passive microwave radiometer deployed on the DMSP F8 satellite to provide measurements of surface wind speed, water vapor column density, liquid water content, and ice concentration. Surface wind speed measurements are derived from this sensor over the ocean areas of the earth by taking advantage of the dependency of emissivity on the state of the sea surface. Along with other SSM/I parameters, satellite-derived measurements of surface wind speeds are currently produced on a real-time basis by Fleet Numerical Oceanographic Center (FNOC). In this paper the results of research being conducted at the Naval Environmental Prediction Research Facility (NEPRF) directed at the assimilation of SSM/I wind speed data into the Navy Operational Global Atmospheric Prediction System (NOGAPS) are reported. The statistical results of comparisons between the SSM/I wind speeds and wind speeds from the NOGAPS multivariate optimum interpolation (MVOI) analysis background are presented for the ocean areas of the world. The data from satellite passes over the Gulf of Mexico on 14-15 September, 1988 (Hurricane Gilbert) are compared with conventional observations. Finally, preliminary results of data assimilation experiments in which SSM/I wind speed data are incorporated into NOGAPS are presented.

2. ASSESSMENT OF SSM/I WIND SPEEDS

NOGAPS consists of a multivariate optimum interpolation analysis (Barker et al., 1988), nonlinear normal mode initialization, and a T47 spectral forecast model. It runs operationally with a 6-hour update cycle so that the background or first-guess fields for the MVOI analysis consist of 6-hour model forecasts valid at the analysis times. In order to assess the quality of the retrieved SSM/I wind speeds, statistics were computed for the differences between these wind speed observations and the MVOI background wind speeds interpolated to the observation locations.

First, SSM/I wind speeds for 6-hour intervals centered on 12 GMT September 14 and 15, 1988 were compared with the respective MVOI backgrounds. After thinning, the number of observations in each interval was approximately 15,000. The observations were stratified into three classes based upon wind speed: 0-5 m/sec, 5-15 m/sec, and greater than 15 m/sec. The respective root mean square (rms) differences between the observations and the backgrounds were 2.1 m/sec, 3.3 m/sec, and 8.1 m/sec. Upon further investigation it was found that about forty percent of the high wind speed reports were the result of contamination from high levels of liquid water or rainfall. The wind speed algorithm in use at this time is still under development. Communication with the algorithm developers revealed that an improved algorithm which would correct such deficiencies would probably be in place by spring of 1989. For the purposes of this study it was found that these observations could be screened out fairly effectively by rejecting any observation whose difference from the background was greater than 8 m/sec.

After screening the contaminated high wind speed observations, the differences between the SSM/I data and the backgrounds were compared with the differences between ship observations of wind speed and the backgrounds for the aforementioned time intervals. There were approximately 1000 ship observations in each interval. Statistics were computed globally and for six ocean basins (North and South Pacific, North and South Atlantic, and North and South Indian). The global rms differences were 3.1 m/sec and 3.3 m/sec, respectively, for the SSM/I and the ships. In each of the ocean basins the rms differences for the SSM/I observations were smaller than those for the ship reports.

The statistical comparisons outlined in this section were also performed for data intervals centered on 12 GMT September 21 and November 21 and 22, 1988. The results found were virtually identical to those reported here for September 14 and 15. Thus, it was concluded that the satellite wind speeds could be utilized in the MVOI analysis with as much confidence as the ship reports of wind speed.

3. DATA ASSIMILATION

The Navy's MVOI analysis is patterned after the volume method introduced by Lorenc (1981). The global analysis of geopotential height and wind is produced for the fifteen standard pressure levels between 1000 mb and 10 mb, inclusive, on a 2.5 x 2.5 degree spherical grid. The data used by the analysis include conventional observations of heights and winds, aircraft and satellite-derived wind observations, and satellite-derived thicknesses between the standard pressure levels. The analysis is such that the weights assigned each observation are chosen so as to minimize the estimated analysis error. The analysis error estimates can be computed along with the analysis itself and are functions of the error variances assigned each observation as well as those assigned to the analysis background. In this section the

analysis error estimates will be used to gauge the potential impact of the assimilation of SSM/I wind speeds into NOGAPS.

In order to use the SSM/I wind speed observations in the MVOI they must first be assigned a direction. A modified version of the analysis is run first which uses all available data other than the SSM/I data and produces analyses at 1000 mb, 850 mb, and 700 mb. The wind direction at 1000 mb from this analysis is interpolated to the location of each SSM/I observation and is assigned to it. All SSM/I observations are assumed to be at 1000 mb and are assigned the same error variance as a wind observation from a ship. In order to make the observational density compatible with a global assimilation system they are further thinned so that typically about 4000 observations are contained in a 6-hour interval.

For 12 GMT 15 September 1988 the MVOI analysis was performed with and without the use of the SSM/I data. Figure 1 displays the satellite observations along with the analysis of 1000 mb wind speed made without them for an area surrounding Hurricane Gilbert in the Gulf of Mexico. Figure 2 displays the same information along with the analysis made using the SSM/I data. Subjectively, the greatest difference between these analyses is just east of the Bahamas where a 25 knot isotach maximum can be seen in Figure 1 but is not evident in the analysis made with the SSM/I data. The ship reports are displayed in Figure 3 along with the 1000 mb D-value analysis made with SSM/I. Here it can be seen that there is no support for the high winds east of the Bahamas and that the SSM/I wind speeds are in good agreement with the wind reports in the Gulf of Mexico surrounding the hurricane. Figure 4 is a blow-up of Figure 2 with expanded SSM/I coverage for a more detailed look at the wind speed reports surrounding Hurricane Gilbert.

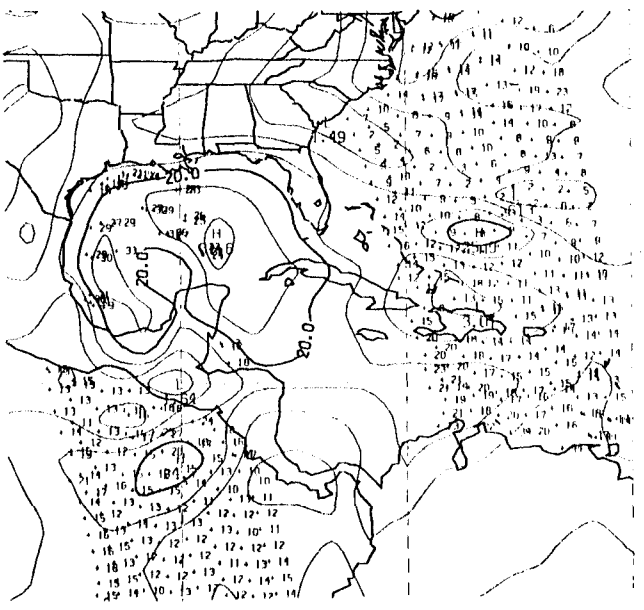

Fig. 1. SSM/I wind speeds in knots and MVOI 1000 mb isotach analysis (without SSM/I) for 12 GMT 15 September 1988.

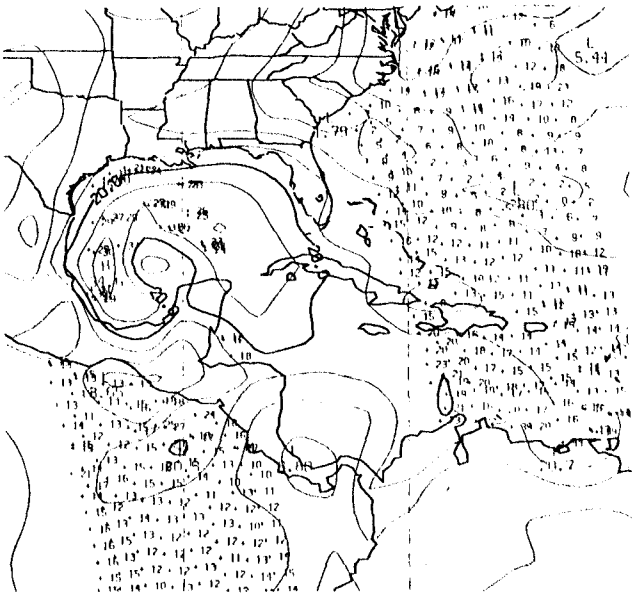

Fig. 2. SSM/I wind speeds in knots and MVOI 1000 mb isotach analysis (with SSM/I) for 12 GMT 15 September 1988.

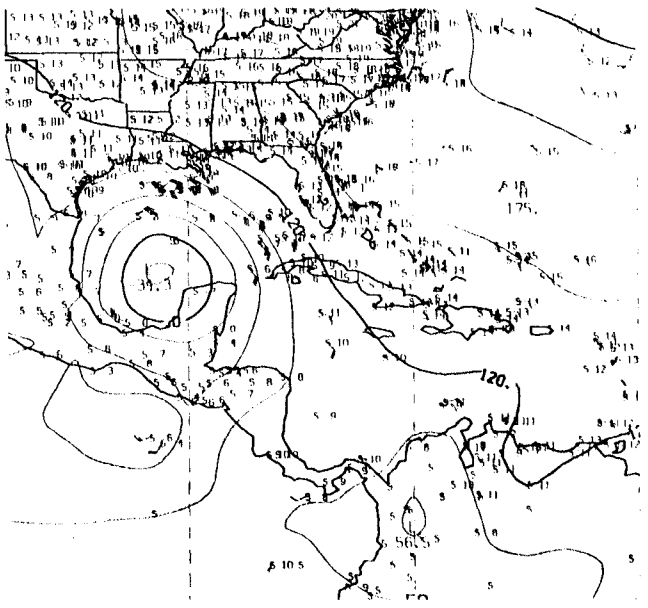

Fig. 3. Conventional surface observations and MVOI 1000 mb D-value analysis in meters (with SSM/I) for 12 GMT 15 September 1988.

In order to assess the potential impact of the SSM/I data on NOGAPS, analysis error estimates were produced for the 1000 mb u-wind and are displayed in Figures 5 and 6 for the conventional analysis and the one made using

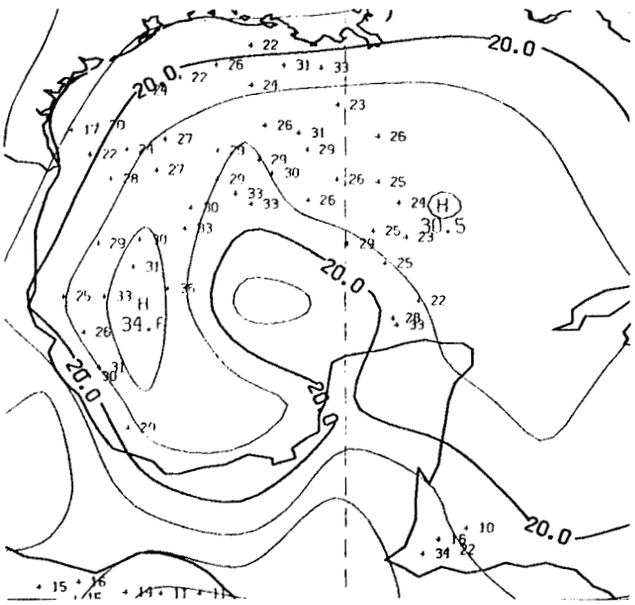

Fig. 4. Expanded coverage of SSM/I wind speeds in knots and MVOI 1000 mb isotach analysis (with SSM/I) for 12 GMT 15 September 1988.

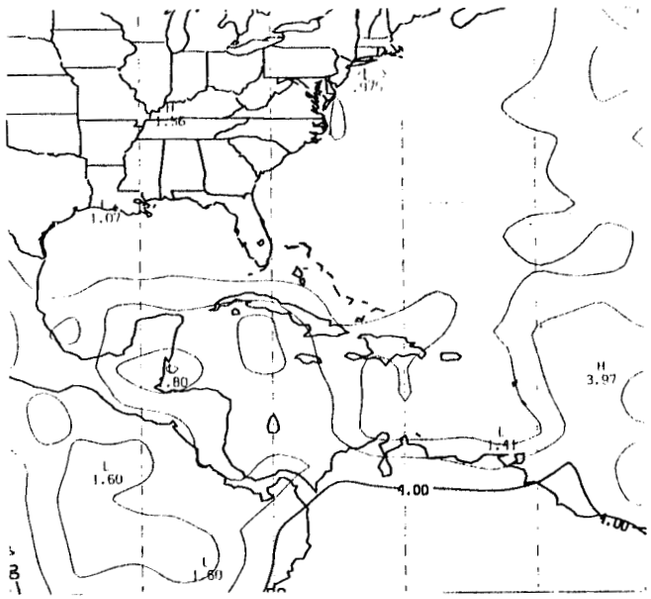

Fig. 6. MVOI 1000 mb u-wind analysis error estimate in m/sec (with SSM/I) for 12 GMT 15 September 1988.

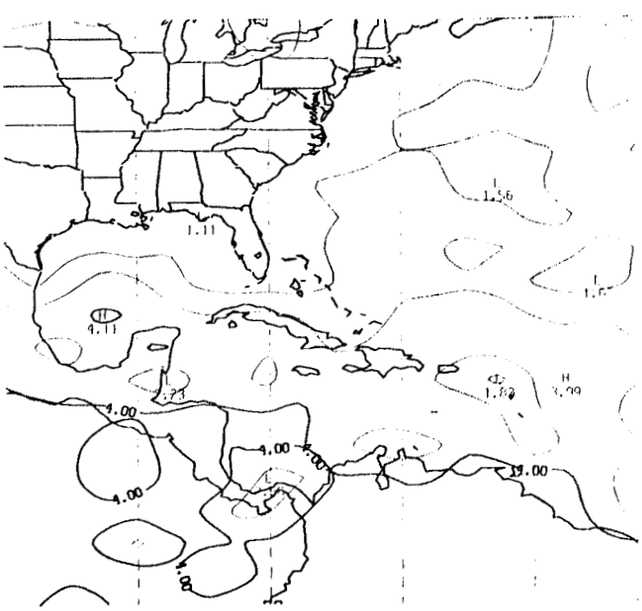

Fig. 5. MVOI 1000 mb u-wind analysis error estimate in m/sec (without SSM/I) for 12 GMT 15 September 1988.

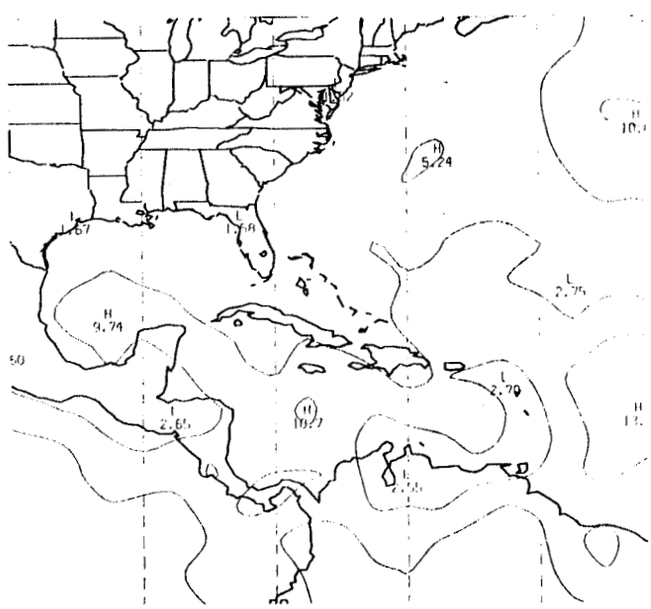

Fig. 7. MVOI 1000 mb height analysis error estimate in meters (without SSM/I) for 12 GMT 15 September 1988.

SSM/I data, respectively. The results for the 1000 mb v-wind were comparable and are not shown. Figures 7 and 8 display similar information for the respective 1000 mb height analyses. As one might expect, Figures 5 and 6 show substantial reduction in the error estimates in the areas covered by SSM/I swaths. The reductions in Figures 7 and 8 for the heights are more subtle although the analysis error estimate near the center of the hurricane is reduced nearly 2.5 m by the presence of surrounding SSM/I observations. This is due to the multivariate nature of the analysis and the geostrophic coupling between the heights and winds.

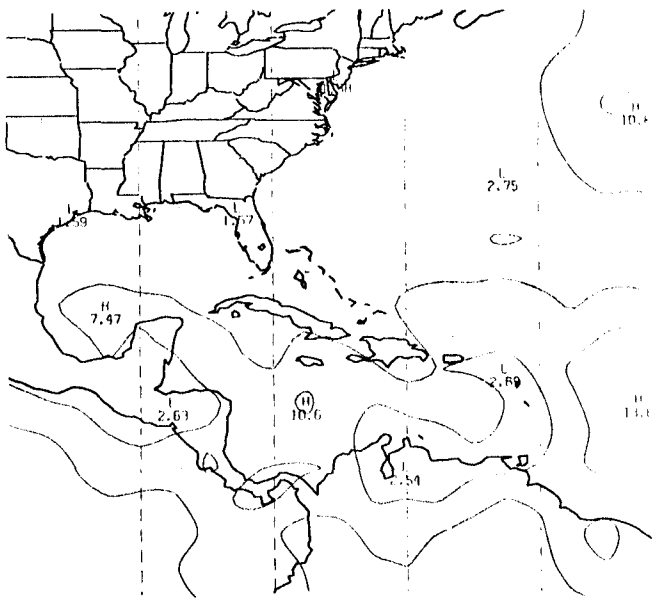

Fig. 8. MVOI 1000 mb height analysis error estimate in meters (with SSM/I) for 12 GMT 15 September 1988.

4. CONCLUSIONS

Examination of the SSM/I wind speed data has revealed that they are certainly of as good quality as the wind speeds reported by ships. Despite problems with the current algorithm, it was found that the data could be successfully assimilated into NOGAPS and estimates of the analysis errors indicate that the impact is likely to be positive. Subjective examination of the SSM/I wind speeds and analyses produced using them is also encouraging. With the implementation of an improved algorithm in spring of 1989, complete NOGAPS data assimilation experiments will be conducted with and without the SSM/I observations in order to determine whether they can indeed have a positive impact upon model forecasts.

5. REFERENCES

Barker, E., J. Goerss, and N. Baker, 1988: The Navy's operational multivariate optimum interpolation analysis method. Preprints Eighth Conference on Numerical Weather Prediction, Baltimore, MD.

Lorenc, A., 1981: A global three-dimensional multivariate statistical interpolation scheme. Mon. Wea. Rev., 109, 701-721.

ASSIMILATION OF AUTOMATED WINDS DERIVED FROM GOES MULTISPECTRAL IMAGERY

Steven D. Swadley and James S. Goerss

Naval Environmental Prediction Research Facility
Monterey, California 93943-5006

1. INTRODUCTION

Cloud motion vectors (CMV's) have been derived from sequences of geostationary satellite images since the late 1960's. Operational use of CMV's in global and regional analyses quickly became routine in the 1970's. With the subsequent implementation of Multivariate Optimum Interpolation (MVOI) schemes at many operational meteorological data processing centers, there existed a need for accurate knowledge of the inherent random observational errors. The determination of the errors, via structure and correlation function analysis (Gandin, 1963; Hillger and Vonder Haar, 1979; Morone, 1986; Swadley, 1988), for each of the various observation types will allow optimal assimilation of all the observational data.

Previous satellite wind impact studies (Lee and Houghton, 1984) have focused attention on describing and understanding the impact of these data on the model simulations. MVOI schemes can provide estimates of the analysis error which can be used to monitor the quality of the analysis. The purpose of this paper is to compare the MVOI analysis error estimates, with and without inclusion of new experimental CMV data, to determine the impact of the additional CMV data upon the analysis.

2. THE NAVY'S MULTIVARIATE OPTIMUM INTERPOLATION SYSTEM

The Navy's current global operational atmospheric prediction system (NOGAPS 3.0) consists of an MVOI analysis, nonlinear normal mode initialization, and a spectral forecast model at T47 resolution. Satellite data assimilation studies utilizing both the SSM/I wind speed data and GOES cloud tracked wind data are currently being conducted at the Naval Environmental Prediction Research Facility (NEPRF) with the NOGAPS system as a tool.

The Navy's operational MVOI system, described by Barker et al. , 1988, is patterned after the volume method of Lorenc (1981). Geopotential heights and u and v wind components are analyzed for 15 standard pressure levels from 1000 mb up to 10 mb on a global spherical grid with 2.5 x 2.5 degree resolution. Observational input data include conventional observations of heights and winds, aircraft winds, satellite wind and wind speed data, and satellite derived thicknesses between the standard pressure layers.

Buell's (1972) relationships for the multivariate background error covariances are used in this MVOI system. The covariances are expressed as products of the vertical and horizontal components. The horizontal structure function for height is a damped cosine function (Franke, 1987), which fits the covariances computed using a history of differences between NOGAPS 3.0 model's first guess and the U.S. and Canadian radiosonde data. An exponential function constructed with standard atmosphere heights is used for the vertical structure function. Satellite thicknesses are used directly, avoiding the necessity of including vertically correlated observational errors, which must be included when satellite data are used as heights.

Deviations from the observations and the model's first guess are interpolated via a bicubic method to the observation locations (Franke, 1985). Observational error variances are similar to those described by Shaw (1987), with the exception of the NASA/MSFC derived cloud tracked wind error variances which were computed by Swadley (1988).

3. NASA/MSFC's AUTOMATED CLOUD MOTION VECTOR SYSTEM

Wilson (1984) introduced a new multispectral technique for deriving mesoscale CMV's from geostationary satellites. The system was designed to produce mesoscale CMV's (approximately 10 km spacing) from 1 km resolution GOES rapid scan imagery. NEPRF has utilized this system with standard GOES imagery at 4 and 8 km resolutions. This provides a much greater areal coverage with nominal CMV spacings of about 40 and 80 km respectively. The current version utilizes the NOGAPS wind and temperature spherical grid fields as input to the system for first guess wind fields and IR blackbody height assignment.

The NASA/MSFC system utilizes "template matching" numbers to determine the relative similarity between an image template and the corresponding image search area (Barnea and Silverman, 1972). This technique, known as the Sequential Similarity Detection Algorithm (SSDA), involves the simple calculation of an absolute value difference between the pixel values in the template and the corresponding pixels in the search area for a given displacement. The displacement which yields the minimum "template matching" number, is considered the best match between the two image subscenes. The NASA/MSFC system employs a simple IR black-body temperature approach for height assignment of the CMV's.

Automatic QC for the NASA/MSFC system utilizes three objective image processing QC parameters. The first involves the elimination of all CMV's with SSDA minima that fall on the search area boundaries.

The other two are template match quality parameters defined as the ratios between the SSDA mean and the SSDA min and SSDA secondary min and the SSDA min. Utilization of these values has allowed a confidence stratification of the resulting CMV's.

4. DATA AND RESULTS

The MVOI analysis is such that the weights assigned each observation are chosen so as to minimize the estimated analysis error. These error estimates can be computed along with the analysis itself (Lorenc, 1981). Global output fields of the estimated analysis error were produced in order to compare the results between parallel runs with and without the NASA/MSFC CMV's.

Cloud motion vector fields were generated with the NASA/MSFC automated satellite wind system for 2330 UTC on 12 April, 1988. The CMV's were then combined with the operational observational data files for inclusion in the analysis. The NOGAPS 3.0 operational root mean square observation errors for both satellite wind and rawinsonde data are compared with the NASA/MSFC wind errors as computed by Swadley (1988).

Table 1. Root mean square observational wind component errors (m/sec).

Level (mb)	Sonde	AIDS/ ASDAR	Sat Winds	NASA/MSFC Winds
1000	2.3	3.5	3.5	1.5
850	2.4	3.5	3.5	1.5
700	2.5	3.5	3.5	2.2
500	2.8	3.5	3.5	2.2
400	3.3	3.5	5.0	3.3
300	3.7	4.0	5.0	3.3
250	3.5	4.5	5.0	3.8
200	3.0	5.0	5.0	4.0

4.1 The Control Case (No NASA/MSFC Winds)

The operationally available 700 mb CMV's for 0000 UTC on 13 April 1988, and corresponding MVOI height analysis are shown in Figure 1. All the CMV's displayed range in height ±1/2 standard pressure layer. The corresponding MVOI estimated analysis error fields for the geopotential height, u and v components are shown in Figures 2, 3 and 4 respectively.

4.2 THE NASA/MSFC WIND ASSIMILATION

The operational 700 mb CMV's for 0000 UTC on 13 April, 1988, combined with the 700 mb NASA/MSFC CMV's, and corresponding MVOI height analysis are shown in Figure 5. The corresponding MVOI estimated analysis error for the geopotential height, u and v components are shown in Figures 6,7 and 8 respectively.

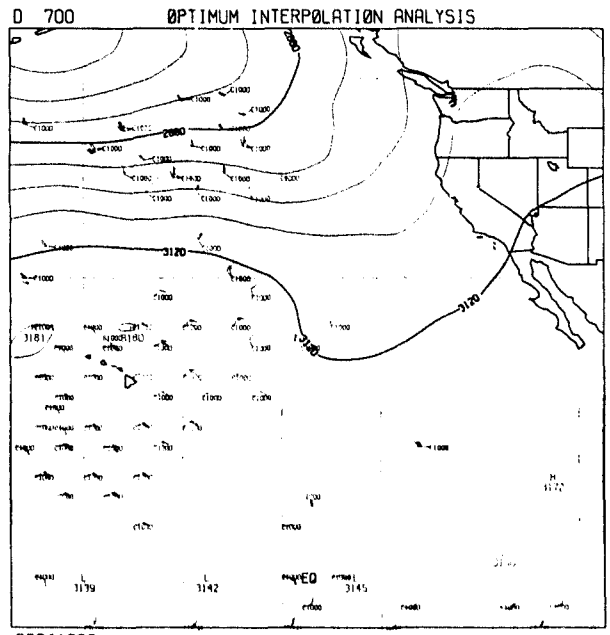

Fig. 1. Operational 700 mb CMV's and height analysis for 0000 UTC on 13 April 1988.

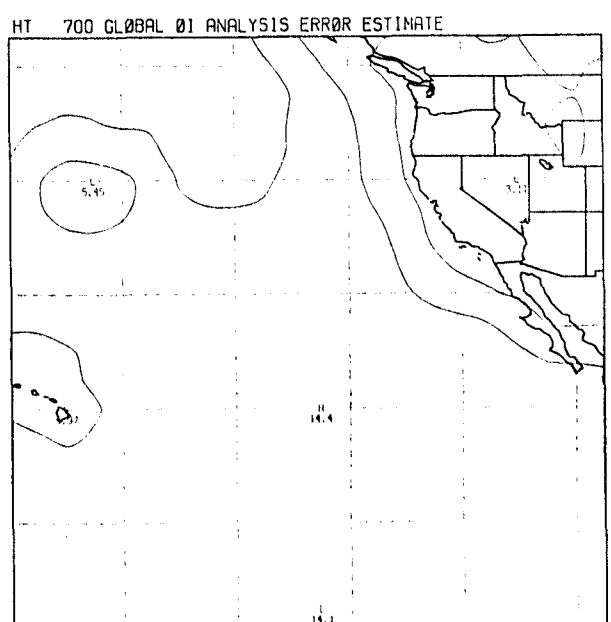

Fig. 2. MVOI 700-mb Analysis error estimate for geopotential height (no NASA/MSFC winds).

Significant lowering of the estimated analysis error occurs in the u and v component fields throughout the region. The height errors have also been lowered in latitudes where the geostrophic coupling is strong. The operational available winds were given the same error variances as the NASA/MSFC winds and some of the differences in the estimated analysis error fields can be attributed to this lack of discrimination between the wind types.

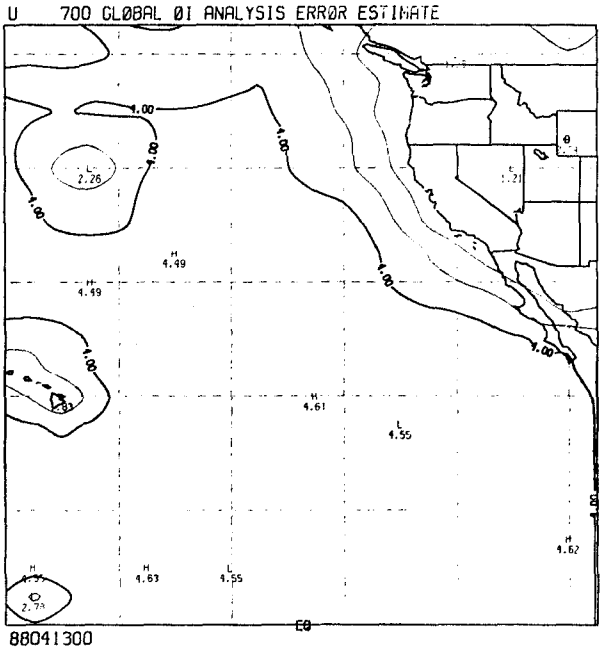

Fig. 3. MVOI 700-mb analysis error estimate for U component of wind (NO NASA/MSFC winds).

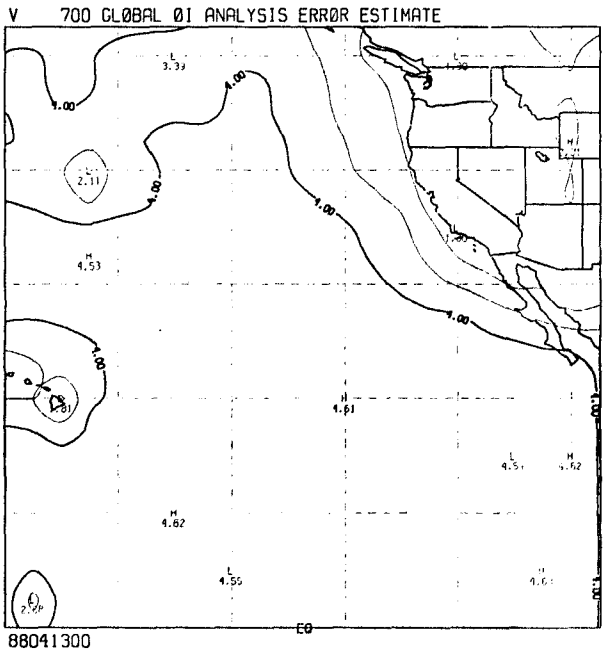

Fig. 4. MVOI 700-mb analysis error estimate for V component of wind (no NASA/MSFC winds).

5. SUMMARY AND CONCLUSIONS

The impact of the NEPRF derived NASA/MSFC cloud motion vectors on the NOGAPS analysis has been investigated via the MVOI's estimated analysis error fields. Significant lowering of the u and v component analysis errors over the eastern Pacific is achieved when the NASA/MSFC winds are included in the operational observational data.

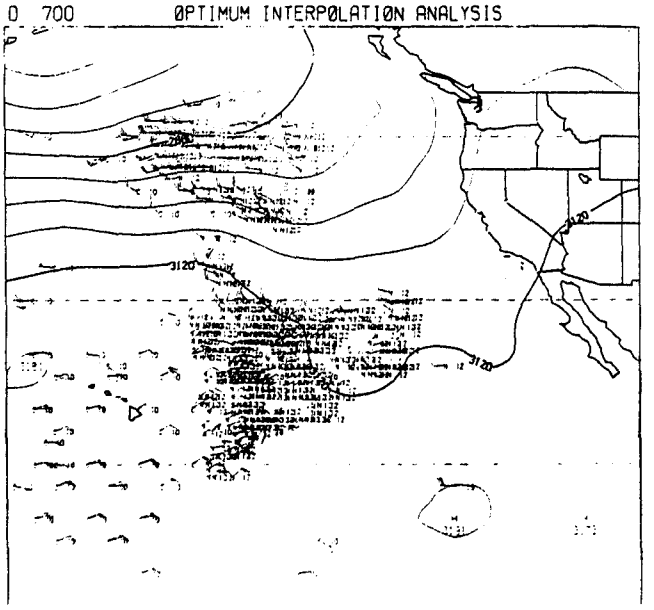

Fig. 5. Operational 700 mb CMV's, NASA/MSFC CMV's, and height analysis for 0000 UTC on 13 April 1988.

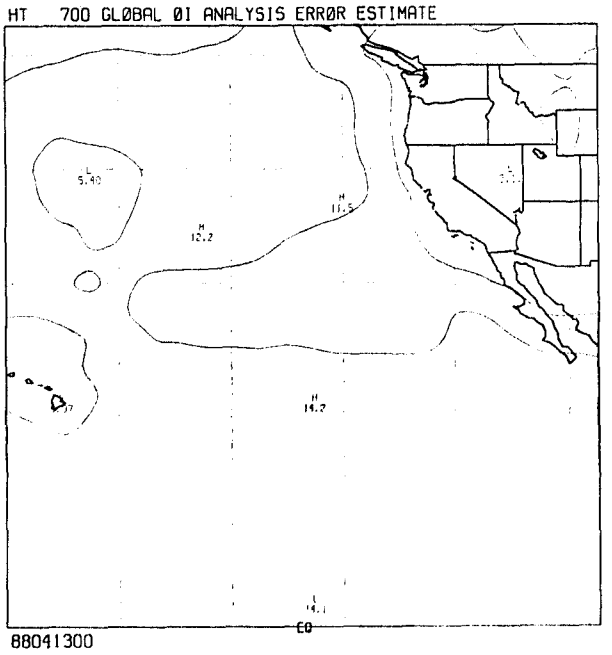

Fig. 6. MVOI 700 mb analysis error estimate for geopotential height (NASA/MSFC winds included).

The NASA/MSFC winds, with lower observational wind component errors, as compared to other satellite wind data, resulted in significantly lower analysis errors in regions where little or no wind data was available. However, the current study did not specify different error variances for the same general types of data, i.e., GMS winds vs. Meteosat winds vs. NASA/MSFC winds. This specification would allow the analysis to discriminate between the satellite wind data types, and give proper weight to the data.

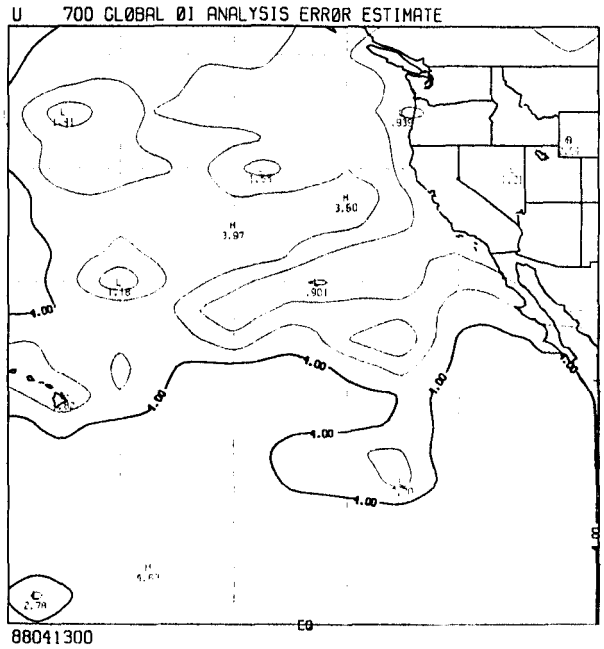

Fig. 7. MVOI 700 mb analysis error estimate for U component of wind (NASA/MSFC winds included).

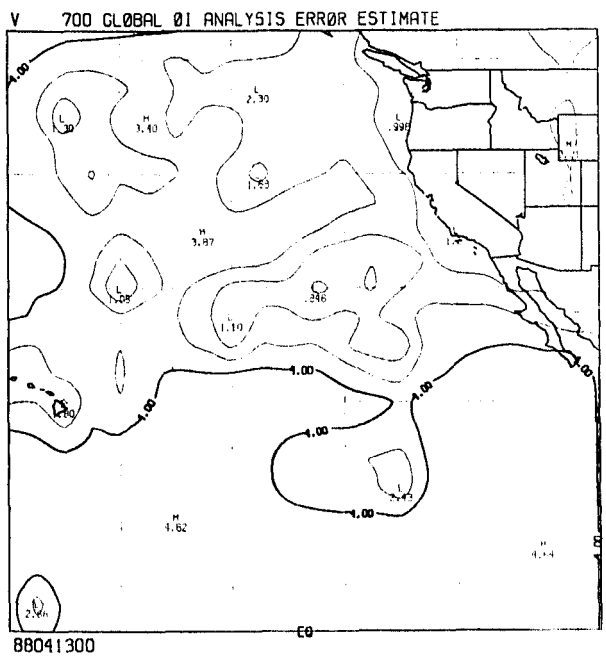

Fig. 8. MVOI 700 mb analysis error estimate for for V component of wind (NASA/MSFC winds included).

The primary goal of this study was to determine the impact of the NASA/MSFC winds on the analysis using NOGAPS' MVOI. Results indicate that the impact on regional analyses is positive and significant enough to warrant a model impact study and operational evaluation of the NASA/MSFC wind data.

6. REFERENCES

Barker, E.H., J.S. Goerss and N.L. Baker, 1988: The Navy's operational multivariate optimum interpolation analysis method. Preprints Eighth Conference on Numerical Weather Prediction, Baltimore, MD.

Barnea, D.I., and H.F. Silverman, 1972: A Class of algorithms for fast digital image registration. IEEE Transactions on Computers. C-21, 179-186.

Buell, C., 1972: Correlation functions for wind and geopotential on isobaric surfaces. J. Appl., 11, 51-59.

Fuelberg, H.E., and P.J. Meyer, 1984: An analysis of the AVE-SESAME I period using statistical structure and correlations functions. Mon. Wea. Rev., **112**, 1562-1576.

Gandin, L.S., 1963: Objective analysis of meteorological fields. Translated from Russian, Israel Program for Scientific Translations, Jerusalem, 242pp. [NTIS TT-65-50007.]

Hillger, D.W., and T.H. Vonder Haar, 1979: An analysis of satellite infrared soundings at the mesoscale using statistical structure and correlation functions. J. Atmos. Sci., **36**, 287-305.

Lee, D.K. and D.D. Houghton, 1984: Impact of mesoscale satellite wind data on numerical model simulations: A case study. Mon. Wea. Rev., 112, 1005-1016.

Lorenc, A., 1981: A global three-dimensional multivariate statistical interpolation scheme. Mon. Wea. Rev., 109, 701-21.

Morone, L.L., 1986: The observational error of automated wind reports from aircraft. Bull. Amer. Meteor. Soc., **67**, 177-185.

Swadley, S.D., 1988: Error analysis of automated winds derived from GOES multispectral imagery. Preprints Third Conference on Satellite Meteorology and Oceanography, Anaheim, CA.

Wilson, G.S., 1984: Automated mesoscale winds derived from GOES satellite imagery. Preprints Conference on Satellite/Remote Sensing and Applications. Clearwater beach, FL.

15.3

ADVANCES IN THE AUTOMATED PRODUCTION OF WIND ESTIMATES FROM GEOSTATIONARY SATELLITE IMAGERY

Robert T. Merrill

Cooperative Institute for Meteorological Satellite Studies
University of Wisconsin -- Madison, WI

1. INTRODUCTION

A complete description of the atmospheric state requires measurements of both mass and wind. The latter is especially important in low latitudes where pressure variability is small and its relationship with the wind is weak.

Retrievals of temperature and moisture from satellite radiances have dominated research in remote sensing because of the inherent mathematical difficulty of the retrieval problem. Estimating winds has received less attention, partly because of the importance of the temperature field for midlatitude analysis, and partially because wind production, at least in principle, is simpler than making soundings.

The original winds system was a human and a pair of satellite images. However, NWP model demands for timely winds over a large area require a largely automated system. The human is replaced with computer code which searches the image(s) for "trackable" features, determines their displacement with time, and assigns to each a height based on the radiometric information. A quality control step then checks the winds against the guess and/or each other and flags or deletes those which are suspect. These steps are generally sequential, while experienced human wind trackers perform all at the same time.

The Cooperative Institute for Meteorological Satellite Studies (CIMSS) automated wind system (Fig. 1) was developed about three years ago. Digital images, global model output, and surface data are extracted from the real-time files on the UW-McIDAS by a pre-processor and written to working files. Target selection, height assignment, tracking, and quality control are then performed sequentially. At the time of writing, we are beginning a two week near-real-time test, the results of which will be summarized at the conference. Here we will concentrate on the mechanics of the system, particularly some of the recent innovations in height assignment and tracking algorithm which we hope will result in more and better satellite derived winds.

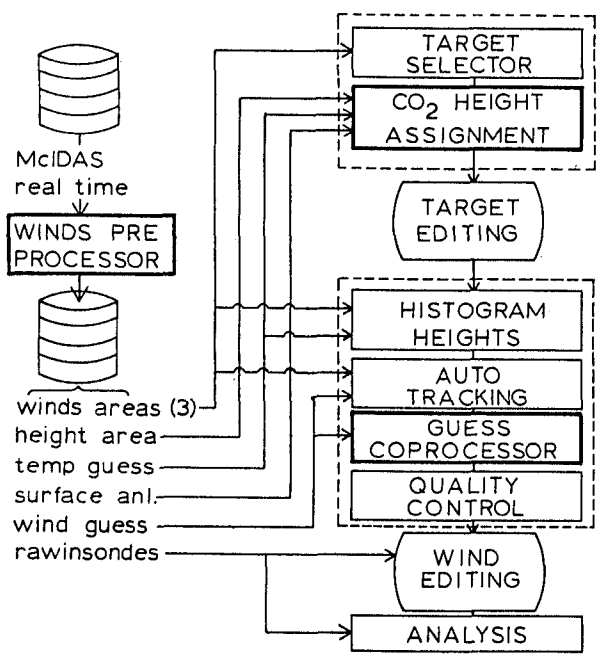

Fig. 1. Flow chart of the CIMSS experimental wind system. Highlighted processes have been substantially upgraded in the past year. Boxes enclose processes, and dashed outlines define single job steps on the UW McIDAS.

2. TARGET SELECTOR

The tracking algorithm is the most computationally expensive part of the system, so rather than apply it at regular intervals across the image we preselect locations (targets) where it is likely to succeed. We desire small scale structures which are coherent in time and located at a single level, but all that can be identified from a single image is structure. Separation of cloud levels through radiometric calculations alone is very difficult, and using multiple images to test for feature longevity means using the tracking algorithm, which is what we seek to minimize.

Fig. 2. illustrates the target selector operation. It considers small sub-areas of image in succession, and within each sub-area locates the maxima in brightness, and of these selects the one associated with the strongest gradient over 3-5 pixels. The operator may specify the minimum acceptable gradient and the maximum and minimum brightnesses to prevent target selection on very weak gradients, the limb, or the terminator. The maximum brightness control also allows a crude height pre-selection when applied to IR channels. The target density is controlled by altering the size of the selector area between 15-25 pixels on a side.

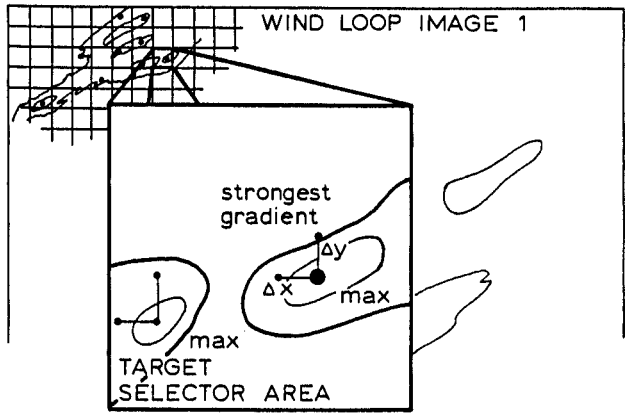

Fig. 2. Schematic of the CIMSS target selector.

Targets are generated for an entire image (up to 500 lines by 2000 elements) in a single job step and then written to a file for later wind tracking. This modular structure allows an interactive step for inserting or deleting targets.

3. HEIGHT ASSIGNMENT

The need for computational efficiency requires assignment of heights to features before tracking them. The tracking algorithm works by finding the best of a possible range of displacements of the feature, and by minimizing this range we can reduce the number of operations considerably. Human operators would use a priori knowledge of the flow, and the automated system imitates this by centering its search around a first guess, typically a 12 h forecast from an NWP model. To interpolate a guess wind from the model output, we must specify the location, which requires that we assign a height to the target.

In addition to being a good source of clouds to track, the 11 micron "window" channel measures their equivalent black body temperature (Tbb). To the extent that the Tbb represents the actual cloud temperature, it can be matched with a forecast sounding to obtain a height (or pressure). Although thick clouds act as black bodies, thin ones, usually cirrus, do not because they have an emissivity less than one and thus appear warmer than they actually are. Direct use of window channel radiances will lead to heights which are too low. Systematic height assignment errors in a vertically sheared atmosphere cause a speed bias in the winds, even if features are perfectly tracked.

A refinement to the above method considers only the colder temperatures and is the present CIMSS "operational" technique (Fig. 3). A histogram of the Tbbs of the tracking area (see Fig. 4) is made, and the coldest class having at least 1.6 percent (5 percent for water vapor imagery) of the pixels is taken as the cloud temperature.

The implicit assumption that at least a few pixels of the feature have an emissivity near one still fails in thin cirrus. This difficulty is partially corrected statistically, by matching a large sample of winds with nearby rawinsondes and determining the "level of best fit"; linear regression on a sample of such matches provides a relationship between the tracer temperature estimated from the histogram and the best fit atmospheric temperature (Hayden and Merrill, 1988; Hayden and Stewart, 1987). Although the regression equation may correct for systematic errors due to thin clouds, it is inherently unable to account for variability in the peak emissivity values of different clouds and will be "tuned" for a typical value. The mean height assignment will be acceptable but heights assigned to thin cloud will be too high, and those assigned to dense cloud will be too low. The result will be a slow bias in winds associated with thin cirrus. Such a slow bias is a consistent deficiency in cloud motion winds, and such height assignment problems may be a partial cause (Bowen and Saunders, 1984).

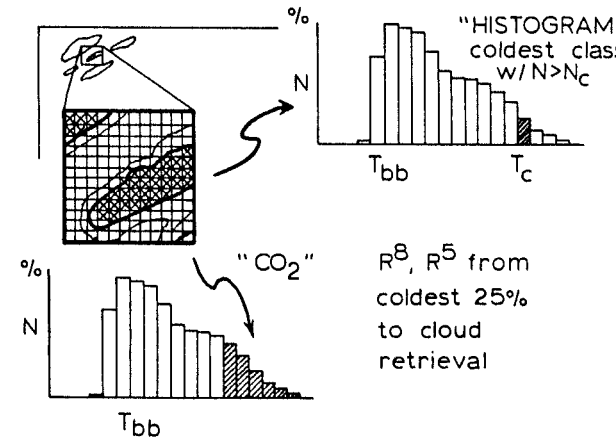

Fig. 3. Schematic of the height assignment algorithm.

In an attempt to improve the height assignments, several winds producers, including CIMSS and the European Space Agency (ESA), have begun to experiment with "multi-spectral" height algorithms. For every tracer there are two unknowns, temperature and emissivity, and therefore two pieces of information are needed to solve the associated radiative transfer problem. The basis of these techniques is

$$R_m^j - R_a^j = n(R_c^j(p) - R_a^j) \qquad (1)$$

where R^j is radiance in channel j, and subscripts m, a, and c denote measured, clear air, and cloudy radiances respectively. Clear and cloudy radiances are computed from a guess sounding using a radiative transfer model; for the cloudy radiance a "black" cloud at pressure is assumed. The effective emissivity is the product of the cloud emissivity and the fraction of the scene filled with cloud. If we assume that the emissivity of the feature is the same for two channels (i.e. 5 and 8), we then can write

$$\frac{R_m^5 - R_a^5}{R_m^8 - R_a^8} = \frac{R_c^5(p) - R_a^5}{R_c^8(p) - R_a^8} \qquad (2)$$

which can be solved iteratively for p.

The upgraded CIMSS height algorithm uses the VAS 11 micron window (Band 8) and the 13.3 micron CO2 band (Band 5) obtained by operating the VAS in Multi-Spectral Image (MSI) mode. At present the coldest 25 percent of the radiances are averaged, but the technique seems to be relatively insensitive to the sampling rate as would be expected from theory.

4. TRACKING ALGORITHM

4.1 Standard method

Fig. 4 illustrates the tracking algorithm. A tracking area 24 pixels square is defined on the first image, centered on a target. The algorithm then goes to the second image in the loop and searches for that 24 pixel square area which best matches the radiances in the tracking area. To minimize computational expense, the search is confined to a "search area" centered around the guess displacement of the target. The match area is that for which

$$F(\underset{\sim}{r}(\underset{\sim}{d})) = \text{minimum} \qquad (3)$$

where F is the tracking function and $\underset{\sim}{r}(\underset{\sim}{d})$ is the radiance difference between potential match area at displacement $\underset{\sim}{d}$ and the tracking area. The solution to (3) is the displacement of the "best" radiance match which can be converted to a velocity. F can be any function with a relative minimum for small arguments so it "rewards" small radiance differences. A typical choice is

$$F(\underset{\sim}{r}(\underset{\sim}{d})) = \underset{\sim}{r}^T(\underset{\sim}{d}) \cdot \underset{\sim}{r}(\underset{\sim}{d}) \qquad (4)$$

which is the sum of squares of the radiance differences.

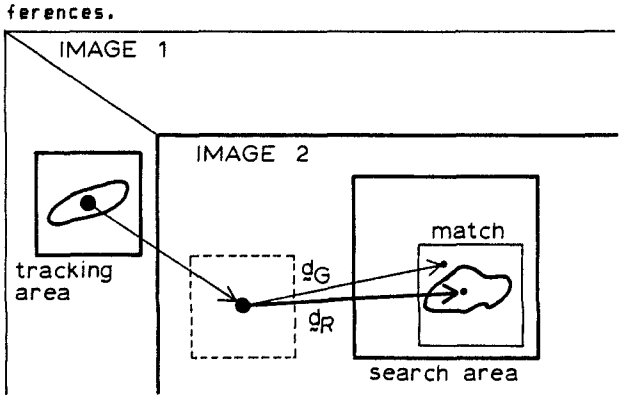

Fig. 4. Schematic of the wind tracking algorithm. The CIMSS system actually produces two vectors per target, the first between images 1 and 2, and the second between images 2 and 3, using the first wind as a "guess."

Another possibility (which we have not yet attempted) is to weight the function towards matches associated with a particular range of radiances associated with cloud at a specified level (Schmetz and Nuret, 1987). However, as with height assignment, differences in cloud emissivity make the Tbb vary across the same tracer. With more sophisticated radiometers, it may someday be possible to track retrieved quantities (cloud temperature or mixing ratio) rather than raw radiances, and image brightness would then have a one-to-one relationship with assigned height. VAS derived imagery of precipitable water has been tracked in this fashion but as it is a vertically integrated quantity it offers no benefits for height assignment.

4.2 Guess co-processing

With numerical models improving faster than satellite instruments, the guess is becoming ever harder to "beat" but also more useful for the retrieval process. Thus far we have used the guess only to economize on the search area, but Eyre (1987) proposes including the guess and its expected error characteristics directly in the "wind retrieval" process through the following modification to the tracking algorithm, based on Bayes' Theorem

$$F(d) = \frac{\underset{\sim}{r}^T(\underset{\sim}{d}) \cdot \underset{\sim}{r}(\underset{\sim}{d})}{N\,\sigma_r^2} + \frac{(\underset{\sim}{d} - \underset{\sim}{d}_g)^T \cdot (\underset{\sim}{d} - \underset{\sim}{d}_g)}{\sigma_g^2} \qquad (6)$$

where d_g is the guess displacement, N is the number of pixels in the tracking area, and σ_r and σ_g are the RMS errors in the radiance measurements and the guess respectively. The second term penalizes the tracking function for deviations from the guess. For a strong signal (small radiometric noise and a target with large variance and small structural changes) the radiance difference will overpower the guess and the selected displacement will nearly that given by minimizing (4), while for a weak signal the guess term will pull the estimated wind back towards the guess. Plots of tracking function and guess term values are shown in Fig. 5.

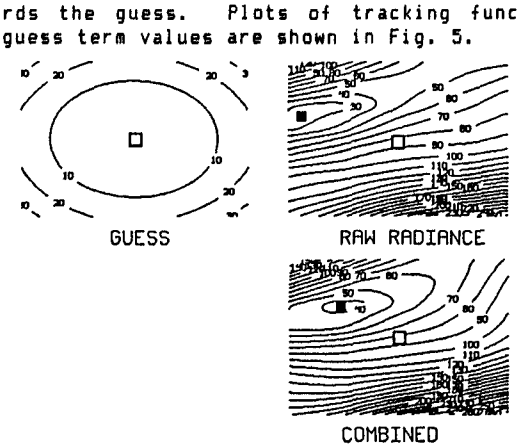

Fig. 5. Plots of the guess error term, the tracking function, and their combination. The open square corresponds to the guess displacement, so the deviation of the minima (solid squares) from the open squares corresponds to the difference between the radiometric or combined displacements and the guess.

It is conceptually straightforward to generalize (6) to include the effects of guess dependence on the height assignment by adding another term. This has not yet been done because of computational limitations. At present, the tracking algorithm computes the value of (4or (5) for each possible (discrete) displacement; this would be impractical for the three-

dimensional form and would require the use of a minimization algorithm.

5. RESOLUTION EFFECTS.

Much attention has been paid to the effects of increasing the resolution, either in time or in space, of the imagery used to derive winds. CIMSS investigations on this topic have revealed some issues which should help clarify future work in this area.

The raw output of a wind algorithm is displacement $\underset{\sim}{d}$ of best fit in pixels. A velocity is obtained by scaling by

$$\underset{\sim}{V} = \underset{\sim}{d}\,(X/T) \qquad (7)$$

where X is the size of an image pixel and T is the time interval of the loop. Since the displacement in pixels is a discrete variable (although spatial interpolation is done to find the minimum) the output of velocity is also discrete, with steps of X/T. If the time interval is shortened without a corresponding decrease in pixel size, these steps will increase proportionally, introducing a random error into the winds.

Eq. (7) also implies guess dependence of winds, whether intended or not. Since the range of possible displacements is the difference in size between the tracking and search areas (the lag size L), the allowable deviation from the first guess is bounded above. The effective displacement range is $L-1$, since whenever the minimum of the tracking function is found for a match area at maximum displacement, a "correlation error" is indicated, since it is likely that the real "best fit" lies at a somewhat larger (and untested) displacement. In practical terms, this constrains all the wind vectors to lie within

$$(u-u_g) \;\text{ or }\; (v-v_g) \leq \frac{(L-2)X}{2T} \qquad (8)$$

of the guess. For X=4 km, T=30 minutes, and a lag size L of 14 pixels, the winds would be constrained to lie within 13 m/s of the guess in each component and 19 m/s in speed. This becomes important when comparing wind vectors obtained at different space and time resolutions. When the same lag size is used for all, the longer loop interval is found to produce fewer vectors but less noisy ones, because they are constrained more closely to the guess. When the lag size is varied to keep the constraint (8) a constant, the longer loop intervals may produce the same or more vectors, and may also be noisier. They also become more expensive, since the number of times (3) must be evaluated is the square of the lag size. There is no "right" loop interval, but these factors must be accounted for when comparing loop intervals against each other.

6. SUMMARY

This paper describes the CIMSS automated wind system, with emphasis on upgraded height assignment and tracking procedures implemented during the past year. We are now entering a period of consolidation and evaluation of these changes, beginning with a two week test of the system from 6-20 February 1989. Results of this test will be summarized at the meeting.

REFERENCES

Bowen, R. A. and R. W. Saunders, 1984: The semi-transparency correction as applied operationally to Meteosat infrared data: a remote-sensing problem. ESA Journal, 8, 131-135.

Eyre, J. R., 1987: A maximum probability method for estimating satellite winds. Unpublished CIMSS manuscript, 12 pp.

Hayden, C. M. and R. T. Merrill, 1988: Recent NESDIS research in wind estimation from geostationary satellite images. Report on ECMWF seminar on data assimilation and the use of satellite data, 5-9 September, 1988, in press.

Hayden, C. M. and T. R. Stewart, 1987: An update on cloud and water vapor tracers for providing wind estimates. 6th AMS Conference on Meteorological Observations and Instrumentation, Jan. 12-16, 1987, 70-75.

Schmetz, J. and M. Nuret, 1987: Automatic tracking of high-level clouds in Meteosat IR images with a radiance windowing technique. ESA Journal, 11, 275-286.

16.2

SATELLITE OBSERVATIONS OF TROPICAL CYCLONES DURING THE 1990's

William E. Shenk and Edward B. Rodgers
Laboratory for Atmospheres
NASA/Goddard Space Flight Center
Greenbelt, MD 20771

Simon Chang
Naval Research Laboratory
Washington, DC 20375

1. INTRODUCTION

There are a number of major developments during the next decade which should lead to substantial improvements in the understanding and the prediction of tropical cyclones. The advances in the measurements made by geosynchronous and low orbiting satellites during this period are expected to be one of the principal keys to their improvement. Besides their diagnostic value, the satellite information will be utilized in dynamical and statistical models which should be the primary means for reducing prediction errors. Part of the increased reliance on satellite data will result from the anticipated continued decline of conventional data over oceanic areas, especially reconnaissance aircraft. The reduction and/or elimination of the reconnaissance aircraft is a very distressing development. Not only do they still provide unique and crucial data (e.g. accurate center location, central pressure estimates) but these data are very important for the verification of satellite techniques (e.g. intensity). We suggest that the reconnaissance program be revitalized and that the measurements from aircraft be combined with satellite information for even better results and for the verification of new and/or improved satellite techniques.

A long range reason for increasing our attention on improving tropical cyclones prediction is the possibility that some of them will become more intense in future decades if the "greenhouse" effect leads to higher sea surface temperatures. Since it will take many years to develop the necessary observational and analysis resources to realize a substantial prediction improvement, it is important that we begin as early as possible in order to be ready if these storms become more intense and/or numerous.

The principal operational satellite advances should be on the GOES I-M and NOAA K-M missions. Since high temporal resolution is very important in monitoring a tropical cyclone, the GOES I-M geosynchronous satellite will be the main data source for tropical cyclones in the North Atlantic and Eastern Pacific basins. Some of the techniques demonstrated from GOES I-M could be utilized with the other geosynchronous satellites around the world, (i.e. Meteosat, GMS, and INSAT). Near the end of the 1990's there is the possibility of more advanced instrumentation in geosynchronous orbit, on the next generation operational series (GOES-N+) and/or on research satellites. The research satellites might be placed at sub-satellite points that would survey tropical cyclones in any portion of the globe.

The operational polar orbiting NOAA K-M satellites will monitor the globe and will have a new microwave sensor that will offer improved temperature and moisture profiling. The operational DOD DMSP series should continue to provide very useful visible and infrared imaging and microwave profiling and imaging. There are two more NASA low orbiting satellites that are planned for launch during the middle and late 1990's that could provide unique data to complement the improved operational system. They are the Tropical Rainfall Measurement Mission (TRMM) which will be in an orbit approximately ±35° from the equator, and the Earth Observing Satellite (EOS), which is planned for polar orbit.

2. MAJOR TROPICAL CYCLONE QUANTITIES AND PROCESSES AND THE REQUIRED PARAMETERS

The investigation of tropical cyclones during the 1990's can be roughly divided into two categories. One is the continuing desire for better satellites measurements of basic quantities such as center location and current motion, strength and intensity. The other category, which also will utilize satellite data, is the increased understanding of tropical cyclone processes (e.g. genesis, intensification, cyclone-environmental interactions, and the transformation of a tropical cyclone into an extratropical system) and the future prediction of motion, strength, and intensity. The future predictions are mainly dependent on the improvements made in both the first category and the better understanding of tropical cyclone processes portion of the second category.

There is a wide variety of scientific hypotheses that are connected with the study of tropical cyclone processes. A good reference that reviews their status is given by Anthes, 1982. There is considerable commonality in the measurement requirements associated with the study of these hypotheses and in the measurements needed to determine the basic tropical cyclone quantities in the first category. Also, the measurement requirements for extratropical cyclones have substantial overlap with these for tropical cyclones and, therefore, similar data sets could greatly benefit the study and prediction of extratropical cyclones.

It is important to estimate what the most significant variables are that are needed for the various tropical cyclone quantities and processes. Then quantitative estimates are needed for the measurement requirements (e.g. resolutions, coverage, accuracies) associated with the basic parameters required to determine the variables.

Table 1
The Variables That Can Be Measured by Satellites During the 1990's for the Determination of Tropical Cyclone Quantities and Processes

Variables	1	2	3	4	5	6	7	8	9
SST'	•			•		•	•		•
Latent Heat Release				•		•			•
CDO & TBB			•	•			•	•	•
CDO & Ht			•	•				•	•
CDO & Shape	•		•	•	•	•		•	•
Rainband Shape	•	•	•	•	•	•		•	•
Eye		•	•	•	•	•	•		•
Thickness							•	•	•
Core ΔT	•	•	•	•	•	•	•	•	•
Tropopause Ht			•	•	•	•	•	•	•
Lower-Trop afc Winds	•	•	•	•	•	•	•	•	•
Upper-trop Winds	•			•		•	•	•	•
Deep-layer Winds	•			•		•	•	•	•
Trop Water Vapor	•			•			•	•	•
Cloud Ice/Water				•		•			•
Lightning				•		•			•
Surface Pressure *	•	•	•	•	•	•	•	•	•

Key: Significant Tropical Cyclone Quantities and Processes

1) Genesis
2) Location
3) Intensity
4) Intensity Change
5) Strength
6) Strength Change
7) Motion-Current and Future
8) Cyclone/Environmental Interaction
9) Transformation (Tropical to Extratropical Cyclone)

& CDO = Central Dense Overcast

Table 1 is our estimate of the key variables that are needed for the nine tropical cyclone quantities and processes that are listed at the bottom of the table. We have made no attempt to indicate the relative importance of any variable to a given quantity or process. It is clear that winds are an extremely important variable and are involved at some tropospheric level in the investigation of all nine processes. Cloud and precipitation information is also vital especially for intensity and strength estimates and their changes. The measurement of the warm temperature anomolies (core ΔT in Table 1) near the center of the cyclone are important for their diagnostic value (e.g. intensity, position) and for what can be determined about cyclone evolution (e.g. changes in intensity, transformation from a warm core to an extratropical system). Sea surface temperature is also an important boundary condition. The degree of value of some variables (e.g. lightning) is unclear at the present time simply because our ability to measure lightning in tropical cyclones has been poor.

Table 2

Tropical Cyclone Observational Guidelines

Parameter	Resolution: Spatial (km)	Resolution: Vertical (km)	Resolution: Temporal	Absolute Accuracy
Temperature:				
o Sea Surface	20-100		6-24 h	±1.0K[a]
o Profiles				
1. Away from eye wall	40-200	1-5[b]	1-3 h	±1-1.5K[c]
2. Eye and eye wall	5-50	1-5	10-60 min	±1-3K[c]
Moisture Profiles:				
1. Away from eye wall	20-100	1-5[b]	1-3 h	±5-15%
2. Eye and eye wall	5-50	1-5	10-60 min	±5-15%
Surface Pressure:				
1. Away from eye wall	40-200		1-3 h	±1-3 mb
2. Eye and eye wall	5-50		10-60 min	±1-3 mb
Winds:				
o Boundary Layer	20-50	0.2-1	30-120 min	±1-3m/sec
o Above Boundary Layer	40-150	1-5	1-3 h	±1-3m/sec
Precipitation:				
o Rate	10-50		15-120 min	±20-50%
o Tes/Ho	10-50		15-120 min	
Cloud Top Height	2-20	0.25	3-30 min	±500m[a]

[a]Relative accuracy should be one-half of these values

[b]0.2 km through inversions.

[c]Relative accuracy ≤1.0K.

Table 2 provides guidelines for what parameters and associated resolutions and accuracies are needed to realize substantial improvement in the understanding of tropical cyclone processes and for a sizeable prediction improvement. The guidelines in Table 2 are very close to what are contained in the Review of Federal Research and Data Collection Programs for Improving Tropical Cyclone Forecasting (1983) and what was published by Shenk, et al (1987). Nearly all of the variables in Table 1 can be derived from the parameters in Table 2. Almost all of the guidelines in Table 2 have a range of values. Most of the improvements to understanding and prediction are expected to come as observations move from the low-resolution end to the high-resolution end of each range. Although observations outside the low-resolution limits can still be of benefit, the greatest increase of improvement should come from the observations within each range. Likewise, to improve observation performance beyond the upper limit is not expected to result in much further improvement.

Table 2 shows that, although a tropical cyclone can be a large system, high spatial and temporal resolution is needed. This is due to the convective processes that contribute to tropical cyclone development and the cyclone environment-interaction processes that affect development and movement, and which result in rapid changes on small to regional scales within and surrounding the relatively large envelope of the cyclone.

3. FUTURE SATELLITE OBSERVING SYSTEM AND IT'S RELATIONSHIP TO THE REQUIRED PARAMETERS

Table 3
Future Instruments and Satellites that are Expected to Derive Key Tropical Cyclone Parameters (From Table 1) During the 1990's

Future Instruments and Satellite Parameters	1	2	3	4	5	6	7	8	9	10	11	12	13	14
SST	•	•		•	•		•	•					•	•
Latent Heat Release		•	•			•		•	•	•			•	
CDO & TAB		•											•	
CDO & Ht		•	•	•	•								•	•
CDO & Shape	•	•	•										•	
Rainband Shape	•	•							•	•			•	
Eye	•	•	•					•	•	•			•	
Thickness				•			•							•
Core ΔT				•			•							•
Tropopause Ht			•	•			•				•			•
Lower-Trop afc Winds	•	•	•	•			•&					•		•&
Upper-Trop Winds *		•	•	•	•		•&							•&
Deep Layer Winds *		•	•	•	•		•&							•&
Middle-Trop Water Vapor			•		•			•						
Cloud Ice/Water								•	•	•			•	
Lightning						•								
Surface Pressure														

Key: Future Instruments and Satellites

1) GOES I-M Imager-Visible
2) GOES I-M Imager-IR
3) GOES I-M Imager-Stereo
4) GOES I-M Sounder-Temperature
5) GOES I-M Sounder-Water Vapor
6) GOES M Lightning Mapper*
7) AMSU-Temperature
8) AMSU-Water Vapor and Imaging
9) SSMI/EOS/TRMM Passive Microwave Radiometers
10) TRMM Radar
11) EOS Total Ozone Mapper
12) EOS Scatterometer
13) NOAA AVHRR and EOS MODIS
14) EOS AIRS

[a] In middle latitudes-derived from mass field
* A research sensor under consideration for flight on GOES M.
&A CDO = Central Dense Overcast

As indicated earlier, the 1990's are expected to contain a major explosion in satellite capability which should have significant impact on tropical cyclone analysis and prediction. Table 3 shows what variables in Table 1 would be measured by the major new satellite and sensor capabilities during the 1990's. Only sensors that are expected to be flown on missions which are in the development stage (e.g. GOES I-M) or in a more advanced planning stage (e.g. EOS) are shown. Thus, future operational or research geosynchronous missions which might occur in the late 1990's or early in the next century are not included. Their impact on tropical cyclone analysis and prediction would also be substantial as indicated by Shenk, et al. (1987). Also not included in Table 3 was the possible flight of profiling measurements from lidar systems on EOS during the 1990's. If flown they would help with temperature, moisture, and pressure profiles away from the main cloud canopy of the cyclone. This would be the only source of direct pressure measurements from satellites.

The instrumentation on the three axis stabilized GOES I-M series is shown in the first 6 columns. The improvements from this system beyond the current GOES series are expected due to better instrumentation, greater operating flexibility, and focus on the survey of significant storm events. The imaging and profiling sensors will have higher spatial resolution, more channels of information, and significantly higher radiometric sensitivity than the current GOES series counterpart, the VISSR Atmospheric Sounder (VAS). The separation of imaging and profiling functions into individual instruments and more sectorizing capability should give much greater operating flexibility. The GOES I-M sensors will be able to provide high resolution winds from cloud motions and moisture motions. Cloud height estimates (in general, with $\leq$1 km accuracy) will be possible, especially if stereo is taken between two of the GOES satellites. Most of the useful profiling information will be taken on the perhipery of the cyclone because of the clouds near the center. There is, however, the possibility of warm temperature anomaly measurements where the eye is large (>20km) and clear, at least in the upper troposphere.

The polar orbiting satellites will provide data mostly at 12-24 hour intervals. The key measurements will be the determination of the mass and moisture fields (e.g. AMSU, AIRS) and precipitation estimates. Most of the mass field data on this time scale will be important for determining the steering flow in the middle latitudes, while the temperature anomalies in the core (e.g. AMSU) will be most important for estimating the intensity. The EOS AIRS should make a substantial improvement in providing accurate mass field data surrounding the cyclone with the approximately factor of two increase in vertical resolution over present profilers and an accuracy increase of about 1K. The precipitation structure (i.e. rainbands) and latent heat release estimates can be made from several of the polar orbiting microwave instruments (i.e. AMSU, SSMI, EOS, TRMM). When these are operating simultaneously it should be possible to generally have higher temporal resolution than 12 hours. The total ozone mapper on EOS will help define the upper tropospheric circulation since it can often detect features that are vertically thin and not easily seen with the temperature profiles (Rodgers, 1988). Detailed cloud structure information will be observed better with the imaging radiometers on board (e.g. AVHRR, MODIS) low orbiting satellites than from geosynchronous orbit, since they will have higher spatial resolution. Surface wind information will be provided by the EOS scatterometer.

Table 4

Evaluation of Satellite Capabilities to Satisfy the Federal Coordinator's Report Tropical Cyclone Observational Guidelines

Parameter	Resolution: Spatial	Resolution: Vertical	Resolution: Temporal	Absolute Accuracy
Temperature:				
o Surface	2[a],1		1,1	2,1
o Profiles				
1. Away from eye wall	1[a],2	3,2	1,4	3
2. Eye and eye wall	4,3	3,3	1,4	3,3
Moisture Profiles:				
1. Away from eye wall	2[a],1	3,2	1,4	3,2
2. Eye and eye wall	4,2	3,3	1,4	4,3
Surface Pressure:				
1. Away from eye wall	4,4		4,4	4,4
2. Eye and eye wall	4,4		4,4	4,4
Winds:				
o Boundary layer	3,3,3[b]	3,4	1,4	2,2[b]
o Above boundary layer	3,4	4,4	1,4	3,4
Precipitation:				
o Rate	2,1		1,4	4,2
o Yes/No	2,1		1,4	
Cloud Top Height	1(2), 1	1(3),1	1,4	1(3),2

[a]Clear and partly cloudy conditions

[b]Surface Winds

1 - Satellite observation fulfills the complete range of the guideline

2 - Satellite observation fulfills most of the range of the guideline

3 - Satellite observation fulfills some of the range of the guideline

4 - Satellite observation fulfils none of the range of the guideline

Table 4 provides a semi-quantitative assessment of how well the combination of the new geosynchronous and low orbiting satellites could satisfy the observational guidelines shown in Table 2. Separate assessments are made for GOES I-M and low orbiting sensors since, with the exception of sea surface temperature, it is not anticipated that the temporal resolution guidelines will be routinely approached with low orbiting data. However, these low orbiting data can still be valuable where 1) larger scale information is needed, 2) no other information source is available (e.g. microwave profiles), 3) to provide more spatial detail than is possible from geosynchronous orbit, and 4) to help verify techniques developed with geosynchronous satellite data. Therefore, assessments were made of the ability of low orbiting instruments to meet the other components of the guidelines.

In Table 4 there are two numbers ranging from 1 to 4 in place of each of the guideline entries. These numbers represent, respectively, an assessment of how well each of the guidelines can be met with the GOES I-M satellite series and the low orbiting satellite sensors shown in Table 3. A "1" indicates that a satellite system is expected to cover the entire range of the guidelines (and may even exceed the range); a "2" means that most of the range can be met; a "3" indicates that some of the range can be satisfied (generally less than ½); and a "4" represents when none of the range can be satisfied. A number in parentheses is a nighttime evaluation, usually resulting from lower spatial resolution measurements.

Table 4 shows some general performance characteristics of each system. The GOES I-M geosynchronous satellite can meet all of the temporal resolution guidelines for the parameters that can measure all parameters except surface pressure. Low-orbiting satellites (assuming two are in orbit that are equidistantly spaced) could provide six-hourly coverage over the tropics. Therefore, the sea surface temperature temporal guideline can be met. Microwave instruments could measure sea surface temperature with approximately 1K accuracy in virtually all weather conditions. High-resolution (approximately 1 km) infrared sensing can give better sea surface temperature accuracy (probably less than ½ K) in areas where cloud cover does not interfere.

The GOES I-M satellite will meet a substantial amount of the spatial resolution guidelines for surface temperature, and temperature and moisture profiles away from the main cloud area in clear and partly cloudy conditions. The spatial resolution for cloud and precipitation estimates (which depend on cloud measurement) will also approach the higher resolution end of the guidelines. For the winds from cloud motions, the "3" evaluation represents the average case. There will be some situations where trackable clouds are numerous and a "1" or "2" evaluation could be given. However, there will be other circumstances where a "4" would be appropriate, especially for clouds above the boundary layer. Daytime performance would be better than at night, since the high resolution (1 km) visible channel is available during the day.

Virtually all of the spatial resolution guidelines could be met with sensors in low-orbit if they were designed specially for tropical cyclone events. However, due to the lack of temporal resolution, low-orbiting instruments are not designed with tropical cyclone events as a high priority. Therefore, the evaluation of the low-orbit instrumentation is based on the expectation of satisfying the resolution guidelines from what is planned to be flown primarily for other purposes. Outside the inner core of a tropical cyclones, the spatial resolution of the sensors in low orbit will be good, relative to the observational needs, and useful data will be obtained even near the center.

However, an especially important area to improve the spatial resolution is the measurement of the upper tropospheric temperature anomolies in the core region. Kidder, et al. (1978) and Velden and Smith (1983) have already demonstrated that profiles derived from current low-orbit microwave profilers (≥110 km resolution) can provide useful surface pressure estimates. The AMSU, with 50 km resolution, meets the very top of the guideline range. The AMSU is expected to improve the Kidder, et al. (1978) and Velden and Smith (1983) results where higher resolution should yield substantially superior performance.

The vertical resolution of the GOES I-M profiler should meet the upper end of the guideline range. In low orbit the EOS AIRS will improve the vertical resolution by about a factor of two over the GOES I-M profiler with a major increase in accuracy (about 1K). The vertical resolution of the imagers on both GOES I-M and the low orbiting satellites will be good to excellent for clouds (a function of the radiometric sensitivity).

Since the determination of the wind profiles from GOES I-M is dependent on using the cloud-motion technique, the vertical resolution of these profiles is a function of how many cloud layers are available and how well the instruments can accurately locate and track them. In the tropics, the cumulus and cirrus-cloud layers predominate and thus provide a single level in the boundary layer and one at the upper troposphere level. Often the cirrus is located at several levels. The stereographic cloud-height technique is especially effective for separating these levels. This technique is also very useful in separating middle level clouds. Unless a Doppler lidar system is flown on the EOS during the late 1990's, there will be no direct wind measurements above the surface. The evaluation entries are for surface wind measurements from the scatterometer.

The areas where the greatest satisfaction of the accuracy guidelines occur (mostly away from the core) are for 1) surface temperature, 2) temperature and moisture profiles from low orbit, 3) winds from cloud motions in the boundary layer, 4) surface winds from the scatterometer, 5) precipitation estimates from TRMM, and 6) cloud top height estimates (especially if the stereographic heights are used from two GOES I-M satellites).

Table 5
Major NASA/NOAA Satellite Launches Planned or Proposed During the 1990's

	Year					
Satellite System	'90	'92	'94	'96	'98	'00
Geosynchronous Orbit						
GOES I	▲					
GOES J		▲				
GOES K			▲			
GOES L				▲		
GOES M					▲	
Low Orbit						
NOAA K			▲			
NOAA L			▲			
NOAA M				▲		
TRMM				▲		
EOS (initial)				▲		

Table 5 shows the expected launch dates for the major satellite systems during the 1990's. There may be more geosynchronous satellite launches in the late 1990's depending on how the plans progress for the next operational series and research satellites (e.g. the NASA geoplatform). For the low orbiting satellites the launch dates for TRMM and EOS may be greatly

altered, since they are in the middle planning stages. The DMSP launch dates are not shown. Thus, by the latter part of the 1990's there will be as many as five satellite systems (including DMSP) which could be used for tropical cyclone analysis and prediction, even if none of the future geosynchronous satellites plans are realized. This combination of satellites offers a tremendous opportunity to develop techniques where the data from more than one satellite is used, (especially the combination involving GOES I-M and a polar orbiting mission (e.g. profiling using infrared and microwave data).

The greatest remaining challenges for tropical cyclone observation from a satellite viewpoint are: 1) virtually continuous temperature and moisture profiles in cloudy areas, 2) the achievement of even higher vertical resolution of the temperature and moisture profiles, 3) the development of an accurate method to determine mesoscale winds from geosynchronous orbit to augment the cloud-motion technique and further improvements in cloud motion measurements, 4) accurate and frequent mesoscale-precipitation estimates, and 5) direct surface-pressure measurements at frequent intervals, with sufficient spatial resolution to cover the inner core of a cyclone, as well as the area surrounding the cyclone.

4. INSERTIONS OF SATELLITE MEASUREMEMTS INTO NUMERICAL MODELS

Another major challenge is the use of satellite data in numerical tropical-cyclone models. Although there have been some attempts with models below the synoptic and global scales, this remains an area where much more needs to be done.

Although, satellites do not always supply simultaneous observations of all of the state parameters (u, v, p, T, and q) that are ideal for numerical simulations and prediction, recent observing system simulation studies have demonstrated the usefulness of properly assimilated satellite observations. Geosynchronous satellites would provide nearly simultaneous observations of the parameters that are measured from that orbit. Scatterometer surface winds, along with cloud-base and cirrus-level winds, are very beneficial in defining and predicting tropical storms. Satellite-sensed temperature profile and D-values can be utilized to initiate the numerical models. The description of the mass field and the deep layer mean winds from water-vapor tracking is crucial to predict tropical storm movement. Recent advances in the theory of tropical storm motions have shown that there is significant interaction between the vortex and the mean flow at intermediate radii from the center. The satellite-measured latent heating rate (or precipitation rate) has been used to define the heating distribution in tropical cyclone models to improve structural and movement forecasts.

5. CONCLUSIONS

We have the opportunity during the next decade to make large improvements in our understanding and prediction of nature's most violent cyclone using measurements from the expected satellites along with their insertion in the rapidly improving numerical models. This could break a three decade period of relative stagnation in prediction skill. Future geosynchronous satellites beyond GOES I-M are expected to provide yet another period of dramatic improvement.

References

Anthes, R. A., 1982: Tropical Cyclones-Their Evolution, Structure and Effects, AMS Meteor. Monograph, Vol. 19, No. 41, 208 pp.

Federal Coordinator for Meteorological Services and Supporting Research, 1983: Review of federal research and data collection programs for improving tropical cyclone forecasting, FCM-R2- 1982, 23 pp. (w/appendices).

Kidder, S. Q., W. M. Gray, and T. H. Vonder Haar, 1978: Estimating tropical cyclone central pressure and outer winds from satellite microwave data, Mon. Wea. Rev., 106, 1458-1464.

Rodgers, E. B., J. Stout, J. Steranka, and S. Chang, 1988: Tropopause adjustment to tropical cyclones is inferred from satellite ozone observations. Preprint, 3rd Conf. on Satellite Meteorology and Oceanography, AMS, 197-202.

Shenk, W. E., T. H. Vonder Haar, and W. L. Smith, 1987: An evaluation of observations from satellite for the study and prediction of mesoscale events and cyclone events, Bull Amer. Meteor. Soc., 68, 21-35.

Velden, C. S. and W. L. Smith, 1983: Monitoring tropical cyclone evolution with NOAA satellite microwave observations, J. Climate and Appl. Meteor., 22, 714-724.

16.3

AUTOMATIC ANALYSIS OF STEREOSCOPIC GOES/GOES AND GOES/NOAA IMAGE PAIRS FOR MEASUREMENT OF HURRICANE CLOUD TOP HEIGHT AND STRUCTURE

A. F. Hasler
Laboratory for Atmospheres

J. Strong
Space Data & Computing Division
NASA/Goddard Space Flight Center
Greenbelt, MD 20771

H. Pierce & R. H. Woodward
General Sciences Corporation
Laurel, MD 20707

1. INTRODUCTION

Cloud height measurements from stereoscopic weather satellite images are very useful for the observation of a broad spectrum of meteorological processes. In particular measurements have been made which have added to our understanding of the structure and dynamics of hurricanes and severe local thunderstorms. In Hasler (1981), (1989), Fujita (1982), Mack *et al.* (1983), and Hasler *et al.* (1983) stereoscopic measurements are presented not only from simultaneous geosynchronous satellite (GEO) image pairs , but also from combination of GEOs with the NOAA Low Earth Orbiters (LEOs). A major obstacle to routine use of manual stereo measurements has been the time consuming nature of detailed cloud height structure analysis. To automate the procedure, a very powerful computer is required to compute the many cross-correlations which are needed. The Massively Parallel Processor (MPP) at Goddard Space Flight Center has made it possible to apply cross correlation techniques to obtain high resolution results for pairs of operational GOES weather satellite images (Hasler *et al.* 1988). The automatically derived height fields give significant structure in much less time than manual analyses (Hasler *et al.* 1988). In this paper we show the results of a baseline study with an idealized (synthetic) stereo image pair. A GEO/LEO image pair from Hurricane Allen (1980) was chosen to illustrate the results achievable from the best quality data available. Finally an analysis is presented from a GEO/GEO image pair of Hurricane Gilbert (1988). Automatic Stereo Analysis (ASA) technique enhancements illustrated in this paper include: selection of optimum correlation search area, and optimum bridging of poor match areas.

2. TECHNIQUES

2.1 Automatic Stereo Analysis

2.1.1 Background

Parallel architectures such as that of the MPP have made it possible to apply computationally intensive cross correlation techniques to obtain high resolution results from large images by the automatic detection of local differences between pairs of images. The algorithm used in this paper for the automated analysis of stereo image pairs to determine elevation information was developed by Strong and Ramapriyan, (1987). The application of automated analysis of stereo pairs from GOES satellites was introduced by Hasler *et al.* (1988).

Local correlation techniques are used in the stereo analysis to compute the parallax between two images caused by cloud-top elevation variation. With local correlation it is necessary to match a reference neighborhood in one image with various candidate matching neighborhoods within a search area in the other. Once the relative locations of matching neighborhoods in the two images are known, cloud top height maps can easily be computed. With typical images one has on the order of 100 billion calculations. The resulting computations are best done with very high-speed computers. The massively parallel architecture of the MPP is ideally suited to this.

2.1.2 Image correction and enhancement

The major difficulties in matching corresponding pixels in the two images are: a) Different brightness levels in the two images, b) Local distortions of the image, c) Low contrast areas and noise. Standard techniques of image normalization, destriping, noise removal, and image enhancement are used to obtain a matching pair of images with maximum signal to noise ratio. Because of the viewing geometry, features in the two GOES images have different dimensions in the stereopsis direction. Thus, the test image is remapped into the coordinate system of the reference image as described by Hasler (1981) so that features at the same elevation have the same shape.

2.1.3 Automatic analysis procedure

Local distortions occur in stereo analysis due to the different viewing angles. Because of the large angular separation of the two satellites (GOES/GOES or GOES/NOAA), which are available for cloud top stereo, it is impossible to see features from both cameras in steeply sloping regions. Errors due to local distortion, residual noise, spatial periodicities and low contrast in the image are reduced by computing matches at nearly every pixel in the image. However, areas of bad matches still remain which require bridging or interpolation.

2.1.4 Synthetic Stereo

The synthetic stereo technique described by Hasler *et al.* (1981) is used here to make stereo pairs from a visible image and a corresponding infrared image. The synthetic technique produces a stereo image pair consisting of an unaltered visible reference image and a derived image made by shifting pixels horizontally (up to 14 pixels in this case) proportional to their infrared temperature. This technique has previously been used as a display technique, but is used here to produce a known stereo pair for the testing of the MPP stereo analysis algorithm.

2.2 Display techniques

Artificial illumination is a display technique which is used to give image data a 3 dimensional quality. The technique is effected by differentiation of the image along the vector coming from a simulated light source. When combined with the original image data, (eg. 60%/40% sum) it becomes easier to detect differences when comparing images.

The perspective techniques used to display the stereo analyses in this paper are described by Hasler *et al.* (1985). The program requires two data arrays: 1) a height field which defines the three dimensional surface to be portrayed and 2) a shading or coloration image which supplies the information to produce the proper texture for the image. Here the MPP stereo parallax image or the infrared image provides the height field; and an illumination image or the corresponding visible image gives the information necessary to produce the texture in the final image. The program combines the two images into a single perspective image. For example, the algorithm constructs an image of a hurricane as it would be seen from an arbitrary eye-point looking towards the given view-point .

3. RESULTS

Fig. 1a. NOAA AVHRR satellite 1 km resolution 11 micron infrared image of Hurricane Allen at 1336 UTC on August 8 1980 when the storm was located in the Gulf of Mexico.

Fig. 2a. Same as infrared image in Fig. 1a, except that the number of brightness levels is reduced from 256 to 14 and an artificial illumination algorithm as been used to highlight the contours. The illumination is performed by differentiation of the image along the vector coming from a simulated light source to the left of the storm.

Fig. 3a. Same as Fig 2a except that the perspective technique described by Hasler *et.al* (1985) is used to display the results with artificial illumination producing the shading. Note how the thin cirrus bands north of the eye are shown to be much lower than the nearby central dense overcast which is caused by their transmission of energy from the warm ocean below.

Fig. 4a. Same as Fig 3a except that the visible image supplies the shading for the perspective technique.

Fig. 1b. NOAA AVHRIR satellite 1 km resolution visible image of Hurricane Allen corresponding to the infrared image shown in Fig. 1a. This image has been remapped into the coordinate system of the GOES East satellite image (see Fig. 1c).

Fig. 2b. Illuminated image of automatically analyzed synthetic stereo heights. The synthetic stereo technique described by Hasler *et al.* (1981) was used to make a stereo image from Figs. 1a and 1b for an automatic Massive Parallel Processor (MPP) stereo analysis algorithm to be tested on. Comparing with Fig. 2a we see fundamentally the same image except for smoothing due to an 11 X 11 cross correlation search area.

Fig. 3b. Same as Fig 2b except that the perspective technique is used to display the results with an artificial illumination producing the shading.

Fig. 4b. Same as Fig 3b except that the visible image supplies the shading for the perspective technique.

Fig. 1c. GOES East 1 km resolution visible image of Hurricane Allen at 1336 UTC on 8/8/80. It is nearly simultaneous to the NOAA image shown in Fig. 1b. The combination of Fig. 1b and this figure constitutes a GEO/LEO stereo pair. A discussion of the production and application of simultaneous GEO/LEO stereo pairs is reported by Hasler *et al.* 1983.

Fig. 2c. Illuminated display of Hurricane Allen cloud top heights from the GOES East and NOAA AVHRIR (GEO/LEO) visible images shown in Figs. 1b and 1c. This view is developed from automatic MPP stereo analysis using a 20 X 20 search area for the cross correlations.

Fig. 3c. Same as Fig 2c except that the perspective technique is used to display the results with an artificial illumination producing the shading. Note the thin cirrus bands north of the eye shown to be nearly as high as the nearby central dense overcast which is not true in the infrared based products shown in Figs 3a and 3b.

Fig. 4c. Same as Fig 3c except that the visible image supplies the shading for the perspective technique.

Many cloud surfaces are difficult to process compared to most geographical surfaces which have been successfully defined previously using ASA. Some of the problems with cloud fields include extremely steep slopes with discontinuities at cloud edges and amorphous cirrus clouds with very little structure. In addition the relatively low quality 6 bit GOES images normally used make the problem even more difficult. For this reason a well behaved test case was chosen with known topography which however, still had real (typical) cloud slopes, discontinuities and texture. A 1 km resolution 8 bit NOAA AVHRR visible and infrared image pair of hurricane Allen was used to construct the test data set. The synthetic stereo technique described by Hasler et al. (1981) was used to produce a test stereo image pair from the data set so that the ASA could be used under optimum conditions.

Figures 1 - 4 consists of 12 images arranged in a full page 3 X 4 matrix to aid in understanding the results. The first column (Figs. 1a, 2a, 3a, 4a) shows a 1 km resolution AVHRR infrared image and various enhancements (eg. illumination & perspective displays). The first row (Figs. 1a, 1b, 1c) adds the corresponding AVHRR visible image and the GOES visible image to make a stereo pair. (Figs 1b and 1c) The remaining images illustrate how the automatic analysis program performs on real and simulated stereo pairs.

3.1 Automatic Stereo Calibration Using Synthetic Stereo

In Fig. 1a. we see a NOAA AVHRR 11 micron infrared image with 1 km resolution of Hurricane Allen at 1336 UTC on August 8, 1980 when the storm was located in the Gulf of Mexico. The NOAA satellite with an orbital height of about 1000 km is considered a Low Earth Orbiter (LEO). The NOAA AVHRR satellite 1 km resolution visible image of Hurricane Allen is shown in Fig. 1b. corresponding to the infrared image of Fig. 1a. This image has been remapped into the coordinate system of the GOES East satellite image (see Fig.1c) and is used together with the temperature information shown in Fig. 1a to produce synthetic stereo images described above. In Fig. 1c. we see the GOES East satellite 1 km resolution visible image of Hurricane Allen at 1336 UTC on August 8, 1980. This view is nearly simultaneous to the NOAA image shown in Fig 1b. The GOES, with a orbital height of about 40,000 km, is a Geosynchronous Earth Orbiter (GEO). The combination of Fig. 1b and 1c constitutes a GEO/LEO stereo pair. A discussion of the production and application of simultaneous GEO/LEO stereo pairs is reported by *Hasler et al.* 1983.

Fig. 2a. is the same as infrared image in Fig. 1a, except that the number of brightness levels is reduced from 256 to 14 and an artificial illumination algorithm as been used to highlight the contours as described above. The synthetic stereo technique described by Hasler et al. (1981) was used to make a stereo image from Figs. 1a and 1b to test the automatic MPP stereo analysis algorithm. The illuminated image of automatically analyzed synthetic stereo heights is shown in Fig. 2b. The synthetic stereo technique uses an image pair consisting of a reference image (Fig. 1b) and a derived image made by shifting pixels horizontally (up to 14 pixels) proportional to their height. Therefore in level areas the images are identical and the automatic stereo analysis should give perfect results. However, where there are cloud surface discontinuities or the slopes are very steep, the automatic analysis is severely tested. An 11 X 11 search area test produced an excellent reproduction of the input field (compare Figs. 2a and 2b) with only a few small areas of bad matches as shown here. However, the comparison between Figs. 2a and 2b also dramatizes the fairly drastic smoothing resulting from cross correlation boxes of this size. In particular the two bands of thin cirrus seen north of the eye in Fig. 2a are not resolved in this image. Figures 3a and 3b use the artificially illuminated perspective rendering display technique to emphasize the basic similarities, as well as the loss of detail due to smoothing. When the illumination from the actual visible image is substituted (see Figs. 4a and 4b), differences between the actual infrared and automatically analyzed infrared are difficult to detect.

3.2 Automatic Stereo Analysis of GEO/LEO Visible Images

The ASA was tested next on the highest quality real stereo data set available. This data set was formed by remapping an 8 bit resolution NOAA AVHRR visible image into the coordinate system of a GOES East visible image. The brightness resolution of the GOES image was only 6 bits, but the combination gave significantly better feature matching than the use of two 6 bit images.

In Fig. 2c. we see an illuminated display of Hurricane Allen cloud top heights from the GOES East and NOAA AVHRR (GEO/LEO) visible images (Figs. 1b and 1c). This view is developed from automatic MPP stereo analysis using a 20 X 20 search area for the cross correlations. The basic features such as the eye, deep trough north of the eye and convective cloud towers west of the eye are resolved similarly to the infrared images. However, in the true stereo thin cirrus features are maintained at the proper height unlike the infrared representations which place them at too low an altitude. Note how the thin cirrus bands north of the eye in the infrared based images (see Figs. 3a and 3b) are shown to be much lower than the nearby central dense overcast. This effect is caused by their transmission of energy from the warm ocean below (see true stereo view in Fig. 3c on right). Comparing Figs. 4a, 4b and 4c where the visible image supplies the shading for the perspective technique, the gross differences between the infrared based and true stereo based heights can still be detected.

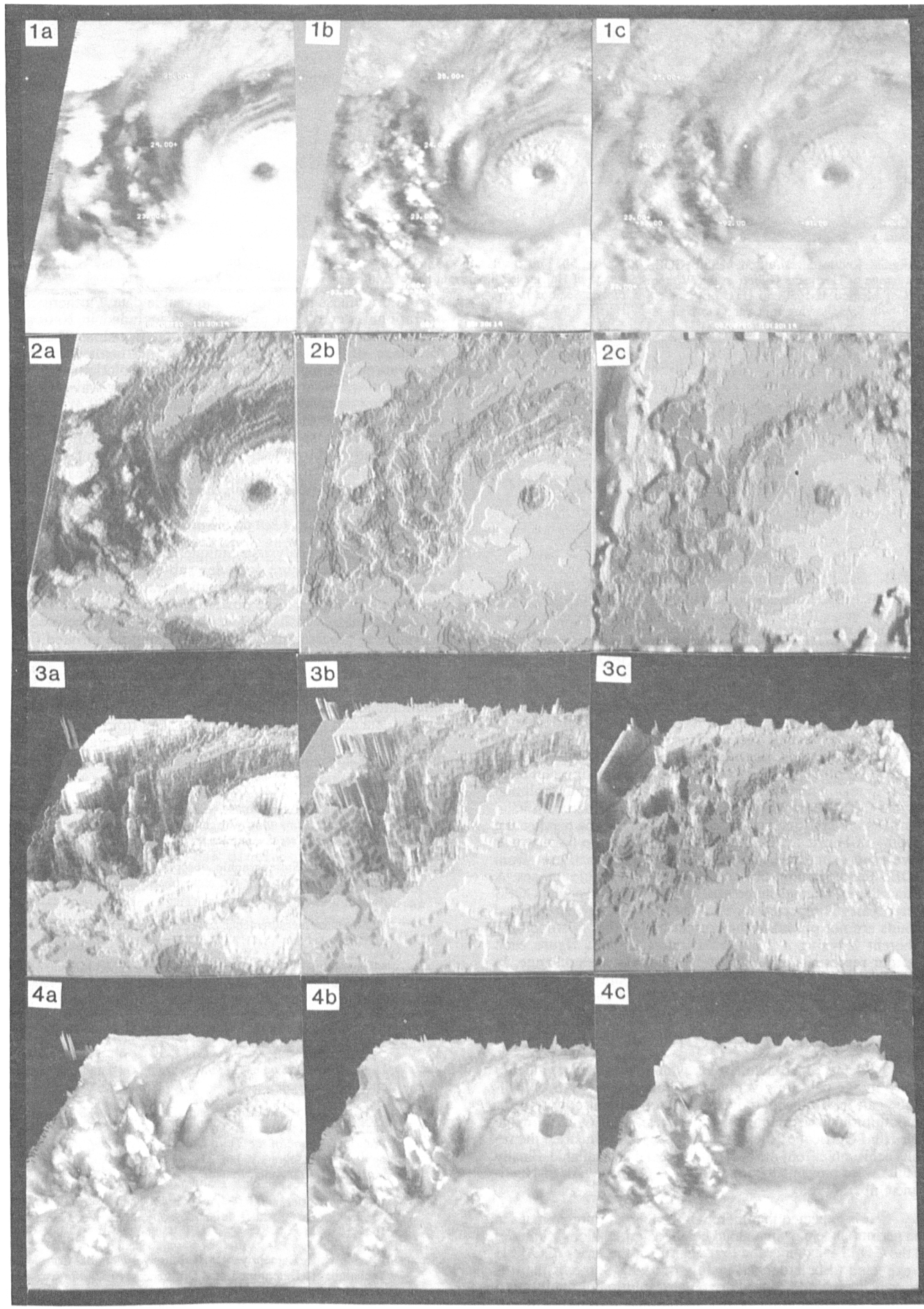
1a
1b
1c
2a
2b
2c
3a
3b
3c
4a
4b
4c

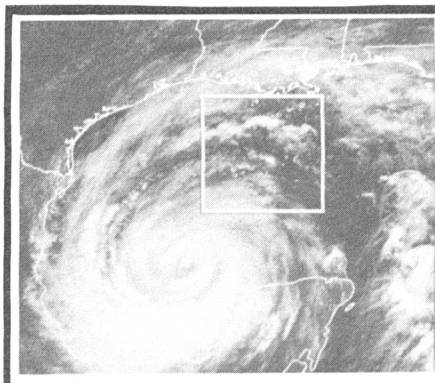

Fig.5a. Reduced resolution visible GOES East image of Hurricane Gilbert in the Western Gulf of Mexico at 16:48:56 UTC on Sept. 15, 1988 with box showing rain band close up region North East of eye.

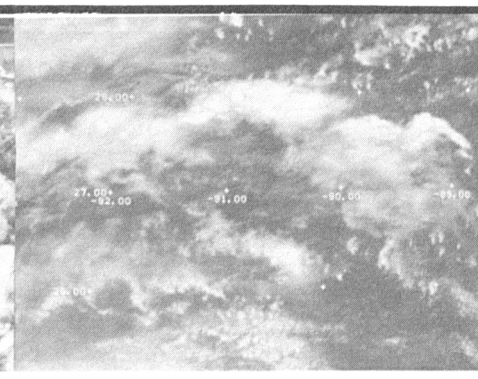

Fig. 5b. Full resolution visible GOES East image of Hurricane Gilbert rain band north east of eye. See box in Fig. 5a.

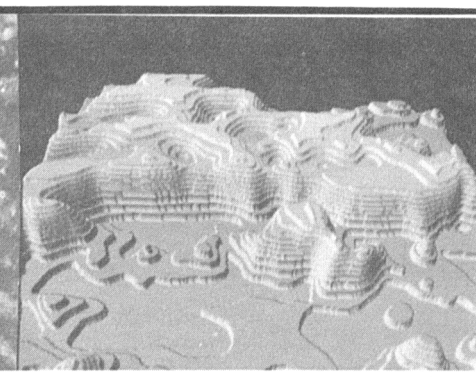

Fig. 6a. perspective display of Hurricane Gilbert rain band cloud top heights.

Fig. 6b. Perspective rendering of the MPP analyzed stereo except that the visible image (Fig. 5b) is used for shading instead of the artificial illumination shown in Fig. 6a.

3.3 Automatic Stereo Analysis of GEO/GEO Visible Images

Stereo GOES satellite image pairs of a Hurricane Gilbert rain band area are used to illustrate the performance of the automatic stereo analysis technique for small isolated clouds. Fig.5a Presents a reduced resolution visible GOES East image of Hurricane Gilbert in the Western Gulf of Mexico at 16:48 UTC on Sept. 15, 1988 with the box showing rain band close-up region northeast of eye. Fig.5b shows a full resolution visible GOES East image of the Hurricane Gilbert rain band northeast of eye (See box in Fig. 5a.) The Fig. 6a perspective display of Hurricane Gilbert rain band cloud top heights was developed using the ASA with a 25 X 25 search area from GOES East (See Fig. 5b) and GOES-West visible images. A discussion of manual stereo analysis from simultaneous GOES stereo pairs is reported by Hasler (1981). Note that isolated clouds are not placed at the correct height due to smoothing inherent in using a 25 X 25 window. In this figure each contour represents approximately 1 km elevation change. In Fig. 6b we see a perspective rendering of the MPP analyzed stereo except that the visible image (5b) is used for shading instead of the artificial illumination shown in Fig. 6a.

4. CONCLUSIONS AND FUTURE WORK

Results of a baseline study with an idealized (synthetic) stereo image pair are given which show that the (ASA) technique can faithfully reproduce cloud top structure, except for smoothing caused by correlation boxes. A GEO/LEO image pair from Hurricane Allen (1980) was used to illustrate the results achievable from the best quality real data available. Finally results were presented from a GEO/GEO image pair of Hurricane Gilbert (1988).

It is expected that there will be a great improvement in the performance of stereo cloud height determination techniques in the GOES-Next era. The first satellite of the series (GOES I) is expected to be launched in July of 1990. Some of the improvements include better horizontal resolution of the infrared channel, over-sampling of the visible and infrared, and improved brightness resolution of the visible data. Furthermore, operational stereo data processing is included in National Weather Service operational plans for the first time. The performance of GOES I improvements pertinent to stereo observations are as follows: 1) One km resolution with 1.7 times over-sampling along the line in the visible wave length, (vs. no over-sampling now). This should give 300 m vertical resolution vs. 500 m on the present GOES. 2) Brightness digitization of 10 bits, (vs. 6 bit on the present GOES). This should greatly improve mid-day stereo. 3) Four km horizontal resolution with 1.7 times over-sampling along the line in the 11 micron IR band , (vs. 8 km on the present GOES). This will make 1.2 km vertical resolution stereo height measurements possible, compared to 4 km on the present GOES.

Automatic analysis technique enhancements to be investigated in the future include: sub-pixel correlation for extraction of fine structure information and use of the infrared image as a first guess. The powerful, but small and economical, workstations which are now on the market will be used in the future to process this type of data. Using the infrared first guess method to limit the search area and correlation algorithms adapted to the workstations, reasonable automatic analysis times should be achievable. With economical processing using automatic analysis techniques described in this paper, higher quality data and routine stereo image pairs from GOES-next, the prospects of operational use of stereo cloud height observations are much brighter.

5. REFERENCES

Fujita, T. T., 1982: Principle of stereoscopic height computations and their applications to stratospheric cirrus over severe thunderstorms.*Jour. Meteor. Soc. Japan.* **60**, 355-368.

Hasler, A. F., 1981: Stereographic observations from satellites: An important new tool for the atmospheric sciences. *Bull. Amer. Meteor. Soc.*, **62**, 194-212.

———, 1989: Stereo measurements. *Silver Anniversary Book on Weather Satellites*, Section VII-4, NOAA. (in press)

———, M. desJardins, & A. Negri, 1981: Artificial stereo presentation of meteorological data fields. Bull. Amer. Meteo. Soc., 62, 970-973.

———, R. Mack, and A. Negri 1983: Stereoscopic observations from meteorological satellites, *Adv. Space Res.* **2**, No.6, pp. 105-113, 1983, Pergamon Press.

———, H. Pierce and J. Dodge 1985: Meteorological data fields "in perspective". *Bull, Amer. Meteor. Soc.* **66**, pp. 795-801.

———, A.F., J. Strong, R. Morris, and H. Pierce, 1988: Automatic analysis of stereoscopic image pairs from GOES satellites, Preprint Volume of the Third Conference on Satellite Meteorology and Oceanography, Jan. 31- Feb 5, 1988. Anaheim, California. pp.187-191. Amer. Meteor. Soc. Boston, MA.

Mack, R. A., A. F. Hasler, and R. F. Adler 1983: Thunderstorm cloud top observations using satellite stereoscopy, *Mon. Wea. Rev.*, **111**, 1949-1964.

Strong, J. P. and H. K. Ramapriyan 1987: Massively Parallel Correlation Techniques to Determine Local Differences. *Proceedings 2nd International Conference on Supercomputing*, June 1987, Santa Barbara CA, International Supercomputer Institute.

16.4

FOURIER TRANSFORM SPECTROSCOPY FOR IMPROVED ATMOSPHERIC SOUNDING FROM SPACE

Steven H. Silverman, and Daniel D. LaPorte
Santa Barbara Research Center
75 Coromar Drive, Goleta, CA 93117 805-562-7330
H. E. Revercomb
University of Wisconsin-Madison,
Cooperative Institute for Meteorological Satellite Studies
1225 West Dayton Street
Madison, Wisconsin 53706 608 262-0544

Santa Barbara Research Center has been developing Michelson interferometer technology for Fourier transform spectroscopy (FTS) since the early part of this decade and has been working closely with the University of Wisconsin to develop the High-resolution Interferometer Spectrometer (HIS) NAS5-27608(1988), Revercomb(1988), Revercomb(1988), Revercomb(1988). This effort has proven the feasibility of the FTS system as an excellent tool for improved atmospheric measurements Smith(1987), Smith(1987), Smith(1988). This technology has matured to a point where space hardware is now under development for NASA of a Mars Thermal Emission Spectrometer (TES).

This paper describes the the application of FTS for improved temperature and trace gas soundings of the earth's atmosphere. It will also describe the instrument characteristics of the HIS aircraft instrument, and the characteristics and expected performance of both a research and operational geostationary orbit (GEO) sounders.

1.THE NEED FOR IMPROVED SOUNDINGS

NOAA will be installing a network of Doppler radar wind profilers across the U.S. In order to use this improved wind data (1m/s and vertical resolution of 1 km) for mesoscale or regional models the accuracy of temperature and moisture soundings from space must be improved in order to allow the finer spatial grid of the GOES measurements to be used. It has been shown that temperature and moisture distributions must be known to 1-2 km vertically, with an accuracy of 1°C for temperature and 3°C for dew point. The path to improved vertical resolution is through increased spectral resolution of the data.

An interferometer has distinct advantages over filter instruments when operated in GEO. The nature of the orbit is one that lends itself to staring systems. This is the ideal match for an interferometer coupled to an area array imaging system. Since all the data are taken simultaneously, longer integration times (and therefor better SNRs) are possible than those achievable with filter wheels, dispersive systems, or Fabry-Perot instruments. The only penalty paid for increased spectral resolution is one of increased data rate.

The HIS instrument provided the test bed to determine performance requirements for a geo-stationary sounder. Figure 1 shows a typical spectrum sensed by the HIS. GOES Next filter bandwidths are shown indicating the degree of smearing of the spectrum by the current GOES Next Sounder.

With this improved spectral data, calculations done at the University of Wisconsin have shown the degree of performance improvement the interferometer has over the expected performance of the GOES I/M filter wheel sounder. Figure 2 shows the improvement in vertical temperature resolution, and Figure 3 shows the improvement in the temperature and water vapor concentration accuracies.

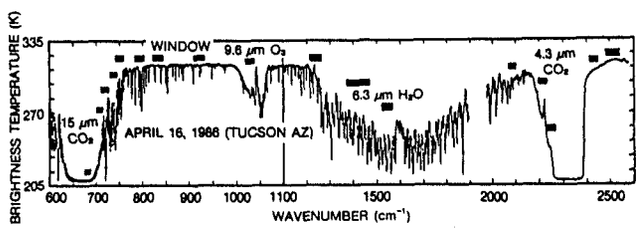

Figure 1. Radiation brightness temperature spectrum as observed by HIS from the NASA U-2 over Tucson, Arizona with the half bandwidths of the GOES-NEXT filters superimposed

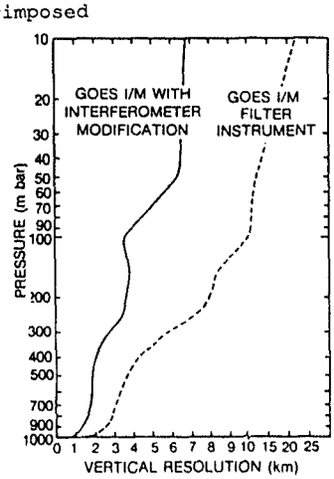

Figure 2. Improvement in vertical temperature profile RMS retrieval errors from modifying GOES L/M to use an interferometer..

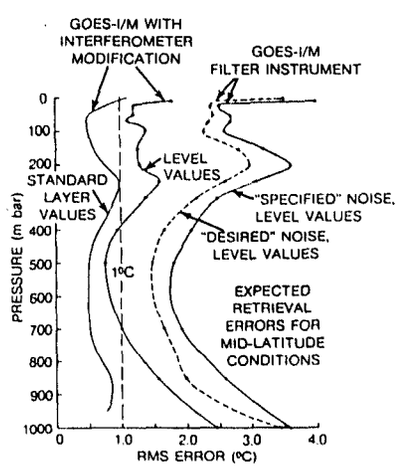

Figure 3. Improvement in vertical temperature profile resolution from modifying GOES L/M to use an interferometer.

2.HIS INSTRUMENT SPECIFICATIONS AND PERFORMANCE

NASA and NOAA jointly funded the development of the HIS aircraft instrument and since its completion in 1985, more than 40 flights aboard the NASA U2/ER2 and the NOAA P-3 have been made. These flights have demonstrated both the technical feasibility of flying an interferometer in a harsh environment, as well as demonstrating the radiometric performance of the instrument NAS5-27608(1988).

Table 1 Provides a list of the HIS aircraft instruments parameters.

Spectral range cm^{-1}	
Band I	590-1080
Band II	1080-1850
Band III	2000-2700
Field of view diameter (mr):	
Telescope	100
Interferometer	30
Blackbody reference sources:	
Emissivity	>0.998
Aperture diameter (cm)	1.5
Temperature stability (K)	±0.1
Auto-aligned interferometer:	modified Bomem BBDA2.1
Beamsplitter:	
Substrate	KC1
Coatings (1/4 Wave at 3.3μm)	$Ge+Sb_2S_3$
Maximum delay double-sided	
Band I (hardware limit is ±2.0)	±1.8
Bands II and III (limited by data system)	+1.2, -0.8
Michelson mirror optical scan rate (cm/s):	.06
Aperture stop (at interferometer exit window):	
Diameter (cm)	4.1
Central obscuration area	0.17
Area (cm^2)	10.8
Area-solid angle product (cm^2-sr):	0.0076
Detectors:	
Type	Ar doped Si
Diameter (cm)	0.16
Temperature (K)	6

Basically, the HIS covers a spectral region from 3.8 to 16.6 μm. The instrument fits in a pod about 3 meters long and 0.5 meters wide. The pod was mounted directly under the the main fuselage of ER2, in very close proximity to the engine and on the P-3 in the turbulent wake of the Radar antenna pod. The modified BOMEM Michelson Interferometer is evacuated and equipped with a dynamic alignment system, thus allowing the interferometer to operate properly even in the harsh vibrational environments of the ER2 and P3.

The radiometric performance of the aircraft instrument is best interpreted by looking at the scene brightness temperature errors when compared to temperatures calculated using FASCODE. The temperature errors are generally from incomplete information input to the FASCODE computation with respect to the temperature and water vapor, atmospheric constituents, as well as deficiencies in the FASCODE equations. Figure 4 shows a representative spectrum along with FASCODE calculation and the associated error.

3. THE GOES HIGH RESOLUTION INTERFEROMETER SOUNDER (GHIS)

Existing filter wheel sounders are limited in their operational flexibility since time sequential measurements are made, limiting the number of spectral channels available during a given observational period. This suggests that an interferometer (which measure spectral information simultaneously) is the ideal instrument to replace the GOES (I-M) filter wheel instrument. A recently study for NOAA has confirmed this assumption RPT81280(1988). Table 2 lists some of the instrument parameters of the GHIS. The important feature here is that the interferometer will only increase the the sensor weight by 6.8 kg, and the average power consumption increases by only 10.7 watts. The sounder data rate will be less than 500 kbs.

Table 2 Key features of GHIS instrument

Simultaneous FOV	4
FOV Defining Element	Field Stop, 242 μrad (8.6 km, Nadir)
Telescope Aperture	31.1 cm (12.25 in) Dia.
Channel Separation,	Dichroic
IR Spectral Definition	Interferometer
Visible Sounding	Fixed Detectors
Radiometric Calibration	Space and 290K Blackbody
Frequency of Space Clamp	2 Minutes
IR Calibration Frequency	20 Minutes
IR Detector Temperature (K)	92, 97, 102, 107
Field Sampling	4 Areas N-S on 10 km Centers
Scan Step Angle	280 μrad (10 km Nadir); Skip-Step and Skip-Line Optional
Step and Dwell Time	0.1 Seconds; 02.s, 0.4s. 0/8 Optional
Scan Capability	Full Earth and Space
Sounding Areas	10 km x 40 km to 60°E-W & 60° N-S
Optical Location	Star Sensing
Output Data	12 Bits
Output Data Rate	<500 kbits Per Second
System Power Average	112W
System Weight:	
Sensor Assembly	202 lb (92.0 kg)
Electronics Module	61 lb (27.9 kg)
Power Supply	14 lb (6.2 kg)
Interferometer Processor	16 lb (7.3 kg)
Total Weight	293 lb (133.4 kg)

The expected performance of the GHIS greatly exceeds the expected performance of the current GOES Next Sounder as illustrated in table 3a & 3b.

Table 3a Expected GHIS NEN performance

NEΔN [mW/sqm/sr/cm-1]

Spectral Resolution	Dwell Time [sec]	Band1 [cm-1] [620 -1150]	Band2 [cm-1] [1210 -1740]	Band3 [cm-1] [2150 -2721]
Low	0.1	0.11	0.06	0.006
Medium	0.4	0.25	0.13	0.014
High	0.8	0.36	0.19	0.021

Table 3b GHIS low resolution mode NEN performance reduced to GOES I/M resolution

Channel Number	Channel Wavenumber	GOES I/M Resolution Δv [cm-1]	GHIS NEΔN [mW/sqm/sr/cm-1] Specified	Desired	Expected
1	680	13	0.66	0.25	0.065
2	696	13	0.58	0.25	0.066
3	711	13	0.54	0.25	0.067
4	733	16	0.45	0.25	0.063
5	748	30	0.44	0.20	0.047
6	790	50	0.25	0.15	0.038
7	832	50	0.16	0.06	0.040
8	907	25	0.16	0.06	0.062
9	1035	25	0.35	0.12	0.071
10	1345	55	0.16	0.05	0.017
11	1425	80	0.12	0.04	0.015
12	1535	60	0.15	0.04	0.018
13	2188	23	0.013	0.004	0.0029
14	2210	23	0.013	0.004	0.0030
15	2245	23	0.013	0.004	0.0030
16	2420	40	0.008	0.003	0.0025
17	2513	40	0.0082	0.003	0.0025
18	2671	100	0.0036	0.002	0.0017

4. A RESEARCH SOUNDER

If we free the sounder from the GOES (I-M) operational requirements and allow it to operate in a research mode, a great deal of improvements can be made to the GHIS concept. The first step is to increase the number of detectors in the focal plane from 4 to 25, which gives better geometric integrity to the data, allows an increase in scene dwell time, and provides a higher degree of spatial simultaneity. The addition of more flexible scene scan scenarios will allow the scientist to carefully studie areas of interest, and increased programmability of the interferometer functions will allow flexibility in the selection of spectral regions and spectral resolutions. Finally, the addition of a visible cloud imaging array will provide simultaneous and instantaneous data for cloud clearing algorithms. Figure 5 is a depiction of the surface "footprint" of the Research Sounder and Figure 6 is an optical schematic of the Research Sounder.

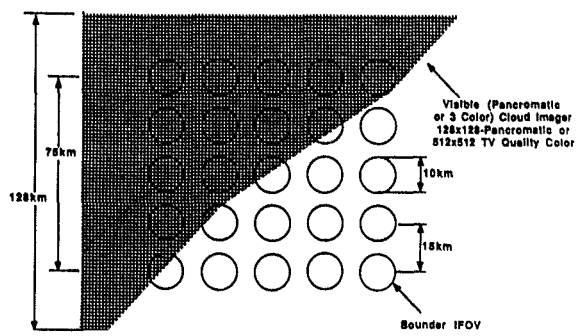

Figure 5. "Footprint" Of the Research Sounder

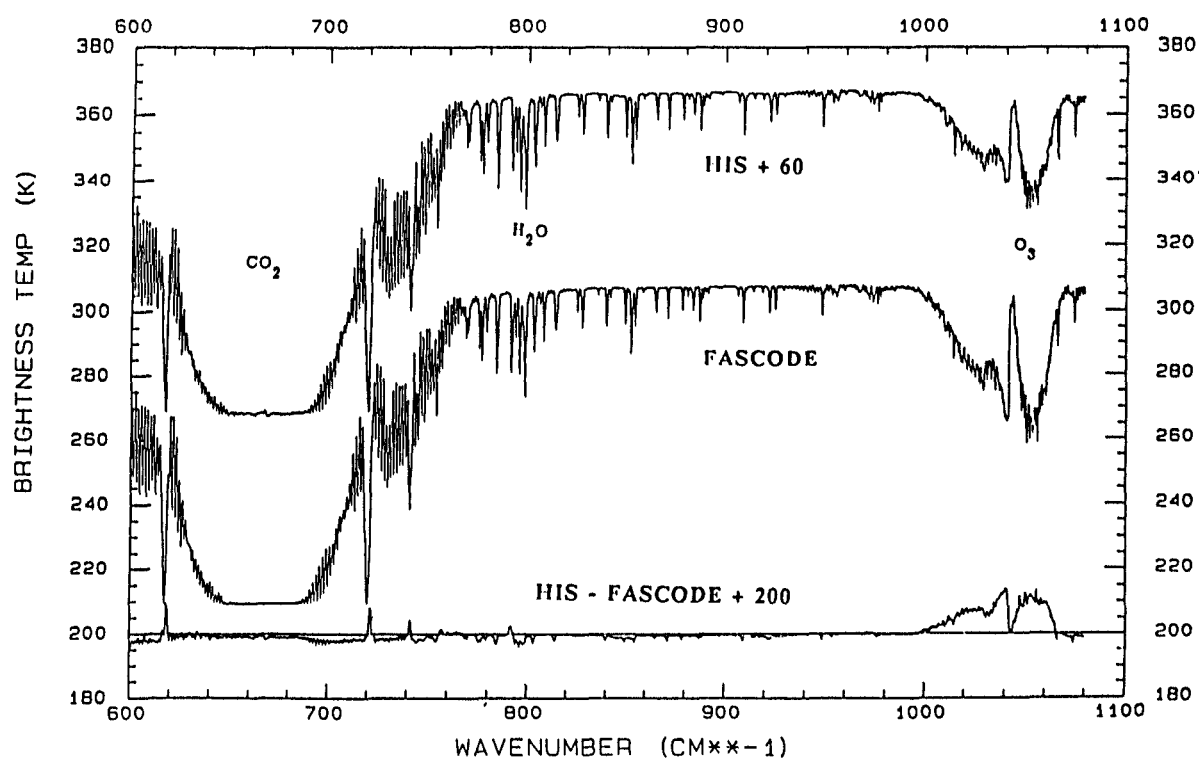

Figure 4. Equivalent blackbody temperature of upwelling radiance from the nadir viewing HIS instrument from the NASA U2 20 km over the desert southwest on April 15, 1986. Also shown is a calculation from FASCOD2 using a nearby radiosonde to yield 0.7 cm^{-1} resolution .

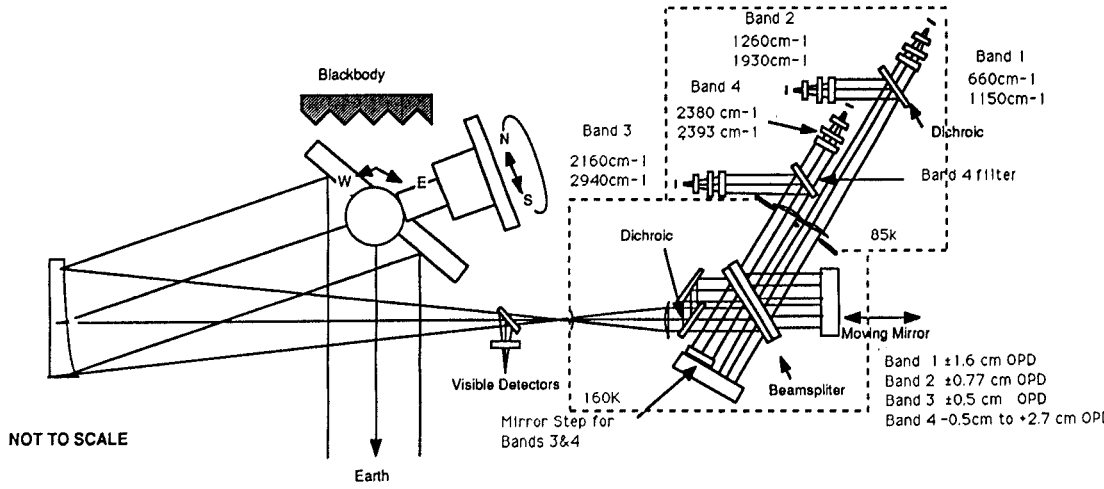

Figure 6. Optical Schematic Of the Research Sounder

Table 4 Research Sounder Characteristics

Coverage:	3000km x 3000km less than 30 min /1000km x 1000km in 3 Min			
Integration Time(sec):	1.00			
	IR (5X5)	VIS (128X128)		
IFOV Diameter [km]:	10	1		
Footprint Center Spacing [km]:	15	1		
Spectral Separation:	Fourier Transform Spectrometer, Four Spectral Bands			
	Band1	Band 2	Band 3	Band 4
Spectral coverage [cm-1]:	660-1150	1210-1930	2160-2940	2380-2393
Avg Apodized Resolution (cm-1):	0.63	2.33	2.33	0.37
Focal Plane Type:	PC HgCdTe	PC HgCdTe	PV HgCdTe	PV HgCdTe
Array Size:	5x5	5x5	5x5	5x5
NEΔN [mW/m^2/sr/cm-1]:	0.128	0.036	0.026	0.004
Telescope:	60 cm Entrance Pupil, Unobscured Confocal Parabolas			
Cooling:	Passive Radiative Cooler Enhanced VAS Type, Passive Radiator for Interferometer			
Data Rate(bits/sec):	2.09E+07			
Instrument Temperatures:	280K Telescope, 140K Interferometer, 80K Detector			
Instrument Weight & Power:	200kg 150-200W			

5.References

NAS5-27608 "High-Resolution Interferometer Sounder (HIS) Phase II", NASA Contract - University of Wisconsin-Madison, Cooperative Institute for Meteorological Satellite Studies, Oct 1988

H.E. Revercomb, D.D. LaPorte, W.L. Smith, H. Buijs, D.G. Murcray, F.J. Murcray, and L.A. Sromovsky, "High-Altitude Aircraft Measurements of Upwelling IR Radiance: Prelude to FTIR from Geosynchronous Satellite", (for 6th International Conference on Fourier Transform Spectrocopy, Vienna, Austria, 24-28 August 1987) Mikrochimica Acta, in Press 1988.

H.E. Revercomb, H. Buijs, H.B. Howell, R.O. Knuteson, D.D. LaPorte, W.L. Smith, L.A. Sromovsky, and H.W. Woolf, "Radiometric Calibration of IR Interferometers: Experience from the High-resolution Interferometer Sounder (HIS) Aircraft Instrument", Presented at International Workshop on Remote Sensing Retrieval Methods, Williamsburg, Virginia, 15-18 December, for publication in Advances in Remote Sensing Retrieval Methods, a. Deepak Publishing, Hampton, Virginia, in Press, 1988.

H.E. Revercomb, H. Buijs, H.B. Howell, D.D. LaPorte, W.L. Smith, and L.A. Sromovsky, "Radiometric Calibration of IR Fourier Transform Spectrometers: Solution to a Problem with the High Resolution Interferometer Sounder",, Applied Optics, 27, 3210-3218, 1988

W.L. Smith, H.M. Woolf, H.B Howell, H. L. Huang and H.E. Revercomb, "Improved Geostationary Satellite Soundings for the Mesoscale Weather Analysis/Forecast Operation", Proc. Symp.. Mesoscale Analysis and Forecasting, Vancouver, Canada, 17-19 August, ESA SP-282, 79-83, 1987.

W.L. Smith H. M. Woolf, H.B. Howell, H.E. Revercomb, and H.-L. Huang, "HIS - A High Resolution Atmospheric Sounder", Paper presented at the 21st International Symposium on Remote Sensing of Environment, Ann Arbor, Michigan, 26-30 October, 1987.

W.L. Smith, H.M. Woolf, H.B. Howell, H. -L. Huang, andH.E. Revercomb, "The Simultaneous Retrieval of Atmospheric Temperature and Water Vapor Profiles - application to Measurements with the high- resolution Interferometer Sounder (HIS)", Sensing Retrieval Methods, Williamsburg, Virginia, 15-18 December, for publication in Advances in Remote Sensing Retrieval Methods A. Deepak Publishing, Hampton, Virginia, in Press, 1988.

RPT81280 "High-Resolution Interferometer Modification of the GOES L/M Sounder: Feasibility Study" NOAA/NESDIS Grant number NA87AA-H, Cooperative Institute for Meteorological Satellite Studies, September 1988

MULTISPECTRAL RETRIEVAL OF RAINFALL RATES USING THE SPECIAL SENSOR MICROWAVE / IMAGER (SSM/I)

William S. Olson, Frank J. LaFontaine, William L. Smith, Barry A. Roth

Cooperative Institute for Meteorological Satellite Studies, University of Wisconsin
Madison, Wisconsin

Christian D. Kummerow

NASA / Goddard Space Flight Center
Greenbelt, Maryland

1. INTRODUCTION

The Special Sensor Microwave/Imager (SSM/I) is a passive multichannel microwave radiometer borne by the DMSP-F8 polar orbiting satellite. The SSM/I is configured with dual-polarization channels at three frequencies (19.35, 37, and 85.5 GHz) and a single-polarization (vertical) channel at 22.235 GHz. Radiance measurements from the SSM/I have been analyzed to yield estimates of a variety of environmental parameters, including suface wind speed and precipitable water over the ocean, sea ice concentration, precipitation rate, and land surface type (see DMSP SSM/I CAL/VAL Team, 1989).

In this article, collocated SSM/I and radar measurements are compared to model-simulated radiances upwelling from precipitating clouds. The model comparisons illustrate the significant variations in the microwave brightness temperature-rainfall rate relationship induced by both variations in fractional coverage of the SSM/I footprint by rain and the vertical distribution and phase of hydrometeors in the precipitating cloud.

The model simulations serve as a guide to the development of statistical rain rate retrieval algorithms, which are derived from the collocated SSM/I and radar data. Regressions of the SSM/I brightness temperatures against rainfall rate yield maximum correlations of .78 over land and .85 over ocean at midlatitudes.

2. METHODOLOGY

Raingages provide the most accurate standard for point estimates of surface rainfall. However, because of the high spatial variability of precipitation intensity and the relatively low sampling density (one measurement every 25 km along-scan) and large footprint dimensions (minimum 13 km x 15 km) of the SSM/I, area-averaged radar rain estimates are utilized as the primary source of ground truth data in this study.

In order to maximize the correlation between the radar rain rate estimates and surface rainfall amounts, only low antenna elevation angle ($\alpha \leq 1^{o}$) plan-position indicator (PPI) scans were used. Also since the radar beam height increases with range, no radar measurements beyond a range of 220 km were considered. Ground clutter and obvious radar artifacts were also screened. The remaining bin reflectivities were converted to rainfall rate using a standard relationship ($Z=200\ R^{1.6}$) and then interpolated to a 5 km cartesian grid.

Typically three radar PPI sweeps bracketing the DMSP-F8 overpass time were processed. All gridded rainfall rates falling within a 625 km^2 circular area of a given SSM/I all-channel brightness temperature scene were time-interpolated to the SSM/I measurement time. The time-interpolated, gridded rain rates were subsequently area-averaged and then stored along with the corresponding seven sensor data record (SDR) brightness temperatures (see Hollinger et al., 1987).

Since individual radar-derived rainfall rate estimates can have a high uncertainty, simultaneous raingage measurements were also recorded for the purpose of calibration.

3. DATA SOURCES

SSM/I brightness temperature measurements coinciding with radar measurements of precipitation were obtained from the Naval Research Laboratory (NRL) archive.

Surface truth for midlatitude validations was obtained from seven radar sites in the United Kingdom operational network and the Patrick Air Force Base (PAFB) radar at Cape Canaveral, Florida (see Table 1 for specifications).

Table 1 Validation radar sites and number of calibrating raingages.

Radar site	Specifications	Number of gages
Camborne, England, UK	10 cm, S-band, 2° beamwidth	3
Upavon, England, UK	10 cm, S-band, 2° beamwidth	3
Clee Hill, England, UK	5.6 cm, C-band, 1° beamwidth	3
Hameldon Hill, England, UK	5.6 cm, C-band, 1° beamwidth	5
Chenies, England, UK	5.6 cm, C-band, 1° beamwidth	5
Shannon, Ireland, UK	10 cm, S-band, 2° beamwidth	0
Castor Bay, Northern Ireland, UK	5.6 cm, C-band, 1° beamwidth	0
Patrick Air Force Base, Cape Canaveral, FL	5 cm, C-band, 1.1^{o} beamwidth	21

Each of these radars provided significant coverage of both land and ocean areas, and were operating almost continuously since the launch of the DMSP-F8.

The United Kingdom data were obtained from archives maintained by the British Meteorological Office (BMO), and the PAFB data were retrieved from laser disk recordings compiled by personnel at the Severe Storms Laboratory at NASA / Goddard Space Flight Center.

Raingage observations from three to five telemetering raingages are recorded operationally for five of the seven United Kingdom sites. If sufficient raingage hourly totals are recorded in the same time frame as a given radar sweep, then a real-time correction is applied to the radar data using the scheme described by Collier, et al. (1983).

Hourly raingage data from National Weather Service (NWS) gages in the vicinity of the PAFB radar site were obtained from National Climatic Data Center archives at Asheville, North Carolina. Twenty-one raingages in the NWS network provided hourly rainfall rate totals within a 200 km radius of the PAFB site.

4. SATELLITE / RADAR DATA GEOLOCATION

Since rainfall is highly variable in both space and time, accurate geolocation of both the satellite and radar data is required for proper statistical comparisons.

Errors as great as 30 km were observed in the position of land-ocean boundaries in the DMSP-F8 SSM/I imagery. Since precipitation fields can vary greatly on spatial scales of 10 km or less, correlations between brightness temperature features in the SSM/I imagery and radar echoes were degraded in many situations. Through a cooperative effort between scientists at University of Wisconsin, University of Massachusetts (UMASS), and the Naval Research Laboratory (NRL), a method was developed to automatically relocate the SSM/I data.

Basically, the method consisted of an optimization routine which searched for corrections in the spacecraft pitch and yaw angles that maximized the correlation between coastal discontinuities in the 85.5 GHz horizontally-polarized SSM/I brightness temperature imagery and the known location of coastal boundaries as specified in the World Data Base II coastline map.

Upon review of 10 to 20 relocated SSM/I images, the automated procedure appeared to locate the satellite data to within about 6 km of the World Data Base II coastline. The WDB II coastline is reported to be accurate to within 3 km.

The radar data were earth-located using the recorded range of the radar bin and the elevation and azimuth angle of the radar antenna. The uncertainty in the earth location of any radar bin is estimated to be on the order of 1-2 km. The estimated total error in the radar ground truth product, including satellite-radar misregistration, is ~45%.

5. DATA SAMPLES

DMSP-F8 overpasses of the United Kingdom and PAFB radar sites during the summer and fall of 1987 and the spring of 1988 provided data for model and statistical comparisons. The United Kingdom (hereafter UK) data set is composed of collocated SSM/I and radar measurements derived from 23 overpasses of the UK radar sites during August and September of 1987. Nine overpasses of the PAFB site during August and November of 1987 and March of 1988 contributed to the Cape Canaveral (hereafter Cape) comparison data set. The total numbers of collocated area-average rain rate estimates and SSM/I all-channel measurements in the UK, Cape and combined data sets are listed in Table 2. Listed separately are the number of collocated measurements over land and ocean backgrounds. Also included are the number of "significant" collocated measurements, defined as those for which the area-average radar rain rate was at least 0.5 mm/hr.

Table 2 Numbers of collocated SSM/I and radar data.

	land	ocean
UK:	2291 (243)	581 (75)
Cape:	369 (120)	343 (117)
Total:	2660 (363)	924 (192)

Despite the large numbers of total collocated data, Table 2 indicates that only a small fraction of the data are associated with rain rates exceeding 0.5 mm/hr. This characteristic of the sample is due to the naturally skewed rainfall rate distribution, which is dominated by light rain rate events. The skewed rain distribution has an important bearing on the statistical analyses to be presented in section 7.

6. MODEL COMPARISONS

In Fig. 1 are plotted SSM/I-measured brightness temperatures versus collocated, radar-derived rainfall rates over the ocean. The UK and Cape data were combined in this plot. Note that although there is a trend of decreasing brightness temperature with rainfall rate, there is a large range of rainfall rates that may be associated with a given brightness temperature.

The scatter of data in Fig. 1 may be explained using model simulations of the upwelling microwave radiances. Horizontally-finite, precipitating "clouds" with random areas ranging from 25 to 2500 km^2 were generated and positioned in random locations with repect to a circular, 625 km^2 radar observation area. The only constraint on the cloud position was that some finite portion of the cloud was required to be within the 625 km^2 area. The rainfall rate within the cloud was also randomly generated between values of 0 and 64 mm/hr. The rainfall rate was assumed to be uniform within the cloud area, while the rainfall rate outside the cloud area was assumed to be zero. The hydrometeors within each cloud included both liquid and ice hydrometeors in a vertical distribution consistent with the structure of strongly convective clouds or thunderstorms.

The microwave brightness temperature upwelling from each model cloud was computed using the modified Eddington solution described in Kummerow and Weinman (1988). The upwelling radiance from a single cloud and the surrounding rain-free atmosphere were then convolved by the SSM/I antenna response pattern in the 85.5 GHz vertical channel to simulate an individual SSM/I measurement. The area-average rainfall rate produced by each cloud within the 625 km^2 observation area was also recorded.

A total of 500 randomly-generated model clouds yielded the distribution of 85.5 GHz brightness temperatures shown in Fig. 2. The data are sorted by the fraction of the 85.5 GHz antenna pattern subtended by each model cloud. For the purpose of display, the actual fraction is multiplied by ten and rounded down to the next lowest integer. Note that the spread of observed brightness temperatures in Fig. 1 can be explained by the varying antenna reponse to each cloud. For a given area-average rainfall rate, the brightness temperature decreases with increasing response by the antenna. An increase in the antenna response may be due to a cloud location closer to the antenna boresight, or a cloud covering a larger area.

Another factor which can cause a variation in the measured radiance at 85.5 GHz is the phase of hydrometeors in the precipitating cloud. The closed dots in Fig. 3 correspond to the convective cloud model simulation previously described. Model clouds containing only liquid precipitation were utilized to generate the distribution of radiances identified by small circles in Fig. 3. The liquid clouds are more representative of stratiform precipitation areas, in which cloud updraft speeds are relatively low.

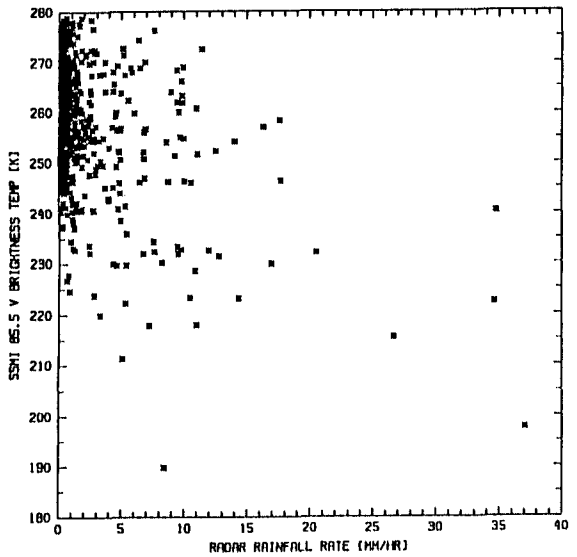

Fig. 1 SSM/I-measured 85.5 GHz vertically-polarized radiances from precipitating clouds over the ocean.

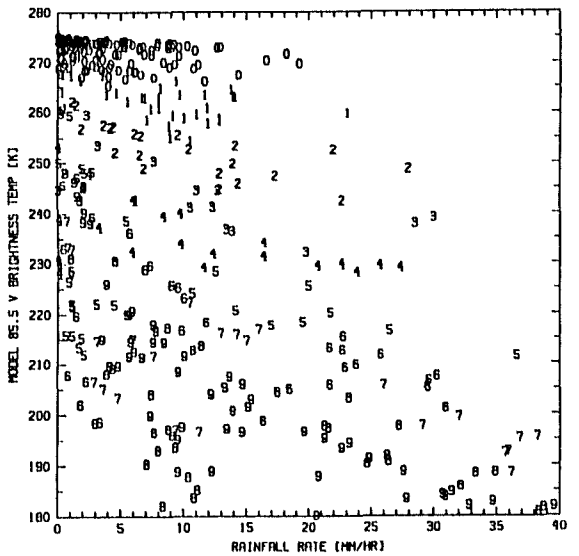

Fig. 2 Modeled 85.5 GHz vertically-polarized radiances from a distribution of precipitating convective clouds over the ocean.

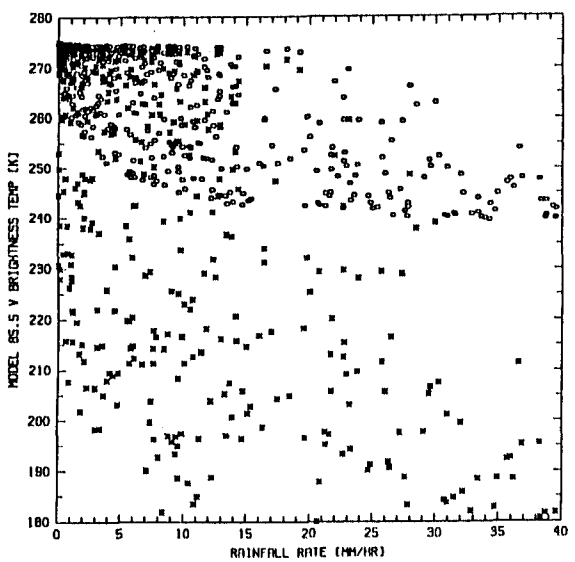

Fig. 3 Modeled 85.5 GHz vertically-polarized radiances from distributions of precipitating convective and stratiform clouds over the ocean.

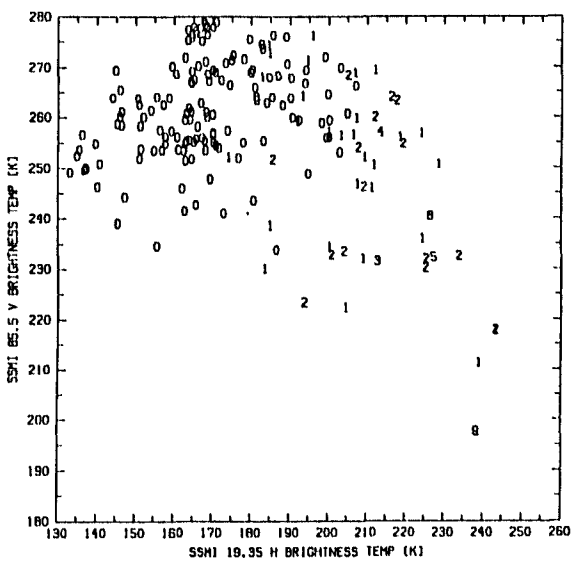

Fig. 4 SSM/I-measured 85.5 GHz vertically-polarized and 19.35 GHz horizontally-polarized radiances from precipitating clouds over the ocean.

Note that the decrease in 85.5 GHz brightness temperatures induced by the liquid clouds is generally much less than in the convective cloud simulations, with a minumum brightness of ~240 K. Precipitating cloud systems typically contain both convective and stratiform precipitation areas (see Houze and Hobbs, 1982).

The observations and model simulations in Figs. 1, 2, and 3 suggest that more than one SSM/I channel or measurement are required to infer a unique estimate of rainfall rate. Fig. 2 indicates that the upwelling brightness is sensitive to the position of, and area subtended by, the cloud within the SSM/I footprint. High resolution visible or infrared data could provide the necessary information on cloud distribution; however, neighboring 85.5 GHz SSM/I measurements could also be utilized to resolve the gross features of the rain distribution, since adjacent measurements are separated by 12.5 km.

Alternatively, the different response of channels at the other SSM/I frequencies and polarizations could also be utilized to remove ambiguity in rain rate estimates. For example, the plot of 85.5 GHz vertical and 19.35 GHz horizontal SSM/I measurements in Fig. 4 indicates that it may be possible to separate classes of rainfall rate using a linear combination of the two channels. The numbers in the plot are the radar-observed rainfall rate divided by four and rounded to the next-lowest integer. A trend of increasing rainfall rate is observed along an axis from the upper-left corner to the lower-right corner of the plot.

7. STATISTICAL RAINFALL RATE RETRIEVAL ALGORITHMS

Prospective retrieval algorithms are derived, based upon stepwise multiple linear regression of the SSM/I brightness temperature data against the collocated, radar-derived rainfall rates from both the UK and Cape radars. Two types of regression model are tested:

$$R = a_0 + \sum_{i=1}^{N} a_i TB_i \qquad (1)$$

and

$$R = \exp\{a_0 + \sum_{i=1}^{N} a_i TB_i\} - c \qquad (2)$$

The rainfall rate R is expressed as a function of N SSM/I-measured brightness temperatures TB_i, with fitted constants a_i. The exponential form (2) is determined by regressing ln(R+c) against the SSM/I brightness temperatures for different values of the constant c. The exponential form sometimes provides a better fit to the data because the magnitude of the incremental rain rate response of the SSM/I in all channels tends to decrease with increasing rainfall rate (see Kummerow and Weinman, 1988). The residuals in all regressions are weighted by the square root of the rainfall rate to compensate for the skewed distribution of rain rates in the collocated data sample.

Results of the regression analyses are presented in Table 3. Cases are coded according to the legend below the table. Although the regressions are based upon the total data sample, the statistics of each regression model are given for radar-derived rain rates ≥ 0.5 mm/hr, to avoid overemphasis of low rain rate events. The number of collocated data n, the mean rain rate Rm, the error standard deviation of the regression estimate σe, and the correlation coefficient r are given for each case.

Table 3 SSM/I regression model statistics.

Case	n	Rm	σe	r
Over land:				
A1	363	2.77	4.48	.598
B1	363	2.77	4.32	.636
C1	363	2.77	3.52	.756
D1	363	2.77	3.60	.752
A2	363	2.77	3.88	.664
B2	363	2.77	3.70	.702
C2	363	2.77	3.26	.784
D2	363	2.77	3.29	.784
Over ocean:				
A1	192	3.25	4.17	.525
B1	192	3.25	3.70	.650
C1	192	3.25	3.35	.730
D1	192	3.25	2.94	.800
A2	192	3.25	3.80	.585
B2	192	3.25	3.30	.715
C2	192	3.25	3.17	.739
D2	192	3.25	2.49	.846

A: regression against 85.5 GHz vertical data only
B: regression against 3x3 neighborhood of 85.5 GHz vertical channel observations
C: regression against all seven SSM/I channel measurements
D: regression against all seven SSM/I channel measurements plus 3x3 neighborhood of 85.5 GHz vertical channel observations
1: linear model; see Eq. (1)
2: exponential model with c = 4.0 mm/hr; see Eq. (2)

Regressions A and B are designed to test whether or not significant rain footprint-filling information is contained in the distribution of 85.5 GHz measurements (see Fig. 2). The linear and exponential models over both land and ocean all yield much better rain estimates when neighboring 85.5 GHz measurements are included as predictors of rain rate. Maximum correlations ~.7 are obatined using the exponential models and a 3x3 neighborhood of 85.5 GHz vertical channel observations.

The accuracy of regression rain rate estimates is further increased with the addition of the other six collocated SSM/I brightness temperature measurements. Again, the exponential models provide a better fit to the data than the linear models, with a maximum correlation of .784 over land and .739 over ocean. Over land, the inclusion of the 3x3 neighborhood of 85.5 GHz vertical channel observations does not have a significant impact on the performance of the regression models, once the full complement of SSM/I channel measurements at all frequencies is considered (see C1, D1, C2, and D2 in Table 3). However, over the ocean substantial improvements in the accuracy of regression estimates are obtained. The correlation increases from .739 to .846 with the addition of the neighboring 85.5 GHz vertical channel data.

8. CONCLUSIONS

Regression analysis of collocated SSM/I brightness temperature measurements and radar-derived rainfall rates show the potential of the SSM/I to provide 25 km resolution rain rate estimates over land and ocean surfaces. Because of their computational efficiency, the regression-based algorithms considered in this study are ideally suited to operational settings (see DMSP SSM/I CAL/VAL Team, 1989, for a detailed description of candidate algorithms).

Radiative transfer model simulations suggest, however, that significant improvements in retrieval accuracy are possible if physical models of the rain field and antenna response are employed. Specifically, an accurate description of the geometry of the cloud field and the vertical distribution of hydrometeors, in combination with existing microwave radiative transfer cloud models, would provide the necessary constraints for the physical retrieval of rainfall rates. Measurements from the SSM/I could be supplemented by visible, infrared, or active microwave measurements to yield the required high-resolution cloud information.

Acknowledgments

The authors would like to thank Jim Hollinger and Gene Poe of the Naval Research Laboratory, and the other members of the SSM/I CAL/VAL Team for their support during all phases of this project. Our special thanks go to Mark Goodberlet of UMASS for providing a spacecraft attitude correction routine for SSM/I data geolocation.

We would also like to thank the personnel of the British Meteorological Office and Dan Rosenfeld and David Wolff of NASA/Goddard Space Flight Center for supplying radar and raingage ground truth for this study.

References

Collier, C. G., P. R. Larke, and B. R. May, 1983: A weather radar correction procedure for real-time estimation of surface rainfall. Quart. J. R. Met. Soc., 109, 589-608.

DMSP SSM/I Cal/Val Team, 1989: DMSP Special Sensor Microwave/Imager Calibration/Validation Final Report. J. Hollinger, ed., (in preparation).

Hollinger, J., R. Lo, G. Poe, R. Savage, and J. Peirce, 1987: Special Sensor Microwave/Imager User's Guide. Naval Research Laboratory, Washington, D. C., 120 pp.

Houze, R. A., and P. V. Hobbs, 1982: Organization and structure of precipitating cloud systems. Advances in Geophysics, 24, 225-315.

Kummerow, C. and J. A. Weinman, 1988: Determining microwave brightness temperatures from horizontally finite and vertically structured clouds. J. Geophys. Res., 93, 3720-3728.

6.1

SSM/I OBSERVATION OF TROPICAL CYCLONE GALE FORCE VICINITY WINDS

Charles R. Holliday and Kenneth R. Waters

Air Force Global Weather Central
Offutt AFB, NE 68113

1. INTRODUCTION

The Defense Meteorological Satellite Program (DMSP) Special Sensor Microwave Imager (SSM/I) data provide several capabilities that are exploitable for operational tropical cyclone analysis. One example is estimation of ocean surface wind speed. The University of Massachusetts (UM), an investigator under the Naval Research Laboratory (NRL) SSM/I calibration and validation effort, recently has developed a revised algorithm for ocean surface wind speed (Goodberlet, 1989). This algorithm shows significant improvement in accuracy and is global in application, whereas earlier algorithm versions were stratified by 9 climate codes.

Of interest is the performance of this revised algorithm in the vicinity of tropical cyclones permitting determination of the near-gale wind ($\geq$15 ms^{-1}) outer boundary. This paper addresses a preliminary assessment of this capability.

2. BACKGROUND

The SSM/I ocean surface wind algorithm uses multiple linear regression techniques (D-matrix) and is based on the relationship between ocean sea state and brightness temperature increase of the ocean scene. Of the four SSM/I sensor frequencies and seven channels, the 19 GHz vertical and 37 GHz horizontal polarized channels are the most sensitive to the ocean roughness and foam (Goodberlet, 1989). The algorithm incorporates two other channels, the 22 GHz vertical and 37 GHz vertical to subtract for atmospheric effects in deriving a surface wind estimate. The 22 GHz channel is used to address water vapor effects while both the 37 GHz channels (vertical and horizontal polarization differential, or 37V-37H) are used to address cloud and liquid water scattering.

Rainfall contaminates the ocean surface signal by generating false foam signatures which result in unrealistically high wind speed values in the algorithm retrievals. The relative percentage of foam generated is proportional to an increase in wind speed (Hollinger and Lo, 1983). The difference in the 37 GHz polarization, however, can be used as an approximation to discriminate between rain and no-rain situations. Environmental Research Technology Inc (ERT) identified polarization differences of 25 or less as a possible rain flag (Lo, 1983).

3. UM GLOBAL WIND SPEED ALGORITHM

The UM global wind speed algorithm is a significant improvement over earlier versions which were stratified by latitude and season using 9 climate codes. These improvements were documented by Goodberlet (1989). The data set used for surface truth consisted of paired comparisons of SSM/I wind estimates with mid-latitude (25-55 deg N) U.S. NOAA fixed buoys. The revised UM algorithm meets the DMSP specification goal for accuracy within 2 ms^{-1} across a range of 3 to 25 ms^{-1} under absence of heavy cloud cover. The restrictive accuracy criteria reflect possible contamination of SSM/I wind speed estimates by total water vapor content and cloudiness. Specifics on the algorithm are listed in Table 1.

Table 1. Global D-matrix algorithm (from Goodberlet, 1989).

Surface Wind (ms^{-1}) = 147.90 + 1.0969 x 19V - 0.4555 x 22V - 1.7600 x 37V + 0.7860 x 37H

Flag	Criteria	Accuracy (SD)
0	37V - 37H > 50 deg	< 2 ms^{-1}
1	37V - 37H < 50 deg	2 - 5 ms^{-1}
2	37V - 37H < 37 deg	5 - 10 ms^{-1}
3	37V - 37H < 30 deg	> 10 ms^{-1}

4. DATA

4.1 Conventional Data

Ship wind speed observations were used to evaluate the UM algorithm in tropical cyclone high wind ($\geq$ 15 ms^{-1}) regions. Although ship wind speeds have inherent measurement differences when compared to fixed buoys (Earle and Wilkerson, 1985), these data are plentiful and most often used by forecasters to delimit the 15 (near gale force) or 17 ms^{-1} (gale force) wind speed boundary for warning purposes. Aircraft reconnaissance in developed tropical cyclones (winds $\geq$ 25 ms^{-1}) usually is confined to the inner core region (< 250 km radius) limiting observation in the outer gale region which may exceed 400 km in hurricanes or typhoons. Fixed buoy observations in tropical cyclones from the U.S. NOAA and Japanese networks were also included in the data set.

4.2 SSM/I Retrievals

The Air Force Global Weather Central (AFGWC) SSM/I data base extractions used for comparison with the conventional data are from a gridded 1/8 mesh (50 km) I-J polar stereographic grid format (AFGWC Real-Time Nephanalysis grid). The individual channel data known as Sensor Data Records (SDRs) were averaged from their original resolution to grid size before the revised algorithm retrievals were computed.

4.3 Data sample

A comparative set of 62 ship and buoy observations was collected in 23 coincident SSM/I tropical cyclone overpasses for preliminary assessment (Table 2). These data covered some 11 well-developed tropical cyclones ($\geq$ 25 ms^{-1} maximum intensity) which were close enough to major shipping lanes for observation and were readily available in AFGWC archives. Ship and buoy observations within three hours of SSM/I overpasses were retained. The data were collected from a latitude range of 10 to 30 deg N. The ERT criteria for rain-free conditions (37V-37H > 25 deg) reduced the final set of observations to 51. Table 3 shows the frequency distribution of the data. Ship and buoy wind speed measurements in the remaining sample ranged from 15 to 26 ms^{-1} with the bulk of the data (86%) confined to the 15-20 ms^{-1} interval. Matching SSM/I 37 GHz polarization differences (37V-37H) for the data set occurred in the 30 to 49 deg range for 90% of the sample.

Table 2. SSM/I tropical cyclone passes and number of coincident ship and buoy reports.

Storm	DTG (UTC)	# Rpts	Storm	DTG (UTC)	# Rpts
TY Thelma	11/2200 Jul 87	5	TY Skip	08/1000 Nov 88	4
TY Betty	18/2200 Aug 87	1	TS Skip	11/1200 Nov 88	2
TS Cary	18/2200 Aug 87	1	TY Tess	05/1100 Nov 88	2
TY Dinah	25/1000 Aug 87	4	TS Florence	09/1200 Sep 88	1
TY Dinah	28/2200 Aug 87	1	HR Gilbert	13/0000 Sep 88	2
TY Dinah	29/1100 Aug 87	1	HR Gilbert	15/1200 Sep 88	4
TY Dinah	29/2200 Aug 87	1	HR Gilbert	16/0100 Sep 88	5
TY Dinah	30/1000 Aug 87	1	HR Gilbert	16/1200 Sep 88	3
TY Pat	20/1100 Oct 88	4	TS Keith	21/1200 Nov 88	4
TY Pat	21/1100 Oct 88	2	TS Keith	23/0000 Nov 88	1
TY Ruby	24/0000 Oct 88	7			
TS Ruby	27/1100 Oct 88	4			
TS Ruby	28/1100 Oct 88	2		total	62

Table 3. Wind speed frequency distribution for ship and buoy observations in rain-free conditions (37V - 37H > 25 deg).

Range (ms^{-1})	# Rpts	Beaufort Force
15-16	19	7 - Near Gale
17-20	25	8 - Gale
21-24	5	9 - Strong Gale
$\geq$ 25	2	10 - Storm
Total	51	

5. DISCUSSION

Table 4 shows the statistics for the final data observation sample when compared to the UM revised wind algorithm retrieval for collocated SSM/I pixels on the display grid. A bias of -1.0 ms^{-1} suggests a tendency for the algorithm to underestimate the wind speed in this high wind speed interval. However, a standard deviation (SD) of 2.2 ms^{-1} and RMSE 2.5 ms^{-1} are relatively low values considering the possible wind speed measurement scatter of ship observations. The standard deviation is considerably less than what would be expected using the UM revised algorithm accuracy criteria (flags 1 and 2) in Table 1.

Table 4. UM algorithm retrievals compared to ship and buoy reports in rain-free conditions (37V - 37H > 25 deg).

Number of data pairs	51
Bias (ms^{-1})	-1.0
Std Deviation (ms^{-1})	2.2
RMSE (ms^{-1})	2.5
Range (ms^{-1})	-6 to +4
Cases > 4 ms^{-1}	6 (12%)

It is useful to note that 70% of the wind estimates are within the 2 ms^{-1} DMSP specification goal. If the accuracy window is opened to 3 ms^{-1}, then 82% of the sample is included. Six observations revealed a greater than 4 ms^{-1} underestimate of the SSM/I retrieval. With one exception these observations occurred within 50 km (one pixel) of a higher SSM/I field of values which would have reduced the difference to 3 ms^{-1} or less. Ship movement (cases of 2 to 3 h differences between observation and pass time), geolocation (ship versus pixel location), as well as observation accuracy might be factors in this discrepancy.

Dedicated platform measurements from fixed buoy and weather ships (table 5) in the sample compare well with the SSM/I. The observations collected from tropical cyclones Dinah, Gilbert, Keith, and Skip within one hour of SSM/I overpass reflect agreement within 2 ms^{-1}.

Table 5. Fixed buoy and weather ship wind speeds in rain-free conditions with corresponding SSM/I retrieval differences.

Site	Lat-Long	Obs (ms^{-1})	SSM/I Diff (ms^{-1})	37 V-H (deg)	Storm	DTG (UTC)
Buoy	28.3 N 126.0 E	15	+ 2	30	Dinah	30/0900 Aug 87
Buoy	26.0 N 93.5 W	17	+ 1	39	Gilbert	16/0100 Sep 88
Buoy	26.0 N 93.5 W	18	+ 1	39	Gilbert	16/1200 Sep 88
Buoy	26.0 N 85.9 W	15	+ 1	36	Keith	23/0000 Nov 88
JBOA	18.6 N 109.4 E	17	0	39	Dinah	28/2100 Aug 87
EREC	14.3 N 109.4 E	25	+ 2	26	Skip	11/1200 Nov 88

In spite of the limited number of paired cases available, the UM revised global wind speed algorithm appears to be capable of rain-free (37V-37H > 25 deg) retrieval accuracies within 3 ms^{-1} in a high percentage of the cases where the wind equals or exceeds 15 ms^{-1}. This is in contrast with the UM criteria which reflect a

deteriorating accuracy as the 37V-37H difference decreases from 50 deg. One explanation is that the ocean roughness emissions are stronger than emissions produced by total water vapor or cloudiness in the high wind regimes (>15 ms^{-1}). Both Rao et al. (1989) and Olson (1987) suggest that even light rain (< 1 mm h^{-1}) has only a secondary effect when compared to formation of ocean surface foam at high wind speed (> 15 ms^{-1}). It is possible much of the UM data accuracy criteria are influenced by observations from lower wind speeds (<15 ms^{-1}) where the ocean roughness and foam signal have less effect.

6. SSM/I RAIN-FREE STORM COVERAGE

It is instructive to examine the rain-free areas which allowed SSM/I wind algorithm retrievals in tropical cyclone high wind regions (>15 ms^{-1}). In the storm cases reviewed from the 23-pass data set, three types are apparent: Type 1) near gale-force winds extending outward 100 to 200 km from a rain masked central core in at least two to three quadrants; Type 2) a large rain-free central area enclosed by one or more major rain contaminated bands; and Type 3) an exposed low-level circulation usually with a rain contaminated area obscuring less than half the circulation. Types 2 and 3 comprised less than 20% of the SSM/I passes reviewed.

Hurricane Gilbert on 16 Sep 1988 as shown in Fig. 1 is illustrative of Type 1. Although the central area is rain-contaminated, SSM/I gale force wind estimates are possible in regions extending some 150 to 200 km outward from the rain boundary regions in the northern and eastern semicircles. A fixed buoy at 26.0° N and 93.6° W verified the UM estimates at 0100 UTC of 18 ms^{-1} in the northern fringe of the storm within 1 ms^{-1}. The western and southern SSM/I gale force extent from the rain boundary is limited to 50 km. At 0000 UTC Ship KIGR observed a wind of 18 ms^{-1} at 19.5° N, 93.9° W, supporting the southern boundary limit. Overall, the average radius of SSM/I gale force winds matched well with the National Hurricane Center advisory issued at 16/0400 UTC which stated radii of 500 km in the NE, NW and SW quadrants and 400 km in the SE quadrant.

Type 2 was characteristic of tropical storms in the South China Sea whose maximum wind radius expanded up to 200 km after passage as a typhoon over the Philippines. The relatively large rain-free center allowed SSM/I wind estimates within the encircling rain-obscured bands. Cary, Pat, and Ruby fit this category with SSM/I winds matching ship observations as high as 20 and 23 ms^{-1} in the storm's central core.

Two tropical storms in the sample exhibited conditions of Type 3. Both Keith (Gulf of Mexico) and Skip (South China Sea) had maximum winds near 25 ms^{-1}. Their deep convective, rain-contaminated, regions were restricted to a half semicircle or less of the wind field and were displaced from the core region to reveal a center of minimum winds. In the case of Keith, on 23 Nov 0000 UTC, a fixed buoy at 26.0° N, 85.9° W verified SSM/I 15 ms^{-1} estimates in the rain-free western semicircle. On 8 Nov 1200 UTC a weather ship (EREC) reported 25 ms^{-1} 100 km southwest of the convective eroded center in

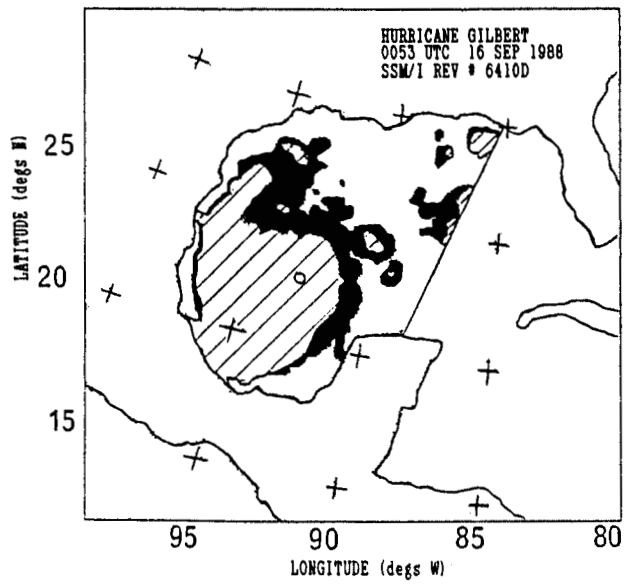

Fig. 1. Hurricane Gilbert, 0053 UTC, 16 Sep 1988. SSM/I estimates delimiting gale-force (> 17 ms) wind (shown in black) and rain contamination region (hatched area). Open circle represents center location.

Skip. This supported a SSM/I estimate within 2 ms^{-1}.

7. SUMMARY

SSM/I detection of gale force vicinity winds is possible in tropical cyclones as long as the rain contamination areas are screened out. The SSM/I retrievals based on the revised global wind speed algorithm appear useful in examining these relatively rain-free environments. The majority, or 82%, of the SSM/I wind speeds estimates in this study were within 3 ms^{-1} of the comparative ship and buoy data in high wind regimes (> 15 ms^{-1}).

Based on this preliminary assessment of the UM global algorithm performance in tropical cyclones, high wind regime retrievals under rain-free conditions can be determined with greater accuracy than reflected in the accuracy SD for flag 1 and 2 (37V-37H, 30 to 50 deg). One possible explanation is that the sea state emission contributes far more in high wind conditions than does total water vapor, cloudiness, or even light rain. Apparently, the UM accuracy SD figures may be influenced by data comparisons at lower wind speeds.

The central core regions of tropical cyclones are not always rain covered. SSM/I retrievals of up to 25 ms^{-1} were confirmed by ship data within an exposed central core area. Typically, these are storms at or below 33 ms^{-1} maximum intensity.

From the data reviewed, high wind (> 15 ms^{-1}) regions of tropical cyclones tend to extend well beyond rain areas in several quadrants, permitting SSM/I near-gale and gale force outer boundary identification.

8. REFERENCES

Earle M.D. and J.C. Wilkerson, 1985: Statistical Comparision of Ship and Buoy

Marine Observations. Report No. MEC85-8, MEC Systems Corp, Manassas, VA, 314pp.

Goodberlet, M.A., 1989: Remote Sensing of Ocean Surface Winds with the Special Sensor Microwave/Imager (SSM/I). Fourth AMS Conference on Satellite Meteorology and Oceanography, San Diego, CA, May 16-19.

Hollinger, J. P. and R.C. Lo, 1983: Project Summary Report, Naval Research Labs Memo. Report 5055, Washington D.C., 106 pp.

Lo, R.C., 1983: A Comprehensive Description of the Mission Sensor Microwave Imager (SSM/I) Environmental Parameter Extraction Algorithm. Naval Research Labs Memo. Report 5199, Washington D.C., 48 pp.

Olson, W.S., 1987: Estimation of rainfall rates in tropical cyclones by passive microwave radiometry. Ph.D. Dissertation, Univ of Wisconsin, 282 pp.

Rao, G.V., E.J. Ciardi, and D.K. Rhudy, 1989: Comparison of SSM/I Rainrates and Surface Winds with the Corresponding Conventional Data in Northwest Pacific Typhoons. Fourth AMS Conference on Satellite Meteorology and Oceanography, San Diego, CA, May 16-19.

OVERVIEW OF THE TROPICAL RAINFALL MEASURING MISSION (TRMM)

Joanne Simpson
Goddard Space Flight Center
Greenbelt, Maryland

1. INTRODUCTION

The Tropical Rainfall Measuring Mission (TRMM) is a proposed space system for measuring tropical rainfall and its variations. Such measurements are critically needed for progress in our knowledge of the overall earth system. Evaporation of water vapor into the atmosphere and its condensation to produce rainfall are at the heart of the earth's hydrological cycle, which is, in turn, essential for life on the planet. The placement of human settlements has been dictated more by the availability of an ample water supply than by any other factor. The nature of the earth's vegetative cover is controlled, to a very large extent, by moisture conditions and particularly by rainfall. The nature of this heat release, coupled with the resulting motions in the atmosphere, concentrates rainfall in the tropics in a thin latitude band called the intertropical convergence zone. We now know that year-to-year variations in the latent heat released in this region are a leading cause of year-to-year global climate variations, including the El Niño/Southern Oscillation (ENSO) phenomenon.

In July 1988, NASA and the Space and Technology Agency of Japan each successfully completed a one-year study of the feasibility of implementing TRMM as a joint space mission with the goal of obtaining improved measurements of rainfall over the global tropics and subtropics. A basic product would be a data set of 30-day average rainfall and its vertical distribution over 5° by 5° areas.

The quantification of global or regional rainfall is a major challenge, due to its high temporal and spatial variability. Moreover, most of the rain in the tropics falls in regions that are relatively inaccessible to in situ measurements. The quantitative distribution over the tropical oceans is uncertain to a multiplicative factor of about two or three.

Remote sensing from space has already been helpful in studying rainfall and promises to be the only useful and economic means of obtaining such measurements worldwide in the future. Spaceborne measurements of the outgoing long-wave radiation now provide our present best climatological estimates of rainfall over the tropical oceans. These have been aided by passive microwave measurements from the electronically scanning microwave radiometer on Nimbus 5, from the scanning multichannel microwave radiometer on Nimbus 7, and since 1987 from the Special Sensor for Microwave Imaging on the Defense Meteorological Satellite. These microwave measurements have all been obtained from polar sun-synchronous orbits. As a result, they do not give representative estimates of the daily rainfall in any one place, owing to the very large diurnal variations of rainfall in the tropics. The same will be true for the microwave measurements to be made on the Eos polar platforms. Present microwave measurements are also more reliable over oceans than over land, where differences in surface emissivity complicate data interpretation.

2. TRMM INSTRUMENTATION AND ORBIT

TRMM will carry three principal instruments (see Table 1). One is a cross-track scanning multichannel passive microwave radiometer, which will give good rainfall measurements over the oceans. TRMM will be the first space mission to include a precipitation radar (14 GHz), which will scan across a narrower track. Use of the passive microwave results to constrain the radar equation will permit vertical profiling of the rainfall over both land and sea. The vertical rain profiles are important because they may be used, with cloud models developed mainly at GSFC, to derive the vertical profiles of latent heat release. General circulation models and theory have shown that the height distributions of latent heating are vital to understand and model the impacts of tropical rain variability on large-scale atmospheric circulations; for example, the hemisphere-wide "teleconnections" associated with an ENSO event. The third payload package comprises two or three channels (visible and infra-red, with a night-time visible channel added, if resources permit) from an advanced very high-resolution radiometer (AVHRR). Data from this device compared with rainfall measurements from the passive microwave and radar instruments can be used to better interpret and calibrate visible/infrared rain estimations from past and future operational satellites, which will be of great value to the World Climate Research Program (WCRP).

The TRMM orbit will be circular at an altitude of 350 km and at an inclination of 35° (Fig. 1).

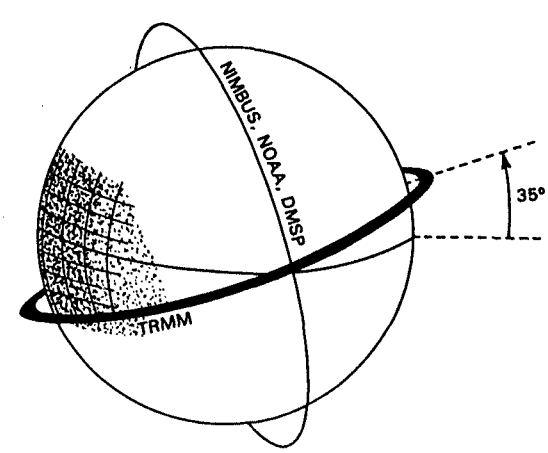

Fig. 1. Schematic of TRMM inclined orbit compared with the more conventional polar orbits. The 5° by 5° latitude boxes for data averaging are indicated under the shading.

TABLE 1. TRMM Sensor Summary

Microwave Radiometers	Radar	Visible/Infrared Radiometer	Orbit
19, 37, 90 GHz (dual polarized) @ 10 km res. 600 km swath	14 GHz 4 km footprint 250 m range res. 220 km swath	VIS and 10μm IR @ 1 km resolution 600 km swath	35° inclination 350 km altitude High resolution,
10 GHz @20 km res *5 GHz @40 km res*	*24 GHz* *600 km swath*	*Moonlight visible* *1.6 μm (phase of H_2O)* *6.7 μm , split window*	

Note: Items in italics desired if resources permit but are not necessary to achieve main TRMM objectives

This orbit will give intensive coverage in the tropics. It has been shown that, if the instruments were perfect, the error due to rain sampling would be less than 10 percent. The 35° inclination causes the orbit to precess, so that it passes over each 5° by 5° box at a different local time each day, so that the diurnal cycle in rainfall may be documented. The instruments' field of view will extend to latitudes as high as 37°, of considerable value to Japan owing to the large percentage of their rainfall occurring from the "Baiu front" which is found at that latitude in spring and summer. An advantage of the relatively low orbital altitude is a smaller instrumental "footprint" and hence higher spatial precision, allowing rainfall variations over smaller spatial scales. A data collection period of not less than three years is planned to begin in the mid 1990's. Both the orbit inclination and altitude would permit recovery of the TRMM payload by the Shuttle for refurbishment and later deployment on the Space Station. Fig. 2 shows the TRMM instruments mounted on the spacecraft, and their scanning patterns on the clouds and earth below.

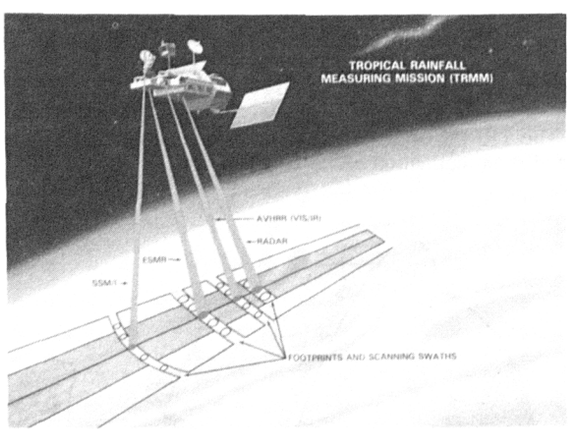

Fig. 2. Schematic of planned TRMM payload on spacecraft, showing the scanning patterns of the instruments. The solar power panel extends downward to the right. The two hemispheres mounted on the rear of the spacecraft send the data to other satellites which relay it to ground.

3. TRMM RAIN RETRIEVALS AND VALIDATION

A preliminary report on TRMM sampling, rain retrievals and planned validation by Simpson et al. (1988) has been followed by a detailed description of the entire mission (TRMM Science Steering Group, 1989). Counterpart studies have been published in Japan. These have received intensive reviews and approvals. It is hoped that the necessary funding for TRMM as an early member of the Earth Probe series will be obtained in FY1991 in order to permit launching on the Japanese H2 rocket in 1995.

Progress in algorithms to calculate rain amounts and vertical profiles has been made. Firstly, an algorithm called Height-Area Rain Threshold (HART) has been developed from earlier surface radar-rainfall studies. If the area of rain above a certain determinable threshold rate is determined, as well as the height of the rain layer within that area, an accurate estimate of rain amount can be made. This new algorithm extends the usefulness of TRMM results to mesoscale studies, since the rainfall may be determined fairly accurately along individual swathes of the rain radar. Secondly, encouraging progress has been made using cloud models to derive latent heat profiles from TRMM-determined precipitation profiles. These models have also been used to simulate real cloud fields in experiments developing and testing rain retrieval methods.

Thirdly, important early steps have been made in showing that vertical precipitation profiles can be obtained under most conditions with the single frequency radar, when the results from the passive microwave instruments are used to constrain the radar equation. Finally, an overall error analysis estimates that TRMM errors in monthly rainfalls over the 5° by 5° areas will, if instrumental and retrieval biases are uncorrelated with rain rates, probably be considerably lower than the discrepancies likely to be found among the various validation methods! The largest component of the estimated errors is due to sampling, which component would be greatly reduced by the presence of a single polar orbiting rain-measuring satellite.

4. REFERENCES

Simpson, J., R. F. Adler, and G. R. North, 1988: A proposed Tropical Rainfall Measuring Mission satellite. *Bull. Amer. Meteor. Soc.*, 69, 278-295.

Tropical Rainfall Measuring Mission Science Steering Group, Ed. J. Simpson, 1989: Report of the Science Steering Group of the Tropical Rainfall Measuring Mission. NASA Publ., Gov't Printing Off. Washington, D.C., 94 pp.

ACKNOWLEDGMENTS: TRMM is a team effort with hundreds of skilled participants in both the U.S. and Japan. Especial appreciation is due to D. Atlas, C. Kummerow, D. Rosenfeld and J. Weinman for major contributions to the retrieval methods discussed here. O. Thiele has made excellent progress in establishing the validation networks. Study Manager T. Keating superbly led the U.S. team of engineers in cooperation with science teams of both nations. The TRMM Science Steering Group provided a large part of the science and project design. Gratitude is due to leaders M. Geller and J. Theon for their support.

ON THE USE OF SATELLITE DERIVED HEATING RATES TO INITIALIZE TROPICAL FORECASTS

William A. Heckley, Graeme Kelly and Michael Tiedtke

European Centre for Medium Range Weather Forecasts
Reading, England.

1. INTRODUCTION

Analysis systems as used to provide initial conditions for numerical weather forecasts usually seek to blend observations together with a background field in a statistically optimum and multivariate manner. The exact form this takes varies. In all cases, however, the success of the technique depends on the quality of the background field, the coverage and quality of the observations, and a knowledge of the statistical stucture of the errors in the background field and in the observations. At ECMWF the background field is a six hour forecast from the previous, initialised, analysis.

In the northern hemisphere extratropics this approach works well. The background field is fairly accurate, usually at least as accurate as the observations, and its error structure can be determined (Hollingsworth et al., 1985). With the notable exception of the Pacific, there is a good coverage of observations.

Within the tropics the situation is quite different. Near the equator there exists no simple relationship between mass and wind fields, making any form of multivariate analysis difficult. The analysis scheme has to become univariate near the equator. Subsequent adjustment can be through variational schemes (e.g. Jones, 1976), model adjustment (e.g. Lyne et al., 1982) or through initialisation. The weak pressure gradients in the tropics present difficulties in that observing techniques frequently lack sufficient accuracy to resolve the gradients, inaccurate observations may frequently degrade rather than enhance the analysis. Lack of high quality mass observations also leads to aliasing between large scale Rossby and Kelvin modes (Cats and Wergen, 1983). Perhaps the most serious problem for tropical analysis is the lack of data. A general paucity of data leads to far greater uncertainty in the analyses than usually occurs in the northern hemisphere extratropics, with the possibility of serious deficiencies in the background field being uncorrected by the analysis. This, in turn, implies difficulies in quality control of data. It is clear that the quality of the tropical analyses will depend crucially on the quality of the background field and of the model used to produce it. Inadequate parameterization of physical processes can lead to large erorrs in the tropical forecasts and these can have a significant effect on the analyses (Tiedtke et al., 1988).

In view of the dominant role of diabatic processes within the tropics, and also the general lack of 'conventional' data, it makes sense to utilise more direct measures of the diabatic forcing within the assimilation. It has frequently been suggested that OLR data may be used to identify regions of deep convection. Puri (1987), working with the ECMWF model, has used OLR to specify heating rates, which are then used in diabatic non-linear normal mode initialisation of the analyses. A major limitation of his study is in the data source used for the OLR, which was twice daily, 2.5 degree gridded, analyses. Specifically, to be of use within the analysis, it is necessary to have an idea of the quality (data coverage) and time of each observation, point by point; and ideally to provide global fields every six hours. Also as it turns out, OLR of itself does not provide a sufficiently good measure of precipitation. This study extends the ideas of Puri (1987) by deriving more suitable estimates of precipitation.

2. PRECIPITATION ANALYSIS

The NOAA series of orbiting satellites provide almost global coverage every six hours and carry, as part of their instrument package, a High resolution Infrared Radiation Sounder (HIRS) sampling 20 channels from .7 to 15 micron. Each measurement resolves a circular area of 30 km diameter at the satellite sub-point and there are 56 fields of view within each scan. Each scan covers approximately 2250 km on the earth's surface and is perpendicular to the satellite track.

Long wave flux (OLR) is calculated from the HIRS data by a regression relation between these channels and OLR using code obtained from 'The Physical Retrieval TOVS Export Package' Smith et al.(1984). At any one analysis time between five and ten orbits are available from a combination of the NOAA 9 and NOAA 10 orbiters, giving typically around 500000 observations of OLR. Coverage is such that at each of the main synoptic hours there are few data voids. Values of OLR are available for each spot of every scan of each orbit. The OLR is converted to brightness temperature. For each spot we have the temperature and the time of the observation. The spots are collected into 7*7 boxes and the fractional coverage of cold cloud is calculated by counting the number of spots colder than 235K. This results in values of fractional coverage of cold cloud at a reduced resolution of about 2.5 degrees.

A Cressman analysis is now carried out of the fractional coverage of cold cloud and of the observation times. A byproduct of the Cressman analysis is a field weights which is a point by point measure of the data density. The weights are rescaled to be between zero and one to reflect confidence limits for the analyses. The analysis of observation times is expressed as departures from the analysis time, and is used to further modify the field of weights such that the values are progressively reduced according to the degree of asynopticity of the data. Finally the weights are subjected to a latitudinal weighting such that they become zero poleward of 35 degrees and can only

reach their maximum value equatorward of 25 degrees. Thus the field of weights now reflects the data distribution, the asynopticity of the observations and air mass type.

Following Arkin and Meisner (1987), the fractional coverage of cold cloud is interpreted, within the tropics, as rainfall rates.

Availability of these 'diagnosed' precipitation rates at each of the main synoptic hours allows their use in place of model generated heating in the diabatic initialisation scheme.

3. USE WITHIN THE ASSIMILATION

Rainfall rate is essentially a measure of the vertically integrated heating rate at that location. These diagnosed heating rates are incorporated into the model through the Kuo parameterization of deep convection. The appropriate input for the Kuo scheme is a moisture convergence into the grid area to produce precipitation but no moistening (moistening parameter β=0). Diagnosed values (DIAG) of moisture convergence are merged with the model generated values (MOD) as

$$(1\text{-wts})*\text{MOD} + \text{wts}*\text{DIAG},$$

depending on confidence in the diagnosed precipitation. Similarly the moistening parameter β is set to (1-wts)*MODβ, where MODβ is the model β parameter. In regions of high confidence the weights (wts) are close to unity, the moisture convergence is defined by the diagnosed precipitation rate and the moistening parameter is set to zero so that all the moisture convergence falls out as rain. Where there is no data, or in the extratropics, or where the data is far from the synoptic time, the weights (wts) will be close to zero and the moisture convergence will be set to its forecast value (MOD), as will the moistening parameter (MODβ). Thus the scheme moves smoothly between forecast and diagnosed convection according to the specified field of confidence weights. The Kuo scheme will generate a field which is consistent with both the diagnosed precipitation and the model parameterization.

The forecast model is integrated for two hours in this manner starting from the uninitialised analyses, the first two timesteps are discarded, and the diabatic tendencies are averaged over the remaining period. These diabatic tendencies are then projected onto the model normal modes. That component which projects onto inertia-gravity modes having a free frequency greater than five hours, and within the first twenty zonal and twenty meridional modes, is used as a constant forcing term in the diabatic non-linear normal mode initialisation. The diagnosed precipitation rates are in this way allowed to influence the initialised analysis in a way which is consistent with the models parameterization.

4. ASSESSMENT OF THE SCHEME.

Comparison of model generated heating rates and diagnosed heating rates shows that the model field is often stronger but tends to be of a disorganised and 'spotty' nature. The diagnosed heating rates display a well organised and plausible structure. Vertical structures are similar. Insertion of the heating through the Kuo scheme works well in some regions, notably the tropical Pacific and Indonesia, but fares less well over the equatorial Atlantic where, presumably due to analysis deficiencies, the flow is initially too stable to support deep convection. Over the tropical continents convection is supported by the model during the day but not at night, due to the stabilising effect of the radiative cooling.

Influence of the scheme on the analyses, through data assimilation, and on subsequent forecasts, is currently being assessed. A parallel data assimilation has been carried out with and without the modified heating. Preliminary investigation shows significant differences in the analysed fields. The figure below shows the differences in the 200 hPa wind field, as streamlines and isotacs, after two days of assimilation (contour interval 1ms^{-1}). Wind field differences of 4 ms^{-1} or larger occur over regions of deep convection. Largest differences are confined to otherwise data sparse areas.

200 hPa wind differences

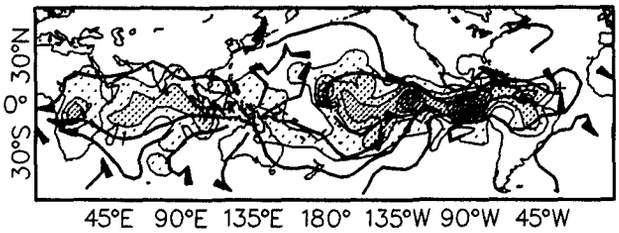

Further results will be presented.

REFERENCES.

Arkin, P A and Meisner, B N, 1987: The relationship between large-scale convective rainfall and cold cloud over the Western hemisphere during 1982-84. Mon.Wea.Rev. 115, pp 51-74.

Cats, G J and Wergen, W, 1983: Analysis of large scale normal modes by ECMWF analysis scheme. ECMWF workshop on current problems in data assimilation pp 343-372.

Hollingsworth, A, Shaw, D B, Lonnberg, P, Illari, L, and Simmons, A J., 1986: Monitoring of observation and analysis quality by a data assimilation system. Mon. Wea. Rev., Vol. 114, pp 861-879.

Lyne, W H, Swinbank, R and Birch, N T, 1982: A data assimilation experiment and the global circulation during the FGGE special observing periods. Quart. J R Met Soc, 457 pp 575 - 594.

Puri, K, 1987: Specification of diabatic heating in the initialization of numerical weather prediction models. ECMWF workshop on Diabatic Forcing, pp 151-176

Smith, W L, Woolf, H M, Hayden, C M, Schreiner, A J, Le Marshall, J F, 1984: The Physical Retrieval TOVS Export Package. Technical Proceedings of the first TOVS study conference. Igls, Austria. W.P. Menzel Editor. Cooperative Institute for Meteorological Satellite Studies. University of Wisconsin, USA.

Tiedtke, M, Heckley, W and Slingo, J, 1988: Tropical forecasting at ECMWF: the influence of physical parametrization on the structure of forecasts and analyses. Q J R Meteorol Soc 114, pp 639-664.

INTERANNUAL VARIABILITY OF THE EARTH'S CLIMATE DURING THE LAST DECADE AS OBSERVED BY THE NIMBUS-7 SPACECRAFT

Philip E. Ardanuy*, H. Lee Kyle, Douglas V. Hoyt*, and Daesoo Han

NASA/Goddard Space Flight Center
Greenbelt, MD 20771

*Research and Data Systems Corporation
Greenbelt, MD 20770

1. THE EARTH RADIATION BUDGET CLIMATOLOGY

The Nimbus-7 satellite, launched in late 1978, recently completed taking a decade of wide-field-of-view (WFOV) observations of the Earth's climate. The Earth Radiation Budget (ERB) instrument continues to take data at this time, and has created an unprecedented data set for the analysis of the time-averaged radiation budget, as well as for the detection of intra-annual and interannual climate variability. The ERB measurements have been used to examine the evolution of the Southern Oscillation (SO), including the major 1982-1983 El Niño/Southern Oscillation (ENSO) event. Teleconnection patterns extending throughout the tropics and extratropics have been identified using the ERB measurements. Here we consider an eight-year set of ERB observations spanning the time period 1979 to 1987.

2. THE TIME-AVERAGED RADIATION BUDGET

Figure 1 illustrates the diurnally averaged, eight-year top-of-the-atmosphere (TOA) net radiation field. The greatest amount of the net downward-directed radiation at the TOA is over the tropical oceans within a narrow equatorial belt. Here, an average of 80 Wm^{-2} is continuously absorbed. In the middle and high latitudes, the net radiation is negative, with the Earth losing more heat to space than it gains from the Sun (with the excess heating and cooling being offset by horizontal and vertical transport by fluxes of sensible and latent heat within the oceans and atmosphere). The net radiation is a minimum over the southern-hemisphere continents. Even more striking is the minimum positioned over the Sahara Desert and northern Africa, where the high albedos combine with the large longwave radiative flux to drive the net radiation below -20 Wm^{-2}. It is this negative net radiative heating that permits the intense subsidence over the region that maintains the desert. The dry adiabatic warming of the descending air balances the radiative cooling.

3. THE ZONALLY AVERAGED RADIATION BUDGET

The distribution of the net radiation shows the latitudinal imbalances in the radiative heating of the planet, modulated primarily by the distribution of the solar insolation. It is possible to infer the latitudinal transport of energy required to balance the Earth's energy budget (Figure 2). A small correction is first made to remove the globally annually averaged bias present in the measurements. Next, the net radiation is integrated over latitude, beginning at the south pole, to infer the required northward flux of heat by the atmosphere and oceans. We see that the meridional

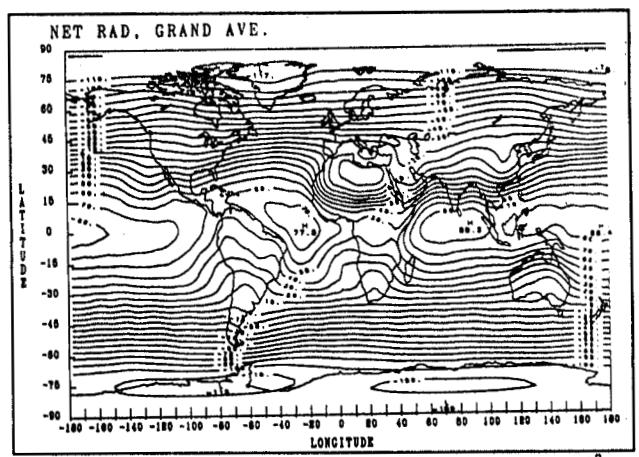

Fig. 1. Eight-year averaged net radiation (Wm^{-2}).

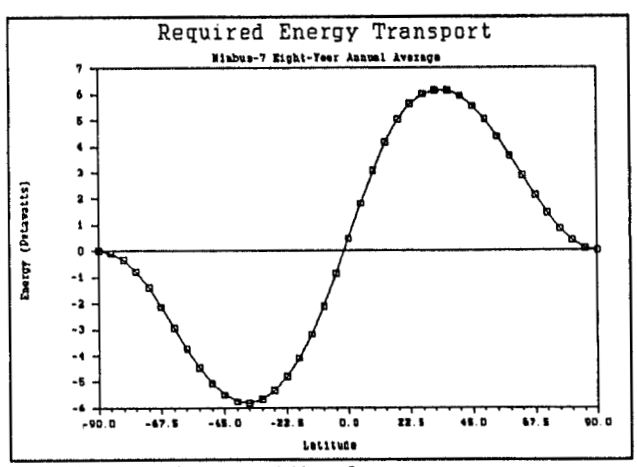

Fig. 2. Required meridional energy transport.

flux reaches a maximum at 30°S and 32°N of -5.81 and 6.16 Petawatts (10^{15} Wm^{-2}), respectively. The equatorial value is 0.47 Petawatts, indicating that an annually averaged northward cross-equatorial energy flux is required to balance the planetary heat budget, perhaps due to the relatively lower albedo of the southern hemisphere.

4. INTERANNUAL CLIMATE VARIABILITY

Climatic variability can occur regularly, due to forcing mechanisms external to the Earth system, such as with the diurnal, annual, and 11-year (sunspot) periods. Internally driven climate variations also occur both intra-annually (e.g., planetary-scale and synoptic-scale midlatitude waves and 30- to 60-day tropical waves) and interannually (e.g., the SO and volcanic eruptions such as El Chichón) due to nonlinear interactions within the

system. The oscillations and perturbations in the Earth climate system (the atmosphere, biosphere, hydrosphere, and cryosphere, as well as to a lesser extent the solid Earth) are observable as variations in the radiation budget at the TOA.

Variability in the net radiation is due to changes in the clear-sky shortwave and longwave radiation fields or changes in the total cloudiness distribution and the cloud properties themselves. Figure 3 displays the standard deviation of the WFOV net radiation annual averages for the eight-year period 1979 to 1986. Two factors are immediately evident. First, there is little interannual variation in this parameter at this timescale. Minima are observable over the high latitude oceans, where the variation in the net radiation (0.3 to 0.5 Wm^{-2}) approaches that expected from a 0.1% solar constant change during the 11-year cycle. Elsewhere, outside of the tropics, the variability in the net radiation is less than 2 Wm^{-2}. Second, the primary source of interannual variation in the net radiation is the SO, particularly the segment associated with the 1982-83 ENSO event. There are two main centers of variation, each of which reach about 10 Wm^{-2}. These correspond to the ENSO bifurcation pattern, which can be seen to perturb the annually averaged net radiative input regionally by about 10 Wm^{-2}; they are found over Indonesia, where the winter monsoon failed during the El Niño, and over the eastern equatorial Pacific Ocean, where the anomalous convection appeared instead. A related maximum is identifiable over northern Brazil. Ardanuy and Kyle (1986) analyzed the interactions between the 1982-83 ENSO event and the TOA radiation budget, as well as the multi-year recovery period following the episode (Ardanuy et al., 1987). The primary mechanism for deviations in the net radiation are cloudiness changes (driven, in turn, by variations in the underlying sea surface temperature). The changes in the annually averaged net radiation examined here are primarily due to cloudiness changes, suggesting that the interannual variability of the net cloud forcing, as measured by an annual standard deviation, is less than 2 Wm^{-2} outside the tropics, and only exceeds 4 Wm^{-2} in response to strong El Niño episodes.

Figure 4 displays annual averages of the TOA outgoing longwave radiation (OLR) field cross-correlated to the value over Darwin, Australia (one of the poles of the SO). The variability of the OLR (and the winter monsoon) are positively correlated from southeast Asia through the southern tip of Australia. The strong positive correlation extends through the South Pacific Convergence Zone (SPCZ) to the tip of South America. Strong negative correlations are present over the central Pacific Ocean (due to the presence of cloudiness related to the El Niño phase of the SO) and across a SPCZ eastward-shifted by 60° to 70° of longitude. Strong negative correlations exceeding -0.6 are also evident in storm tracks over California and the southeastern U.S. (The implication is that, when the Darwin/winter monsoon fails, there is increased cloudiness over these regions. Many other apparent teleconnections exist across the tropics that are statistically significant.

Figure 5 displays the anomalies in total cloud cover for January 1983 as derived from instruments on the Nimbus-7 satellite (Stowe et al., 1988). The failure of the winter monsoon is evident in the -51% cloud anomaly over Indonesia, while the convection over the equatorial Pacific Ocean extending to the coast of South America is also Noteworthy due to the large positive anomaly. To

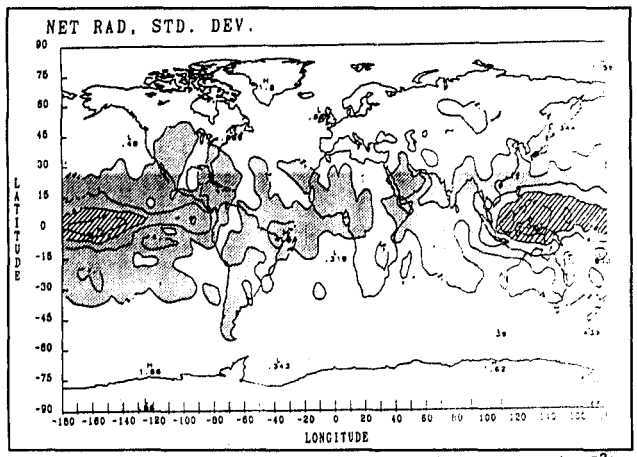

Fig. 3. Annual net radiation STD deviation (Wm^{-2}).

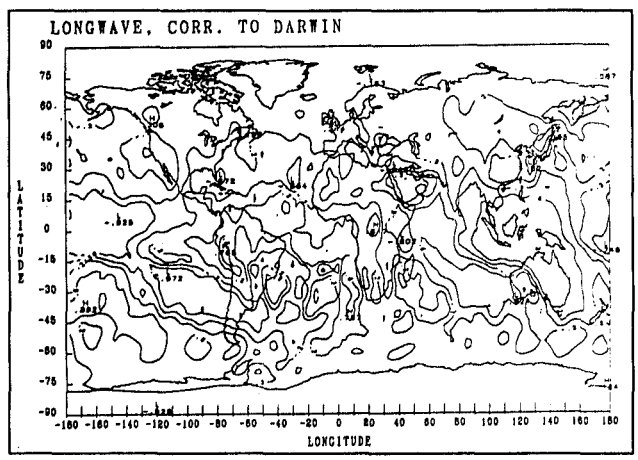

Fig. 4. LW radiation annual correlation to Darwin.

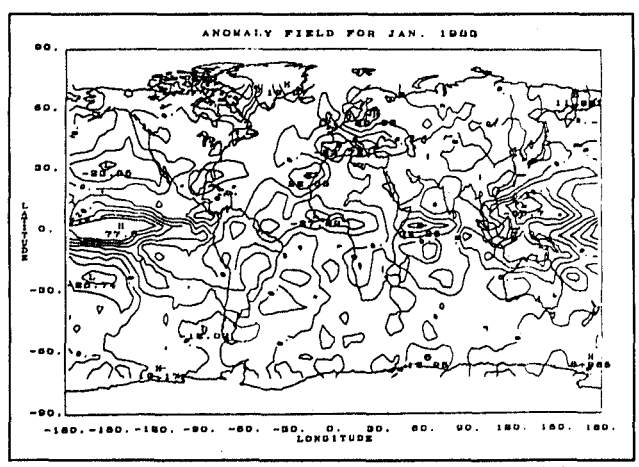

Fig. 5. Total cloud anomalies for Jan 83 (%).

the north and south of this convective area are regions where the ENSO-related convection forced thermally direct Hadley circulations, with corresponding descending branches and -25% cloud anomaly minima at 30°N and 30°S latitudes. It is this variation in cloudiness, coupled with changes in the clear-sky radiation budget, that have generated the interannual variability analyzed above.

5. THE GLOBALLY AVERAGED RADIATION BUDGET

Figure 6 presents the eight-year time series of the monthly averaged net radiation for each hemisphere and for the globe. The two hemispheres are

six months out of phase, with the net radiation a maximum in each summer hemisphere, and a minimum in each winter hemisphere. The seasonal cycle of the net radiation is largest in the southern hemisphere due, in part, to its lower albedo, the greater thermal inertia of the oceans, and the Earth's elliptical orbit around the Sun (closest during southern summer; farthest during southern winter). The 20 Wm^{-2} annual cycle of the global net radiation is almost entirely explained by the 23 Wm^{-2} seasonal variation of the solar insolation. The long-term average of the net radiation is biased 6 Wm^{-2} from a perfect balance. This bias may be explained, in part, by an undersampling of the polar caps (1.3 Wm^{-2}) and by a 0.4% overestimate in the value of the solar constant (1.6 Wm^{-2}). The balance may be physically meaningful, but is more likely explained by a 1% error in the absolute calibration of the radiometers. A trend of about 0.2 Wm^{-2}/year is evident in the annually averaged net radiation values. While such a trend may indicate the signature of the buildup of CO_2 and other trace greenhouse gases in the atmosphere (the trend is driven by a 0.2 Wm^{-2}/year decrease in the longwave flux; the albedo is stable), the <0.1%/year longwave drift is within the present uncertainty of the relative calibration of the ERB instrument.

Figure 7 illustrates those radiation budget parameters key to the Earth's heat balance: the solar insolation, the reflected solar radiation, the absorbed solar radiation, and the emitted longwave radiation. The latter two terms describe the energy input and output from the Earth's climate system; their difference is the global net radiation. Neither the planetary albedo nor the planetary radiative temperature respond fully to the variations in the solar insolation; indeed, the energy output is completely out of phase with the energy input. We see that the outgoing longwave flux at the TOA is completely out of phase with the incident solar insolation, with the greatest emission and equivalent blackbody temperature of the Earth occurring during northern summer. To understand this apparent contradiction, Ardanuy et al. (1987) divided the Earth into four regions corresponding to the tropics and extratropics of each hemisphere (Figure 8). In the extratropics, the longwave radiation is seen to be proportional to the hemispheric insolation, with the northern hemisphere experiencing the greatest seasonal cycle. The seasonal cycle for the northern hemisphere mean surface temperature greatly exceeds that of the southern hemisphere. This difference is caused by the differing amounts of land and ocean in the two hemispheres. The two tropics, on the other hand, behave in a converse manner, with the OLR the highest in the winter hemisphere. This is the direct result of cloud feedback, where the tropical convection in the Intertropical Convergence Zone closely tracks the solar declination. The resultant cloud forcing, caused by the large swings in cloud amount and the surface minus cloud-top temperature difference (Ardanuy et al., 1989), reverses the phase of the tropical longwave flux relative to the insolation. When these four contributions are combined, the northern hemisphere extratropics provides the dominant amplitude which drives the global average.

REFERENCES

Ardanuy, P. E. and H. L. Kyle, 1986: El Niño and Outgoing Longwave Radiation: Observations from N-7 ERB, Mon. Wea. Rev., 114, 415-433.

Ardanuy, P. E., H. L. Kyle, and H.-D. Chang, 1987: Evolution of the Southern Oscillation as Observed by the Nimbus-7 ERB Experiment, Mon. Wea. Rev., 115, 2615-2625.

Ardanuy, P. E., L. L. Stowe, A. Gruber, M. Weiss, and C. S. Long, 1989: Longwave cloud radiative forcing as determined from Nimbus-7 observations. J. Climate, in press.

Stowe, L. L., C. G. Wellemeyer, T. F. Eck, H. Y. M. Yeh, and the Nimbus-7 Cloud Data Processing Team, 1988: Nimbus-7 global cloud climatology, Part I: Algorithm and validation, J. Climate, 1, 445-470.

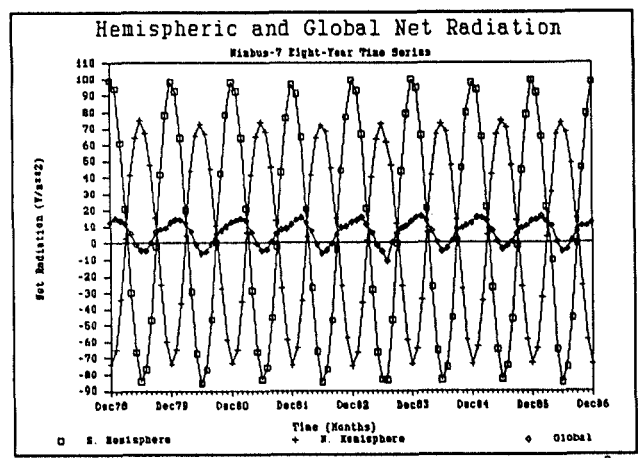

Fig. 6. Global and hemispheric net radiation (Wm^{-2}).

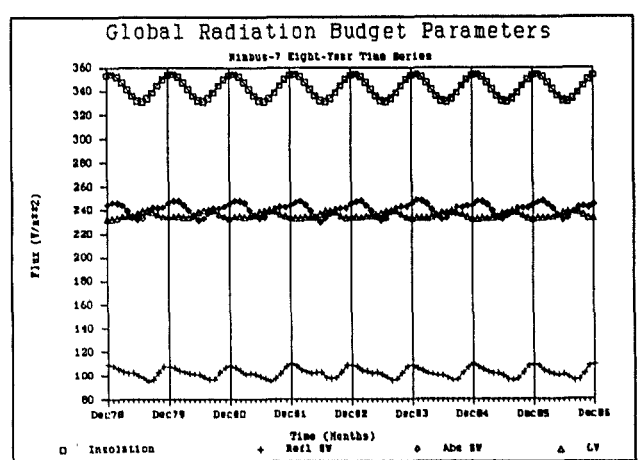

Fig. 7. Key radiation budget parameters (Wm^{-2}).

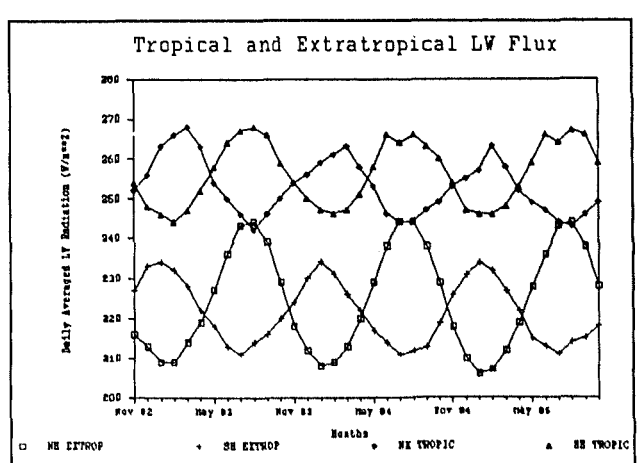

Fig. 8. Tropical and extropical LW radiation (Wm^{-2}).

PASSIVE MICROWAVE RETRIEVALS OF RAINFALL AND RAIN SYSTEM STRUCTURE

Christian Kummerow [1]
Ida M. Hakkarinen [2]

[1]Universities Space Research Association
USRA Visiting Scientist Program
Goddard Space Flight Center
Greenbelt, MD 20771

[2] General Sciences Corporation
Laurel, MD 20707

1. INTRODUCTION

One of the major objectives of both the Tropical Rainfall Measuring Mission (TRMM) and the Earth Observing System (EOS) is the quantitative mapping of rainfall and rain system vertical structure. The latter is extremely important in determining the vertical profile of the latent heat release associated with precipitation which, in turn, governs the nature of the 30-60 day oscillations in the tropics. Algorithms are currently being developed in connection with TRMM to retrieve both rain, and rain vertical structure from passive microwave radiometry. Aircraft observations made at the frequencies proposed for TRMM are used to simulate the expected resolution (~5 km) which will be available from the TRMM satellite.

Many single- and dual-channel rainfall retrieval algorithms have been developed in the past (*e.g.*, Wilheit *et. al.*, 1977, Spencer, 1986). The major obstacles which these algorithms have had to overcome are large, incompletely-filled footprints and the dependence of brightness temperatures not only on the rainfall rate, but also on the vertical profile of hydrometeors. Low-earth orbiting satellites, such as TRMM and EOS, with planned resolutions of <10 km, will eliminate the first of these two problems. Preliminary evidence will be presented here to suggest that the second may be overcome by a multi-channel algorithm which simultaneously retrieves the rainfall rate and the rain system structure.

2. RETRIEVAL ALGORITHM

A self-consistency approach developed by Kummerow *et al.* (1989) is used to retrieve the surface rain rate from aircraft measurements of microwave brightness temperatures obtained during the COoperative Huntsville Meteorological EXperiment (Dodge *et al.*, 1986). The retrieval method is essentially an improved version of the piece-wise linear, multi-channel statistical method first described by Chang and Milman (1982). The rain rate in these methods is inferred from microwave brightness temperatures (TB) by relationships of the form:

$$R = a_0 + \sum_i a_i TB_i \qquad (1)$$

where "i" represents all available channels (18H, 18V, 37H, 37V and 92 GHz in the present study). The regression coefficients a_0 and a_i are obtained from radiative transfer calculations through modeled clouds in which the geophysical parameters of interest (typically the rain rate, cloud liquid water and surface temperature) are varied randomly. Since the TB-rain rate relations are known to be non-linear, regression statistics are carried out over smaller portions of the rain rate range. In the present analysis, six intervals (0-3, 3-6, 6-10, 10-20, 20-40, > 40 mmhr^{-1}) are used for the rainfall rate. Details of the procedure are found in Kummerow *et al.* (1989).

Microwave brightness temperatures, however, are affected not only by rain rate, cloud liquid water and surface temperature, but also by the vertical structure of hydrometeors. Warm, orographic rain, for example, produces a very different TB signature than convective precipitation of the same rain rate. This is due to the higher concentrations of ice in the convective situation, which significantly reduces the upwelling radiances at the higher frequencies.

Since regression statistics are based upon an assumed cloud model, they become sensitive to errors when the underlying rain system is not properly replicated. A method for verifying that the model used to generate the statistics corresponds to the actual rain scene is therefore needed. The process by which this is accomplished is shown diagrammatically in Fig. 1. It is intuitively clear that, if the cloud radiative model accurately represents the underlying rainfall scene, then it will generate multi-frequency sets of TB values which are very similar to the observed TB values. This, in turn, produces retrieved quantities whose corresponding brightness temperatures closely resemble observations. The converse of this statement, unfortunately, is true only if a given set of TB values correspond to a unique set of geophysical parameters. Although no proof is given, it appears that the seven channels of the proposed TRMM sensor ranging from 19 to 85 GHz, provide sufficient independent information to overcome the non-uniqueness problem in a gross sense. Non-uniqueness problems in the neighborhood of the correct answer do not pose a serious problem because small errors are acceptable in pixel-by-pixel rain rate retrievals, as long as they are not systematic.

The retrieval procedure used here utilizes a large number of cloud radiative models. For each model, regression statistics are generated and the variable geophysical parameters are retrieved. Unique to the current retrieval approach is the fact that the set of retrieved geophysical parameters for each point are then inserted *back* into the cloud radiative model used to

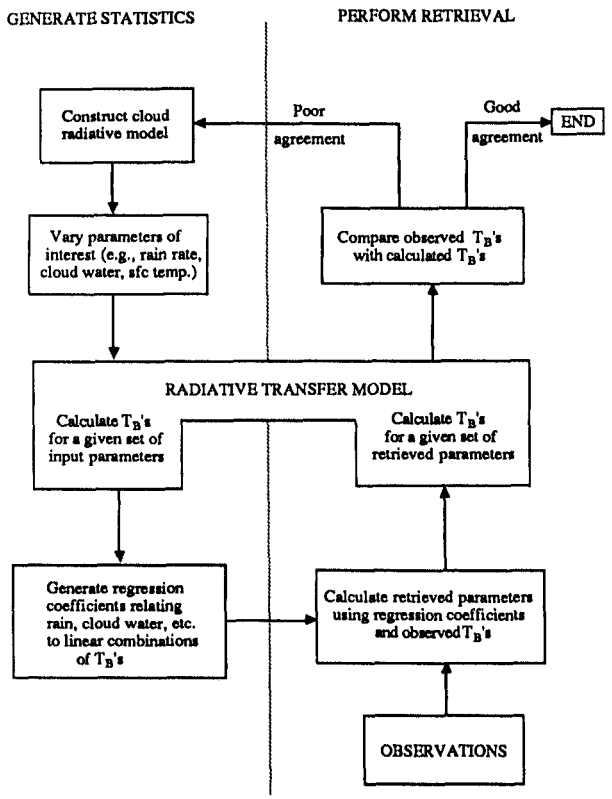

Fig. 1 Schematic representation of retrieval algorithm

generate the statistics for that case, and the resulting brightness temperatures (*the retrieved brightness temperatures*) are compared to the observations at each point. The cloud radiative models used represent a wide variety of scenes: strong convection over land, anvil cirrus, clear ocean, stratiform precipitation over water. These models are constructed from reports in the literature of what rain of the specified type might look like. For each model, a record is kept of the retrieved geophysical parameters and the associated difference between retrieved and observed brightness temperatures. The final step in the retrieval procedure is the merging of all model results. For each point, the geophysical parameters corresponding to the cloud radiative model having the smallest difference between observed and retrieved brightness temperatures are used as the final result. Thus, since the retrieval algorithm selects the cloud radiative model which best fits the data, the original choice of models is quite arbitrary. Preliminary investigations with high resolution data seem to indicate that root-mean-square differences of approximately 5°K between observed and retrieved TB's generally produce good results.

In the present retrieval, eighteen cloud radiative models were used. Nine models correspond to convective systems which contain large fractions of liquid water above the freezing level. Five models correspond to stratiform precipitation in which little water is found above the freezing level. Two models are used for no-rain situations, where only the surface temperature and the cloud liquid water over land and ocean are retrieved, respectively. Three models correspond to anvil structures, consisting of mostly frozen hydrometeors aloft, with no liquid water found near the surface.

3. DATA

Aircraft observations made by the high-altitude NASA ER-2 research aircraft on 29 June and on 1 July 1986 are used in this study. In order to demonstrate the versatility of the retrieval scheme and to simulate large satellite footprints, the observed brightness temperatures for the two days were combined using a linear interpolation over a 10 km distance. Thus it was possible to obtain a continuous data set of ~1000 km covering intense convective systems, frontal rain over the ocean, and anvil cirrus clouds. The top panel of Fig. 2 shows 18 GHz and 37 GHz horizontally-polarized brightness temperatures from the Microwave Precipitation Radiometer (MPR) and the 92 GHz nadir temperatures from the Advanced Microwave Moisture Sounder (AMMS). The MPR vertically polarized temperatures are not shown. The MPR data have been empirically adjusted to the AMMS data to account for the difference in viewing geometries (45° ahead of the aircraft for the MPR, nadir for the AMMS). The adjustment for the June 29 data over the intense convection used a polynomial regression to match the TB minima and maxima. A constant time offset was used for the July 1 data. The segment from 275 to 285 km corresponds to the linear interpolation between these two flight days.

Region A, from 0 to 40 km in panel 1 of Fig. 2 represents open land. Region B corresponds to an intense convective system over northern Virginia on 29 June 1986. Region C is where anvil material is being blown off over the ocean. Region D is the area where the two flight lines are joined. Since the second flight line begins over land, while the first line ends over water, the effect of this joining appears as a small "island" in the microwave data. Region E represents a frontal rain system with associated light, stratiform precipitation. Finally, region F corresponds to almost clear ocean.

Panel 2 of Figure 2 shows the corresponding rainfall rates deduced from coincident radar data obtained from the NASA SPANDAR radar at Wallops Island, VA. Low-level reflectivities were converted to rain rate using the Z-R relation of Wexler (1947) for thunderstorm rain in the heavy convection region (90-180 km), and Marshall and Palmer (1948) for the stratiform region (340-490 km).

4. RETRIEVAL RESULTS

Panel 3 of Figure 2 shows the retrieved rainfall rate for 1 km resolution brightness temperatures. The solid line is the retrieved rain rate in $mmhr^{-1}$ while the dashed curve indicates the difference between the observed and the retrieved TB's obtained for each point These values correspond to the root-mean-square (RMS) differences between all five channels. One is most confident of those results which show a small RMS deviation, indicating that the particular model used to obtaine the retrieved rain rate probably was a good description of the underlying rain scene. A good example of this is the region between 70 and 90 km where, with the exception of a few points, most deviations are < 5K. In contrast, there is a large peak in the RMS deviations between 275 and 285 km. It should be recalled that this is the region where the two flight lines were joined by interpolation. These data have no correspondence to any modeled scene. Careful comparisons between the rain rates deduced from radar (Panel 2) and from the high-resolution passive microwave retrievals (Panel 3) further reveal that the agreement is generally better when the

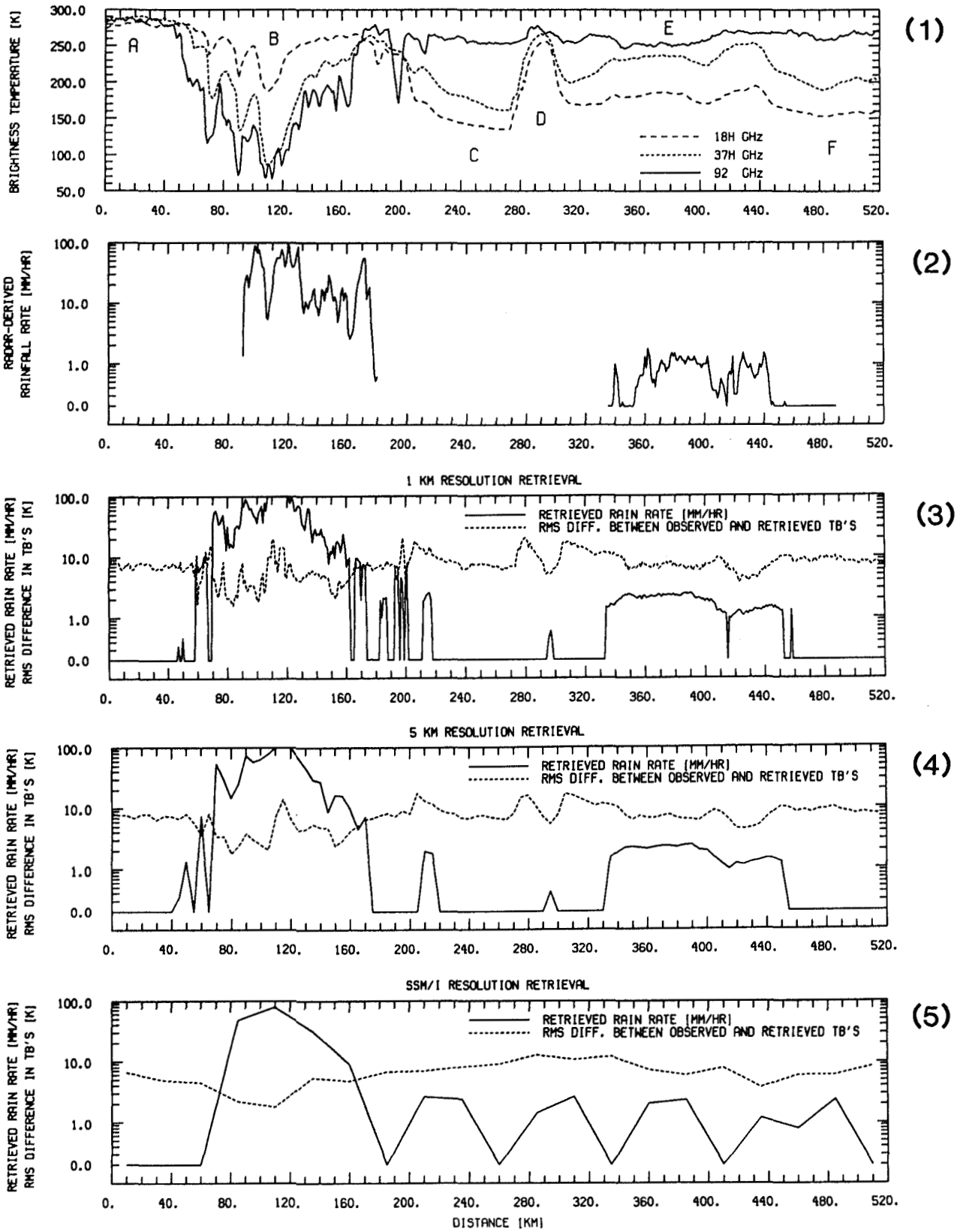

Fig. 2 Panel 1: Aircraft measured TB (1 km resolution); Panel 2: Rdar-derived rain rate; Panel 3: 1 km resolution rain rate retrieval; Panel 4: 5 km resolution rain rate retrieval; Panel 5: Rain rate retrieval using SSM/I resolution data.

RMS deviations between retrieved and observed brightness temperatures are low. The inverse is also true.

Panel 4 shows the results obtained from the same retrieval technique when the resolution of the data is degraded to 5 km, corresponding to approximately the resolution of TRMM. Although some of the fine structure is lost, there appears to be little difference between the 5 km and the 1 km resolution retrievals.

Panel 5 of Fig. 2 shows the retrieved results when the resolution is degraded to that of the SSM/I. High resolution data were convolved with approximate antenna gain functions applicable to the SSM/I. The sampling distance of 25 km, equal to that of the SSM/I was used. The retrieved results in this case differ somewhat from the previous retrievals, in that partial footprint filling was considered as a variable in the retrieval. The results, given the very coarse resolution of the data, seem to show general agreement with the 1 km and the 5 km resolution retrievals.

5. DISCUSSION

Although the spatial variabilities considered in this study are only one-dimensional rather than two-dimensional, they probably give a reasonable representation of data to be expected from a satellite such as TRMM. Table 1 presents summary comparisons between the radar-derived rain rate and the retrieved results at various spatial resolutions. The data are divided into thunderstorm rain (0 - 260 km) and frontal rain (260 - 520 km). Only those regions along the flight path which are covered by the radar are considered.

The microwave retrievals are larger than the radar-derived rain rates by ~50% in the thunderstorm region. This is also true in the stratiform rain region. It should be noted that the thunderstorms on June 29 were some distance away from the radar. The radar-derived rain rate for the thunderstorm region corresponds to the lowest available elevation angle of the radar. This represents an echo height of ~5.0 km at the 90 km distance mark and an echo height of 2.5 km at the 180 km distance. Thus, the radar was not observing rainfall at the surface, and might therefore be underestimating the total rainfall. The stratiform rain region was relatively close to the radar, hence the reflectivity more nearly represents the values at the surface.

TABLE 1

Thunderstorm (0 - 260 km)	Total # of pixels covered by radar	# of raining pixels	Average rain rate [mm/hr]
Radar 1 km res.	91	91	27.38
Microwave 1 km res.	91	83	43.27
Microwave 5 km res.	19	17	42.52
Microwave SSM/I res.	4	4	41.92

Stratiform rain (260-520 km)	Total # of pixels covered by radar	# of raining pixels	Average rain rate [mm/hr]
Radar 1 km res.	154	100	0.83
Microwave 1 km res.	154	118	1.36
Microwave 5 km res.	31	24	1.38
Microwave SSM/I res.	7	5	1.26

TABLE 2

	Thunderstorm (0 - 260 km)		Stratiform rain (260-520 km)	
	Convective rain (%)	Stratiform rain (%)	Convective rain (%)	Stratiform rain (%)
Microwave 1km res.	55.6	44.4	0.9	99.1
Microwave 5km res.	55.5	44.5	1.1	98.9
Microwave SSM/I res.	50.9	49.1	0.0	100.

Table 2 shows the relative contribution from convective and stratiform precipitation for the thunderstorm and the stratiform rain region. The division into convective or stratiform rain was accomplished by referring to the cloud radiative model which was selected by the retrieval procedure for each pixel. Again, the results appear to be relatively homogeneous. However, it should be noted that the results for the SSM/I resolution were achieved only after partial footprint filling was considered. Assuming completely-filled footprints for the SSM/I resolution resulted in most of the precipitation being retrieved to be associated with stratiform cloud radiative models.

6. REFERENCES

Chang, A. T. C. and A. S. Milman, 1982: Retrieval of ocean and atmospheric parameters from multichannel microwave radiometric measurements. *IEEE Trans. on Geoscience and Remote Sensing*, 20, 217-224.

Dodge, J., J. Arnold, G. Wilson, J. Evans, and T. Fujita, 1986: The Cooperative Huntsville Meteorological Experiment. *Bull. Amer. Meteor. Soc.*, 67, 417-419.

Kummerow, C., R. A. Mack, and I. M. Hakkarinen, 1989: A self-consistency approach to improve microwave rainfall rate estimation from space. *J. Appl. Meteor.*, accepted.

Marshall, J. S. and W. M. Palmer, 1948: The distribution of raindrops with size. *J. Meteorol.*, 5, 165-166.

Spencer, R. W., 1986: A satellite passive 37 GHz scattering-based method for measuring oceanic rain rates. *J. Climate Appl. Meteor.*, 25, 754-766.

Wexler, R., 1947: Radar detection of a frontal storm 18 June 1946. *J. Meteorol.*, 4, 38-44.

Wilheit, T. T., A. T. C. Chang, M. S. V. Rao, E. B. Rodgers, and J. S. Theon, 1977: A satellite technique for quantitatively mapping rainfall rates over the ocean. *J. Appl. Meteor.*, 16, 551-560.

J1.5

CLOUD MODEL-BASED SIMULATIONS OF SATELLITE MICROWAVE DATA AND THEIR APPLICATION TO AN SSM/I RAIN ALGORITHM

Robert F. Adler[1]
Andrew J. Negri[1]
N. Prasad[2]
Wei-Kuo Tao[1]

NASA/Goddard Space Flight Center[1]
Severe Storms Branch/Code 612
Greenbelt, MD 20771

General Sciences Corporation[2]
Laurel, MD 20707

1. INTRODUCTION

The objective of this work is to simulate satellite microwave observations of convective rain systems using a three-dimensional cloud model and a microwave radiative transfer model. The simulated data sets are then used as a basis to derive rain estimation algorithms which are tested on actual satellite data. In this paper a tropical simulation will be accomplished and the algorithms applied to SSM/I (Special Sensor Microwave/Imager) data.

2. CLOUD MODEL/RADIATIVE MODEL RESULTS

The cloud model used in this study is a three-dimensional, multi-cloud model described by Tao and Soong (1986) and Tao et al. (1987). The model contains microphysical parameterization for both water and ice (three classes) and has a horizontal resolution of 1.5 km and a domain of approximately 100 km on a side. The radiative transfer model is an improved version by Szejwach et al. (1986) of the plane-parallel model by Wilheit et al. (1982). The improvements include a mixed phase layer, 19 layers in the vertical, and updated scattering coefficients.

Some results of the use of the cloud model/ radiative model combination have been described by Adler et al. (1988). The results in this paper use the instantaneous surface rain rate distribution over the model domain for a particular time (210 min.) into the model run of a simulation of a tropical oceanic squall line. The resulting radiance calculation at 86 GHz (vertical polarization [V]) shows a sharp decrease in brightness temperature (T_B) from the ocean background of about 270 K in the precipitation areas. A minimum T_B of below 100 K is located in conjunction with the heaviest rain. The T_B (86 GHz) shows the most variation in the light to medium rain rate areas and tends toward saturation in the heavier rain areas. Calculations were also made at other frequencies, including those on SSM/I. Three sets of radiance calculations were made using the same set of cloud model hydrometeor profiles: 1) The original ocean background case; 2) An ocean background case with environmental humidity profiles reduced to 75% of the original values; and 3) a land background case with emissivity of 0.95.

Next, the satellite observations are simulated by area-averaging the T_B values, originally at 1.5 km resolution, into 12 km by 12 km boxes, the approximate resolution of the SSM/I 86 GHz channels. The cloud model rain rates are also area-averaged. The results are shown in Fig. 1 for both 37 and 86 GHz and 12 km averaging, even though the SSM/I 37 GHz spatial resolution is about 25 km. Over water both frequencies show the polarization differences in clear air and tend toward zero polarization at heavier rain rates (the radiative model only considers spherical particles). The ocean/land difference is also obvious.

3. MODEL-BASED ALGORITHMS

The area averaged T_B's and rain rates shown in Fig. 1 (plus those from the third, less humid run) were used with a regression approach to produce SSM/I algorithms. In each case only those area-averaged data points with ≥ 0.1 mm h^{-1} rain were included in the regression data set. Three algorithms will be examined in this paper: A) Combination of 86 GHz V and H polarizations to separate land/ocean differences and raining from non-raining areas, B) 86 GHz (V) alone to determine the loss of information, if any, in using just one polarization, and C) a combination of 86 GHz (H) and 37 GHz (H) to examine a frequency-difference algorithm, and one applicable to the current situation where the 86 GHz (V) channel is unusuable because of instrument problems.

The regression equations are given in Table 1. For algorithm A, which uses the two polarizations at 86 GHz, the regression equation can be manipulated so that a new parameter, $\hat{T}$, can be derived which is a linear combination of the two channels and has the property that $\hat{T} = T_V = T_H$ when $T_H = T_V$, i.e. when the polarization difference is zero. The resulting equation is:

$$R = 36.65 - .1398\,\hat{T}, \qquad (1)$$

where $\hat{T} = 1.422\,T_V - 0.422\,T_H$. The $\hat{T}$ parameter is similar to the Polarization Corrected Temperature (PCT) of Spencer et al. (1988).

The results of applying the derived algorithms back on the cloud-model-based data set are shown in Table 1 and Fig. 2. Table 1 shows that there is not much difference among the algorithms either in the correlation coefficient in raining (≥ 1 mm h^{-1}) areas or in the rain/no rain discrimination capability seen in the other statistics (e.g. CSI). It is surprising that the 86 V algorithm did just as well as the other two algorithms. This result is probably due to the relatively moist environment in this case producing fairly high T_B's over the clear, simulated ocean.

The results for this model-based, dependent data set define, in certain ways, the upper limit to the retrieval of rain. This is because this "perfect" data set has the T_B's connected to the rain rate through the physics of the cloud

model and radiative transfer model. The scatter in Fig. 2 and the errors defined in Table 1 are a result only of the failure of the modeled system to produce a unique rain-T_B relation. This is due to the complex nature of the convective precipitation process and the associated rain and T_B fields, which are well captured by the models.

4. APPLICATION TO SSM/I DATA

As a test of this approach, the model-based algorithms are applied to SSM/I data for August 5, 1987, coinciding with ground-based radar data from the NASA 10 cm radar at Wallops Island, Virginia. The resulting rain rate maps are shown in Fig. 3 along with the radar rain rate distribution. The patterns are very similar and this is also apparent from the statistics in Table 2 and the scatter plot in Fig. 4.

The application to real data indicates that the model-based approach has promise, although there has been a sharp drop in the correlation coefficient (0.9 to 0.7 and in the CSI (0.8 to 0.5) from the simulated data to the real SSM/I data set. This drop in accuracy may be due more to the difficulties of doing radar-satellite time/space matchups than to differing T_B-rain relations, although both effects are probably inbedded in the results.

Table 3 gives the totals for the area and indicates that the techniques are getting the total rainfall approximately correct, but tend to underestimate the area and overestimate the rain rate. Since this is only one case, no strong conclusions should be drawn based on these statistics.

Fig. 5 shows the application of the techniques to other examples of SSM/I data with no verification. The results appear reasonable, but many more cases with verification need to be examined.

5. CONCLUSIONS

The cloud model-radiative transfer model combination appears to be a viable way of studying area-averaged T_B-rain rate relations and using the simulated data to develop algorithms. Application of model-based algorithms to SSM/I data was successful with little discernible loss in accuracy in using a frequency difference algorithm (C) rather than a polarization algorithm (A). Even an 86 V only algorithm was successful in this limited application. Although this work to date has accented the frequencies in which the scattering process dominates, inclusion of all the available frequencies should produce an overall better result. Application of techniques such as that of Kummerow et al. (1989) using an iterative approach with a radiative transfer model should enhance the utilization of the model-generated data sets.

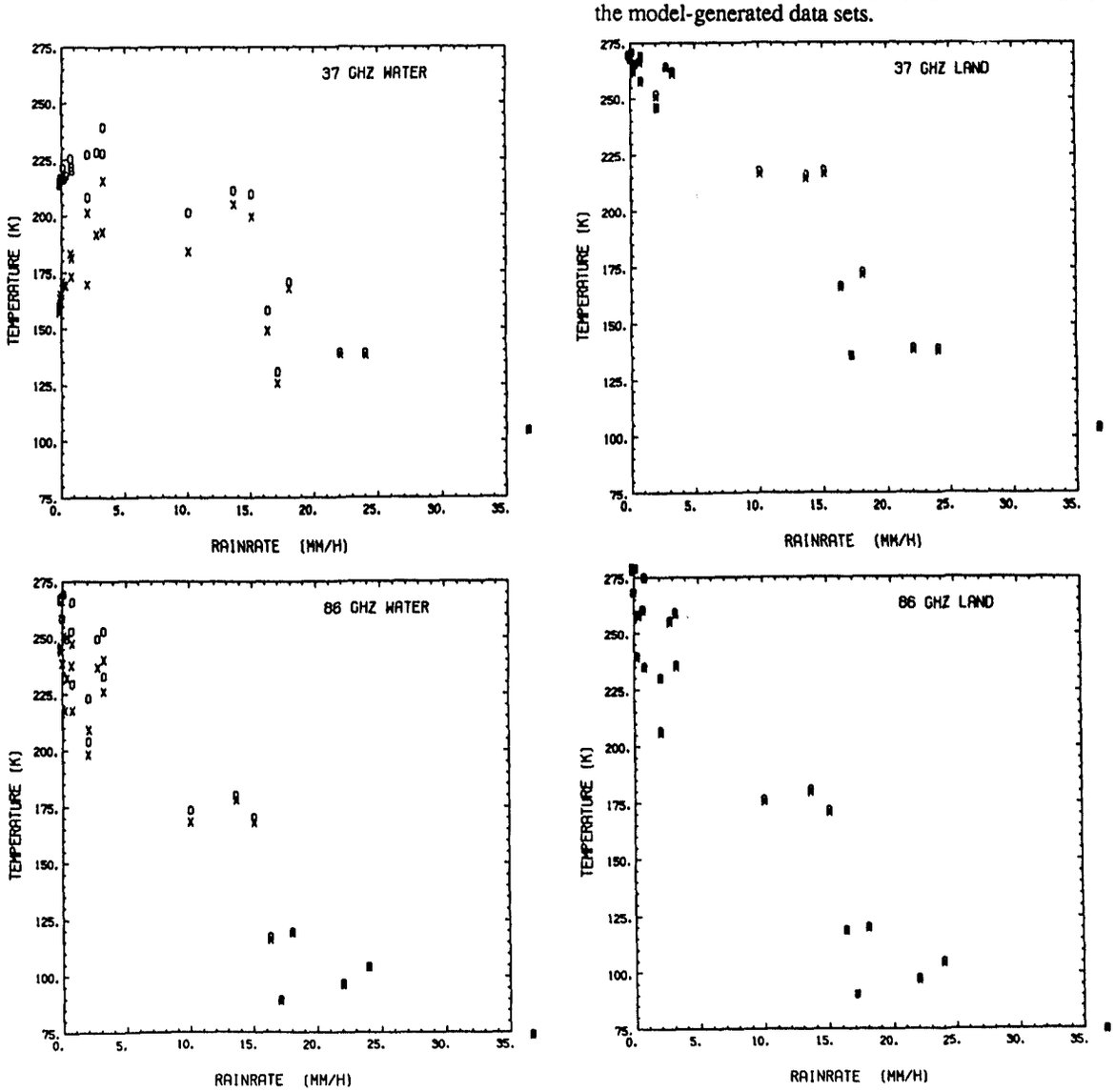

Fig. 1 Area-averaged T_B versus rain rate (12 km x 12 km) over the cloud model domain. Results are shown for 37 and 86 GHz with both a land and a water background. The circles are the vertical polarization and the x's are horizontal polarization.

REFERENCES

Adler, R. F., W.-K. Tao, N. Prasad, J. Simpson, and H.-Y. Yeh, 1988: Satellite microwave rainfall simulations with a three-dimensional cloud model. Preprint volume, 3rd Conference on Satellite Meteorology and Oceanography, 290-295.

Kummerow, C., R. A. Mack, and I. M. Hakkarinen, 1989. A self-consistency approach to improve microwave rainfall rate estimation from space. J. Appl. Meteor., (accepted).

Spencer, R. W., H. M. Goodman, and R. E. Hood, 1989: Precipitation retrieval over land and ocean with the SSM/I, Part 1: Identification and characteristics of the scattering signal. J. Atmos. and Ocean Tech., (in press).

Szejwach, G. R. F. Adler, I. Jobard, and R. A. Mack, 1986: A cloud model-radiative model combination for determining microwave T_B-rain rate relations. Preprints, 2nd Conference on Satellite Meteorology/Remote Sensing and Applications, Amer. Meteor. Soc., Williamsburg, VA, 444-449.

Tao, W.-K. and S.-T. Soong, 1986: The study of the response of deep tropical clouds to mesoscale processes: Three-dimensional numerical experiments. J. Atmos. Sci., 43, 2653-2376.

Tao, W.-K., J. Simpson, and S.-T. Soong, 1987: The statistical properties of a cloud ensemble: A numerical study. J. Atmos. Sci., 44, 3175-3187.

Wilheit, T. T., J. L. King, E. B. Rodgers, R. A. Nieman, B. M. Krupp, A. S. Milman, J. S. Stratigos, and H. Siddalingaiah, 1982: Microwave radiometric observations near 19.35, 35, 92, and 183 GHz of precipitation in tropical storm Cora. J. Appl. Meteor., 21, 1137-1145.

TABLE 2

Statistical analysis of regression-generated rain rates derived from SSM/I brightness temperatures and Wallops radar-derived rainrates averaged over 13 km on a side. RHO, POD, FAR, CSI and %ERR calculated from 1444 data points. A rain threshold of 1.0 mm/h was used to determine rain/no-rain.

SCHEME	RHO	POD	FAR	CSI	%ERR
A	0.739	0.66	0.30	0.48	0.09
B	0.731	0.55	0.31	0.44	0.10
C	0.746	0.59	0.30	0.47	0.10

TABLE 3

Comparison of Volume Rainrate (VRR), Rain Area (A_r) and Mean Raining Area Rainrate (MRR) for the 2×10^5 km^2 area viewed by the Wallops radar.

SCHEME	FREQ'S	VRR (10^{10} kg/h)	A_r (10^4 km^2)	MRR (mm/h)
A	86H, 86V	11.89	3.35	3.55
B	86V	11.22	3.15	3.56
C	86H, 37H	13.30	3.20	4.16
RADAR		12.93	4.10	3.15

TABLE 1

Statistical analysis of model-generated rainrates and brightness temperatures. Regression coefficients and correlation coefficient (RHO) computed from 63 temperatures with associated rainrates greater than 0.1 mm/h. Probability Of Detection (POD), False Alarm Ratio (FAR), Critcal Success Index (CSI) and Percent Error (%ERR) calculated from the regression applied to the original 192 data points. A rain threshold of 1.0 mm/h was used to determine rain/no-rain.

SCHEME	REGRESSION EQUATION	RHO	POD	FAR	CSI	%ERR
A	-0.1988 T(86v) + 0.0590 (T86h) + 36.6532	-0.933	0.90	0.16	0.78	0.06
B	-0.1440 T(86v) + 37.0796	-0.933	0.93	0.19	0.76	0.06
C	-0.1679 T(86h) + 0.0279 (T37h) + 35.3567	-0.926	0.90	0.21	0.73	0.07

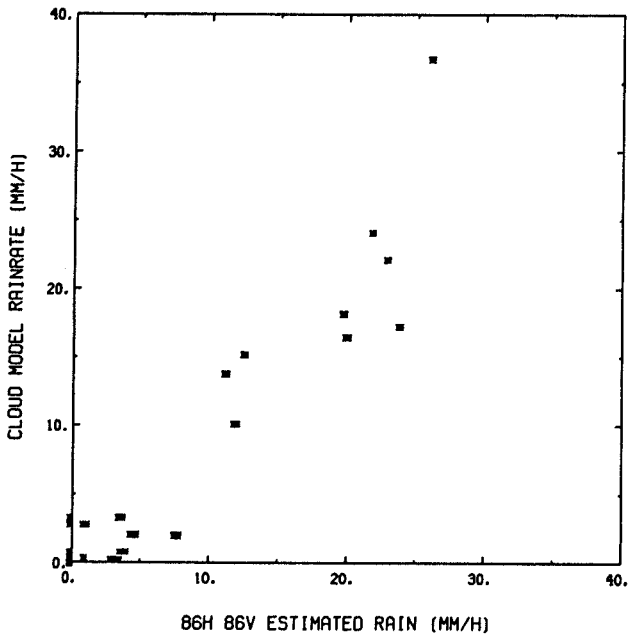

Fig. 2 Scatter plot of algorithm A applied to the model-based, dependent data sets.

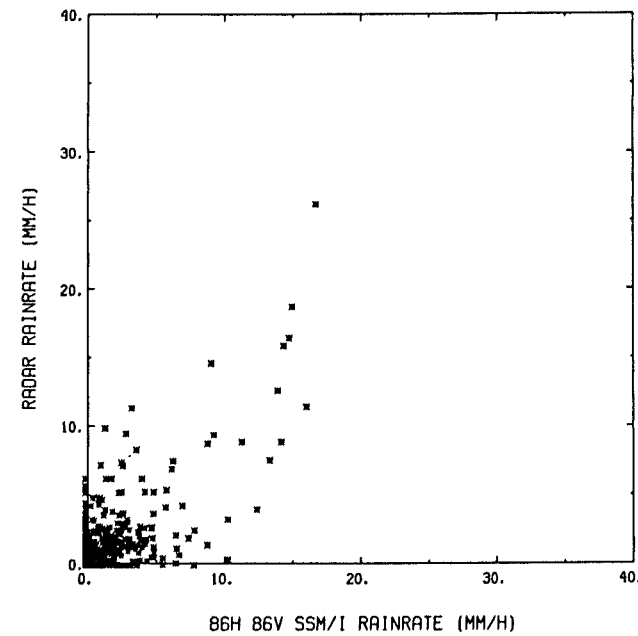

Fig. 4 Scatter plot of algorithm A applied to the SSM/I data and compared to Wallops Island radar data on August 5, 1987.

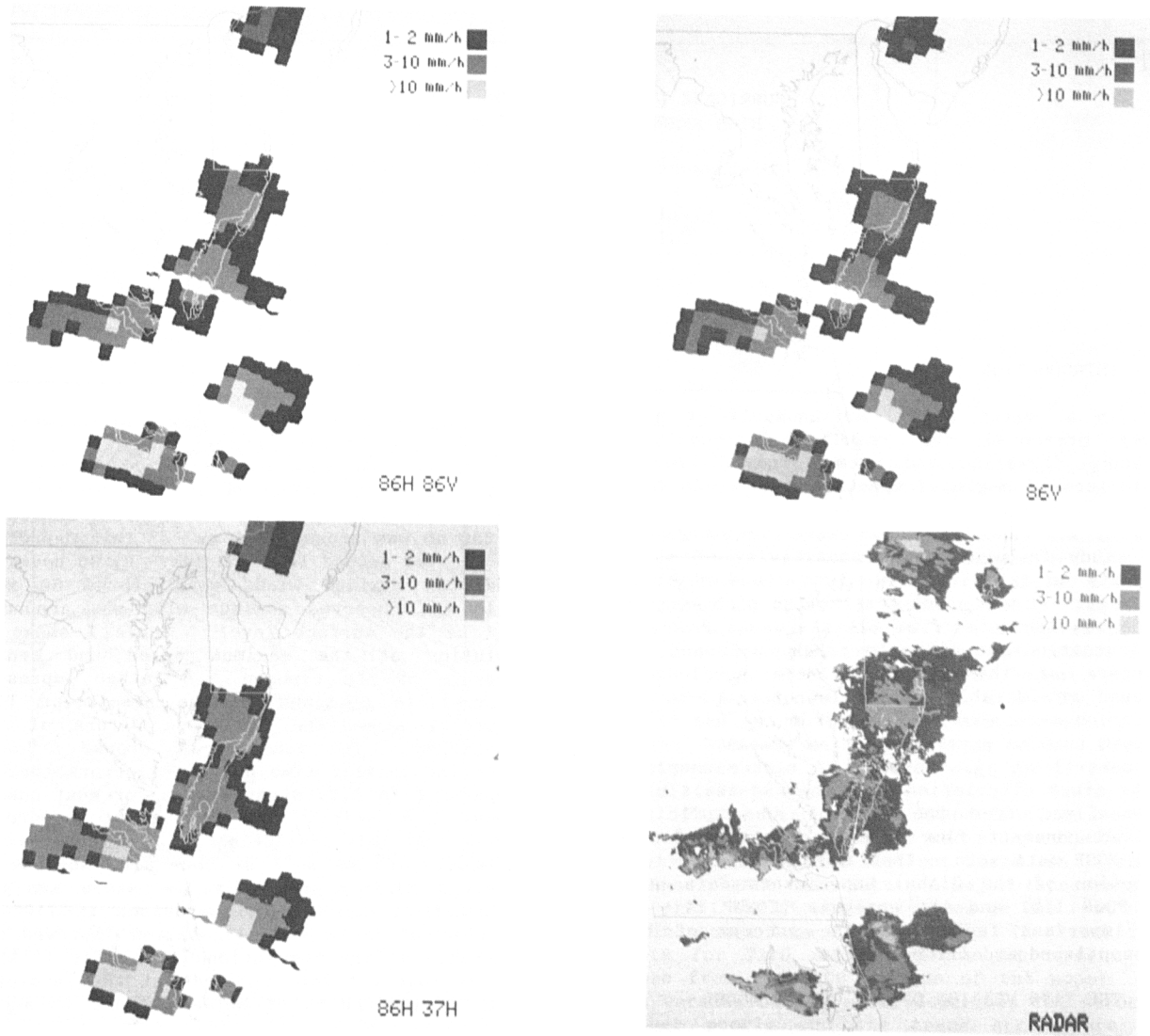

Fig. 3 Result of applying algorithms A (upper left), B (upper right), and C (lower left) to SSM/I data in a comparison with Wallops Island ground-based radar data (lower right) 2346 GMT August 5, 1987.

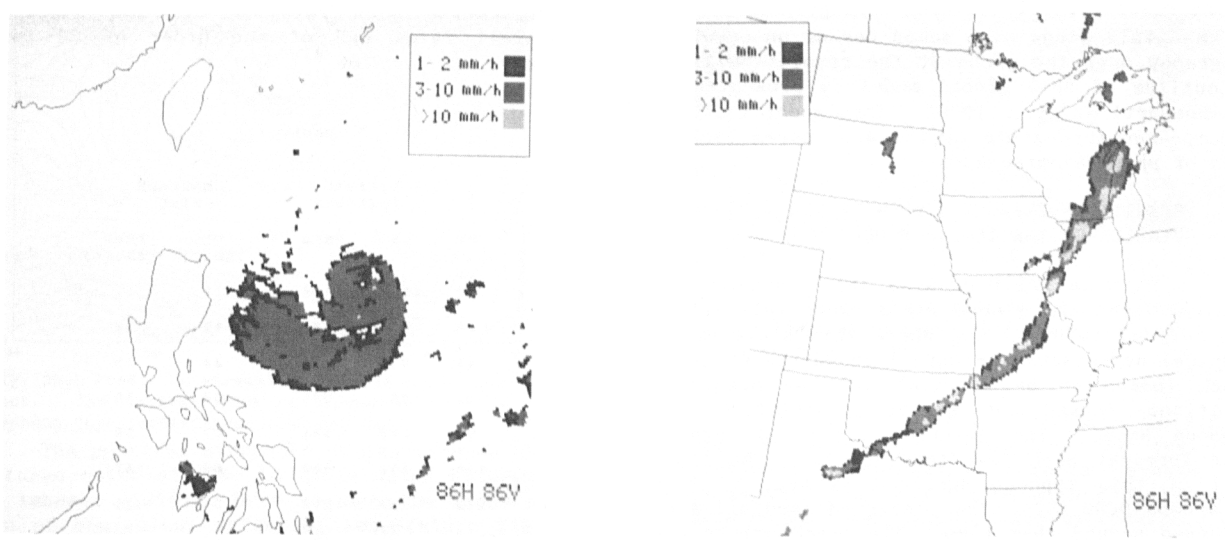

Fig. 5 Application of algorithm A to a tropical cyclone (July 11, 1987, 2130 GMT) and a mid-latitude squall line (August 17, 1987, 0052 GMT).

J2.1

HURRICANE (TYPHOON) MOTION FROM VERY HIGH RESOLUTION MODEL FORECASTS

T.N. Krishnamurti, H.S. Bedi and D. Oosterhof

Florida State University
Tallahassee, Florida

1. INTRODUCTION

In a recent study, Krishnamurti et al., (1989) presented the results on hurricane (typhoon) formation and motion from different resolutions of a global spectral model. In that study, the prediction of several storms over the Atlantic and Pacific ocean were investigated. That study focused on the sensitivity of storm forecasts to data sets, resolution and physical processes. It was noted that as the global resolution was increased from T21 (21 waves triangular truncation) to T106 the track, size and the structure of the storms in the predictions improved considerably. Major improvements in the prediction were also realized from the use of an improved cumulus parameterization scheme, Krishnamurti et al., (1983). A closer coupling of the storm circulation with the air-sea fluxes was realized from the use of an explicitly resolved constant flux layer. The use of the final FGGE data sets - that included the delayed collection of the Global Experiments data sets (The FGGE IIb) and its analysis (ECMWF IIIb) - were important factors in the success of the aforementioned modelling efforts.

2. THE T170 VERSION OF THE GLOBAL MODEL

The present study primarily focuses on the results from a T170 version of the global model. The transform grid at this resolution consists of 512 grid points in the zonal direction and 256 grid points along the meridional direction. Near 20N the resolution of the transform grid is around 50 km. This study also makes use of an envelope orography over the globe at the resolution T170. An outline of this global model is presented in Krishnamurti et al., (1989). This model includes a comprehensive, state of the art, parameterization of physical processes.

3. RESULTS OF TYPHOON HOPE WITH THE T170 VERSION OF THE GLOBAL MODEL

Here we shall examine the forecasts for typhoon Hope; the global fields were initialized for July 27 1979, 12 UTC where this storm was a tropical depression. Figure 1 shows the observed track (based on best track) and the predicted positions (based on surface vorticity) for typhoon Hope. The position errors throughout this forecast were less than 300 km. The landfall of this typhoon occurred on Aug. 2, 1979 at around 0600 UTC. The predicted landfall also occurred around that time. The track errors are extremely small at this resolution. The position error at day 5.7 was around 300 km. The predicted streamline and isotach field, at hours 0 and 96, are shown in fig. 2 a, b respectively. The isotachs exhibit the development of a strong wave number one type asymmetry around the storm center as is typical in hurricanes and typhoons. The initial wind speed in the tropical depression at 850 mb was around 15.6 ms^{-1}. This depression was located around 143E and 19N. By 96 hours the predicted maximum winds were around 50 ms^{-1}, while the observed maximum wind was around 67 ms^{-1} at the surface level. Table 1 shows the evolution of the maximum speed and central pressure of the typhoon. A rather impressive forecast is obtained at the resolution T170. Figure 1 shows the positions errors at this resolution. The landfall at around 5.7 days after the initial time has model errors that are comparable to 2 to 3 day errors for most conventional statistical and equivalent barotropic models. At this resolution the predicted maximum speed reached 60 ms^{-1} at hour 120, whereas the observed maximum speed in the storm was also around that value. In comparison to T106 the strength of the storm circulation improved considerably at the resolution T170. Fig. 3 shows the 24 hourly rainfall totals at the resolution T170. Rainfall rates between hours 48 and 72 reached as high as 463 mm/day when the predicted storm reached supertyphoon intensity. The rainfall rates at T170 were about 100% higher than from T106 in the first 72 hours, Krishnamurti et al., (1989). The rainfall pattern shows a very interesting broad band that exhibits a counterclockwise slow rotation; in the bands the rainfall rates are of the order of 30 to 40 mm/day.

TABLE 1

	CENTRAL PRESSURE		MAXIMUM WIND	
HR	OBS	PRED	OBS (SURF)	PRED (850MB)
0	1008	1008	10	17
24	999	994	18	30
48	972	986	34	35
72	932	981	44	40
96	898	981	67	50
120	920	980	62	61
132	NA	993	54	35
*138	NA	998	44	25

* DENOTES TIME AT LANDFALL

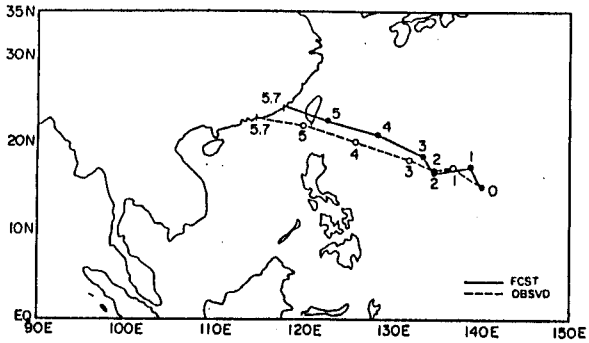

Fig. 1. The observed and the predicted track of Typhoon Hope.

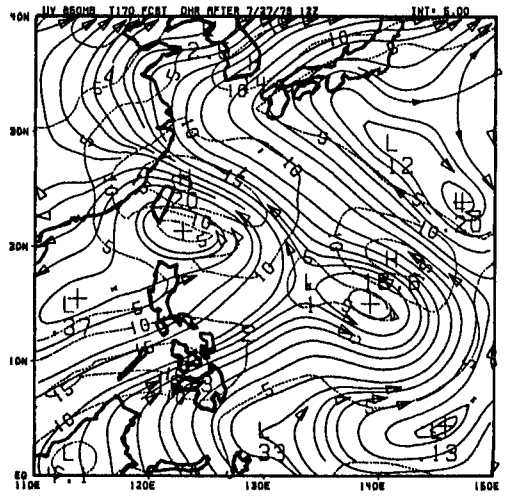

Fig. 2a. Streamlines at 850 mb on day 0 of forecast. Note a tropical depression near 143E and 19N with maximum winds around 15.5 ms^{-1}. (Speed lines are dashed).

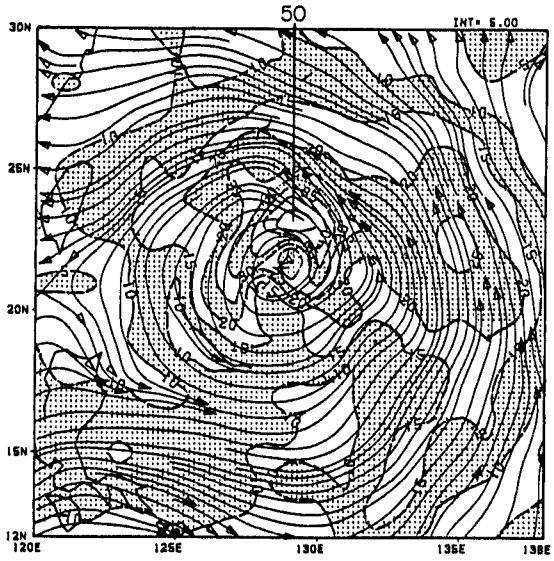

Fig. 2b. Predicted streamlines on day 4 of forecast. The maximum wind is around 50 ms^{-1} in Typhoon Hope located near 129E and 23N.

The vertical structure of the typhoon shows features quite similar to those noted by Hawkins and Imbembo (1976). Here we show the cross section of equivalent potential temperature fig. 4 that illustrates near neutral constant θe structure along the vertical near the storm center. Away from the storm center the θe minimum and conditional instability is reasonably maintained.

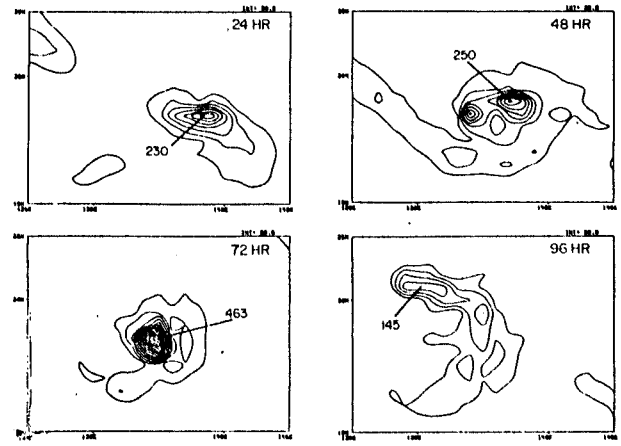

Fig. 3. Predicted 24 hourly rainfall amounts, units mm/day. Maximum rainfall between hours 48 and 72 is around 463 mm/day.

The features in the vertical cross sections of wind speed, vorticity and temperature anomaly (not shown), at T170, were quite similar to typical sections shown in Anthes (1982). The inner rain area of the storm, within a radius of 100 km, is not properly resolved by the current model at the resolution T170. The lowest surface pressure was around 980 mb at hours 72, 96 and 120. While the observed minimum pressure was around 898 mb at around hour 96. Fig. 5 illustrates the predicted sea level pressure field at 96 hours.

Further increase in resolution, is however, needed to obtain sharper radial gradients that are seen in cross-sections based on aircraft reconnaissance data sets. A major improvement in the predicted structure is seen as the resolution is increased from T106 to T170. The track forecasts for T170 show a slight improvement over those from the T106 version of the model. The T63 version of the model describes the structure rather poorly and its track errors are also somewhat larger.

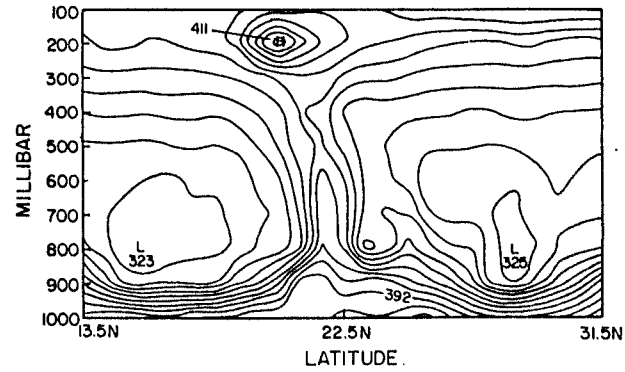

Fig. 4. Vertical cross section of equivalent potential temperature across the storm center on day 4 of forecast. Units °K.

Based on numerous forecasts of similar storms at very high resolution, we feel that operational forecasting efforts should aim towards very high resolution with global models. Medium range forecasting of storms require a global modelling effort. The aforementioned results require, aside from a sophisticated model, a FGGE-type of data collection and analysis effort.

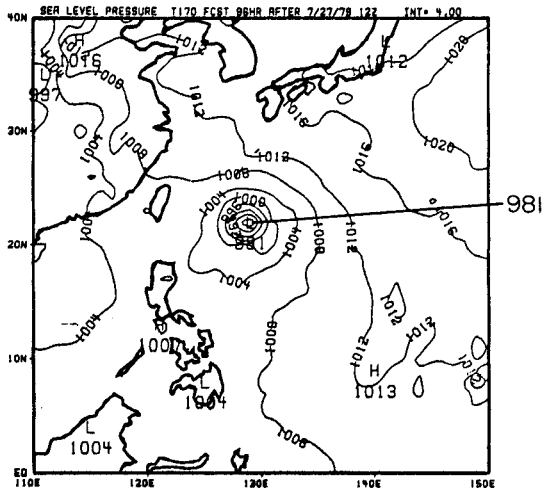

Fig. 5. Predicted field of sea level pressure on day 4 of forecast. Units mb. Storms minimum pressure=981 mb.

4. MIXED RESOLUTION EXPERIMENTS

The computer time required to run a comprehensive model at the resolution T170 on the several supercomputers ranges from 4 to 8 hours for a 24 hour run. The model can be run in a mixed resolution mode, Krishnamurti et al., (1989). In that study we also ran the dynamics at a resolution of T42 and physics at a resolution of T106. For that combination the phase speed of tropical waves was too slow. In a recent study we reversed the resolution for dynamics (T106) and physics (T42). We noted that a reasonable phase speed is obtained by having the dynamics at a very high resolution; the detailed results with respect to dynamics and physics at different resolutions will be presented. Since the dynamics part of the code is fully vectorized, this approach is shown to be economical for high resoluted modelling.

5. DEGRADING THE MODEL

A number of recent studies on typhoon motion have focused on the interactions of the steering flow and a vortex in the context of barotropic dynamics. The high resolution global model was degraded sequentially to examine the validity of such studies. We have found that the storm motion and its interaction with the dynamics is rather closely linked to the vigorous convection in a hurricane. Degrading the multilevel global model with physics into a global barotropic model, although useful as an academic exercise, has very little bearing to the interaction of a hurricane (or typhoon) with its environment. The inner convection is critical for the maintenance of divergent circulation in a hurricane. These in turn maintain the azimuthal circulations. The barotropic instability of the circulate vortex cannot be studied in isolation from the source of energy that maintains the vortex. Degrading the model is shown to produce erroneous tracks, erroneous steering and a poor coupling of the storm with its environment. Several examples on the storm track and its relationship to dynamical parameters such as vorticity advection, orientation of beta gyres and their degradation will be illustrated.

REFERENCES

Anthes, R.A., 1982: Tropical cyclones, their evolution, structure and effects. Sci. Press, 208 pp.

Hawkins, H.F. and S.M. Imbembo, 1976: The structure of a small, intense hurricane, Inez 1966. Mon. Wea. Rev., 104, 418-442.

Krishnamurti, T.N., S. Low-Nam and R.J. Pasch, 1983: Cumulus parameterization and rainfall rate II. Mon. Wea. Rev., 111 815-828.

Krishnamurti, T.N., D. Oosterhof, and N. Dignon, 1989: Hurricane Prediction with a High Resolution Global Model, Monthly Weather Review, March, 1989.

ON GENERALIZING THE THEORY OF TROPICAL CYCLONES TO INCLUDE ENVIRONMENTAL INFLUENCES

Robert T. Merrill

Cooperative Institute for Meteorological Satellite Studies
University of Wisconsin -- Madison, WI

1. INTERNAL DYNAMICS

Tropical cyclones (TCs) are fundamentally a cooperative interaction between a nearly balanced vortex, the planetary boundary layer (PBL), and moist convection. High winds enhance the PBL fluxes and with reduced surface pressure elevate the θ_e of the inflow. Though but a small fraction of the energy conversion of the TC, the "θ_e boost" is critical because it maintains the slight instability to moist ascent necessary for a secondary circulation which both spins up and warms the vortex. Low-level convergence increases the tangential winds and latent heat release in the unstable air slightly exceeds the adiabatic cooling by the mean ascent. At higher rotation rates, the compensating cloud-scale subsidence becomes focused into an eye. Lower pressure increases the θ_e boost and maintains *instability even as the vortex warms aloft*, and deepening continues.

Though details of the above mechanism have driven as many arguments as storms, after 25 years of study it is apparent that internal processes alone, though energetically dominant, cannot explain all TC behavior. TC research has thus expanded to include environmental conditions and as we observe and begin to simulate them we must generalize our conceptual model of the TC as a local instability to include environmental effects without compromising what we know of the internal dynamics. It is not possible to fully understand one without an active awareness of the other.

For brevity we limit the discussion to changes in the maximum winds or minimum pressure (intensity change) though this is only one mode of TC structure change. I believe that the keys to understanding observed intensity changes are those processes which cause a TC to <u>stop</u> deepening. Intensifying TCs eventually warm aloft so much that even with increasing inflow θ_e boost, stability for moist ascent develops and further balanced spin-up of the mass and wind fields is no longer possible in the stabilized area. This happens most easily at the eye wall and when it does intensification ceases, though the outer circulation may continue to spin up. *Even under "ideal" conditions (yet undefined)* there is apparently an upper limit, or "potential intensity" (PI) for TCs, dependent on sea surface temperature (SST) and tropopause (or outflow) temperature (Emanuel, 1988; Merrill, 1988). Most TCs never approach their PI value.

Environmental influences interact with the vortex and hasten (or sometimes delay) the development of stability to moist ascent in the TC core. They can act either by interfering with the θ_e boost (landfall is the most obvious example) or by accelerating the warming aloft. Note that warming aloft intensifies the cyclone only if it occurs in the eye; beyond this it broadens but does not deepen the TC and may even prevent further deepening by suppressing the eye wall.

2. VERTICAL SHEAR

Vertical shear of the environmental flow is apparently the dominant environmental influence. Since TCs move with the deep layer mean flow (Pike, 1987), shear implies relative motion between vortex and surroundings at some level(s). Riehl (1979) describes the effect as "ventilation" of the warm core by cooler, drier relative flow, which both reduces the core column warming and therefore the pressure drop and also affects convection by diluting updrafts and stimulating downdrafts (Black and Marks, 1987). The results of Willoughby et. al. (1984) suggest another shear mechanism; they relate the <u>S</u>tationary <u>B</u>and <u>C</u>omplex (SBC) to relative low level flow, such as expected with shear. The resulting secondary circulation is shown in Fig. 1. This model is also supported by 6.7 micron (water vapor) satellite imagery, which often shows strong drying on the upshear side and an asymmetric expansion of cold cloud tops on the opposite side of the TC.

Given that the interaction of vortex and shear establishes an SBC and that ventilation stimulates downdrafts, shear influence on intensity change follows directly. The downdrafts with convective bands can reduce the PBL θ_e by over 10 K and also establish an inversion to prevent recovery except in a shallow layer (Powell, 1985), resulting in a loss in buoyancy available to the eyewall (or any other convection located inward and counterclockwise) which *receives this modified air. What is unknown are* the factors determining the magnitude of this

effect, i.e. vortex size, shear strength and orientation (directional, speed, or mixed), latitude, and orientation of the inflow trajectories relative to the SST cold wake.

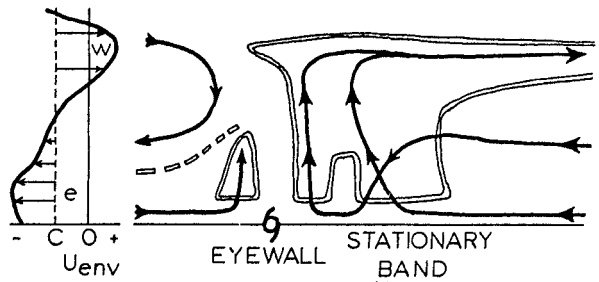

Fig. 1. Zonal cross section through a TC embedded in the sheared environmental flow shown at left. Arrows show cyclone-relative radial flow.

3. OUTFLOW EFFECTS

Though the subject of most of the research on environmental influences, the outflow layer remains an enigma. Its low inertial stability and asymmetric structure make it a logical place for environmental interaction (Holland and Merrill, 1984), who also suggest that eddy absolute angular momentum (AAM) flux convergence stimulates upper level outflow and compensating mid-tropospheric inflow, completing a secondary circulation which removes heat from the TC core and maintains moist instability (Fig. 2). Rawinsonde composites offer limited evidence for a cooler upper troposphere in intensifying TCs (Edson, 1987), and Molinari and Vollaro (1989) find a correlation between eddy AAM imports and intensification. Merrill (1988) compared composite outflows of TCs well below PI and found that non-intensifying ones had a stronger outflow layer anticyclone beyond 1000 km radius, also consistent with reduced AAM imports.

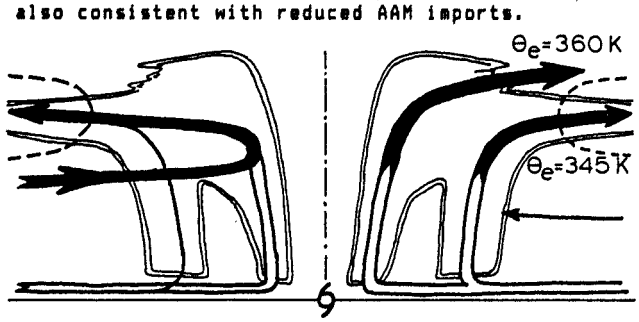

Fig. 2. Cross section through a TC showing outflow layer interactions. Left. Eddy AAM flux convergence (dashed outline) may stimulate a secondary circulation. Right. High eyewall θ_e may result in outflow at significantly different levels.

Fig. 2 also shows an interesting limitation of this model. Because of the θ_e boost, we expect a 10-15 K difference in outflow temperature between the eyewall and outer convection, and rawinsonde composites indicate that the latter probably dominates the outflow in the eddy AAM flux convergence zone. If the higher level flow is very different, we may be missing crucial evidence of how the environment and TC interact to influence eyewall static stability and convection explicitly when we treat the "outflow layer" as a vertically homogeneous region as has always been done.

Three dimensional analysis of the outflow layer of some well observed TCs is thus necessary before we can proceed with hypothesis development. Isentropic potential vorticity (IPV) analysis is suggested because of the proximity to the tropopause, and eyewall outflow should be marked by tropospheric IPV but stratospheric θ_e.

4. SUMMARY

We have suggested a generalized TC theory in which internal feedbacks between convection, vortex, and boundary layer are energetically dominant and the environment influences intensity change by interacting with the vortex and modifying the core static stability either directly or by convective band effects on the PBL. We have specified explicitly the interaction for vertical shear; this hypothesis awaits study with satellite and in situ observations and numerical simulation. It is suggested that interactions between outflow layer asymmetries and the vortex also affect the core static stability and thereby convection and intensity change. Knowledge of the three-dimensional mass and wind structure of the outflow layer is essential for progress in this area, and IPV analysis of individual cases is urged as an initial step towards a definite hypothesis.

REFERENCES

Black, P. G., and F. D. Marks, Jr., 1987: Environmental interactions associated with hurricane supercells. 17th AMS Conf. on Hurricanes and Trop. Meteor., Miami, FL, 7-10 April, 416-419.

Edson, R. E., 1987: A rawinsonde study of tropical cyclone intensification characteristics. 17th AMS Conf. on Hurricanes and Trop. Meteor., Miami, FL, 7-10 April, 280.

Emanuel, K. A., 1988: The maximum intensity of hurricanes. J. Atmos. Sci., 45, 1143-1155.

Holland, G. J., and R. T. Merrill, 1984: On the dynamics of tropical cyclone structural changes. Quart. J. Roy. Meteor. Soc., 110, 723-745.

Merrill, R. T., 1988: Environmental influences on hurricane intensification. J. Atmos. Sci., 1678-1687.

Molinari and Vollaro, 1989: External influences on hurricane intensity: Part I. Outflow layer eddy AAM fluxes. accepted by J. Atmos. Sci.

Pike, A. C., 1987: A comparison of wind components and geopotential heights as statistical predictiors of tropical cyclone motion, 17th AMS Conf. on Hurricanes and Trop. Meteor., Miami, FL, 7-10 April, 101-103.

Powell, M., 1987: Boundary layer structure in convective hurricane rainbands. 17th AMS Conf. on Hurricanes and Trop. Meteor., Miami, FL, 7-10 April, 373-376.

Riehl, H., 1979: Climate and Weather in the Tropics. Academic Press, 611 pp.

Willoughby, H. E., F. D. Marks, Jr. and R. J. Feinberg, 1984: Stationary and moving convective bands in hurricanes. J. Atmos. Sci., 41, 3189-3211.

THE UTILITY OF SPECIAL SENSOR MICROWAVE/IMAGER DATA IN THE OPERATIONAL ANALYSIS OF TROPICAL CYCLONES

Edward N. Rappaport

NOAA National Hurricane Center
Coral Gables, Florida

Peter G. Black

NOAA Hurricane Research Division
Miami, Florida

1. INTRODUCTION

The National Hurricane Center (NHC) of the National Oceanic and Atmospheric Administration (NOAA) has statutory responsibility for the analysis and forecast of tropical cyclones in the Atlantic and Eastern Pacific basins. The accuracy of NHCs operational products depends upon the quality and resolution of real-time data. At present, the NHC relies on a suite of instrumented platforms, including reconnaissance aircraft and geostationary satellites.

Recently, several studies have shown that microwave measurements from polar-orbiting satellites can be used to infer rain rates and wind speeds over tropical cyclones (e.g., Black *et al*, 1985; Hawkins and Black, 1982). Satellite microwave measurements over tropical cyclones will soon become available operationally to the NHC.

The Special Sensor Microwave/Imager (SSM/I) is a polar-orbiting passive microwave radiometer launched by the Defense Meteorological Satellite Program (DMSP) in June 1987. The imager is intended to provide estimates of several meteorological parameters in real time. In this study the utility of the SSM/I as a supplemental source of data in tropical cyclones was evaluated.

The evaluation focused on the reliability of the data-delivery system and the accuracy of SSM/I rain rate and wind speed retrievals. The evaluation used data collected during a 1988 field program designed by the NHC, NOAA Hurricane Research Division (HRD) and Office of Aircraft Operations (OAO), and the U. S. Air Force Chief, Aerial Reconnnaissance Coordination, All Hurricanes (CARCAH) for a comparison of SSM/I products with similar products available from NOAA WP-3D aircraft. In this paper we present the initial findings of the evaluation.

2. DATA AND METHOD OF ANALYSIS

2.1 SSM/I

The SSM/I measures upwelling radiation over a ~1400 km wide swath. Measurements are made for both vertical (v) and horizontal (h) polarizations (pol) at three frequencies, 19.35, 37.0 and 85.5 GHz, and at 22.235 GHz for v-pol only. Although the radiation is determined every 25 km (12.5 km at 85.5 GHz) along the earth's surface, the dimensions of SSM/I samples range from 69 km x 43 km at 19.35 GHz to 15 km x 13 km at 85.5 GHz. Each SSM/I sample is converted to a brightness temperature during preliminary processing.

Brightness temperatures for SSM/I orbit number 6410, including the satellite's overpass of Hurricane Gilbert at about 0050 UTC, 16 September 1988, were obtained on magnetic tape from the Naval Research Laboratory (NRL) of the U. S. Department of the Navy. The brightness temperatures were corrected for feedhorn spillover loss and cross-polarization coupling using the procedure described by Hollinger *et al.* (1987). The side lobe correction proposed by Hollinger *et al.* (1987) was not applied because of the uncertainties that they noted. Subsequent study showed that this correction does not significantly improve the accuracy of SSM/I wind speeds.*

The mean surface wind speed (W) in m/s at 19.5 m was calculated using:

$$W = 147.90 + 1.0969 \times TB19V - 0.455 \times TB22V - 1.76 \times TB37V + 0.786 \times TB37H \quad (1),$$

where TB19V, TB22V and TB37V are the corrected v-pol brightness temperatures at 19.35, 22.235 and 37 GHz, respectively, and TB37H is the corrected h-pol 37 GHz brightness temperature.

Rain rate (R) in mm/h was obtained from:

$$R = 26.09023 + 0.07980 \times TB19H - 0.14376 \times TB85V \quad (2),$$

where TB19H and TB85V are the corrected brightness temperatures for h-pol 19.35 GHz and v-pol 85.5 GHz, respectively. These equations gave the most accurate estimates of wind speed and rain rate in the NRL's calibration and validation study. Hollinger *et al.* (1987) describe further the SSM/I calibration procedures and this "D-Matrix" approach to regression equations.

SSM/I earth location data were renavigated using a procedure provided by the University of

* Goodberlet, M. A., (1989), Univ. of Mass., Dept. of Computing and Electrical Eng., Amherst, MA, personal communication.

Massachusetts. The procedure uses modified pitch and yaw angles for the DMSP spacecraft to minimize navigation errors. Comparison of the renavigated data with known geographical landmarks shows the corrected locations to be accurate to within one pixel (25 km).

2.2 Aircraft

WP-3D data from 0020 to 0245 UTC 16 September 1988 were used to evaluate the SSM/I. The aircraft flew a "figure 4" pattern that was centered approximately at the storm's center and extended outward to a radius of about 200 km. The aircraft flew at an altitude of about 1500 m.

SSM/I wind speeds were compared to the WP-3D flight-level winds. In making the comparisons, it is noted that 19.5-m level wind speeds are usually 80% of flight-level wind speeds at 1500 m (Powell, 1980).

Radar reflectivities from the WP-3D lower fuselage radar were used to evaluate SSM/I rain rates. A composite analysis of radar reflectivity data, as described and justified by Marks (1985), was constructed for 0020 to 0245 UTC. The analysis also used an objectively determined storm track (Willoughby and Chelmow, 1982) and mapped reflectivities into a storm-relative coordinate system. The 0050 UTC storm center positions determined from aircraft data (22.57°N, 93.81°W) and estimated from SSM/I 85.5 GHz data agree to within about 20 km.

The radar reflectivity factor Z was converted to rain rate using the relationship developed by Jorgensen and Willis (1982),

$$R = (Z / 300)^{1/1.35} \qquad (3).$$

Jorgensen (1984) lists additional characteristics of the WP-3D instrumentation and describes data processing techniques. Marks (1985) discusses the accuracy of WP-3D rain rates.

3. RESULTS

The SSM/I's polar orbit and limited swath width result in data-void areas between adjacent swaths at low latitudes. Table 1 shows the probability of SSM/I overpasses at 20°N as a function of time for one imager. The first observation of a tropical cyclone center may not occur for more than 48 h. In fact, it is possible for a tropical cyclone to progress through its entire life cycle without being observed by the imager. It is further noted that SSM/I observations from a single imager are too infrequent to resolve temporal variations in tropical cyclone structure, strength and motion over periods less than 12 to 24 h.

The SSM/I's swath intercepted Hurricane Gilbert at about 0050 UTC 16 September. Figures 1 and 2 show the SSM/I fields of rain rate and wind speed, respectively, for that overpass. Although the western edge of the swath is not displayed, the figures show the large area observed. Upon closer inspection, the data sampling interval (25 km) for these fields can also be seen.

The algorithms used to create Figs. 1 and 2 apply only over the ocean. Three problems with the data were detected. First, the black, arched bands extending across the images denote missing data. This form of data loss occurs a few percent of the time. Second, the long narrow bands of constant

TABLE 1

SSM/I overpass probabilities near 20°N.

Overpasses	Probability (%)			
≥ 4	0	0	0	30
≥ 3	0	0	35	45
≥ 2	0	45	55	55
≥ 1	50	60	75	70
0	50	40	25	25
Period (h)	12	24	36	48

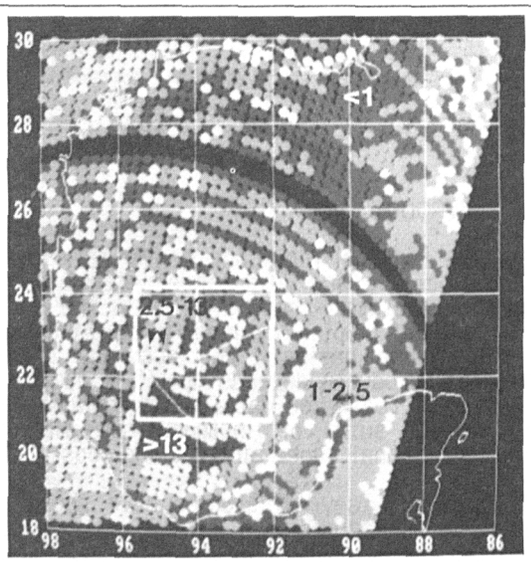

Fig. 1. SSM/I precipitation pattern at about 0050 UTC 16 September 1988. Rain rates (mm/h) shown by pixels shaded dark gray (≥ 13), light gray (1 to < 2.5), gray (< 1) and black (no data). Other shading for 2.5 to 13 mm/h. White box and enclosed contour indicate area of quantitative evaluation and WP-3D flight track, respectively.

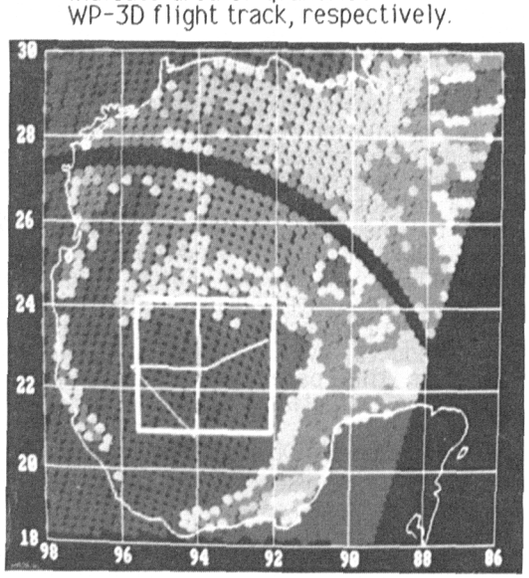

Fig. 2. As in Fig. 1, except for wind speeds (kt) denoted by dark gray (> 50), white (> 40 to 50), gray (> 30 to 40) and light gray (> 20 to 30).

(non-zero) rain rate aligned parallel to the missing data in Fig. 1 probably result from calibration or measurement errors.

The colocation of the broad area of high wind speed (Fig. 2) and rain (more clearly identified in color images of Fig. 1) is an example of the third problem. The correspondence occurs because, at the frequencies used by the SSM/I, rain obscures the wind speed signal from sea-surface emission, and contributes a signal that is incorrectly interpreted as a wind speed. (This artifact should not be confused with the physically realistic rainband-scale relationships between rain and wind in hurricanes [e.g., Parrish *et al.*, 1982].) In effect, where it is raining, the map of wind speeds should be interpreted as an uncalibrated depiction of rain. This critical limitation, combined with the coarse resolution of data, prevents an accurate SSM/I representation of wind speed in the inner core of tropical cyclones.

Quantitative comparisons between the SSM/I and WP-3D were made for the boxed region shown in Figs. 1 and 2. Figure 3 shows a close-up view of SSM/I rain rates there. Rain rates range generally from 5 to 15 mm/h. It is difficult to identify with confidence mesoscale features such as an eyewall or spiral band.

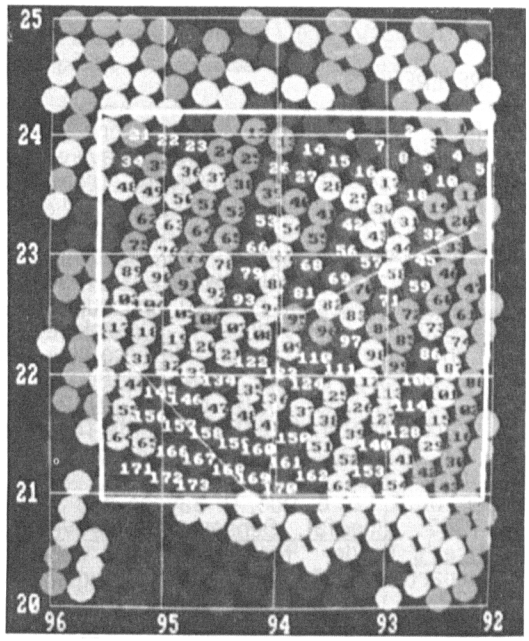

Fig. 3. As in Fig. 1, except for close-up view of boxed region. Pixels used in the comparison with WP-3D radar reflectivity data are numbered from 1 to 173.

Figure 4 shows a low-level Plan Position Indicator (PPI) of rain rates derived from 1.5 km x 1.5 km resolution WP-3D radar reflectivity data over the boxed region in Fig. 3. Most of the area is rain free, but Gilbert's eyewall can be seen near the center of the figure. A broken inner eyewall and a broad outer rainband can also be seen in the PPI. Rain rates range mostly from 4 to 8 mm/h there.

The center of a radar bin was defined at the center of each numbered SSM/I pixel in Fig. 3. Radar data within a 14.1 km radius of these centers were averaged together to obtain a PPI (Fig. 5) of degraded horizontal resolution (14.1 km was the radius used by the NRL in their derivation of the rain rate algorithm). Figure 6 shows a plot of the SSM/I rainfall as a function of the degraded resolution WP-3D rain rates. Figure 6 shows that the SSM/I algorithm significantly overestimated the area and rate of precipitation.

Even if the accuracy of the SSM/I rain rate algorithm can be improved, the utility of the product will always be limited by the coarse spatial

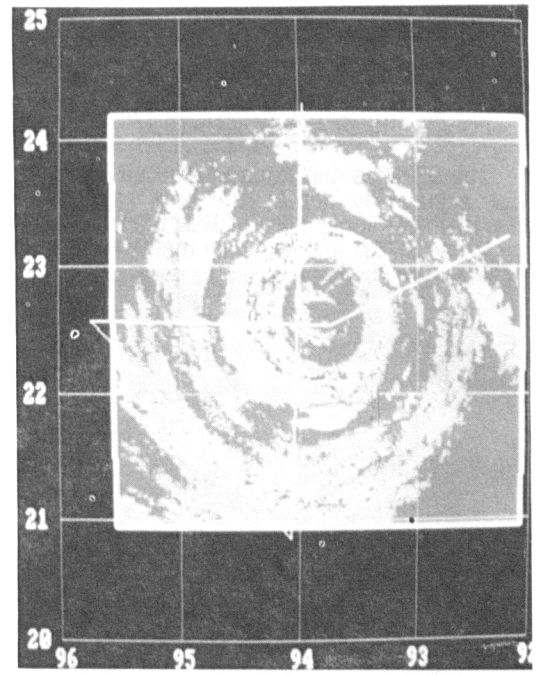

Fig. 4. Composite analysis of WP-3D lower fuselage radar reflectivity data from 0020 to 0245 UTC 16 September 1988, for the boxed region shown in Figs. 1-3. Rain rates (mm/h) denoted by gray (< 2.5), white (2.5 to 9) and dark gray (> 9). Horizontal resolution of data is 1.5 km x 1.5 km. Thin white contour indicates WP-3D flight track.

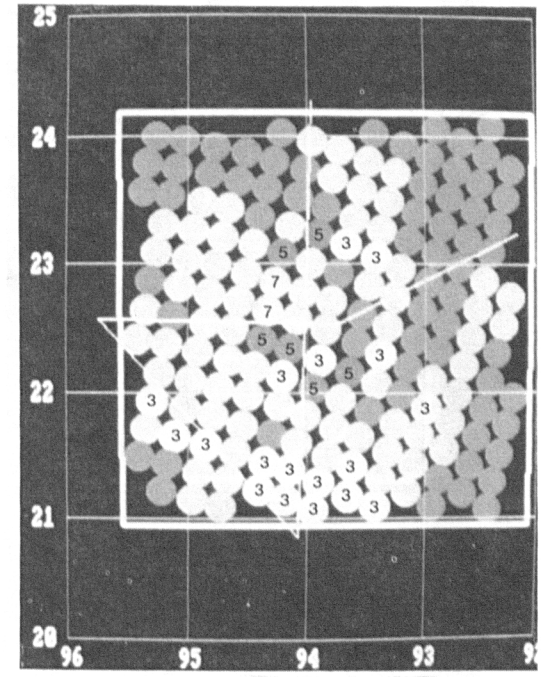

Fig. 5. As in Fig. 4, except for a horizontal resolution of 14.1 km and numbers show approximate rain rates in mm/h for all pixels with rates exceeding 2.5 mm/h.

resolution of the sensors. The degraded PPI (Fig. 5) essentially represents the best possible SSM/I rain rate display.

The SSM/I's poor resolution and the contamination by rain obscure details of Gilbert's inner wind field (Fig. 7). SSM/I indicated speeds ≥ 50 kt over most of the analysis area. The aircraft found from < 5 kt to 97 kt there. Also, the SSM/I has a maximum distinguishable wind speed of 50 kt. This is too low to resolve winds of hurricane force (≥ 64 kt).

4. CONCLUSIONS AND DISCUSSION

The SSM/I algorithms evaluated in this study did not accurately depict the rain rate and wind speed within the inner core of Hurricane Gilbert.

Other SSM/I applications merit further study.

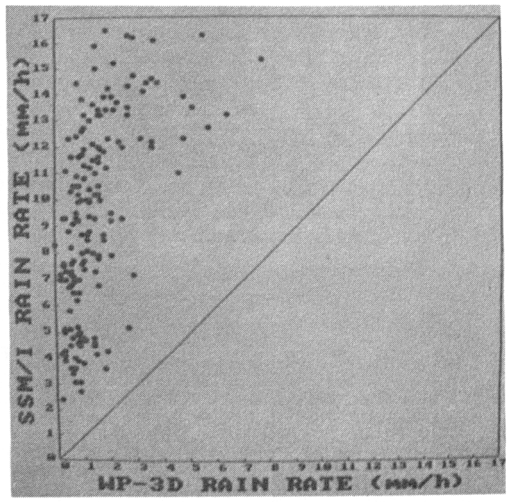

Fig. 6. Plot of SSM/I rain rate as a function of WP-3D lower fuselage rain rate for pixels enclosed by boxes in Figs. 3 and 5.

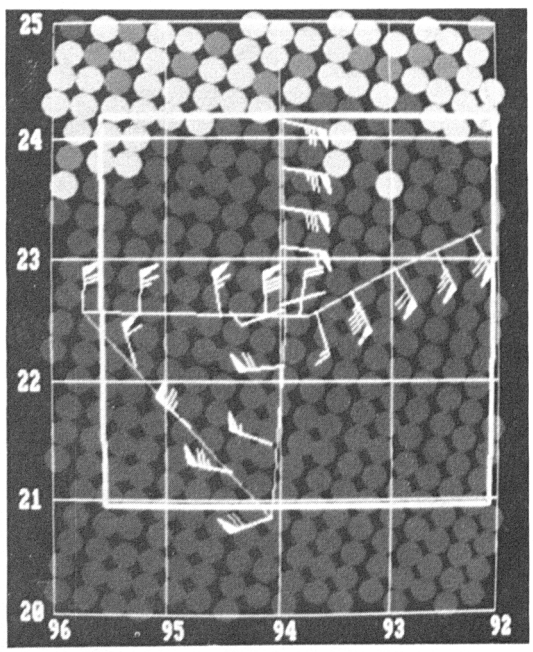

Fig. 7. Wind speeds (kt) near Hurricane Gilbert at about 0050 UTC. SSM/I winds denoted by dark gray (> 50), white (> 40 to 50) and gray (> 30 to 40) pixels. Wind barbs for WP-3D data with flag for 50 kt, barb for 10 kt, half barb for 5 kt and solitary mast for 3 kt.

New rain rate algorithms should emphasize 85.5 GHz data. These fields have a high spatial resolution (see Velden *et al*, this Proceedings) and, for Gilbert, resembled the pattern of WP-3D radar reflectivities. The accuracy of wind speed retrievals away from rain needs to be evaluated and a follow-up field program to test the accuracy of SSM/I wind speeds in the outer regions of tropical cyclones (e.g., near the 30 kt wind radius) is recommended.

Some of SSM/I's limitations may be overcome by other remote sensing microwave instruments (e.g., the Stepped-Frequency Microwave Radiometer [SFMR] on the WP-3D [Black and Swift, 1984]). Despite the SSM/I's deficiencies, advances in the application of microwave frequency technology continue to hold promise for the real-time analysis of tropical cyclones.

ACKNOWLEDGMENTS

Dr. Frank D. Marks, Jr. made important contributions to the design and execution of the field program and directed preliminary processing of the WP-3D radar data. Dr. Robert C. Sheets, HRD scientists and OAO and CARCAH personnel helped make the SSM/I field program successful. Mr. Mark A. Goodberlet and Dr. William S. Olson made available the SSM/I coefficients.

REFERENCES

Black, P. G., R. C. Gentry, V. J. Cardone, and J. D. Hawkins, 1985: Seasat microwave wind and rain observations in severe tropical and midlatitude marine storms. *Adv. in Geophys.*, **27**, 197-277.

Black, P. G., and C. T. Swift, 1984: Airborne stepped frequency microwave radiometer measurements of rainfall and surface wind speed in hurricanes. Preprints, 22nd Conference on Radar Meteorology, Amer. Meteor. Soc., Boston, pp. 433-438.

Hawkins, J. D., and P. G. Black, 1982: Seasat scatterometer detection of gale force winds near tropical cyclones. *J. Geophys. Res.*, **88**, 1674-1682.

Hollinger, J., R. Lo, G. Poe, R. Savage and J. Pierce, 1987: Special Sensor Microwave/Imager User's Guide. Naval Research Laboratory, Department of the Navy, Washingtion D. C., 177 pp.

Jorgensen, D. P., 1984: Mesoscale and convective-scale characteristics of mature hurricanes. Part I: General observations by research aircraft. *J. Atmos. Sci.*, **41**, 1268-1285.

_____, and P. T. Willis, 1982: A Z-R relationship for hurricanes. *J. Appl. Meteor.*, **21**, 356-366.

Marks, F. D., Jr., 1985: Evolution and structure of precipitation in Hurricane Allen (1980). *Mon. Wea. Rev.*, **113**, 909-930.

Parrish, J. R., R. W. Burpee, F. D. Marks, Jr., and R. Grebe, 1982: Rainfall patterns observed by digitized radar during the landfall of Hurricane Frederic (1979). *Mon. Wea. Rev.*, **110**, 1933-1944.

Powell, M. D., 1980: Evaluations of diagnostic marine boundary layer models applied to hurricanes. *Mon. Wea. Rev.*, **108**, 757-766.

Willoughby, H. E., and M. B. Chelmow, 1982: Objective determination of hurricane tracks from aircraft observations. *Mon. Wea. Rev.*, **110**, 1298-1305.

IMPROVING OBJECTIVE SATELLITE ESTIMATES OF TROPICAL CYCLONE INTENSITY

Raymond M. Zehr

Regional and Mesoscale Meteorology Branch, NOAA/NESDIS
Cooperative Institute for Research in the Atmosphere (CIRA)
Colorado State University, Fort Collins, CO 80523

1. INTRODUCTION

Satellite images have been used to track tropical cyclones and also to estimate their intensity. In recent years, with the availability of digital satellite data and computer technology, objective estimates of current intensity are possible. This paper reports on improvements and adjustments to the approach given by Dvorak (1984) and proposes an alternate technique. Both computations use infrared pixel brightness temperatures.

2. NW PACIFIC TYPHOONS — DVORAK METHOD

The algorithm developed by Dvorak (1984) extracts two temperatures from the IR data and relates them to current intensity (Fig. 1). A 55 km (30 n mi) circle centered on the eye is used to find the surrounding temperature. Intensity increases as the surrounding temperature decreases. The warmest IR pixel in the eye is the other temperature, and intensity increases as eye temperature increases. Dvorak expresses intensity in terms of an index or T-no. corresponding to typical daily intensity changes. T-no. can be converted to maximum sustained wind speed and minimum sea-level pressure (MSLP).

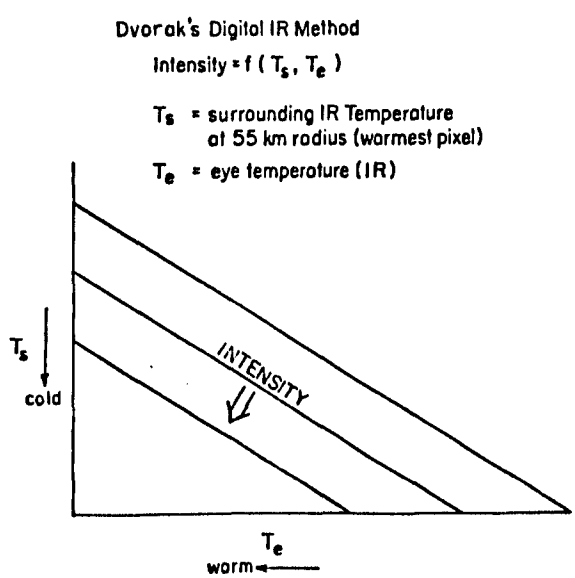

Fig. 1. Dvorak algorithm to estimate hurricane intensity from digital IR satellite data.

Dvorak's digital IR technique was developed with Atlantic hurricanes and GOES IR digital data. Three-hourly, 10-km resolution IR data from the GMS (140 deg E long.) have been available since July, 1983. Ten typhoons from 1983-1984 were used to test Dvorak's algorithm with the GMS data for NW Pacific cases. Those results led to some improvements and adjustments to Dvorak's original table, and the following results have incorporated those changes.

Figure 2 shows the satellite estimates of MSLP for Typhoon Marge (1983) compared with the aircraft MSLP observations. Note that the 3-h values (Fig. 2a) are quite noisy and show unrepresentative short-term changes. Therefore, time-averaging of the satellite MSLP estimates is desirable. Figure 2b has plots of satellite MSLP with the current value averaged with the 7 previous time periods (24-h running mean). Note that the 24-h time averaged satellite estimates correlate best with aircraft observations. This was generally true for all ten typhoons, however in some portions of the life cycle with some cases, a shorter averaging period related better to aircraft MSLP. The fact that a 24-h running mean of satellite MSLP estimates relates better to current intensity implies that the satellite estimates of intensity changes precede the aircraft measured MSLP changes. However, Fig. 2a shows there is little or no lead time from the satellite intensity estimates to predict the period of rapid deepening. Therefore, this computational approach should be regarded as a nowcast tool, which has little or no predictive capability other than extrapolation. Additional research is needed to refine this methodology to average the satellite computations over time to obtain the best correlation with current aircraft observations of intensity.

Of the ten typhoons, a qualitative evaluation of the algorithm performance given by plots as shown in Fig. 2, resulted in seven good cases, one poor case, and two marginal evaluations. Additional research is needed to try to recognize those very few typhoons where the satellite intensity estimates may be unreliable.

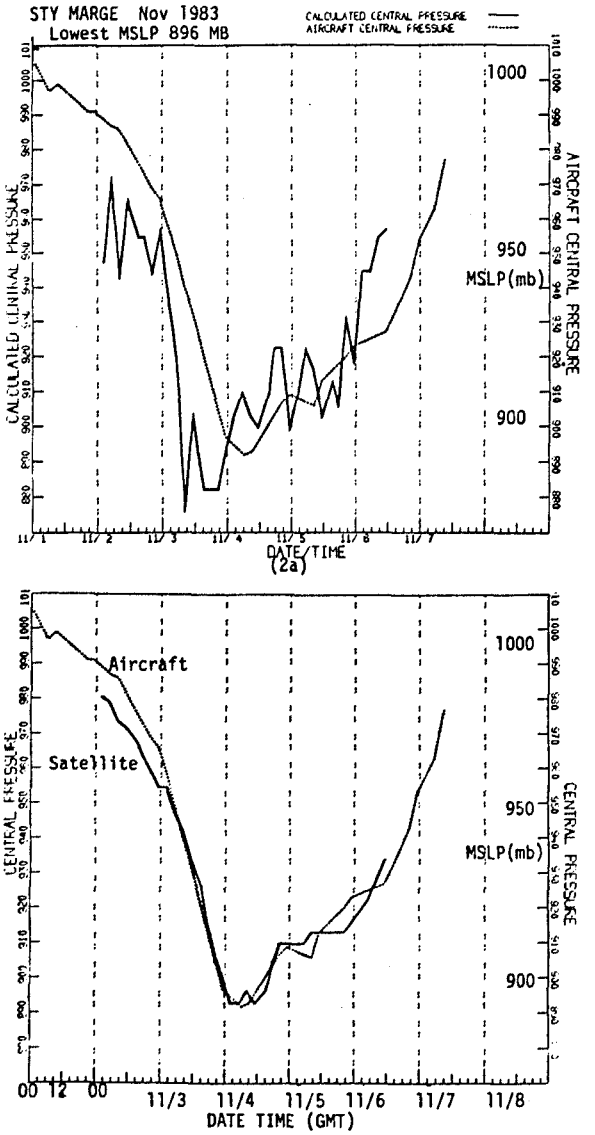

Fig. 2. Typhoon Marge (1983) Dvorak digital IR method satellite estimates of MSLP and aircraft observations of MSLP. a. 3-h interval satellite estimates. b. 24-h running mean of satellite estimates.

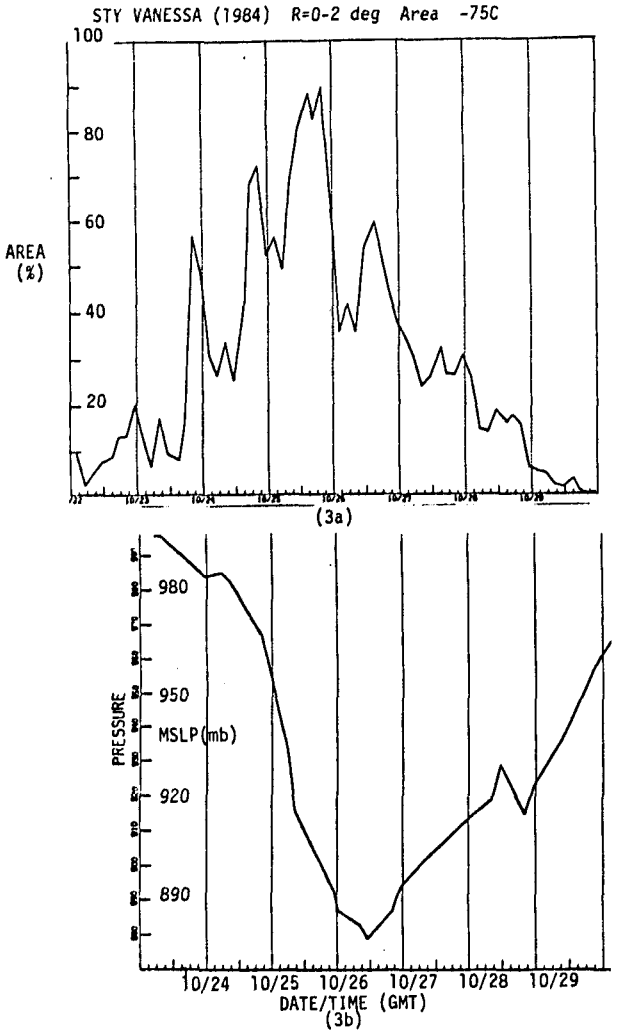

Fig. 3. Typhoon Vanessa (1984). a. Area with IR temperature less than -75 degrees C for radius 0-2 degrees lat. from center. b. MSLP.

3. AN ALTERNATE APPROACH

An objective approach different from that of Dvorak (1984) was developed in which there appears to be a direct relationship between cold IR cloud areas within two degrees latitude of the typhoon center and intensity CHANGE. Figure 3 illustrates this with a time series plot of area colder than -75C for Typhoon Vanessa (Fig. 3a) and aircraft observations of MSLP on the same time scale (Fig. 3b). Note that the time when convection (as measured by the R=0-2 deg IR area colder than -75C) is greatest corresponds to the time when MSLP is decreasing most rapidly. Thus, this objective computation corresponds in time to rate of intensity change as opposed to current intensity using the digital IR Dvorak algorithm. Note the diurnal variation of the cold IR areas in Fig. 3a (Zehr, 1987). Figure 4 illustrates how computations of this type might be related to intensity change after compensation for the diurnal variation (e.g. a 24-h running mean). Additional research is needed to refine a technique based on this concept which might then be used to complement or be combined with the Dvorak algorithm. This approach offers some short-term predictive capability since it provides an estimate of intensity change rather than current intensity.

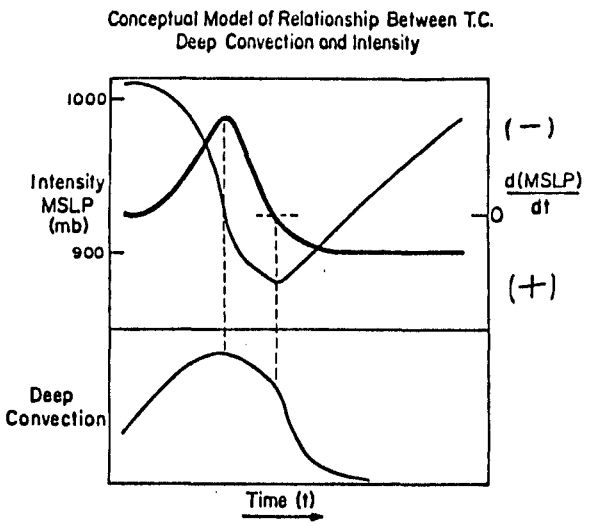

Fig. 4. Relationship between IR-defined cold cloud areas and tropical cyclone intensity change.

4. ADDITIONAL IMPROVEMENTS TO THE DVORAK ALGORITHM

As previously mentioned, the short term variability of Dvorak's digital IR computation is a significant drawback to obtaining reliable satellite estimates of current intensity. For example, hourly values of Dvorak's digital IR T-No. along with MSLP observations for Hurricane Gilbert are plotted in Fig. 5. A time-averaging routine is needed to give consistency to the satellite estimates of current intensity.

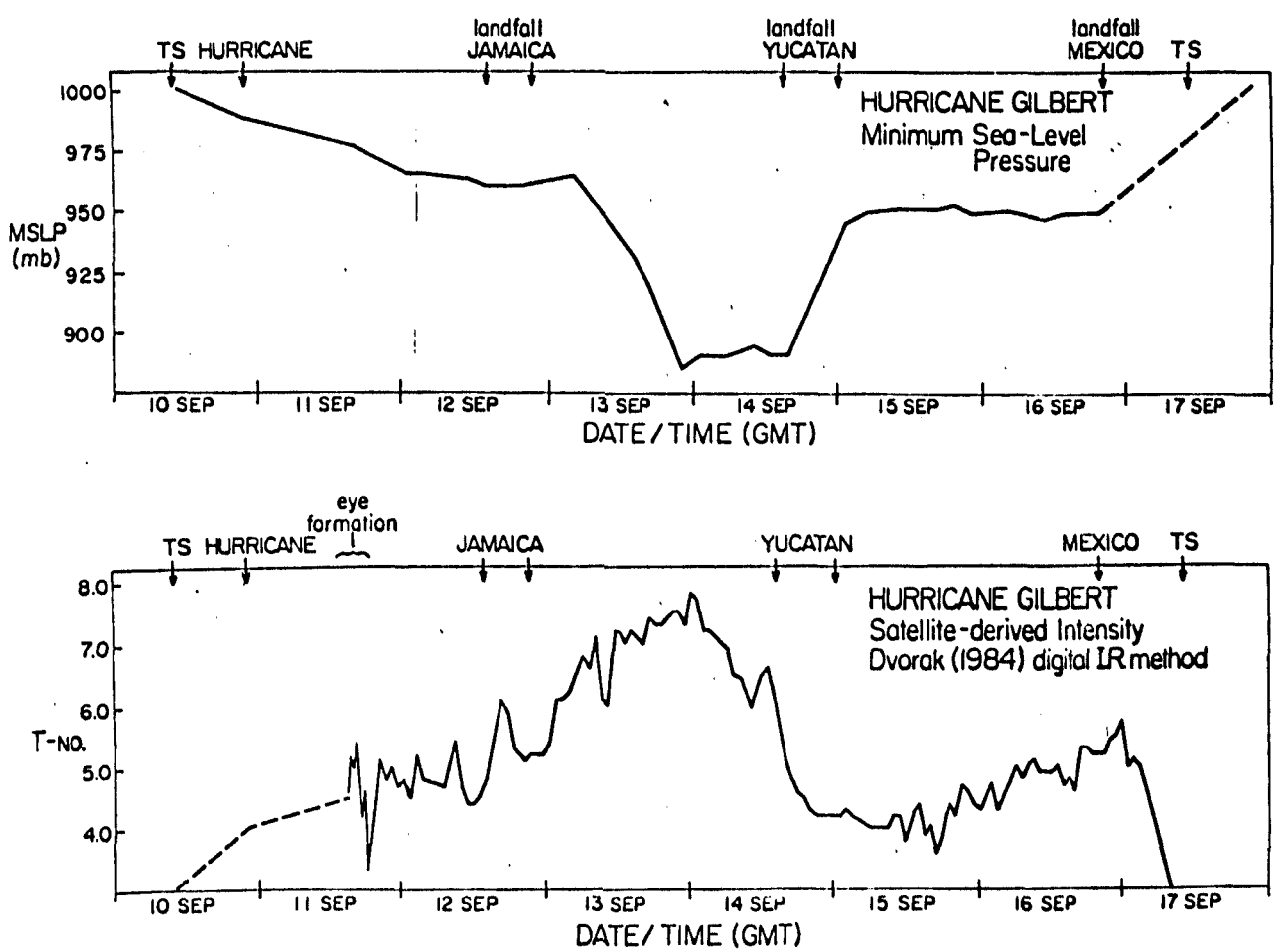

Fig. 5. Hourly digital IR T-no. computations and aircraft observations of MSLP for Hurricane Gilbert.

Preliminary results have shown that a multi-radius computation following the Dvorak approach may also help remove some of the short-term variability. The computation of "surrounding temperature" is done at various radii for circles both smaller and larger than the Dvorak-prescribed 55-km radius circle. The maximum resultant intensity estimate might then be used to indicate current intensity. Preliminary indications are that a tropical cyclone which has a maximum intensity as given by the Dvorak algorithm on a circle of relatively large radius, has a large potential for further deepening. Testing of the multi-radius computations and their capability for diagnosing intensity and structure of NW Pacific typhoons is underway. Additional information on eye size and shape can be estimated by both aircraft and satellite. Those data may eventually be introduced to the computations following some of the relationships found by Weatherford (1987) relating eye size and tropical cyclone structure.

5. ACKNOWLEDGEMENTS

Portions of this research were supported by NOAA Grant NA-85-RAH-0545. The author has benefited from discussions with Prof. William M. Gray, CSU, and a number of his project members.

6. REFERENCES

Dvorak, V.F., 1984: Tropical cyclone intensity analysis using satellite data. NOAA Tech. Report NESDIS-11, 47 pp.

Weatherford, C.L., 1987: Typhoon structural evolution. Dept. of Atmos. Sci. Ph. D. Dissertation, Colo. State Univ., Fort Collins, CO, 198 pp.

Zehr, R.M., 1987: The diurnal variation of deep convective clouds and cirrus with tropical cyclones. Preprints, 17th Conf. on Hurricanes and Tropical Meteorology, AMS, April 7-10, Miami, FL.

J5.1

TECHNIQUES DEVELOPMENT PROGRAM AT THE JOINT TYPHOON WARNING CENTER

Joel D. Martin

Detachment 1, 1st Weather Wing (MAC)
Nimitz Hill, Guam

1. INTRODUCTION

In June 1988 Air Weather Service established a techniques development cell of two people - one officer and one noncommissioned officer - at Detachment 1, 1st Weather Wing (Det 1), Nimitz Hill, Guam. The position supports both the tropical cyclone satellite reconnaissance mission of Det 1 and the warning agency role of the Joint Typhoon Warning Center (JTWC). The author serves as the Techniques Development Officer and this paper is a report on development actions underway at JTWC and Det 1.

2. ROLE OF TECHNIQUES DEVELOPMENT

JTWC and Det 1 have neither the responsibility nor the resources to carry out academic-style tropical cyclone research. A close liaison between the research community, who can complete detailed studies, and Det 1/JTWC, who can identify requirements and apply research results is required. Two recent examples illustrate how the techniques development position can work to benefit both operational and research interests.

Dr. Greg Holland recently visited JTWC as part of an Office of Naval Research (ONR) staff role. Using his published research (Holland 1980) and other notes, we were able to develop a diagnostic technique that improves our tropical cyclone wind-radii estimates. Dr. Holland concluded his visit with a two-hour seminar on selected tropical cyclone topics for members of JTWC and Det 1.

Similarly, Dr. Mark Lander visited from the University of Hawaii, also as part of an ONR-sponsored project. He developed an "in-house" micro-computer version of the Colorado State University Model (CSUM) (Matsumoto 1984) that, for the first time, gives JTWC forecasters a way to run local "what-if" scenarios with an operational model. His work also verified problems with CSUM statistical coefficients in the Indian Ocean—corrective action would have been missing without his expertise. We also adapted his streamline analysis techniques for our warning center's training program.

Both cases show how research knowledge can be used to assist Det 1 and JTWC. But the relationship works two ways. Both researchers gained valuable insight into our operational needs which, in turn, focuses their organizations' research efforts. These scientists also obtained the latest information on data archives available here as well as specific recent case studies of particular research interest. In addition, they coordinated JTWC and Det 1 support for the proposed 1990 tropical cyclone motion experiment.

3. PROGRAM ORGANIZATION

3.1 Personnel

The Techniques Development Officer is a full-time atmospheric science master's degree position. The officer draws part-time help from the pool of satellite analysts and Typhoon Duty Officers (TDO) at JTWC.

3.2 Resources

At present, microcomputers provide graphical and numerical processing of data and access to more powerful computers such as those at the Fleet Numerical Oceanography Center(FNOC), Monterey, Ca., and via the Defense Data Network (DDN). A Zenith Z-248 microcomputer allows use of the Navy's Automated Tropical Cyclone Forecasting (ATCF) system. Through the ATCF system, the Techniques Development Officer can access real-time and archived tropical cyclone data sets. That information can then be used in the process of developing and evaluating new techniques. A Navy Apple Macintosh SE microcomputer allows a link to satellite imagery stored on larger in-house computers. Once transferred to the Macintosh, a variety of enhancements can be applied to images. High quality graphic analyses are produced on a connected LaserWriter. Necessarily, these systems allow parallel development of techniques without disrupting the operational work routine.

Since research must be pulled in for techniques development, JTWC must maintain a research library of technical reference material applicable to the operational mission. The JTWC library was recently reorganized and located with the techniques development function to meet those needs. The library should also serve as an excellent workplace for visiting researchers who need archived data and consolidated tropical cyclone reference literature.

3.3 Future

Both geostationary and polar-orbiter satellite imagery can be exploited for operational techniques. The Air Weather Service is presently selecting a sophisticated satellite imagery processing system for Det 1. Using a mini- or super-microcomputer, multiple graphics planes, high-resolution displays, and large capacity storage, the techniques development shop will be able to do more detailed examination of potential techniques. This capability would give a significant boost to efforts that translate research results into operational tools.

4. DIAGNOSTIC TECHNIQUES

Techniques development efforts are generally separated into two areas: diagnostics and forecasting.

Diagnostic techniques focus on removing as much uncertainty as possible about the location, motion, intensity, structure, and synoptic environment of a tropical cyclone *before* a forecast is generated. Better diagnosis of initial conditions is assumed to produce better forecasts—depending on how the better diagnostic knowledge is translated into forecast results.

Diagnostic techniques are also important in setting a standard for forecast error computations. After-the-fact analysis of all data regarding a tropical cyclone yields a post-analysis best-track. Thus, as diagnostic techniques improve, the best-track improves, which also improves the forecast error calculations.

4.1 Position/Motion Diagnostics

Center fixes are accomplished primarily from satellite imagery by Det 1 analysts and a network of polar-orbiter imagery receiving sites. Center fixes are subjective, based on a set of patterns and rules. These fixes are used for a comprehensive working track of cyclone motion and intensity. Objective curve-fit schemes aid the final subjective working track determination.

Techniques have been explored to track the deep convection envelope as well as the routine center fix to see if a better conservative motion vector can be obtained. These techniques show some promise but arguably provide no more information than a more aggressive use of image animation to obtain a motion estimate.

Methods that will provide an objective and conservative motion vector from satellite imagery are needed. Improvements in working track formulation techniques are also a high priority.

4.2 Intensity Diagnostics

Currently a modified Dvorak (1984) scheme is employed to infer a tropical cyclone's intensity. Six-hour updates on intensity and intensity trends are provided to the TDO. The technique appears quite consistent, but prone to occasional large errors. Ground truth estimates by direct aircraft measurements are no longer available and synoptic measurements are scarce.

Det 1 and JTWC do not have the tools in place to objectively analyze satellite data as done in the latest research. Techniques development and subsequent operational advances in this area will likely await new satellite processing tools.

4.3 Structure Diagnostics

Satellite imagery provides our only consistent inference of tropical cyclone structure and structural change. Image looping, or animation, is not available to us in a center-relative mode. That center-relative tool is preferred by many tropical cyclone satellite researchers for structural change studies.

New color enhancement tables, adapted from several researchers, have been added to our image processing systems. These color enhancements make trends in deep convection easier to observe.

A diagnostic scheme was developed by G. Holland and J. Martin (1988) to aid in establishing critical wind-radii parameters. The technique uses cyclone size parameters inferred from enhanced infrared convection signatures and current intensity estimates. Operational and research verification have yielded promising results to date.

4.4 Synoptic Environment Diagnostics

Both 00 UTC and 12 UTC gradient- and 200 hPa-level analyses of streamlines and isotachs comprise the primary local analysis tools. Analysis charts for all standard levels and NOGAPS model initialization are provided by FNOC. National Meteorological Center (NMC) and Air Force Global Weather Central(AFGWC) analysis products are also received via a facsimile circuit.

Recent work has centered on synthesizing more of the large volume of information available to the forecaster. A "back to basics" approach using more composite and trend charts, such as the Hovmöller trough-and-ridge diagram (Hovmöller 1949), have been tested.

Work is continuing to better consolidate forecast information. New techniques are needed in this area.

5. FORECAST TECHNIQUES

The second area for techniques development is the forecast process. The 48- and 72-hour forecasts are critical for the JTWC's customers. Consequently, techniques development has focused on improving forecasters' basic meteorological skills and available tools that are necessary for improvements in that extended range. Forecasts in the 12- and 24- hour range are important as well, dependent on the size and speed of movement of a particular storm. The point we want to make is that some may be more critical to JTWC's customers than others.

5.1 Track Forecasts

A track forecast is produced by first updating the working track of a tropical cyclone's motion. The updated information is submitted into the forecast aids package that is processed by FNOC. The forecaster looks at the returned aids results (dynamic, statistical, climatological, analog) and subjectively determines a track forecast based on an evaluation of the forecast situation with regard to typical aids' performance and personal experience.

Capt John D. Pickle, a TDO at JTWC, has worked several areas for track forecast technique improvement. His work is two-fold. First he looks to statistically screen objective aid performance based on the synoptic situation. A second area he's exploring is use of composite rawinsonde information to provide statistical aids in track forecasting. Both approaches may give forecasters better awareness of their forecast situation and an increased probability of selecting the best forecast tools for the situation.

Tropical cyclone motion forecasting is a tough problem. Not only the average track forecast error, but the chance for the large single forecast error need to be minimized. Consistent objective aids are needed. Statistical aids at present appear to offer great opportunity for advances. Sparse synoptic data in the JTWC area of responsibility may make numerical model improvements more difficult. Optimization of existing forecast aids is also a high priority. Updates to our current aids as well as updates to our analog (forecast) data bases are also needed.

5.2 Intensity Forecasts

Our only available tool for the intensity forecast is the Dvorak (1984) pattern matching scheme. Current image processing tools preclude application of objective deep convection analysis. Some researchers indicate forecast signals may be present from trends in the deep convection.

Better image processing hardware and software combinations are needed at Det 1 and JTWC to exploit some of the latest research results. A design and specification study for procurring this capability is currently underway, and rapid progress should be noted once such tools are available.

5.3 Structure Forecasts

Wind-radii diagnostic tools are applied by the forecaster to a subjective forecast of intensity and size for the cyclone. To date, JTWC has demonstrated minimal skill over persistence in this forecast area. Forecasts of abrupt cyclone structural changes, such as changing vertical shear conditions, also have been a problem.

Research in this area by Candis Weatherford and others at Colorado State University is promising. As new tools are made available to Det 1 and JTWC, more of the physics of cyclone structural change may be observed and understood.

5.4 Synoptic Environment Forecasts

The Navy Operational Global Atmospheric Prediction System (NOGAPS) numerical forecast package from the FNOC is the primary tool of the TDO at JTWC. AFGWC, NMC, and European Center for Medium-Range Weather Forecast (ECMWF) products are also generally available in varying orders of timeliness and display utility. Objective aids are processed from NOGAPS field information at FNOC.

More work is needed in studying synoptic scale interaction with tropical cyclones. Pattern recognition of the synoptic environment centered on improved analog forecast aids is an important objective.

6. CONCLUSION

Det 1 and JTWC are evolving rapidly from grease-pencil plots and reliance on aircraft reconnaissance reports to satellite imagery and computer integrated workstations. The evolution has caused rethinking in every area of the operation. As a consequence, techniques development has been elevated as a management function that must lead the way in the technology revolution.

It's an exciting time that requires a special bond between researchers and forecasters to tackle the tough challenges. Clearly it's an opportune time for the more formalized techniques development program at Det 1 and JTWC.

NOTES

More information regarding Det 1 and JTWC operations may be found in the current issue of JTWC's Annual Tropical Cyclone Report.

This paper was intended as a general survey, and guide to researchers, of techniques development at JTWC and Det 1. If you have more specific information needs please write:

Techniques Development Officer
Detachment 1, 1st Weather Wing
COMNAVMAR Box 20
FPO San Francisco 96630

REFERENCES

Dvorak, V.F., 1984: Tropical Cyclone Intensity Analysis Using Satellite Data. NOAA Technical Memorandum NESDIS 11, US Dept. of Commerce, Washington DC, 47 pp.

Holland, G., 1980: An Analytical Model of the Wind and Pressure Profiles. *Monthly Weather Review*, 108, 1212-1218.

Holland, G. and Martin, J., 1988: Wind-Radii Profiler and Beta Motion Tool. Documentation available from: Techniques Development Officer, Det 1, 1 WW (MAC), FPO San Francisco 96630-1066.

Hovmöller, E., 1949: The Trough-and-Ridge Diagram. *Tellus*, 1, 62-66.

Matsumoto, C., 1984: A Statistical Method for One- to Three-Day Tropical Cyclone Track Prediction. Dept. of Atmos. Sci. Paper No. 379, Colo. State Univ. Fort Collins, CO, 201 pp.

J5.2 FORECASTING TYPHOONS WITHOUT AIRCRAFT RECONNAISSANCE AT THE JOINT TYPHOON WARNING CENTER

Daniel McMorrow, Lt Col, USAF

Joint Typhoon Warning Center
Det 1, First Weather Wing
Nimitz Hill, Guam

1. Introduction

The Joint Typhoon Warning Center (JTWC) was established by the United States Pacific Command in 1959 to protect Department of Defense (DOD) forces operating in the western Pacific from the damaging and potentially crippling effects of tropical cyclones. Over the last thirty years the area of forecast responsibility for JTWC has been expanded to include the Indian Ocean, the Arabian Sea, and the entire Southern Hemisphere from the dateline westward to the African coast. As a 24 hour-a-day forecast center, JTWC now issues warnings on about 60 tropical cyclones each year. Approximately 25% of the time, the center is issuing warnings on multiple cyclones. While the Center is chartered to provide forecast and warning support for the United States forces, many countries around the Pacific rim have come to rely upon the JTWC forecasts for the protection of their populations and resources.

Much of the forecast focus is in the western North Pacific because most DOD assets operate in that region. Traditionally, this has been a primary area for many of the the world's tropical cyclones (Gray, 1978) and the cyclones that do develop are generally larger and stronger than those found in other basins. This provides an ideal laboratory for studying tropical cyclones.

From 1945 to 1971 both the Navy and Air Force were actively involved in aircraft reconnaissance of tropical cyclones. While the emphasis was on accurate storm track forecasts to assist operational customers, much valuable

In 1986, the last full year of aircraft operations, the cost of aircraft reconnaissance had risen to $20 million a year or $80 thousand per fix mission. The Air Force decision to end the era of in-situ measurements generated considerable controversy. Many experts predicted large degradations in the accuracy of track forecasting and an increased risk to DOD forces operating in the Pacific. The speed with which the decision was implemented in 1987, placed an additional burden on JTWC to quickly convert its approach to the operational forecasting problem from a system that relied heavily on aircraft observations to one based on remotely sensed satellite data.

2. The Conversion Process

In the spring of 1987 there was still considerable disagreement among the scientific and operational communities on the impact of the loss of dedicated reconnaissance for the upcoming storm season which usually begins in June. The Naval Oceanography Command and the Air Weather Service agreed to conduct an operational evaluation to determine where the potential problems lay and to formulate ways to cope with the loss of the aircraft data. This "test", which consisted of two teams, one with aircraft data, and one without, was not designed to prove or disprove the need for aircraft reconnaissance, but rather to assist in the transition process. The participants were temporarily assigned to JTWC for only two months (15 June to 15 August). With the 1 Oct 87 deadline for deactivation of the WC-130 flying unit at Andersen Air Force Base, there was considerable pressure to remove the aircraft from Guam in early July. In the end, the last mission was flown on 14 August 87 by the one remaining aircraft. Eight tropical cyclones occurred during the test period.

The results of this evaluation contained many expected results, but also some surprises. The biggest surprise was the lack of a degradation in forecast track accuracy of the experimental team (no aircraft data) when their forecasts were compared against the operational JTWC best track. The experimental team was not able to

position storms as accurately as JTWC (initial position error of 42 km compared to 33 km) but the forecast accuracy of both teams at 24, 48 and 72 hours was approximately the same. Martin (1988) who compared forecast track errors based on no aircraft data within twelve hours of the warnings against forecasts made with recent aircraft data noted a similar result after investigating eight years of data for the NW Pacific basin. The experimental team did have larger standard deviations in its forecast. Post analyses showed that intensity estimates for the experimental team, based solely on Dvorak (1984) satellite interpretation techniques, were slightly better than those produced by the JTWC forecasters that had access to the aircraft data. While the summary numbers from this test led to considerable discussions on the need for aircraft reconnaissance to forecast tropical cyclones, at JTWC, the concern was focused on where did we error and how could we compensate.

A major discovery during the test was that the experimental team operated differently than the operational JTWC team. In JTWC, the satellite operations section was traditionally discouraged from interacting with the Typhoon Duty Officers (TDO), or track forecaster, for fear of biasing the independent satellite positions. The experimental team, however, maintained a constant dialog between the satellite analyst and the track forecaster. The 10 to 12 years forecasting experience of the satellite analyst often helped the TDO recognize changing synoptic conditions and this enabled the team to put out a superior track forecast. The TDO, in exchange, often noted subtle features in the satellite imagery that the mid-latitude trained satellite analyst expert had overlooked. This synergistic approach to the operational forecast problem evolved into the team forecasting system used at JTWC today.

Another important modification in the forecast process involved the modification of the empirical Dvorak intensity estimation technique from twice a day to four times a day based upon enhanced infra-red imagery. This adaptation allowed the satellite analyst to catch changes in the tropical cyclone intensity quickly.

Perhaps the most fundamental change was the realization that the key JTWC product for our customers was an accurate forecast of damaging winds within 48 hours. Rather than approach the forecast problem in our traditional way of time stepping the short range (observational intensive) forecasts into the future, JTWC shifted its focus into making accurate forecast of the synoptic situation at the 72 hour point and then backstepping the forecast to the present. This approach required longer range estimates of the typhoon intensity from the satellite analyst and a deeper understanding of the dynamics of the mid-latitude forcing by the TDO. Forecasts of shearing patterns, beta drift predictions, strengthening and timing of approaching troughs became techniques used to quantify not only the tropical cyclone but also the synoptic environment upstream of the cyclone. Early results of this approach are encouraging but problems still exist. Weak systems (30-40 kts) frequently are not driven by the synoptic patterns, and forecasting the tracks of weak systems remains a major problem.

3. NEW HARDWARE

Until 1988, JTWC warnings were computed by manual methods. The time required to build a typical warning was about 90 minutes. In the spring of 1988 JTWC converted the warning preparation onto the Automated Tropical Cyclone Forecasting (ATCF) system. This interactive graphics system was developed by Tsui and Miller at the Navy Environmental Prediction Research Facility (NEPRF) in Monterey, Ca. NEPRF worked closely with JTWC in bringing the ATCF system on-line and making software changes as required through a rapid prototyping approach. As a result, most of the typhoon warnings in 1988 were produced on the ATCF in about 15 minutes. It is difficult to evaluate the shift in the focus of the TDO from putting out error free messages to thinking more about the forecast; however, it appears the ATCF has significantly contributed to maintaining our skill in 1988, a very difficult forecasting year.

A second major upgrade at JTWC was the introduction of hourly digital geostationary satellite imagery. This enhancement was possible with the acquisition of the Navy Medium Data Utilization System Replacement program. This upgrade allowed JTWC to identify transitory features that were frequently lost in imagery received every three hours. An added benefit was the ability of the satellite analyst to more accurately monitor the tropical cyclone by examining trends in the imagery.

The third major improvement in the warning process was the installation of a low resolution animation capability of geostationary data by the Air Force. Animation of the tropical cyclone imagery proved very valuable in detecting changes in the tracks by precursive changes in the imagery. Animation has been especially useful in detecting the early signs of recurvature of the systems.

Another change in the operational capability at JTWC was the installation of the Air Force Pacific Digital Facsimile System. For the first time, JTWC had real time access to synoptic forecasts produced from spectral models at the Air Force Global Weather Center and the National Meteorological Center. This complemented the guidance routinely provided by the Fleet Numerical Oceanography Center at Monterey, Ca. This modest upgrade enabled the TDOs to blend their forecasts and frequently detect changes in the track faster than before.

4. Results

The conversion of JTWC's forecasting operation to a satellite based system was a logical evolution. Figure 1 shows the trend in aircraft fixes for NW Pacific Tropical Cyclones over the period from 1971 to 1987. Starting in 1977 less than 18 percent of the fixes were done by aircraft.

The 1987 typhoon season in the NW Pacific was a very typical year. Approximately half the tropical cyclones recurved, there were six super typhoons, six tropical storms, and the cyclone tracks were very similar to the 10 year mean conditions. There were some anomalies, such as the absence of systems induced by tropical upper-tropospheric troughs but the systems were well defined and they lasted on average seven days. It was a busy year for JTWC, with over 389 warnings that verified at 72 hours. The forecast track errors for the year are summarized in table 1. While aircraft data was available for the first third of the season, the overall track errors remained relatively low even after the aircraft was unavailable. Standard deviations in the track errors were nearly the same as the long term averages, and the initial position error (35 km) was also consistent with the long term mean.

The 1988 season was completely different from 1987 and one of the most anomolous on record. The season started late and ended early, yet there were two more storms than in 1987. The abnormal poleward position of the monsoonal trough spawned many tropical cyclones north of 20 N. These storms were very short-lived (less than three days), and seldom achieved the characteristics of the Pacific typhoons. Only one supertyphoon developed and thirteen systems never reached typhoon intensity. Accurate forecasting of cyclone tracks (Odessa) and translation speeds (Pat) were problems on several of these weakly defined systems. Only 183 forecasts verified at 72 hours, 47 percent of the 1987 total. Although 1988 was a difficult forecasting year, the mean track errors showed a slight improvement as compared to the long term means (see Table 1.)

TIME/YEARS	1979-86		1987		1988	
INITIAL POSITION	43* (630)	SD	33 (657)	SD	35 (465)	SD
24 HOURS	220 (523)	146	198 (563)	111	211 (373)	135
48 HOURS	442 (406)	283	377 (465)	205	400 (262)	266
72 HOURS	673 (304)	436	561 (389)	316	583 (183)	374

* 35 km BETWEEN 1982-1986

TABLE 1. MEAN FORECAST TRACK ERRORS (km) AND STANDARD DEVIATIONS (km) FOR NW PACIFIC TROPICAL CYCLONES. NUMBER OF CASES ARE IN PARENTHESIS

After two seasons of forecasting without aircraft reconnaissance, JTWC has learned a great deal. One of the most important lessons is that in the western North Pacific basin, aircraft data is not required to routinely make accurate operational forecasts. JTWC track forecasting is now at least as accurate as it was in the aircraft era. So far the initial position errors and the forecast variance have changed very little from the long term averages.

The satellite positioning and intensity estimation techniques currently used at JTWC work best for large intense typhoons, which are the critical forecast problems for most customers. JTWC still has difficulty in forecasting the tracks of weak tropical storms and much of the yearly forecast error is attributed to errors in these poorly defined systems. Deciding on the initial track of developing cyclones remains an area of concern.

Team forecasting has worked well at JTWC, as has the use of multiple data sources in developing the blended forecast. Automation of the warning process in 1988 has also had a significant impact on the procedures used to develop the forecast.

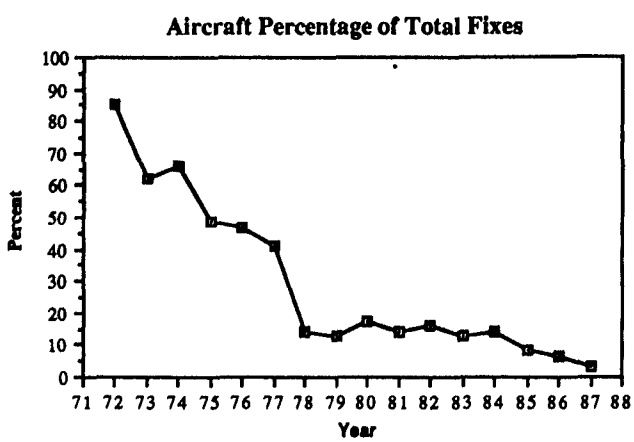

FIG 1. CHANGE IN PERCENT OF AIRCRAFT FIXES FOR NW PACIFIC TROPICAL CYCLONES

While the loss of dedicated aircraft reconnaissance data has had little impact on the operational role of JTWC, we remain concerned about the long term affects of the loss of ground truth for developing new forecasting techniques from satellite imagery. Verification of new techniques will have to be accomplished in other basins were tropical cyclones have different characteristics and the impetus to produce breakthrough techniques in remote sensing methods are not as pressing as they are in the Pacific.

5. Conclusions

JTWC has demonstrated an ability to make accurate operational forecasts without aircraft data for two diverse typhoon seasons. Forecasting techniques currently available have allowed JTWC to accurately forecast large intense typhoons. Forecast accuracy for weak tropical storms remains a problem.

References:

Dvorak, V.F., 1984: Tropical Cyclone Intensity Analysis Using Satellite Data. NOAA Tech Report NESDIS 11, U.S. Dept Of Commerce, NOAA, NESS, Wash. D.C., 46 pp

Gray, W.M., 1968: Global View of the Origin Of Tropical Distrubances and Storms, Mon. Wea. Rev. 10, 669-698

Martin, J.D., 1988: Tropical Cyclone Observation and Forecasting With and Without Aircraft Reconnaissance, Atmos Science Paper No 428, Dept of Atmos Science, Colorado State Univ., 114 pp

TROPICAL CYCLONE CENTER-FIXING USING DMSP SSM/I DATA

Christopher S. Velden, William S. Olson, Barry A. Roth

University of Wisconsin-Space Science and Engineering Center
Madison, Wisconsin

1. INTRODUCTION

With the loss of aircraft reconnaissance flights into typhoons in the NW Pacific, and the potential phasing out in the Atlantic, meteorological satellites will be heavily relied upon to provide accurate center fixes of tropical cyclones (TC's). In many cases, conventional visible and IR imagery can be used to get a relatively accurate position. These cases are usually characterized by storms with an eye, or an exposed low-level center.

There exists, however, a fairly large percentage of TC cases where center-fixing from conventional satellite imagery is limited, and in some cases can lead to large position errors. These cases are characterised by storms with an expansive central dense overcast and no apparent eye. This problem is especially prominant at night, when visible imagery is not available. This limitation has been noted for a long time, but has gotten considerable attention recently with the curtailment of the reconnaissance flights (Gray et al., 1989).

Recently, a new meteorological satellite data source has become available. The Special Sensor Microwave Imager (SSM/I) instrument aboard the polar-orbiting Defense Meteorological Satellite Program (DMSP) F8 satellite provides high resolution microwave imaging capability. A preliminary examination of this data reveals that information from this instrument can be used in certain cases to more accurately estimate TC center positions.

Statistics are presented comparing TC center fixes (estimates) from the SSM/I imagery with operational fixes from reconnaissance aircraft and conventional geostationary satellite imagery. The data set includes 20 cases from the 1988 North Atlantic TC season. The cases are stratified by whether or not an eye is apparent in the conventional IR imagery. The inherent subjectivity involved in center-fixing using this information is also examined. The statistics are discussed, and examples shown of some extreme cases where the SSM/I imagery could be very helpful in delineating TC structure, organization and center location. The operational availability, potential, and limitations are also addressed.

2. INSTRUMENT DESCRIPTION

The first SSM/I was launched in June, 1987. The data swath width is 1400 km, and results in near-global coverage over a 24 hour period. The SSM/I is a 7 channel, 4 frequency, linearly polarized passive microwave radiometric system. The four frequencies include 19.35, 22.23, 37.0 and 85.5 GHz (Hollinger et al., 1987). This data will be available in the near future to TC forecasting offices such as the National Hurricane Center (NHC) and the Joint Typhoon Warning Center (JTWC).

The SSM/I provides relatively high resolution imagery in the microwave frequencies which have the ability to penetrate clouds and provide a radar-like view of TC's. One practical application of this imagery is to locate and fix TC centers. The optimal SSM/I channel available to accomplish this is the horizontally-polarized 85.5 GHz band, which has a horizontal resolution of 12.5 km, and is sensitive to convective cloud and precipitation over oceanic regions. Scattering of the 85.5 GHz radiances by precipitation and ice hydrometeors associated with the TC results in depressed brightness temperatures. The high resolution and sensitivity of this channel provides an excellent depiction of the mesoscale precipitation patterns associated with tropical cyclones. Some examples are shown in Fig. 1.

3. DATA AVAILABILITY

The current SSM/I scenerio (one in orbit) provides nearly complete global coverage in a 24 hour period, except in tropical areas (Fig. 2). Unfortunately, the latitude where data gaps exist coincides with that of greatest TC activity. It is possible to get up to two passes per day over a geographical point on the earth. However, in tropical regimes, there will be times when there is no coverage. It is important to know the expected availability of the SSM/I data for center-fixing TC's in an operational environment. To get an estimate of this, SSM/I data were collected (via the Naval Research Laboratory) for selected 1988 North Atlantic TC's (Table 1). In this sample, there are a total of 22 storm days, resulting in 44 possible overpasses. It is found that 29 of the 44 possible overpasses actually covered the TC's, resulting in a coverage frequency of 67%. The TC's happened to fall in the data void areas in the remaining 15 cases. This translates into

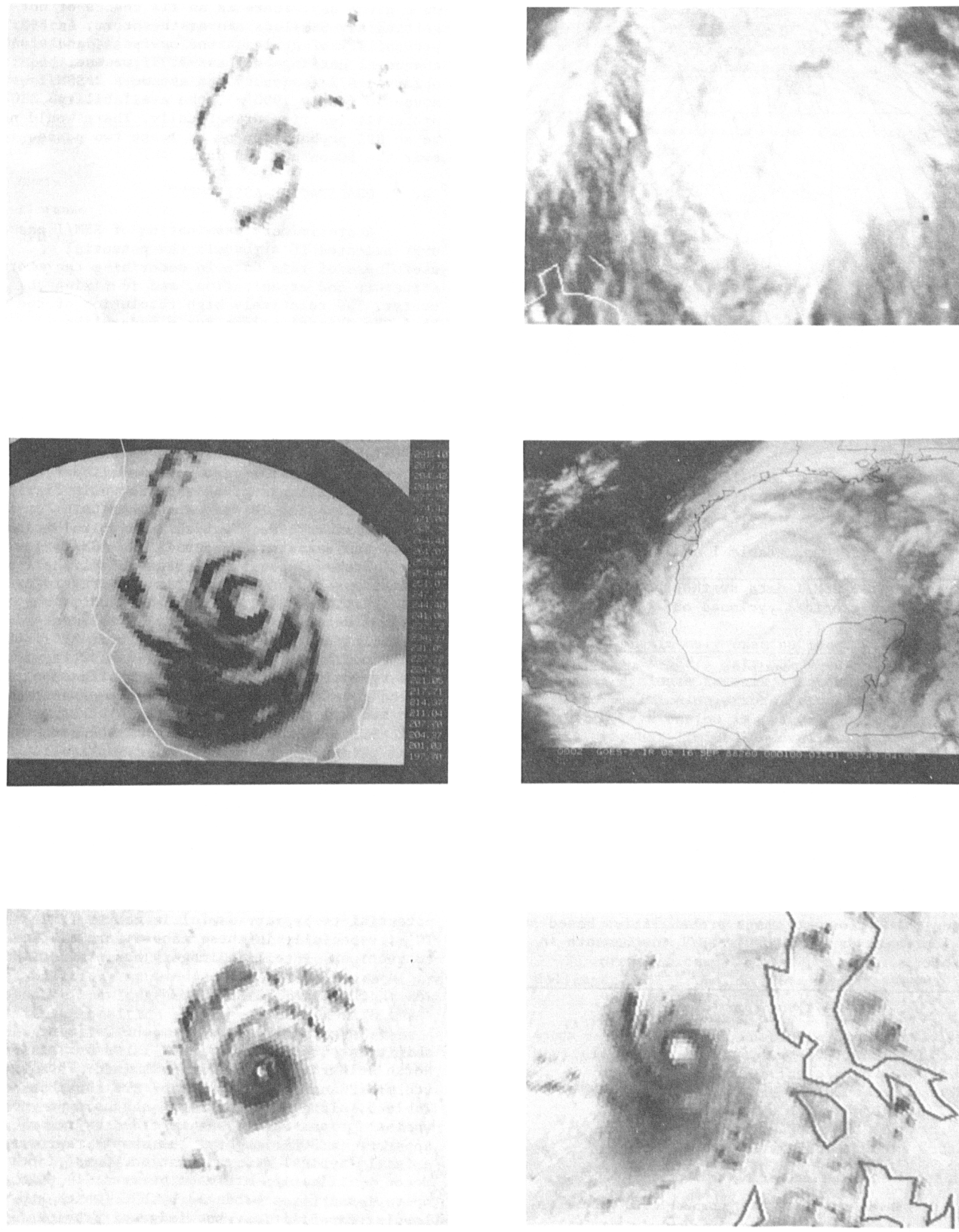

Fig. 1. Examples of SSM/I 85.5 GHz imagery over selected tropical cyclones: a) Tropical Storm Emily (1987), b) Emily GOES IR, c) Hurricane Gilbert (1988), d) Gilbert GOES IR, e) Typhoon Wynne (1987), f) Typhoon Betty (1987).

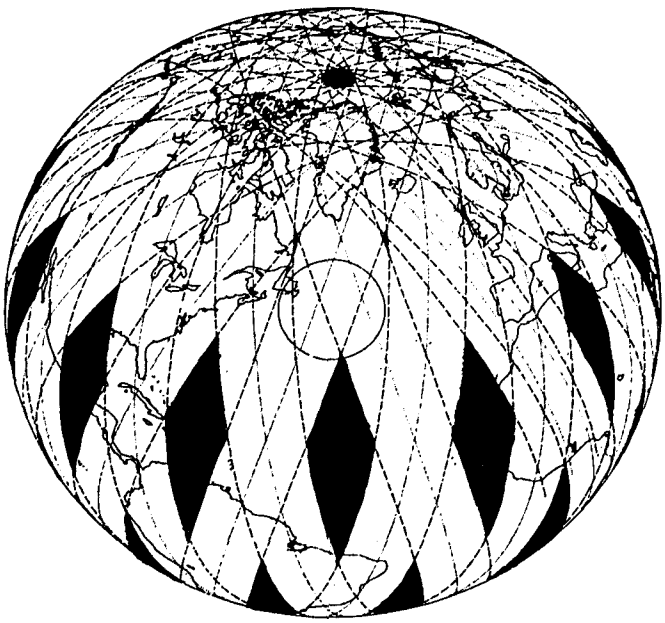

Fig. 2. Coverage of SSM/I in 24 hours. Black areas indicate data gaps (from Hollinger et al., 1987).

Table 1

Percentage of SSM/I data swaths that overpassed the desired tropical cyclones on 22 selected days.

Storm name	Possible	Attained	
Chris	2	1	
Florence	6	5	
Gilbert	12	7	
Joan	18	11	
Keith	6	5	
	44	29	= 67%

Table 2

Tropical cyclone overpass probabilities based on 1 (current) or 2 (future) SSM/I instruments in orbit.

1 SSM/I scenerio (observed)	
# of passes/day	probability over storm
0	11%
at least 1	89%
2	44%

2 SSM/I scenerio (theoretical)	
# of passes/day	probability over storm
0	1%
at least 1	99%
at least 2	89%
at least 3	59%
4	20%

the availability probabilities shown in Table 2. On a given day, there is an 11% chance of not getting any SSM/I data over the storm, an 89% probability of at least one overpass, and a 44% chance of getting two passes. If we use the observed 67% frequency and assume a 2 SSM/I scenerio (early 1990's), the availability probabilities rise dramatically. There would now be an 89% probability of at least two passes over the TC on a given day.

4. QUALITATIVE ASSESSMENT

A preliminary examination of SSM/I passes over selected TC's reveals the potential usefulness of this data in describing the storm structure and organization, and in fixing the center. The relatively high resolution of the 85.5 GHz channel allows for a radar-like depiction of the rainband and eye-wall regions. In many cases, an eye is apparent (Fig. 1). This depiction can be especially useful for center-fixing purposes in cases where conventional satellite data (IR) does not clearly reveal the center. In these cases, a thick cirrus overcast, or "ball" of convection exists which prohibits the conventional IR imagery from delineating an eye. A good example of this is shown in Fig. 1 for TC Emily. The IR data shows a cluster of convection, but the organization (spiral rain bands) and eye are apparent in the SSM/I view.

From an operational standpoint, there are limitations to the use of this data regarding center-fixing abilities. As discussed in the previous section, availability of this data is quite limited, especially in the current 1 SSM/I scenerio. There may also be a 1-4 hr delay in data reception as the satellite must pass over a ground receiving station before the data can be ingested and transmitted to the forecast offices. The absolute accuracy of the center fix using this imagery is, of course, navigation dependent. The current earth location methods yield accuracies on the order of 6 km. Finally, the center-fixing is subjective at this point. While some cases are clear-cut, others are open to image interpretation (further addressed in the next section).

From a qualitative standpoint, it is quite apparent that the SSM/I data has the potential to be very useful in center-fixing TC's, especially in those cases where conventional satellite imagery has problems.

5. QUANTITATIVE ASSESSMENT

To get an idea of the center-fixing ability/accuracy of this data, a number of 1988 North Atlantic TC cases are examined. The five storms (20 cases) investigated are shown in Table 3, along with the storm stages, and whether or not an eye was recorded by recon, or apparent in GOES imagery. The sample represents a fairly typical diversification. Comparisons to recon verification are made between: 1) GOES operational fixes produced by NHC (which had looping capabilities, knowledge of previous storm track, and possible knowledge of recon fix positions); 2) GOES research fixes (done subjectively in non real-time by the first author without looping or recon fix knowledge); 3) SSM/I fixes (#1) generated by the first author (fairly experienced in image interpreta-

Table 3

Tropical cyclone cases used to compare SSM/I position estimates to recon verification. TS=tropical storm; HURR=hurricane; recon eye=eye reported in recon data; GOES eye=eye apparent in GOES data.

Storm name	Storm stage TS	HURR	Recon eye	GOES eye
Chris	1	0	0	0
Florence	4	1	2	1
Gilbert	0	6	6	6
Joan	5	0	3	1
Keith	3	0	0	0
	13	7	11	8

tion); and 4) SSM/I fixes (#2) produced by the third author (inexperienced in image interpretation). The two independent SSM/I estimates allows for an appraisal of the subjectivity involved in center-fixing with this data.

The results of the comparisons are presented in Table 4. The average error, RMSE, worst case, and the number of cases where each method performed superior to the others (ties are counted) are shown. Comparisons to recon verification are made for the entire sample, and for just those cases where an eye is not apparent in the GOES imagery. The comparisons show that for the entire sample, which includes cases with well-defined eyes, the SSM/I #1 estimates are comparable in accuracy to the operational GOES estimates of storm position, and much improved over the GOES research estimates. It should be noted that the operational GOES estimates are quite good in this sample, especially in comparison with the independent GOES research estimates which contain large position errors up to 145 km. This also shows the subjectivity that can exist using conventional IR center-fixing techniques (Mayfield et al., 1988). The spread is not nearly as great between the two independent SSM/I fixes, suggesting less subjectivity.

An encouraging finding is the fact that the SSM/I #1 fixes are superior, overall, in cases where an eye is not discernible in the GOES imagery (Table 4). Despite looping capabilities, knowledge of past storm track, and possible knowledge of past recon fixes that can limit the position errors associated with the operational GOES estimates, the average error and RMSE associated with the SSM/I #1 position estimates are reduced over that of the operational GOES estimates. It is cautioned, however, that image interpretation is still important using this data as evidenced by the increased differences between the independent SSM/I estimates in this sample. It is notable, however, that the SSM/I #2 estimates (no previous image interpretation experience) in both samples are much improved over that of the research GOES IR estimates.

Table 4

SSM/I center fixes compared to recon verification for all 20 cases, and for cases when an eye is not apparent in the GOES IR imagery.

Comparisons to recon verification

20 cases (all)

	GOES (Research)	GOES (Operational)	SSM/I (#1)	SSM/I (#2)
Ave. Error	55 (km)	22	21	34
RMSE	70	29	25	42
Worst case	145	61	58	87
Sup. Perf.	3	9	10	5

12 Cases (Negative GOES eye)

	GOES (Research)	GOES (Operational)	SSM/I (#1)	SSM/I (#2)
Ave. Error	85 (km)	28	23	42
RMSE	90	40	28	49
Worst Case	145	61	58	87
Sup. Perf.	0	5	7	4

6. SUMMARY

A preliminary examination of the usefulness of SSM/I data in center-fixing tropical cyclones reveals a potential for reduced positioning errors, especially in cases where the eye region is obscured by clouds. While somewhat limited in availability, and subject to image interpretation in some cases, these data provide important supplemental information to augment existing satellite capabilities.

7. REFERENCES

Gray, W., C. Guard, C. Neumann, and T. Tsui, 1989: The impact of aircraft reconnaissance on tropical cyclone analysis/forecasting. Manuscript in preparation.

Hollinger, J., R. Lo, G. Poe, R. Savage, and J. Pierce, 1987: Special Sensor Microwave/Imager user's guide. Naval Research Lab., Washington, D.C., 120 pp.

Mayfield, M., C. McAdie, and A. Pike, 1988: A preliminary evaluation of the dispersion of tropical cyclone position and intensity estimates determined from satellite imagery. NOAA NHC research paper, National Hurricane Center, Coral Gables, Fl., 16 pp.

J5.5

THE AMS STUDY OF IMPACT OF AIRCRAFT RECONNAISSANCE ON TROPICAL CYCLONE ANALYSIS--FORECASTING

W. Gray (CSU, Ft. Collins, CO)
C. Guard (Hd., AWS, Scott AFB, IL),
C. Neumann (NOAA, Miami, FL),
T. Tsui (NEPRF, Monterey, CA)

1. INTRODUCTION

This talk gives background information on the AMS Tropical Meteorology and Tropical Cyclones ad hoc committee study of the impact of aircraft reconnaissance upon tropical cyclone (TC) observation and forecasting. This study has been motivated by the 1987 Department of Defense (DOD) decision to discontinue aircraft reconnaissance in the Northwest (NW) Pacific Ocean and the suggestion of some DOD officials that it may also be technically justified to discontinue DOD aircraft reconnaissance in the Atlantic as well.

To what extent can reliable Atlantic tropical cyclone (TC) forecast warnings be issued without the observations of the current Atlantic DOD aircraft reconnaissance program?

A comprehensive assessment of the need for aircraft reconnaissance in the Atlantic has yet to be accomplished. Studies of this type are long overdue. Prior and subsequent to discontinuance of NW Pacific reconnaissance in the Summer of 1987, internal Air Force studies indicated that the loss of aircraft reconnaissance with appropriate compensatory actions would not seriously affect the ability of the Joint Typhoon Warning Center (JTWC) in Guam to perform its TC warning mission in the NW Pacific. JTWC's lower than average forecast errors during 1987 and 1988 lend support to this Air Force assessment for the Pacific.

The role of reconnaissance in the Pacific may not necessarily reflect the situation in the Atlantic since these two reconnaissance programs have distinct differences in their mission and modes of application. In addition, the storm characteristics (e.g. size, intensity, season) and their environmental influences (e.g. latitudinal zone) are known to be different in these two oceans. Storm surge and its destructive potential is a major problem along the US coastline, while it is not a major consideration for US interests in the NW Pacific. Thus, some of the judgments relative to the NW Pacific discontinuance of aircraft reconnaissance may not be valid with respect to US and Caribbean Basin coastal areas.

AMS Study Group. The discontinuance of aircraft reconnaissance in the NW Pacific and its possible demise in the Atlantic has prompted several recent technical studies on the TC observation/forecasting issue. Recent studies are beginning to give much new quantitative information on the many complex technical aspects of this question. This study has only considered conditions as they current exist and are likely to exist in the next few years.

The goal of this special AMS study group has been to assess, as objectively as possible, the impact of potential loss of aircraft reconnaissance observing platform on Atlantic TC forecasting and warnings as it currently exists. Can the other observing platforms provide adequate information in the absence of aircraft reconnaissance? Clearly, there is redundancy between the different platforms and, in particular, the aircraft and satellite.

The central question being studied is the accuracy of the current weather satellites are for specifying TC position, current motion, intensity and outer radius wind distribution without the support of aerial reconnaissance. Many TC specialists feel that this is an unresolved question which needs more study. Most of the important TC satellite fixes and intensity estimates in the Atlantic have not been made independent of aircraft information. Where reconnaissance flights were not made, ground truth information as to how accurate the satellite estimates are is typically not available. It is important that this question be more thoroughly studied.

2. CURRENT STUDY

Table 1 gives a chronology of the events associated with this special AMS reconnaissance study. Recent studies directed towards more information on the reconnaissance question have been primarily initiated by R. Sheets, M. Mayfield, C. McAdie, A. Pike at NHC; J. Martin, D. Shoemaker, W. Gray at CSU; C. Guard and others of AWS, and R. Black out of the Federal Coordinator for Meteorology (FCM) office. Table 2 lists most of the new references which have been used in the writing of this report.

Our four-member write-up team met for 3 days in August 1988 and drafted a preliminary report which was based primarily on the references of Table 2. This first draft was reviewed by R. Elsberry (NPG), G. Holland (BMRC), R. Merrill (U. of Wis.), and R. Sheets (NHC). This approximately 50-page double-spaced report was then altered and sent in early November 1988 to about 60 of our countrys' most experienced tropical cyclone operational forecasters and researchers. Written responses from slightly more than 45 of these specialists. Many of the

TABLE 1
AMS Reconnaissance Study Chronology

1. January 1987 - AWS announces plan to discontinue Guam Reconnaissance.
2. April 1987 - Commander AWS talk at AMS Hurricane Meeting, Orlando, Florida indicating that DOD may have to discontinue Atlantic reconnaissance due to budget restrictions.
3. April 1987 - AMS Tropical Meteorology Committee votes to form an ad hoc group to study the technical aspects of the reconnaissance question
4. 1987-1989 - Various reconnaissance studies are performed.
5. April 1988 - Commander AWS talk at AMS Hurricane Meeting, Atlanta, Georgia, reiterating AWS intention to discontinue DOD aircraft reconnaissance by 1990.
6. August 1988 - W. Gray, C. Guard, C. Neumann, T. Tsui meet for 3 days and write a 1st report draft which is reviewed by R. Elsberry, G. Holland, R. Merrill and R. Sheets.
7. Early November 1988 - Preliminary draft sent to 60 of some of our countries' most experienced TC experts. Written replies were received from about 45 of these individuals.
8. 14-16 January 1989 - Gray, Guard, Neumann, Tsui meet again for integrations of replies and preparation of a second draft.
9. New research by C. Neumann and others is made to better classify points raised in the review of the first draft.
10. Spring 1989 - Other inputs and final alteration of second draft.
11. Spring 1989 - Preparation of a short AMS position paper based on this study.
12. Summer 1989 - Submission of final draft for publication consideration as an AMS Bulletin article. Also submission of short policy statement for AMS council review.

respondees took considerable time and gave much careful thought and effort in their responses.

Our write-up team met again for 3 days in January 1989 to integrate all responses as best we could. A second revised draft is being prepared this winter and will, with additional inputs, hopefully be completed at the time of this San Diego meeting. It is our plan to send this manuscript for AMS Bulletin publication consideration in the early summer of 1989. It is planned that a shorter 3-4 page position paper based on this study also be prepared for AMS council consideration.

3. SUMMARY

Space is not available to discuss the technical assessments of this study. Some general statements can be made however.

1) There has been insufficient attention to the question of the impact of aircraft reconnaissance on TC analysis and forecasting. Having had reconnaissance for over 40 years, most American TC forecasters and researchers have not felt the need to make quantitative studies of how beneficial aircraft reconnaissance may have been. New research is now beginning to focus on this topic.

2) The technical aspects of the reconnaissance question are exceedingly complex. There is a very wide variety of views and opinions on this topic.

3) It is likely to be beneficial to the US tropical cyclone community that the broad ranging technical aspects associated with the aircraft reconnaissance issue be aired in open forum and widely discussed.

4) Assessments of the needs and benefits of aircraft reconnaissance in the NW Pacific basin do not necessarily directly carry over to the Atlantic.

TABLE 2
PRIMARY REFERENCES USED FOR THIS STUDY

1. American Meteorological Society (AMS), 1986: Policy statement on hurricane detection, tracking and forecasting. Bull. Amer. Soc., 67, 1508-1510.
2. Guard, C. D., 1988: Results of a tropical cyclone accuracy study using polar orbiting satellite data. Office of the Federal Coordinator, Tropical Cyclone Studies Rept FCM-R11-1988, Part 3.
3. Hope, J. R., 1971: Position error of tropical cyclones vs. frequency of aircraft fixes. J. Appl. Meteor., 10, 1035-1036.
4. Martin, J. D., 1988: Tropical cyclone observation and forecasting with and without aircraft reconnaissance. Dept. Atmos. Sci. Paper No. 428, Colo. State Univ., Ft. Collins, CO, 114 pp.
5. Mayfield, M., C. McAdie, and A. Pike, 1988: A preliminary evaluation of the dispersion of tropical cyclone position and intensity estimates determined from satellite imagery. NOAA NHC research paper, 16 pp.
6. McBride, J. L. and G. J. Holland, 1987: Tropical cyclone forecasting: A worldwide summary of techniques and verification statistics. Bull. Amer. Meteor. Soc., 68, 1230-1238.
7. Modified Operations Evaluation, 1987: Prepared by special forecast team of JTWC, 120 pp. Available from Hq. Air Weather Service, Scott AFB, IL, 62225-5008.
8. Sheets, R. C., 1985: Hurricane tracking using a mass field envelope approach-impacts of forecast tracks. Extended abstracts volume, 16th Conference on Hurricanes and Tropical Meteorology, May 14-17, 1985, Houston, TX, Published by American Meteorological Society, Boston, MA, 02108, 38-30.
9. Sheets, R. C., 1986: Hurricane tracking using an envelope approach-impacts on forecast tracks. NOAA Technical Memo. NWS NHD 33, National Hurricane Center, Miami, FL, 42 pp.
10. Sheets, R. C., 1988: Impact of aircraft reconnaissance "fixes" on tropical cyclone track predictions. 7 pp. Recent informal rept.

11. Sheets, R. C. and P. Grieman, 1975: An evaluation of the accuracy of tropical cyclone intensities and locations determined from satellite pictures. NOAA Tech. Memo. ERL WMPO-20, NOAA, US Dept. of Commerce, Boulder, CO, 33 pp.

12. Sheets, R. and C. McAdie, 1988: Preliminary results of a study of the accuracy of satellite-based tropical cyclone position and intensity estimates. NOAA NHC research paper, 49 pp.
13. Shoemaker, D. N., 1988: Influence of synoptic track aircraft reconnaissance on JTWC TC track errors. Internal report, 5 pp.

REMOTE SENSING OF OCEAN SURFACE WINDS WITH THE SPECIAL SENSOR MICROWAVE/IMAGER (SSM/I)

Mark A. Goodberlet

University of Massachusetts
Amherst, MA

1. INTRODUCTION

The Defense Meteorological Space Program (DMSP) Special Sensor Microwave/Imager (SSM/I) wind speed retrieval algorithm developed by Environmental Research and Technology Inc. (ERT) under contract from Hughes Aircraft is called the D-matrix algorithm and has the following form [Lo, 1983].

$$SW = C0(j) + C1(j).TB(19H) + C2(j).TB(22V) + C3(j).TB(37V) + C4(j).TB(37H) \quad (1)$$

Equation (1) is valid only over open ocean where the wind speed, SW, is in m/s and referenced to a height of 19.5 m above the surface. Equation (1) also contains the terms TB(x) which represent the SSM/I measured brightness temperature of frequency/polarization combination "x" and the D-matrix coefficients, Ci(j), where "j" is the climate code index and varies from 1 to 9. Each of the 9 distinct climate codes represents a particular season and latitude band [Lo, 1983].

The amount of microwave energy being emitted from the ocean surface is dependent on the wave structure and foam coverage [Ulaby et al., 1986] which, in turn, are influenced by wind speed. Therefore, by measuring the ocean surface microwave emission, the SSM/I is able to predict ocean surface wind speed. Microwave emission at the SSM/I frequencies which is coming from the ocean surface is effectively masked by the emission and attenuation characteristics of rain and large amounts of water vapor in the earth's atmosphere. Realizing this, ERT suggested the use of the rain-flags 0, 1, and 2 which identify the conditions of no rain, possible rain, and heavy rain respectively. These flags are set based on predetermined thresholds for TB(19H) and the difference between TB(37V) and TB(37H) [Lo, 1983].

The DMSP accuracy specification for wind speed retrievals under rain-free conditions (i.e., rain-flag = 0) is ± 2 m/s (standard deviation) over the range 3 m/s to 25 m/s. Accuracy was not specified for wind retrievals from cells flagged either 1 or 2. In fact, the original D-matrix algorithm did not attempt to retrieve winds under rain-flag 2 conditions.

2. NOAA BUOY SYSTEM AND CRITERIA FOR COMPARISON

Validation of the SSM/I wind speed retrievals was done using the anemometer measured winds of open ocean buoys maintained by the National Oceanic and Atmospheric Administration (NOAA). These buoys make an 8.5 minute average of the wind once every hour with an accuracy of ± 0.5 m/s for winds less than 10 m/s and 5% for winds greater than 10 m/s [Gilhousen, 1986].

To avoid land contamination of ocean brightness temperatures and to insure that the land did not restrict the wind speed fetch distance necessary for creating fully developed seas [Ulaby et al., 1986.], only buoys further than 100 km from land were chosen for the validation. Nineteen of the NOAA buoys were used and their wind speed observations, taken at heights of either 5 or 10 meters above the surface, were converted to equivalent winds at 19.5 meters above the surface [Liu, et al., 1984] so that they could be compared directly to the 19.5 meter referenced D-matrix winds. Converted buoy winds and D-matrix winds were paired only when the SSM/I retrieval was located within 25 km of the buoy position and the SSM/I overpass time was within 30 minutes of the buoy wind speed measurement. Based on the work of Monaldo [1988], the error introduced by the average values of these spatial and temporal differences is less than 10% of the total standard deviation of 2 m/s.

3. REQUIRED NUMBER OF COMPARISONS

In determining the required number of buoys for the validation, one must consider how often each buoy lies within the swath of an SSM/I overpass. The number of SSM/I overpasses depends on the latitude, LAT, of the buoy and can be approximately calculated using equation (2) which is reasonably accurate up through 60 degrees latitude, above which the error exceeds 15%.

$$\text{SSM/I Overpasses in 30 Days} = 30/cos(LAT) \quad (2)$$

The accuracy specification of ± 2 m/s for D-matrix wind speed retrievals is interpreted as the standard deviation of the comparison between D-matrix winds and buoy winds in any sub-interval of the 3-25 m/s wind speed range. Shown in Table 1 is the number of comparisons out of 1,000 for which the buoy wind speed falls within each of 6 selected sub-intervals of the 3-25 m/s range. These comparison counts are based on the global distribution of winds given by Schroeder, et al. [1986].

It is preferable to have a sample size of 30 or more when doing statistical analysis of the data. For wind speed sub-intervals 1, 2, and 3, it appears that this sample size can be obtained by collecting approximately 140

Table 1. Expected number of D-matrix/buoy wind speed comparisons per 1000 which fall into selected subintervals of the 3 m/s to 25 m/s wind speed range.

I.D.	Range (m/s)	Comparisons per 1000
1	3-6	260
2	6-10	395
3	10-14	215
4	14-18	50
5	18-22	25
6	22-25	1

comparisons. Approximately 15% of the data are rain-flagged and since the comparisons are made only with data which is not rain-flagged, the sample size required for each climate code must be increased 15% from 140 to 161. Other factors affecting the total required buoy count include lost data due to periodic buoy maintenance and the likelihood of encountering wind speeds distributed according to Schroeder et al. [1986]. These factors were determined from actual climatic summaries for the individual data buoys which are available from the National Data Buoy Center [Gilhousen, et al., 1986]. The climatic summaries established that the 19 buoys selected could more than satisfy the low wind speed validation requirements. However, the low probability of observing winds greater than 15 m/s makes it difficult to evaluate the overall performance of the D-matrix algorithm in the range 15-25 m/s.

4. VALIDATION RESULTS

Performance of the climate code 5 (25-50 degs latitude, Spring and Fall) version of the original D-matrix algorithm is shown by the scatter-plot in Figure 1. Given in the legend of Figure 1 is the y-intercept (bias) and slope of the regression line, which has been chosen to minimize the sum of the squares of the horizontal distances from each point to the regression line. The SD is the standard deviation of the quantity, (D-matrix winds minus buoy winds). The term "CORR(R)" is the correlation coefficient [Book, 1977] between buoy winds and D-matrix winds, and the term "#OBS" represents the number of observations or data points in the scatterplot. The poor performance of the climate code 5 algorithm is typical of all 9 versions of the original D-matrix algorithm. To correct this problem new coefficients were generated using standard linear regression of buoy wind speed on the coincident SSM/I brightness temperature measurements, TB(19H), TB(22V), TB(37V), and TB(37H) and the rain flag criteria was revised. Performance of the new climate code 5 D-matrix algorithm is shown in Figure 2. Performance of the revised 9-version D-matrix algorithm is summarized in Table 2 and the new coefficients are given in the SSM/I Cal/Val final report [Hollinger, 1988]. Despite the apparent good performance of the new algorithm, additional improvements are necessary.

In Figure 3, the D-matrix wind speed residual is plotted as a function of buoy measured wind speed using data from climate code 5. Dividing the region of Figure

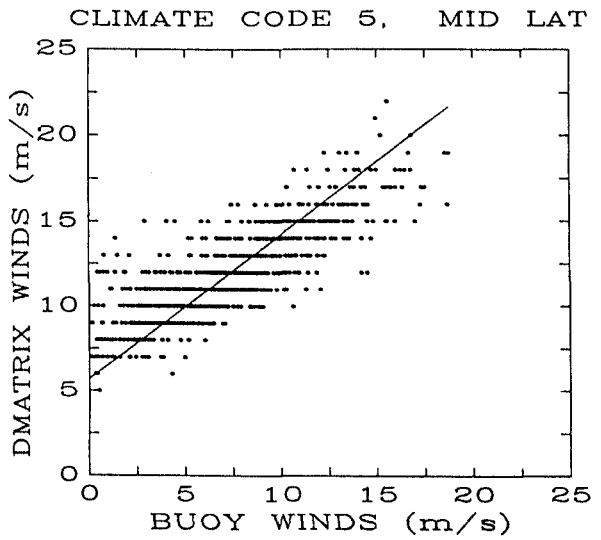

Figure 1. Performance of the original D-matrix algorithm for climate code 5. Bias = 5.7 m/s, slope = 0.85, S.D. = 5.1 m/s, corr (R) = 0.82, # obs = 998.

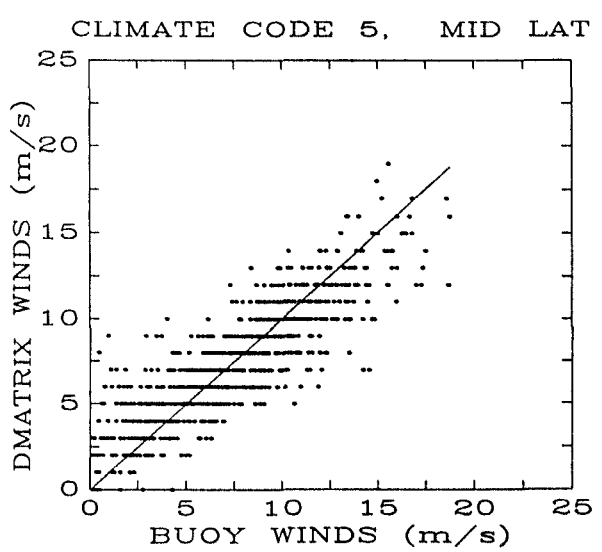

Figure 2. Performance of the revised D-matrix algorithm for climate code 5. Bias = 0.0 m/s, slope = 1.0 m/s, S.D. = 1.9 m/s, corr (R) = 0.85, # obs = 998.

Table 2. Performance of the 9 climate code D-matrix algorithm.

Climate Code	S.D. m/s	Percentage Rain Flagged	Number of Comparisons
1	1.5	17	376
2	1.4	10	63
3	1.5	8	109
4	1.5	9	43
5	1.8	13	1296
6	1.5	12	643
7	1.9	18	516
8	1.8	19	279
9	1.6	9	277

3 into a number of vertical bins and calculating the SD and bias (i.e., average) of the points falling within each bin results in the "interpreted" residual plot shown in Figure 4 which indicates that the accuracy of the D-matrix retrievals is best near the global average wind speed of 7 m/s and becomes worse for predictions away from 7 m/s.

Discontinuity of the retrieved winds across climate code boundaries is another problem with the 9-version D-matrix algorithm. The average discontinuity across each latitude band boundary was calculated using actual SSM/I data and was found to be as high as 2.0 m/s but was typically 1.0 m/s.

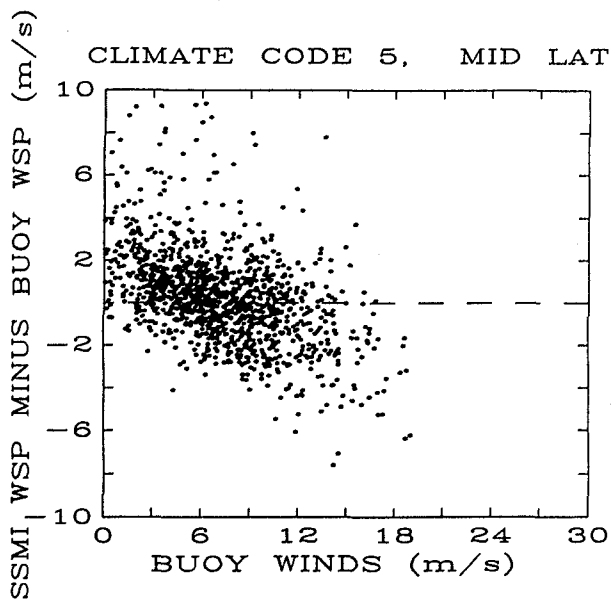

Figure 3. D-matrix residual plotted as a function of the coincident buoy winds for climate code 5.

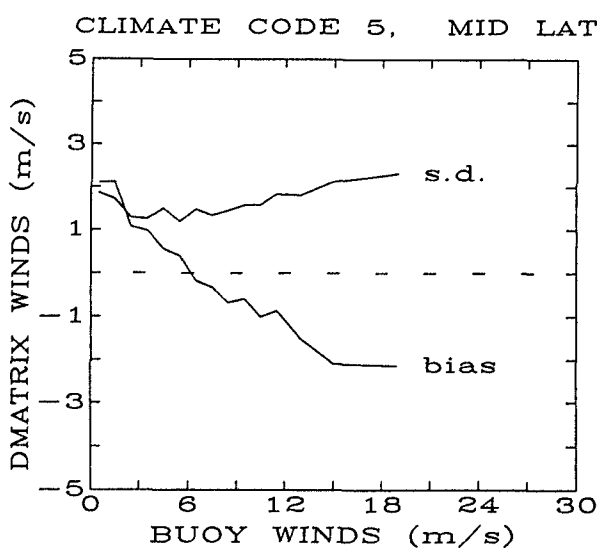

Figure 4. Standard deviation and bias of the D-matrix retrieved winds plotted as a function of buoy wind speed for climate code 5.

The fact that the accuracy of the SSM/I wind speed retrievals deteriorates rapidly in areas where rain and heavy cloud cover are found, severely limits the ability of this instrument to map the wind field in and around typhoons, hurricanes and tropical storms. Figure 5 shows the rain-flagged areas of typhoon Wynne as it appeared on July 25, 1987 at approximately 2040Z. According to aircraft reconnaissance data collected by the Air Force/Navy Joint Typhoon Warning Center, the rain-flag 3 area outline corresponds roughly to the 25 m/s wind speed radius of this storm which had visually observed winds as high as 60 m/s near its center.

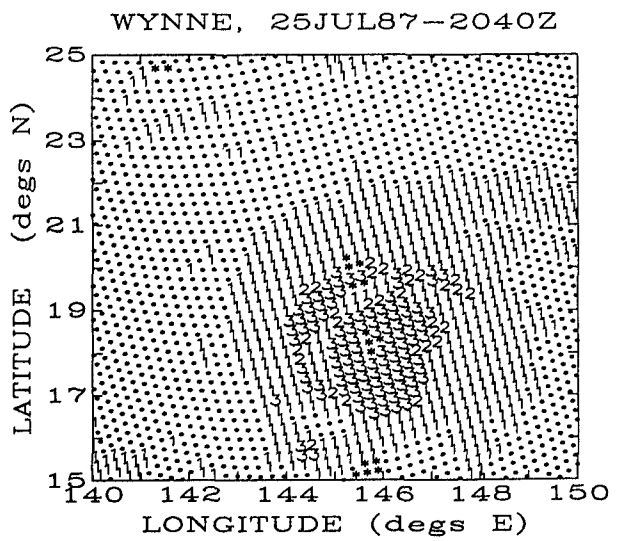

Figure 5. Rain-flagged areas of typhoon Wynne on 25 July 1987. The dots and asterisks indicate rain-flag zero areas and land (Mariana Isles) respectively. The numbers 1, 2, and 3, correspond to rain-flags 1, 2 and 3.

5. ALTERNATE WIND SPEED ALGORITHM

A single D-matrix algorithm, valid at all latitudes and during all seasons was developed and found to meet the ± 2 m/s accuracy specification under rain-free conditions. Details of the global algorithm are given in Table 3. Note the use of the four rain-flags and their interpretation which differs considerably from the rain-flag criteria of the original ERT algorithm. It is recommended that wind speeds be calculated under all conditons and that the associated rain-flag be the user's guide to the accuracy of the retrieval.

The global wind speed algorithm was developed using 100 randomly selected SSM/I buoy match-ups from each of the 9 climate codes. Out of this 900 point data set, only the 708 which were rain-flagged either 0 or 1 were retained and used to develop the new algorithm. In this way, the global algorithm was based on data from types of weather systems where accurate wind speed retrievals were likely while at the same time being made somewhat tolerant of rain.

Coefficients for the algorithm were generated using a weighted linear regression [Draper, et al., 1981] of the buoy wind speeds on the coincident SSM/I brightness temperatures of TB(19V), TB(22V), TB(37V), and TB(37H). Note that the new algorithm uses TB(19V) since it resulted in slightly more accurate retrievals than if the ERT suggested TB(19H), was used. The weights used in the regression were set equal to one over the square root of the wind speed density function [Schroeder et al., 1986],

Table 3. Specifications of the global D-matrix algorithm.

$$SW = 147.90 + 1.0969 \cdot T_B(19V) - 0.4555 \cdot T_B(22V) + - 1.7600 \cdot T_B(37V) + 0.7860 \cdot T_B(37H)$$

Rain Flag	Criteria	Accuracy
0	$T_B(37V) - T_B(37H) > 50$ $T_B(19H) < 165$	$< 2\ m/s$
1	$T_B(37V) - T_B(37H) < 50$ $T_B(19H) > 165$	$2 - 5\ m/s$
2	$T_B(37V) - T_B(37H) < 37$	$5 - 10\ m/s$
3	$T_B(37V) - T_B(37H) < 30$	$> 10\ m/s$

Wind Speed Cutoff at 25 m/s

evaluated at the particular buoy wind speed. This type of weighting has the effect of making all wind speed ranges equally important in the creation of the new algorithm. In contrast, the unweighted regression used previously tends to emphasize those wind speed ranges where there is a lot of data and de-emphasize the ranges where little data was collected. This is precisely why the original D-matrix performed well near the global average wind speed of 7 m/s and performed poorly (both in terms of SD and bias) in the high (>15 m/s) range.

True performance of the alternate global wind speed algorithm under rain-free conditions is indicated by the "interpreted" residual plot shown in Figure 6. Comparison of Figure 6 with Figure 4 shows that much of the high wind speed bias associated with the original D-matrix retrievals has been removed by the weighted regression technique. The average retrieval SD of the new algorithm is found to be 2.0 m/s which meets the ± 2 m/s DMSP accuracy specification.

6. CONCLUSIONS

Although wind speed retrievals from the ERT 9-version D-matrix algorithm did not meet the DMSP accuracy specification of ± 2 m/s, regeneration of the coefficients using standard linear regression resulted in a set of algorithms whose retrievals did meet specifications.

An alternate global D-matrix algorithm with a single set of coefficients has been developed which meets retrieval accuracy specifications and does not have the zonal discontinuity and high wind speed bias problems found in the original ERT algorithm.

The rain-flag criteria was revised to be more restrictive and the global algorithm now uses the four rain-flags, 0, 1, 2, and 3, which indicate retrieval accuracy SD's of <2 m/s, 2-5 m/s, 5-10 m/s and >10 m/s, respectively. During any particular day, approximately 85% of the D-matrix retrieved ocean surface winds will have an accuracy of ± 2 m/s. The remaining 15% of the time, the scene will be rain-flagged and retrieval accuracies will be worse than ± 2 m/s. Since a majority of the scene in and around typhoons and hurricanes is rain-flagged, the SSM/I appears to have limited use for studying the wind field of these weather systems. Additionally, the spatial resolutions of the 19, 22 and 37 Ghz channels (55, 49 and 32 km) are incapable of resolving accurately any wind speeds in areas where high wind speed gradients exist.

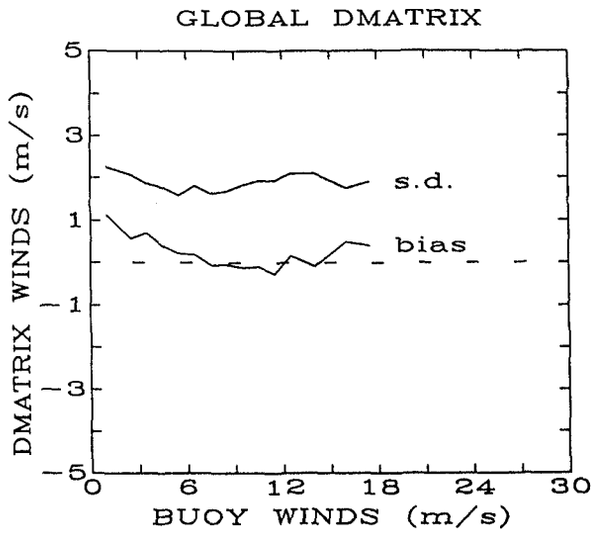

Figure 6. Standard deviation and bias of the global D-matrix retrieved winds plotted as a function of buoy wind speed.

REFERENCES

[1] Book, S.A., *Statistics*, p. 221, McGraw-HIll, New York, NY., 1977

[2] Draper, N.R. and H. Smith, Applied Regression Analysis, 2nd edition, p. 108, John Wiley and Sons, New York, NY., 1981

[3] Gilhousen, D.B., An Accuracy Statement for Meteorological Measurements Obtained from NDBC Moored Buoys, Proc. MDS '86 Marine Data Systems International Symposium, Marine Tech. Soc., New Orleans, La., 1986a

[4] Gilhousen, D.B., M.J. Changery, R.G. Baldwin, T.R. Karl, and M.G. Burgin, Climatic Summaries for NDBC Data Buoys, National Data Buoy Center publication, NSTL, Ms., 1986b

[5] Hollinger J.P. et al, DMSP Special Sensor Microwave/Imager Calibration/Validation, Naval Research Labs, Washington D.C., 1988

[6] Liu, W.T. and T.V. Blanc, The Liu, Katsaros and Businger (1979) Bulk Atmospheric Flux Computational Iteration Program in FORTRAN and BASIC, Naval Research Labs memorandum report 5291, Washington D.C., 1984

[7] Lo, R.C., A Comprehensive Description of the Mission Sensor Microwave Imager (SSM/I) Environmental Parameter Extraction Algorithm, Naval Research Labs memo. report 5199, Washington D.C., 1983

[8] Monaldo, F.M., Expected Differences between Buoy and Radar Altimeter Estimates of Wind Speed and Significant Wave Height and their Implications on Buoy-Altimeter Comparisons, J. Geophys. Res., 93, 2285-2302, 1988

[9] Schroeder, L.C. and J.L. Sweet, Merge and Archival of SEASAT-A Satellite Data and Insitu at Selected Illuminated Sites Over the Ocean, NASA Langley tech. memo., Hampton, Va., 1986

[10] Ulaby, F.T., R.K. Moore, and A.K. Fung, *Microwave Remote Sensing Active and Passive*, vol. 3, p. 1440-1467, Artech House, Norwood, Ma., 1986

J11.2 UPPER-TROPOSPHERIC INFLUENCES ON WESTERN PACIFIC TROPICAL CYLONE INTENSITY CHANGE AS INFERRED FROM SATELLITE OZONE OBSERVATIONS

Edward B. Rodgers
Laboratory for Atmospheres
NASA/Goddard Space Flight Center
Greenbelt, MD 20771

John Stout
General Sciences Corporation
Laurel, MD 20785

1. INTRODUCTION

The Nimbus-7 Total Ozone Mapping Spectrometer (TOMS) was used to map the distribution of total ozone within and surrounding 45 mature (i.e. storm stage and greater) Western North Pacific tropical cyclones (1979-1982). Rodgers et al. (1988) found that the TOMS-observed total ozone distribution within the subtropical ocean regions during the tropical cyclone season corresponded well with the upper-tropospheric and tropopause topography, similar to previous middle-latitudinal observations (Reed, 1955). This relationship made it possible to monitor the propagation of upper-tropospheric subtropical transient waves with the TOMS. Since the intensity change of mature tropical cyclones have been suggested to be related to upper-tropospheric forcing (Holland and Merrill, 1984), the TOMS-observed total ozone was examined for its potential to help differentiate intensifying from non-intensifying mature tropical cyclones.

To demonstrate the feasibility of diagnosing tropical cyclone intensity change from TOMS, this paper examines the relationship between upper-tropospheric environmental total ozone distribution and intensity for a tropical cyclone case study and then examines the climatological total ozone patterns for the purpose of identifying upper-tropospheric features that could help differentiate intensifying from non-intensifying Western Pacific tropical cyclones (1979-1982).

2. NIMBUS-7 TOMS

The TOMS, which was flown on Nimbus-7 and launched in October, 1978 into a sun-synchronous polar orbit, is a scanning instrument that uses six wavelengths from 312.5 to 380.0 nm to separate the effects of ozone absorption, molecular scattering, and surface reflection. From these wavelengths, total ozone in a column is determined from TOMS measurements to within 2% relative to ground-based observations (Shapiro, et al., 1982). Additional information about Nimbus-7 TOMS and the TOMS total ozone algorithm can be found in the Nimbus-7 User Guide (Nimbus Project, 1975).

3. CASE STUDY/TROPICAL CYCLONE TIP (7-13 October, 1979)

To examine the mutual adjustment between a tropical cyclone's intensity and its upper-tropospheric environment, Fig. 1 shows the TOMS observed total ozone anomalies (TOA) (observed minus the climatological mean TOMS-observed total ozone at a given location) and aircraft-measured central pressure for tropical cyclone Tip (7-13 October). TOA were averaged over a 10° latitude. These averages were computed every 1.25° longitude, extending 16° east and west of Tip's center. During the period of observation, Tip headed in a general westward direction traversing the open western Pacific south of 20° N and east of 135° W.

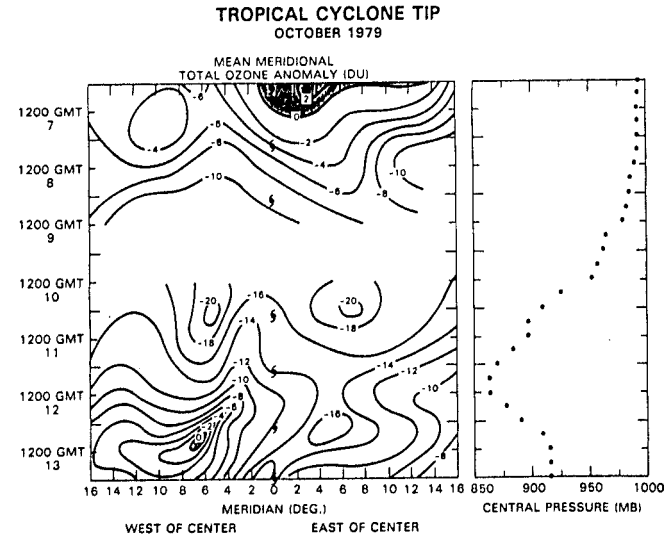

Fig. 1 The left panel delineates the contours of the total ozone anomalies (2 Dobson Units [DU] interval) on a time vs longitude scale for tropical cyclone Tip (7-13 October, 1979). Shaded regions depict positive total ozone anomalies. The hurricane symbol delineates Tip's center and time of observation. The right panel depicts Tip's 6 h interval aircraft observed central pressure (mb). TOMS-measured total ozone data on 10 October, 1979 was missing.

The major points of interest depicted by the figure are that prior to 11 October as Tip intensified, TOA within 8° longitude of the center rapidly decreased under the influence of the enhanced ascending branch associated with the strengthening jet induced secondary circulation (Rodgers et al., 1988). The minimum of TOA (-20 DU) on 11 October depicts the time when the jet influences were the greatest. Also, it is observed that Tip's deintensification on 12 October appears to be related to the intrusion of upper-tropospheric air, since the changes in lower-tropospheric influence were minimal (i.e. sea surface temperatures). Reed's (1955) total ozone and upper-tropospheric wave model suggest that Tip had interacted with the subsiding ozone rich region of an middle-latitudinal upper-tropospheric trough.

4. CLIMATIC STUDY/WESTERN PACIFIC TROPICAL CYCLONES (1979-1988)

The climatological TOA maps were generated using the proceedure documented by Rodgers et al. (1988), which included rotating all the tropical cyclones to a common direction.. Mature tropical cyclones during tropical cyclone months between July-October (1979-1988) that traverse the open Western Pacific ocean equatorward of 35° N and between 124° W and 160° W were sampled.

To examine the variation of total ozone distribution according to tropical cyclone intensity change, TOA were stratified with respect to direction of motion and intensity change that occurred over the 12 h period, 6 h after the TOMS observation. The westward moving storms (225° ≤ Dir ≤ 315°) were considered to be equatorward of the 500 mb subtropical ridge, while northward moving storms (315° ≤ Dir 45°) were considered to be west and north of the 500 mb subtropical ridge. The steady state/weakening systems 12 h central pressure change were ≥ 0 mb, while intensifying system's central pressure change were ≤ 0 mb.

The sample size, mean intensity during observation, mean intensity change, and mean center latitude for the non-intensifying (intensifying) tropical cyclones were 26 (62), 944 mb (978 mb) + 6 mb/12 h (-10 mb/12 h), and 19° N (17° N), respectively, for the westward moving system and 46 (32), 954 mb (968), +6 mb/12h (-8 mb/12 h), and 24° N (19° N), respectively, for the northward moving systems.

Figs. 2 and 3 show the difference between the mean TOA of the intensifying and the non-intensifying westward and northward moving tropical cyclones, respectively and the regions where the probability that the difference in the mean is due to chance is less 10% [student-t test (Panofsky and Brier, 1968)]. It can be seen from Fig. 2 that the most significant environmental TOA feature (region A within the stippled region) that differentiates intensifying from non-intensifying westward moving systems is the large positive TOA region to the right (north) of the center. Considering the total ozone and upper-troposphere wave model (Reed, 1955) and the northward justaposition of the tropical upper-tropospheric trough (TUTT) needed to intensify tropical cyclones south of the subtropical ridge (Sadler, 1976), it is most likely that this region delineates the preferred location of the axis of the dry, sinking, cold TUTT for tropical cyclone intensification.

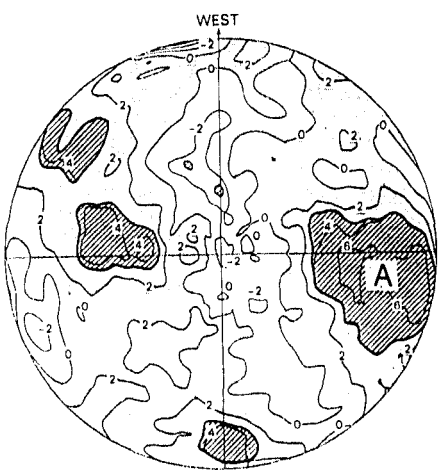

Fig. 2 Difference in the mean Nimbus-7 TOMS measured total ozone anomalies (2 DU interval) between intensifying and non-intensifying westward moving tropical cyclones. Shaded areas have positive total ozone anomalies. Radius of circle is 2222 km. The storms' have been rotated so that their forward motion is towards the top of the page (see text). The stipple regions delineates the area where the probability that the difference of the mean is due to chance is less than 10%.

The TOA difference map for the northward moving tropical cyclones (Fig. 3) is quite similar to the one observed with the North Atlantic tropical cyclones (Rodgers et al., 1988). As with the North Atlantic tropical cyclones, the favorable positioning of the upper-tropospheric middle-latitudinal trough for northward moving Western Pacific tropical cyclones to intensify is to have the trough situated to west and north of the system (Sadler, 1976). The TOA

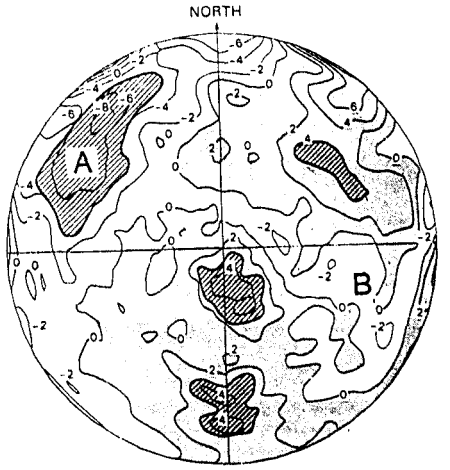

Fig. 3 Same as Fig. 2, except for northward moving tropical cyclones.

difference maps reflect the preferred positioning of these troughs for tropical cyclone intensification with positive TOA in the forward-left quadrant (northwest of the center) near to the center and negative TOA in the forward-left quadrant at larger distances from the center (region A within the stippled area). The TOA difference maps suggest that the distance between upper-tropospheric troughs and tropical cyclones need to be less for intensification to occur. Another common TOA difference feature, that delineates intensifying from non-intensifying North Atlantic and Pacific tropical cyclones, although less prominant for the North Pacific systems, is the region of negative TOA (region B) in the rear-right quadrant (southeast of the center). Since low values of TOA are caused by the ascending branch of the thermally indirect circulation in the exit region (Rodgers et al., 1988), this TOA pattern suggest that the radial extent of the outflow jet is greater for intensifying systems as compared to non-intensifying system. This finding is consistent with Merrill (1988), who observed from the composite of North Atlantic tropical cyclone satellite winds that the radial extent of the outflow was greater for intensifying tropical cyclones than those that did not intensify.

5. REFERENCES

Holland, G.L., and R. T. Merrill, 1984: On the dynamics of tropical cyclone structure change. Quart. J. Roy. Meteor. Soc., 110, 722-745.

Nimbus Project, 1978: Nimbus-7 User Guide, Nimbus Project, National Space Science Data Center, Goddard Space Flight Center, Greenbelt, MD 20771, 263 pp.

Panofsky H.A. and G. W. Brier, 1968: Some Applications of Statistics to Meteorology. The Pennsylvania State Univ., 224 pp.

Rodgers E. B., J. Stout, J. Steranka, and S Chang, 1988: Tropopause adjustment to tropical cyclones as inferred from satellite ozone observations. Preprints, Third Conf. on Satellite Meteorology and Oceanography, Amer. Meteor. Soc., 197-202.

Reed, R. J., 1955: A study of a characteristic type of upper-level frontogenesis. J. Meteor., 12, 226-237.

Sadler, J. C., 1976: Tropical cyclone initiation by the tropical upper-tropospheric trough. Mon. Wea. Rev., 104, 1266-1278.

Shapiro, M.A., A.J. Krueger, and P. J. Kennedy, 1982: Nowcasting,. K. A. Browning Ed., Academic Press. London, 256 pp.

FORECASTING 30 KNOT WIND RADIUS IN WEST PACIFIC TROPICAL CYCLONES USING GEOSTATIONARY INFRARED SATELLITE DATA

Capt. Daniel N. Shoemaker, USAF

Dept. of Atmospheric Science, Colorado State University
Fort Collins, CO, 80523

1. INTRODUCTION

1.1 Why This Study?

Due to the discontinuance of aircraft reconnaissance in the Northwest Pacific, forecasters have lost their best tool for measuring outer wind distribution in NW Pacific Ocean tropical cyclones. A forecast scheme is presented here to specify the 30 knot wind radius for tropical storms in this basin based on GMS data. Infrared cloud areas colder than four thresholds (0°C, -25°C, -50°C, and -75°C) are summed and plotted from three hourly images. Cold cloud areas are used to estimate the mean radius of 30 and 50 knot wind (R30 and R50) and their changes.

1.2 Working Hypothesis

The premise behind this study is that convection affects outer winds in tropical cyclones. Convection at any given time doesn't correlate with outer winds, so it was decided to examine the total convection in a storm's recent past and see if outer winds correlated with sustained convection. It appears that the one to two day history of convection relates to outer wind distribution.

2. DATA SETS

2.1 Satellite Data

The satellite data set consists of three hourly 10km resolution Japanese GMS digitized infrared images for 1983-1984. Images were navigated to storm-centered coordinates to create a vortex-referenced coordinate system. Seven annuli were analyzed at four temperature thresholds (≤ 0, ≤ -25, ≤ -50, ≤ -75°C) to find the best signal for predicting different parameters of R30. Areas sampled were 0-1° latitude (0-111km) 0-2°, 0-4°, 0-6°, 1-4°, 2-4° and 2-6°.

2.2 Pixel Processing

A pixel is the smallest unit that the satellite can resolve. Counting pixels colder than a given threshold gives a number equivalent to area. A plot of these "raw" counts taken over time (multiple images) shows a distinct diurnal variation in convection (Zehr, 1987). A running mean over 24 hours would take out the diurnal variation, but the author did not want to average out any signal that might be present. It was decided to take a cumulative sum of the infrared cloud areas (counts) to see if total convection was related to R30. Thus, the first image processed would have the same magnitude for both raw and cumulative counts, but time two of the cumulative areas equals time one plus time two of the raw counts, and so on. The 24 hour slope of the cumulative count plot is equivalent to the temperature-defined area averaged over 24 hours. A greater slope means greater convection, and when the slope goes to zero, active convection colder than the selected threshold has stopped.

2.3 Aircraft Data

The aircraft data consists of all USAF reconnaissance missions for 1983-1984 in the NW Pacific Ocean basin. These missions were typically flown at 700mb and data included flight level winds and sea level pressure. Surface wind speeds were considered to be 85 percent of the flight level winds (Weatherford and Gray, 1988). A curve representing where 35 and 59 knot winds occurred was drawn for each mission. A four quadrant average of this hand-drawn radius was taken to represent the mean radius of 30 and 50 knot winds (R30 and R50). Therefore, R30 and R50 are an azimuthal average of the radial extent of winds greater than 30 and 50 knots. Twelve storms were selected for detailed analysis due to good continuity of both aircraft measurements and satellite data over their life cycles.

3. RESULTS

3.1 R30 Increase

The convection slope ≤ -25°C at 0-6° radius over the previous 24 to 48 hours relates to the rate of R30 increase. More convection (a greater slope or a larger cloud area) means a greater rate of R30 growth. There is a direct linear relationship that explains approximately 2/3rds of the variance of R30 with convection (Fig. 1). This allows an estimated rate of R30 increase which can be used to forecast R30 at a future time.

3.2 Maximum R30

The change of the slope of the same deep convection (≤ -75°C) at radius 2-4° gives a signal as to when the maximum R30 will occur. There are two types of storms that need to be defined for the results to be meaningful. Typical storms are those where R30 continues to

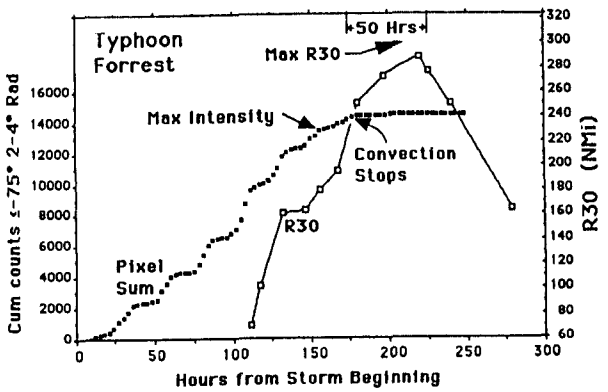

Fig. 1. Maximum R30 for a typical storm. Note that the end of convection gives a 48-hour signal for maximum R30. Maximum intensity occurred almost two days before maximum R30.

increase after intensity has reached maximum. Simultaneous storms (1/3rd of the sample) are those where R30 and maximum intensity occur at approximately the same time. For typical storms, when the slope of cumulative convection ≤ -75°C in the annulus 2-4° shows a leveling off (convection ending), this is the signal that the maximum R30 will occur approximately 48 hours later (Fig. 2). For simultaneous storms, the point of maximum R30 and maximum intensity is reached within 12 hours (±) of when the deep convection ends (Fig. 3). The forecaster has a 48 hour lead time for determining maximum R30 occurrence in typical storms, and a nowcast tool verifying that maximum R30 has been reached for simultaneous storms.

3.3 R30 Decrease

Specification of R30 decrease (after maximum R30) probably can't be achieved with infrared satellite data because the deep convection is typically absent with these filling storms. A statistical rate of R30 decrease based on the entire 83-84 storm data set measured by aircraft gives an average rate of -26 n mi/day for the R30 decrease. The standard deviation is 8 n mi/day.

3.4 Initial R30

Direct measurements of outer wind distribution are generally not available. A 45 knot maximum wind intensifying tropical storm (T3 on the Dvorak scale or 991mb MSLP in the NW Pacific) should have an R30 established. This is taken to be the initial time of the storm for purposes of obtaining R30. The slope of the convection ≤ -25°C at 0-2° radius explains approximately 50% of the variance of R30 for this 45 knot storm. More convection in the past means a larger radius of 30 knot winds. One can adjust initial R30 up or down based on the previous convection rates.

3.5 R50 Determination

The best way to determine R50 was to use the statistical relationship that R50 = [(.5 * R30) - 11] (n mi). This explained 2/3rds of the variance of R50, and allows one to specify R50 after determining R30.

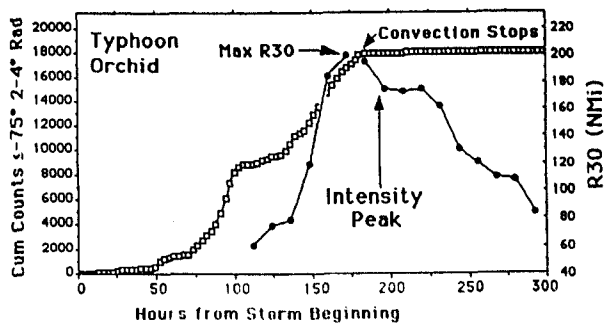

Fig. 2. Maximum R30 for a simultaneous storm. Maximum R30 and maximum intensity occur within 12 hours of the end of the deep convection, although not necessarily simultaneously.

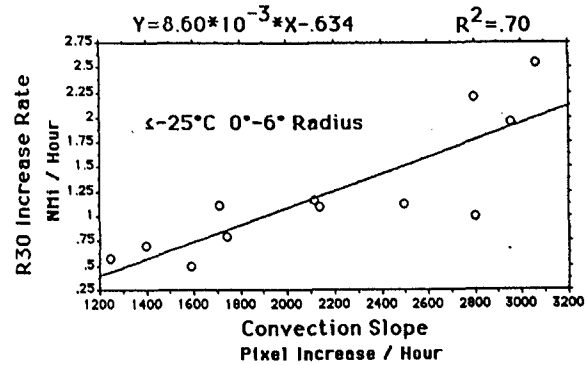

Fig. 3. Comparison of cumulative convection counts to R30 increase slope. More convection equates to a greater rate of R30 increase with 70 percent of the variance explained.

4. CONCLUSION

Combining these four techniques allows forecasters to estimate:

1. The initial R30 for a 45 knot tropical storm.
2. The rate of R30 (R50) growth.
3. The time of maximum R30 (R50).
4. The rate of R30 (R50) decrease after maximum R30.

These aids are being developed for use on NW Pacific tropical cyclones at the Joint Typhoon Warning Center (JTWC) on Guam. The methodology can probably be used in all ocean basins with some adjustments for different climatological storm structure characteristics. It is hoped that this and other similar studies will help fill the knowledge gap caused by lack of observed data on tropical cyclone wind profiles.

5. REFERENCES

Weatherford, C., and W. M. Gray, 1988: Typhoon structure as revealed by aircraft reconnaissance: Part II: Structural variability. Mon. Wea. Rev., Vol. 116, 5, 1044-1056.

Zehr, R. M., 1987: The diurnal variation of deep convective clouds and cirrus with tropical cyclones. Preprints, 17th Conf. on Hurricanes and Tropical Meteorology, AMS, April 7-10, Miami, FL.

J11.4

A USE OF WATER VAPOR IMAGERY IN FORECASTING HURRICANE MOTION

James B Lushine

Weather Service Forecast Office
Miami, Florida

1. INTRODUCTION

Forecasting the motion of tropical cyclones is a difficult task however much progress has been made in hurricane numerical modelling especially in the 1980s. At the same time more sophisticated geostationary satellite imagery has become available which senses the atmosphere in 12 channels of the infra-red spectra, Smith (1983). One of the most promising of these spectra available to the operational forecaster is the 6.7 micron water vapor imagery which can be received and animated hourly. The 6.7 micron imagery has its maximum sensitivity near 400 mb but is responsive to radiation from about 700 to 100 mb. Since the motion of hurricanes is best related to deep layer (1000-100 mb) steering with the single most highly correlated level near 400 mb, Dong (1986), it would seem plausible that the 6.7 micron water vapor imagery could be useful in hurricane motion forecasting. The 6.7 micron water vapor imagery although displaying a pleasing continuous grey shade pattern is often quite ambiguous as to the height and vertical extent of the moisture. This ambiguity is least when dryness through a deep layer of the troposphere is depicted as a dark grey shaded area, Weldon (1983). If these dark areas can be related to anticyclones or ridges in the middle to upper levels of the troposphere useful information about the steering of hurricanes may be inferred. Of course many of the dark areas in water vapor imagery are not associated with a deep layer anticyclone or ridge. Among other things dark areas may be related to mid and upper level cold air advection, Weldon (1983), jet streaks, deformation zones, vorticity maxima and cyclones, Anderson(1982). Therefore care and cunning must be employed in identifying the dark areas and their movements in the water vapor imagery that are associated with the deep layer anticyclone or ridge. Complicating this identification process is the fact that thin layers of moisture associated with features such as short wave troughs, vorticity maxima and jet streaks may mask at least temporarily the deep layer dry areas associated with ridges and anticyclones. An example of this will be given in the case of Hurricane Helene. Once the dark areas on the water vapor imagery that are associated with the deep layer ridges and anticyclones are identified their relationship to hurricane motion can be examined.

2. DATA

The tracks of Hurricanes Florence, Gilbert and Helene all of which occurred in September of 1988 were monitored in near real time by use of conventional and reconnaissance data along with half hourly visible and infra-red satellite imagery. In addition near real time hourly 6.7 micron water vapor imagery was available in animation and hard copy. The National Hurricane Center (NHC) mean upper level (600-200 mb) chart, Simpson (1971), available daily about 3 hours after 0000 and 1200 UTC corresponds the closest to the layer observed by the 6.7 micron water vapor imagery and was useful in interpreting features seen in the satellite imagery.

3. INDIVIDUAL CASES

Hurricane Florence formed in the central Gulf of Mexico on September 7 at the tail end of a frontolysis zone. After slowly acquiring tropical characteristics Florence drifted east then north for 24 to 36 hours at 5 knots or less. During this time the official forecast track was for a continued northward drift of around 5 knots with landfall expected along the northeast Gulf coast in 72 hours. On the morning of September 9, Florence accelerated northward reaching a maximum forward speed of 15 knots at midday and reached the Louisiana coast early on the morning of September 10, 48 hours earlier than originally forecast. Observing the animated water vapor imagery during this time a band of dark grey indicating dryness through a deep layer of the

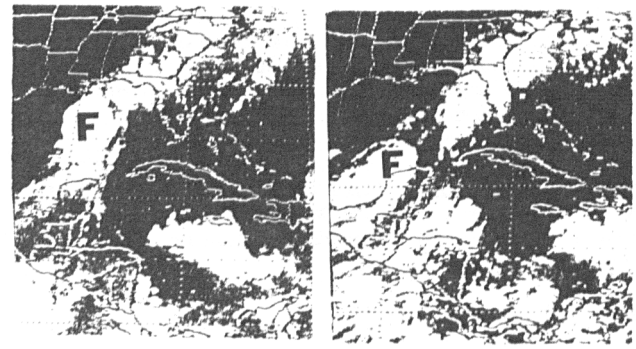

Fig. 1. 6.7 micron water vapor imagery at 1900 UTC Sep 8 1988 (Right) and 1200 UTC Sep 9 1988 (Left) showing approach of dark band (A-B) toward Hurricane Florence (F) in the Gulf of Mexico.

upper and middle troposphere was seen advancing westward from the Bahamas across Florida and into the eastern Gulf of Mexico along the same latitude as Florence (See Figure 1). When the leading edge of this dark area moved to within 5 degrees of Florence the hurricane began its acceleration to the north. It is hypothesized that the dark area was associated with a ridge of high pressure in the mid and upper troposphere which built westward and caused the northward acceleration of Florence. The building of the ridge as suggested by the water vapor imagery is supported by examining the mean upper level (600-200 mb) chart which showed height rises moving westward across the western Bahamas and Florida on September 9.

Powerful Hurricane Gilbert formed in the eastern Caribbean Sea on September 8 and moved on a steady west northwest course at near 15 knots until making final landfall on the northeast coast of Mexico on September 17. The official forecasts of motion were very good until the hurricane reached the west central Gulf of Mexico at which time a turn to the northwest or north was considered a distinct possibility. The water vapor imagery during its entire lifetime showed a large dark area to the north of Gilbert (See Figure 2) which by examining the upper level mean chart was found to be associated with a ridge of high pressure. This dark area propagated west northwestward in tandem with Gilbert and the possible northward motion of Gilbert never materialized until well after landfall.

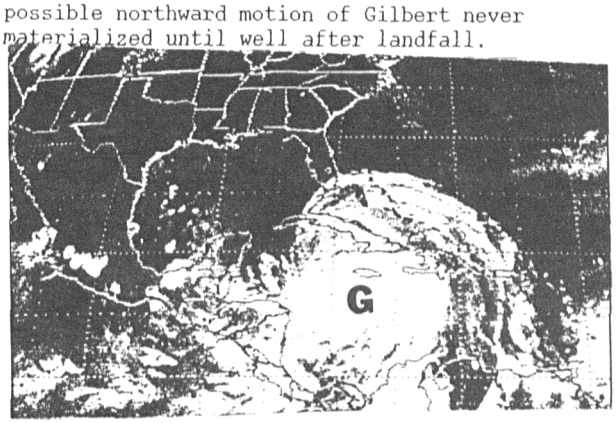

Fig. 2. 6.7 micron water vapor imagery at 0600 UTC Sep 13 1988 showing mid-upper level ridge (A-B-C) north of Hurricane Gilbert (G).

Hurricane Helene, the second of three major hurricanes of the 1988 season, formed in the eastern Atlantic on September 20 and after moving west for three days turned to the northwest then made a gradual recurvature to the north then northeast on September 24-30. Some numerical guidance forecasted the northwestward turn 24 hours before it began but because of the uncertainty in the models the official forecast called for a westerly track. Water vapor imagery in this case revealed a nearly circular dark area most likely related to a mid to upper level anticyclone located initially to the north of the hurricane. The western boundary of this dark area was observed to remain stationary in satellite animation as Hurricane Helene traveled westward along the southern periphery of the anticyclone. When Helene reached the western boundary of this dark area (See Figure 3) the hurricane turned to the northwest just as some of the numerical models had forecasted.

As was mentioned above, locating the dark areas associated with mid to upper level anticyclones can be complicated by thin layers of moisture moving through them. A portion of the deep layer anticyclone around which Hurricane Helene was being steered was partially obscured by a thin moist layer moving ahead of a mid to upper level shortwave trough in the westerlies. During this time it was difficult to determine whether the anticyclone was moving or not. Eventually the strong subsidence associated with the anticyclone overcame the moisture associated with the upper level trough and the boundary of the dark area reappeared.

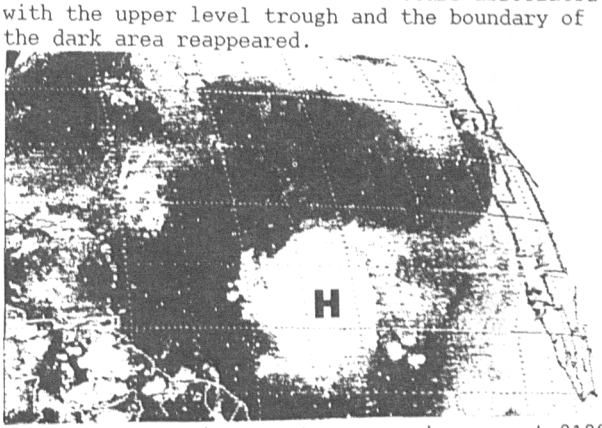

Fig. 3. 6.7 micron water vapor imagery at 0100 UTC Sep 23 1988 showing mid-upper level anticyclone (A-B-C-D-E) north of Hurricane Helene (H).

4. DISCUSSION AND CONCLUSIONS

In each of the three cases noted above, features were seen in the 6.7 micron water vapor imagery which helped explain the motion of the hurricane. This knowledge could have been used to operationally better assess the numerical model guidance and give the forecaster more confidence in predicting the track of the hurricane. During other periods of tropical cyclone activity in 1988 it was also noted that the steering of tropical cyclones of less than hurricane strength did not follow the guidelines mentioned above. This is not surprising in that the single level best correlated to tropical storm motion is near 700 mb, Dong (1986).

REFERENCES

Anderson, R.K., J. Gurka and S. Steinmetz, 1982: Application of VAS Multispectral Imagery to Aviation Forecasting. Preprints, AMS 9th Conference on Weather Forecasting and Analysis, June 1982, Seattle, Wash.

Dong, K. and C.J. Neumann, 1986: The Relationship Between Tropical Cyclone Motion and Environmental Geostrophic Flows. Mon. Wea. Rev., 114, 115-122.

Simpson, R.H., 1971: The Decision Process In Hurricane Forecasting, NOAA Tech Memo., NWS SR-53, National Weather Service, 35pp.

Smith, W.L., 1983: The Retrieval Of Atmospheric Profiles From VAS Geostationary Radiance Observations. J. Atmo. Sci.,40, 2025-2035.

Weldon, R. and S. Steinmetz, 1983: Characteristics Of Water Vapor Imagery. Training Notes. Satellite Applications Lab., NOAA/NESDIS.

J11.5

PRECIPITABLE WATER AND LIQUID WATER IN TROPICAL CYCLONES AS ESTIMATED FROM SSM/I

Huo-Jin (Alex) Huang
Atmospheric Sciences Program
University of North Carolina
at Asheville, Asheville, NC 28804

Franklin R. Robertson
Earth Sciences and Applications Division
NASA/Marshall Space Flight Center
Huntsville, AL 35812

1. INTRODUCTION

Remote sensing measurements from satellites have facilitated studies of tropical cyclones for almost three decades. Surface wind speeds (Fett, 1966; Gentry *et al.*, 1980) and cyclone intensity (Dvorak, 1975) have been inferred using visible and infrared data. Passive microwave measurements have provided a measure of internal storm structure relating to water vapor and liquid water content and the associated latent heat release (Allison *et al.*, 1974; Adler and Rogers, 1978; Rosenkranz *et al.*, 1978). The passive microwave measurements available from SSM/I (Special Sensor Microwave Imager) since July 1987 offer a data set of uprecedented quality and temporal coverage for studying tropical systems. The present study uses SSM/I data to investigate the distribution of precipitable water and liquid water in and near several tropical cyclones in the western Pacific during September 1987. We will examine how precipitable water in the storm environment and the production of total liquid water are related to the evolution and intensity of these tropical cyclones.

2. DATA AND ALGORITHMS

Passive microwave data used in this study were obtained from Remote Sensing Systems, Inc., courtesy of Dr. Frank Wentz. The retrievals are column-integrated water vapor, or precipitable water, and column-integrated total liquid water. The retrieval algorithm is based on a radiative transfer model for brightness temperature that accounts for scattering and emission by the sea surface and radiative absorption and emission by an intervening cloudy atmosphere (Wentz, 1983). Because of its low emissivity, the ocean appears as a radiometrically cold background at frequencies flown on the SSM/I. Radiation emitted by liquid water and water vapor contribute to the upwelling radiance and result in elevated brightness temperatures as detected by the sensor. The separate contributions by water vapor and liquid water are distinguished by the brightness temperature model. The SSM/I data were navigated and composited in digital image form on the MSFC McIDAS (Man computer Interactive Data Access System). The tracks and intensities of western Pacific tropical storms were obtained from the 1987 annual Tropical Cyclone Report (1987) published by the Joint Typhoon Warning Center in Guam. Additional analyses of precipitable water calculated using the ECMWF global analyses obtained from NCAR.

3. DISCUSSION

The tracks of two of the systems being studied are shown in Fig. 1. Typhoon Freda (September 4-17, 1987) and Super Typhoon Holly (September 5-15, 1987) both developed while following a similar type track, moving west/northwest before recurving northward to about 35° N and then transforming into subtropical cyclones. Freda appeared first as a persistent cluster of convection in the Eastern Caroline Islands on September 1. It gradually drifted northwestward and intensified to tropical storm strength at 0600 UTC September 5. Freda reached maximum strength, 125 k on September 10 and weakened therafter as it continued northward. On September

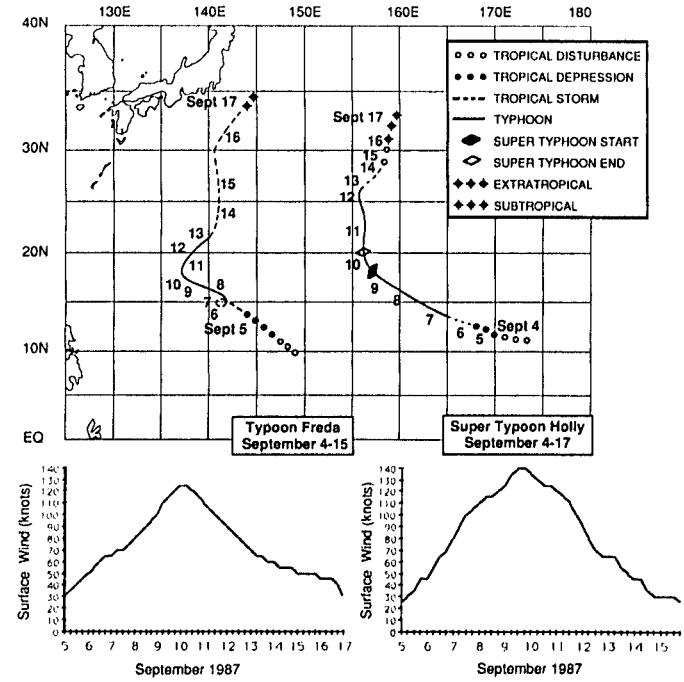

Figure 1. Positions and intensities of western Pacific storms Freda and Holly during September 1987.

16, the storm began to interact with an eastward moving mid-level trough, resulting in a more northeastward track. Holly was spawned in the active monsoonal trough in the central Pacific and reached typhoon strength while moving northwestward on September 7. On September 9, Holly reached an intensity of 140 k at 1200 UTC and its track shifted toward the north. It slowly drifted northward and weakened, acquiring subtropical characteristics after September 14.

Fig. 2 shows precipitable water derived from ECMWF analyses on 10 September while both storms were close to peak intensity. The tropical cyclones are located in environments with greater than 5 g cm^{-2} precipitable water. However, drier air lies immediately to the north of both storms. Fig. 3 shows precipitable water along an SSM/I swath covering Freda near 2300 UTC 10 September. The Dark gray areas indicate generally high water vapor contents (over 5 g cm^{-2} in the storm environment. The tongue of dry air northeast of Freda and the moist air (> 5 g cm^{-2}) near southern Japan agree well with the ECMWF analysis. Apparent also in Fig. 3 is a dry spiral banded feature lying south and east of Freda at a radius of about 3°. Furthermore near the core of the storm (black circular region) and at two locations in the spiral band, precipitable water is not retrieved. These are regions where the precipitable water algorithm fails because of extremely high liquid water concentrations. A comparison of Fig. 3 to total liquid water in Fig. 4 shows this correspondence readily. Total liquid water contents in the spiral band begining south-

west of the storm are generally 50 to 200 mg cm^{-2}. Within the core of the storm these values exceed several hundred mg cm^{-2} but may not be reliable (Wentz, 1983). In reality it is likely that within a radius of 5.0° of Freda, the regions shown drier than 5 g cm^{-2} are at least this moist. Further analysis of SSM/I precipitable water and total liquid water distributions, and their relationship to storm intensity will be presented at the conference.

4. ACKNOWLEDGEMENTS

The authors express their thanks to Dr. Frank Wentz, Remote Sensing Systems, Inc., for supplying the Ocean Products Tapes, and to Dr. Roy Spencer for the use of image processing software. This research is supported by the NASA Global Scale Processes Research Program, Dr. Ramesh Kakar, Program Manager.

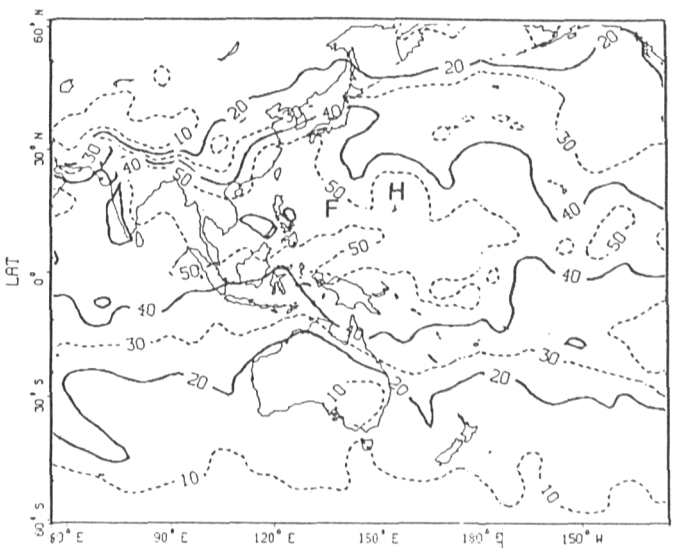

Figure 2. Mean precipitable water (mm) from 00 and 12 UTC September 10, 1987 ECMWF analysis.

5. REFERENCES

Adler, R. T., and E. B. Rogers, 1977: Satellite-observed latent heat release in a tropical cyclone. *Mon. Wea. Rev.*, 105, 956-963.

Allison, L. J., E. B. Rogers, T. T. Wilheit and R. W. Fett, 1974: Tropical cyclone rainfall as measured by the Nimbus 5 electrically scanning radiometer. *Bull. Amer. Meteor. Soc.*, 55, 1074-1089.

Dvorak, V. F., 1975: Tropical cyclone intensity analysis and forecasting from satellite imagery. *Mon. Wea. Rev.*, 103, 420-430.

Fett, R. W., 1966: Upper-level structure of the formative tropical cyclone. *Mon. Wea. Rev.*, 94, 9-18.

Gentry, R. C., E. Rogers, J. Steranka and W. S. Shenk, 1980: Predicting tropical cyclone intensity by using satellite-measured equivalent blackbody temperatures of cloud tops.

Rosenkranz, P. W., and D. H. Staelin, 1978: Typhoon June (1975) viewed by a scanning microwave spectrometer. *J. Geophys. Res.*, 83, 1858-1868.

Wentz, F. J., 1983: A model function for ocean microwave brightness temperatures. *J. Geophys. Res.*, 88, 1892-1908.

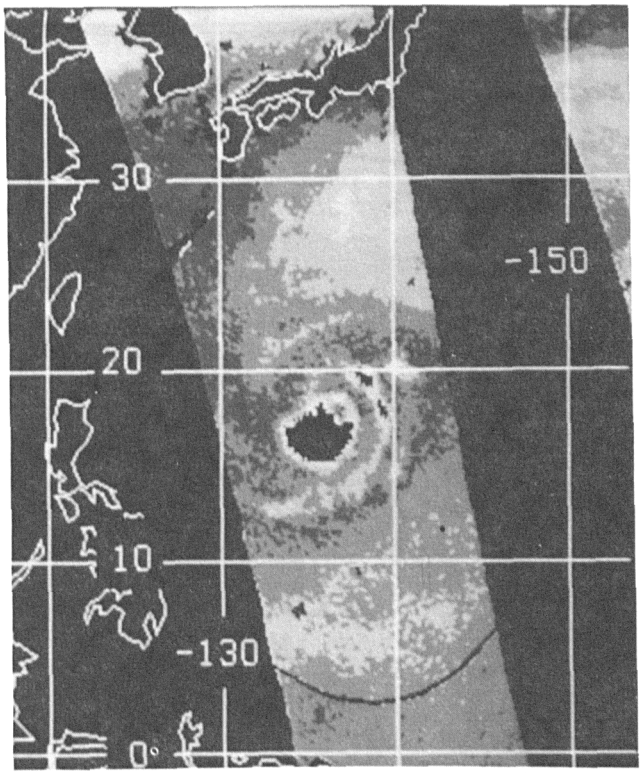

Figure 3. SSM/I precipitable water 0600 Local 10 September. Four gray shades (light --> dark) correspond to amounts greater than 2.0, 3.0, 4.0, 5.0 cm of total water vapor. Black regions in data swath (land and storm core) have no retrieved values.

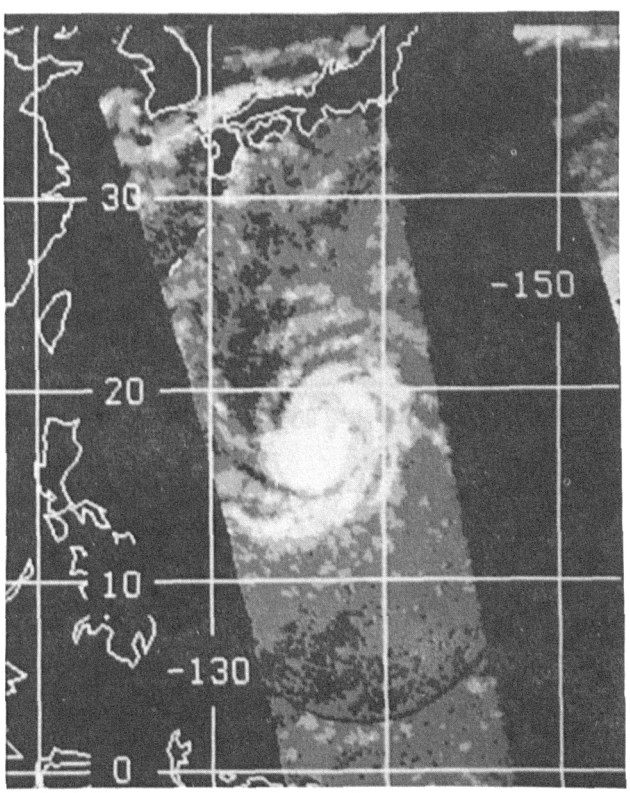

Figure 4. SSM/I Total liquid water (cloud + rain). Gray shades (dark gray --> white) correspond to amounts greater than 16, 64, 128 and 256 mg cm^{-2}.

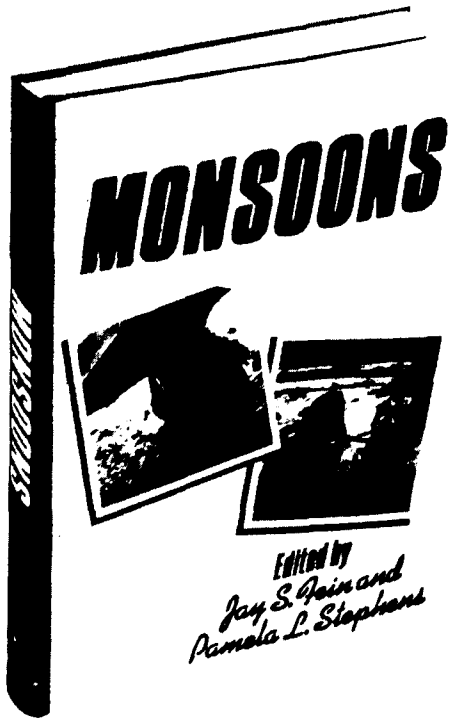

MONSOONS

Edited by

Jay S. Fein and Pamela L. Stephens

Monsoons is the first work that attempts to unravel the entire mystery. What is a monsoon? And how far have we come in our ability to tell when it will arrive and how abundant the rainfall will be? *Monsoons* goes beyond being a technical analysis to present a broad, fascinating review that explains, in terms anyone can understand, the meteorology of monsoons, their economic impact and their history and folklore.

This comprehensive volume covers the monsoon from many perspectives, including: the influence of the monsoon on traditional culture; an economic analysis of the value of weather and climate data in developing countries; the evolution of the concept of the monsoon as a weather and climate systems from the early mariners to today's scientists; a most thorough treatment of monsoon variability on paleoclimate time scales; an in-depth look at topographical influences on monsoons; ocean-monsoon interactions, and interactions of monsoons with other global weather and climate events; the latest information on the tools being used to predict the variability of monsoons.

Plus, it examines an intriguing hypothesis, which states that it is inherently easier to predict the average behavior of the monsoon on monthly and seasonal time scales than to forecast monsoon weather patterns a few days in advance—a topic of great concern to atmospheric scientists and policymakers in developing countries.

Illustrated with ocean circulation charts, data tables on long-term statistics of monsoon precipitation and its variability, and extensive bibliographies, *Monsoons* is the first work to take a broad, multidisciplinary look at this dramatic product of nature. An ideal sourcebook for meteorologists and climatologists, oceanographers, environmental scientists, folklorists, and policymakers in monsoon regions—for anyone interested in a phenomenon that so greatly affects so much of mankind.

To order please send $74.95 plus $3.00 postage and handling
to

AMERICAN METEOROLOGICAL SOCIETY
45 BEACON STREET
BOSTON, MA 02108

MESOSCALE METEOROLOGY AND FORECASTING

Edited by PETER S. RAY

This volume provides a comprehensive survey of the important topics in mesoscale meteorology. It is designed to supplement a practicing meteorologist's experience with new material and ideas on mesoscale processes, and to acquaint the student meteorologist with the broad range of topics embraced by the classification "mesoscale" meteorology.

Illustrations, complete bibliographic references, and a comprehensive index are included. The text comprises contributions from 44 distinguished scientists in mesoscale meteorology. The 31 chapters are organized within these general headings:

INTRODUCTION

Kerry A. Emanuel
Glen Rasch
Daniel Smith
T.T. Fujita
Joseph T. Schaefer
Fred L. Zuckerberg

OBSERVING TECHNIQUES

Donald Burgess
Joseph H. Golden
Ronald D. McPherson
Peter S. Ray
Robert Serafin
Joseph Facundo
Vincent Lally
James F.W. Purdom
Roderick A. Scofield
Dennis W. Thomson

INTERNALLY GENERATED CIRCULATIONS

Robert W. Burpee
William H. Hooke
Douglas Lilly
Howard B. Bluestein
Charles F. Chappell
Daniel Keyser

MESOSCALE CONVECTIVE SYSTEMS

Diana L. Bartels
Kenneth W. Howard
Robert Maddox
Richard Rotunno
Carl Hane
Joseph B. Klemp
Dennis M. Rodgers
Morris L. Weisman

EXTERNALLY FORCED CIRCULATIONS

Joe F. Boatman
Roger A. Pielke
Roger F. Reinking
Moti Segal
Dale R. Durran
Raymond T. Pierrehumbert
Joseph T. Schaefer

MESOSCALE MODELING

Richard A. Anthes
John B. Hovermale
William R. Cotton
Donald J. Perkey

SHORT-RANGE FORECASTING TECHNIQUES

Charles A. Doswell
Bruce B. Ross
John McGinley
Thomas W. Schlatter

As a textbook of mesoscale meteorology, the volume will provide to the operational and practicing meteorologist, as well as student meteorologists, the principal new observations and theories in this interdisciplinary topic.

List price $50*
AMS Member/NOAA Employee $40*

*(Plus $5.25 shipping and handling)

Send order and remittance to:
AMERICAN METEOROLOGICAL SOCIETY
45 Beacon Street
Boston, MA 02108

RADAR IN METEOROLOGY

Edited by David Atlas

Dedicated to the memory of Prof. Louis J. Battan, this volume had its origin in the 40th Anniversary Radar Meteorology Conference (Boston, November 1987) which commemorates the anniversary of the first radar conference (MIT, March 1947).

The book is organized in three segments: history, critical reviews of progress and status, and panel reports. The histories cover the people, events and institutions which played pivotal roles in about the first two decades. The critical reviews cover technological, scientific and operational topics, authored by experts in each of the subject areas. The panel reports following each review represent the consensus of a group of specialists and provide a broader perspective of the review's topic as well as a look into future development. With more than 200 contributors, the volume is a product of the entire community and represents an unprecedented compendium of knowledge in this field.

This is much more than a narrow treatise on radar meteorology. Although the technological chapters deal explicitly with various aspects of the instruments, the remaining chapters discuss a broad spectrum of scientific and operational problems in meteorology. The papers cover scientific subjects ranging from cloud microphysics and dynamics to global climate, and operational topics such as nowcasting, severe storm detection and warning, and hazards to aviation such as low-level wind shear.

The book is especially timely since the field is about to explode with the forthcoming widespread installation of the most modern Doppler radars throughout the United Sates. These include the Next Generation Weather Radars (NEXRAD), VHF and UHF wind profiling radars, and Terminal Doppler Weather Radars (TDWR) for wind shear detection. Corresponding developments are taking place in Europe and Asia. When viewed in the context of the striking advances in parallel fields of space observation,, computer technology, information handling and display, communications, and numerical modeling of meteorological and oceanic phenomena, the outlook for the future is breathtaking. The rich variety of planned and ongoing experiments on storm and mesoscale problems and climate provide the stage on which much of the future research and operational activity will be played out.

This landmark treatise brings alive the remarkable achievements of the past four and one-half decades and provides a visionary path toward the exciting advances yet to come. In addition to its value for radar meteorologists, substantial portions of the volume will be of special value to students, scientists, technologists, and operational staffs in forecasting and aviation meteorology. It will also serve as a guidebook to decision-makers who must set the priorities for the future.

AMS publication date: Summer 1989

For futher information, please contact:
American Meteorological Society
45 Beacon Street
Boston, Ma. 02108
617-227-2425

TROPICAL CYCLONES
Their Evolution, Structure and Effects
by Richard A. Anthes

Tropical cyclones and hurricanes, long feared for the death and destruction that often accompanies them, are among the most fascinating of atmospheric phenomena. Created by thermodynamic processes, they unleash vast amounts of energy and influence a wide variety of natural processes along their paths.

In *Tropical Cyclones—Their Evolution, Structure and Effects*, the author, Richard A. Anthes, tells the story of their creation and destruction, of meteorology's successes in understanding, modeling and predicting their behavior, and of the attempts to modify them.

Chapter Topics Include:

- *Structure and Life Cycle of Tropical Cyclones*
- *Physical Processes in Tropical Cyclones*
- *Simulation of Tropical Cyclones by Numerical Models*
- *Hurricane Modification*
- *Oceanic Response to Tropical Cyclones*
- *Tropical Cyclone Forecasting*

208 Pages
11 Pages of References
17 Photos, 99 Figures
Hardcover

A unique feature of this book, which may be used in the home, laboratory, or classroom, is a thorough treatment of the interactions between storm and ocean, with both observations and theory being integrated to provide a complete description.

$30 AMS Members
$40 Nonmembers

(add $3.00 postage/handling)

Send orders and remittance to:

AMERICAN METEOROLOGICAL SOCIETY
45 Beacon St.
Boston, Mass. 02108

Meteorological Monographs, Vol. 19, No. 41
American Meteorological Society

ISBN: 0-933876-54-8
ISSN: 0065-9401